

SPACE SCIENCE ACTIVITIES IN CHINA

NATIONAL REPORT 2014-2016



**CN-COSPAR
JULY 2016 BEIJING**

Members of the Chinese National Committee for COSPAR (CNCOSPAR)

President

XIANGLI Bin, Vice President, Chinese Academy of Sciences (CAS)

Vice Presidents

HUANG Weidong, Researcher

LI Ming, Researcher, China Academy of Space Technology (CAST)

HAO Zhaoping, Researcher, China Academy of Launch Vehicle Technology (CALT)

JING Guifei, Researcher, National Remote Sensing Center, Ministry of Science and Technology (MOST)

Membership

JIANG Jingshan, Academician, National Space Science Center, CAS

AI Guoxiang, Academician, National Astronomical Observatories, CAS

HU Wenrui, Academician, Institute of Mechanics, CAS

WANG Shui, Academician, University of Science and Technology of China (USTC)

OUYANG Ziyuan, Academician, National Astronomical Observatories, CAS

GONG Huixing, Academician, Shanghai Institute of Technical Physics, CAS

TU Chuanyi, Academician, Department of Geophysics, Peking University

LÜ Daren, Academician, Institute of Atmospheric Physics, CAS

LI Tabei, Academician, Institute of High Energy Physics, CAS

GU Yidong, Academician, Technology and Engineering Center for Space Utilization, CAS

WU Yirong, Academician, Institute of Electronics, CAS

GUO Huadong, Academician, Institute of Remote Sensing and Digital Earth, CAS

WANG Weihua, Academician, Institute of Physics, CAS

ZHOU Zhixin, Academician, Beijing Institute of Remote Sensing Information

XU Ronglan, Researcher, National Astronomical Observatories, CAS

XIAO Zuo, Professor, Department of Geophysics, Peking University

CAI Zhenbo, Researcher, China Academy of Space Technology (CAST)

LI Yinghui, Researcher, Beijing Institute of Space Medico-Engineering

WANG Jianyu, Researcher, Chinese Academy of Sciences Shanghai Branch

GAN Weiqun, Researcher, Purple Mountain Observatory, CAS

YAN Yihua, Researcher, National Astronomical Observatories, CAS

YU Qi, Deputy Director General, Department of System Engineering, China National Space Administration

ZHANG Xingwang, Researcher, Institute of Semiconductors, CAS

DOU Xiankang, Professor, University of Science and Technology of China (USTC)

WANG Chi, Researcher, National Space Science Center, CAS

WANG Jingsong, Researcher, China Meteorological Administration

CAO Jinbin, Professor, Beijing University of Aeronautics and Astronautics

FANG Guangyou, Researcher, Institute of Electronics, CAS
WANG Shijie, Researcher, Institute of Geochemistry, CAS
FENG Xueshang, Researcher, National Space Science Center, CAS
DONG Xiaolong, Researcher, National Space Science Center, CAS
LU Feng, Researcher, Institute of Geographical Sciences and Natural Resources Research, CAS
JIANG Luhua, Researcher, Institute of High Energy Physics, CAS
GAO Ming, Researcher, Academy of Opto-Electronics, CAS
LONG Mian, Researcher, Institute of Mechanics, CAS
CHEN Hongbin, Researcher, Institute of Atmospheric Physics, CAS
LU Jinying, Senior Engineer, China Academy of Space Technology (CAST)
SUN Yeqing, Professor, Institute of Environmental System Biology, Dalian Maritime University
CHAI Chunlin, Researcher, Institute of Semiconductors, CAS
CHANG Jin, Researcher, Purple Mountain Observatory, CAS
PAN Mingxiang, Researcher, Institute of Physics, CAS
WEI Jianyan, Researcher, National Astronomical Observatories, CAS
ZHANG Tao, Researcher, Shanghai Institute of Technical Physics, CAS
DING Mingde, Professor, Department of Astronomy, Nanjing University
LI Chunlai, Researcher, National Astronomical Observatories, CAS
HUANG Maohai, Researcher, National Astronomical Observatories, CAS
XUE Hongwei, Shanghai Institute for Biological Sciences, CAS
LIU Lin, Professor, Department of Astronomy, Nanjing University
XU Minqiang, Professor, Harbin Institute of Technology
DENG Yulin, Professor, Beijing Institute of Technology
LIU Siqing, Researcher, National Space Science Center, CAS
SUN Yueqiang, Researcher, National Space Science Center, CAS

Secretary General

WU Ji, Researcher, National Space Science Center, CAS

Deputy Secretary General

LI Lei, Researcher, National Space Science Center, CAS
WANG Zhenyu, Division Director, Bureau of International Cooperation, CAS
YAN Jingye, Researcher, National Space Science Center, CAS

Secretariat Contact

LI Xiaoyu, XU Yongjian
CN-COSPAR Secretariat
c/o NSSC, No.1 Nanertiao, Zhongguancun, 100190, Beijing, China
Tel: 86 10 6258 6404
Fax: 86 10 6263 2257
E-mail: xuyongjian@nssc.ac.cn

SPACE SCIENCE ACTIVITIES IN CHINA

CONTENTS

Space Research Plan of China's Space Station	GU Yidong, GAO Ming, ZHAO Guangheng	(1)
Progress of Strategic Priority Program on Space Science	WU Ji, FAN Quanlin, CAO Song	(5)
Vision and Voyages for Deep Space Exploration	ZOU Yongliao, WANG Qin	(11)
New Progress in China's Lunar Exploration Program	ZOU Yongliao, XU Lin, WANG Qin	(14)
Main Science Results from Chinese Meridian Project (2014–2015)	WANG Chi on behalf of the Meridian Project team	(22)
The Space Sciences and Application Projects in Space Laboratory	Gu Yidong, Gao Ming, Zhao Guangheng	(27)
Status of the Hard X-ray Modulation Telescope (HXMT) Project	LU Fangjun	(33)
Progress of Microgravity Experimental Satellite SJ-10	HU Wenrui, TANG Bochang, KANG Qi	(36)
Space-based multi-band astronomical Variable Objects Monitor	WEI Jianyan	(48)
Developing the TanSat Mission: A Progress Report		
.....LIU Yi, YIN Zengshan, ZHENG Yuquan, YAN Changxiang, YANG Zhongdong, TIAN Xiangjun, LÜ Daren		(50)
Space Solar Physics in China: 2014–2016	GAN Weiqun	(58)
A Brief Review of Interplanetary Investigations in China from 2014 to 2016		
.....ZHAO Xinhua, ZHANG Min, WANG Yuming, HE Jiansen, KONG Xiangliang		(61)
Magnetospheric Physics in China: 2014–2015	CAO Jinbin, YANG Junying	(88)
New Understanding Achieved from 2 Years of Chinese Ionospheric Investigations	LIU Libo, WAN Weixing	(144)
Advances in the Researches of the Middle and Upper Atmosphere in China in 2014–2016		
.....CHEN Zeyu, XU Jiyao, HU Xiong, CHEN Hongbin, CHEN Wen, WEI Ke, BIAN Jianchun, TIAN Wenshou, ZHANG Shaodong, REN Rongcai, DOU Xiankang		(165)
Development of Operational Space Environment Technology System		
.....GONG Jiancun, CAI Yanxia, LIU Siqing, SHI Liqin, LU Guorui, CHEN Zhaofeng, BAO Lili		(177)
Observations from FENGYUN Satellites	Tang Yunqiu, Li Yingying, Zhang Jiashen, Wang Jingsong	(185)
Progress of 2014–2016 China's Earth Observation and Earth Science	GUO Huadong, XIAO Han, MA Jianwen	(192)
National Report on Space Medicine Progress in 2014–2016		
LI Yinghui, ZHANG Xiaoyou, WAN Yumin, DING Bai, LIU Zhaoxia, LING Shukuan, BAI Yanqiang, CHEN Shanguang		(201)
Space Life Science of China in 2015	MA Hong, LÜ Xuefei, DAI Rongji, LI Yujuan, ZHANG Yongqian, LI Xiaoqiong, WANG Rui, QING Hong, LI Qiang, SUI Li, ZHUANG Fengyuan, DENG Yulin	(207)
Microgravity Material Research in China: 2016	XIE Wenjun, LUO Xinghong, ZHANG Xingwang, YU Yude	(222)

Space Research Plan of China's Space Station

GU Yidong, GAO Ming, ZHAO Guangheng

Technology and Engineering Center for Space Utilization, Chinese Academy of Sciences, Beijing 100094

* E-mail: zhangwei@csu.ac.cn

Key words

China's space station
Space science
Research planning
Research facilities
Research racks
Onboard and ground support

Abstract

China's manned spaceflight missions have been introduced briefly, and the research planning of space sciences for China's Space Station (CSS) has been presented with the topics in the research areas, including: life science and biotechnology, microgravity fluid physics and combustion science, space material science, fundamental physics, space astronomy and astrophysics, earth sciences and application, space physics and space environment, experiments of new space technology. The research facilities, experiment racks, and supporting system planned in CSS have been described, including: multifunctional optical facility, research facility of quantum and optic transmission, and a dozen of research racks for space sciences in pressurized module, etc. In the next decade, significant breakthroughs in space science and utilization will hopefully be achieved, and great contributions will be made to satisfy the need of the social development and people's daily life.

1 Brief Introduction to China's Manned Spaceflight Missions

China Manned Space Program (CMSP) was started in 1992. According to its roadmap, a space laboratory named Tiangong-2 will be launched in September, 2016, and then docked with Shenzhou-11 manned spaceship and Tianzhou-1 cargo ship in 2017. A permanent space station, China's Space Station (CSS), will be started to build in 2018, and completed in 2022 or later. Tiangong-2 is the first space laboratory of CMSP that weighs about 8 tons with 2 to 4 years of lifetime. The Tianzhou-1 weighs 13 tons with cargo transportation capacity of 6 tons. According to the preliminary design, the main part of CSS is a combination of 3 modules including a core module and two experiment-carrying modules and will be assembled in orbit. In addition, there is an independent flight module for optical astronomy in the same orbit near enough to the space station to dock for upgrades and ser-

ving. The total weight of CSS is more than 66 tons. The orbit parameters of CSS are the same as Tiangong-2, attitude accuracy of 0.1° and attitude stabilization of $10^{-3} (^\circ) \cdot s^{-1}$, predicted microgravity level of 10^{-3} , payload weight of 15 tons with 12 kW power supply, crew number of 3, communication of down link through relay satellite of 1.1 Gbps with 90% global coverage. The lifetime of CSS will be more than 10 years. A series of science projects will be carried out onboard Tiangong-2, Tianzhou-1 and CSS.

2 Space Sciences Research Planning for CSS

Space sciences research planning for CSS has been carried out, which aims to advance the development of space sciences in China and get to the frontier in some important research areas, to achieve significant breakthroughs in technologies of space utilization, and make contribu-

tions to satisfy the need of the social development and people's daily life.

2.1 Research Planning of Space Sciences for CSS

The research areas of space sciences for CSS include life science and biotechnology, microgravity fluid physics and combustion science, material science, fundamental physics, space astronomy and astrophysics, space physics and space environment, Earth science and application, and experiment of new space technology. The research topics which are planned in every area are presented as follows.

(1) Life Science and Biotechnology

It focuses on fundamental biology by investigating the response and mechanism of some kinds of ground living organism in space, to get better understanding of the nature of life. It also conducts biotechnology experiments to improve the existence capability of humans in space, and benefit the human health, drugs industry, agriculture, and so on. The research topics include fundamental biology, radiation biology, space biotechnology, fundamental research of Closed Ecology and Life Supporting System (CELSS), and the frontier exploration (space biomechanics, sub-magnet biology, molecular biology related to life origin, and so on).

(2) Microgravity Fluid Physics and Combustion Science

Microgravity fluid physics is aimed at finding the special law of fluids in space (driven by surface tension, heat and solute gradient) which is masked by convection, sedimentation or hydrostatic pressure on the ground. Chemical kinetics is studied to understand the microgravity combustion process. Research in this area also help to improve the process of producing and processing on the ground, fluid management, energy utilization, propulsion, and fire protection and extinguishing. The topics in this area include hydrodynamics, complex fluid (colloid, foam and particle plasma), two-phase system and combustion dynamics, and related technologies demonstration which can be transferred to the industry.

(3) Space Material Science

Space material science focuses on the mechanism of material formation, crystallization, as well as new method of producing material in space which could deliver new knowledge and benefits for material science and industry in China. The topics in this area include kinetics of material growth under microgravity, preparation on high-value

materials, measurement of thermal physical property, performance study of space function materials and intelligence materials.

(4) Fundamental Physics

Fundamental physics is an emerging area in microgravity science, with purpose of verifying current physics theory, finding new physics phenomena, and promote new fundamental physics theory study such as gravitational gauge field theory, grand unified theory, Standard Model of new particle physics. The topics in this area include ultracold atom physics and curious quantum phenomena, high accuracy time-frequency system in space and related physics experiment, gravitational physics, test of the equivalence principle, condensed matter physics.

(5) Space Astronomy and Astrophysics

This area focuses on the significant issues related to the nature of the universe such as black hole, dark matter and dark energy, and the origin of universe, galaxy formation and evolution, and extraterrestrial life. The topics in this area include: precise multi-band photometry and all sky spectrum survey, detection of high-energy cosmic ray and dark matter, probing of the change of celestial body and burst phenomena (the Sun is included), and the study of new technologies of space astronomy.

(6) Earth Sciences and Application

It utilizes the Earth observation sensors on the space station to obtain dynamic, real and overall information of land, ocean and atmosphere to better understanding the key issues related with global changes, alterations of the environment and natural resources due to human activities. The topics in this area include the development and application of new remote sensor, the research of earth sciences related to global change, the monitoring of natural resources and environment, and the detection of natural disasters.

(7) Space Physics and Space Environment

The orbit of space station at medium and low latitude is suitable for relationship study of the sun, magnetosphere, and ionosphere. The sun is the primary source that influences the sun-earth space environment, especially the energy release process of the solar flare and Coronal Mass Ejections (CME). The emphasis of the study in this area is striving to guarantee the safe existence for space station and astronauts by predicting space environment and monitoring burst of the sun, and to investigate structure of ionosphere at medium and low latitude as well as exploration of thermosphere physics.

(8) Experiments of New Space Technology

Space station is a perfect space technology demonstration platform due to the participation of astronauts. The focus in this area is on space communication and information technology of new generation, laser energy transmission, microsatellite, 3D printing in space, novel space robots, and trials of components in space application.

2.2 Research Facilities, Experiment Racks, and Supporting System in CSS

Researches on board the CSS will be conducted over 10 years. The research facilities, experiment racks and related supporting systems are planned in CSS to facilitate the space science experiments. Most of the facilities are being developed nowadays.

2.2.1 Major Research Facilities

(1) Multifunctional Optical Facility

Multifunctional optical facility is to implement multi-band photometry and all sky spectrum survey, with a primary mirror of 2 meters in diameter. The facility is to study the mechanism of accelerating expansion of the universe and the nature of dark energy, validate the universe model, and explore the properties of dark matter. The three-dimensional structure of the galaxy and the origin and evolution of stars, black holes, galaxies and quasars are also included.

The facility will also be utilized to conduct sub-millimeter observation to study the trace components of interstellar matter in early universe and those of the earth atmosphere. Multi-wavelength and multi-mode laser sensors are adopted to measure the profile wind field of atmosphere, distribution of cloud and aerosol, biomass of sub-surface of the ocean and the earth vegetation which are for earth science and application.

(2) Research Facility for Cosmic Ray and Dark Matter (TBD)

It is utilized to implement accurate measurement of high-energy cosmic ray with wide energy region, to study on the components, origin, transmission and accelerating mechanism of cosmic ray in galaxy. Possible annihilation spectrum of dark matter is also to be investigated. The facility is with the energy range 5GeV–50TeV, acceptance of $5 \text{ m}^2 \cdot \text{sr}$, and γ/p resolution better than 1×10^{-7} , and the detection capability is hoped to be competitive in the world.

In the area of space astronomy, an all sky X-ray moni-

tor, a high sensitive detector of solar high-energy emission, and a research facility for extreme physics of neutron star are also planned in CSS.

(3) Research Facility of Quantum and Optic Transmission

It is utilized to carry out quantum science study, which includes quantum relay demonstration based on quantum memory and nonlocal test of quantum mechanics with the participation of free will. It also supports to test space-Earth, space-space entanglement quantum distribution with high fidelity and high-speed laser communication with different modulation method.

2.2.2 Research Racks for Space Sciences

A dozen of research racks are planned in pressurized module to accommodate series of scientific experiments by changing experiment units or samples. The research racks for different research areas are described as follows.

(1) Life Science and Biotechnology

Two research racks are arranged. One is Life and Ecology research Rack (LER), which is utilized to conduct experiments for biological individuals (plants, microorganism and small animals) and CELSS. One small centrifuge is assembled in it to compare the results under different gravity level. The other is Biotechnology research Rack (BTR), which is utilized to conduct experiments for biological macromolecules, cells, tissues and small mammals. The two racks have the capability of life support, dynamic monitoring and fine observation by microscope, fluorescence detector, spectrum analyzer, CCD camera, and so on.

(2) Microgravity Fluid Physics and Combustion Science

Three racks are arranged. The first one is Fluid Physics research Rack (FPR), which is utilized for experiments of complex fluids and all kinds of transparent system. The second one is Two-Phase System research Rack (TPSR), which is utilized for experiments of two-phase fluids, phase transition, and heat transfer. The third one is Combustion Sciences research Rack (CSR), which is utilize for combustion experiment of gas, liquid (droplet) and solid. These experiment racks is assembled with advanced observation devices such as digital holography, shadow, high-speed CCD, infrared thermal image, PIV, thermochromic liquid crystal, dynamic light scattering, rheology, optical spectrum, mass spectrum, *etc.*

(3) Space Material Science

There are two racks for material science. One is High-

Temperature Materials research Rack (HTMR), which is utilized for experiments for melt growth and solidification of different kind of samples sealed in ampoules. It can achieve the temperature of 1600°C, provide different temperature fields like gradient, isothermal, zone melting, and is equipped with X-ray and optical diagnostic devices. The other one is Container-less Materials Processing Rack (CMPR), which adopts electrostatic levitation to realize container-less processing. The highest temperature is over 3000°C and it can support the study of material undercooling and thermal properties measurement.

(4) Fundamental Physics

Three experiment racks are developing. One is Cold Atom Physics research Rack (CAPR), which is utilized to implement quantum degenerate gas of 10^{-12} K, which cannot be achieved on the Earth, by means of magneto-optical trap and optical lattice under microgravity. New quantum phenomena could be studied by using it. The second one is High Precision Time-Frequency System (HPTFS), which aims to build a time-frequency system composed of hydrogen clock, cold atomic clock and optical clock as well as laser and microwave link chain. The daily stability and uncertainty of the system predicted the order of 10^{-17} – 10^{-18} , which enables to conduct the fundamental physics research such as the change of fine structure constant and gravitational redshift. The third one is High Microgravity Level research Rack (HMLR), which achieves a level of microgravity 2 to 3 times better than in the pressurized module by means of isolating micro-vibration through suspension. In this rack the test of equivalence principle by means of gyro-accelerometer and cold atom interferometer can be carried out.

(5) Some Universal Experiment Racks

The Glovebox & Cold Storage Rack (GCSR) facilitates the astronauts to operate experiments in isolated and sealed space. It can also provide three storage temperatures which are 4°C, –20°C and –80°C (for biology samples). The second one is Variable Gravity Research Rack (VGR). It can provide variable gravity environment to differentiate the effects of microgravity and other space

environmental factors by simulating gravity varying from 0.01*g* to 2*g* with centrifuge. The third one is On-orbit Maintenance and Manipulation Workbench (MMW), which can serve the assembly, operation and test of fine mechanical structure and electronics devices, to improve the maintenance support capability in orbit.

(6) Exposed Experiment Facilities

Three exposed experiment facilities are arranged. A biology research exposed facility is utilized for radiation biology research and life science experiments in extreme environment. A material research exposed facility is utilized for the study of the material service performance in space. The components test exposed facility is to verify the performance of new space components in space.

2.2.3 Onboard and Ground Support Segment for Space Sciences and Application

An integrated information system based on FC-AE-1553 bus fiber optic network has been designed to support the control and information management of hundreds of payloads on CSS. Its bit-rate achieves 4Gbps in each pathway, the storage capability is up to 1000 Tb, and the capability of in-orbit information processing is over 10TFlops. The system can satisfy various needs of the change of task, expansion and in-orbit maintenance.

In order to support complex inter-disciplinary mission design, parallel development, testing, space operation, scientific research and application in space station, an advanced support segment on the ground is presented, which includes capabilities of mission planning, parallel design, integrated simulation and validation, flexible integration testing, operation and control of payloads, scientific data processing and service, *etc.* It adopts Model Driven System Engineering (MDSE) and the approach of parallel engineering to implement collaborative design of multiple disciplinary payloads. The testing of payloads is conducted with flexible intelligent test technology. The operation of complex mission is based on the space-Earth collaborative approach. Besides, high performance calculation system is developed to provide powerful capability of data processing for space sciences and application missions.

Progress of Strategic Priority Program on Space Science

WU Ji, FAN Quanlin, CAO Song

National Space Science Center, Chinese Academy of Sciences, Beijing 100190

* E-mail: wuji@nssc.ac.cn

Key words

SPP on space science
Satellite
Science objective

Abstract

The most important all-round progress in China's Space Science in recent years is the official go-ahead of Strategic Priority Program (SPP) on Space Science in 2011, which marks China's space science has entered a new stage. SPP on Space Science includes 4 satellites (DAMPE, SJ-10, QUESS and HXMT), the Intensive Study of Future Space Science Missions, and the Advanced Research of Space Science Missions and Payloads. It is expected that the innovative breakthroughs will be achieved, and the great leaps of related high-technology will be driven through both independent space science missions and international cooperation. The implementation of the SPP on Space Science will enable the rapid development of China's space science endeavor, and contribute to the progress of human civilization.

Since the launch of Dongfanghong-1, the China's first satellite, a relatively comprehensive satellite system for various applications have been established in China, and China has gradually developed into one of the world's space powers. With respect to space science development, we have developed a series of space science missions over the past 50 years, *i.e.* sounding rockets, Shijian series scientific experiment satellites, manned spaceflight, Double Star Program, lunar exploration program, *etc.* Substantial progress has been achieved in space science study, exploration technology, as well as experiment technology. Nevertheless, the most important all-round progress in China's Space Science in recent years is the official go-ahead of Strategic Priority Program (SPP) on Space Science in 2011, which marks China's space science has entered a new stage. Through both independent space science missions and international cooperation, it is expected that the innovative breakthroughs will be achieved, and great leaps of related high-technology will be driven by the strategic role of space science in national development.

SPP on Space Science includes 4 satellites—Dark Matter Particle Explorer (DAMPE), Shijian-10 (SJ-10), Quantum Experiments at Space Scale (QUESS) and Hard X-ray Modulation Telescope (HXMT), the Intensive Study of Future Space Science Missions, and the Advanced Research of Space Science Missions and Payloads (See Figure 1)^[1–2].

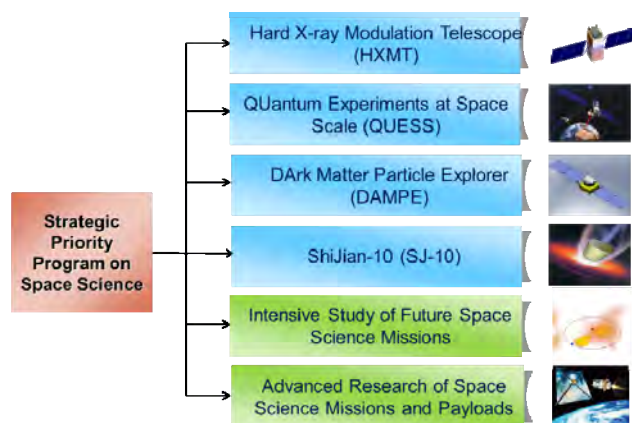


Fig. 1 Structure of SPP on Space Science

1 DAMPE

The main scientific goals of DAMPE (see Figure 2), also called Wukong, are to detect high energy electron and gamma-ray spectra with high energy resolution and in wide energy range, and make a breakthrough in the field of dark matter search; to detect electrons and heavy nuclei beyond 1 TeV, and answer the question about the origin of cosmic rays; and to carry out high energy gamma-ray survey^[3].

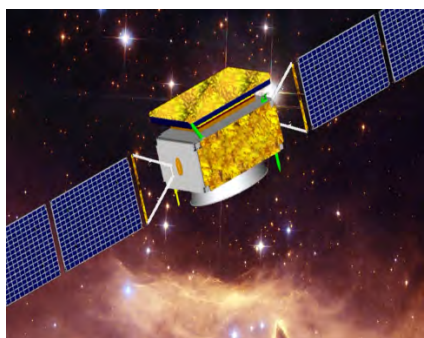


Fig. 2 Artist's view of DAMPE satellite in orbit

DAMPE mission was formally approved in December 2011, with Preliminary Design Review (PDR) completed in April 2013 and Critical Design Review (CDR) in September 2014. All flight models of the satellite system were completed in May 2015. Three beam calibration experiments were conducted in European Organization for Nuclear Research (CERN) in October 2012, October 2014 and March 2015 (see Figure 3). The satellite was lifted off on December 17, 2015 (see Figure 4) and officially delivered to the scientific user after three months' in-orbit tests.

DAMPE operates at sun-synchronous orbit with an altitude of 500 km and an inclination of 97.3065°, with a 3-year lifetime. Its total mass is less than 1900 kg.

As to the output, we have received 2833 tracks of data up to June 20, 2016, with electric charge equivalent to AMS, *i.e.* the resolution of O is 0.185, and that of Fe is 0.389. Its gamma-ray sky map fits well with FERMI's, proving its ability to identify direction of measured particle.

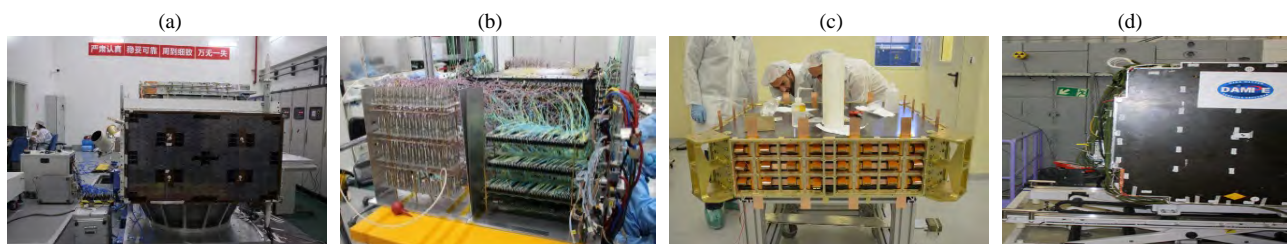


Fig. 3 Development of DAMPE: flight model of the satellite (a), BGO calorimeter (b), Silicon-Tungsten tracker (c) and beam calibration experiment in CERN (d)



Fig. 4 Launch of DAMPE satellite



Fig. 5 Artist's view of SJ-10 satellite

2 SJ-10

The major scientific objectives of SJ-10 (see Figure 5) are to get innovative achievements in the kinetic properties of matter and the rule of life activities by carrying out various scientific experiments in the space environment.

SJ-10 mission was formally approved in December 2012. The satellite PDR was completed in September 2013, the satellite CDR completed and entered flight model phase in December 2014 (see Figure 6).

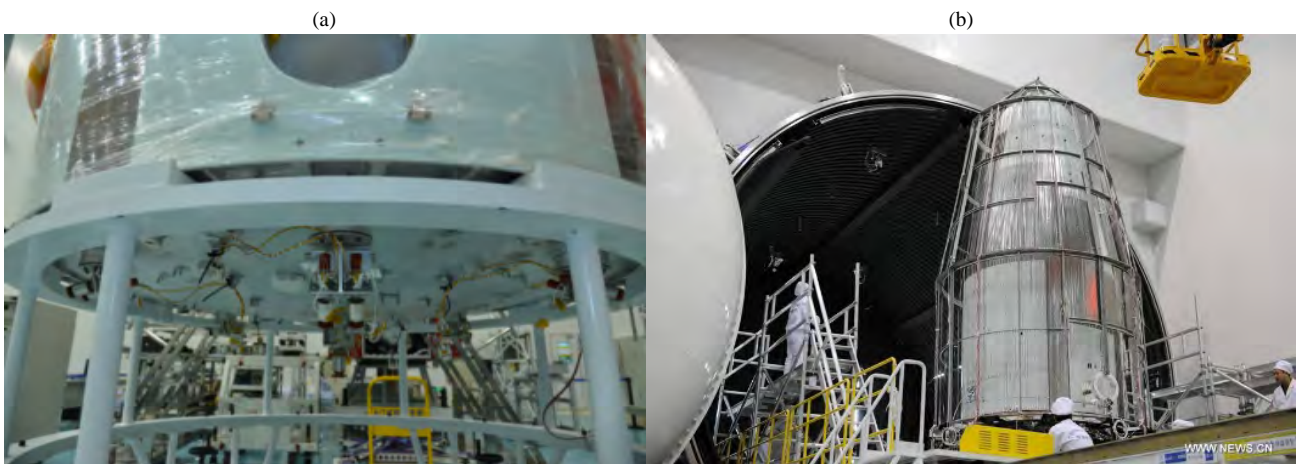


Fig. 6 SJ-10 flight model system level tests (a) and SJ-10 satellite under development (b)

SJ-10 operates at a circular orbit with an altitude of 252 kilometers and orbit inclination 43° . The mass of SJ-10 satellite is 3363 kg, and the orbiting capsule's lifetime is 15 days^[4].

SJ-10 was launched on April 6, 2016, and the re-entry capsule landed in Inner Mongolia on April 18, 2016 (see Figure 7). Results were achieved in orbit for the first time in the following aspects in kinetic theory of granular flow: formation of cluster, granule cooling behavior, and double bin separation Maxwell's demon phenomenon. The mammal embryos were developed in space for the first time.

3 QUESS

The scientific objectives of QUESS (see Figure 8) are to carry out satellite-ground experiments of high-speed quantum key distribution, and, based on it, do further

experiments of the long-distance quantum key network, in order to make breakthroughs in the realization of space-based practical quantum communications; carry out experiments on quantum entanglement distribution as well as quantum teleportation at the space scale, and fundamental tests of quantum mechanics at space scale^[5].

QUESS was formally approved in December 2011, with PDR completed in November 2012 and CDR in December 2014. The spacecraft and payloads entered flight model phase in December 2014. Besides, the construction of two optical ground stations in Xinjiang and Qinghai provinces were respectively completed in September 2015 (see Figure 9).

QUESS was launched in August 16, 2016 (see Figure 10), and will operate in the sun-synchronous orbit with an altitude of 600 km and an inclination of 97.79° , with a 2-year lifetime. Its mass is 631 kg.

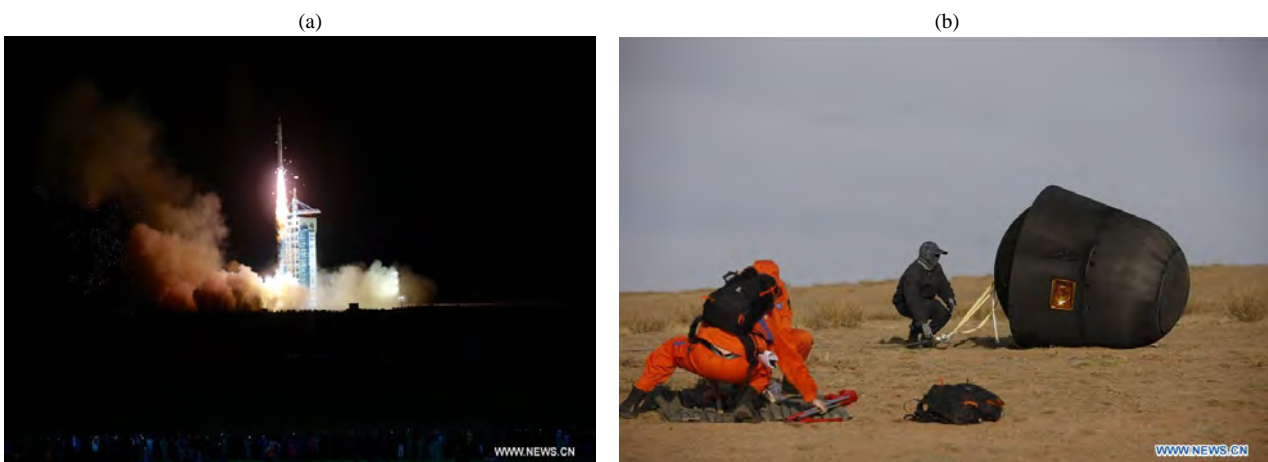


Fig. 7 Launch of SJ-10 satellite (a) and the landing of SJ-10 re-entry capsule (b)



Fig. 8 Artist's view of QUESS satellite



Fig. 9 Qualification models of QUESS payloads (a) and the optical telescope (b)



Fig. 10 Launch of QUESS satellite

4 HXMT

The scientific objectives of HXMT (see Figure 11) are to perform repeated scanning surveys of the galactic plane, in order to monitor galactic variable sources and to detect new galactic transient sources; make large-area sky observations, in order to study the cosmic variance of the cosmic X-ray background; obtain the broad band X-ray spectra of bright AGNs, in order to constrain the geometry of the various components in the AGN unified model; and observe X-ray binaries with broad band spectral and timing capabilities, in order to understand the physics under the extreme physical conditions near compact objects^[1, 6].

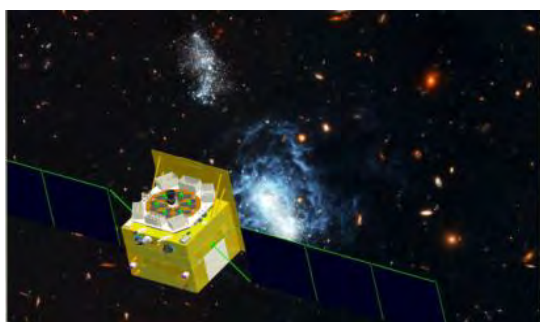


Fig. 11 Artist's view of HXMT in orbit

HXMT was formally approved in March 2011, with PDR completed in June 2012 and CDR in December 2013. All the space qualification models and their environment tests were completed in late 2014. HXMT is now in flight model phase.



Fig. 12 Development of HXMT payloads

The total mass of HXMT is about 2700 kg. It will be launched in late 2016 into an orbit with an inclination of 43° and height 550 km. Its operating lifetime is 4 years.

5 Intensive Study of Future Space Science Missions

The Intensive Study of Future Space Science Missions aims to carry out intensive studies on the selected future science missions including their scientific objectives, their payload definitions, and related key technologies, preparing for the implementation of the missions during the “Thirteenth Five-Year Plan” period (2016–2020).

The missions include Magnetosphere-Ionosphere-Thermosphere (MIT) Coupling Constellation Mission, Solar Polar Orbit Telescope (SPORT), X-ray Timing and Polarization mission (XTP), Space Millimeter VLBI Array (S-VLBI), Search for Terrestrial Exo-Planets (STEP), Einstein Probe (EP), Advanced Space-based

Solar Observatory (ASO-S) and Water Cycle Observation Satellite (WCOM). The final reviews of above-mentioned 8 missions' intensive study phase have been completed in the first half of 2016.

Among the 8 missions, EP, WCOM, MIT and ASO-S (see Figure 13) are expected to be the first ones to enter the satellite development phase. EP mainly focuses on frontier questions in time-domain astronomy. It explores the electromagnetic counterparts of black-holes and the sources of gravitational wave bursts in order to discover the processes and laws in extreme physical conditions of intense gravitation. WCOM focuses on water cycle's changes under the background of global changes, and on mechanisms governing water cycle's response and feedback to global changes. MIT is targeting the coupling processes of the Earth's magnetosphere-ionosphere-thermosphere system. The mission's science objectives focus on the acceleration mechanism and the origin of upflow ions and other related scientific questions. ASO-S mainly focuses on frontier studies on solar magnetic fields and solar eruptions, in order to unveil the inter-relationship between solar flare, coronal mass ejections, and the solar magnetic fields and their formation rules^[1, 6].

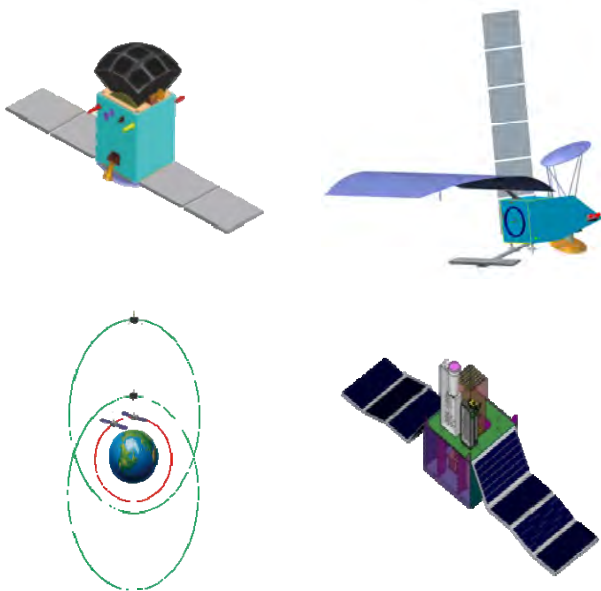


Fig. 13 Illustration of EP, WCOM, MIT and ASO-S satellites (from left to right)

SMILE (See Figure 14) is an ESA-CAS joint scientific space mission, which will determine when and where transient and steady magnetopause reconnection

dominates; define the substorm cycle, including timing and flux transfer amplitudes; define the development of CME-driven storms, including whether they are sequences of substorms. It will operate at $5000 \text{ km} \times 19 R_e$ orbit, with a mass not heavier than 300 kg and a 3-year lifetime. It is scheduled for launch in 2021^[7].

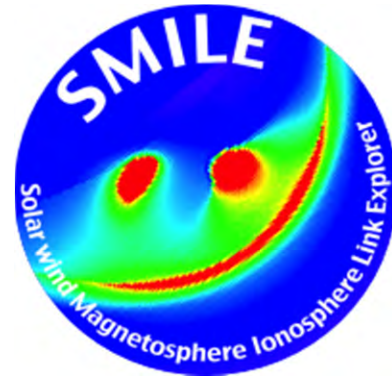


Fig. 14 SMILE mission's logo

6 Advanced Research of Space Science Missions and Payloads

The Advanced Research of Space Science Missions and Payloads is targeted for the advanced research on key technologies for future space science satellites by planning a cluster of research subjects, including innovative concepts of space science missions, key technologies of payloads, ground calibrations as well as short-time flight demonstrations^[1, 6].

The project includes nearly 100 research subjects in total, laying a solid foundation for China's future space science missions.

Space science is honored as a jewel in the crown of space exploration. It is not only an important frontier of natural science, but also playing a significant role in driving space technology. At present, good opportunities arise for China's space science^[8]. The dark matter explorer mission Wukong, the first Chinese microgravity and life sciences mission SJ-10, and the first quantum satellite QUESS have been launched, and the scientific data has been received and analyzed successfully so far, which shows that the mission is very promising in new discoveries. The implementation of the SPP on Space Science will enable the rapid development of China's space science endeavor, advance China's economic and social interests and make contribution to the progress of human civilization.



References

- [1] WU Ji, SUN Lilin. Strategic Priority Program on Space Science [J]. *Chin. J. Space Sci.*, 2014, 34(5): 505-515
- [2] Team of Strategic Priority Program on Space Science. Strategic Priority Program on Space Science: Turning a new page of Chinese space endeavor [J]. *Bull. Chin. Acad. Sci.*, 2014, 29(6): 754-763(中国科学院空间科学战略性先导科技专项研究团队. 开启中国认识宇宙的新篇章 [J]. *中国科学院院刊*, 2014, 29(6): 754-763)
- [3] CHANG J, ADAMS J H, H. AHN S, et al. An excess of cosmic ray electrons at energies of 300–800 GeV [J]. *Nature*, 2008, 456: 362-365
- [4] HU W R, ZHAO J F, LONG M, et al. Space Program SJ-10 of Microgravity Research [J]. *Microgravity Sci. Tech.*, 2014, 26: 159-169
- [5] YIN J, REN J G, LU H, et al. Quantum teleportation and entanglement distribution over 100-kilometre free-space channels [J]. *Nature*, 2012, 11332: 185-188
- [6] LU Yonglong, AN Jianji, GONG Haihua. Science in the Chinese Academy of Sciences - A Sponsored Supplement to Science [J]. *Science*, 2012: 1-49
- [7] WU J. *Calling Taikong: A Study Report on the Future Space Science Program in China* [M]. Beijing: Science Press, 2016
- [8] BIEVER C, PEARSON H, HAYDEN E C, et al. Science stars of China [J]. *Nature*, 2016, 534: 456-461

Vision and Voyages for Deep Space Exploration

ZOU Yongliao, WANG Qin

National Astronomical Observatories, Chinese Academy of Sciences, Beijing 100012

* E-mail: wangqin@bao.ac.cn

Key words

Deep space exploration
Mars
Moon

Abstract

More than 50 years of space exploration has not only satisfied human curiosity and built up international cooperation, but also improved life on Earth. Space exploration is an open-ended process which started 50 years ago. It enables access to unknown terrains with robots and humans, thereby opening new frontiers. Progress of goal deep space exploration was reviewed. China's current deep space missions are also briefly introduced. Focused on the vision and voyages for China's deep space exploration in 5 or 10 years. Like the Chinese Lunar Exploration Program (CLEP), we embark on a journey to Mars. We will spend few decades on Mars with the robotic explorers. Unlike CLEP, scientists proposed to build moon research station by 2030.

1 Introduction

After more than 50 years since humans ventured into orbit for the very first time, space exploration has evolved in terms of destinations, duration, objectives and partnerships.

The United States, Russia, Europe, Japan, China, India and other countries and organizations have launched more than 200 space probes, visited seven planets and Pluto in the solar system, implemented the moon, Mars, Venus, Titan, asteroids and comets landing detections, achieved sample return from the moon, asteroids and comets particle, implemented six manned lunar landings and sent 12 astronauts to the moon.

The challenges encountered on the way and the number of involved participants added to the level of complexity, but significantly increased the sustainability and the relevance to our common future on planet Earth. By 2030, there will be approximate 16 lunar explorations, 12 Mars missions. Missions to Mars are the ultimate challenge, which include the return of samples in 2025 and the close cooperation between robots and humans on the surface of the Red Planet in 2035.



Fig. 1 ESA artist's concept of a moon village

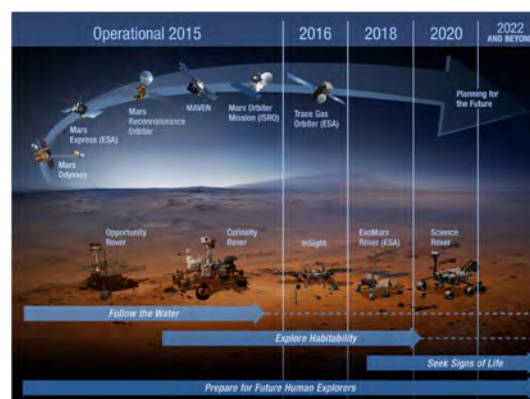


Fig. 2 On the red planet: robotic Mars missions

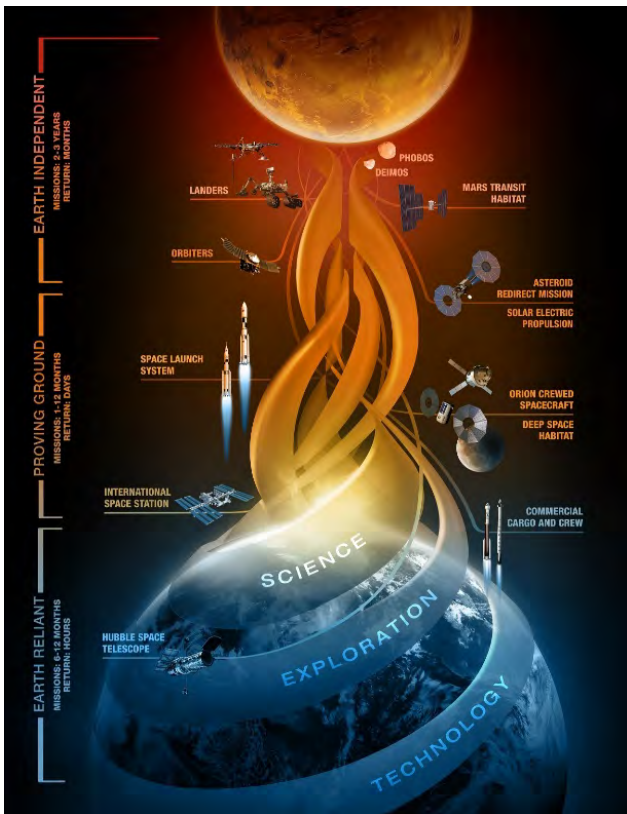


Fig. 3 NASA: three phases on the journey to Mars

2 China's current situation

The Chinese Lunar Exploration Program (CLEP) is an ongoing series of robotic moon missions. The CLEP is divided into three main operational phases, with each mission serving as a technology demonstrator in preparation for future missions. CE-1 & CE-2 are lunar orbiters, and has now been completed effectively. CE-3 is ongoing, and incorporates spacecraft capable of soft-landing on the Moon and deploying lunar rovers. CE-5 will entail a lunar sample return mission in 2018. More than 10 years of CLEP has not only achieved a series of progresses, but has also made favorable conditions for future deep space exploration.

3 Scientific objectives

With emphasis on the Moon and Mars, the future deep space exploration will carry out terrestrial planets, giant planets, and small objects exploration. It will obtain many important research findings about the origin and evolution of the solar system, disastrous impact on the Earth by the Sun and small bodies, extraterrestrial life exploration and other research fields, and will also promote astron-

omy, space science and technology applications.

4 General Conception of Future Deep Space Exploration

By 2020, CLEP three phases will be comprehensively implemented: circling, landing and returning. China also proposes a series of Mars sample return, asteroids, Jovian system, interstellar exploration in the next 15 years.

4.1 The Moon

Chang'E-4 mission, phase two of China Lunar Exploration Program, represents China's first attempt to explore far side of lunar surface. CE-4 mission includes lander, rover and a telecommunication relay, presently scheduled to launch in 2018.

The scientific objects of the future lunar exploration are space and astronomy, geology and structure, resources and environment. Proposed future lunar missions include robotic lunar missions and human lunar exploration. China is currently working on robotic missions to conduct scientific research and support future human surface missions. Robotic science missions would detect lunar south/north pole and collect sample and return to the Earth. So the robotic missions will continue well into the next decade to meet high-priority science objectives and to prepare for future human missions to the Moon. Human lunar exploration would include human orbiter lunar exploration, manned lunar-landing and manned lunar scientific station.

4.2 Mars

The Mars program consists of two missions to be launched in 2020 and 2030, respectively. The first phase is circling, landing, in-situ and rover exploration, and second phase is sample return.

Mars is the horizon goal for space pioneering; it is the next tangible frontier for expanding human presence. Our robotic mission will scout Mars' geological evolution and climate cycles, which were comparable to Earth's at one time and suitable for life, to detect Mars' space physical, atmospheric and meteorological characteristics, Martian surface environment; to research topography formation, Martian soil composition, structure, physical characteristics; to find valuable resources such as water ice just below the surface; to study the internal structure and the evolution of planetary systems, and comparative planetology.

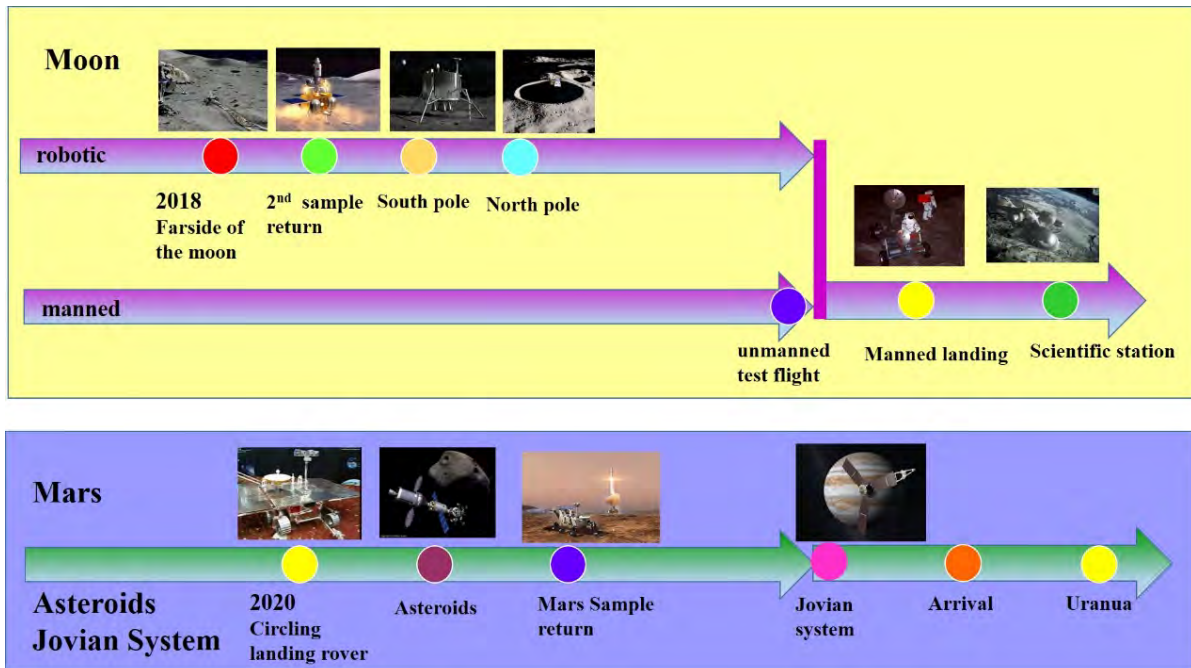


Fig. 4 Poposal for deep space exploration mission development route

4.3 Asteroid

By 2024, scientists suggested asteroid mission could focus on flying by, touchdown, sample return, with a serious of multi-purpose explorations, to detect the formation and evolution of asteroid, assess risks of impact on the Earth, and study the solar system origin, evolution and how life began on Earth.

4.4 Jovian System

By 2030, scientists proposed to carry out Jovian system orbiter exploration. To research the structure of Jupiter’s magnetosphere, Europa space/surface environment and ice shell characteristics.

Arriving at Uranus is planned in 2048.

New Progress in China's Lunar Exploration Program

ZOU Yongliao, XU Lin, WANG Qin

National Astronomical Observatories, Chinese Academy of Sciences, Beijing 100012

* E-mail: xul@nao.cas.cn

Key words

China's Lunar Exploration Program
Chang'E-3
Scientific results

Abstract

Chang'E-1 and Chang'E-2 of China's Lunar Exploration Program (CLEP) have successfully achieved their mission. At the present time, only Chang'E-3 is still in operation, which was successfully launched on December 2, 2013. Chang'E-3 probe is the third robotic lunar mission of CLEP, which consists of a lander and a rover, with eight payloads boarded on the spacecraft. Up to December 21, 2015, more than 2.86 TB raw data were received from these instruments onboard Chang'E-3 probe. A series of research results have been achieved. This paper gives a detailed introduction to the new scientific results obtained from Chang'E-3 missions.

1 Introduction^[1–16]

A total of three lunar spacecrafts of Chinese Lunar Exploration Program (CLEP) have been launched. Chang'E-1 and Chang'E-2 have successfully achieved the mission's science goals. Currently, Chang'E-3 is still in operation, which was successfully launched on December 2, 2013, and soft-landed on December 14, 2013. Chang'E-3 is the third robotic probe of CLEP, which consists of a lander and a rover (Yutu). There are eight scientific payloads onboard Chang'E-3: the Landing Camera (LCAM), the Terrain Camera (TCAM), the Extreme Ultraviolet Camera (EUVC) and the Moon-based Ultraviolet Telescope (MUVT) onboard the lander; the Panoramic Camera (PCAM) and the Visible/Near-Infrared Imaging Spectrometer (VNIS), the Active Particle-induced X-ray Spectrometer (APXS) and the Lunar Penetrating Radar (LPR) on the rover Yutu. Their main scientific goals include: investigating the lunar local surface topography, geological structure and chemical compositions, monitoring the structure and dynamics of

the Earth's plasmasphere, and conducting Moon-based astronomical observations.

Up to December 21, 2015, more than 2.86 TB raw data were received from these instruments onboard Chang'E-3. These raw data were pre-processed by channel processing, unpacked, calibrated and corrected, and so on, and produced data which scientists can use. The various data processing methods have provided scientists with help in further research.

LCAM and TCAM on the lander, and PCAM on the rover were used to investigate the surface topography and geological structure around the landing area. Through systematical processing of the data obtained by LPR, VNIS and APXS, we obtained the data on chemical composition and mineral abundance of lunar soil at the landing site and the superficial structure of lunar regolith and crust. It is the first attempt to explore the lunar subsurface structure by using high-resolution LPR. In addition, EUVC and MUVT on the lander made observations of the terrestrial plasmasphere and stars.

2 Preliminary Scientific Results for China's Lunar Exploration Program

2.1 Lunar Rover Yutu has Revealed the Volcanic History of the Imbrium Basin^[17–18]

Scientists have found that the data from LPR, VNIS and APXS can reveal large volcanic eruptions extending to 2500 Ma ago, probably induced by the local enrichment of radioactive elements in the landing area. In addition, the lunar regolith layer may be thicker than the previous estimates. These results provide important scientific constraints on the volcanic history of the Imbrium basin and the evolution of the Moon.

During the first 2 months, Yutu successfully carried out two APXS and four VNIS analyses on the lunar soils and performed a 114-meter-long LPR profile along the rover track in the landing area (Fig. 1).

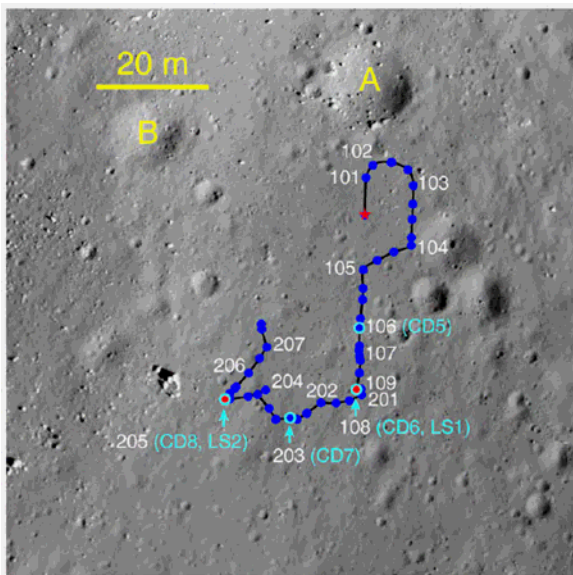


Fig. 1 Chang'E-3 landing site and the rover Yutu's track. The red star represents the landing position. A and B represent two large impact craters. The black line is the track of Yutu. LS1 and LS2 are positions of 2 APXS analyses, and CD5–8 are positions of 4 VNIS analyses.

2.1.1 Major and Trace Elements of the Lunar Soils

The APXS of the rover Yutu generates X-Ray by the artificial radioactive elements as the source. When the lunar soil is irradiated by the X-Ray beam, it will emit X-ray fluorescence. Based on the intensities of X-ray fluorescence, the chemical composition of the lunar soil can be calculated. The background of X-ray fluores-

cence is very low when using an X-ray beam as source. Therefore, the APXS of the rover Yutu can detect not only the major elements, such as Mg, Al, Si, Ca, Ti, K, Fe and Cr, but also 4 trace elements, such as Sr, Y, Zr and Nb. According to the APXS data, the team obtained the contents of the 12 elements in the measured lunar soils (Table 1). In order to improve the accuracy the results, the team carried out a number of calibration experiments on 10 rock standards in laboratory, and established a complete data processing method.

The outer most lunar surface is covered by a thin layer of regolith due to 20–40 billion years long impact of numerous asteroids. The regolith measured by the Yutu can actually represent the underlying rock, which is a distinct type of mare basalt based on the APXS data. Compared with the Apollo and Luna soil samples, these soils are rich in Fe and Ti contents and poor in Al contents. In addition, they are enriched in K, Zr, Y, and Nb, indicating assimilation of 10%–20% of the KREEP component—last remnants of lunar magma ocean, highly enriched in radioactive and incompatible elements, phosphorous, rare Earth elements and potassium. Thus, the basalt could be derived via partial melting of ilmenite-rich mantle reservoir, then assimilated by the residual KREEP layer crust as it ascended, finally erupted into the Imbrium basin.

Table 1 Chemical compositions of the lunar soil measured by APXS

Sample name	LS1	±	LS2	±
SiO ₂	42.8		43.2	
MgO	9.9	1.5	8.9	1.9
Al ₂ O ₃	11.5	0.9	10.5	1.0
K ₂ O	0.18	0.01	0.15	0.01
CaO	10.4	0.3	10.9	0.4
TiO ₂	4.0	0.2	4.3	0.2
FeO	21.3	1.7	22.1	1.9
Total	100.0		100.0	
Cr, ppm	877	162	825	161
Sr, ppm	139	19	198	29
Y, ppm	34	10	54	13
Zr, ppm	200	26	168	49
Nb, ppm	13	2	14	10

In wt %, normalized to 100 wt %. LS1, lunar soil 1; LS2, lunar soil 2.

2.1.2 Mineral Abundances and Optical Maturity Index

The research team obtained the mineral abundances and optical maturity index of the lunar soils based on the VNIS data. The VNIS, mounted at the front of the Yutu, can acquire the visible to near-infrared spectra of the surface soils and exposed rocks in the landing area.

Compared with the previous orbital detections, the VNIS of the Yutu provided the highest spatial resolution. However, it showed significant shadow effect due to the observation angle and surface roughness. The team presented a method to effectively correct the shadow effect, decoded the spectral data of VNIS, and obtained iron and titanium contents, mineral abundances and optical maturity index of the lunar soils. The calibrated spectra with typical characteristics of space weathering are similar to that of the mare soil samples, and display lower reflectance than highland soils. In addition, the 4 VNIS analyses have variable optical maturity. The optical maturity and reflectance tend to increase towards the lander, probably reflecting that the upper most surface soil was blown away during the landing process.

2.1.3 A Thicker Lunar Regolith Layer than Expected

The Yutu's LPR is the first radar deployed on the lunar surface since human exploration of the Moon. The team acquired the thickness and structure of the lunar regolith, and identified three layers of basalt and their thickness based on the LPR data. The LPR has two working frequency: high frequency channel of 500 MHz with detection depth of tens of meters and resolution of > 30

cm; low frequency channel of 60 MHz with detection depth of hundreds of meters and resolution at meter level. In order to obtain accurate and clear results, instantaneous frequency spectrum analysis and migration method in the field of seismic exploration have been used for data processing.

The lunar was covered by a homogeneous "dust" layer, which is about 0.7 m thick. This result is consistent with those of borehole core method by the Apollo program. The thickness of the lunar regolith in the mare area was previously estimated to about 2 to 4 m because this region with young ages should have a thinner regolith layer. However, the LPR results indicate a regolith thickness of about 5 m, which is significantly higher than previous estimation. Although the thick regolith layer may be partially attributed to the ejecta deposits from a large crater close to the landing site, high resolution topography images show that this impact is limited. Since the lunar soil is the most important reservoir of helium-3 and hydrogen, this result is very important for future exploitation of lunar resources (Fig. 2).

2.1.4 The Moon is Still Active in Its Old Age

Another important achievement is the identification of

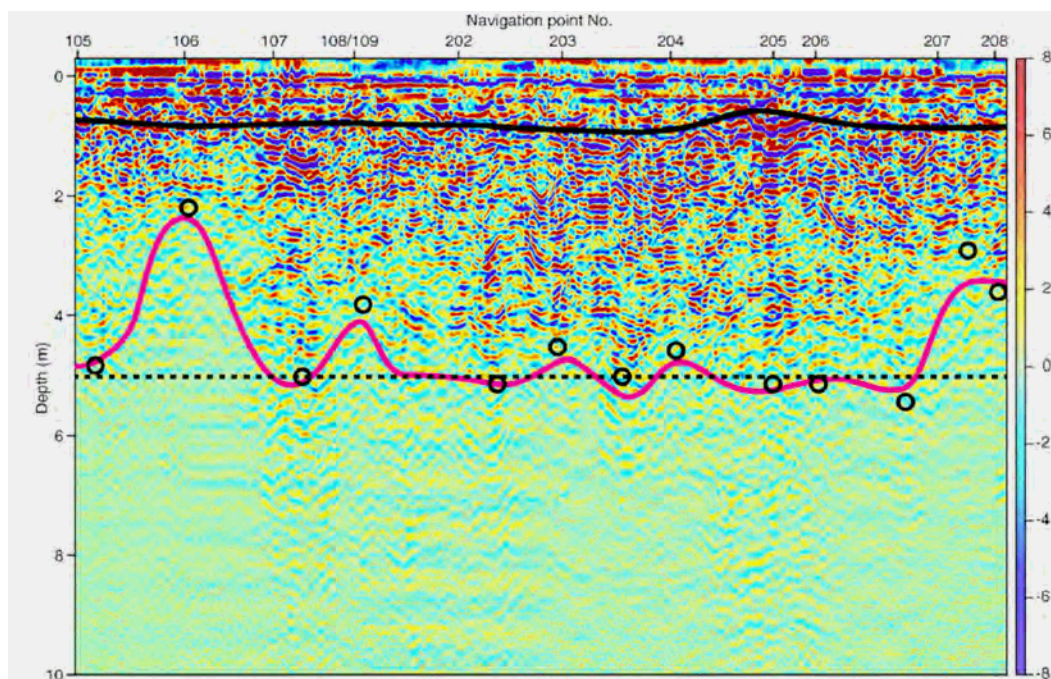


Fig.2 Migration result of high frequency channel of LPR. Bold black and red curves denote the lunar soil sublayer and regolith bottoms, respectively. Bold black circles are the depths of lunar regolith picked up from the key traces by time-frequency analyses after migration. The dashed black line (at 5 m depth) denotes the best depth estimation of the lunar regolith at the research area.

three reflecting interfaces in the deep interior, based on which, thicknesses of 3 suits of basalts can be calculated. The thickness of the latest basalt unit is about 195 meters, showing that there were still huge basalt magma eruptions during lunar old age (about 2500 million years ago). The Moon experienced asteroid bombardment at about 3.9 billion years, forming basins with different sizes on the surface. These basins were then filled by basaltic magma at about 3.8–3.1 Ga. After that, the Moon entered its old age, and the magmatism tended to stop. However, the Yutu data showed that strong volcanic activity of the mare area lasted until 2.5 Ga. The lunar soils of the landing site contain 10%–20% of KREEP component, indicating assimilation of the residual KREEP layer crust as the magma ascended. The KREEP is enriched in radioactive elements, which provided the major energy of the long term magmatism (Fig. 3).

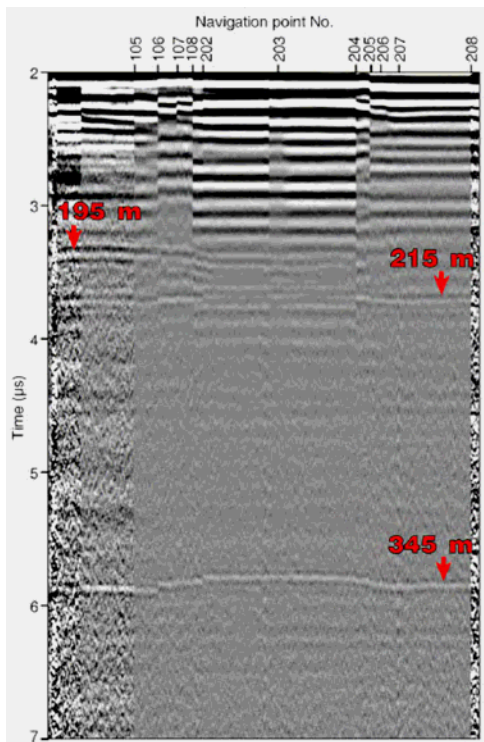


Fig. 3 The LPR profile of low frequency channel, showing 2 reflection interfaces at 195 m, 215 m, and 345 m, respectively.

2.2 Layered Subsurface Structure and Complex Geological History of Chang'E-3 Landing Site are Revealed^[19–22]

The Lunar Penetrating Radars (LPR) onboard Yutu rover has firstly detected the subsurface structure of the landing site. The shallow surface stratigraphic structure

over the Chang'E-3 landing site was systematically studied based mainly on the high-frequency LPR data, along with the optical images acquired by the descending and terrain cameras. The results reveal four major stratigraphic zones from the surface to a depth of ~ 20 m: a layered reworked zone (< 1 m), an ejecta layer (~ 2–6 m), a paleo-regolith layer (~ 4–11 m), and the underlying mare basalts. Combining with the regolith thickness estimation, the LPR observations indicate a larger accumulation rate of lunar surface regolith as compared with previous estimation at the Apollo landing sites (Fig. 4).

Low-frequency radar obtained deeper structure information. Data inversion and interpretation, combining with local and regional geological characteristics, six more layered rock units have been revealed: 8– ~35 m basalts, ~35– ~45 m paleo-regolith, 45– ~140 m massive basalts, 140– ~240 m layered volcanic/pyroclastic rocks, 240– ~360 m and below 360 m massive basalts. The upper layer Eratosthenian basalts (~2.5 Ga) extend to a depth of ~35 m, which is filled above a ~10 m thick paleo-regolith layer formed at the surface of underlying Imbrian basalts (~3.3 Ga) (Fig. 5). It is suggested that there is at least three Imbrian volcanic eruption events to the depth of ~400 m. These layered lava and pyroclastic rocks are inter-bedded by space weathering formed regolith during the interval of volcanic events. Relatively accurate knowledge on regolith thickness and shallow surface structure of lunar crust was obtained, which provides reliable structural constraints to study the lunar volcanism history and estimate the reserve of lunar He-3 resources.

2.3 A New Rock Type on Lunar Surface is Discovered^[23]

According to Lunar Magma Ocean (LMO) model, the mineral composition and their spatial distribution on lunar surface are determined by the initial global differentiation and later magmatic activities. The elemental and major mineral (olivine, pyroxene, plagioclase and ilmenite) contents across lunar surface are keys to understand lunar evolution history. Comprehensive study of the datasets obtained from Active Particle-induced X-ray Spectrometer (APXS) and Visible and Near-infrared Imaging Spectrometer (VNIS) aboard rover Yutu (Fig. 6 and Fig. 7), we obtained the compositional and mineralogical information of lunar rock/soil at Chang'E-3 landing site. The analysis indicates a new type of mare basalt rich in

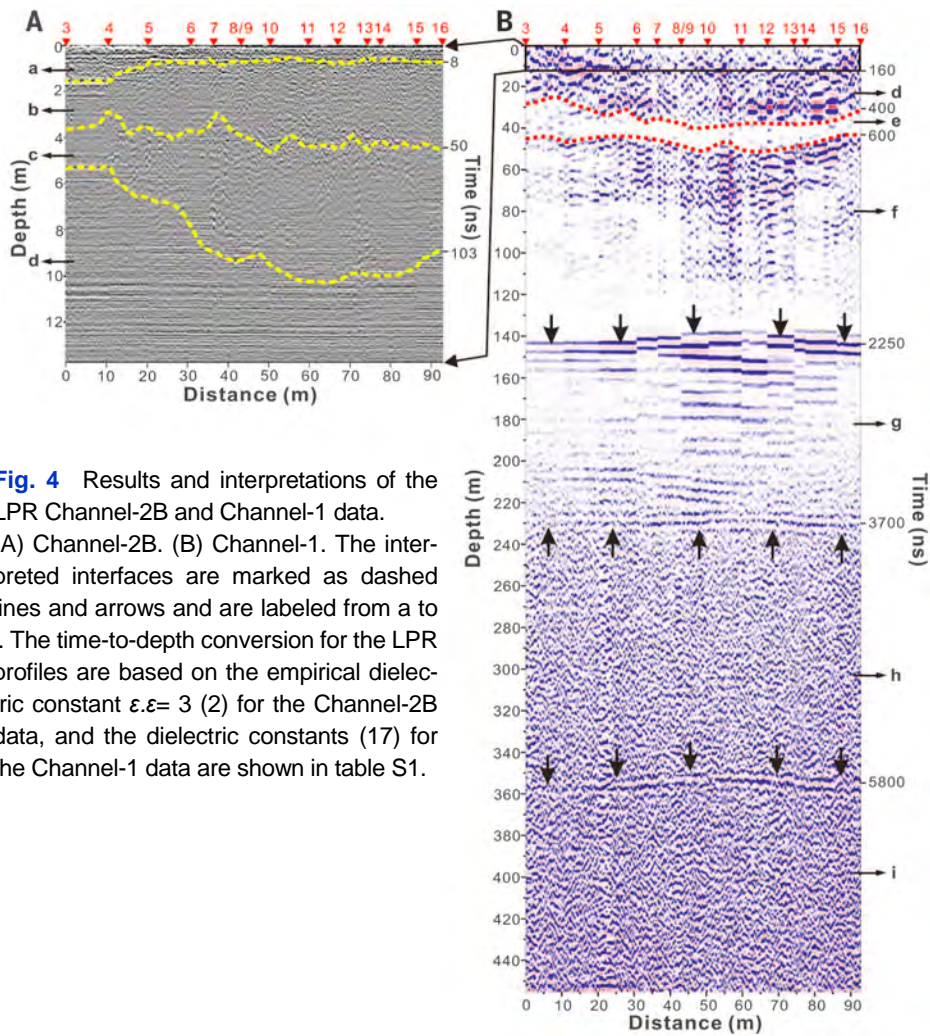


Fig. 4 Results and interpretations of the LPR Channel-2B and Channel-1 data. (A) Channel-2B. (B) Channel-1. The interpreted interfaces are marked as dashed lines and arrows and are labeled from a to i. The time-to-depth conversion for the LPR profiles are based on the empirical dielectric constant $\epsilon_r = 3$ (2) for the Channel-2B data, and the dielectric constants (17) for the Channel-1 data are shown in table S1.

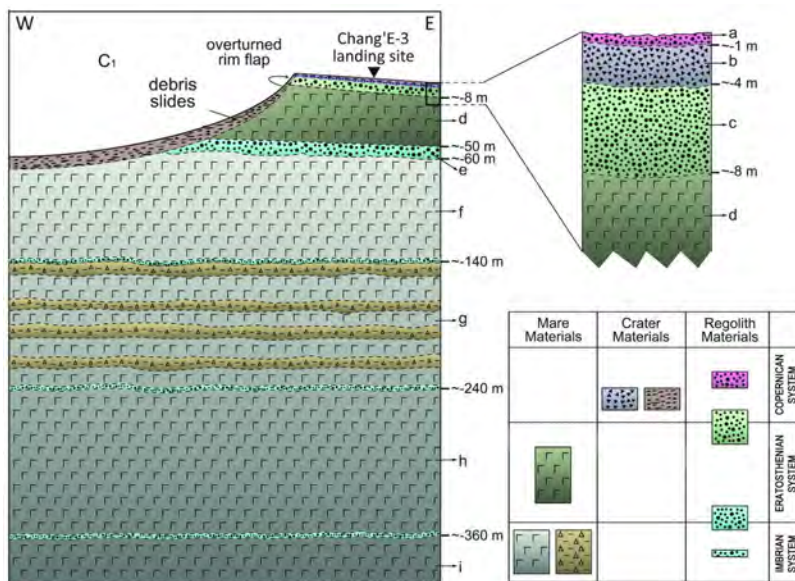


Fig. 5 Sketched geological cross section and an inferred profile of the CE-3 landing site. Yutu has detected seven subsurface interfaces, which formed from Imbrian to Copernican. Letters a to i indicate interpreted subsurface layers based on LPR data (Fig. 4).

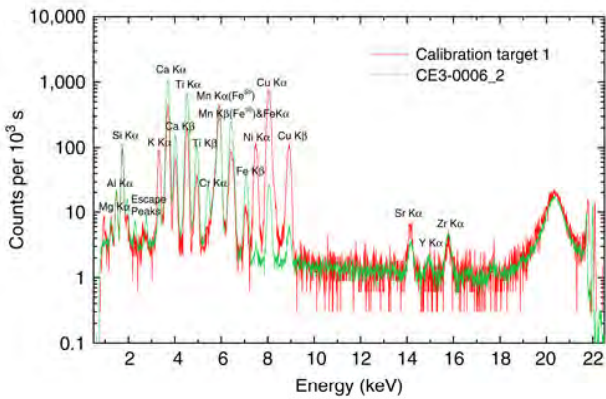


Fig. 6 X-ray spectrum and chemical compositions of Chang'E-3 soils from APXS. APXS spectrum CE3-0006_2 overlain on the calibration spectrum.

olivine and ilmenite within the “Guang Han Gong” that has not been sampled by previous Apollo and Luna missions and lunar meteorite collections. Thus Chang'E-3 landing site (“Guang Han Gong”) has become a new calibration site with ground truth for lunar remote sensing studies, providing critical constraints for later-stage lunar volcanism as well as the mechanism of magmatic evolution.

2.4 Space Weathering Process and Products are Quantify Constrained^[24–25]

Lunar surface regolith carries important information on space weathering processes, the lunar environment and is very important for lunar explorations. On the first lunar day after the rover deployment, the onboard Panoramic Camera (PCAM's) captured the first in-situ lunar opposit

ion effect since the Apollo era. The in-situ lunar phase curve, covering the phase angle range from 2° to 141°, was extracted from the PCAM's images and by performing photometric inversions the physical properties of the upper regolith have been inferred. The major results include: the surface regolith porosity is around photometric inversions the physical properties of the upper regolith have been inferred. The major 0.68, the regolith grains may be more transparent than the average maria, and the average slope angle ranges from 11° to 18° which is also smaller than the average maria.

2.5 EUV Camera—An Overview on Observations of the Earth's Plasmasphere with EUV Camera on Board Chang'E-3^[26–34]

The Earth's plasmasphere, composed of dense and cold plasma coming from the ionosphere, has been observed for more than six decades since 1950s. Space missions play important roles in explorations of the plasmasphere. The Extreme Ultraviolet Imager working at a wave band of 30.4nm on the Imager for Magnetopause-to-Aurora Global Exploration (IMAGE) satellite brings us great knowledge although this mission ended several years ago. In its elliptical orbit, 90° inclination with an apogee altitude of 7 R_E and perigee of 1000 km, IMAGE can only make observations in polar views with short exposure time. In 2008 the Telescope of Extreme Ultraviolet (TEX) working at a wave band of 30.4 nm on a Japanese satellite named KAGUYA provided the first sequential images of the plasmasphere in meridian views. Due to some problems in the instrument, TEX can only provide

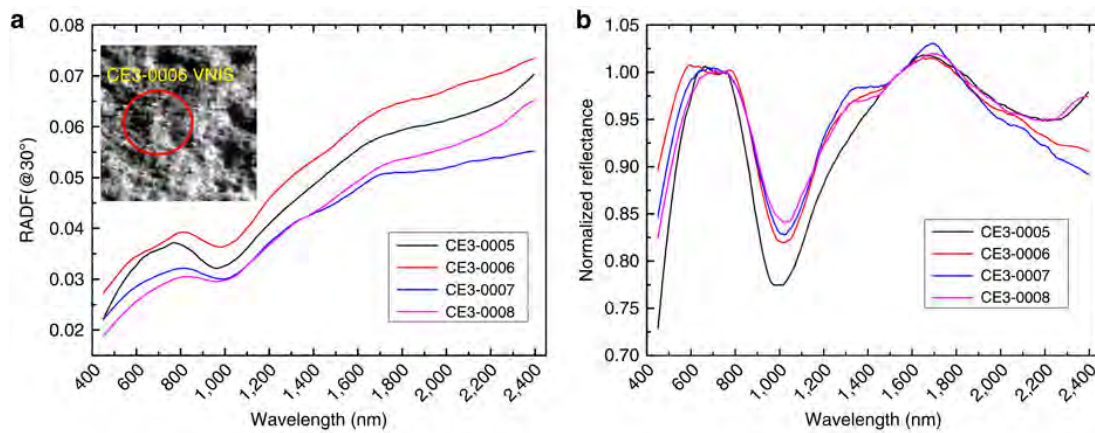


Fig. 7 Visible-NIR spectral properties and mineral chemistry of Chang'E-3 soils from VNIS (a) Combined VNIS spectra (450–2,400 nm) from sites 0005, 0006, 0007 and 0008. The inset image is from site CE3-0006 of the VNIS (450–950 nm) image mode at 750 nm. The dashed circle indicates the region measured by the VNIS-point spectral mode (900–2,400 nm). (b) VNIS spectra after continuum removal.

observational data with a half field of view during its short life time.

In order to observe the Earth's plasmasphere in a global scale meridian view, a moon based EUV camera (EUVC) made observations at a wave band of 30.4 nm and with a field of view of 15° during the period of December, 2013 to June, 2014. On the top deck of Chang'E-3, this camera obtained more than 1000 images of the Earth's plasmasphere with an angular resolution of 0.1° and a temporal resolution of 10 minutes within some time intervals of moon's day. More than 20 hours continuous observations were made in February, April and May of 2014, respectively. Combining with other space observations, we study the plasma density configuration, velocity fields and global structure evolution in the Earth's plasmasphere.

By reconstructing the global plasmaspheric configuration based on the EUVC images observed during 20-22 April 2014, we show that in the observing period, the plasmasphere had three bulges which were located at different geomagnetic longitudes. The inferred midnight transit times of the three bulges, using the rotation rate of the Earth, coincide with the expansion phase of three substorms, which implies a causal relationship between the substorms and the formation of the three bulges on the plasmasphere. Instead of leading to plasmaspheric erosion as geomagnetic storm does, magnetospheric substorms initiated on the night side of the earth cause local inflation of plasmasphere in the midnight region.

The plasmopause locations determined from the EUVC images and the auroral boundaries determined from the Defense Meteorological Satellite Program (DMSP) Special Sensor Ultraviolet Spectrographic Imager (SSUSI) images are used to investigate the plasmaspheric evolutions during substorms. The most important finding is a nightside pointing plasmaspheric plume observed at 23:05 UT on 21 April 2014 under very quiet geomagnetic conditions. High correlations between the plasmopause evolutions and the auroral signatures exist during substorms. After substorm onset, the plasmopause erosion and the equatorward expansion of the auroral oval occur almost simultaneously in both MLT and UT, and then both the erosion and the expansion propagate westward and eastward. The enhanced convection during substorms or Earthward propagation of dipolarization fronts produces plasmasphere erosion and MLT propagations, and the substorm dipolarization causes

pitch angle scattering of plasma sheet electrons and the resulting precipitation excites aurora emissions at the same time.

2.6 LUT Observations^[35–42]

By using the LUT observations with extremely low stray light pollution caused by sunshine, Wang *et al.*^[35] reported an unprecedented upper limit of the content of the OH radicals in lunar exosphere through the in-situ measurements of the diffuse sky background. The column density and surface concentration of the OH radicals are obtained to be $<10^{11} \text{ cm}^{-2}$ and $<10^4 \text{ cm}^{-3}$, respectively, basing upon the resonance fluorescence emission at 3081\AA . This results is the best known of the OH content in the lunar exosphere to date (being lower than the previously reported value given by HST by about two orders of magnitude), and is close to the prediction of the sputtering model.

Spectral datasets from NUV to optical band were constructed by Wang *et al.*^[36] for 44 International Ultraviolet Explorer (IUE) standards, because of the LUT's relatively wide wavelength coverage. With the spectral datasets, Wang *et al.*^[37] shows a highly stable photometric performance during LUT's 18-months operation. The magnitude zero point is determined to be 17.53 ± 0.05 mag, which is independent of the spectral type of the standard from which the magnitude zero point is determined. Qi *et al.*^[38] presented an astrometric solution of LUT to calibrate the basic information (attitude, CCD constants, etc.) of LUT, not only for the accurate pointing and tracking of celestial objects but also for target detection on CCD images.

Meng *et al.*^[39] developed a dedicated data processing pipeline for LUT point observations that monitor variable objects in NUV band. The procedures of the pipeline include stray light removing, astrometry, flat fielding employing superflat technique, source extraction and cosmic ray rejection, aperture and PSF photometry, aperture correction, and catalogues archiving, etc. The resulted photometric accuracy is typically ~ 0.02 mag for LUT 10 mag stars (30s exposure).

Qian *et al.*^[40] analyzed the NUV light curve of short-period eclipsing binary GQ Dra observed by LUT, which suggests an long term increase of orbital period at a rate of $(3.48 \pm 0.23) \times 10^{-7} \text{ days} \cdot \text{yr}^{-1}$ and a mass transfer rate of $(9.57 \pm 0.63) \times 10^{-8} M_{\odot} \text{ yr}^{-1}$. Zhu *et al.*^[41] obtained a photometric solution of semi-detached binary V548 Cygni in NUV band. The solution suggests that there

are three cyclic variations that are interpreted by the light travel-time effect via the presence of three additional stellar companions. The photometric solution of the well-known Algol-type binary TW Dra was obtained by Liao *et al.*^[42] by analyzing the first NUV light curve obtained by LUT. Based on 589 available data spanning more than one century, the authors identify three cyclical changes. The two cyclical changes with short periods can be explained as the result of two circum-binary companions orbiting around TW Dra.

Acknowledgements

We thank Lin Yangting, Yang Wei, Hu Sen, Xiao Long, Ling Zongcheng, Wang Huaning, He Han, Wei Jianyan, Wang Jing for providing reference materials. This work was supported by the Key Research Program of the Chinese Academy of Sciences, Grant No. KGZD-EW-603.

Reference

- [1] Chen, B., Song, K. F., Li, Z. H., *et al.* 2014, RAA (Research in Astronomy and Astrophysics), 14, 1654
- [2] Dai, S., Su, Y., Xiao, Y., *et al.* 2014, RAA (Research in Astronomy and Astrophysics), 14, 1642
- [3] Fang, G.-Y., Zhou, B., Ji, Y. C., *et al.* 2014, RAA (Research in Astronomy and Astrophysics), 14, 1607
- [4] Feng, J.-Q., Liu, J.-J., He, F., *et al.* 2014, RAA (Research in Astronomy and Astrophysics), 14, 1664
- [5] Fu, X.-H., Li, C.-L., Zhang, G.-L., *et al.* 2014, RAA (Research in Astronomy and Astrophysics), 14, 1595
- [6] He, Z.-P., Wang, B.-Y., Lu, G., *et al.* 2014, RAA (Research in Astronomy and Astrophysics), 14, 1567
- [7] Li, C.-L., Mu, L.-L., Zou, X.-D., *et al.* 2014, RAA (Research in Astronomy and Astrophysics), 14, 1514
- [8] Lin, X., & Ouyang, Z. 2014, *Chin. J. Space Sci.*, 34, 525
- [9] Liu, B., Li, C.-L., Zhang, G.-L., *et al.*, 2014, RAA (Research in Astronomy and Astrophysics), 14, 1578
- [10] Liu, J.-J., Yan, W., Li, C.-L., *et al.* 2014, RAA (Research in Astronomy and Astrophysics), 14, 1530
- [11] Ren, X., Li, C.-L., Liu, J.-J., *et al.* 2014, RAA (Research in Astronomy and Astrophysics), 14, 1557
- [12] Su, Y., Fang, G.-Y., Feng, J.-Q., *et al.* 2014, RAA (Research in Astronomy and Astrophysics), 14, 1623
- [13] Tan, X., Liu, J.-J., Ren, X., *et al.* 2014, RAA (Research in Astronomy and Astrophysics), 14, 1682
- [14] Wang, F.-F., Liu, J.-J., Ren, X., 2014, RAA (Research in Astronomy and Astrophysics), 14, 1543
- [15] Wen, W.-B., Wang, F., Li, C.-L., *et al.* 2014, RAA (Research in Astronomy and Astrophysics), 14, 1674
- [16] Zhang, H.-B., Zheng, L., Su, Y., *et al.* 2014, RAA (Research in Astronomy and Astrophysics), 14, 1633
- [17] Zhang, J., Yang, W., Hu, S., Lin, Y., Fang, G., Li, C., Peng, W., Zhu, S., He, Z., Zhou, B., Lin, H., Yang, J., Liu, E., Xu, Y., Wang, J., Yao, Z., Zou, Y., Yan, J., Ouyang, Z. 2015. Volcanic history of the Imbrium basin: A close-up view from the lunar rover Yutu. *Proc Natl Acad Sci U S A*, 112, 5342–5347
- [18] Hu, S., Lin, Y.T., Liu, B., Yang, W., He, Z.P., Xing, W.F. 2015. Reflectance calibration and shadow effect of VNIS spectra acquired by the Yutu rover. *Research in Astronomy & Astrophysics*, 15, 1587–1596.
- [19] Xiao L, Zhu P M, Fang G Y, *et al.* A young multilayered terrane of the northern Mare Imbrium revealed by ChangE-3 mission. *Science*, 2015, 347 (6227): 1226–1229
- [20] Zhao J, Huang J, Qiao L, Huang, Wang J, He Q, Xiao L, 2014. Geologic characteristics of the Chang'E-3 exploration region. *SCIENCE CHINA Physics, Mechanics & Astronomy*, 57 (3): 1–8
- [21] Fa W Z, Zhu M, Liu T, *et al.* Regolith stratigraphy at the Chang'E-3 landing site as seen by Lunar Penetrating Radar. *Geophys Res Lett*, 2015, doi: 10.1002/2015 GL 066537
- [22] Qiao Le, Xiao Zhiyong, Zhao Jiannan, Xiao Long. Subsurface Structures at the Chang'E-3 Landing Site: Interpretations from Orbital and in-situ Imagery Data. *J. Earth Science*. 2016, doi: 10.1007/s12583-015-0655-3
- [23] Ling Z C, Jolliff B L, Wang A L, *et al.* Correlated compositional and mineralogical investigations at the Chang'E-3 landing site. *Nat Commun*, 2015, 6: 8880 doi: 10.1038/ncomms9880 (2015)
- [24] 24-Zhang H, Yang Y Z, Yuan Y, *et al.* In-situ optical measurements of Chang'E-3 landing site in Mare Imbrium 1: Mineral abundances inferred from spectral reflectance. *Geophys Res Lett*, 2015, 42: 6945–6950
- [25] Jin W D, Zhang H, Yuan Y, *et al.* In-situ optical measurements of Chang'E-3 landing site in Mare Imbrium 2: Photometric properties of the regolith. *Geophys Res Lett*. 2015, 42: 8312–8319
- [26] Fei He, Xiao-Xin Zhang, Bo Chen, Mei-Ching Fok, and Yong-Liao Zou (2013), Moon-based EUV imaging of the Earth's Plasmasphere: Model simulations, *JGR*, 118, 7085–7103
- [27] Feng, J. Q., J. J. Liu, F. He, W. Yan, X. Ren, X. Tan, L. P. He, B. Chen, W. Zuo, W. B. Win, Y. Su, Y. L. Zou, C. L. Li (2014), Data processing and initial results from the CE-3 Extreme Ultraviolet Camera, *RAA*, 14, 1664-1673, doi: 10.1088/1674-4527/14/12/014
- [28] Bo, Chen, Kefei, Song, Zhaohui, Li *et al.* (2014), Development and calibration of the Moon-based EUV camera for Chang'E-3, *RAA*, 14, 1654–1663
- [29] Chen, Zheng, Jingsong, Ping, *et al.* (2015), Geocentric position preliminary detection from the extreme ultraviolet images of Chang'E-3, *ApSS*, 358, 28–39
- [30] Yan, Yan, Huaning Wang, *et al.* (2016), Analysis of observational data from Extreme Ultra-Violet Camera onboard Chang'E-3 mission, *ApSS*, 361, 76–83
- [31] He, F., X.-X. Zhang*, X.-Y. Wang, and B. Chen (2015), EUV emissions from solar wind charge exchange in the Earth's magnetosheath: Three-dimensional global hybrid simulation, *JGR*, 120, 138–156, doi: 10.1002/2014JA020521
- [32] He, F., X.-X. Zhang*, B. Chen, M.-C. Fok, and S. Nakano (2016), Determination of the Earth's plasmapause location from the CE-3 EUVC images, *JGR*, 121, 296–304, doi:10.1002/2015JA021863
- [33] Zhang, X.-X., F. He*, B. Chen, M.-C. Fok, S. Nakano (2016), Plasmaspheric evolutions during substorms observed by CE-3 EUVC, *GRL*, under review
- [34] Han, He, Chao, Shen, Huaning, Wang, *et al.* (2016), Plasmaspheric evolutions during substorms observed by CE-3, Scientific reports, under review
- [35] Wang, J., Wu, C., Qiu, Y. L., *et al.* An unprecedented constraint on water content in the sunlit lunar exosphere seen by Lunar-based Ultraviolet Telescope of Chang'E-3 mission. 2015c, *P&SS*, 109, 123
- [36] Wang, J., Cao, L., Meng, X. M., *et al.* Photometric Calibration of the Lunar-based Ultraviolet Telescope for Its First Six Months of Operation on the Lunar Surface, 2015a, *RAA*, 15, 1068
- [37] Wang, J., Meng, X. M., Han, X. H., *et al.* 18-Months operation of Lunar-based Ultraviolet Telescope: a highly stable photometric performance, 2015b, *Ap&SS*, 360, 10
- [38] Qi, Z. X., Yu, Y., Cao, L., *et al.* 2015, Astrometric Support for the Lunar-based Ultraviolet Telescope, *PASP*, 127, 1152
- [39] Meng, X. M., Cao, L., Qiu, Y. L., *et al.* Data processing pipeline for pointing observations of Lunar-based Ultraviolet Telescope, 2015, *Ap&SS*, 358, 47
- [40] Qian, S.B., Zhou, X., Zhu, L. Y., *et al.* LUT Reveals a New Mass-transferring Semi-detached Binary, 2015, *AJ*, 150, 193
- [41] Zhu, L. Y., Zhou, X., Hu, J. Y., *et al.* LUT Reveals an Algol-type Eclipsing Binary With Three Additional Stellar Companions in a Multiple System, 2016, *AJ*, 151, 107
- [42] Liao, W. P., Qian, S. B., Zejda, M., *et al.* Lunar-based Ultraviolet telescope study of the well-known Algol-type binary TW Dra, 2016, *RAA*, accepted.

Main Science Results from Chinese Meridian Project (2014–2015)

WANG Chi on behalf of the Meridian Project team

State Key Laboratory of Space Weather, National Space Science Center, Chinese Academy of Sciences, Beijing 100190

* E-mail: cw@spaceweather.ac.cn

Key words

Space Weather
Ground-based observation

Abstract

The Chinese Meridian Space Weather Monitoring Project (Meridian Project for short) is a ground-based geospace monitoring chain in China. It consists of a chain of 15 ground-based observatories located roughly along 120°E longitude and 30°N latitude. Each observatory is equipped with multiple instruments to measure key parameters such as the baseline and time-varying geomagnetic field, the middle and upper atmosphere and ionosphere from about 20 to 1000 kilometers. This project started collecting data in 2012. Here we will give a brief overview of the Chinese Meridian Project, and present most recent science results mainly in the ionospheric and atmospheric studies.

1 Brief Overview of Chinese Meridian Project

The Chinese Meridian Space Weather Monitoring Project (for short Meridian Project) is a ground-based geo-space monitoring chain in China. (Wang C., 2010). It consists of a chain of 15 ground-based observatories located roughly along 120°E longitude and 30°N latitude. Each observatory is equipped with multiple instruments to measure key parameters such as the baseline and time-varying geomagnetic field, as well as the middle and upper atmosphere and ionosphere from about 20 to 1000 kilometers. This project was funded by China's National Development and Reform Commission as a part of a series of major scientific infrastructure construction projects. Including 15 stations, 38 observing sites and 94 instruments, after 58 months of construction, the world's most extensive and integrated ground-based system for geospace weather monitoring passed the national acceptance review in Beijing on October 23, 2012, started officially to collecting data to support scientific research and space weather forecast.

By the end of 2015, the Chinese Meridian Project has collected more than 3.45 TB geo-space environment data. A total of 185 papers have been published in peer-reviewed journals. The data from the Chinese Meridian Project has been used to support the space weather forecast for Chinese space activities, including the Chinese manned-space flight and lunar missions. The main science results in 2014–2015 will be reviewed in the following sections.

2 Main Science Results

The Meridian Project has provided the scientists with the first-hand monitoring data of the near Earth geospace environment over China. Some important space weather phenomena and dynamical processes have been identified. A series of significant research achievements have been made.

2.1 Concentric Gravity Waves over Northern China Observed by an Airglow Imager Network and Satellites

The first gapless OH airglow all-sky imager network was

established in northern China in February 2012. The network is composed of six all-sky airglow imagers that make observations of gravity waves and cover an area of about 2000 km from east to west and about 1400 km from south to north. An unusual outbreak of Concentric Gravity Wave (CGW) events were observed by the network nearly every night during the first half of August 2013. These events were coincidentally observed by satellite Fengyun-2 (FY-2), Atmospheric Infrared Sounder (AIRS)/Aqua, and Visible Infrared Imaging Radiometer Suite (VIIRS)/Suomi National Polar-orbiting Partnership (NPP). Combination of the ground imager network with satellites provides multilevel observations of the CGWs from the stratosphere to the mesopause region. Xu *et al.* (2015) studied two representative CGW events in August 2013 in details: first is the CGW on the night of 13 August 2013, likely launched by a single thunderstorm. The temporal and spatial analyses indicate that the CGW horizontal wavelengths follow freely propagating waves based on a GW dispersion relation within 300 km of the storm center. In contrast, the observed more distant gravity wave field exhibits a smaller horizontal wavelength of ~20 km, and the analysis strongly suggests this wave field represents a ducted wave. A second event, exhibiting multiple CGWs, was induced by two very strong thunderstorms on 9 August 2013. Multiscale waves with horizontal wavelengths ranging from less than 10 km to 200 km were observed.

2.2 First Report of Sporadic K Layers and Comparison with Sporadic Na Layers at Beijing, China (40.6°N, 116.2°E)

A double-laser beam lidar was successfully developed to simultaneously measure K and Na layers at Beijing (40.6°N, 116.2°E) in 2010 (Jiao *et al.*, 2015). Statistical analysis on the lidar data over 2 years was performed to determine the parameters of sporadic K (K_s) and sporadic Na (Na_s) layers, and different characteristics were found. The average K_s occurrence (2.9%) was lower than that of Na_s (5.9%); the Na_s occurrence had a maximum (19.3%) in May/June and a minimum (1.6%) in January/February, while the K_s occurrence had a maximum (4.9%) in January/February and a minimum (1.0%) in September/October; most K_s peaks tended to appear around 93 km, which was ~2 km lower than that of Na_s (~95 km); the K_s peak density was often at least 1 order of magnitude lower than that of Na_s ; notably, two K_s with high peak

densities ($>1000 \text{ cm}^3$) were observed, which were much higher than K density (15–300 cm^3) reported before. The ascending time of K_s was often longer than its descending time, but an opposite trend occurred for Na_s . During the 152 cases of joint observation for the K and Na layers, 21% (32/152) were cases in which K_s and Na_s events simultaneously occurred, while 79% (120/152) were cases in which only strong K_s or Na_s exhibited.

2.3 Statistical Study of Atmospheric Gravity Waves in the Mesopause Region Observed by a Lidar Chain in Eastern China

Atmospheric gravity wave activities in the mesopause region have been observed and statistically investigated with a sodium lidar chain in eastern China (Gong *et al.*, 2015). In total, there were 471 gravity waves identified from over 5400h of observations at Hainan (19.99°N, 110.34°E), Hefei (31.87°N, 117.23°E), and Beijing (40.47°N, 115.97°E). These waves typically had vertical wavelengths of $\lambda_z=2\sim 4$ km, observed periods of $T_{ob}=1\sim 4$ h, amplitude growth factors of $\beta=-0.025\sim +0.05 \text{ km}^{-1}$, and wave amplitudes of 1.5%~6%. Strong systematic parameter relationships were found, and they agree with the predictions of diffusive filtering theory. Statistical results show that the seasonal variability of gravity wave activity had a summer-maximum and winter-minimum characteristic in the mesopause region over eastern China. A qualitative interpretation is proposed regarding the seasonal and geographic variability observed by the lidar chain, based on analysis of source properties and influences from background wind, which vary by season.

2.4 Comparison of Rotational Temperature Derived from Ground-based OH Airglow Observations with TIMED/SABER to Evaluate the Einstein Coefficients

Ground-based observations of the OH (9–4, 8–3, 6–2, 5–1, and 3–0) band airglows over Xinglong, China (40°24'N, 117°35'E) from December 2011 to 2014 are used to calculate rotational temperatures (Liu *et al.*, 2015). The temperatures are calculated using five commonly used Einstein coefficient data sets. The kinetic temperature from Thermosphere, Ionosphere, Mesosphere, Energetics and Dynamics (TIMED) /Sounding the Atmosphere by Broadband Emission of Radiation (SABER) is completely independent of the OH rotational temperature. SABER temperatures are weighted vertically by weight-

ing functions calculated for each emitting vibrational state from two SABER OH volume emission rate profiles. By comparing the ground-based OH rotational temperature with SABER's, five Einstein coefficient data sets are evaluated. The results show that temporal variations of the rotational temperatures are well correlated with SABER's; the linear correlation coefficients are higher than 0.72, but the slopes of the fit between the SABER and rotational temperatures are not equal to 1. The rotational temperatures calculated using each set of Einstein coefficients produce a different bias with respect to SABER; these are evaluated over each of the vibrational levels to assess the best match. It is concluded that rotational temperatures determined using any of the available Einstein coefficient data sets have systematic errors. In order to get a set of optimal Einstein coefficients for rotational temperature derivation, their ratios from ground-based OH spectra and SABER temperatures are derived statistically using 3 years of data. The use of a standard set of Einstein coefficients will be beneficial for comparing rotational temperatures observed at different sites.

2.5 Mesoscale Field-Aligned Irregularity Structures (FAIs) of Airglow Associated with Medium-scale Traveling Ionospheric Disturbances (MSTIDs)

Sun *et al.* (2015) reported the evolution (generation, amplification, and dissipation) of optically observed mesoscale Field-Aligned Irregularity Structures (FAIs) (~150 km) associated with a Medium-Scale Traveling Ionospheric Disturbance (MSTID) event. There have been no observations of mesoscale FAIs of airglow before. The mesoscale FAIs were generated in an airglow-depleted front of southwestward propagating MSTIDs that were simultaneously observed by an all-sky imager, a GPS monitor, and a digisonde around Xinglong (40.4°N, 30.5° magnetic latitude), China, on 17/18 February 2012. A normalized cross-correlation method has been used to obtain the velocities of mesoscale FAIs and MSTIDs. The mesoscale FAIs had an obvious northwestward relative velocity to MSTIDs main body (about 87.0 m·s⁻¹ in average). The direction of this relative velocity was roughly parallel to the depleted fronts. Furthermore, the evolution of the mesoscale FAIs was mostly controlled by the intensity of the depleted fronts. Occurring in a highly elevated ionosphere that had a total electron content depletion associated with large negative airglow perturbations (-25%), the mesoscale FAIs grew rapidly when they ex-

perienced southeastward wind, which had a speed of about 100 m·s⁻¹ and were measured by a Fabry-Perot interferometer. A northeastward polarization electric field within a depleted airglow front can play a controlling role in the development of the mesoscale FAIs. The electric field can significantly elevate the ionosphere and move the mesoscale FAIs northwestward by the $E \times B$ drift. The processes for the generation and development of the polarization electric field and the mesoscale FAIs, however, need further study.

2.6 Ionospheric Plasma Bubbles Observed Concurrently by Multi-instruments over Low-latitude Station Hainan

Previous studies have shown that the ionospheric "Strong range Spread F" (SSF) closely correlates with the occurrence of scintillations caused by equatorial plasma bubbles. However, there is no report on concurrent observations of SSF and bubbles. Wang *et al.* (2015) discussed two cases of concurrent observations with a DPS4 digisonde and a collocated scintillation monitor at the low-latitude station Hainan (19.5°N, 109.1°E), and compared the observations with in-situ ion density measurements made by the ROCSAT-1 satellite. Two case studies were made for 10 and 23 April 2004, respectively. In both cases, the SSF occurred before midnight and lasted more than 3.5 hours. The scintillations started earlier and ended later than the SSF. Concurrently, the ROCSAT-1 satellite observed plasma bubbles over Hainan station. In the first case, two bubbles were observed by the satellite with east-west sizes of more than ~200 km over Hainan station. Two bubbles were also observed in the second case with east-west extensions of about 220 km and 35 km, respectively. For the first time, direct observational evidence is provided for the causal relationship between equatorial plasma bubbles and the concurrent occurrence of SSF and strong scintillations.

2.7 Ionospheric and Geomagnetic Disturbances Caused by the 2008 Wenchuan Earthquake: A Revisit

Previous works have shown that Co-seismic Ionospheric Disturbances (CIDs) after the tsunamigenic 2011 Tohoku earthquake (Tohoku EQ, Mw9.1) covered a vast area and were observed thousands of kilometers away from the epicenter. For the purpose of making a comprehensive comparison between powerful oceanic and inland EQs, Zhao and Hao (2015) conducted a retrospective investi-

gation of CIDs and geomagnetic responses to the 2008 Wenchuan EQ (Mw7.9) using a combination of techniques, total electron content, HF Doppler, and ground magnetometer. It is the very first study to present CIDs recorded by different techniques at co-located sites and profiled with regard to changes of both ionospheric plasma and current (geomagnetic field) simultaneously. The integrated observation also shows that (1) in the Wenchuan case, most of the ionospheric and geomagnetic disturbances were observed within 1000 km distance which is far less than the Tohoku case; (2) two groups of CIDs were found with maximum amplitudes in the direction of azimuth 150° and 135° , respectively; and (3) the geomagnetic changes were only registered by three magnetometers located to the east and southeast of the epicenter. All the facts indicate that the main directional lobe of Wenchuan EQ energy propagation is to southeast and perpendicular to the direction of the fault rupture, but this kind of directivity is not that distinct in the Tohoku case. It is suggested that the different fault slip (inland or submarine) affecting the way of couplings of lithosphere with atmosphere may contribute to the discrepancies between the two events.

2.8 Seasonal Variations of MLT Tides Revealed by a Meteor Radar Chain Based on Hough Mode Decomposition

Seasonal variations of different tides in the mesosphere and lower thermosphere are investigated from wind observations of a meteor radar chain on the basis of Hough mode decomposition (Yu *et al.*, 2015). First, the observed winds are decomposed into different (diurnal, semidiurnal, and terdiurnal) tidal components. Different seasonal patterns are revealed for each component. Pronounced Semiannual Oscillation (SAO) is presented in the diurnal component, while latitude-dependent seasonal variation is found in the semidiurnal and terdiurnal components. At the low/mid-latitude stations, the semiannual/annual oscillation is relatively stronger. Then, Hough mode decomposition is utilized to extract the dominant tidal modes of each decomposed component. It is found that each component is dominated by one of its symmetric tidal modes with strong seasonal dependency. Apparent SAO is observed in the dominant (1, 1) mode; (2, 4) mode is strong in the autumn and winter months (after the September equinox). Based on the extracted results we further map the three-dimensional distribution (latitude \times altitude \times season) of each tidal component. The mapped

results are finally compared with the corresponding values observed by the Thermosphere Ionosphere Mesosphere Energetics and Dynamics Doppler Interferometer (TIDI) and modeled from the Global Scale Wave Model (GSWM). Each mapped tidal component agrees well with corresponding TIDI observation in the seasonal variation. Meanwhile, coincidences are found in the seasonal dependency of the diurnal component between the mapped values and the modeled results from GSWM, while difference between them exists in that of the semi-diurnal one.

2.9 Strong Correlation between Quasiperiodic Echoes and Plasma Drift in the E Region

Simultaneous observations of QuasiPeriodic (QP) echoes and plasma drift in the ionospheric E region were conducted in Fuke (19.5°N , 109.1°E), Hainan province, China, to investigate the QP striation tilts under varying plasma drift conditions (Chen *et al.* 2015). The E region Field-Aligned Irregularities (FAIs), observed using the Hainan VHF radar, and the drift velocities of the plasma blobs in the E_s layer, recorded by the Hainan Digisonde operating in drift mode, are reported. The QP echoes and drift data recorded during the entire year of 2013 were analyzed and compared. A surprising consistency between the striation tilt of the QP echoes and the drift direction of the plasma blobs was discovered. A negative echo striation of the QP FAIs was recorded when the measured drift direction of the plasma blobs was southward, whereas a positive echo striation was observed during the northward drift. Furthermore, the echo trace was continuous, whereas the QP striation changed from negative to positive, and vice versa. Thus, it can be concluded that the morphology of the QP echoes may be controlled by the background wind fields in the E region. The northward/southward-drifting striated FAIs in the observation region of a coherent scatter radar might induce the positive/negative QP echo striation in the range-time-intensity plots.

2.10 Diurnal Variation of Winter F Region Ionosphere for Solar Minimum at both Zhongshan Station, Antarctica and Svalbard Station, Arctic

Diurnal variation features of wintertime F_2 peak electron density (N_mF_2) representative for solar minimum at both Zhongshan station, Antarctica, and Svalbard station are compared and analyzed (Zhang *et al.*, 2015). Both sta-

tions are located around cusp latitude and are almost on the same geomagnetic meridian plane in both hemispheres. For quiet time period, typical N_mF_2 diurnal variation features at Svalbard station show double peaks with a decrease of N_mF_2 around magnetic local noon (\sim UT + 3 h); N_mF_2 diurnal variation at Zhongshan station shows one major peak around magnetic local noon (\sim UT+ 1.75 h), followed by a sharp decrease of N_mF_2 , and a subpeak around 15:00 UT. Simulation results of the high-latitude ionospheres in both hemispheres agree well with observations at both stations. It is found that the major difference of N_mF_2 variation between both stations can be explained by the unique location of each station relative to the sunlit demarcation line during the day. For quiet time period, photoionization from lower latitude contributes to the major peak of N_mF_2 in the diurnal variation at Zhongshan station, while the interaction between horizontal convection and auroral precipitation is the main cause for N_mF_2 variation at Svalbard station. For active time period, both stations show the increase of N_mF_2 due to transportation of higher plasma density from lower latitudes on the dayside with the expansion of the polar cap and the additional ionization from precipitating soft electrons.

2.11 GIC Due to Storm Sudden Commencement in Low-latitude High-voltage Power Network in China

The impact of Geomagnetically Induced Currents (GIC) on the power networks at middle and low latitudes has attracted attentions in recent years with the increasing of large-scale power networks. Zhang *et al.* (2015) reported the GIC monitored at two low latitude 500 kV substations of China during the large storm event of 17 March 2015. The GIC due to the SSC was much higher than that during the storm main phase. This phenomenon is more likely to happen at low latitude locations, highlighting the importance of SSC in inducing GIC at low latitude power networks. Furthermore, a global MHD model was run to simulate the GIC during this event by using the solar wind observation as input. The model results reproduced the main features of the GIC. It is also shown that the eastward component of the geo-electric field is dominant for low latitude locations due to the SSC events; topology and electrical parameters of the power grids make significant differences in the GIC levels.

3 Summary

The Chinese Meridian Project has been operated smoothly so far for more than 3 years, and provided valuable space

environment parameters along 120°E longitude and 30°N latitude in China. Significant scientific achievements have been made by the Chinese space weather community, mainly in the ionospheric and atmospheric studies. With the accumulation of data, combined with spaceborne observations and other ground-based observations, more science results and better understanding of the geospace are expected. Furthermore, Chinese Meridian Project also provides real-time data for space weather warning and predictions.

References

- [1] Wang, C. New Chains of Space Weather Monitoring Stations in China. *Space Weather*, 2010, 8, S08001, doi:10.1029/2010SW000603
- [2] Xu *et al.* Concentric gravity waves over northern China observed by an airglow imager network and satellites. *J. Geophys. Res. Atmos.*, 2015, 120, 11,058–11,078, doi: 10.1002/2015JD023786
- [3] Jiao *et al.* First report of sporadic K layers and comparison with sporadic Na layers at Beijing, China(40.6°N, 116.2°E). *J. Geophys. Res.*, 2015, 120(6), 5214–5225
- [4] Gong *et al.* Statistical study of atmospheric gravity waves in the mesopause region observed by a lidar chain in eastern China. *J. Geophys. Res. Atmos.*, 2015, 120, doi:10.1002/2014JD022673
- [5] Liu, W., J. Xu, A. K. Smith, and W. Yuan. Comparison of rotational temperature derived from ground-based OH airglow observations with TIMED/SABER to evaluate the Einstein coefficients. *J. Geophys. Res. Space Physics*, 2015, 120, doi:10.1002/2015JA021886
- [6] Sun, L., J. Xu, W. Wang, X. Yue, W. Yuan, B. Ning, D. Zhang, and F. C. de Meneses. Mesoscale field-aligned irregularity structures (FAIs) of airglow associated with medium-scale traveling ionospheric disturbances (MSTIDs). *J. Geophys. Res. Space Physics*, 2015, 120, 9839–9858, doi:10.1002/2014JA020944
- [7] Wang, G. J., J. K. Shi, B. W. Reinisch, X. Wang, and Z. Wang. Ionospheric plasma bubbles observed concurrently by multi-instruments over low-latitude station Hainan. *J. Geophys. Res. Space Physics*, 2015, 120, doi:10.1002/2014JA020245
- [8] Zhao, B., and Y. Hao. Ionospheric and geomagnetic disturbances caused by the 2008 Wenchuan earthquake: A revisit. *J. Geophys. Res. Space Physics*, 2015, 120, 5758–5777
- [9] Yu, Y., W. Wan, Z. Ren, B. Xiong, Y. Zhang, L. Hu, B. Ning, and L. Liu. Seasonal variations of MLT tides revealed by a meteor radar chain based on Hough mode decomposition. *J. Geophys. Res. Space Physics*, 2015, 120, 7030–7048
- [10] Yu, Y., W. Wan, Z. Ren, B. Xiong, Y. Zhang, L. Hu, B. Ning, and L. Liu. Seasonal variations of MLT tides revealed by a meteor radar chain based on Hough mode decomposition. *J. Geophys. Res. Space Physics*, 2015, 120, 7030–7048
- [11] Chen, G., H. Jin, X. Huang, D. Zhong, C. Yan, and G. Yang. Strong correlation between quasiperiodic echoes and plasma drift in the E region. *J. Geophys. Res. Space Physics*, 2015, 120, doi:10.1002/2015JA021566
- [12] Zhang, B.-C., S.-G. Yang, S. Xu, R.-Y. Liu, I. Häggström, Q.-H. Zhang, Z.-J. Hu, D.-H. Huang, and H.-Q. Hu. Diurnal variation of winter F region ionosphere for solar minimum at both Zhongshan Station, Antarctica, and Svalbard Station, Arctic. *J. Geophys. Res. Space Physics*, 2015, 120, doi:10.1002/2015JA021465
- [13] Zhang J.J., C. Wang, T.R. Sun, C.M. Liu, and K.R. Wang (2015), GIC due to storm sudden commencement in low-latitude high-voltage power network in China: Observation and simulation. *Space Weather*, 13(10), 643–655

The Space Sciences and Application Projects in Space Laboratory

GU Yidong, Gao Ming, Zhao Guangheng

Technology and Engineering Center for Space Utilization, Chinese Academy of Sciences, Beijing 100094

* E-mail: zhangwei@csu.ac.cn

Key words

Space sciences and application
Tiangong-2
Tianzhou-1
Space Laboratory
Microgravity

Abstract

Space sciences and application projects arranged in Tiangong-2 space laboratory and Tianzhou-1 cargo ship have been described in detail, covering research areas of the fundamental physics, space astronomy, microgravity fluid physics and materials science, space life science, and earth science. These experiments and researches will hopefully produce great scientific results and social benefits in several fields, including: universe evolution, quantum communication, material development, global climate change and earth environment, etc.

Over a dozen of space sciences and application projects are arranged in Tiangong-2 space laboratory and Tianzhou-1 cargo ship, covering research areas of fun-

damental physics, space astronomy, microgravity fluid physics and material science, space life science and Earth science. The projects are described as follows.

Table 1 Space sciences and application projects onboard Tiangong-2 and Tianzhou-1

Research Area	Project	Platform
Fundamental physics	Cold atom clock experiment in space	Tiangong-2
	Quantum key distribution experiment	Tiangong-2
Space Astronomy	Electrostatic levitation accelerometer and active vibration control experiment	Tianzhou-1
	Polarization detection of gamma-ray burst	Tiangong-2
Microgravity fluid physics and materials science	Thermo-capillary convection in liquid bridge	Tiangong-2
	Two-phase fluid experiment	Tiangong-2
Space life science	Multiple sample materials processing	Tianzhou-1
	Higher plants cultivation experiment	Tiangong-2
Earth science	The influence of microgravity on cell proliferation and differentiation	Tianzhou-1
	Multi-angle polarization and wide-band spectrum imager	Tiangong-2
Earth science	Interferometry imaging radar altimeter	Tiangong-2
	Multi-band ultraviolet limb imager	Tiangong-2

1 Fundamental Physics

(1) Cold Atom Clock Experiment in Space

The space-borne cold atom clock could get precise

time frequency signal because of microgravity environment in which the temperature of cold atoms could be down to the order of $\mu\text{K}^{[1]}$. In this experiment, the rubidium atoms are utilized under ultra-high vacuum condi-

tion^[2] and are captured by laser while cold atoms are led into microwave cavity. Two interactions take place both at head and tail sides of microwave cavity to form Ramsey interference fringe. Since there is no free fall of atomic cluster under microgravity condition, the period of interaction between cold atoms and microwave is remarkably lengthened. Therefore, the frequency stability of 2 or 3 orders of magnitude higher than on the ground can be achieved. The number of cold atoms is more than 10^6 . The predicted Ramsey line width will be 0.1–0.2 Hz. The frequency stability of clock will hopefully achieve the order of 10^{-16} . It will be the first space cold atom clock experiment in the world. The Ramsey curve of cold atom clock taken on the ground is shown in Fig.1.

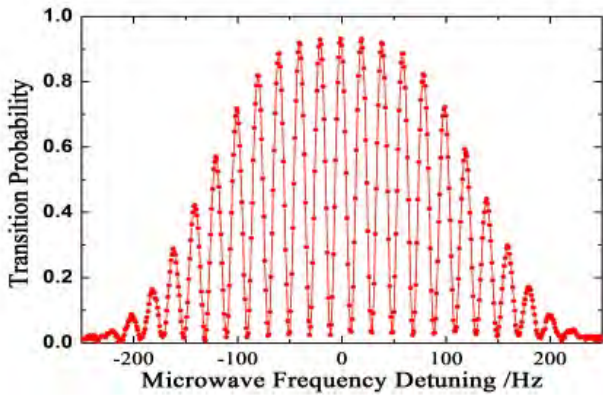


Fig. 1 Transition probability as a function of microwave frequency for ⁸⁷Rb on the ground

(2) Quantum Key Distribution Experiment

In this experiment, the photons as quantum key will be sent from LRO to the ground by utilizing named “Decoy State Method” in which the photons are modulated in

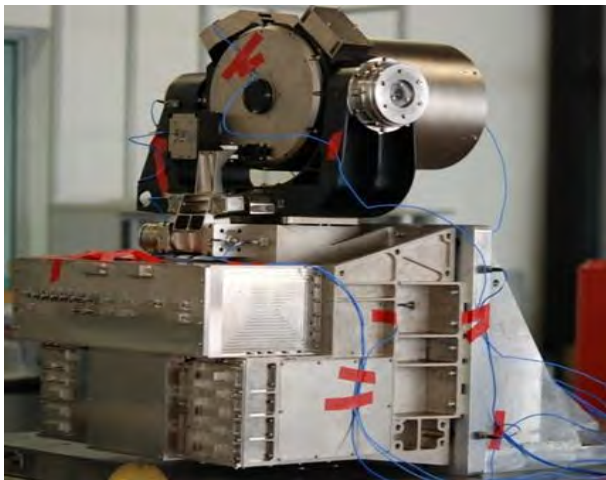


Fig. 2 Space to ground quantum key distribution experiment facility

polarization angle. The key technology on the generation, distribution and distillation of quantum keys and the stabilization of optical channels^[3-4] will be demonstrated. The dynamic accuracy of onboard ATP is better than $10 \mu\text{rad}$. Raw quantum key rate will be 3 Kbps. Space to ground laser communication will also be implemented with bit rate of 1.6 Gbps.

(3) Electrostatic Levitation Accelerometer and Active Vibration Control Experiment

The aim of this project is to explore potential “non-Newtonian force in 5–10 μm range” in microgravity^[5] which is predicted by Extra Dimension Theory, and study the “hierarchy problems” of grand unified theory. The resolution of electrostatic levitation accelerometers is better than $3 \times 10^{-10} \text{ m} \cdot \text{s}^{-2} \cdot \text{Hz}^{-1/2}$ ^[6]. In order to reduce the mechanical inference of various vibration sources, an active electromagnetic vibration attenuation device is developed as well.

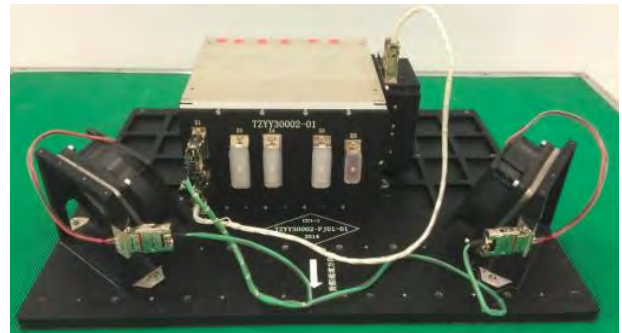


Fig. 3 Electrostatic levitation accelerometer and active vibration attenuation device

2 Space Astronomy - Polarization Detection of Gamma-ray Burst

The Gamma-Ray Burst Polarimeter (POLAR), is a novel compact space-borne polarimeter designed for a precise measurement of hard X-ray/Gamma-ray polarization and optimized for the polarization detection of the prompt emission of Gamma-Ray Bursts (GRB) in the energy range of 50–500 keV^[7]. In this experiment, novel polarization measurement approach is utilized, which inversely calculates the angle of incidence and degree of polarization based on the trajectory of recoil electrons generated by gamma photon’s Compton scattering. The detailed measurement of the polarization of GRB will lead to a better understanding of the geometry of radiation region and emission mechanisms. Due to its large effective area, POLAR will be able to reach a minimum detectable po-

larization of less than 10% for GRBs with a flux large than $3 \times 10^{-5} \text{ erg} \cdot \text{cm}^{-2}$ and open a new window for high energy astronomy. This instrument is developed under international collaboration of China, Switzerland and Poland. The calibration result of modulation factor of POLAR is shown in Fig. 4^[8].

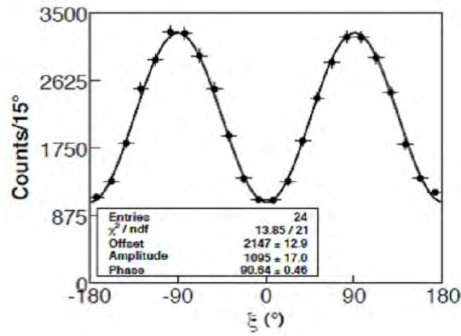


Fig. 4 Modulation curve measured with 100% polarized hard X-ray beam at 200 keV

3 Microgravity Fluid Physics and Materials Science

(1) Thermo-capillary Convection in Liquid Bridge

The experiment is focused on thermo-capillary convection instability, turning and second turning, temperature oscillation, and the mechanism in liquid bridge with large Prandtl number^[9-10]. The experimental facility consists of liquid bridge and pulling mechanism, liquid storage and injection unit, liquid bridge clearance unit, temperature controllers, etc. The aspect ratio and volume ratio could be adjusted on a liquid bridge with diameter of 20 mm.

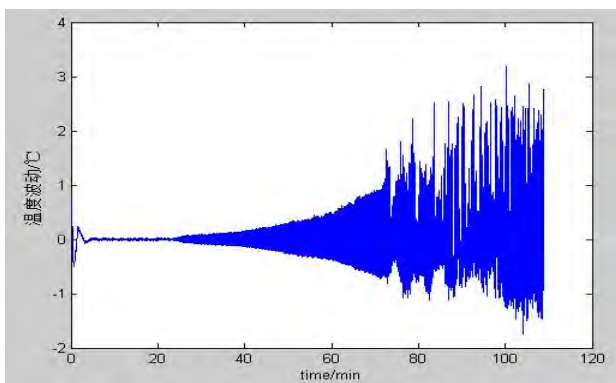


Fig. 5 Temperature oscillation curve measured from liquid bridge experiment on the ground

(2) Two-phase Fluid Experiment

The purpose of this project is to investigate the phase transition kinetics of liquid evaporation and condensation,

gas-liquid-solid contact dynamics as well as two phase fluid transportation in microgravity, and demonstrate key technologies related to two-phase system experiment rack of CSS. It will provide theoretical foundation and data for fluid management of spacecraft, two-phase fluid heat transfer with high efficiency, and industrial applications on the ground^[11]. The evolution of liquid film evaporation thermal patterns and heat flux measured at heating solid substrate on the ground is shown in Fig.6^[12].

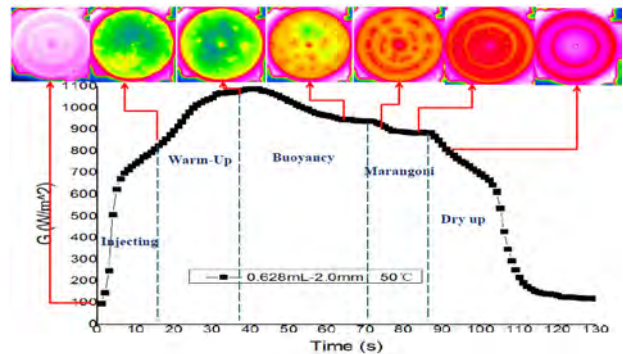


Fig. 6 Evaporation thermal patterns and heat flux during the liquid film evaporation on the ground

(3) Multiple Sample Materials Processing

A Multiple sample Materials Processing Furnace (MMPF) with double zone resistance heater provides opportunity for various material processing and formation mechanism study^[13-14]. The sample candidates include semiconductor, optoelectronics materials, metal alloys and metastable materials, functional single-crystal, nanometer and composite materials. The furnace is with ampoule number of 6 each batch, ampoule size of 16 mm × 260 mm, temperature range of 500–950°C, temperature gradient of 6–45°C·cm⁻¹ and temperature stability of ± 0.5°C. The movement speed of material sample is 0.5–100 mm·h⁻¹. In the experiment, astronauts will replace the samples in orbit and send completed experimental samples back to Earth for analysis. The structure of MMPF is depicted in Fig.7.

4 Space Life Science

(1) Higher Plants Cultivation Experiment

The aim of this project is to study the growth and development laws of higher plants from seed to seed in gravity and explore the photoperiod induced florescent regulation and adjusting mechanism of both long day plants and short day plans in microgravity condition. A long day plant (*Arabidopsis thaliana*) and a short day

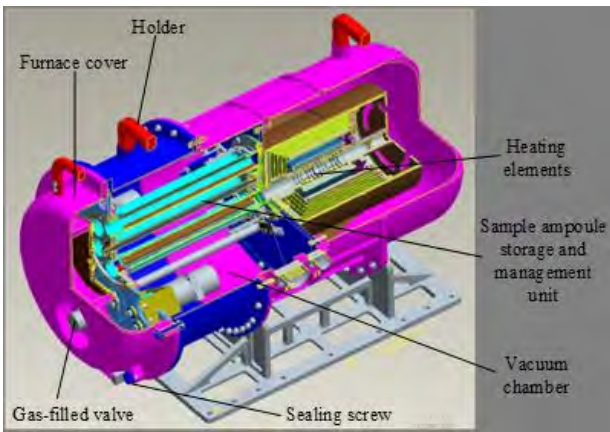


Fig. 7 Structure of Multiple sample Materials Processing Furnace (MMPF)

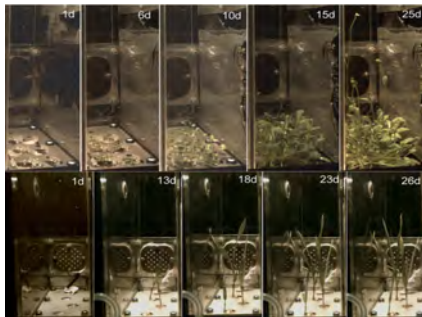


Fig. 8 Growing states of Arabidopsis thaliana and rice in the plant incubator on the ground

plant (rice) are respectively used as samples in the experiments and an exclusive plant incubator, which has the temperature range of 17–28°C, humidity range of 60%–100% and adjustable illumination intensity and cycle, is also developed for this project. The most significant changes during the whole plant growth procedure appear from planting to blooming, because of the influences from both environment and internal spreading signals. It is a new way of investigation to carry out experiments in mixed conditions of microgravity and varying rhythm in order to understand the mechanism.

(2) Influence of Microgravity on Cell Proliferation and Differentiation

This project will conduct eight animal cell experiments in space, including the differentiation of mammal stem cell in microgravity condition, the development of different embryonic stem cells, pathogenetic mechanism and countermeasures of metabolism disturbance of osteoblast and osteoclast, etc. Besides the scientific meaning in cytological research, this project also has the medical research potential and the prospect of application. For instance, the research result of stem cells can be used for

treatments of heart and liver disease, the study of embryonic stem cells can provide a new way to explore the application potential in tissue engineering and regenerative medicine, and the learning of bone cells can be helpful to prevent and heal bone diseases in space and on the ground and even support the development of molecular targeted drugs.

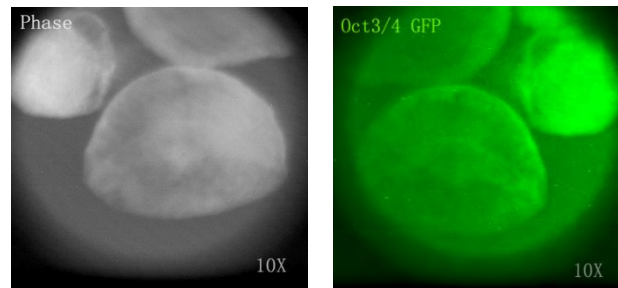


Fig. 9 Mouse embryonic stem cell observed by fluorescence microscope (right)

5 Earth Science

(1) Multi-angle Polarization and Wide-band Spectrum Imager

It consisted of two imagers. One is wide-band imager, which is able to measure the precise spectral information of oceans, atmosphere and lands, with spectrum range of 0.4–10 μm, spectral resolution of 5–10 nm (VNIR), imaging resolution of 100 m(VNIR)–400 m (SWIR and LWIR), FOV of 42° and swath of 300 km. The other is multi-angle polarization imager using super wide-angle optics and filter wheel technique which achieves wide coverage of 87.6° (770 km), image resolution of 3 km, and the polarization observation capability with angle measurement number of 12. The tungsten halogen lamp, neophane glass, and black body are used for in-orbit spectrum and radiometric calibration in VNIR, SWIR and LWIR channel of wide-band imager respectively to issue application with quantitative determination. The wide-band spectrum imager and multi-angle polarization will be utilized for the study of Earth environment and the application of remote sensing of land, ocean and atmosphere. Fig.10 shows an image in VNIR of spectrum imager on the ground.

(2) Interferometry Imaging Radar Altimeter (InIRA)^[15–16]

A new generation of radar altimeter, which integrates synthetic aperture, interferometry and height tracking technology, is developed to measure, in a wide swath, the ocean environmental factors including the Sea Surface



Fig. 10 Outdoor image in VNIR of spectrum imager

Height (SSH), the Significant Wave Height (SWH) as well as the Sea Surface Wind Speed (SSWS), and study the ocean dynamics. It also provides important data for the study of global climate change and protection of maritime activities. The principle of InIRA is to use high-accuracy capability of interferometric phase measurement owing to a small off-nadir observation geometry with short baseline and high coherent two-channel receiving, to accurately retrieve the three dimensional information of the target with the help of waveform tracking. To improve the azimuth resolution, synthetic aperture processing is adopted. The measurement parameters of InIRA are swath of 30 km, image resolution of 100 m \times 100 m, measurement accuracy of SSH of 10 cm, SWH of 10 cm or 10%, SSWS of ± 2 m \cdot s $^{-1}$. Fig. 11 shows the interferometric image of water surface measured by InIRA.

(3) Multi-band Ultraviolet Limb Imager

This instrument will obtain ultraviolet and wider bandwidth spectrum emitted from Earth atmosphere by limb observation. There are two limb spectrum Imagers. An Ring shaped Imager (RI) is with field of view of 360°, and 3 spectrum channels of 265 nm (± 10 nm), 295 nm (± 10 nm), 360 nm (± 20 nm). The geometric resolution is

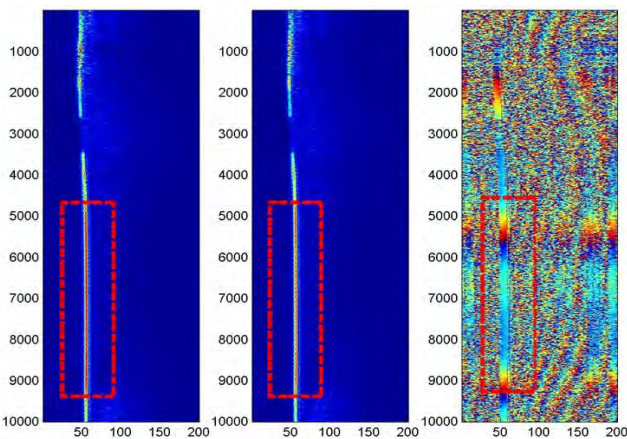


Fig. 11 Interferometric images of water surface obtained by InIRA

4 km. The other is a Front view limb Imager (FI) to observe along with the flight direction of spacecraft. It is with field of view of $0.05^\circ \times 3.3^\circ$, geometric resolution of 4 km, bandwidth from 280 nm to 1000 nm, spectrum resolution of 1.8 nm@290 nm. The ultraviolet limb imager could obtain 3D dynamic distribution of air density, ozone and aerosol in Earth atmosphere, etc. The study will improve understanding the interactions of different layers of atmosphere, and the relationship between solar activity and atmosphere processes^[17-18].

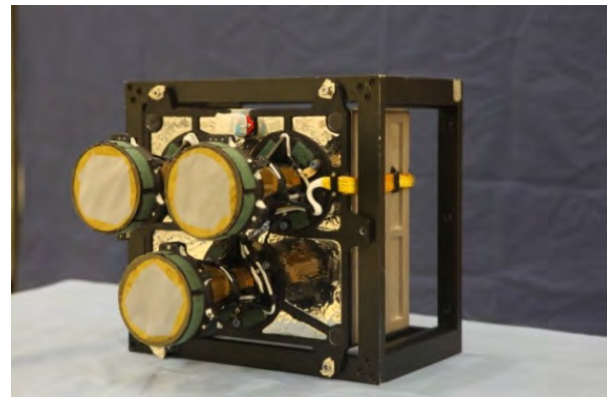


Fig. 12 The ring shaped spectrum imager in the multi-band ultraviolet limb imager

At present, all the payloads supporting space sciences and application in Tiangong-2 space laboratory have already been completed and are ready for launch, while the prototype development of payloads in Tianzhou-1 cargo ship have been finished.

References

- [1] Qiuzhi Qu, Bin Wang, Desheng Lu, Jianbo Zhao, Meifeng Ye, Wei Ren, Jingfeng Xiang, and Liang Liu. Integrated design of a compact magneto-optical trap for space applications. *Chin. Opt. Lett.*, 2015, 13(6): 061405. doi:10.3788/COL201513.061405
- [2] Wei Ren, Jingfeng Xiang, Yuantao Zhang, Bin Wang, Qiuzhi Qu, Jianbo Zhao, Meifeng Ye, Desheng Lü, Liang Liu. Development of an ultra-high vacuum system for space cold atom Clock. *Vacuum*, 2015, 116(6): 54. doi:10.1016/j.vacuum.2015.03.001
- [3] Wang J Y, Yang B, Liao S K, Zhang L, Shen Q, Hu X F, Wu J C, Yang S J, Jiang H, Tang Y L, Zhong B, Liang H, Liu W Y, Hu Y H, Huang Y M, Qi B, Ren J G, Pan G S, Yin J, Jia J J, Chen Y A, Chen K, Peng C Z, Pan J W. Direct and full-scale experimental verifications towards ground-satellite quantum key distribution. *Nature Photonics* 7, (2013), 387-393
- [4] Nauerth S, Moll F, Rau M, Fuchs C, Horwath J, Frick S, Weinfurter H. Air-to-ground quantum communication. *Nature Photonics*, 2013, 7: 382-386
- [5] Guan Shengguo, Tu Liangcheng, Zhou Zebing, Luo Jun. Proposal for



- testing non-Newtonian gravitational force in space. *J. Jpn. Soc. Microgravity Appl. Special Issue: Sixth Japan/China Workshop on Microgravity Sciences*, 2007, 24: 86-90
- [6] Tu H B, Bai Y Z, Zhou Z B, Liu L, Cai L, Luo J. Performance measurements of an inertial sensor with a two-stage controlled torsion pendulum. *Class Quantum. Grav.*, 2010, 27: 205016
- [7] Orsi S, Hass D, Hajdas W, et al. Response of the Compton polarimeter POLAR to polarized hard X-rays. *Nuclear Instruments and Methods in Physics Research A*, 2011, 648: 139-154
- [8] Xiao H L, Hajdas W, Bao T W, et al. Calibration of Gamma-ray Burst Polarimeter POLAR, arXiv:1512.02784
- [9] Hu W R, Tang Z M. Influence of liquid bridge volume on the floating zone convection. *Crystal Research and Technology*, 2003, 38: 627-634
- [10] Zhu P, Duan L, Kang Q. Transition to chaos in thermocapillary convection. *International Journal of Heat and Mass Transfer*, 2013, 57: 457-464
- [11] Liu Qiusheng, Nie Yuxing, Feng Meifu, Hu Wenrui. Progress on Microgravity Sciences in China. *Chin. J. Space Sci.*, 2006, 26 (Supp): 150-159
- [12] Chen X, Zhu Z Q, Liu Q S, Wang X W. Thermodynamic Behaviors of Macroscopic Liquid Droplets Evaporation from Heated Substrates. *Microgravity Science and Technology*, 2015, 27:353-360, Online (DOI 10.1007/s12217-015 -9426-0)
- [13] Liu Y, Ai F, Feng C, Yu Q, Tan X. *Space Technology*, 2006, 26: 124-126
- [14] Liu Y, Ai F, Zhou Y, Pan X, Jin W. *Journal of the Japan Society of Microgravity Application*, 2007, 24(1): 23-25
- [15] Yunhua Zhang, Xiangkun Zhang, et al., An Interferometric Imaging Altimeter Applied for both Ocean and Land Observation, *IGARSS 2007, Barcelona*, 2007: 3821-3824
- [16] Yunhua Zhang, Wenshuai Zhai, et al. Experimental Demonstration for the Attitude Measurement Capability of Interferometric Radar Altimeter, 15th International Radar Symposium, IRS-2014 Conferences Proceedings, pp.422-425, Gdansk, Poland, 2014: 424-427
- [17] Yu Xiangyang, Wang Shurong, Huang Yu, Lin Guangyu. *Acta Optica Sinica*, 2012, 32(12): 1211004
- [18] Xue Qingsheng, Lin Guanyu, Chen Wei. *Chinese Journal of Scientific Instrument*, 2012, 33(5): 1167-1173

Status of the Hard X-ray Modulation Telescope (HXMT) Project

LU Fangjun

Institute of High Energy Physics, Chinese Academy of Sciences, Beijing 100049

* E-mail: lufj@ihep.ac.cn

Key words

Hard X-ray Modulation Telescope (HXMT)
Payloads of HXMT
Calibration

Abstract

The Hard X-ray Modulation Telescope (HXMT) is China's first X-ray (1–250 keV) astronomical satellite officially approved in 2011. It will scan the Galactic plane to detect new transient sources and do pointed observations of X-ray sources to study their spectra and multi-wavelength temporal properties. Now the flight model of the satellite is in the final testing stage, and the expected launch date is late 2016.

1 Scientific Objectives

HXMT will do both scan imaging and pointed observations in 1–250 keV. The main targets of the scanning observation are the Galactic plane, the Galactic center, and the Galactic bulge regions. It is anticipated that in the scan a large number of new transient events will be detected, while with the pointed observations the multiwavelength X-ray variabilities and the broad band X-ray spectra of some bright sources can be studied in details. Specifically, HXMT has the following scientific objectives:

- Scan the Galactic Plane, Galactic Center and Galactic Bulge regions frequently, to find new transient sources and the new activities of known sources.
- Observe the Galactic X-ray binaries with high cadence, to understand the mechanism behind their state transitions.
- High statistics observations of bright Galactic sources, to study the fundamental physics in accretion black holes and neutron stars.
- Detect a large number of gamma-ray bursts in 300–3000 keV, and to search for the electro-magnetic counterparts of gravitational wave events.

2 Payloads onboard HXMT

HXMT carries three slat-collimated instruments, the High Energy X-ray Telescope (HE), the Medium Energy X-ray Telescope (ME), and the Low Energy X-ray Telescope (LE). HE consists of 18 NaI/CsI phoswich modules (main detectors) with a total detection area of about 5000 cm². Its energy band is 20–250 keV. ME uses 1728 Si-PIN detectors read out by ASIC. The energy coverage of ME is 5–30 keV, and the total detection area is 952 cm². LE uses Swept Charge Device (SCD) as the detectors, which is sensitive in 1–15 keV with a total detection area of 384 cm².

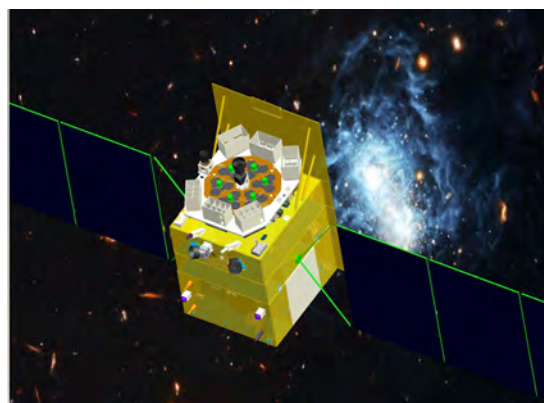


Fig. 1 An illustration of the HXMT satellite

3 Development of the Flight Models

We started the development of the HXMT flight models in 2014. By the end of 2015, all the payloads except two out of the three ME detector boxes, had been finished, and those two ME detector boxes were integrated to the

satellite at the beginning of May 2016. On May 31rd, the satellite is in the final vacuum test, which will be finished in middle June as expected. Figure 2 shows the 18 HE main detectors and their energy resolution at 59.5 keV. Figure 3 shows the payload assembly in the process mounting to the satellite.

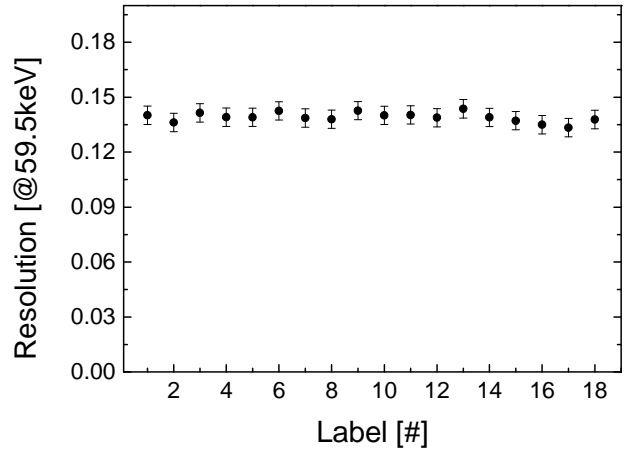


Fig. 2 The 18 HE main detectors that will be onboard HXMT (left panel) and their spectral resolution at 59.5 keV (right panel)



Fig. 3 The payload assembly of HXMT in the process of integrating to the satellite

4 Calibration

All the X-ray detectors of HXMT had been calibrated before they were integrated to the satellite. Two calibration facilities working in 1–30 keV and 15–150 keV respectively have been built. Both of them use X-ray machines to generate X-ray radiation and double-crystal mono-chromators to get the mono-energy X-ray beams. The formal facility (Figure 4, left panel) is for LE and ME, while the later one (Figure 4, right panel) is for HE.

As examples of the calibration results, Figure 5 shows the detection efficiency curves of HE main detectors and Figure 6 shows the energy-channel relation as a function of working temperature of an LE module.

5 Future Plan

It is expected that the satellite will be ready in late September 2016, and then to be transported to the Jiuquan Satellite Launching Center. The scheduled launch time is in late November of 2016.



Fig. 5 The calibration facilities for HXMT in 1–30 keV (left panel) and 15–150 keV (right panel)

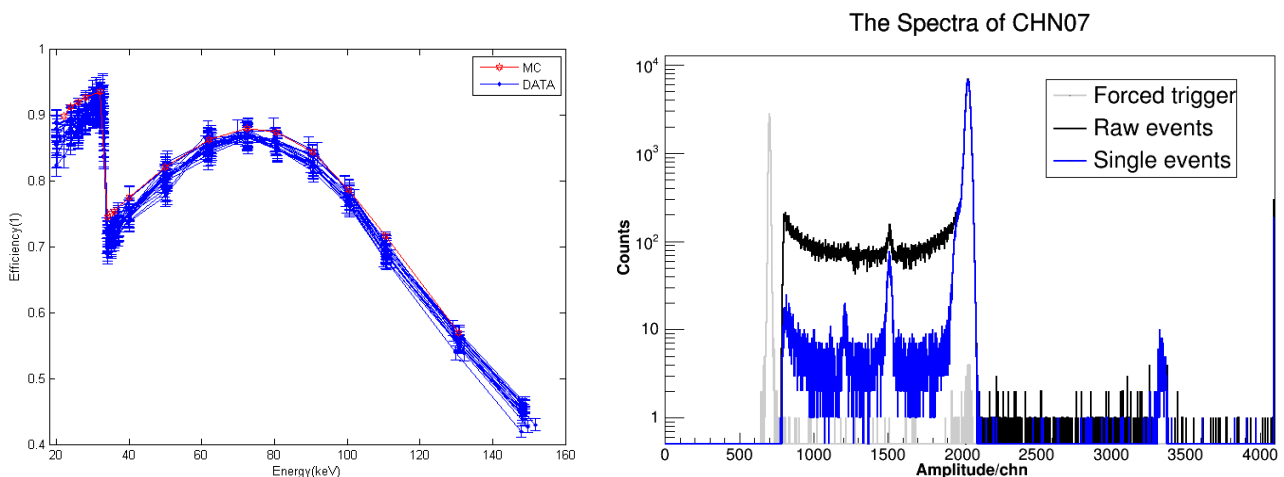


Fig. 6 The detection efficiency curves of the 18 HE main detectors (left panel) and the response of an LE detector at -45°C to the 4.5 keV photons (right panel). The black line in the right panel represents the measured spectrum with all events included, the blue line represents the one only with the single pixel events included, and the grey line is from the forced trigger events that represent the system background

Progress of Microgravity Experimental Satellite SJ-10

HU Wenrui¹, TANG Bochang², KANG Qi¹

1. Institute of Mechanics, Chinese Academy of Sciences, Beijing 100190

2. Chinese Academy of Space Technology, Beijing 100094

Key words

Scientific satellite
SJ-10
Microgravity science
Space life science
Recoverable satellite

Abstract

The program SJ-10 is one of the scientific satellite programs in the Strategic Priority Research Program on Space Science, the Chinese Academy of Sciences, and was launched in April 6, 2016. There are totally 19 scientific payloads with a payload of multi-function furnace for 8 materials research missions and a payload of three-dimensional cell culture for the neural stem cell mission and the hematopoietic stem cell mission respectively. The recoverable satellite consists mainly of two capsules: a recoverable capsule was recovered on April 18, 2016 with all payloads of life science in addition of the payload of the multi-function furnace and the payload for measurements of Soret Coefficients of Crude Oil (SCCO), and an un-recoverable capsule persisted to work in additional 3 days of all other physical payloads. The experiments were operated via tele-operations, and all experimental data were received by the ground station in real time. The satellite was launched on April 6, 2016, and the recoverable capsule returned on the ground on April 18, 2016. The data and recoverable samples are analyzed by the teams of experimental program.

1 Introduction

Microgravity experiments for long period, which could be performed only in the space facilities such as space station, space shuttle, and satellite, are essential for the development of microgravity science and space life science. The recoverable satellite is a useful and efficient tool for space experiments in the microgravity environment (Hu 2008; Li *et al.* 2008), and such kind of satellites have been launched successfully 23 times in China (Li *et al.* 2008). Space microgravity experiments in China have been completed mainly aboard the recoverable satellites since the late 1980's (Zhong and Lin 1997) and the spaceships Shenzhou since the late 1990's. The launch of the satellite SJ-8 was a turning point of transportation the mission purpose from Earth observation mainly to microgravity experiments. The main scientific results of SJ-8 missions were published in a spe-

cial issue of Microgravity Science and Technology (2008, vol. 20, no.2). The space experiments of microgravity fluid physics, including one in cooperation with the Russian scientists aboard the Mir space station, were summarized by Hu *et al.* (2009). The program of SJ-10 satellite was organized by the Chinese National Space Administration (CNSA) in the middle of 2000's. 10 experiments of microgravity science and 10 experiments of space life science were selected from more than 200 applications of SJ-10 mission in the early of 2005. The mission proposal of space experiments was reviewed in the October of 2005. The engineering proposal of satellite platform was reviewed in May of 2006 by the CNSA. Then, the demonstration working group on "recoverable satellite of scientific experiments for space environment utilization" was formally organized, and the mission was determined as SJ-10. Unfortunately, the demonstrative phase was stopped after one year due to

the reform of CNSA, and re-started when the government of China determined to move the national management of scientific satellite from CNSA to the Chinese Academy of Sciences (CAS) in 2011. The re-started demonstration phase was completed in the end of 2012, and the engineering phase of program SJ-10 was started since the beginning of 2013. Then, the satellite was launched on April 6, 2016. In SJ-10 program, there are 6 experiments in the field of microgravity fluid physics, 3 in microgravity combustion, 8 in space material science, 3 in radiation biology, 3 in gravitational biology, and 4 in space biotechnology. Main scientific purposes of these experiments may be summarized as follows.

- To promote the basic research of fluid physics and biology experiments;
- To support the manned space flight for fire safety research;
- To improve the human health by biotechnology studies;

- To develop the high-technology by experiments of coal combustion, materials processing and biotechnology.

The issues of selected space experiments are listed respectively in Table 1 for microgravity science and Table 2 for space life science.

2 Recoverable Satellite of SJ-10

The recoverable satellite is a very useful spacecraft for microgravity experiments (see, for example, Li *et al*, 2008), and the satellite of SJ-10 is the 25th recoverable satellite of China. The structure of SJ-10 satellite is shown in Fig.1.

The SJ-10 satellite flies in a circular orbit of 255 km, and its main parameters are given as follows.

- Total mass: $\leq 3600\text{kg}$
- Orbital Inclination: 43°
- Orbital altitude: $\sim 255\text{ km}$
- Life span: $12 + 3\text{ days}$

Table 1 List of microgravity science experiments

Program	Experiments	PI
A1-1	Microgravity Space experiment of evaporation and Fluid physics fluid interfacial effects	Q.S. Liu (Inst. Mech., CAS)
A1-2	Phase separation and dynamic clustering in granular gas	M.Y. Hou (Inst. Phys., CAS)
A1-3	Thermal dynamical behavior of vapor bubble during pool boiling	J.F. Zhao (Inst. Mech., CAS)
A1-4	Space experimental on surface wave of thermocapillary convection	Q. Kang (Inst. Mech., CAS)
A1-5	Study on the colloidal assembling	Y.R. Wang (Inst. Mech., CAS)
A1-6	Soret coefficients of crude oil (SCCO)	A. Verga (ESA), and Z.W. Sun (Inst. Mech., CAS)
A2-1	Combustion on ignition, soot emission and smoke distribution of wire insulations by overload	W.J. Kong (Eng. Inst. Thermophys., CAS)
A2-2/3	Investigation of the coal combustion and pollutant formation characteristics under microgravity	H. Zhang (Tsinghua Univ.) and M.H. Xu (Huazhong Sci. & Tech.)
A2-4	Ignition and burning of solid materials in microgravity	S.F. Wang (Inst. Mech., CAS)
A3	Solidification and crystal growth in space	X.W. Zhang (Inst. Semiconductor, CSA, <i>et al</i>)

Table 2 List of space life science experiments

Program	Experiments	PI
B1-1	Molecular biology mechanism of space radiation mutagenesis	Y.Q. Sun (Dalian Maritime Univ.)
B1-2	Roles of space radiation on genomic DNA and its genetic effects	H.Y. Hang (Inst. Biophysics, CAS)
B1-3	Effects of space environment on silkworm embryo development and mechanism of mutation & Ecology	Y.P. Huang (Inst. Plant Physiology, CAS)
B2-1	Biological effects and the signal transduction of microgravity stimulation in plants	W.M. Cai (Inst. Plant Physiology, CAS)
B2-2	Biomechanics of mass transport of cell interactions under microgravity	M. Long (Inst. Mech., CAS)
B2-3	Photoperiod-controlling flowering of Arabidopsis and rice in microgravity	H.Q. Zheng (Inst. Plant Physiology & Ecology, CAS)
B3-1	Three-dimensional cell culture of neural stem cells in space	J.W. Dai (Inst. Genetics & Developmental Biology, CAS)
B3-2	Three-dimensional cell culture of hematopoietic stem cells in space	Y. Zhao (Inst. Zoology, CAS)
B3-3	Development of mouse early embryos in space	E.Q. Duan (Inst. Zoology, CAS)
B3-4	Potential and molecular mechanism of osteogenic differentiation from human bone mesenchymal stem cells	J.F. Wang (Zhejiang Univ.)

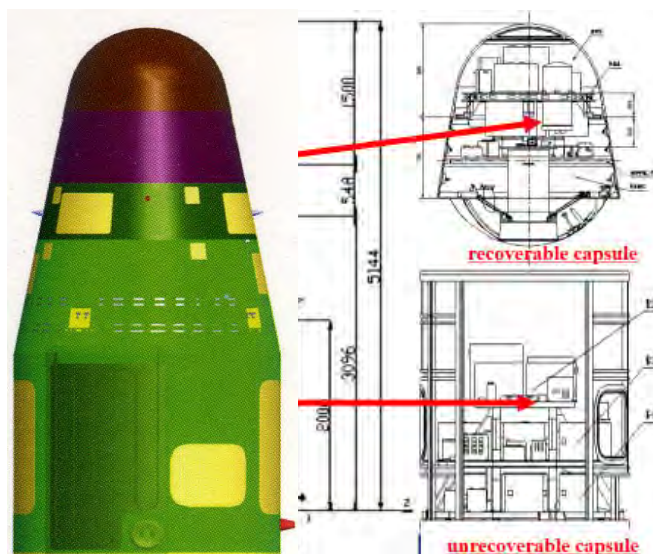


Fig. 1 Schematics of SJ-10. The structure is in left part is, and recoverable capsule and un-recoverable capsule are shown respectively in the right upper and right lower part.

- Gravitation level: Better than 10^{-3} g
- Payload: 270 kg (recoverable capsule)
280 kg (un-recoverable capsule)
- Rocket: CZ-2D
- Launch date: April 6, 2016

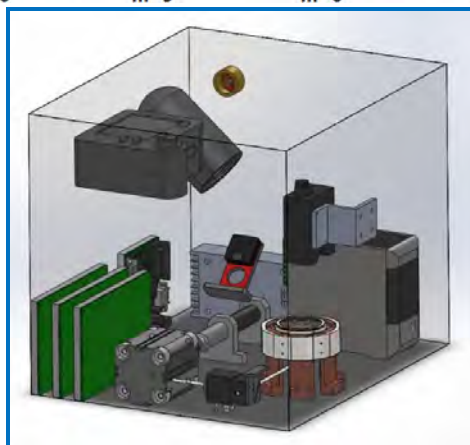
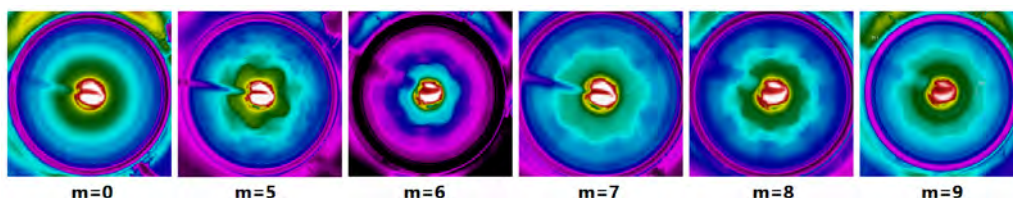
3 Scientific Facilities on Board SJ-10

There are 19 scientific payloads with 28 scientific objectives. The scientific purposes of the missions are described as follows.

3.1 Convection and Diffusion

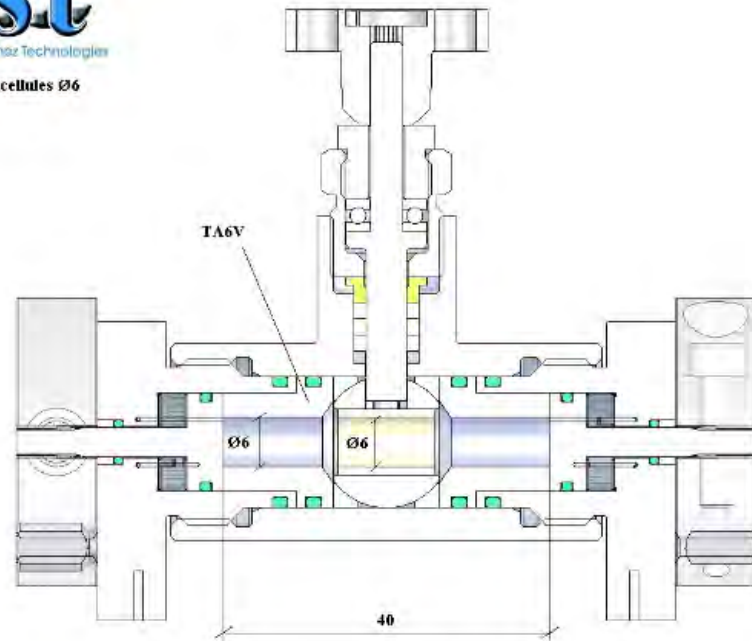
A1-4: Space Experimental on Surface Wave of Thermocapillary Convection

The goal is to study the volume effect and the scale effect on oscillation and transition process of thermocapillary convection.



A1-6: Soret Coefficients Measurement in Microgravity Condition (SCCO)

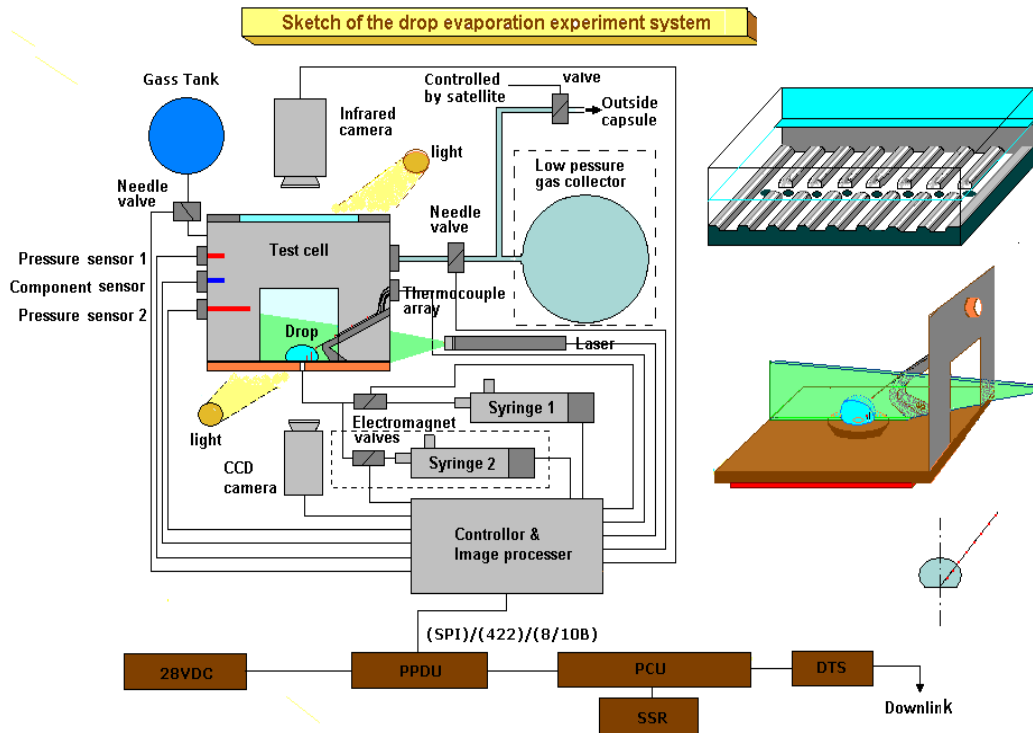
The goal is to measure the Soret coefficient to accurately predict petroleum composition distribution, etc.



3.2 Multi-phase Flow

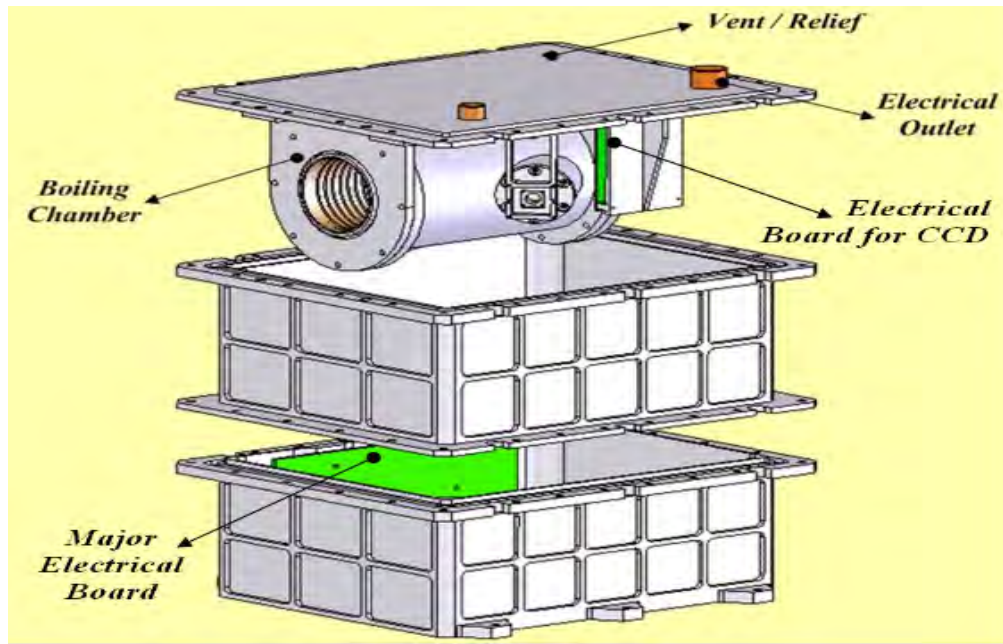
A1-1: Space Experiment of Evaporation and Fluid Interfacial Effects

The goal is to study the evaporation of heat and mass transfers, and to observe the non-equilibrium evaporation and thermal convection in real-time.



A1-3: Thermal Dynamical Behavior of Vapor Bubble during Pool Boiling

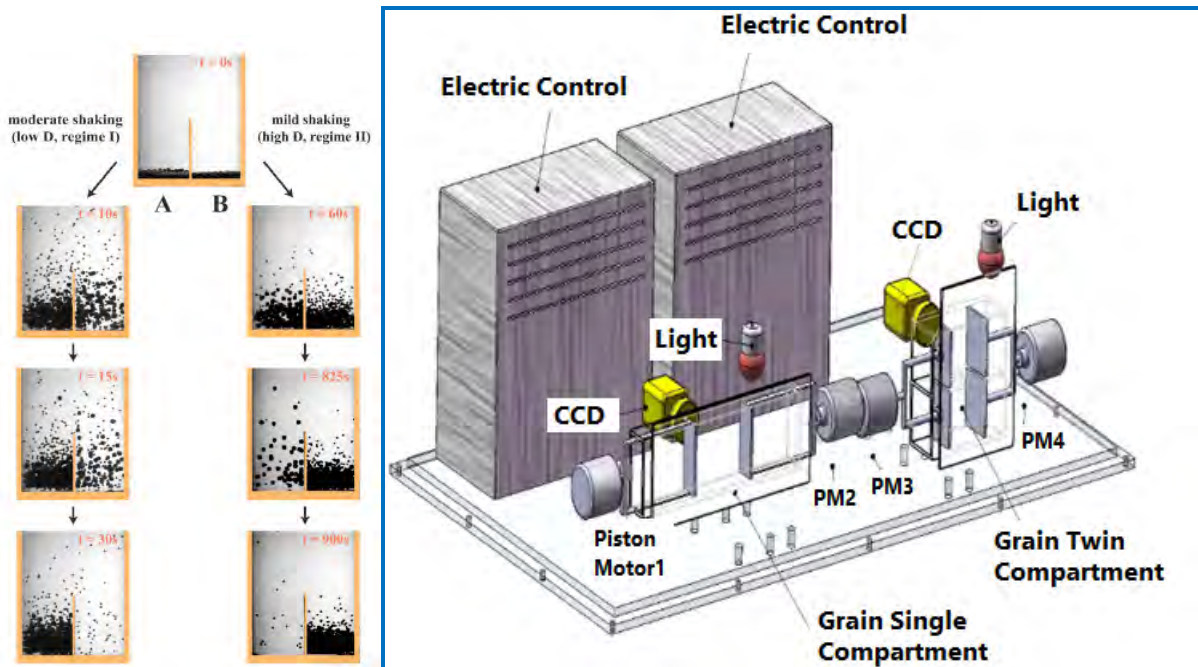
The goal is to study the phase change of time - space scale, and flow and temperature fields for boiling heat transfer mechanism research.



3.3 Complex Fluid

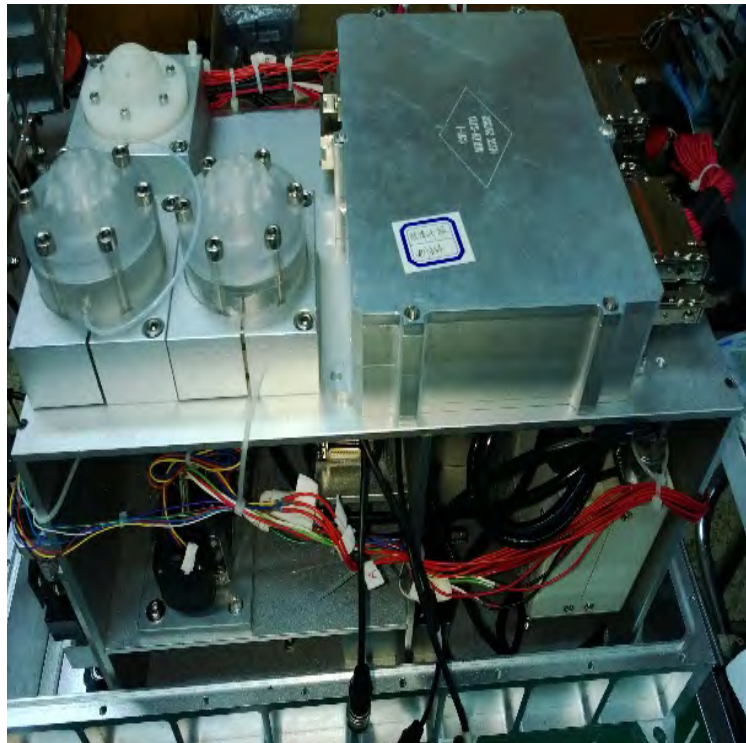
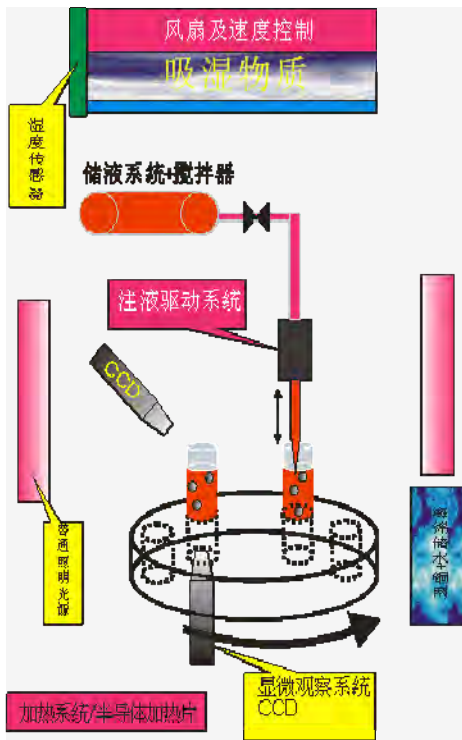
A1-2: Phase Separation and Dynamic Clustering in Granular Gas

The goal is to study the separation - accumulation phenomenon in particle system, and transport particulate matter in micro-gravity.



A1-5: Study on the Colloidal Assembling and New Materials

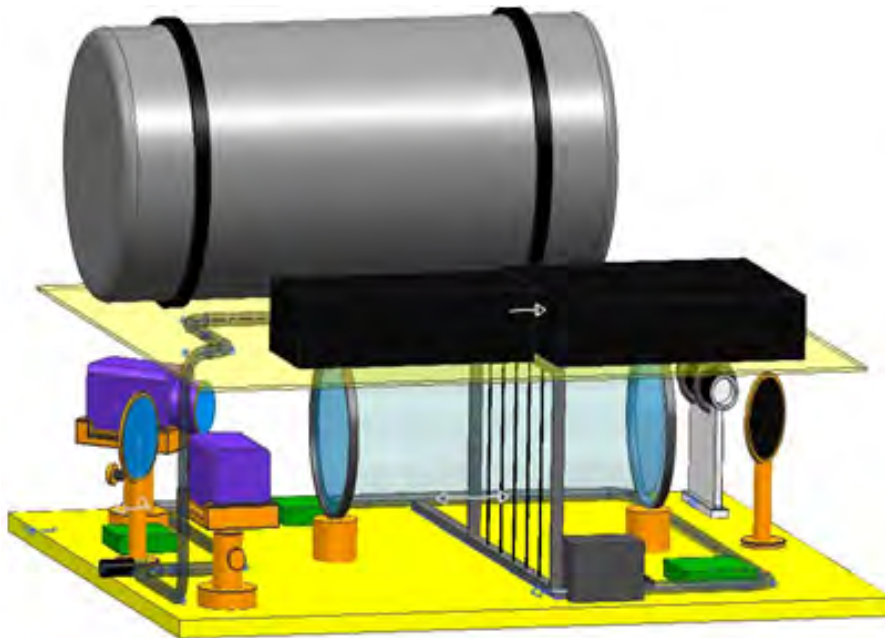
The goal is to study the colloid self-assembly phenomenon of large scale range (nanometers to microns), and multi-effects of fluid mechanics, chemistry and materials science.



3.4 Combustion for Fire Safety

A2-1: Study on Ignition, Soot Emission and Smoke Distribution by Overload

The goal is to study latent "ignition source" and explore scientific theory of novel and reliable fire monitoring and fire early warning in microgravity.



A2-4: Study on Ignition and Combustion of Typical Non-metallic Materials

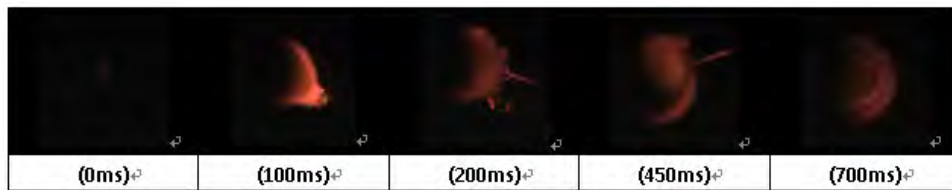
This project focus on microgravity combustion of thermal thick materials, and evaluation of the gas environment's effects.



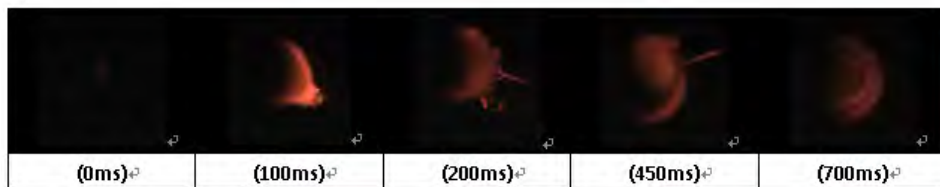
3.5 Coal Combustion and Pollutant Formation

A2-2/3: Investigation of the Coal Combustion and Pollutant Formation Characteristics under Microgravity

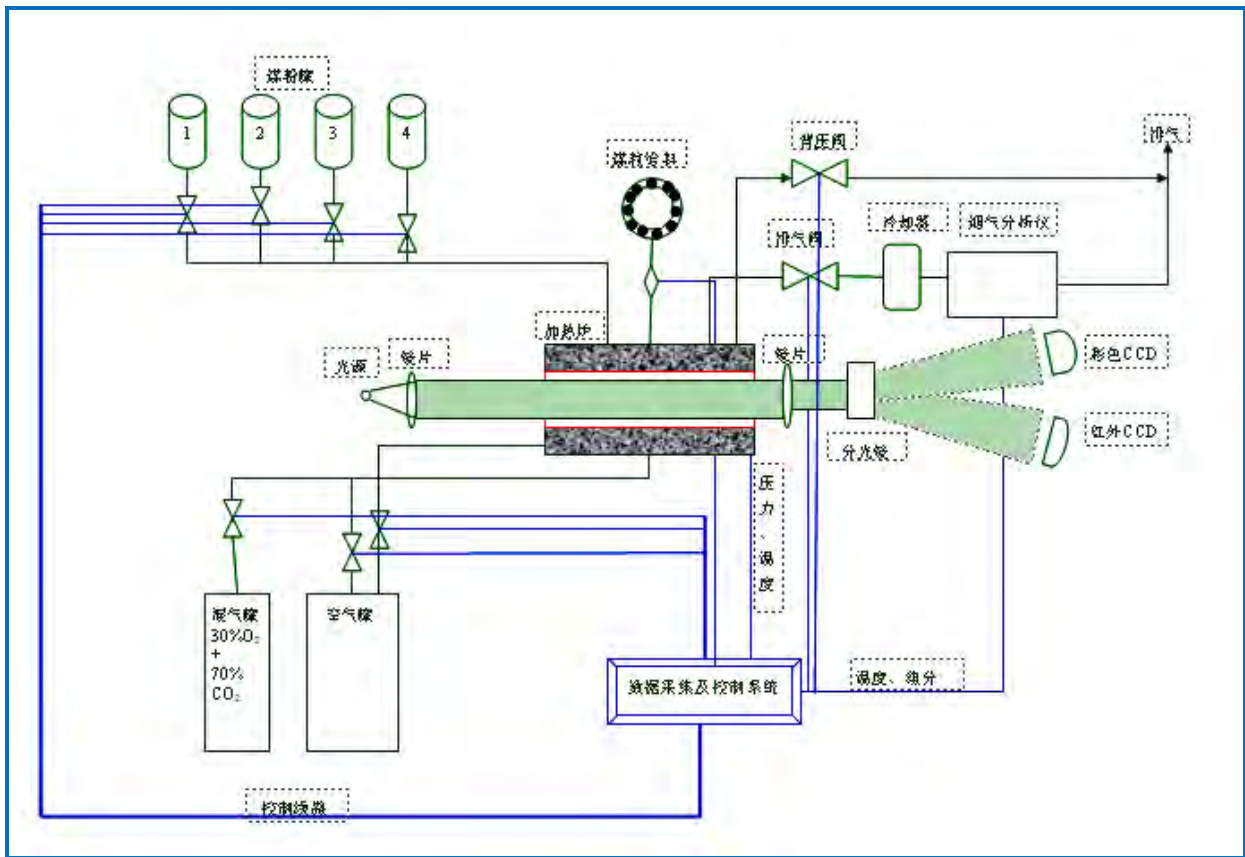
The goals include: to discover the fundamental phenomena and control mechanisms in the entire combustion process of single particles and pulverized clouds of a few kinds of typical China coals, to obtain ideal experimental data that is useful for the validation of theory and model for coal ignition and combustion, to improve the modelling and theory development for ground coal combustion; and to study the entire coal combustion process in long-duration microgravity. High-temperature furnace is used to study the entire coal combustion process, which is close to the actual case.



mg



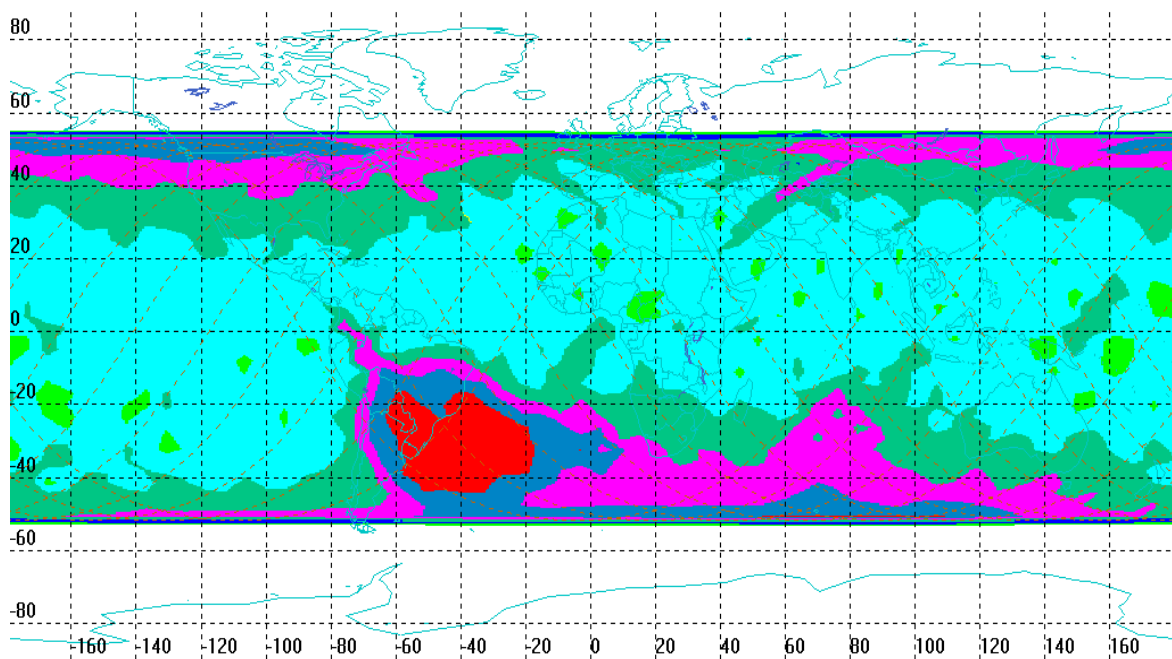
1g



3.6 Radiation Biology

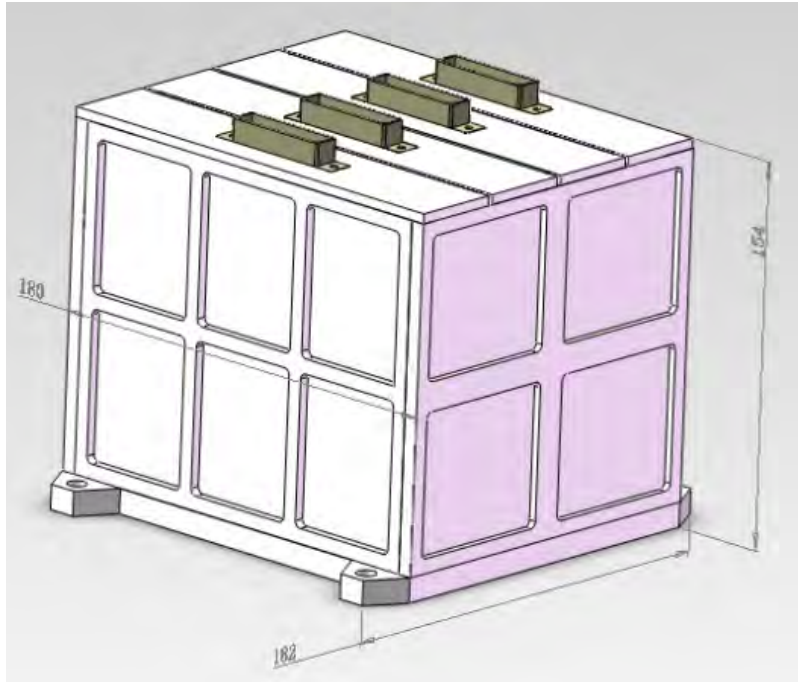
B1-1: Molecular Biology Mechanism of Space Radiation Mutagenesis

The research work includes high throughput data mining, new generation molecular biology, assessment technology of space radiation biological effect.



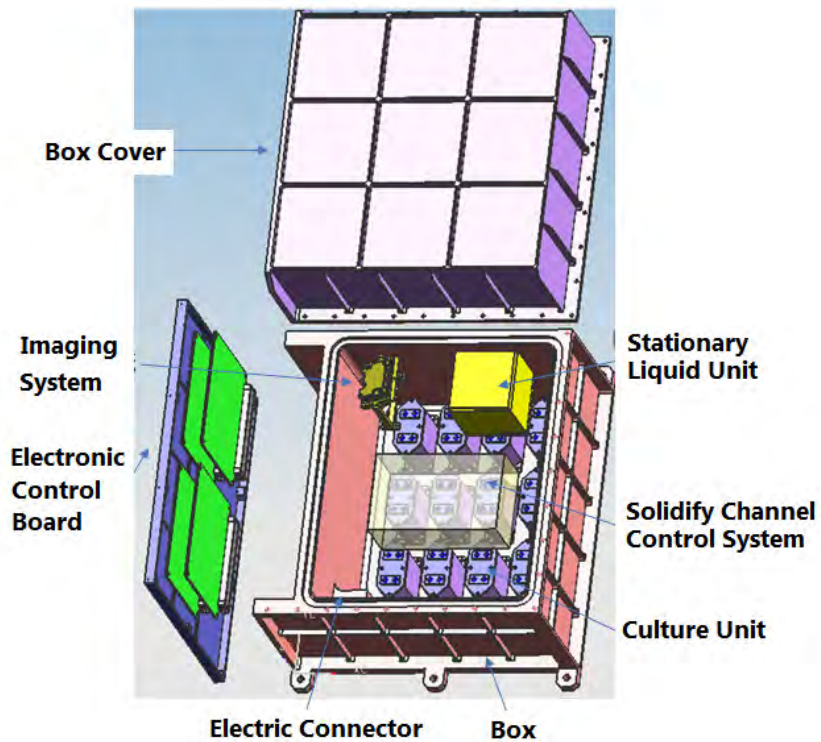
B1-2: Roles of Space Radiation on Genomic DNA and its Genetic Effects

The goal is to study the quantitative effects of space radiation on genomic stability and discover novel sensitive biological molecules as space radiation markers.



B1-3: Effects of Space Environment on Silkworm Embryo Development and Mechanism of Mutation

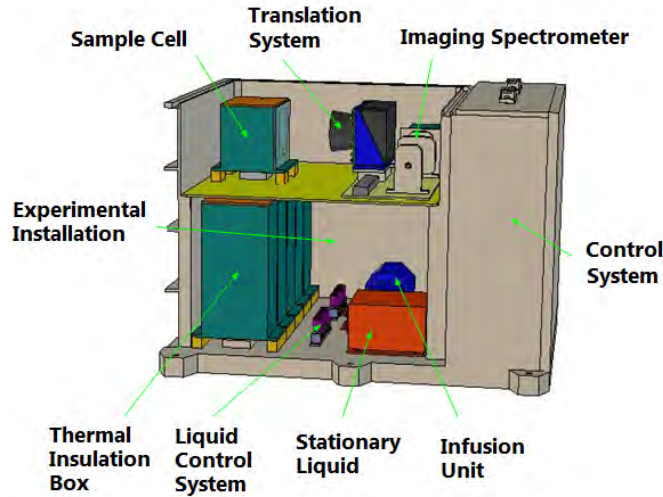
This is the first time to explore the mechanism of silkworm mutant internationally.



3.7 Gravitational Biology

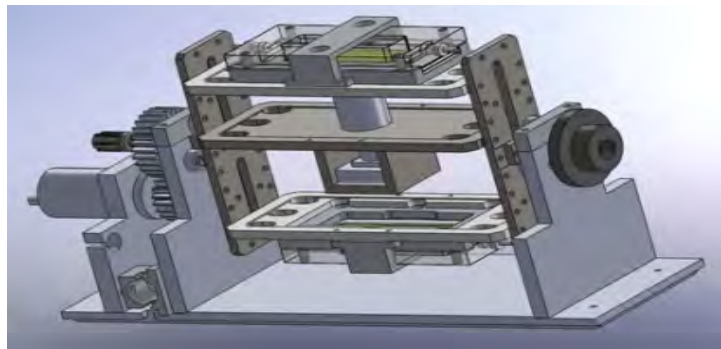
B2-1: Biological Effects and the Signal Transduction of mg Stimulation in Plants

Proteomic methods are used to obtain more information of biological effect on rice, model plant, and important crop.



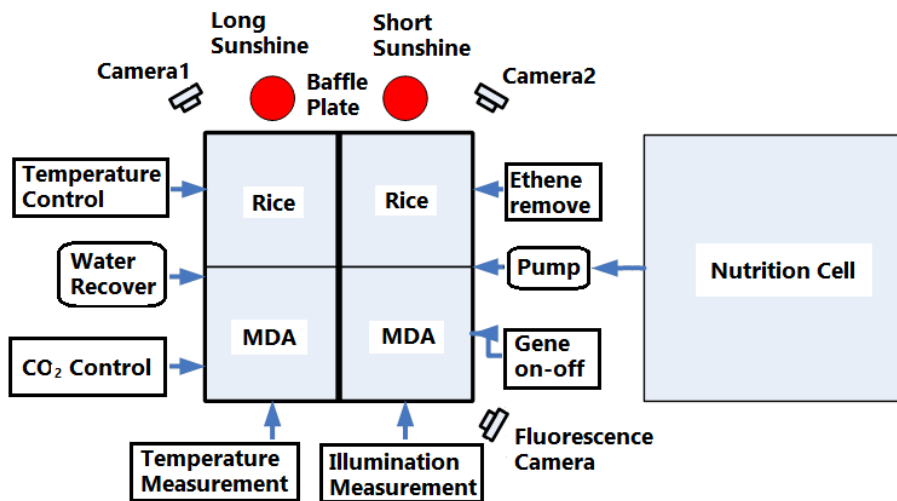
B2-2: Biomechanics of Mass Transport of Cell Interactions under Microgravity

A new hardware is obtained in the first time under well defined medium flow for major functions of typical mammal cells.



B2-3: Photoperiod-controlling Flowering of Arabidopsis and Rice in Microgravity

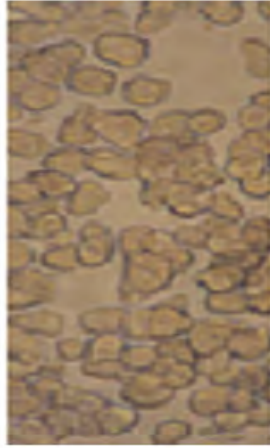
The goal is to illustrate photoperiod induce flowering mechanism for crop cultivation and quality of breeding on agriculture



3.8 Biological Technology

B3-1/2: Three-dimensional Cell Culture of Neural and Hematopoietic Stem Cells in Space

The goal is to study three-dimensional cell culture of neural and hematopoietic stem cells in space, and prepare three-dimensional scaffold materials and three-dimensional cell culture system.



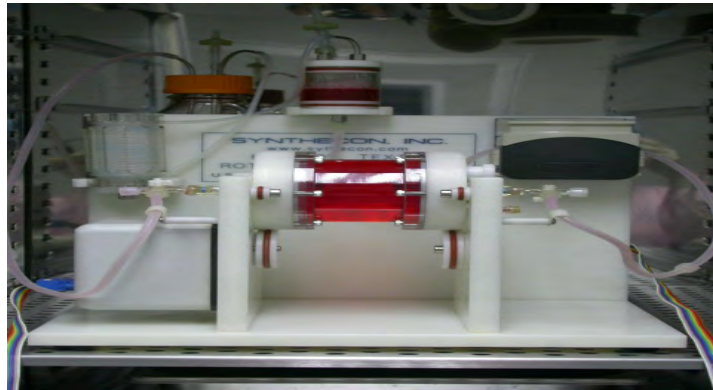
2D-culture



3D-culture

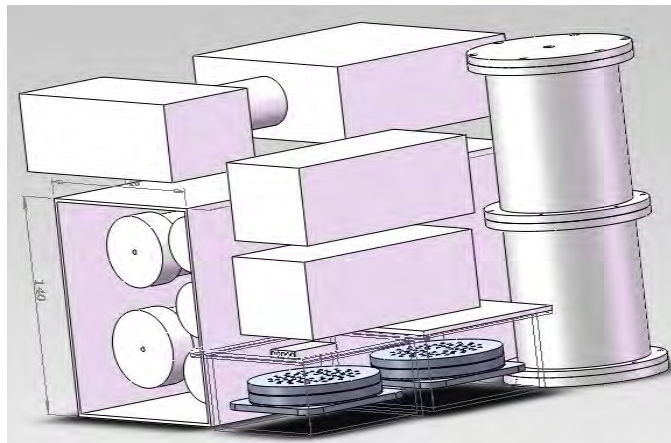
B3-3: Space Development of Mouse Early Embryos

The research items include: mammalian early embryos develop in space, embryonic stem cells into embryoid bodies batch amplification, and directional differentiation to the myocardial cells.



B3-4: Potential and Molecular Mechanism of Osteogenic Differentiation from Human Bone Mesenchymal Stem Cells

This is an osteogenic differentiation experiment of human bone mesenchymal stem cells in mg environment.



4 Research and Design of SJ-10 Space Experimental Operation

The satellite program development is scheduled to be 36 months, and the phases are arranged as follows.

(1) Scheme Design Phase(2013-01-01–2013-09-29)

- (i) Through detailed analysis of various payload demands, full consideration of all the needs of the payloads and related constraints of satellite, to establish effective load service and support system;
- (ii) Determining the load and payload service, support systems and satellite mechanical and electrical interface, and load and payload service, support systems electrical interface;
- (iii) Verification test on the key technology involved, to develop a scheme to meet the load demand.

(2) Prototype Phase(2013-09-30–2014-10-31)

- (i) An effective load and load service and support system prototype sample product development, to complete product identification level environmental test;
- (ii) Payload subsystem debugging, in the desktop united debugging of the satellite system electrical parts.

(3) Flight Model Phase(2014-11-01–2016-04-06)

- (i) An effective load and load service and support system prototype sample product development, complete acceptance level environmental test;
- (ii) Load debugging by systems, after flight model's delivery of overall, varies debug-

ging of the flight model, various tests before leaving the factory and in the launch site included.

(4) Flight test phase (2016-04-06–2016-04-21)

- (i) Flight in the designed orbit;
- (ii) Perform the space science experiment in order, and transfer the scientific data to the ground station;
- (iii) Analyze the scientific data in real time of space experiments;
- (iv) Analyze the scientific results from the recoverable facilities.

The method of tele-science was used during the experimental period. The space experiments were operated by the flight control system as follows, and the PIs can adjust the experimental parameters during the experimental period.

5 Conclusion

The Chinese recoverable satellite is a useful infrastructure for microgravity science and space life science, and the microgravity experimental satellite SJ-10 was launched on April 6, 2016 and recovered on April 18, 2016 successfully.

References

- [1] Hu, W.R. Microgravity experiments on board the Chinese recoverable satellite. *Microgravity Sci. Tech.*, 2008, 20: 59
- [2] Hu, W.R., Long, M., Kang *et al*. Space program SJ-10 of microgravity research, *Microgravity Sci. Tech.*, 2014, 26: 159
- [3] Li, C., Zhao, H., Ni, R. China's recoverable satellite and their on board experiments. *Microgravity Sci. Tech.*, 2008, 20: 61
- [4] Zhong, X.R., Lin, L.Y. GaAs single crystal growth in space. In: *Space Science in China*. New York: Gordon & Breach, 1997: 333

Space-based Multi-band Astronomical Variable Objects Monitor

WEI Jianyan

National Astronomical Observatories, Chinese Academy of Sciences, Beijing 100012

* E-mail: wjy@nao.cas.cn

Space-based multi-band astronomical Variable Objects Monitor (SVOM) is a proposed mission dedicated for studying Gamma-Ray Bursts (GRBs). The mission has been approved jointly by both Chinese and French space agencies. It is planned to be in the orbit in 2021 with an altitude ≤ 600 km and an inclination $\leq 30^\circ$. The System Requirement Review (SRR) in Phase B studies has been taken in Beijing in June 2015, and the Preliminary Design Review (PDR) in Phase B studies will be held at Yantai, China, in July 2016.

GRBs are extremely luminous transient sources appearing when a newborn stellar mass black hole or magnetar emits an ultra-relativistic jet towards the Earth. Consequently, the study of GRBs not only has the potential to expand or revolutionize our understanding of key astrophysical issues on the mechanisms driving stellar explosions and the radiation processes of relativistic jets. In the next years GRBs will also undoubtedly shed new light on the evolution of the young universe, particularly on the history of star formation, the metal enrichment of galaxies, and the reionization of the intergalactic medium.

In order to take advantage of the astrophysical potential of GRBs, SVOM is designed to:

- permit the detection of all known types of GRBs,
- provide fast, reliable GRB positions,
- measure the spectral shape of the GRB prompt emission from visible to MeV,
- measure the temporal properties of the GRB prompt emission from visible to MeV,
- identify quickly the afterglows of detected GRBs at both X-ray and visible bands, including the ones that are highly redshifted ($z > 5$),

- measure the spectral shape of the early and late GRB afterglow from visible to X-rays,
- measure the temporal evolution of the early and late GRB afterglow from visible to X-rays.

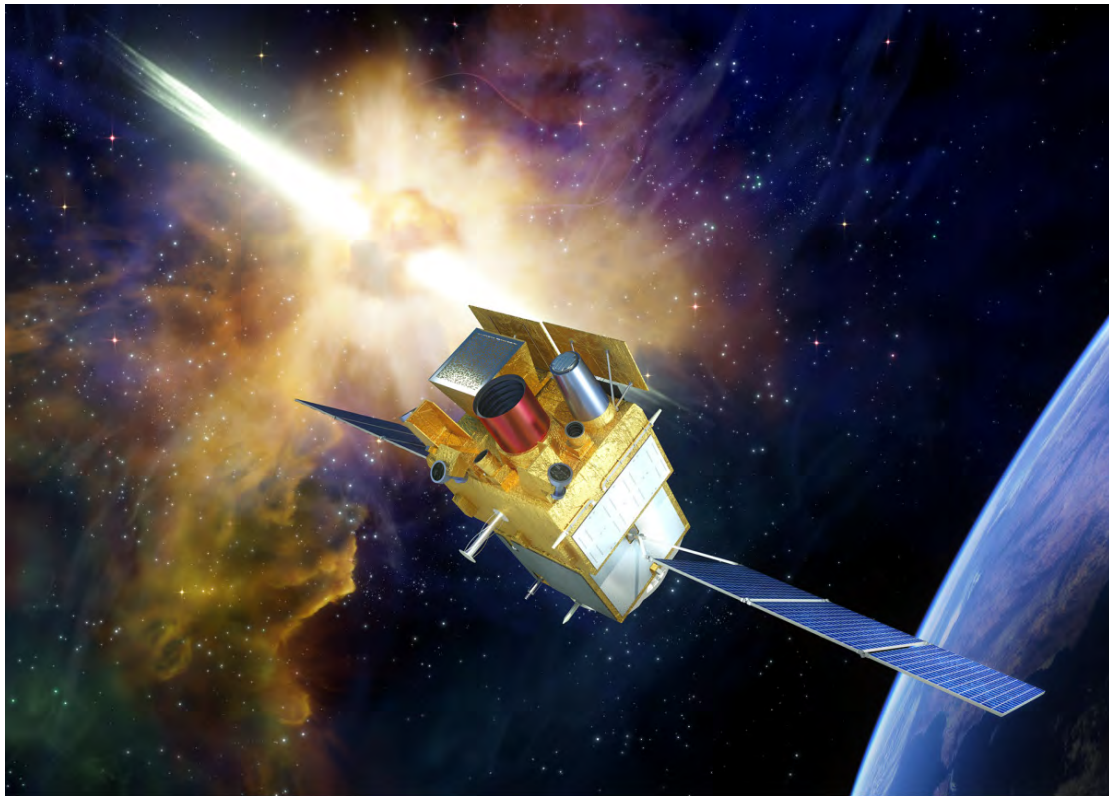
SVOM mission is designed to consist of a set of scientific instruments to implement the synergy between space and ground observations. The space-based instruments include:

- ECLAIRs, a wide field-of-view hard X-ray imager and spectrometer;
- GRM, a wide field-of-view soft gamma-ray spectrometer,
- MXT, a narrow field-of-view low-energy X-ray telescope;
- VT, a narrow field-of-view visible/near infrared (NIR) telescope.

And the ground-based instruments include:

- GFTs, two follow-up telescopes (one of which featuring efficient NIR capabilities);
- GWAC, an array of wide field-of-view cameras in visible band.

At the beginning of the next decade, SVOM will be the main provider of GRB positions and spectral parameters. The SVOM instruments will operate simultaneously with a wide range of powerful astronomical devices, which include not only multi-wavelength ones but also multi-message ones (such as gravitational wave observatories and high-energy neutrino detectors). The SVOM instruments, primarily designed for GRB studies, compose a unique multi-wavelength observatory that must be very helpful for the whole astronomy community beyond the specific objectives related to GRBs.



Artist view of the SVOM satellite

Developing the TanSat Mission: A Progress Report

LIU Yi¹, YIN Zengshan², ZHENG Yuquan³, YAN Changxiang⁴,
YANG Zhongdong⁵, TIAN Xiangjun⁶, LÜ Daren⁷

1. Institute of Atmospheric Physics, Chinese Academy of Sciences
2. Shanghai Engineering Center for Microsatellites
3. Changchun Institute of Optics, Fine Mechanics and Physics
4. Changchun Institute of Optics, Fine Mechanics and Physics
5. National Satellite Meteorological Center, China Meteorological Administration
6. Institute of Atmospheric Physics, Chinese Academy of Sciences
7. Institute of Atmospheric Physics, Chinese Academy of Sciences

* E-mail: liuyi@mail.iap.ac.cn

Key words

Chinese Carbon Dioxide
Observation Satellite
TanSat
Science interpretation
Payload
Platform
Validation

Abstract

The Chinese Carbon Dioxide Observation Satellite (TanSat) was sponsored by the Ministry of Science and Technology of China and the Strategic Priority Research Program of the Chinese Academy of Sciences in 2011. TanSat will carry two instruments: the High Resolution Hyperspectral Sensor for carbon observation Grating Spectrometer (HRHS-GS) and the moderate-resolution Polarization Imaging spectrometer for Cloud and Aerosol (CAPI). HRHS-GS will provide accurate space-based measurements of the column-averaged dry-air mixing ratio of carbon dioxide (XCO_2) at global and regional scales, enabling the quantification of terrestrial sources and sinks of CO_2 . CAPI is used to correct the interference of aerosol. This report summarizes the current development of the TanSat scientific capabilities, satellite observation modes, instrument manufacturing, calibration results, the development of retrieval algorithms and their application to Greenhouse Gases Observing Satellite (GOSAT) data and, finally, the future validation plans. With its launch in December 2016, TanSat will become the third, in-orbit satellite to monitor CO_2 from space.

1 Introduction: Scientific Capabilities

Carbon (e.g., CO_2 , CO, and CH_4) can be released into the atmosphere or absorbed from the atmosphere by processes at the surface. Since the beginning of the industrial age, humans have disrupted the carbon balance through the use of fossil fuels and deforestation. It is well known that the increase in atmospheric CO_2 has resulted in global warming and subsequent climate change. As the largest developing country, China has

the highest level of greenhouse gas (GHG) emissions. To pursue sustainable development and reduce GHG emissions, quantification of the carbon budget at global and regional scales is critical and has become a significant challenge. It has been demonstrated that the column-averaged dry-air mixing ratio of carbon dioxide (XCO_2) can be measured from satellites with high precision. The Greenhouse Gases Observing Satellite (GOSAT), launched in 2009^[1], and the Orbiting Carbon Observatory-2 (OCO-2), launched in

2014, have been designed to exploit this measurement approach^[2].

2 Mission Overview

The Chinese carbon dioxide observation satellite (TanSat: “The Global Carbon Dioxide Monitoring Scientific Experimental Satellite”) was established to aid Earth observation by the National High Technology Research and Development Program of China (863 Program). The main objective of the TanSat was to monitor the XCO₂ and CO₂ flux at regional and global scales. The TanSat satellite consists of an agile platform and two scientific instruments. The High Resolution Hyperspectral Sensor for carbon observation Grating Spectrometer (HRHS-GS) is designed to measure the near-infrared absorption by CO₂ at 1.61 and 2.06 μm, and the molecular oxygen (O₂) A-band in reflected sunlight at 0.76 μm. The instrument has a spatial resolution of 2 km × 2 km. Table 1 shows the specifications of HRHS-GS^[3-6].

Table 1 High Resolution Hyperspectral Sensor for carbon observation Grating Spectrometer (HRHS-GS) specifications

	O ₂ -A	CO ₂ Weak	CO ₂ Strong
Spectral Range (nm)	758-778	1594-1624	2042-2082
Spectral Resolution (nm)	0.038-0.047	0.120-0.142	0.160-0.182
Signal to Noise Ratio (SNR)	360	250	180
Spatial Resolution	2 × 2 km		
Swath	20 km		

The Cloud and Aerosol Polarimetry Imager (CAPI) is used to compensate for CO₂ measurement errors, which are caused by clouds and aerosols, and is based on high-resolution measurements at 0.38, 0.67, 0.87, 1.38, and 1.64 μm. Moreover, CAPI is able to perform polarimetric measurements at 0.67 and 1.64 μm to correct for the interference from clouds and aerosols^[4,7]. Table 2 shows the specifications of the CAPI instrument.

Table 2 Moderate-resolution Polarization Imaging spectrometer for Cloud and Aerosol (CAPI) specifications

Band	(nm)	SNR	Polarization (deg)	Pixel Number
VNIR	365-408	260		1600
	660-685	160	0°,60°,120°	1600
	862-877	400		1600
SWIR	1360-1390	180		800
	1628-1654	110	0°,60°,120°	800

VNIR: visible and near-infrared. SWIR: Short-wavelength infrared

3 Carbon Dioxide Retrieval Algorithm and Flux Inversion

Previous studies have shown a significant influence of the atmospheric and surface status on the spectra received at the top of the atmosphere^[8], and this can induce errors in retrieval. A full physical algorithm is appropriate for deriving XCO₂ due to the simulation of radiance transfer on a physical basis. An XCO₂ retrieval algorithm was developed and named after the Institute of Atmospheric Physics, Chinese Academy of Science (IAPCAS), to support the TanSat mission. Early versions were introduced as an application of the TanSat algorithm on GOSAT observations^[9]. Validation with Total Column Carbon Observing Network (TCCON) measurements indicated that only a 1% (4 ppm) error remained in XCO₂ retrieval, and it will therefore serve as the TanSat operational algorithm.

Recently, some improvements to the IAPCAS algorithm have been made based on a previous version. This includes the modification of radiative transfer calculations, aerosol parameters, and retrieval method. The GOSAT L1B data were used in the retrieval experiments. Nine TCCON sites at different latitudes and on different continents were selected for the validation study. Most of the validation bias was lower than 1 ppmv, while most of the root-mean-square deviation (RMSD) was lower than 2 ppmv. Statistical data from all validation sites had a bias of 0.15 ppmv and an RMSE of 1.48 ppmv, which is sufficiently accurate for the study of carbon fluxes^[10].

The final product of TanSat will be the CO₂ flux at regional and global scales. To derive the CO₂ flux from XCO₂, we have developed a novel framework (“TanTracker”) for assimilating observations of atmospheric CO₂ concentrations, based on the POD-based ensemble four-dimensional variational data assimilation method (PODEn4DVar). An experiment for assimilating the real dry-air column CO₂ retrievals (XCO₂) from the Japanese GOSAT further demonstrated its potential for numerous applications^[11,12]. Methane (CH₄) is the second most important greenhouse gas (GHG). Based on GOSAT data, sensitivity studies have demonstrated the possibility of CH₄ retrieval in the short-wavelength infrared (SWIR) band, and have shown that the 1.65 μm band, associated with the 2.06 μm CO₂ band, retains more than 90% of the CH₄ and CO₂ information content^[13].

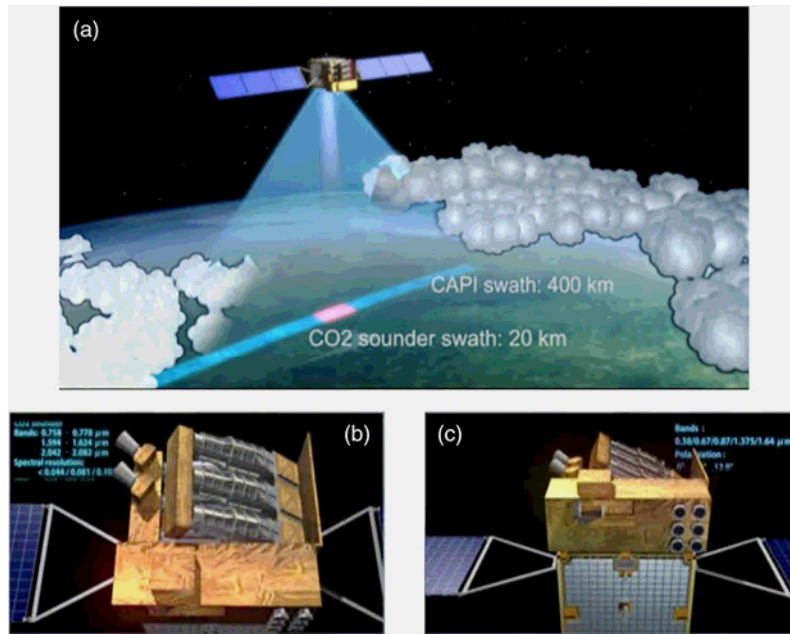


Fig. 1 Artistic conception of Tan-Sat. (a) High Resolution Hyperspectral Sensor for carbon observation Grating Spectrometer (HRHS-GS) swath is 20 km and Moderate-resolution Polarization Imaging spectrometer for Cloud and Aerosol (CAPI) swath is 400 km. CAPI has continuous spatial coverage swath and higher spatial resolution than HRHS-GS to detect the aerosol spatial distribution and cloud cover. (b) The outer structure of HRHS-GS. (c) The outer structure of CAPI.

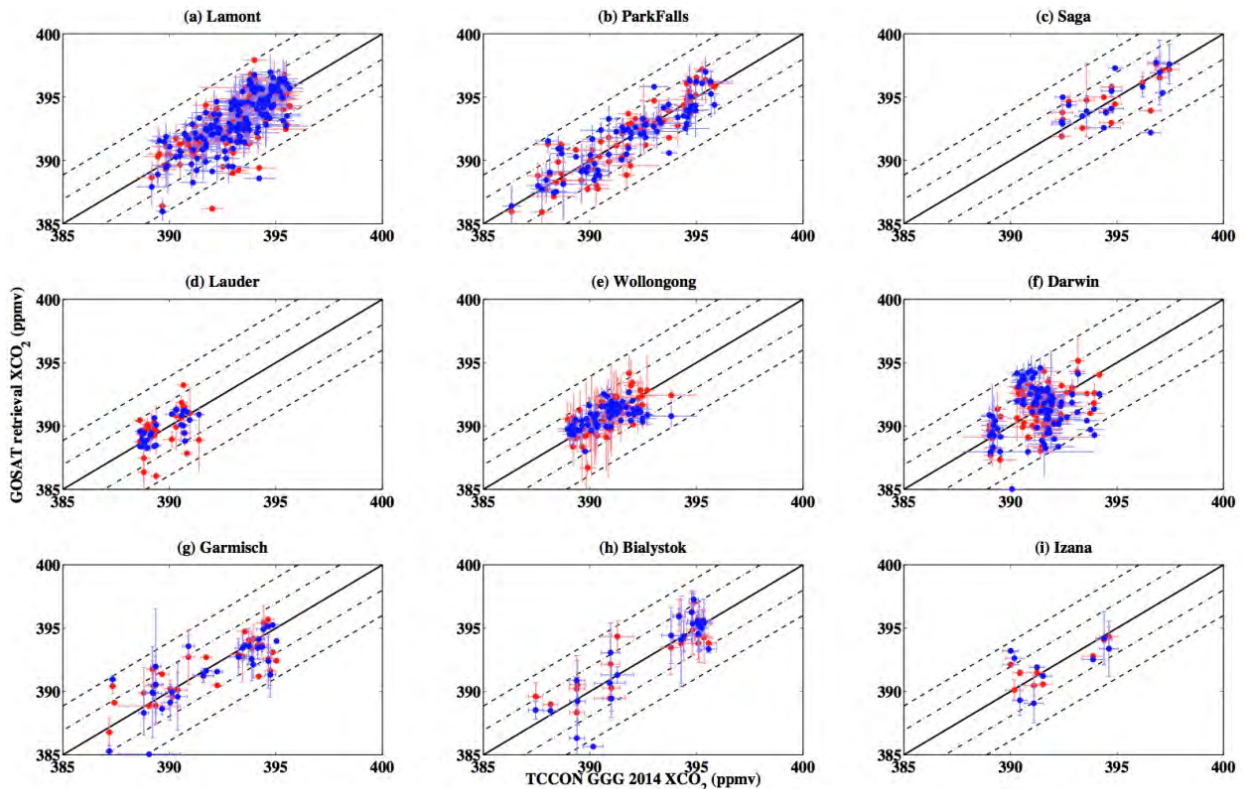


Fig. 2 The validation and inter-comparison of the Institute of Atmospheric Physics, Chinese Academy of Science (IAPCAS) - Greenhouse Gases Observing Satellite (GOSAT) XCO₂ product with Total Column Carbon Observing Network (TCCON) GGG 2014 and GOS OCFP V5.2 over nine TCCON sites (a-i) respectively. Red and blue represent GOS OCFP V5.2 and IAPCAS-GOSAT XCO₂ products respectively. The black solid line is the 1:1 line, while the dot-dash line and dash line indicate 0.5 and 1% error regions.

An algorithm for retrieving surface pressure from hyper-spectral measurements in oxygen A-band has been developed and will be applied in TanSat surface pressure retrievals^[14].

4 Satellite Observation Modes

To meet the mission requirements, the TanSat satellite operates in three observation modes: nadir mode, sun-glint mode, and target mode. In nadir mode, the satellite can obtain the most high-resolution data, and this mode is usually used for CO₂ observations of land surface. In target mode, the satellite observes a target point or area on the Earth from different view angles, ranging from -60° to 60° . Target mode is useful for CO₂ detection over hot-spots. It can also be used to observe ground CO₂ monitoring stations, so that the space-based observation data can be compared and validated against ground based data. In sun-glint mode, the satellite observes the sun glint point of the Earth, with the instrument boresight within five degrees of the principal plane^[2, 3].

5 Observation Instrument

5.1 HRHS-GS

The optical system of HRHS-GS is designed for high spectral resolution and detecting low levels of stray/scattered radiation. Figure 3 shows the optical layout of the HRHS-GS. It consists of a pointing mirror; an afocal system (a system without focus), with double off-axis parabolic mirrors; a dichotic splitter; a focusing system; an entrance slit; a collimating system; a large-area plane diffraction grating; and a spectral imaging system. The key components of the tri-channel grating spectrometer are the diffraction gratings. The three spectral bands are coupled to common fore optics. The three gratings disperse radiation of different spectral ranges onto the focal plane arrays (FPAs) in the direction orthogonal to the long dimension of the entrance slit. There is an area array detector at the focus of each channel of the spectrometer to record the spectrum. One dimension measures the different spectra, while the other measures field angles along the entrance slit.

For the O₂ A-band in the spectral range from 758 to 778 nm, the spectral resolution is 0.04 nm and the ground resolution is 2×2 km, with a 20-km swath. To

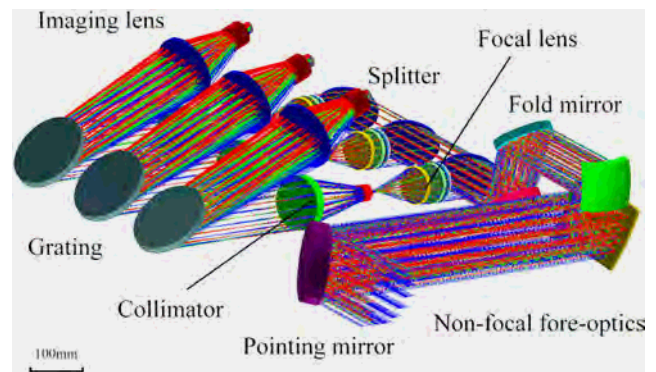


Fig. 3 Optical layout of High Resolution Hyperspectral Sensor for carbon observation Grating Spectrometer (HRHS-GS).

meet mission requirements, the silicon detector E2V55-30 is chosen for the O₂ A-band channel. The E2V55-30 detector is manufactured by E2V Technologies (Chelmsford, United Kingdom). Standard three-phase clocking and buried channel charge transfer are employed. About 320 pixels are used out of the 576 in the spatial dimension parallel to the entrance slit. To improve the signal-to-noise ratio (SNR), 16 adjacent pixels are merged to produce 20 spatially averaged “super pixels”. Due to the small dark signal, the O₂ A-band detector does not need a cooler.

The detectors in the two CO₂ channels use mercury cadmium telluride (HgCdTe) as the photosensitive material. The SATURN SW LSF24 detector (Sofradir, Châtenay-Malabry, France) was chosen for the 1.61 and 2.06- μm bands. It consists of a 500×240 pixel array, with a pixel pitch of 30 μm . The detector array operates in full staring mode, with simultaneous integration of charges during the readout of a previous frame. Similar to the O₂ A-band, 240 pixels of spatial dimension are binned to 20 pixels for a better SNR. Because the dark noise of the HgCdTe detectors increases with rising temperature, a Stirling cryocooler is used to maintain the HgCdTe detectors at their operating temperature (150 K)^[5].

5.2 Calibration

For the hyperspectral sensor, the laboratory calibration experiments were a critical step for future on-board calibration. The laboratory spectral calibration of HRHS-GS was used to determine the instrument line shape (ILS) function, center wavelength, and spectral resolution. The ILS profiles were derived from the testing of the tunable diode-laser. For the three different spectral

bands, three models of tunable diode-laser (Newport Corp., Irvine, CA, USA) were used. The HRHS-GS was placed in a thermal-vacuum chamber at a pressure of less than 1 Pa and at a temperature of 253 K.

The tunable diode-laser continuously output the single-frequency light at regular intervals, scanning the entire spectral range of each band. The laser scanning intervals were 0.005, 0.01, and 0.02 nm for the 0.76, 1.61, and 2.06 μm bands, respectively. The scanning range for a signal pixel was greater than three full widths at half maximum (FWHM). The laser-based spectral calibration system is shown in Figure 4. For a 1 km \times 2 km ground resolution, 16 spatial pixels were merged to produce up to 20 spatially averaged “super pixels”. The ILS profiles of different fields of views and different spectral channels are shown in Figures 5–6. Figure 7 shows the SNR measured in three bands. The results satisfied the requirements of the TanSat design^[4].

6 Satellite Platform Experiments

During the manufacture and integration of instruments and the satellite platform from 2014 to 2016, many tests were conducted (*e.g.*, the mechanical test, integrated test, thermal balance test, and an electromagnetic compatibility (EMC) test). Figure 8 shows the configuration of TanSat. Figure 9 shows the thermal balance test and the mechanical test. Each unit functions within the range required and the whole system meets the requirements of the delivery and pre-launch conditions.

7 Ground Segment-data Receiving and Processing

The National Meteorological Satellite Center (NSMC), China Meteorological Administration, is managing the TanSat ground segment. This system mainly consists of a data management subsystem and products retrieval

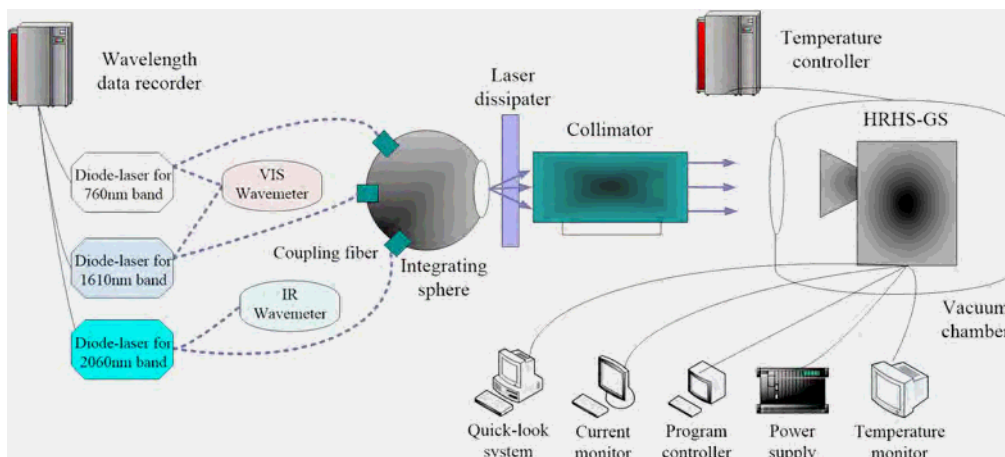


Fig. 4 Schematic of the laser-based spectral calibration system.

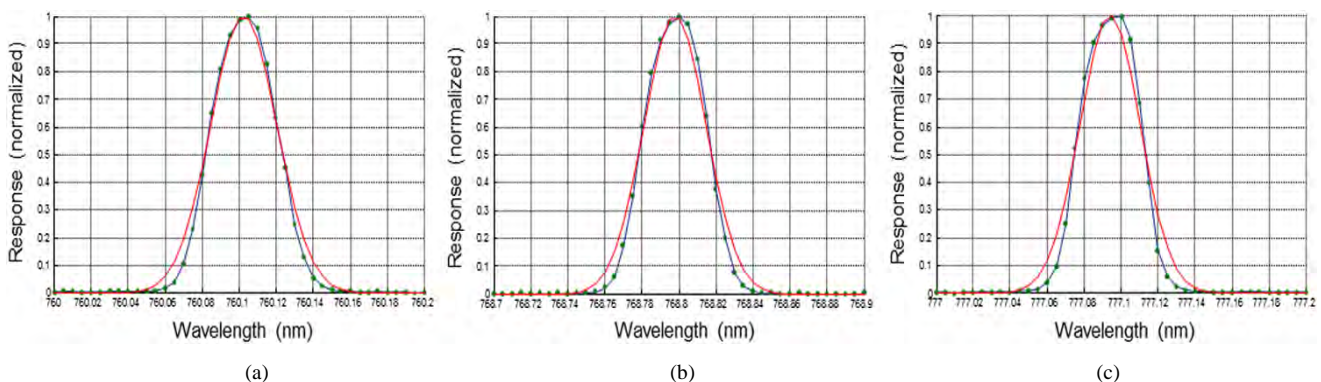


Fig. 5 Spectral response function (ILS) of several different channels on three spatial positions for the 0.76- μm band (FOV represents spatial pixel and channel represents spectral pixel): (a) FOV = 3, channel = 153, FWHM = 0.0401 nm, center wavelength = 760.103 nm; (b) FOV = 10, channel = 642, FWHM = 0.0398 nm, center wavelength = 768.798 nm; (c) FOV = 17, channel = 1181, FWHM = 0.0393 nm, center wavelength = 777.094 nm.

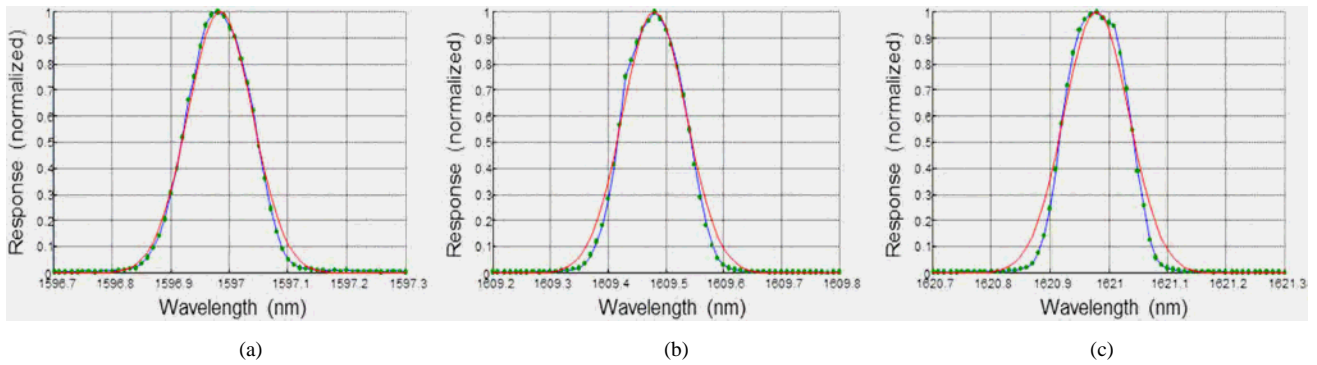


Fig. 6 Spectral response instrument line shape (ILS) function of several different channels on three spatial positions for the 1.61- μm band (the field of view (FOV) represents spatial pixels and the channel represents spectral pixels): (a) FOV = 3, channel = 58, full width at half maximum (FWHM) = 0.1330 nm, center wavelength = 1596.983 nm; (b) FOV = 10, channel = 258, FWHM = 0.1279 nm, center wavelength = 1609.476 nm; (c) FOV = 17, channel = 468, FWHM = 0.1307 nm, center wavelength = 1620.968 nm.

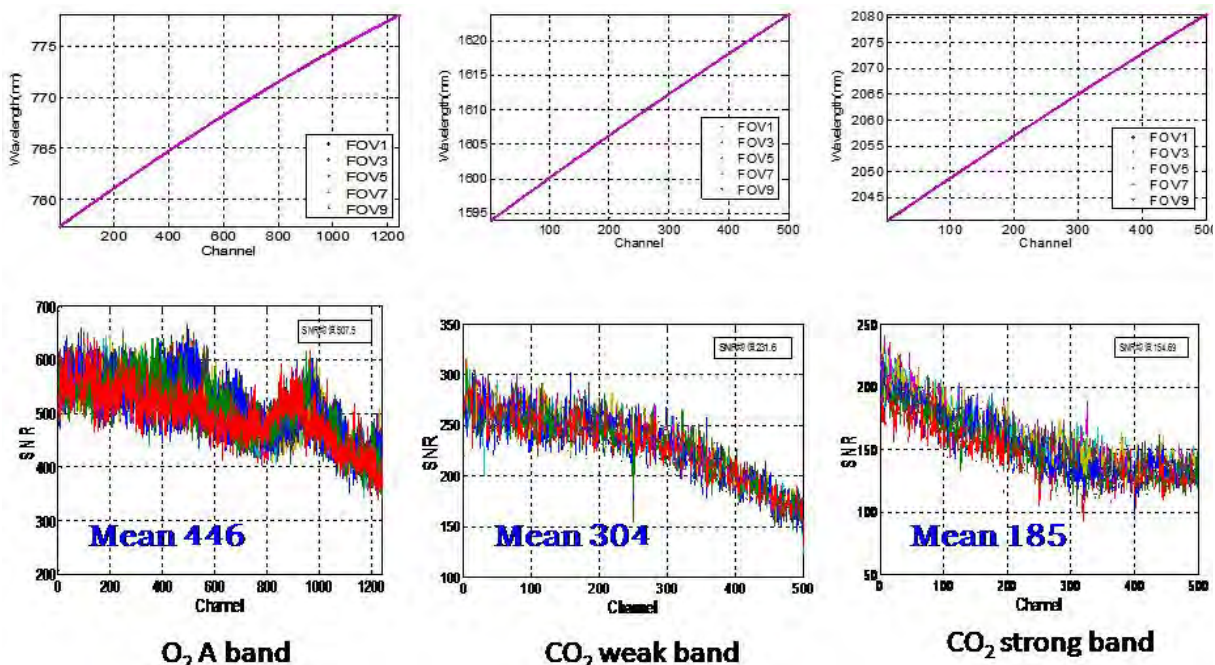


Fig. 7 Signal to noise ratio (SNR) measurements from the three channels

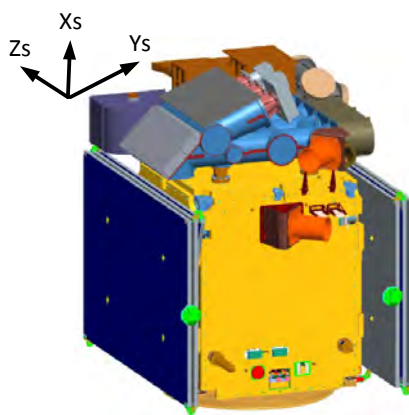


Fig. 8 Configuration of TanSat

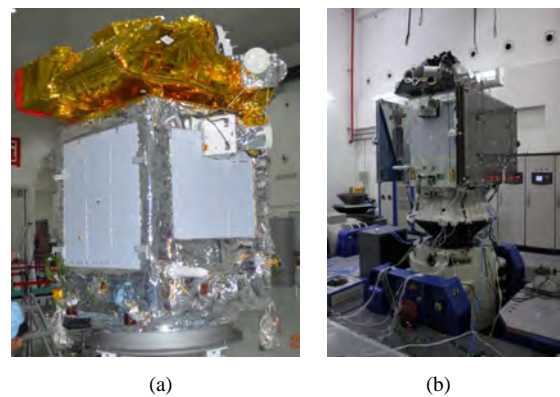


Fig. 9 TanSat integration test: (a) Thermal balance test, (b) Mechanical test.

system. The ground data management subsystem provides operations management of the satellite, and receives, processes, and archives data. Its construction was based on the ground segment of China's FENGYUN (FY) meteorological satellites, and shares some of the FY infrastructure and subsystems. The products retrieval subsystem will process TanSat Level 2 (L2), Level 3 (L3), and Level 4 (L4) products. TanSat L2 products include XCO₂, aerosol optical parameters, and surface pressure retrieved from the HRHS-GS and CAPI data. TanSat L3 products include grid data, such as the monthly mean XCO₂ data. TanSat L4 products include the CO₂ surface flux and CO₂ concentration at global and regional scales. Currently, the L2 and L4 retrieval software has been implemented in the NMSC. Section 3 briefly described the retrieval algorithms and gave a scientific explanation of these products. More detailed information is provided in the Algorithm Theoretical Basis Document and Product Description Document of TanSat. Generally, TanSat will adopt the policy of data sharing, to encourage domestic and international science teams to apply TanSat data in their researches and feedback the results to TanSat science team.

8 Validation Plan

The ground-based Fourier transform infrared spectroscopy

(FTIR) Total Carbon Column Observing Network (TCCON) has become a useful tool to validate XCO₂ from the retrieval results of satellite observations. TCCON is a network of ground-based FTIR instruments, providing highly accurate and precise column-averaged dry-air mixing ratios of atmospheric components, including CO₂, CH₄, and N₂O, for the validation of the corresponding satellite products, such as GOSAT and Orbiting Carbon Observatory 2 (OCO-2). All of the TCCON stations use GGG software to derive the gas column concentrations. Unfortunately, there is no Chinese station in the TCCON yet, but some studies had been conducted using FTIR measurements in Shenzhen to develop a retrieval method^[15] or by analyzing TCCON measurements to validate GOSAT XCO₂ and XCH₄ glint ocean data^[16]. The TanSat science team will seek the international cooperation with some of the TCCON stations and will apply these data to validate TanSat observations. There are several IFS125 FTIR instruments and optical spectrum analyzers located in different sites over China. Figure 10 shows the location of the TanSat validation site and the instrument in each site. These instruments are managed by the Institute of Atmospheric Physics, Chinese Academy of Sciences, National Satellite Meteorological Center, China Meteorological Administration, and other organizations. These sites and their measurements could be coordinated more

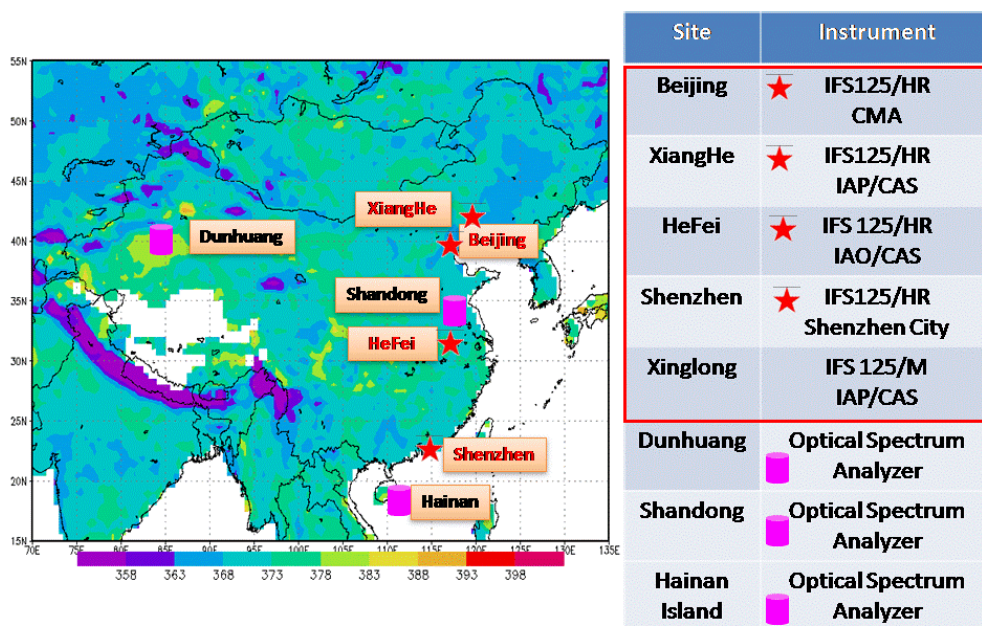


Fig. 10 TanSat surface validation station: (Left) Location of station. (Right) Instruments at the station (IFS125/HR FTIR instruments and optical spectrum analyzers).

efficiently to form a domestic surface validation network to validate TanSat observations.

9 Summary and Perspective

After five years of effective work by the TanSat team, the TanSat mission has completed the following stages. (1) TanSat payloads and platform have been designed, and the manufacture, optimization, laboratory testing and integration of instruments have been completed for the whole satellite. (2) The scientific capabilities have been investigated, and the XCO₂ and CO₂ flux retrieval algorithms and implementation of the software in the data processing system are completed. (3) Surface calibration and validations have been undertaken and a plan for a validation campaign has been determined. After the successful launch of TanSat, its data will be widely used by different science teams, general users, and government agencies^[17, 18].

Acknowledgments

This work was supported by the National High-tech Research and Development Program (2011AA12A104) and the Strategic Priority Research Program-Climatic Change: Carbon Budget and Relevant Issues (XDA050-40200)

Reference

- [1] Yoshida Y, Ota Y, Eguchi N et al. (2011) Retrieval algorithm for CO₂ and CH₄ column abundances from short-wavelength infrared spectral observations by the greenhouse gases observing satellite. *Atmos Meas Tech* 4: 717–734.
- [2] Crisp D. (2015) Measuring atmospheric carbon dioxide from space with the orbiting carbon observatory-2 (OCO-2). *Proc SPIE*, 2015: 1–7.
- [3] Wen Chen, Yonghe Zhang, Zengshan Yin, et al. (2012) The Tansat mission: Global CO₂ observation and monitoring, 63rd International Astronautical Congress, Naples, Italy. IAC-12-B4.4.12, 1–7.
- [4] Yi Liu, Zengshan Yin, Yuquan Zheng, et al. (2012) “Chinese carbon dioxide satellite (TanSat) status and plans,” in Proc. Of American Geophysical Union 2012 Fall Meeting, American Geophysical Union.
- [5] Hang Zhang, Chao Lin, Yuquan Zheng, et al. (2016) “Development and characterization of Carbon Observing Satellite,” *J. Appl. Remote Sens.* 10(2), doi: 10.1117/1.JRS.10.024003.
- [6] Yi Liu, Zhaonan Cai, Dongxu Yang et al. (2014) Effects of spectral sampling rate and range of CO₂ absorption bands on XCO₂ retrieval from TanSat hyperspectral spectrometer. *Chin. Sci. Bull.* 59(14): 1485–1491.
- [7] Guangming Shi, Chengcai Li et al. (2014) Sensitivity Analysis of Single-Angle Polarization Reflectance Observed by Satellite. *Chin. Sci. Bull.* 59(14): 1519–1528.
- [8] Zhaonan Cai, Yi Liu, Dongxu Yang (2014) Analysis of XCO₂ retrieval sensitivity using simulated Chinese Carbon Satellite (TanSat) measurements. *Science China: Earth Sciences*, doi: 10.1007/s11430-013-4707–1.
- [9] Yi Liu, Dongxu Yang, Zhaonan Cai (2013) A retrieval algorithm for TanSat XCO₂ observation: Retrieval experiments using GOSAT data. *Chin. Sci. Bull.* 58(13): 1520–1523.
- [10] Dongxu Yang, Yi Liu, Zhaonan Cai et al. (2015) An advanced carbon dioxide retrieval algorithm for satellite measurements and its application to GOSAT observations. *Chin. Sci. Bull.* 60(23): 2063–2066.
- [11] Xiangjun Tian, Zhenghui Xie, Zhaonan Cai et al. (2014) The Chinese carbon cycle data-assimilation system (Tan-Tracker). *Chin. Sci. Bull.* 59(14): 1541–1546.
- [12] Xiangjun Tian, Zhenghui Xie, Yi Liu et al. (2014) A joint data assimilation system (Tan-Tracker) to simultaneously estimate surface CO₂ fluxes and 3-D atmospheric CO₂ concentrations from observations. *Atmos. Chem. Phys.*, 14, 13281–13293.
- [13] JianBo Deng, Yi Liu, Dong Xu Yang et al. (2014) CH₄ retrieval from hyperspectral satellite measurements in shortwave infrared: sensitivity study and preliminary test with GOSAT data. *Chin. Sci. Bull.* 59(14): 1499–1507.
- [14] Hailei Liu, Minzheng Duan, Daren Lu et al. (2014) Algorithm for retrieving surface pressure from hyper-spectral measurements in oxygen A-band. *Chin. Sci. Bull.* 59(14): 1492–1498.
- [15] Jian Li, Chengcai Li, Jietai Mao et al. (2014) Retrieval of column-averaged volume mixing ratio of CO₂ with ground-based high spectral resolution solar absorption. *Chin. Sci. Bull.* 59(14): 1536–1540.
- [16] Minqiang Zhou, Bart Dils, Pucal Wang et al. (2015) Validation of TANSO-FTS/GOSAT XCO₂ and XCH₄ glint mode retrievals using TCCON data from near-ocean sites, *Atmos. Meas. Tech. Discuss.*, 8, 10897–10935.
- [17] Yi Liu, Daren Lu, Hongbin Chen et al. (2011) Advances in technologies and methods for satellite remote sensing of atmospheric CO₂. *Remote Sensing Technology and Appl.*, 26(2): 247–254 (in Chinese).
- [18] Yuquan Zheng (2011) Development status of remote sensing instruments for greenhouse gases. *Chinese Optics*, 4(6): 546–561 (in Chinese).

Space Solar Physics in China: 2014–2016

GAN Weiqun

Key Laboratory of Dark Matter and Space Astronomy, Purple Mountain Observatory, Chinese Academy of Sciences, Nanjing 210008

* E-mail: wqgan@pmo.ac.cn

Key words

Space astronomy
Solar physics

Abstract

The activities of Chinese space solar physics in 2014–2016 were mainly undertaken within the framework of Strategic Priority Program on Space Science, sponsored by CAS, which include: to accomplish the last version for the mid and long-term (2016–2030) plan of Chinese space solar physics; to subsidy a few of pre-study projects of space solar physics; to implement two intensive study projects, ASO-S and SPORT. This paper summarizes these activities briefly.

1 Strategic Study for 2016 to 2030

The primary draft of “The Strategic Report of Mid and Long-term (2016–2030) Plan of Chinese Space Solar Physics” was finished in 2014. In the early 2015, National Space Science Center (NSSC), CAS arranged international peer reviews for the report. Taking into account almost all of comments of the referees, we submitted the revised version to NSSC in October 2015. The final report, as an appendix of “Prospect for Space Science in 2016–2030”, will be published in 2016.

The current prospect, based on the two prospects previously proposed in 2008 and 2012, is more concise and more extensive and puts more emphases on the actuality and feasibility. The core contents are on the one hand to aim at the vital scientific objectives on the physical formation of solar magnetic fields, solar flares, and Coronal Mass Ejections (CMEs), their mutual interactions and relations; on the other hand, to take the opportunity of the 25th solar activity maximum to make a breakthrough from zero in the approval of a solar satellite proposal. Subsequently, at the early time of the “14th Five-Year Plan”, it is targeted to realize the breakthrough from zero in the solar observations made by our own mission. The ultimate goal is to become one of the key members in the international community of

space solar physics by 2030.

2 Financing Some Pre-study Projects

During this period, the third batch of pre-study projects was got partially support from Strategic Priority Program on Space Science, sponsored by CAS. Among them 4 projects belong to solar physics:

- (i) Key technique studies on a new type Bi-refraction filter (January 2015–December 2016).
- (ii) Further technique studies on space-borne solar full-disc vector magnetograph (January 2015–December 2016).
- (iii) Key technique studies on detection of solar energetic particles with a high accuracy (January 2016–December 2016).
- (iv) Key technique studies on inner coronagraph at L5 (January 2015–December 2016).

Due to financial problem, these projects were delayed by one or two years to start and the scale of budget were also reduced.

3 Some Mission-level Projects

As described in previous reports^[1–6], although there are some mission-level projects, like Deep Space Solar Observatory (DSO, a heritage of Space Solar Observatory), Kuafu (a solar-terrestrial mission), Advanced Space-

based Solar Observatory (ASO-S), and Solar Polar Orbit Telescope (SPORT), none of these mission projects has formally been developed into the engineering phase. From 2014 to 2016, both DSO and Kuafu did not seem to have made great progress on the way to the approval of the engineering stage. We therefore describe only ASO-S and SPORT here. Another project, LASGA (Large Area Solar GAMMA-ray spectrometer) is also described, since it is a new mission which has been accepted as a payload aboard the future Chinese space station.

(1) ASO-S

ASO-S is a mission proposed for the 25th solar maximum by the Chinese solar community^[7]. The scientific objectives are to study the relationships among solar magnetic field, solar flares, and Coronal Mass Ejections (CMEs). ASO-S consists of three payloads: Full-disk Magnetograph (FMG), Lyman-alpha Solar Telescope (LST), and Hard X-ray Imager (HXI), to measure solar magnetic field, to observe CMEs and solar flares, respectively. ASO-S has a solar synchronous orbit at an altitude of 720 km with an inclination angle of around 98.2°. ASO-S is almost finished by now its so-called intensive studies (similar to phase-B). Explicitly, during 2014–2015, following works have been accomplished: the preliminary design of ASO-S satellite system; the requirement analysis on rocket system, launch site system, measurement and control system, and ground support system; the preliminary design of scientific application system; the schematic design and key techniques for scientific payloads of FMG, LST, and HXI; some prototypes (e.g., HXI) or key components of payloads; and so on.

On October 30–31, 2014, ISSI-BJ organized an international forum especially on ASO-S^[8]. Twenty-five participants reached an agreement after this two-day meeting: “ASO-S has well-defined scientific objectives and will measure fundamental and important parameters of solar magnetic field, solar flares, and CMEs. The mission is not overloaded and is still ambitious. It has focus and is in good balance between the advanced scientific objectives and resources. Therefore, the mission is very probable to be successful”.

ASO-S is now ready for the competition with other proposals for phase-C study.

(2) SPORT

SPORT is intended to be the first mission from a polar orbit around the Sun to measure the solar high-latitude magnetism leading to eruptions and the fast solar

wind, and to image the interplanetary propagation of CMEs in the ecliptic. The payload aboard SPORT includes a solar ultraviolet imager (121.6 and 13.1 nm), a solar vector magnetograph, a large-angle coronagraph (white light and 121.6 nm), a heliospheric imager, an energetic neutral atom imager, a solar wind plasma analyzer, a fluxgate magnetometer, a radio and plasma wave instrument, and an energetic particle and composition analyzer.

A Chinese CZ-5E rocket with upper stage is envisioned to be the launch vehicle for SPORT. The spacecraft is designed to first travel along a big elliptic transfer orbit towards Jupiter. Using the gravity assist of Jupiter, the mission will achieve an elliptic polar orbit around the Sun with an inclination angle of 62°, a perihelion at 0.7 AU, and an aphelion at 5 AU. Further multiple gravity assists from Venus will shrink the solar polar orbit within 2 AU and increase the inclination angle to 70°. Imaging observations of the Sun and interplanetary space will be activated, when SPORT is within 2 AU from the Sun. Because of the high-inclination angle, the total mass of the mission has to be no more than 1050 kg.

During the intensive study between 2012–2015, the SPORT team made the following progress: a schematic design of the spacecraft orbit and platform, booms and antennas deployable in space, attitude stability and control, and full-prototypes and key components of some instruments (e.g., the coronagraph, heliospheric imager and ultraviolet imager). The ISSI-BJ SPORT forum held on 24–25 November 2013 concluded that SPORT will be a “great mission” having both imaging and in situ capabilities out of the ecliptic^[9]. SPORT will compete for selection and implementation during China’s 13th Five-Year Plan period of 2016–2020.

(3) LASGA

It is an accepted proposal for the payload aboard Chinese space station which will be launched in 2020 or in 2022. The scientific goals are: (i) to observe solar high energy radiation with a high sensitivity, for studying the relationship between accelerated electrons and protons, as well as the frequency distributions; (ii) to observe solar gamma-ray spectra with a high energy resolution, for studying the energy spectra of accelerated protons, their acceleration mechanisms, and temporal variations; (iii) to observe inner links between solar energetic radiation and disaster space weather, for studying the forecasting method of disaster space

weather; (iv) to observe cosmic gamma-ray bursts, for studying GeV excess near galactic center and burst mechanisms. The energy range is from 10 keV to 2.5 GeV with energy resolution of 2.8% at 662 keV. The effective area is 1600 cm². By now LASGA is in the stage of schematic design. If everything goes smoothly, LASGA is expected to work in the orbit for over ten years and cover a whole period of the 25th solar cycle.

Acknowledgments The author is grateful to Dr. Ying Liu for providing the material of SPORT. The work is supported by NNSFC *via* grants 11233008 and 11427803.

References

- [1] Gan W Q, Xue S J. Space astronomy in China: 2002–2004. *Chin. J. Space Sci.*, 2004, **22**(Suppl.): 99-101
- [2] Gan W Q. Space astronomy in China during 2004–2006. *Chin. J. Space Sci.*, 2006, **26**(Suppl.): 76-78
- [3] Gan W Q. Space astronomy in China: 2006–2008. *Chin. J. Space Sci.*, 2008, **28**(5): 424-425
- [4] Gan W Q, Zhang S N, Yan Y H, Chang J. Space astronomy in China: 2008–2010. *Chin. J. Space Sci.*, 2010, **30**(5): 424-426
- [5] Zhang S N, Yan Y H, Gan W Q. China's space astronomy and solar physics in 2011–2012. *Chin. J. Space Sci.*, 2012, **32**(5): 605-617
- [6] Gan W Q. Space Solar Physics in 2012–2014. *Chin. J. Space Sci.*, 2014, **34**(5): 563-564
- [7] Gan W Q, Deng Y Y, Li H, Wu J, Zhang H Y, *et al.* ASO-S: Advanced Space-based Solar Observatory. Proc. of SPIE, 2015, 9604: 96040T
- [8] Gan W Q, Feng L. Exploring solar eruptions and their origins. *IS-SI-BJ Magazine*, 2015 (5): 1-11
- [9] Xiong M, Liu Y. An out-of-ecliptic view of our Sun. *ISSI-BJ Magazine*, 2014 (4): 1-19

A Brief Review of Interplanetary Investigations in China from 2014 to 2016

ZHAO Xinhua¹, ZHANG Min², WANG Yuming², HE Jiansen³, KONG Xiangliang⁴

1. (State Key Laboratory of Space Weather, Center for Space Science and Applied Research, Chinese Academy of Sciences, Beijing 100190)
2. (CAS Key Laboratory of Geospace Environment, Department of Geophysics and Planetary Sciences, University of Science and Technology of China, Hefei 230026)
3. (School of Earth and Space Sciences, Peking University, Beijing 100871)
4. (Shandong Provincial Key Laboratory of Optical Astronomy and Solar-Terrestrial Environment, and Institute of Space Sciences, Shandong University, Weihai, Shandong 264209)

* E-mail: fengx@spaceweather.ac.cn

Key words

Solar wind
Coronal mass ejection
Solar flare
Interplanetary transients
Space weather

Abstract

Great progress has been made in the research of solar corona and interplanetary physics by the Chinese scientists during the past two years (2014–2016). Nearly 100 papers were published in this area. In this report, we will give a brief review to these progresses. The investigations include: solar corona; solar wind and turbulence; superhalo electron and energetic particle in the inner heliosphere; solar flares and radio bursts; Coronal Mass Ejections (CMEs) and their interplanetary counterparts; Magnetohydrodynamic (MHD) numerical modeling; CME/shock arrival time prediction; magnetic reconnection; solar variability and its impact on climate. These achievements help us to better understand the evolution of solar activities, solar eruptions, their propagations in the heliosphere, and potential geoeffectiveness. They were achieved by the Chinese solar and space scientists independently or *via* international collaborations.

1 Solar Corona

A jet is a considerable amount of plasma being ejected from the chromosphere or lower corona into the higher corona and is a common phenomenon. Usually, a jet is triggered by a brightening or a flare, which provides the first driving force to push plasma upward. In this process, magnetic reconnection is thought to be the mechanism to convert magnetic energy into thermal, nonthermal, and kinetic energies. However, most jets could reach an unusual high altitude and end much later than the end of its associated flare. This fact implies that there is another way to continuously transfer magnetic energy into kinetic energy even after the reconnection.

The picture described above is well known in the community, but how and how much magnetic energy is released through a way other than reconnection is still unclear. By studying a prominence-like jet observed by the Atmospheric Imaging Assembly (AIA) on board the Solar Dynamics Observatory (SDO) and the Extreme Ultraviolet Images (EUVI) telescope onboard Solar TERrestrial RELations Observatory Ahead (STEREO-A), Liu *et al.*^[1] found that the continuous relaxation of the post-reconnection magnetic field structure is an important process for a jet to climb up higher than it could through only reconnection. The kinetic energy of the jet gained through the relaxation is 1.6 times that gained from the reconnection. The resultant energy flux is hun-

dreds of times larger than the flux required for the local coronal heating, suggesting that such jets are a possible source to keep the corona hot. Furthermore, rotational motions appear all the time during the jet. The analysis suggests that torsional Alfvén waves induced during reconnection could not be the only mechanism to release magnetic energy and drive jets.

As one of the most intriguing phenomena occurring in the solar atmosphere, solar jets have been studied extensively and deeply in the past few decades. The potential relations and interactions between jets and CMEs are intriguing and could enrich their knowledge of the various physical processes in the solar atmosphere. Liu *et al.*^[2] presented multi-point, multi-wavelength observations and analysis of a solar coronal jet and Coronal Mass Ejection (CME) event. Employing the GCS model, they obtained the real (three-dimensional) heliocentric distance and direction of the CME and found it to propagate at a high speed of over $1000 \text{ km}\cdot\text{s}^{-1}$. The jet erupted before the CME and shared the same source region. The temporal and spatial relationship between these two events leads to the possibility that the jet triggered the CME and became its core. This scenario holds the promise of enriching their understanding of the triggering mechanism of CMEs and their relations to coronal large-scale jets. This work was highlighted by the American Astronomical Society NOVA website in its front page on November 18.

Zhang *et al.*^[3] presented multi-wavelength observations of a prominence eruption originating from a quadrupolar field configuration, in which the prominence was embedded in a side arcade. Within the two-day period prior to its eruption on 2012 October 22, the prominence was perturbed three times by chromospheric fibrils underneath, which rose upward, became brightened, and merged into the prominence, resulting in horizontal flows along the prominence axis, suggesting that the fluxes carried by the fibrils were incorporated into the magnetic field of the prominence. These perturbations caused the prominence to oscillate and to rise faster than before. The absence of intense heating within the first two hours after the onset of the prominence eruption, which followed an exponential increase in height, indicates that ideal instability played a crucial role. The eruption involved interactions with the other side arcade, leading up to a twin coronal mass ejection, which was accompanied by transient surface brightenings in the central arcade, followed by transient dimmings and

brightenings in the two side arcades. They suggest that flux feeding from chromospheric fibrils might be an important mechanism to trigger coronal eruptions.

Liu *et al.*^[4] combined observations of the Coronal Multi-channel Polarimeter and the SDO/AIA to study the characteristic properties of (propagating) Alfvénic motions and quasi-periodic intensity disturbances in polar plumes. This unique combination of instruments highlights the physical richness of the processes taking place at the base of the (fast) solar wind. The (parallel) intensity perturbations with intensity enhancements around 1% have an apparent speed of $120 \text{ km}\cdot\text{s}^{-1}$ (in both the 171 and 193 Å passbands) and a periodicity of 15 minutes, while the (perpendicular) Alfvénic wave motions have a velocity amplitude of $0.5 \text{ km}\cdot\text{s}^{-1}$, a phase speed of $830 \text{ km}\cdot\text{s}^{-1}$, and a shorter period of 5 minutes on the same structures. These observations illustrate a scenario where the excited Alfvénic motions are propagating along an inhomogeneously loaded magnetic field structure such that the combination could be a potential progenitor of the magnetohydrodynamic turbulence required to accelerate the fast solar wind.

Liu *et al.*^[5] reported the observation of an X-class long-duration flare which is clearly confined. It appears as a compact-loop flare in the traditional EUV passbands (171 and 195 Å), but in the passbands sensitive to flare plasmas (94 and 131 Å), it exhibits a cusp-shaped structure above an arcade of loops like other long-duration events. Inspecting images in a running difference approach, they find that the seemingly diffuse, quasi-static cusp-shaped structure consists of multiple nested loops that repeatedly rise upward and disappear approaching the cusp edge. Over the gradual phase, they detect numerous episodes of loop rising, each lasting minutes. A differential emission measure analysis reveals that the temperature is highest at the top of the arcade and becomes cooler at higher altitudes within the cusp-shaped structure, contrary to typical long-duration flares. With a nonlinear force-free model, the analysis shows that the event mainly involves two adjacent sheared arcades separated by a T-type Hyperbolic Flux Tube (HFT). One of the arcades harbors a magnetic flux rope, which is identified with a filament that survives the flare owing to the strong confining field. They conclude that a new emergence of magnetic flux in the other arcade triggers the flare, while the preexisting HFT and flux rope dictate the structure and dynamics of the flare loops and ribbons during the long-lasting decay

phase, and that a quasi-separatrix layer high above the HFT could account for the cusp-shaped structure.

Gou *et al.*^[6] performed a Differential Emission Measure (DEM) analysis of candle-flame-shaped flares observed with the Atmospheric Imaging Assembly onboard the SDO. The DEM profile of flaring plasmas generally exhibits a double peak distribution in temperature, with a cold component around $\lg T \approx 6.2$ and a hot component around $\lg T \approx 7.0$. Attributing the cold component mainly to the coronal background, they propose a mean temperature weighted by the hot DEM component as a better representation of flaring plasma than the conventionally defined mean temperature, which is weighted by the whole DEM profile. Based on the corrected mean temperature, the majority of the flares studied, including a confined flare with a double candle-flame shape sharing the same cusp-shaped structure, resemble the famous Tsuneta flare in temperature distribution, *i.e.*, the cusp-shaped structure has systematically higher temperatures than the rounded flare arcade underneath. However, the M7.7 flare on 19 July 2012 poses a very intriguing violation of this paradigm: the temperature decreases with altitude from the tip of the cusp toward the top of the arcade; the hottest region is slightly above the X-ray loop-top source that is co-spatial with the emission-measure-enhanced region at the top of the arcade. This signifies that a different heating mechanism from the slow-mode shocks attached to the reconnection site operates in the cusp region during the flare decay phase.

The second peak in the Fe XVI 33.5 nm line irradiance observed during solar flares by the Extreme-Ultraviolet Variability Experiment (EVE) is known as the EUV late phase. Liu *et al.*^[7] defined the extremely large late phase because it not only has a bigger peak in the warm 33.5 irradiance profile, but also releases more EUV radiative energy than the main phase. Through detailed inspection of the EUV images from three points of view, it was discovered that aside from the later-phase loop arcades, the main contributor of the extremely large late phase is a hot structure that fails to erupt. This hot structure is identified as a flux rope, which is quickly energized by the flare reconnection and later on continuously produces the thermal energy during the gradual phase. Together with the late-phase loop arcades, the flux rope failing to erupt with the additional heating create the extremely large EUV late phase.

Liu *et al.*^[8] studied a Coronal Mass Ejection (CME) associated with an X-class flare whose initiation is clearly observed in the low corona with high-cadence, high-resolution EUV images, providing a rare opportunity to witness the early evolution of an energetic CME in detail. The eruption starts with a slow expansion of cool overlying loops (~ 1 MK) following a jet-like event in the periphery of the active region. Underneath the expanding loop system, a reverse S-shaped dimming is seen immediately above the brightening active region in hot EUV passbands. The dimming is associated with a rising diffuse arch (~ 6 MK), which they interpret as a preexistent, high-lying flux rope. This is followed by the arising of a double hot channel (~ 10 MK) from the core of the active region. The higher structures rise earlier and faster than lower ones, with the leading front undergoing extremely rapid acceleration up to $35 \text{ km} \cdot \text{s}^{-2}$. This suggests that the torus instability is the major eruption mechanism and that it is the high-lying flux rope rather than the hot channels that drives the eruption. The compression of coronal plasmas skirting and overlying the expanding loop system, whose aspect ratio h/r increases with time as a result of the rapid upward acceleration, plays a significant role in driving an outward-propagating global EUV wave and a sunward-propagating local EUV wave, respectively.

2 Solar Wind and Turbulence

The edge of the Active Region (AR) is possibly associated with the source of the slow/intermediate solar wind. How the plasma is supplied to the solar wind is not yet investigated. Zhang *et al.*^[9] conducted detail study of the edge of the AR 10977. They selected three small regions with positive correlations between the temporal profiles of the radiation intensity and Doppler shift for all the five emission lines as labelled by white boxes in Fig.1. One of the regions show “weak dimming”, while the other two show “weak brightening”, indicating a slow draining (replenishing) of plasma in the solar wind flux tubes. They suggest that the plasma supply of the slow/intermediate solar wind at the source region is intermittent and with alternation of draining and replenishing.

Traditionally the out layer of the solar atmosphere is composed of photosphere, chromosphere, transition region, corona. The energy and mass flow to the corona and the solar wind must pass through the transition re-

gion. The transition region is important for understanding the heating of the corona and the heating and acceleration of the solar wind. Recently, transit transition region embedded below the traditional transition region was reported by Yan *et al.*^[10]. The appearance of the chromospheric absorption lines like Ni II and Fe II, and the self-absorption of Si IV lines formed in the transition region temperature, with additional estimated density information, suggest that the magnetic reconnection occurs in the middle chromosphere and the plasma is heated to the transition region temperature. The self-absorption of Si IV lines is first reported here.

The interchange reconnection scenario, with foot-point shearing flow being used to energize the system and drive the reconnection, is probably an effective way to supply the mass and energy to solar wind. Fast-propagating Magnetosonic Waves (FMWs) has been directly observed by the SDO/AIA. Yang *et al.*^[11] performed a numerical investigation of the excitation of FMWs in the interchange reconnection scenario. The modelling results show that the hot (~10 MK) reconnection outflows and FMWs owing to the interaction between plasmoids and the ambient magnetic field in the outflow region, both appear under the interchange reconnection scenario. The estimated energy flux of FMWs is ~50 times smaller than the energy flux related to the tube-channeled reconnection outflow, indicating that the energetically and dynamically reconnection outflow is far more important than the waves in the energy and mass supply to the solar wind.

Superhalo electrons appear to be continuously present in the interplanetary medium, even during very quiet times, with a power-law spectrum at energies above ~2 keV. Yang *et al.*^[12] investigated the generation of superhalo electrons by magnetic reconnection in the solar wind source region, using magnetohydrodynamics and test particle simulations for both single X-line reconnection and multiple X-line reconnection. They find that the direct current electric field, produced in the magnetic reconnection region, can accelerate electrons from an initial thermal energy of $T \sim 10^5$ K up to hundreds of keV. After acceleration, some of the accelerated electrons, together with the nascent solar wind flow driven by the reconnection, propagate upwards along the newly-opened magnetic field lines into interplanetary space, while the rest move downwards into the lower atmosphere. Similar to the observed superhalo electrons at 1 AU, the flux of upward-traveling accel-

ated electrons versus energy displays a power-law distribution at ~2–100 keV, $f(E) \sim E^{-\delta}$, with a δ of ~1.5–2.4. For single (multiple) X-line reconnection, the spectrum becomes harder (softer) as the anomalous resistivity parameter α (uniform resistivity η) increases. These modelling results suggest that the acceleration in the solar wind source region may contribute to superhalo electrons.

The wave-particle interaction processes occurring in the solar wind provide crucial information to understand the wave dissipation and simultaneous particle heating in plasma turbulence. One requires observations of both wave fluctuations and particle kinetics near the dissipation range, which have, however, not yet been analyzed simultaneously. He *et al.*^[13] showed new evidence of wave-particle interactions by combining the diagnosis of wave modes with the analysis of particle kinetics on the basis of measurements from the WIND spacecraft with a high cadence of about 3 s. Solar wind protons appear to be highly dynamic in their velocity distribution consisting of varying anisotropic core and beam components. The basic scenario of solar wind proton heating through wave-particle interaction is suggested to be the following. Left-handed cyclotron resonance occurs continuously, and is evident from the observed proton core velocity distribution and the concurrent quasi-parallel left-handed Alfvén cyclotron waves. Landau and right-handed cyclotron resonances are persistent and indicated by the observed drifting anisotropic beam and the simultaneous quasi-perpendicular right-handed kinetic Alfvén waves in a general sense.

Traditionally, the energy in solar wind turbulence is considered to be cascaded by the non-linear interaction between counter-propagating Alfvén Waves (AWs). However, the precise connection between the turbulent fluctuations and the particle kinetics has not yet been established. For the first time, He *et al.*^[14] reported the simultaneous observation of counter-propagating magnetohydrodynamic waves in the solar wind turbulence and present clear evidence of plasma turbulence heating. As opposed to the traditional paradigm with counter-propagating Alfvén Waves (AWs), anti-sunward AWs are encountered by Sunward slow Magnetosonic Waves (SMWs) in this new type of solar wind compressible turbulence. The counter-propagating AWs and SMWs correspond, respectively, to the dominant and sub-dominant populations of the imbalanced Elsässer variables.

Nonlinear interactions between the AWs and SMWs are inferred from the non-orthogonality between the possible oscillation direction of one wave and the possible propagation direction of the other. The associated protons are revealed to exhibit bi-directional asymmetric beams in their velocity distributions: sunward beams appear in short, narrow patterns and anti-sunward in broad extended tails. It is suggested that multiple types of wave-particle interactions, *i.e.*, cyclotron and Landau resonances with AWs and SMWs at kinetic scales, are taking place to jointly heat the protons perpendicular and in parallel.

The dissipation of SMWs may play a significant role in heating the solar wind and SMWs contribute essentially to the solar wind compressible turbulence. The interaction between anti-sunward AWs and sunward SMWs has been reported in the new type of solar wind compressible turbulence. It becomes important for people to investigate the role of the SMWs in simulation. Most previous identifications of slow waves utilized the characteristic negative correlation between $\delta|B|$ and $\delta\rho$. However, that criterion does not well identify quasi-parallel slow waves, for which $\delta|B|$ is negligible compared to $\delta\rho$. Zhang *et al.*^[15] presented a new method of identification of slow waves, which applicable for the three-dimensional (3D) compressible simulation. It is based on two criteria: (1) that $V_p B_0$ (phase speed projected along B_0) is around $v_A > c_s$, and that (2) there exists a clear correlation of δv_{\parallel} and $\delta\rho$. This research demonstrates that if $v_A > c_s$, slow waves possess correlation between δv_{\parallel} and $\delta\rho$, with $\delta\rho/\delta v_{\parallel} \approx \pm\rho_0/c_s$. This method helps to distinguish slow-mode waves from fast and Alfvén waves, both of which do not have this polarity relation. The criteria are insensitive to the propagation angle θ_{KB} , defined as the angle between wave vector k and B_0 ; they can be applied with a wide range of β if only $v_A > c_s$. Four cases of slow wave trains are identified with this method in their numerical simulation. The slow wave trains seem to deform, probably caused by interaction with other waves; as a result, fast or Alfvén waves may be produced during the interaction and seem to propagate bi-directionally away. Their identification and analysis of the wave trains provide useful methods for investigations of compressible turbulence in the solar wind or in similar environments, and will thus deepen understandings of slow waves in the turbulence.

Based on theories, the beam instability induced by

shock-accelerated ions can generate Upstream-Propagating Alfvén Waves (UPAWs) with a power spectral bump near 0.03 Hz, while the nonlinear wave-wave interaction favors an inverse cascade to create a power law spectrum. Wang *et al.*^[16] presented the first observational evidence for the Upstream-Propagating Alfvénic Fluctuations (UPAFs) with power law spectra. They totally found 35 UPAWs and 47 UPAFs with power law spectra, ~47% of which are associated with energetic ion events (>30 keV). These UPAWs and UPAFs are mostly observed in the slow solar wind. However, their occurrence rate and power behave differently in dependence on the radial distance from the Earth.

The UPAWs related to the Earth's bow shock is often reported. However, the really sunward propagating AWs is rarely reported. Using measurements from the WIND spacecraft, He *et al.*^[17] report the observation of sunward propagating AWs in solar wind that is magnetically disconnected from the Earth's bow shock. In the sunward magnetic field sector, they find a period lasting for more than three days in which there existed (during most time intervals) a negative correlation between the flow velocity and magnetic field fluctuations, thus indicating that the related AWs are mainly propagating sunward. The simultaneous observations of counter-streaming suprathermal electrons and non-appearance of interplanetary coronal mass ejection suggest that these AWs are indeed sunward AWs not owing to the deflection of an open magnetic field line. As the scale goes from the magnetohydrodynamic down to the ion kinetic regime, the wave vector of magnetic fluctuations usually becomes more orthogonal to the mean magnetic field direction, and the fluctuations become increasingly compressible, which are both features consistent with quasi-perpendicular kinetic AWs. However, this case shows clear signatures of quasi-parallel sunward propagating ion cyclotron waves. Concurrently, the solar wind proton velocity distribution reveals a sunward field-aligned beam that drifts at about the local Alfvén speed. This beam is found to run in the opposite direction of the normally observed (anti-sunward) proton beam, and is apparently associated with sunward propagating Alfvén/ion cyclotron waves. The results and conclusions of this study enrich their knowledge of solar wind turbulence and foster their understanding of proton heating and acceleration within a complex magnetic field geometry.

MHD discontinuities are ubiquitous in the solar wind and are often found at the origin of turbulence intermittency. They may also play a key role in the turbulence dissipation and heating of the solar wind. How the discontinuities formed or excited has not been yet well studied. Yang *et al.*^[18] investigated how the discontinuities, especially Rotational Discontinuities (RDs), are formed in MHD turbulence. In a simulation of the decaying compressive three-dimensional (3D) MHD turbulence with an imposed uniform background magnetic field, they detect RDs with sharp field rotations and little variations of magnetic field intensity, as well as mass density. Based on the analysis of the magnetic field and plasma parameters of one of the identified RDs, the identified RD evolves from the steepening of the Alfvén wave with moderate amplitude, which is caused by the nonuniformity of the Alfvén speed in the ambient turbulence.

The Tangential Discontinuities (TDs) and Rotational Discontinuities (RDs) are found to be the two most important types of discontinuities. Recently, the connection between turbulence intermittency and proton thermodynamics has been observationally investigated. Zhang *et al.*^[19] presented numerical results from a three-dimensional MHD simulation with pressure anisotropy and defined new methods for identifying and distinguishing TDs and RDs. Three statistical results obtained for the relative occurrence rates and heating effects were highlighted: (i) RDs tend to take up the majority of the discontinuities along with time; (ii) the thermal states embedding TDs tend to be associated with extreme plasma parameters or instabilities while RDs do not; (iii) TDs have a higher average T as well as perpendicular temperature T_{\perp} . The simulation shows that TDs and RDs evolve and contribute to solar wind heating differently.

The power-spectrum index of magnetic fluctuations is a crucial parameter for the characterization of nonlinear interactions affecting the solar wind turbulence. Most previous observations were made for large- and moderate amplitude magnetic fluctuations, which include current sheets and intermittent structures. By using measurements from the WIND spacecraft, Wang *et al.*^[20] presented magnetic spectral features as derived by the fast Fourier transform method from six-minute time series of magnetic fluctuations with low relative amplitudes ($\delta B/B_0$) of only 0.05–0.11. When comparing their spectra with those of moderate-amplitude fluctua-

tions ($\delta B/B_0 \approx 0.4$), they found that for the low-amplitude fluctuations the averaged magnetic spectral indices are -1.67 and -1.46 , respectively, for small and large sampling angles, i.e., the angle between the Sun-to-Earth radial direction and the mean magnetic field direction. However, for the moderate-amplitude fluctuations, these two indices are -1.89 and -1.70 , respectively. This result of the moderate-amplitude fluctuations is consistent with that of previous analyses, which, by using the wavelet technique, revealed spectral anisotropy of magnetic fluctuations and yielded an index of -2 in the parallel direction and $-5/3$ in the perpendicular direction. However, the result found here for the low amplitude fluctuations has not been reported before, and thus will probably initiate new studies aiming to better understand the turbulent nature of such low-amplitude fluctuations. Future studies will help to understand why the spectral anisotropy differs for fluctuations of different amplitudes.

Turbulence in the solar wind was recently reported to be anisotropic, with the average power spectral index close to -2 when sampling parallel to the local mean magnetic field B_0 and close to $-5/3$ when sampling perpendicular to the local B_0 . This result was widely considered to be observational evidence for the Critical Balance Theory (CBT), which is derived by making the assumption that the turbulence strength is close to one. However, this basic assumption has not yet been checked carefully with observational data. Wang *et al.*^[21] presented for the first time the scale dependent magnetic-field fluctuation amplitude, which is normalized by the local B_0 and evaluated for both parallel and perpendicular sampling directions, using two 30-day intervals of Ulysses data. From the results, the turbulence strength is evaluated as much less than one at small scales in the parallel direction. An even stricter criterion is imposed when selecting the wavelet coefficients for a given sampling direction, so that the time stationarity of the local B_0 is better ensured during the local sampling interval. The spectral index for the parallel direction is then found to be -1.75 , whereas the spectral index in the perpendicular direction remains close to -1.65 . These two new results, namely that the value of the turbulence strength is much less than one in the parallel direction and that the angle dependence of the spectral index is weak, cannot be explained by existing turbulence theories, like CBT, and thus will require new theoretical considerations and promote further observations of so-

lar-wind turbulence.

Intensive studies have been conducted to understand the anisotropy of solar wind turbulence. However, the anisotropy of Elsässer variables (Z^\pm) in 2D wave-vector space has yet to be investigated. Yan *et al.*^[22] first verified the transformation based on the projection-slice theorem between the power spectral density $\text{PSD}_{2\text{D}}(\mathbf{k}_\parallel, \mathbf{k}_\perp)$ and the spatial correlation function $\text{CF}_{2\text{D}}(\mathbf{k}_\parallel, \mathbf{k}_\perp)$. Based on the application of the transformation to the magnetic field and the particle measurements from the WIND spacecraft, they investigate the spectral anisotropy of Elsässer variables (Z^\pm), and the distribution of residual energy E_R , Alfvén ratio R_A , and Elsässer ratio R_E in the $(\mathbf{k}_\parallel, \mathbf{k}_\perp)$ space. The spectra $\text{PSD}_{2\text{D}}(\mathbf{k}_\parallel, \mathbf{k}_\perp)$ of B , V , and Z_{major} (the larger of Z^\pm) show a similar pattern that $\text{PSD}_{2\text{D}}(\mathbf{k}_\parallel, \mathbf{k}_\perp)$ is mainly distributed along a ridge inclined toward the \mathbf{k}_\perp axis. This is probably the signature of the oblique Alfvénic fluctuations propagating outwardly. Unlike those of B , V , and Z_{major} , the spectrum $\text{PSD}_{2\text{D}}(\mathbf{k}_\parallel, \mathbf{k}_\perp)$ of Z_{minor} is distributed mainly along the \mathbf{k}_\perp axis. Close to the \mathbf{k}_\perp axis, $|E_R|$ becomes larger while R_A becomes smaller, suggesting that the dominance of magnetic energy over kinetic energy becomes more significant at small \mathbf{k}_\parallel . R_E is larger at small \mathbf{k}_\parallel , implying that $\text{PSD}_{2\text{D}}(\mathbf{k}_\parallel, \mathbf{k}_\perp)$ of Z_{minor} is more concentrated along the \mathbf{k}_\perp direction as compared to that of Z_{major} . The residual energy condensate at small \mathbf{k}_\parallel is consistent with simulation results in which E_R is spontaneously generated by Alfvén wave interaction.

The heliocentric orbits of STEREO-A and B with a separation in longitude increasing by about 45° per year provided Liu *et al.*^[23] the unique opportunity to study the evolution of the Heliospheric Plasma Sheet (HPS) on a time scale of up to ~ 2 days and to investigate the relative locations of HPSs and Heliospheric Current Sheets (HCSs). Previous work usually determined the HCS locations based only on the interplanetary magnetic field. A recent study showed that a HCS can be taken as a global structure only when it matches with a Sector Boundary (SB). Using magnetic field and suprathermal electron data, it was also shown that the relative location of HCS and SB can be classified into five different types of configurations. However, only for two out of these five configurations, the HCS and SB are located at the same position and only these will therefore be used for their study of the HCS/HPS rela-

tive location. They find that out of 37 SBs in their data set, there are 10 suitable HPS/HCS event pairs. They find that an HPS can either straddle or border the related HCS. Comparing the corresponding HPS observations between STEREO-A and B, they find that the relative HCS/HPS locations are mostly similar. In addition, the time difference of the HPSs observations between STEREO-A and B match well with the predicted time delay for the solar wind coming out of a similar region of the Sun. They therefore conclude that HPSs are stationary structures originating at the Sun.

In general, the Heliospheric Current Sheet (HCS), which defines the boundary of sunward and anti-sunward magnetic field, is encased by the slow solar wind. The Stream Interface (SI) represents the boundary between the solar wind plasmas of different origin and/or characteristics. According to earlier studies using data of low time resolution, the SI and HCS get closer further away from the Sun, and the two structures coincide with each other around 5 AU. Huang *et al.*^[24] used STEREO data of a much higher time resolution to reveal an unusual case where the SI and HCS are coincident near 1 AU and separated from the so-called True Sector Boundary (TSB) at which the suprathermal electrons change their relative propagation directions. Preliminary analysis suggests that the closed loops in pseudo-streamers continually have interchange reconnection with the open-field lines that lead them, resulting not only in the coincidence of HCS and SI but also in the separation of the TSB from the HCS/SI. They therefore conclude that the interchange reconnection plays an important role in the evolution of slow solar wind.

In general, near 1 AU the Heliospheric Current Sheet (HCS) will be separated from the Stream Interface (SI) by several hours. However, a recent study found a coincidence case of these two structures that differs from those in former studies. This paper presents a statistical study with multi-spacecraft data during 2007 to 2010 to investigate a classification scheme and the stability of the coincidence cases. Based on the relative locations of HCS and True Sector Boundary (TSB), which is defined by the suprathermal electrons strahl changing pitch angles, and the existence of Heat Flux Dropouts (HFDs) that relate to disconnected magnetic field lines, Huang *et al.*^[25] found eleven coincidence cases that can be classified into three categories (Type I–III). Among

them, type I coincidence cases, which connect to ideal HCSs, are the majority (nine cases). Type II, having separated TSB and HCS, may relate to complicated interchange reconnection processes (one case). Type III has a close connection with HFDs (one case). The statistical results suggest: a) during 2007 to 2010 they observed eleven coincidence cases near 1 AU that can be classified into three types; b) only three out of eleven coincidence cases are observed by several spacecraft with large separation distances, indicating that the coincidence structures may not be stable for a long time; c) interchange reconnection and pseudostreamers should play a role in forming these coincidence cases.

Dynamic Pressure Pulses (DPPs) in the solar wind are a significant phenomenon closely related to the solar terrestrial connection and physical processes of solar wind dynamics. In order to automatically identify DPPs from solar wind measurements, Zuo *et al.*^[26] developed a procedure with a three-step detection algorithm that is able to rapidly select DPPs from the plasma data stream and simultaneously define the transition region where large dynamic pressure variations occur and demarcate the upstream and downstream region by selecting the relatively quiet status before and after the abrupt change in dynamic pressure. To demonstrate the usefulness, efficiency, and accuracy of this procedure, they have applied it to the Wind observations from 1996 to 2008 by successfully obtaining the DPPs. The procedure can also be applied to other solar wind spacecraft observation data sets with different time resolutions.

Zuo *et al.*^[27] performed a statistical survey on the properties of DPPs near 1 AU based on nearly 20 years of observations from the WIND spacecraft. It was found that only a tiny fraction of DPPs (around 4.2%) can be regarded as interplanetary shocks. For most DPPs, the total pressure (the sum of the thermal pressure and magnetic pressure) remains in equilibrium, but there also exists a small fraction of DPPs that are not pressure balanced. The overwhelming majority of DPPs are associated with solar wind disturbances, including coronal mass ejection-related flows, corotating interaction regions, as well as complex ejecta. The annual variations of the averaged occurrence rate of DPPs are roughly in phase with the solar activity during solar cycle 23, and during the rising phase of solar cycle 24.

Turbulence is a chaotic flow regime filled by irregular flows. The dissipation of turbulence is a fundamental problem in the realm of physics. Theoretically, dissipa-

tion ultimately cannot be achieved without collisions, and so how turbulent kinetic energy is dissipated in the nearly collisionless solar wind is a challenging problem. Wave particle interactions and Magnetic Reconnection (MR) are two possible dissipation mechanisms, but which mechanism dominates is still a controversial topic. Wang *et al.*^[28] analyzed the dissipation region scaling around a solar wind MR region. They found that the MR region shows unique multifractal scaling in the dissipation range, while the ambient solar wind turbulence reveals a monofractal dissipation process for most of the time. These results provide the first observational evidences for intermittent multifractal dissipation region scaling around a MR site, and they also have significant implications for the fundamental energy dissipation process.

3 Superhalo Electron and Energetic Particle in the Inner Heliosphere

Wang *et al.*^[29] have derived the particle injections at the Sun for ten good electron/³He-rich solar energetic particle (SEP) events, using a 1.2 AU particle path length. The inferred solar injections of high-energy (~10 to 300 keV) electrons and of ~MeV/nucleon ions (carbon and heavier) start with a delay of 17 ± 3 min and 75 ± 14 min, respectively, after the injection of low-energy (~0.4 to 9 keV) electrons. The injection duration (averaged over energy) ranges from ~200 to 550 min for ions, from ~90 to 160 min for low-energy electrons, and from ~10 to 30 min for high-energy electrons. Most of the selected events have no reported H α flares or GOES SXR bursts, but all have type III radio bursts that typically start after the onset of a low-energy electron injection. All nine events with the coverage of the Large Angle and Spectrometric CORonagraph (LASCO) on Solar and Heliospheric Observatory (SOHO) have a relatively fast (> -570 km·s⁻¹), mostly narrow (~30°), west-limb Coronal Mass Ejection (CME) that launches near the start of the low-energy electron injection, and reaches an average altitude of ~1.0 and 4.7 R_s , respectively, at the start of the high-energy electron injection and of the ion injection.

Wang *et al.*^[30] presented a statistical survey of ~20–200 keV superhalo electrons measured at 1 AU by the WIND 3D Plasma & Energetic Particle instrument during quiet-time periods from 1995 January through 2013 December. The observed omnidirectional differential flux of these quiet-time superhalo electrons generally

fits to a power-law spectrum, with β ranging from ~ 1.6 to ~ 3.7 and the integrated density n_{sup} ranging from 10^{-8} to 10^{-5} cm^{-3} . In solar cycle 23 (24), the distribution of β has a broad maximum between 2.4 and 2.8 (2.0 and 2.4). Both β and the logarithm of n_{sup} show no obvious correlation with sunspot number, solar flares, solar wind core population, *etc.*

Yang *et al.*^[31] presented a comprehensive study of the angular distribution of ~ 20 – 200 keV superhalo electrons measured at 1 AU by the WIND 3DP instrument during quiet times from 1995 January through 2005 December. They found that for $\sim 96\%$ of the selected quiet-time samples, superhalo electrons have isotropic angular distributions, while for $\sim 3\%$ ($\sim 1\%$) of quiet-time samples, superhalo electrons have outward anisotropic (inward-anisotropic) angular distributions. All three groups of superhalo electrons show no correlation with the local solar wind plasma, interplanetary magnetic field, turbulence, and energetic electrons accelerated/reflected at the terrestrial bow shock.

Tao *et al.*^[32] presented a statistical survey of the energy spectrum of solar wind suprathermal (~ 0.1 – 1.5 keV) electrons measured by the WIND 3DP instrument at 1 AU during quiet times at the minimum and maximum of solar cycles 23 and 24. They separate the halo and strahl electrons based on their different angular behaviors and fit the energy spectrum of halo/strahl to a kappa function. They find a strong positive correlation between kappa and effective temperature T_{eff} for both strahl and halo electrons, and a strong positive correlation between the strahl number density and halo number density, likely reflecting the nature of the generation of these suprathermal electrons.

Wu *et al.*^[33] reported observations of the acceleration and trapping of energetic ions and electrons between a pair of Corotating Interaction Regions (CIRs). The event occurred in Carrington Rotation 2060. Observed by the STEREO-B spacecraft, the two CIRs were separated by less than 5 days. In contrast to other CIR events, the fluxes of the energetic ions and electrons in this event reached their maxima between the trailing edge of the first CIR and the leading edge of the second CIR. The radial magnetic field (B_r) reversed its sense and the anisotropy of the flux also changed from Sunward to anti-Sunward between the two CIRs. Furthermore, there was an extended period of counter streaming suprathermal electrons between the two CIRs. Similar obser-

vations for this event were also obtained with the Advanced Composition Explorer and STEREO-A. They conjectured that these observations were due to a U-shaped, large-scale magnetic field topology connecting the reverse shock of the first CIR and the forward shock of the second CIR. Such a disconnected U-shaped magnetic field topology may have formed due to magnetic reconnection in the upper corona.

A rapid radiocarbon ^{14}C increase of 1.2% in AD774–775 has been reported in cedar and oak tree rings. So far, the origin of the ^{14}C increase is still uncertain and the possible origin is either supernova or solar particle event. The most possible origin of ^{14}C increase is strong solar flares and Coronal Mass Ejections (CMEs) with strong particles emission. Comprehensive approaches to identify the strong historical solar particle events based on the rapid $^{14}\text{C}/^{10}\text{Be}$ increase in tree/coral rings and ice cores, long duration strong auroras and geomagnetic storms are introduced. Evidence of the super auroras in AD775 was first found by Zhou *et al.*^[34] in a Chinese Chronicle Jiutangshu and it supports the views that the rapid ^{14}C increase and strong auroras around AD775 are most possibly caused by strong solar storms with intense particles emission. It was identified that the solar event around AD775 would be the strongest solar particle event in the past 11400 years. The discovery is significant for the research on the history of solar activities, space weather and forecast, radiation of solar energetic particles and protection.

Wang *et al.*^[35] investigated the conditions for producing rapid variations of Solar Energetic Particle (SEP) intensity commonly known as “dropouts”. In particular, they used numerical model simulations based on solving the focused transport equation in the three-dimensional Parker interplanetary magnetic field to put constraints on the properties of particle transport coefficients in both directions perpendicular and parallel to the magnetic field. Their calculations of the temporal intensity profile of 0.5 and 5 MeV protons at the Earth show that the perpendicular diffusion must be small while the parallel mean free path is long in order to reproduce the phenomenon of SEP dropouts. When the parallel mean free path is a fraction of 1 AU and the observer is located at 1 AU, the perpendicular to parallel diffusion ratio must be below 10^{-5} if they want to see the particle flux dropping by at least several times within 3 h. When the observer is located at a larger solar radial distance,

the perpendicular to parallel diffusion ratio for reproducing the dropouts should be even lower than that in the case of 1 AU distance. A shorter parallel mean free path or a larger radial distance from the source to observer will cause the particles to arrive later, making the effects of perpendicular diffusion more prominent and SEP dropouts disappear. All of these effects require the magnetic turbulence that resonates with the particles to be low everywhere in the inner heliosphere.

A fundamental statement in diffusion theory is provided by the so-called theorem on reduced dimensionality. The latter theorem is saying that if the dimensionality of the turbulence is reduced, charged particles are tied to a single magnetic field line. If there is pitch angle scattering and therewith parallel diffusion, this usually means that perpendicular transport is subdiffusive. Subdiffusive transport was found in numerous simulations for slab turbulence. However, it was unclear whether the theorem is valid for other models with reduced dimensionality such as the two-dimensional model. Qin and Shalchi^[36] simultaneously traced magnetic field lines and energetic particles and they computed the distance between the particle and the initial field line. They confirm the aforementioned theorem for slab turbulence but they cannot confirm it for two-dimensional turbulence. They also showed that particles are not tied to field lines for two-component turbulence.

Wang *et al.*^[37] investigated the onset time of solar energetic particle (SEP) events with numerical simulations and analyzes the accuracy of the Velocity Dispersion Analysis (VDA) method. Using a three-dimensional focused transport model, they calculate the fluxes of protons observed in the ecliptic at 1 AU in the energy range between 10 MeV and 80 MeV. In particular, three models are used to describe different SEP sources produced by flare or coronal shock, and the effects of particle perpendicular diffusion in the interplanetary space are also studied. They have the following findings. When the observer is disconnected from the source, the effects of perpendicular diffusion in the interplanetary space and particles propagating in the solar atmosphere have a significant influence on the VDA results. As a result, although the VDA method is valid with impulsive source duration, low background, and weak scattering in the interplanetary space or fast diffusion in the solar atmosphere, the method is not valid with gradual source duration, high background, or

strong scattering.

A gradual Solar Energetic Particle (SEP) event observed by multi-spacecraft has been simulated by Qin and Wang^[38]. The time profiles of SEP fluxes accelerated by an interplanetary shock in the three-dimensional interplanetary space are obtained by solving numerically the Fokker-Planck focused transport equation. The interplanetary shock is modeled as a moving source of energetic particles. By fitting the 1979 March 01 SEP fluxes observed by Helios 1, Helios 2, and IMP 8 with their simulations, they obtain the best parameters for the shock acceleration efficiency model. And they also find that the particle perpendicular diffusion coefficient with the level of ~1%–3% of parallel diffusion coefficient at 1 AU should be included. The reservoir phenomenon is reproduced in the simulations, and the longitudinal gradient of SEP fluxes in the decay phase, which is observed by three spacecraft at different locations, is more sensitive to the shock acceleration efficiency parameters than that is to the perpendicular diffusion coefficient.

The spatial and temporal invariance in the spectra of energetic particles in gradual solar events is reproduced in simulations. Based on a numerical solution of the focused transport equation, Wang and Qin^[39] obtained the intensity time profiles of Solar Energetic Particles (SEPs) accelerated by an interplanetary shock in 3D interplanetary space. The shock is treated as a moving source of energetic particles with a distribution function. The time profiles of particle fluxes with different energies are calculated in the ecliptic at 1 AU. According to their model, they find that shock acceleration strength, parallel diffusion, and adiabatic cooling are the main factors in forming the spatial invariance in SEP spectra, and perpendicular diffusion is a secondary factor. In addition, the temporal invariance in SEP spectra is mainly due to the effects of adiabatic cooling. Furthermore, a spectra invariant region, which agrees with observations but is different from the one suggested by Reames *et al.* is proposed based on their simulations.

An approximate analytic description of a diffusion coefficient, including the effect of adiabatic focusing, has been developed by Wang and Qin^[40]. This description is formulated with the aid of stochastic differential equations and the steady perturbation solution of the Fokker-Planck transport equation. The analytical formula is based on three important assumptions. First, the pitch-angle diffusion coefficient is set to be separable

from the spatial coordinate and the pitch-angle cosine. Second, the spatial dependence of the ratio between the mean-free path and focusing length is assumed to be weak. Third, the pitch-angle distribution relaxes quickly to a steady state. The new analytic formula could be applied to calculate the spatial diffusion coefficient in the interplanetary and interstellar space.

Studying the access of the Cosmic Rays (CRs) into the magnetosphere is important to understand the coupling between the magnetosphere and the solar wind. Chu and Qin^[41] numerically studied CRs' magnetospheric access with vertical geomagnetic cutoff rigidities using the method proposed by Smart and Shea (1999). By the study of CRs' vertical geomagnetic cutoff rigidities at high latitudes they obtain the CRs' window (CRW) whose boundary is determined when the vertical geomagnetic cutoff rigidities drop to a value lower than a threshold value. Furthermore, they studied the area of CRWs and found out they are sensitive to different parameters, such as the z component of Interplanetary Magnetic Field (IMF), the solar wind dynamic pressure, AE index, and Dst index. It was found that both the AE index and Dst index have a strong correlation with the area of CRWs during strong geomagnetic storms. However, during the medium storms, only AE index has a strong correlation with the area of CRWs, while Dst index has a much weaker correlation with the area of CRWs. This result on the CRW can be used for forecasting the variation of the cosmic rays during the geomagnetic storms.

Experimental data from Cluster have shown that entropy density can be generated across Earth's bow shock. These new observations are a starting point for a more sophisticated analysis that includes computer modeling of a collisionless shock using observed shock parameters as input. Yang *et al.*^[42] presented the first comparison between observations and particle-in-cell simulations of such entropy generation across a collisionless shock. The ion heating at the shock is dominated by the phase mixing of reflected and directly transmitted ions, which are separated from the incident ions. The electron heating is a nearly thermal process due to the conservation of their angular momentum. For both species, they calculate the entropy density across the shock, and obtain good consistency between observations and simulations on entropy generation across the shock. They also find that the entropy generation rate is reduced as the

shock Mach number decreases.

Wei *et al.*^[43] reviewed current models, which have been used to describe gradual SEP events and their applications. Generally, there are two major approaches to model gradual SEP events: some studies include the acceleration mechanisms of SEPs induced by CME driven shocks, while others assume a fixed particle injecting source at the shock. In addition, some researchers also consider the effects of perpendicular diffusion on SEPs propagation in 3D interplanetary magnetic fields. These models can partially reproduce the observed properties for SEP events. Then, they make a brief review of numerical MHD simulation models, such as Space Weather Modeling Frame (SWMF), CORonal and HELiospheric (CORHEL) model, Solar Inter Planetary-Conservative Element Solution Element (SIP-CESE) model, CORonal INTERplanetary (COIN) model. All these models can be used to work out the propagation parameters of CME and CME-driven shocks, which are expected to provide inputs to the particle model. Finally, some discussions of the future work about how to combine MHD and particle models were presented.

Solar Energetic Particles (SEPs) pose one of the most serious hazards to spacecraft systems and constrain human activities in space. Thus, it is of importance to forecast SEP events. Several theories and numerical models are applied to simulate SEP events. Each model makes some assumptions to simplify the complex acceleration and transportation processes within such events. In general, SEP will interact with ambient solar wind and background magnetic field during transportation. It is recognized that interplanetary transport effects must be taken into account at any analysis of SEP propagation. In the previous simulation, it was always assumed Parker magnetic field and fixed solar wind speed as the input parameters. However, these assumptions are too simple when compared with the real conditions. In order to get better results, it is necessary to use more accurate background conditions. Recently, Wei *et al.*^[44] changed the fixed solar wind speed into spatial dependent speed profile based on Parker's theory, and replaced the Parker magnetic field with another Parker like magnetic field based on in situ data at 1 AU. By solving the focused transport equation with simulation of time-backward stochastic processes method, their results show that: (i) Under fast solar wind speed assumption, it

is clear that the omnidirectional flux decreases faster than that for the situation with slow solar wind speed in the decay phase. They suggest that it is due to the adiabatic cooling effect. Fast solar wind speed has a significant effect on the adiabatic cooling, which leads the SEPs to lose energy more quickly during transportation. However, slow solar wind speed has less impact on the time profiles of SEP flux and anisotropy. They also compare the time profiles of SEP event observed at different observatories and energies, the results remain the same as previous; (ii) When applying in situ data of magnetic field observed by WIND during different Carrington Rotations, the omnidirectional flux time profiles vary greatly, and the main results are as follows: the peak flux appears to be delayed, multi-peak occur, anisotropy also has some differences. They think it results from the magnetic field polarity, which affects the pitch angle, and, furthermore, modulates the momentum. The characteristics are similar in solar minimum and solar maximum, while the peaks seem to be more when solar activity is active. They conclude that the real magnetic field polarity may exert a significant influence during the propagation of SEP. In the future, they will try to use the real-time background conditions which obtain from MHD models in their simulations, in order to make a thorough study of the SEP propagation.

Voyager 2 (V2) observed multiple crossings of the heliospheric Termination Shock (TS) on 2007 August 31 to September 1 at a distance of 84 AU from the Sun. Here, for the first time, Yang *et al.*^[45] presented two-dimensional Particle-in-Cell (PIC) simulations of the TS self-consistently including Pickup Ions (PUIs), and compare the simulation results with V2 observations. They find that: (i) PUIs play a key role in the energy dissipation of the TS, and most of the incident ion kinetic energy is transferred to the thermal energy of PUIs. The PIC simulation indicates that, for the upstream parameters chosen for V2 conditions, the density of PUIs is about 25% and the PUIs gain the largest fraction (approximately 86.6%) of downstream thermal pressure. (ii) The simulated heliosheath ion distribution function is a superposition of a cold core formed by transmitted solar wind ions (SWIs), with the shoulders contributed by the hot reflected SWIs and directly transmitted PUIs, and the wings of the distribution dominated by the very hot reflected PUIs. The V2 Faraday cups observed the cool core of the distribution, and so they only saw the tip of the iceberg. (iii) The nonstationarity of the shock front

is mainly caused by ripples along the shock front which form even if the percentage of PUIs is high. These simulation results agree reasonably well with the V2 experimental data. The relevance of the shock front ripples to the multiple TS crossings observed by V2 is also discussed in this paper.

Based on a hybrid galactic cosmic-ray transport model, which incorporated MHD global heliospheric data into Parker's cosmic-ray transport equation, Luo *et al.*^[46] studied the behavior of the transport of galactic cosmic rays and the corresponding gradients in their flux near the Heliopause (HP). They found that: (i) by increasing the ratio of the parallel diffusion coefficient to the perpendicular diffusion coefficient in the interstellar magnetic field of the outer heliosheath, the simulated radial flux near the HP increases as well. As the ratio multiplying factor reached 10^{10} , the radial flux experienced a sudden jump near the HP, similar to what Voyager 1 observed in 2012. (ii) The effect of changing the diffusion coefficients' ratio on the radial flux variation depends on the energy of the cosmic rays, the lower the energy, the more pronounced the effect is. (iii) The magnitude of the diffusion coefficients also affect the radial flux near the HP, the modulation beyond the HP varies by adjusting the magnitude multiplying factor.

4 Solar Flares and Radio Bursts

Ruan *et al.*^[47] presented the observation of a major solar eruption that is associated with fast sunspot rotation. The event includes a sigmoidal filament eruption, a coronal mass ejection, and a GOES X2.1 flare from NOAA active region 11283. The filament and some overlying arcades were partially rooted in a sunspot. The sunspot rotated at $\sim 10^\circ \cdot \text{h}^{-1}$ during a period of 6 h prior to the eruption. In this period, the filament was found to rise gradually along with the sunspot rotation. Based on the Helioseismic and Magnetic Imager (HMI) observation, for an area along the polarity inversion line underneath the filament, they found gradual pre-eruption decreases of both the mean strength of the photospheric horizontal field (B_h) and the mean inclination angle between the vector magnetic field and the local radial (or vertical) direction. These observations are consistent with the pre-eruption gradual rising of the filament-associated magnetic structure. In addition, according to the nonlinear force-free field reconstruction of the coronal magnetic field, a pre-eruption magnetic

flux rope structure is found to be in alignment with the filament, and a considerable amount of magnetic energy was transported to the corona during the period of sunspot rotation. Their study provides evidence that in this event sunspot rotation plays an important role in twisting, energizing, and destabilizing the coronal filament-flux rope system, and led to the eruption. They also proposed that the pre-event evolution of B_h may be used to discern the driving mechanism of eruptions.

Ruan *et al.*^[48] presented a study of the persistent and gradual penumbral decay and the correlated decline of the photospheric transverse field component 10–20 h before a major flare (X1.8) eruption on 2011 September 7. This long-term pre-eruption behavior is corroborated by the well-imaged pre-flare filament rising, the consistent expansion of the coronal arcades overlying the filament, and the nonlinear force-free field modeling results in the literature. They suggested that both the long-term pre-flare penumbral decay and the transverse field decline are photospheric manifestations of the gradual rise of the coronal filament-flux rope system. They also suggested that the C3 flare and the subsequent reconnection process preceding the X1.8 flare play an important role in triggering the later major eruption.

Chen *et al.*^[49] examined simultaneous radio and Extreme Ultraviolet (EUV)/white-light imaging data for a solar type II radio burst occurring on 2010 March 18 to deduce its source location. Using a bow-shock model, they reconstructed the three-dimensional EUV wave front (presumably the type-II-emitting shock) based on the imaging data of the two STEREO spacecraft. It is then combined with the Nancay radio imaging data to infer the three-dimensional position of the type II source. It is found that the type II source coincides with the interface between the Coronal Mass Ejection (CME) EUV wave front and a nearby coronal ray structure, providing evidence that the type II emission is physically related to the CME-ray interaction. This result, consistent with those of previous studies, is based on simultaneous radio and EUV imaging data for the first time.

Feng *et al.*^[50] studied a multi-lane solar type II radio burst that was observed by several solar spectrographson 16 February 2011. The event was also recorded by the Nancay Radio heliograph (NRH) at several metric wavelengths, by the AIA onboard the SDO, and by the EUVI onboard the STEREO in a number of EUV passbands. These multi-wavelength data provide a rare opportunity to reveal the emission source of the multiple

type II lanes. Their study shows that all lanes are associated with a single EUV wave, presumably the radio-emitting shock. The EUV wave was driven by a CME associated with an M1.6 flare and a filament eruption. With the NRH data and the 3D bow-shock reconstruction that they built using the multi-viewpoint data of the EUV wave, they were able to deduce the 3D coordinates of the radio sources. They concluded that all the three type II lanes originated from the western flank of the shock, with two of them from closely adjacent locations on the southern part, the other one from a distinct location on the northern part. This case study demonstrates how the type II origin can be pinpointed by combining analyses of different data sets.

Kong *et al.*^[51] examined two solar type II radio bursts, separated by ~24 h in time together. Both events are associated with CMEs erupting from the same active region (NOAA 11176) beneath a well-observed helmet streamer. They found that the type II emissions in both events ended once the CME/shock fronts passed the white-light streamer tip, which is presumably the magnetic cusp of the streamer. This leads them to conjecture that the closed magnetic arcades of the streamer may play a role in electron acceleration and type II excitation at coronal shocks. To examine such a conjecture, they conducted a test-particle simulation for electron dynamics within a large-scale partially closed streamer magnetic configuration swept by a coronal shock. They found that the closed field lines play the role of an electron trap via which the electrons are sent back to the shock front multiple times and therefore accelerated to high energies by the shock. Electrons with an initial energy of 300 eV can be accelerated to tens of keV concentrating at the loop apex close to the shock front with a counter-streaming distribution at most locations. These electrons are energetic enough to excite Langmuir waves and radio bursts. Considering the fact that most solar eruptions originate from closed field regions, they suggested that the scenario may be important for the generation of more metric type IIs. This study also provides an explanation of the general ending frequencies of metric type IIs at or above 20–30 MHz and the disconnection issue between metric and interplanetary type IIs.

In many type II solar radio bursts, the fundamental and/or the harmonic branches of the bursts can split into two almost parallel bands with similar spectral shapes

and frequency drifts. However, the mechanisms accounting for this intriguing phenomenon remain elusive. Du *et al.*^[52] reported a special band-splitting type II event in which spectral features appear systematically earlier on the upper band (with higher frequencies) than on the lower band (with lower frequencies) by several seconds. Furthermore, the emissions carried by the splitting band are moderately polarized with the left-hand polarized signals stronger than the right-hand ones. The polarization degree varies in a range of -0.3 to -0.6 . These novel observational findings provide important constraints on the underlying physical mechanisms of band-splitting of type II radio bursts.

One popular interpretation of band split of type II radio bursts is that the splitting bands are emitted from the shock upstream and downstream, respectively, with their frequency ratio (γ) determined by the shock compression ratio. This interpretation has been taken as the physical basis of many published references. Du *et al.*^[53] reported on an observational analysis of type II events with a nice split selected from ground-based RSTN data from 2001 to 2014, in the metric-decametric wavelength. They investigated the temporal variation and distribution of γ , and conducted correlation analyses on the deduced spectral values. It is found that γ varies in a very narrow range with $>80\%$ of γ (one-minute averaged data) being between 1.15 and 1.25. For some well-observed and long-lasting events, γ does not show a systematic variation trend within observational uncertainties, from the onset to the termination of the splits. In addition, the parameters representing the propagation speed of the radio source (presumably the coronal shock) show a very weak or basically no correlation with γ . They suggested that these results do not favor the upstream-downstream scenario of band splits.

Vasanth *et al.*^[54] performed a statistical analysis of the geoeffectiveness of Coronal Mass Ejections (CMEs) that are associated with interplanetary (IP) type II bursts in Solar Cycle 23 during the period 1997–2008. About 47% (109 out of 232) of IP type II bursts are found to be associated with geomagnetic storms. Of these 47%, 27% are associated with moderate, 14% with intense, and 6% with severe geomagnetic storms. They found that the IP type II bursts and their corresponding end frequencies can be used as indicators of CME geoeffectiveness: the lower the type II burst end frequency, the higher the possibility of having a stronger storm. In addition, they showed that various combinations of CME

remote-sensing and IP type II parameters can be used to improve geomagnetic storm forecasting.

5 Coronal Mass Ejections and Their Interplanetary Counterparts

Cheng *et al.*^[55] addressed the formation of a Magnetic Flux Rope (MFR) that erupted on 2012 July 12 and caused a strong geomagnetic storm event on July 15. Through analyzing the long-term evolution of the associated active region observed by the Atmospheric Imaging Assembly and the Helioseismic and Magnetic Imager on board the Solar Dynamics Observatory, it is found that the twisted field of an MFR, indicated by a continuous S-shaped sigmoid, is built up from two groups of sheared arcades near the main polarity inversion line a half day before the eruption. The temperature within the twisted field and sheared arcades is higher than that of the ambient volume, suggesting that magnetic reconnection most likely works there. The driver behind the reconnection is attributed to shearing and converging motions at magnetic foot points with velocities in the range of 0.1 – $0.6 \text{ km}\cdot\text{s}^{-1}$. The rotation of the preceding sunspot also contributes to the MFR buildup. Extrapolated three-dimensional non-linear force-free field structures further reveal the locations of the reconnection to be in a bald-patch region and in a hyperbolic flux tube. About 2 hr before the eruption, indications of a second MFR in the form of an S-shaped hot channel are seen. It lies above the original MFR that continuously exists and includes a filament. The whole structure thus makes up a stable double-decker MFR system for hours prior to the eruption. Eventually, after entering the domain of instability, the high-lying MFR impulsively erupts to generate a fast coronal mass ejection and X-class flare; while the low-lying MFR remains behind and continuously maintains the sigmoidicity of the active region.

It is generally accepted that CMEs are the results of eruptions of Magnetic Flux Ropes (MFRs). However, there is heated debate on whether MFRs exist prior to the eruptions or if they are formed during the eruptions. Several coronal signatures, *e.g.*, filaments, coronal cavities, sigmoid structures, and hot channels (or hot blobs), are proposed as MFRs and observed before the eruption, which support the pre-existing MFR scenario. There is almost no reported observation of MFR formation during the eruption. Song *et al.*^[56] presented an intriguing

observation of a solar eruptive event that occurred on 2013 November 21 with the AIA on board the SDO, which shows the formation process of the MFR during the eruption in detail. The process began with the expansion of a low-lying coronal arcade, possibly caused by the flare magnetic reconnection underneath. The newly formed ascending loops from below further pushed the arcade upward, stretching the surrounding magnetic field. The arcade and stretched magnetic field lines then curved in just below the arcade vertex, forming an X-point. The field lines near the X-point continued to approach each other and a second magnetic reconnection was induced. It is this high-lying magnetic reconnection that led to the formation and eruption of a hot blob (~ 10 MK), presumably an MFR, producing a CME. They suggested that two spatially separated magnetic reconnections occurred in this event, which were responsible for producing the flare and the hot blob (CME).

Song *et al.*^[57] reported for the first time the detailed temperature evolution process of the magnetic flux rope in a failed solar eruption. Occurring on 2013 January 05, the flux rope was impulsively accelerated to a speed of $\sim 400 \text{ km}\cdot\text{s}^{-1}$ in the first minute, then decelerated and came to a complete stop in two minutes. The failed eruption resulted in a large-size high-lying (~ 100 Mm above the surface), high-temperature “fire ball” sitting in the corona for more than two hours. The time evolution of the thermal structure of the flux rope was revealed through the differential emission measure analysis technique, which produced temperature maps using observations of the SDO/AIA. The average temperature of the flux rope steadily increased from ~ 5 MK to ~ 10 MK during the first nine minutes of the evolution, which was much longer than the rise time (about three minutes) of the associated soft X-ray flare. They suggest that the flux rope is heated by the energy release of the continuing magnetic reconnection, different from the heating of the low-lying flare loops, which is mainly produced by the chromospheric plasma evaporation. The loop arcade overlying the flux rope was pushed up by ~ 10 Mm during the attempted eruption. The pattern of the velocity variation of the loop arcade strongly suggests that the failure of the eruption was caused by the strapping effect of the overlying loop arcade.

Hot Channels (HCs), high-temperature erupting structures in the lower corona of the Sun, have been pro-

posed as a proxy of Magnetic Flux Ropes (MFRs) since their initial discovery. However, it is difficult to provide definitive proof given the fact that there is no direct measurement of the magnetic field in the corona. An alternative method is to use the magnetic field measurement in the solar wind from in situ instruments. Song *et al.*^[58] observed an HC prior to and during a Coronal Mass Ejection (CME) by the Atmospheric Imaging Assembly high temperature images. The HC is invisible in the EUVI low-temperature images, which only show the cooler Leading Front (LF). However, both the LF and an ejecta can be observed in the coronagraphic images. These are consistent with the high temperature and high density of the HC and support that the ejecta is the erupted HC. Meanwhile, the associated CME shock was identified ahead of the ejecta and the sheath through the COR2 images, and the corresponding ICME was detected by the Advanced Composition Explorer (ACE), showing the shock, sheath, and Magnetic Cloud (MC) sequentially, which agrees with the coronagraphic observations. Further, the MC average Fe charge state is elevated, containing a relatively low-ionization-state center and a high-ionization-state shell, consistent with the preexisting HC observation and its growth through magnetic reconnection. All of these observations support that the MC detected near the Earth is the counterpart of the erupted HC in the corona for this event. The study provides strong observational evidence of the HC as an MFR.

A Hot Channel (HC) is a high temperature (~ 10 MK) structure in the inner corona first revealed by the SDO/AIA. Eruptions of HCs are often associated with flares and CMEs. Results of previous studies have suggested that an HC is a good proxy for a Magnetic Flux Rope (MFR) in the inner corona as well as another well known MFR candidate, the prominence-cavity structure, which has a normal coronal temperature ($\sim 1\text{--}2$ MK). In this paper, Song *et al.*^[59] reported a high temperature structure (HTS, ~ 1.5 MK) contained in an interplanetary CME induced by an HC eruption. According to the observations of bidirectional electrons, high temperature and density, strong magnetic field, and its association with the shock, sheath, and plasma pile-up region, they suggest that the HTS is the interplanetary counterpart of the HC. The scale of the measured HTS is around $14 R_{\odot}$, and it maintained a much higher temperature than the background solar wind even at 1 AU. It is significantly different from the typical magnetic clouds, which usu-

ally have a much lower temperature. The study suggests that the existence of a corotating interaction region ahead of the HC formed a magnetic container to inhibit expansion of the HC and cool it down to a low temperature.

Filament eruptions often lead to CMEs, which can affect critical technological systems in space and on the ground when they interact with the geo-magnetosphere at high speeds. Therefore, it is important to investigate the acceleration mechanisms of CMEs in solar/space physics. Based on observations and simulations, the resistive magnetic reconnection and the ideal instability of magnetic flux ropes have been proposed to accelerate CMEs. However, it remains uncertain whether both of them play a comparable role during a particular eruption. It has been extremely difficult to separate their contributions as they often work in a close time sequence during one fast acceleration phase. Song *et al.*^[60] reported an intriguing filament eruption event, which shows two apparently separated fast acceleration phases and provides an excellent opportunity to address the issue. Through analyzing the correlations between velocity (acceleration) and soft (hard) X-ray profiles, they suggested that the instability and magnetic reconnection make a major contribution during the first and second fast acceleration phases, respectively. Further, they found that both processes have a comparable contribution to the filament acceleration in this event.

Among various factors affecting the space weather effects of a CME, its propagation trajectory in the interplanetary space is an important one determining whether and when the CME will hit the Earth. Many direct observations have revealed that a CME may not propagate along a straight trajectory in the corona, but whether or not a CME also experiences a deflected propagation in the interplanetary space is a question, which has never been fully answered. Here by investigating the propagation process of an isolated CME from the corona to interplanetary space during 12–19 September 2008, Wang *et al.*^[61] present solid evidence that the CME was deflected not only in the corona but also in the interplanetary space. The deflection angle in the interplanetary space is more than 20° toward the west, resulting a significant change in the probability the CME encounters the Earth. A further modeling and simulation-based analysis suggests that the cause of the deflection in the interplanetary space is the interaction between the CME and the solar wind, which is different

from that happening in the corona.

The dynamic process of CMEs in the heliosphere provides the key information for evaluating CMEs' geoeffectiveness and improving the accurate prediction of CME-induced shock arrival time at the Earth. Shen *et al.*^[62] presented a data-constrained 3D magnetohydrodynamic (MHD) simulation of the evolution of the CME in a realistic ambient solar wind for the 12–16 July 2012 event by using the 3-D corona interplanetary total variation diminishing (COIN-TVD) MHD code. A detailed comparison of the kinematic evolution of the CME between the observations and the simulation is carried out, including the usage of the time elongation maps from the perspectives of both STEREO-A and STEREO-B. In this case study, they find that their 3-D COIN-TVD MHD model, with the magnetized plasma blob as the driver, is able to reproduce relatively well the real 3D nature of the CME in morphology and their evolution from the Sun to the Earth. The simulation also provides a relatively satisfactory comparison with the in situ plasma data from the Wind spacecraft.

A geomagnetic storm is mainly caused by a frontside CME hitting the Earth and then interacting with the magnetosphere. However, not all frontside CMEs can hit the Earth. Thus, which CMEs hit the Earth and when they do so are important issues in the study and forecasting of space weather. In previous work, the deprojected parameters of the full-halo coronal mass ejections (FHCMEs) that occurred from 1 March 2007 to 31 May 2012 were estimated, and there are 39 frontside events that could be fitted by the Graduated Cylindrical Shell model. In this work, Shen *et al.*^[63] studied whether and when these frontside FHCMEs (FFHCMEs) hit the Earth. It is found that 59% of these FFHCMEs hit the Earth, and for central events, whose deviation angles, which are the angles between the propagation direction and the Sun-Earth line, are smaller than 45° , the fraction increases to 75%. After checking the deprojected angular widths of the CMEs, they found that all of the Earth-encountered CMEs satisfy a simple criterion that the angular width is larger than twice the deviation angle. This result suggests that some simple criteria can be used to forecast whether a CME could hit the Earth. Furthermore, for Earth-encountered CMEs, the transit time is found to be roughly anti-correlated with the deprojected velocity, but some events significantly deviate from the linearity. For CMEs with similar velocities, the differences of their transit times can be up to several

days. Such deviation is further demonstrated to be mainly caused by the CME geometry and propagation direction, which are essential in the forecasting of CME arrival.

Mass is one of the most fundamental parameters characterizing the dynamics of a CME. It has been found that CME apparent mass measured from the brightness enhancement in coronagraphs increases during its evolution in the corona. However, the physics behind it is not clear. Does the apparent mass gain come from the outflow from the dimming regions in the low corona, or from the pileup of the solar wind plasma around the CME? Feng *et al.*^[64] analyzed the mass evolution of six CME events. Based on the coronagraph observations from STEREO, they find that their masses increased by a factor of 1.3–1.7 from 7 to 15 R_s , where the occulting effect is negligible. They then adopt the “snow-plow” model to calculate the mass contribution of the piled-up solar wind. The result gives evidence that the solar wind pileup probably makes a non-negligible contribution to the mass increase. In the height range from about 7 to 15 R_s , the ratio of the modeled to the measured mass increase is roughly larger than 0.55 though the ratios are believed to be overestimated. It is not clear yet whether the solar wind pileup is a major contributor to the final mass derived from coronagraph observations, but it does play an increasingly important role in the mass increase as a CME moves further away from the Sun.

Ding *et al.*^[66] investigated the eruption and interaction of two CMEs during the large 2013 May 22 solar energetic particle event using multiple spacecraft observations. Two CMEs, having similar propagation directions, were found to erupt from two nearby Active Regions (ARs), AR11748 and AR11745, at ~08:48 UT and ~13:25 UT, respectively. The second CME was faster than the first CME. Using the graduated cylindrical shell model, they reconstructed the propagation of these two CMEs and found that the leading edge of the second CME caught up with the trailing edge of the first CME at a height of ~6 solar radii. After about two hours, the leading edges of the two CMEs merged at a height of ~20 solar radii. Type II solar radio bursts showed strong enhancement during this two hour period. Using the velocity dispersion method, they obtained the Solar Particle Release (SPR) time and the path length for energetic electrons. Further assuming that energetic protons propagated along the same interplanetary magnetic

field, they also obtained the SPR time for energetic protons, which were close to that of electrons. These release times agreed with the time when the second CME caught up with the trailing edge of the first CME, indicating that the CME-CME interaction (and shock-CME interaction) plays an important role in the process of particle acceleration in this event.

Magnetic Clouds (MCs) are the interplanetary counterparts of CMEs, and usually modeled by a flux rope. By assuming the quasi-steady evolution and self-similar expansion, Wang *et al.*^[66] introduced three types of global motion into a cylindrical force-free flux rope model and developed a new velocity-modified model for MCs. The three types of the global motion are the linear propagating motion away from the Sun, the expanding, and the poloidal motion with respect to the axis of the MC. The model was applied to 72 MCs observed by WIND spacecraft to investigate the properties of the plasma motion of MCs. They find that some MCs had a significant propagation velocity perpendicular to the radial direction and confirm the previous results that the expansion speed is correlated with the radial propagation speed and most MCs did not expand self-similarly at 1 AU. Most interestingly, they find that a significant poloidal motion did exist in some MCs. These findings advance their understanding of the MC's properties at 1 AU and the dynamic evolution of CMEs from the Sun to interplanetary space.

Space weather refers to dynamic conditions on the Sun and in the space environment of the Earth, which are often driven by solar eruptions and their subsequent interplanetary disturbances. It has been unclear how an extreme space weather storm forms and how severe it can be. Liu *et al.*^[67] reported and investigate an extreme event with multi-point remote-sensing and in situ observations. The formation of the extreme storm showed striking novel features. They suggest that the in-transit interaction between two closely launched coronal mass ejections resulted in the extreme enhancement of the ejecta magnetic field observed near 1 AU at STEREO-A. The fast transit to STEREO-A (in only 18.6 h), or the unusually weak deceleration of the event, was caused by the preconditioning of the upstream solar wind by an earlier solar eruption. These results provide a new view crucial to solar physics and space weather as to how an extreme space weather event can arise from a combination of solar eruptions.

In 2012 March the Sun exhibited extraordinary activities. In particular, the active region NOAA AR 11429 emitted a series of large Coronal Mass Ejections (CMEs) which were imaged by the STEREO as it rotated with the Sun from the east to west. The study of Liu *et al.*^[68] demonstrated that these sustained eruptions are expected to generate a global shell of disturbed material sweeping through the heliosphere. A cluster of shocks and interplanetary CMEs were observed near the Earth, and are propagated outward from 1 AU using an MHD model. The transient streams interact with each other, which erases memory of the source and results in a large Merged Interaction Region (MIR) with a preceding shock. The MHD model predicts that the shock and MIR would reach 120 AU around 2013 April 22, which agrees well with the period of radio emissions and the time of a transient disturbance in galactic cosmic rays detected by Voyager 1. These results are important for understanding the “fate” of CMEs in the outer heliosphere and provide confidence that the heliopause is located around 120 AU from the Sun.

From 2012 September 30 to October 1, the Earth underwent a two-step geomagnetic storm. Liu *et al.*^[69] examined the Sun-to-Earth characteristics of the Coronal Mass Ejections (CMEs) responsible for the geomagnetic storm with combined heliospheric imaging and in situ observations. The first CME, which occurred on 2012 September 25, is a slow event and shows an acceleration followed by a nearly invariant speed in the whole Sun-Earth space. The second event, launched from the Sun on 2012 September 27, exhibits a quick acceleration, then a rapid deceleration, and finally a nearly constant speed, a typical Sun-to-Earth propagation profile for fast CMEs. These two CMEs interacted near 1 AU as predicted by the heliospheric imaging observations and formed a complex ejecta observed at WIND, with a shock inside that enhanced the pre-existing southward magnetic field. Reconstruction of the complex ejecta with the in situ data indicates an overall left-handed flux-rope-like configuration with an embedded concave-outward shock front, a maximum magnetic field strength deviating from the flux rope axis, and convex-outward field lines ahead of the shock. While the reconstruction results are consistent with the picture of CME-CME interactions, a magnetic cloud-like structure without clear signs of CME interactions is anticipated when the merging process is finished.

The largest geomagnetic storms of solar cycle 24 so

far occurred on 2015 March 17 and June 22 with *Dst* minima of -223 and -195 nT, respectively. Both of the geomagnetic storms show a multi-step development. Liu *et al.*^[70] examined the plasma and magnetic field characteristics of the driving Coronal Mass Ejections (CMEs) in connection with the development of the geomagnetic storms. A particular effort is to reconstruct the in situ structure using a Grad-Shafranov technique and compare the reconstruction results with solar observations, which gives a larger spatial perspective of the source conditions than one-dimensional in situ measurements. Key results are obtained concerning how the plasma and magnetic field characteristics of CMEs control the geomagnetic storm intensity and variability: (i) a sheath-ejecta-ejecta mechanism and a sheath-sheath-ejecta scenario are proposed for the multi-step development of the 2015 March 17 and June 22 geomagnetic storms, respectively; (ii) two contrasting cases of how the CME flux-rope characteristics generate intense geomagnetic storms are found, which indicates that a southward flux-rope orientation is not a necessity for a strong geomagnetic storm; and (iii) the unexpected 2015 March 17 intense geomagnetic storm resulted from the interaction between two successive CMEs plus the compression by a high-speed stream from behind, which is essentially the “perfect storm” scenario proposed by Liu *et al.* (*i.e.*, a combination of circumstances results in an event of unusual magnitude), so the “perfect storm” scenario may not be as rare as the phrase implies.

For follow-up study on Sun-to-Earth propagation of fast Coronal Mass Ejections (CMEs), Liu *et al.*^[71] examined the Sun-to-Earth characteristics of slow CMEs combining heliospheric imaging and in situ observations. Three events of particular interest, the 2010 June 16, 2011 March 25, and 2012 September 25 CMEs, were selected for this study. They compared slow CMEs with fast and intermediate-speed events, and obtained key results complementing the attempt of Liu *et al.* to create a general picture of CME Sun-to-Earth propagation: (i) the Sun-to-Earth propagation of a typical slow CME can be approximately described by two phases, a gradual acceleration out to about 20–30 solar radii, followed by a nearly invariant speed around the average solar wind level; (ii) comparison between different types of CMEs indicates that faster CMEs tend to accelerate and decelerate more rapidly and have shorter cessation distances for the acceleration and deceleration; (iii) both intermediate-speed and slow CMEs would have speeds compa-

able to the average solar wind level before reaching 1 AU; (iv) slow CMEs have a high potential to interact with other solar wind structures in the Sun-Earth space due to their slow motion, providing critical ingredients to enhance space weather; and (v) the slow CMEs studied here lack strong magnetic fields at the Earth but tend to preserve a flux-rope structure with an axis generally perpendicular to the radial direction from the Sun. They also suggest a “best” strategy for the application of a triangulation concept in determining CME Sun-to-Earth kinematics, which helps to clarify confusions about CME geometry assumptions in the triangulation and to improve CME analysis and observations.

Wang *et al.*^[72] examined two successive flare eruptions (X5.4 and X1.3) on 2012 March 7 in the NOAA active region 11429 and investigate the magnetic field reconfiguration associated with the two eruptions. Using an advanced non-linear force-free field extrapolation method based on the SDO/HMI vector magnetograms, they obtained a stepwise decrease in the magnetic free energy during the eruptions, which is roughly 20% – 30% of the energy of the pre-flare phase. They also calculate the magnetic helicity and suggest that the changes of the sign of the helicity injection rate might be associated with the eruptions. Through the investigation of the magnetic field evolution, they find that the appearance of the “implosion” phenomenon has a strong relationship with the occurrence of the first X-class flare. Meanwhile, the magnetic field changes of the successive eruptions with implosion and without implosion were well observed.

Wang *et al.*^[73] studied the role of the coronal magnetic field configuration of an Active Region (AR) in determining the propagation direction of a Coronal Mass Ejection (CME). The CME occurred in the AR 11944 (S09W01) near the disk center on 2014 January 7 and was associated with an X1.2 flare. A new CME reconstruction procedure based on a polarimetric technique is adopted, which shows that the CME changed its propagation direction by around 28° in latitude within $2.5 R_s$ and 43° in longitude within $6.5 R_s$ with respect to the CME source region. This significant non-radial motion is consistent with the finding of Möstl *et al.* They use nonlinear force-free field and potential field source surface extrapolation methods to determine the configurations of the coronal magnetic field. They also calculate the magnetic energy density distributions at different heights based on the extrapolations. Their re-

sults show that the AR coronal magnetic field has a strong influence on the CME propagation direction. This is consistent with the “channeling” by the AR coronal magnetic field itself, rather than deflection by nearby structures. These results indicate that the AR coronal magnetic field configuration has to be taken into account in order to determine CME propagation direction correctly.

Wang *et al.*^[74] presented an analysis of SDO observations of an X1.4 class flare on 12 July 2012 (SOL-2012-07-12T15:37L082C105), which was associated with a pronounced sunspot rotation in the associated active region. Based on the magnetograms taken with the SDO/HMI, they measured the rotational speed of the sunspot. They also used a technique, called the differential affine velocity estimator for vector magnetograms (DAVE4VM), to determine the horizontal velocities and the magnetic helicity flux transport. The helicity flux rate due to shearing motion changed sign after the onset of the eruption. A high correlation between the sunspot rotation speed and the change in the total accumulated helicity was found. They also calculated the net fluxes of the respective magnetic polarities and the net vertical currents. The net current in the region of interest showed a synchronous change with the sunspot rotation rate. The magnetic configurations of the sigmoid filament in the active region and the associated possible interaction between different structures were further investigated by means of a nonlinear force-free field extrapolation. They identified a possible magnetic reconnection region from the three-dimensional magnetic fields and its association with EUV structures. These results suggest that the major eruption of this active region was connected with the sunspot rotation.

It has been proved from the observations and numerical simulations that the collision between solar Coronal Mass Ejections (CMEs), the largest plasmoids in the heliosphere, could be super-elastic. Shen *et al.*^[75] suggested that the CMEs' magnetic energy and thermal energy could be converted into kinetic energy through a more efficient way. However CME collisions are not always super-elastic, which means that this distinct property of plasmoids is probably excited conditionally. As the first attempt, they carry out a series of three-dimensional numerical experiments, and establish a diagram showing the dependence of the collision nature on the CME speed and k-number, the ratio of the CME's

kinetic energy to the CME's total energy. It is found that the super-elastic nature of CMEs appears at the relatively low approaching speed, and most of the previous case studies are in agreement with this diagram. Their study firmly advances the understanding of the super-elastic property of plasmoids, and does give new clues to deeply understand why and how the magnetic energy and/or thermal energy of the colliding plasmoids can be converted into kinetic energy in such an efficient way.

6 MHD Numerical Modeling

Solar-interplanetary space involves many features, such as discontinuities and heliospheric current sheet, with spatial scales many orders of magnitude smaller than the system size. The scalable, massively parallel, block-based, Adaptive-Mesh Refinement (AMR) promises to resolve different temporal and spatial scales on which solar-wind plasma occurs throughout the vast solar-interplanetary space with even less cells but can generate a good enough resolution. Feng *et al.*^[76] carried out the Adaptive Mesh Refinement (AMR) implementation of their Solar-Interplanetary space-time Conservation Element and Solution Element (CESE) Magneto-hydrodynamic model (SIP-CESE MHD model) using a six-component grid system. The AMR realization of the SIP-CESE MHD model is naturalized directly in hexahedral meshes with the aid of the parallel AMR package PARAMESH available at <http://sourceforge.net/projects/paramesh/>. At the same time, the topology of the magnetic field expansion factor and the minimum angular separation (at the photosphere) between an open field foot point and its nearest coronal-hole boundary are merged into the model in order to determine the volumetric heating source terms. Their numerical results for the validation study of the solar-wind background of Carrington rotation 2060 show overall good agreements in the solar corona and in interplanetary space with the observations from the SOHO and spacecraft data from OMNI.

Feng *et al.*^[77] introduced a new 3D MHD numerical model to simulate the steady state ambient solar wind from the solar surface to $215 R_{\odot}$ or beyond, and the model adopts a splitting finite-volume scheme based on a six-component grid system in spherical coordinates. By splitting the MHD equations into a fluid part and a magnetic part, a finite volume method can be used for

the fluid part and a constrained-transport method able to maintain the divergence-free constraint on the magnetic field can be used for the magnetic induction part. This new second-order model in space and time is validated when modeling the large-scale structure of the solar wind. The numerical results for Carrington rotation 2064 show its ability to produce structured solar wind in agreement with observations.

The dynamic process of coronal mass ejections (CMEs) in the heliosphere provides the key information for evaluating CMEs' geoeffectiveness and improving the accurate prediction of CME-induced shock arrival time at the Earth. Shen *et al.*^[78] presented a data-constrained 3D MHD simulation of the evolution of the CME in a realistic ambient solar wind for the 12–16 July 2012 event by using the 3D corona interplanetary total variation diminishing (COIN-TVD) MHD code. A detailed comparison of the kinematic evolution of the CME between the observations and the simulation is carried out, including the usage of the time elongation maps from the perspectives of both STEREO-A and STEREO-B. In this case study, they find that their 3D COIN-TVD MHD model, with the magnetized plasma blob as the driver, is able to reproduce relatively well the real 3D nature of the CME in morphology and their evolution from the Sun to the Earth. The simulation also provides a relatively satisfactory comparison with the in situ plasma data from the Wind spacecraft.

Zhang and Zhou^[79] applied the MacCormack scheme to the time-independent MHD equations in spherical coordinates with a six-component grid for the 3D interplanetary solar wind simulation. The use of six-component grid system can better body-fit the spherical shell domain of interplanetary space as well as avoid the singularity and the mesh convergence near the poles. The radial coordinate is treated as a time-like coordinate, thus can significantly reduce the computational time. The inner boundary distribution is determined by the empirical relations and observation. Five kinds of inner boundary conditions used formerly by MHD modelers are comparatively used to simulate the Carrington Rotation (CR) 1922 solar wind background. The numerical results show that all these boundary conditions can produce consistent large-scale solar wind structure with the observation, and better result in agreement with observations can be achieved when adopting the following inner boundary condition: the radial speed is obtained by the empirical relationship proposed by McGregor *et al.*

in 2011, the magnetic field is obtained by Horizontal Current Sheet (HCCS) model, an assumption of constant momentum flux is used to derive number density, and temperature is chosen to assure that the total pressure is uniform at the inner boundary.

Wang *et al.*^[80] successfully applied the space-time Conservation Element and Solution Element (CESE) method in general curvilinear coordinates to the 3D MHD simulations of the interaction between the solar wind and Saturn's magnetosphere on a six-component grid system. As a new numerical model modified for the study of the interaction between the solar wind and Saturn's magnetosphere, they obtain the large-scale configurations of Saturn's magnetosphere under the steady solar wind with due southward Interplanetary Magnetic Field (IMF) conditions. The numerical results clearly indicate that the global structure of Saturn's magnetosphere is strongly affected by the rotation of Saturn as well as by the solar wind. The subsolar standoff distances of the magnetopause and the bow shock in their model are consistent with those predicted by the data-based empirical models. Their MHD results also show that a plasmoid forms in the magnetotail under the effect of the fast planetary rotation. However, somewhat differently from the previous models, they found that there are two flow vortices generated on the duskside under due southward IMF at Saturn. On the duskside, the clockwise one closer to the planet is excited by the velocity shear between the rotational flows and the sunward flows, while the anticlockwise one is generated from the velocity shear between the tailward flows along the magnetopause and the sunward flows.

The Coronal Mass Ejection (CME) event on 3 April 2010 is the first fast CME observed by STEREO Sun Earth Connection Coronal and Heliospheric Investigation (SECCHI)/Heliospheric Imager (HI) for the full Sun-Earth line. Such an event provides a good opportunity to study the propagation and evolution of CME from the Sun up to 1 AU. Zhou *et al.*^[81] studied the time-dependent evolution and propagation of this event from the Sun to Earth using the 3D SIP-CESE MHD model. The CME is initiated by a simple spherical plasmoid model: a spheromak magnetic structure with high-speed, high-pressure, and high-plasma density plasmoid. The simulation performs a comprehensive study on the CME by comparing the simulation results with STEREO and WIND observations. It is confirmed

from the comparison with observations that the MHD model successfully reproduces many features of both the fine solar coronal structure and the typical large-scale structure of the shock propagation and gives the shock arrival time at Earth with an error of ~ 2 h. Then they analyzed in detail the several factors affecting the CME's geo-effectiveness: the CME's propagation trajectory, span angle, and velocity.

Fu and Feng^[82] proposed a new hybrid numerical scheme of combining an E-CUSP (Energy-Convective Upwind and Split Pressure) method for the fluid part and the Constrained Transport (CT) for the magnetic induction part. In order to avoid the occurrence of negative pressure in the reconstructed profiles and its updated value, a positivity preserving method is provided. Furthermore, the MHD equations are solved at each physical time step by advancing in pseudo time. The use of dual time stepping is beneficial in the computation since the use of dual time stepping allows the physical time step not to be limited by the corresponding values in the smallest cell and to be selected based on the numerical accuracy criterion. This newly established hybrid scheme combined with positivity preserving method and dual time technique has demonstrated the accurateness and robustness through numerical experiments of benchmark problems such as the 2D Orszag-Tang vortex problem and the 3D shock-cloud interaction problem.

To model the steady state solar wind, Zhang and Feng^[83] developed an implicit dual-time stepping scheme based on the finite volume method in spherical coordinates with a six-component grid system. By adding a pseudo-time derivative to the Magnetohydrodynamics equations for the solar wind plasma, the governing equations are solved implicitly at each physical time step by advancing in pseudo time. As a validation, ambient solar wind for Carrington rotation 2048 has been studied. Numerical tests with different Courant factors show its capability of producing structured solar wind and that the physical time step can be enlarged to be one hundred times that of the original one. Their numerical results have demonstrated overall good agreements with the observations.

Wang *et al.*^[84] presented a newly developed global MHD model to study the responses of the Earth's magnetosphere to the solar wind. The model is established by using the space-time Conservation Element and So-

lution Element (CESE) method in general curvilinear coordinates on a six-component grid system. As a preliminary study, they present the model's numerical results of the quasi-steady state and the dynamics of the Earth's magnetosphere under steady solar wind flow with due northward Interplanetary Magnetic Field (IMF). The model results are found to be in good agreement with those published by other numerical magnetospheric models.

Feng *et al.*^[85] presented a time-dependent 3D MHD solar wind simulation from the solar surface to the Earth's orbit driven by time-varying line-of-sight solar magnetic field data. The simulation is based on the 3D Solar-Interplanetary (SIP) Adaptive Mesh Refinement (AMR) space-time Conservation Element and Solution Element (CESE) MHD (SIP-AMR-CESE MHD) model. In this simulation, they first achieve the initial solar wind background with the time-relaxation method by inputting a potential field obtained from the synoptic photospheric magnetic field and then generate the time-evolving solar wind by advancing the initial 3D solar wind background with continuously varying photospheric magnetic field. The model updates the inner boundary conditions by using the projected normal characteristic method, inputting the high-cadence photospheric magnetic field data corrected by solar differential rotation, and limiting the mass flux escaping from the solar photosphere. They investigate the solar wind evolution from 1 July to 11 August 2008 with the model driven by the consecutive synoptic maps from the Global Oscillation Network Group. They compare the numerical results with the previous studies on the solar wind, the solar coronal observations from the Extreme ultraviolet Imaging Telescope (EIT) board on the SOHO, and the measurements from OMNI at 1 Astronomical Unit (AU). Comparisons show that the present data-driven MHD model's results have overall good agreement with the large-scale dynamical coronal and interplanetary structures, including the sizes and distributions of the coronal holes, the positions and shapes of the streamer belts, the heliocentric distances of the Alfvénic surface, and the transitions of the solar wind speeds. However, the model fails to capture the small-sized equatorial holes, and the modeled solar wind near 1 AU has a somewhat higher density and weaker magnetic field strength than observed. Perhaps better pre-processing of high-cadence observed photospheric magnetic field (particularly 3D global measurements),

combined with plasma measurements and higher resolution grids, will enable the data-driven model to more accurately capture the time-dependent changes of the ambient solar wind for further improvements. In addition, other measures may also be needed when the model is employed in the period of high solar activity.

Solar Active Region (AR) 11283 is a very magnetically complex region and it has produced many eruptions. However, there exists a non-eruptive filament in the plage region just next to an eruptive one in the AR, which gives Jiang *et al.*^[86] an opportunity to perform a comparison analysis of these two filaments. The coronal magnetic field extrapolated using the CESE-MHD-NLFFF code reveals that two Magnetic Flux Ropes (MFRs) exist in the same extrapolation box supporting these two filaments, respectively. Analysis of the magnetic field shows that the eruptive MFR contains a Bald-Patch Separatrix Surface (BPSS) cospatial very well with a pre-eruptive EUV sigmoid, which is consistent with the BPSS model for coronal sigmoids. The magnetic dips of the non-eruptive MFRs match H α observation of the non-eruptive filament strikingly well, which strongly supports the MFR-dip model for filaments. Compared with the non-eruptive MFR/filament (with a length of about 200 Mm), the eruptive MFR/filament is much smaller (with a length of about 20 Mm), but it contains most of the magnetic free energy in the extrapolation box and holds a much higher free energy density than the non-eruptive one. Both the MFRs are weakly twisted and cannot trigger kink instability. The AR eruptive MFR is unstable because its axis reaches above a critical height for torus instability, at which the overlying closed arcades can no longer confine the MFR stably. On the contrary, the quiescent MFR is very firmly held by its overlying field, as its axis apex is far below the torus-instability threshold height. Overall, this comparison investigation supports that an MFR can exist prior to eruption and the ideal MHD instability can trigger an MFR eruption.

In the solar corona, the magnetic flux rope is believed to be a fundamental structure that accounts for magnetic free energy storage and solar eruptions. Up to the present, the extrapolation of the magnetic field from boundary data has been the primary way to obtain fully three-dimensional magnetic information about the corona. As a result, the ability to reliably recover the coronal magnetic flux rope is important for coronal field

extrapolation. Jiang and Feng^[87] examined their coronal field extrapolation code with an analytical magnetic flux rope model proposed by Titov & Démoulin, which consists of a bipolar magnetic configuration holding a semi-circular line-tied flux rope in force-free equilibrium. By only using the vector field at the bottom boundary as input, they test their code with the model in a representative range of parameter space and find that the model field can be reconstructed with high accuracy. In particular, the magnetic topological interfaces formed between the flux rope and the surrounding arcade, i.e., the “hyperbolic flux tube” and “bald patch separatrix surface,” are also reliably reproduced. By this test, they demonstrate that their CESE–MHD–NLFFF code can be applied to recovering the magnetic flux rope in the solar corona as long as the vector magnetogram satisfies the force-free constraints.

Wu *et al.*^[88] presented a 3D MHD model based on an observed eruptive twisted flux rope (sigmoid) deduced from solar vector magnetograms. This model is a combination of their two very well tested MHD models: (i) data-driven 3D MHD active region evolution (MHD-DARE) model for the reconstruction of the observed flux rope and (ii) 3D MHD global coronal- heliosphere evolution (MHD-GCHE) model to track the propagation of the observed flux rope. The 6 September 2011, AR11283, event is used to test this model. First, the formation of the flux rope (sigmoid) from AR11283 is reproduced by the MHD-DARE model with input from the measured vector magnetograms given by SDO/HMI. Second, these results are used as the initial boundary condition for their MHD-GCHE model for the initiation of a Coronal Mass Ejection (CME) as observed. The model output indicates that the flux rope resulting from MHD-DARE produces the physical properties of a CME, and the morphology resembles the observations made by STEREO/COR-1.

Zhang and Feng^[89] presented a comparative study of divergence cleaning methods of magnetic field in the solar coronal 3D numerical simulation. For such purpose, the diffusive method, projection method, generalized Lagrange multiplier method and constrained-transport method are used. All these methods are combined with a finite-volume scheme in spherical coordinates. In order to see the performance between the four divergence cleaning methods, solar coronal numerical simulation for Carrington rotation 2056 has been stud-

ied. Numerical results show that the average relative divergence error is around $10^{-4.5}$ for the constrained-transport method, while about $10^{-3.1}$ – $10^{-3.6}$ for the other three methods. Although there exist some differences in the average relative divergence errors for the four employed methods, their tests show they can all produce basic structured solar wind.

7 CME/Shock Arrival Time Prediction

One of the major solar transients, Coronal Mass Ejections (CMEs) and their related interplanetary shocks have severe space weather effects and become the focus of study for both solar and space scientists. Predicting their evolutions in the heliosphere and arrival times at Earth is an important component of the space weather predictions. Various kinds of models in this aspect have been developed during the past decades. In this paper, Zhao and Dryer^[90] presented a view of the present status (during Solar Cycle 24 in 2014) of the space weather’s objective to predict the arrival of coronal mass ejections and their interplanetary shock waves at Earth. This status, by implication, is relevant to their arrival elsewhere in the solar system. Application of this prediction status is clearly appropriate for operational magnetospheric and ionospheric situations including A→B→C...solar system missions. They review current empirical models, expansion speed model, drag-based models, physics-based models (and their real-time prediction’s statistical experience in Solar Cycle 23), and MHD models. New observations in Solar Cycle 24, including techniques/models, are introduced as they could be incorporated to form new prediction models. The limitations of the present models and the direction of further development are also suggested.

Predicting the arrival times of Coronal Mass Ejections (CMEs) and their related waves at Earth is an important aspect of space weather forecasting. The Shock Propagation Model (SPM) and its updated version (SPM2), which uses the initial parameters of solar flare-Type II burst events as input, have been developed to predict the shock arrival time. Zhao and Feng^[91] continued to investigate the influence of solar disturbances and their associated CMEs on the corresponding Interplanetary (IP) shock’s arrival at Earth. It has been found that IP shocks associated with wider CMEs have a greater probability of reaching the Earth, and the CME speed obtained from coronagraph observations can be

supplementary to the initial shock speed computed from Type II radio bursts when predicting the shock's arrival time. Therefore, the third version of the model, i.e., SPM3, has been developed based on these findings. The new version combines the characteristics of solar flare-Type II events with the initial parameters of the accompanying CMEs to provide the prediction of the associated IP shock's arrival at Earth. The prediction test for 498 events of Solar Cycle 23 reveals that the prediction success rate of SPM3 is 70%–71%, which is apparently higher than that of the previous SPM2 model (61%–63%). The transit time prediction error of SPM3 for the Earth-encountered shocks is within 9 h (mean-absolute). Comparisons between SPM3 and other similar models also demonstrate that SPM3 has the highest success rate and best prediction performance.

Prediction of the shocks' arrival times (SATs) at the Earth is very important for space weather forecast. There is a well-known SAT model, Shock Time of Arrival (STOA), which is widely used in the space weather forecast. However, the shock transit time from STOA model usually has a relative large error compared to the real measurements. In addition, STOA tends to yield too much "yes" prediction, which causes a large number of false alarms. Therefore, Liu and Qin^[92] worked on the modification of STOA model. First, they give a new method to calculate the shock transit time by modifying the way to use the solar wind speed in STOA model. Second, they develop new criteria for deciding whether the shock will arrive at the Earth with the help of the sunspot numbers and the angle distances of the flare events. It is shown that their work can improve the SATs prediction significantly, especially the prediction of flare events without shocks arriving at the Earth.

8 Magnetic Reconnection

Kinetic effects resulting from the two-fluid physics play a crucial role in the fast collisionless reconnection, which is a process to explosively release massive energy stored in magnetic fields in space and astrophysical plasmas. In-situ observations in the Earth's magnetosphere provide solid consistence with theoretical models on the point that kinetic effects are required in the collisionless reconnection. However, all the observations associated with solar wind reconnection have been analyzed in the context of MHD although a lot of solar wind reconnection exhausts have been reported. Be-

cause of the absence of kinetic effects and substantial heating, whether the reconnections are still ongoing when they are detected in the solar wind remains unknown. By dual-spacecraft observations, Xu *et al.*^[93] reported a solar wind reconnection with clear Hall magnetic fields. Its corresponding Alfvénic electron outflow jet, derived from the decouple between ions and electrons, is identified, showing direct evidence for kinetic effects that dominate the collisionless reconnection. The turbulence associated with the exhaust is a kind of background solar wind turbulence, implying that the reconnection generated turbulence has not much developed.

9 Solar Variability and its Impact on Climate

Based on the well-calibrated systematic measurements of sunspot numbers, the reconstructed data of the Total Solar Irradiance (TSI), and the observed anomalies of the Earth's averaged surface temperature (global, ocean, land), Zhao and Feng^[94] investigated the periodicities of both solar activity and the Earth's temperature variation as well as their correlations on the time scale of centuries using the wavelet and cross correlation analysis techniques. The main results are as follows. (i) Solar activities (including sunspot number and TSI) have four major periodic components higher than the 95% significance level of white noise during the period of interest, *i.e.* 11-year period, 50-year period, 100-year period, and 200-year period. The global temperature anomalies of the Earth have only one major periodic component of 64.3-year period, which is close to the 50-year cycle of solar activity. (ii) Significant resonant periodicities between solar activity and the Earth's temperature are focused on the 22- and 50-year period. (iii) Correlations between solar activity and the surface temperature of the Earth on the long time scales are higher than those on the short time scales. As far as the sunspot number is concerned, its correlation coefficients to the Earth temperature are 0.31–0.35 on the yearly scale, 0.58–0.70 on the 11-year running mean scale, and 0.64–0.78 on the 22-year running mean scale. TSI has stronger correlations to the Earth temperature than sunspot number. (iv) During the past 100 years, solar activities display a clear increasing tendency that corresponds to the global warming of the Earth (including land and ocean) very well. Particularly, the ocean temperature has a slightly higher correlation to solar activity



than the land temperature. All these demonstrate that solar activity has a non-negligible forcing on the temperature change of the Earth on the time scale of centuries.

The solar impact on the Earth's climate change is a long topic with intense debates. Based on the reconstructed data of Solar Sunspot Number (SSN), the local temperature in Vostok (T), and the atmospheric CO₂ concentration data of Dome Concordia, Zhao and Feng^[95] investigated the periodicities of solar activity, the atmospheric CO₂ and local temperature in the inland Antarctica as well as their correlations during the past 11,000 years before AD 1895. They find that the variations of SSN and T have some common periodicities, such as the 208-year, 521-year, and ~1000-year cycles. The correlations between SSN and T are strong for some intermittent periodicities. However, the wavelet analysis demonstrates that the relative phase relations between them usually do not hold stable except for the millennium-cycle component. The millennial variation of SSN leads that of T by 30~40 years, and the anti-phase relation between them keeps stable nearly over the whole 11000 years of the past. As a contrast, the correlations between CO₂ and T are neither strong nor stable. These results indicate that solar activity might have potential influences on the long-term change of Vostok's local climate during the past 11000 years before modern industry.

Reference

- [1] Liu J J, Wang Y M, Liu R, Zhang Q H, Liu K, Shen C L, Wang S. When and how does a prominence-like jet gain kinetic energy. *Astrophys. J.*, 2014, 782: 94
- [2] Liu J J, Wang Y M, Shen C L, Liu K, Pan Z H, Wang S. A solar coronal jet event triggers a coronal mass ejection. *Astrophys. J.*, 2015, 813: 115
- [3] Zhang Q H, Liu R, Wang Y M, *et al.* A prominence eruption driven by flux feeding from chromospheric fibrils. *Astrophys. J.*, 2014, 789: 133
- [4] Liu J J, McIntosh S W, Moortel I D, Wang Y M. On the parallel and perpendicular propagating motions visible in polar plumes: An incubator for (fast) solar wind acceleration. *Astrophys. J.*, 2015, 806: 273
- [5] Liu R, Titov V, Gou T Y, *et al.* An unorthodox X-Class long-duration confined flare. *Astrophys. J.*, 2014, 790: 8
- [6] Gou T Y, Liu R, Wang Y M. Do all candle-flame-shaped flares have the same temperature distribution. *Sol. Phys.*, 2015, 290: 2211-2230
- [7] Liu K, Wang Y M, Zhang J, *et al.* Extremely large EUV late phase of solar flares. *Astrophys. J.*, 2015, 802: 35
- [8] Liu R, Wang Y M, Shen C L. Early evolution of an energetic coronal mass ejection and its relation to EUV waves. *Astrophys. J.*, 2014, 797: 37
- [9] Zhang J B, He J S, Yan L M, *et al.* Plasma draining and replenishing near a solar active region inferred from cross-correlation between radiation intensity and Doppler shift. *Science China Earth Sciences*, 2015, 58: 830, doi:10.1007/s11430-014-4999-9
- [10] Yan L M, Peter H, He J S, *et al.* Self-absorption in the solar transition region. *Astrophys. J.*, 2015, 811: 48, doi: 0.1088/0004-637X/811/1/48
- [11] Yang L P, Zhang L, He J S, *et al.* Numerical simulation of fast-mode magnetosonic waves excited by plasmoid ejections in the solar corona. *Astrophys. J.*, 2015, 800: 111
- [12] Yang L P, Wang L H, Z He J S, *et al.* Numerical simulation of superhalo electrons generated by magnetic reconnection in the solar wind source region. *RAA*, 2015, 15: 348-362
- [13] He J S, Wang L H, Tu C Y, *et al.* Evidence of Landau and cyclotron resonance between protons and kinetic waves in solar wind turbulence. *Astrophys. J.*, 2015, 800: L31
- [14] He J S, Tu C Y, Marsch E, *et al.* Proton heating in solar wind compressible turbulence with collisions between counter-propagating waves. *Astrophys. J.*, 2015, 813: L30(6pp)
- [15] Zhang L, Yang L P, He J S, *et al.* Identification of slow magnetosonic wave trains and their evolution in 3D compressible turbulence simulation. *Ann. Geophys.*, 2015, 33: 13-23
- [16] Wang X, Tu C Y, Wang L H, *et al.* The upstream-propagating Alfvénic fluctuations with power law spectra in the upstream region of the Earth's bow shock. *Geophys. Res. Lett.*, 2015, 42: 3654-3661
- [17] He J S, Pei Z T, Wang L H, *et al.* Sunward propagating Alfvén waves in association with sunward drifting proton beams in the solar wind. *Astrophys. J.*, 2015, 805: 176
- [18] Yang L P, Zhang L, He J S, *et al.* The formation of rotational discontinuities in compressive three-dimensional MHD turbulence. *Astrophys. J.*, 2015, 809: 155
- [19] Zhang L, He J S, Tu C Y, *et al.* Occurrence rates and heating effects of tangential and rotational discontinuities as observed from three-dimensional simulation of magnetohydrodynamic turbulence. *Astrophys. J.*, 2015, 804: L43
- [20] Wang X, Tu C Y, He J S, *et al.* The spectral features of low-amplitude magnetic fluctuations in the solar wind and their comparison with moderate-amplitude fluctuations. *Astrophys. J.*, 2015, 810: L21
- [21] Wang X, Tu C Y, Marsch E, *et al.* Scale-dependent normalized amplitude and weak spectral anisotropy of magnetic field fluctuations in the solar wind turbulence. *Astrophys. J.*, 2016, 816: 15
- [22] Yan L M, He J S, Zhang L, *et al.* Spectral anisotropy of Elsässer variables in two-dimensional wave-vector space as observed in the fast solar wind turbulence. *Astrophys. J.*, 2016, 816: L24
- [23] Liu Y C M, Huang J, *et al.* A statistical analysis of heliospheric plasma sheets, heliospheric current sheets, and sector boundaries observed in situ by STEREO. *J. Geophys. Res. Space Physics*, 2014, 119: 8721-8732
- [24] Huang J, Liu Y C M, Klecker B, Chen Y. Coincidence of heliospheric current sheet and stream interface: Implications for the origin and evolution of the solar wind. *J. Geophys. Res. Space Phys.*, 2016, 121: 19-29
- [25] Huang J, Liu Y C M, *et al.* Statistical study of the coincidence of heliospheric current sheet and stream interface. *J. Geophys. Res. Space Physics*, 2016JA022842, under review
- [26] Zuo P B, Feng X S, Xie Y Q, *et al.* Automatic detection algorithm of dynamic pressure pulses in the solar wind. *Astrophys. J.*, 2015,

- 803: 94
- [27] Zuo P B, Feng X S, Xie Y Q, *et al.* A statistical survey of dynamic pressure pulses in the solar wind based on WIND observations. *Astrophys. J.*, 2015, 808: 83
- [28] Wang Y, Wei F S, Feng X S, *et al.* Energy dissipation processes in solar wind turbulence. *Astrophys. J. Supp.*, 2015, 221: 34
- [29] Wang L H, Krucker S, Mason G M, Lin R P, Li G. The injection of ten electron^βHe-rich SEP events [J]. *Astron. Astrophys.*, 2016, 585: A119
- [30] Wang L H, Yang L, He J S, *et al.* Solar wind ~20–200 keV superhalo electrons at quiet times. *Astrophys. J.*, 2015, 803: L2
- [31] Yang L, Wang L H, Li G, *et al.* The angular distribution of solar wind superhalo electrons at quiet times. *Astrophys. J.*, 2015, 811: L8
- [32] Tao J W, Wang L H, Zong Q G, *et al.* Wimmer-Schweingruber R F, He J S, Tu C Y, Bale S D. Quiet-time suprathermal (~0.1–1.5 keV) electrons in the solar wind. *Astrophys. J.*, 2016, accepted
- [33] Wu Z, Chen Y, Li G, *et al.* Observations of energetic particles between a pair of corotating interaction regions. *Astrophys. J.*, 2014, 781: 17
- [34] Zhou D Z, Wang C, Zhang B Q, *et al.* Super solar particle event around AD775 was found. *Chin. Sci. Bull.* 2014, 59(22): 2736-2742
- [35] Wang Y, Qin G, Zhang M, Dalla S. A numerical simulation of solar energetic particle dropouts during impulsive events. *Astrophys. J.*, 2014, 789: 157
- [36] Qin G, Shalchi A. Perpendicular diffusion of energetic particles: Numerical test of the theorem on reduced dimensionality. *Phys. Plasmas*, 2015, 22, 012905
- [37] Wang Y, Qin G. Estimation of the release time of solar energetic particles near the Sun. *Astrophys. J.*, 2015, 799: 111
- [38] ¹¹Qin G, Wang Y. Simulations of a gradual solar energetic particle event observed by HELIOS 1, HELIOS 2, and IMP 8. *Astrophys. J.*, 2015, 809: 177
- [39] Wang Y, Qin G. Simulations of the spatial and temporal invariance in the spectra of gradual solar energetic particle events. *Astrophys. J.*, 2015, 806: 252
- [40] Wang Y, Qin G. Effect of adiabatic focusing on diffusion of energetic charged particles. *Astrophys. J.*, 2016, 820: 61
- [41] Chu W, Qin G. The geomagnetic cutoff rigidities at high latitudes during different solar wind and geomagnetic conditions. *Ann. Geophys.*, 2016, 34: 45-53
- [42] Yang Z W, Liu Y D, *et al.* Full particle electromagnetic simulations of entropy generation across a collisionless shock. *Astrophys. J.*, 2014, 793: L11
- [43] Wei W W, Shen F, Zuo P B. Research progress on the solar energetic particle model based on magnetohydrodynamic simulation. *Prog. Astron.*, 2015, 33: 1
- [44] Wei W W, Shen F, Zuo P B, *et al.* Effects of the solar wind background field on the numerical simulation of the Solar Energetic Particle (SEP) transportation. *Chin. J. Geophys.*, 2016, 59(3): 767- 777
- [45] Yang Z W, Liu Y D, Richardson J D, *et al.* Impact of pickup ions on the shock front nonstationarity and energy dissipation of the heliospheric termination shock: Two-dimensional full particle simulations and comparison with Voyager 2 observations. *Astrophys. J.*, 2015, 809: 28
- [46] Luo X, Zhang M, Potgieter M, *et al.* A numerical simulation of cosmic-ray modulation near the heliosopause. *Astrophys. J.*, 2015, 808: 82
- [47] Ruan G P, Chen Y, Wang S, *et al.* A solar eruption driven by rapid sunspot rotation. *Astrophys. J.*, 2014, 784: 165
- [48] Ruan G P, Chen Y, Wang H M. Gradual magnetic evolution of sunspot structure and filament-corona dynamics associated with the X1.8 flare in AR11283. *Astrophys. J.*, 2015, 812: 120
- [49] Chen Y, Du G H, Feng L, *et al.* A solar type II radio burst from CME-coronal ray interaction: simultaneous radio and EUV imaging. *Astrophys. J.*, 2014, 787:59
- [50] Feng S W, Du G H, Chen Y, *et al.* Simultaneous radio and EUV imaging of a multi-lane coronal Type II radio burst. *Sol. Phys.*, 2015, 290: 1195-1205
- [51] Kong X L, Chen Y, Guo F, *et al.* The possible role of coronal streamers as magnetically closed structures in shock-induced energetic electrons and metric Type II radio bursts. *Astrophys. J.*, 2015, 798: 81
- [52] Du G H, Chen Y, Lv M S, *et al.* Temporal spectral shift and polarization of a Band-splitting solar Type II radio burst. *Astrophys. J. Lett.*, 2014, 793: L39
- [53] Du G H, Kong X L, Chen Y, *et al.* An observational revisit of Band-split solar Type-II radio bursts. *Astrophys. J.*, 2015, 812: 52
- [54] Vasanth V, Chen Y, Kong X L, Wang B. Investigation of the geoeffectiveness of CMEs associated with IP Type II radio bursts. *Sol. Phys.*, 2015, 290:1815-1826
- [55] Cheng X, Ding M D, Zhang J, *et al.* Formation of a double-decker magnetic flux rope in the sigmoidal solar active region 11520. *Astrophys. J.*, 2014, 789: 93
- [56] Song H Q, Zhang J, Chen Y, Cheng X. Direct observations of magnetic flux rope formation during a solar coronal mass ejection. *Astrophys. J. Lett.*, 2014,792: L40
- [57] Song H Q, Zhang J, Cheng X, *et al.* Temperature evolution of a magnetic flux rope in a failed solar eruption. *Astrophys. J.*, 2014, 784: 48
- [58] Song H Q, Chen Y, Zhang J, *et al.* Evidence of the solar EUV hot channel as a magnetic flux rope from remote-sensing and in situ observations. *Astrophys. J. Lett.*, 2015, 808: L15
- [59] Song H Q, Zhang J, Chen Y, *et al.* First taste of hot channel in interplanetary space. *Astrophys. J.*, 2015, 803: 96
- [60] Song H Q, Chen Y, Zhang J, *et al.* Acceleration phases of a solar filament during its eruption. *Astrophys. J. Lett.*, 2015, 804: L38
- [61] Wang Y M, Wang B Y, Shen C L, *et al.* Deflected propagation of a coronal mass ejection from the corona to interplanetary space. *J. Geophys. Res.*, 2014, 119: 5117-5132
- [62] Shen F, Shen C L, Zhang J, *et al.* Evolution of the 12 July 2012 CME from the Sun to the Earth: Data-constrained three-dimensional MHD simulations. *J. Geophys. Res.*, 2014, 119: 7128- 7141
- [63] Shen C L, Wang Y M, Pan Z H, *et al.* Full halo coronal mass ejections: Arrival at the Earth. *J. Geophys. Res.*, 2014, 119: 5107-5116
- [64] Feng L, Wang Y M, Shen F, *et al.* Why does the apparent mass of a coronal mass ejection increase. *Astrophys. J.*, 2015, 812: 70
- [65] ¹¹Ding L G, Li G, Jiang Y, *et al.* Interaction between two coronal mass ejections in the 2013 May 22 large solar energetic particle event. *Astrophys. J. Lett.*, 2014, 793: L35
- [66] Wang Y M, Zhou Z J, Shen C L, *et al.* Investigating plasma motion of magnetic clouds at 1 AU through a velocity-modified cylindrical force-free flux rope model. *J. Geophys. Res.*, 2015, 120: 1543-1565
- [67] Liu Y D, Luhmann J G, Kajdič P, *et al.* Observations of an extreme storm in interplanetary space caused by successive coronal mass ejections. *Nat. Commun.*, 2014, 5:3481,doi: 10.1038/ncomms4481
- [68] Liu Y D, Richardson J D, Wang C, Luhmann J G. Propagation of



- the 2012 March coronal mass ejections from the Sun to heliopause. *Astrophys. J.*, 2014, 788: L28
- [69] Liu Y D, Yang Z W, Wang R, *et al.* Sun-to-Earth characteristics of two coronal mass ejections interacting near 1 AU: Formation of a complex ejecta and generation of a two-step geomagnetic storm. *Astrophys. J. Lett*, 2014, 793: L41
- [70] Liu Y D, Hu H D, Wang R, *et al.* Plasma and magnetic field characteristics of solar coronal mass ejections in relation to geomagnetic storm intensity and variability. *Astrophys. J. Lett.*, 2015, 809: L34
- [71] Liu Y D, Hu H D, Wang C, *et al.* On Sun-to-Earth propagation of coronal mass ejections: II. Slow events and comparison with others. *Astrophys. J.* 2016, 222(Supp): 23
- [72] ¹¹Wang R, Liu Y D, Yang Z W, Hu H D. Magnetic field restructuring associated with two successive solar eruptions. *Astrophys. J.*, 2014, 791: 84(8pp)
- [73] Wang R, Liu Y D, Dai X H, Yang Z W, Huang C, Hu H D. The role of active region coronal magnetic field in determining coronal mass ejection propagation direction. *Astrophys. J.*, 2015, 814: 80(9pp)
- [74] Wang R, Liu Y D, Wiegelmann T, Cheng X, Hu H D, Yang Z W. Relationship between sunspot rotation and a major solar eruption on 12 July 2012. *Solar Phys*, 2016, DOI 10.1007/s11207-016-0881-6
- [75] Shen F, Wang Y M, Shen C L, Feng X S. Turn on the super-elastic collision nature of coronal mass ejections through low approaching speed. *Scientific Reports*, 2016, 6:19576, DOI: 10.1038/srep19576
- [76] Feng X S, Xiang C Q, Zhong D K, Zhou Y F, Yang L P. SIP-CESE MHD model of solar wind with adaptive mesh refinement of hexahedral meshes. *Computer Physics Communications*, 2014, 185: 1965-1980
- [77] Feng X S, Zhang M, Zhou Y F. A new three-dimensional solar wind model in spherical coordinates with a six-component grid. *Astrophys. J. Supp.*, 2014, 214:6(12pp)
- [78] Shen F, Shen C L, Zhang J, Hess P, Wang Y M, Feng X S, Cheng H Z, Yang Y. Evolution of the 12 July 2012 CME from the Sun to the Earth: Data constrained three-dimensional MHD simulations. *J. Geophys. Res. Space Phys.*, 2014, 119:7128-7141
- [79] Zhang M, Zhou Y F. Three-dimensional steady state interplanetary solar wind simulation in spherical coordinates with a six-component grid (in Chinese). *Chin. J. Space Sci.*, 2014, 34(6): 773-784
- [80] Wang J, Feng X S, Du A M, Ge Y S. Modeling the interaction between the solar wind and Saturn's magnetosphere by the AMR-CESE-MHD method. *J. Geophys. Res. Space Physics*, 2014, 119: 9919-9930
- [81] Zhou Y F, Feng X S, Zhao X H. Using a 3D MHD simulation to interpret propagation and evolution of a coronal mass ejection observed by multiple spacecraft: The 3 April 2010 event. *J. Geophys. Res. Space Physics*, 2014, 119: 9321-9333
- [82] Fu H Z, Feng X S. Splitting based scheme for three-dimensional MHD with dual time stepping. *Chin. J. Space Sci.*, 2015, 35(1): 9-17
- [83] Zhang M, Feng X S. Implicit dual-time stepping method for a solar wind model in spherical coordinates. *Computers & Fluids*, 2015, 115: 115-123
- [84] Wang J, Du A M, Zhang Y, Zhang T L, Ge Y S. Modeling the Earth's magnetosphere under the influence of solar wind with due northward IMF by the AMR-CESE-MHD model. *Science China: Earth Sciences*, 2015, doi: 10.1007/s11430-015-5056-z
- [85] Feng X S, Ma X P, Xiang C Q. Data-driven modeling of the solar wind from 1 Rs to 1 AU. *J. Geophys. Res. Space Physics*, 2015, 120, doi:10.1002/2015JA021911.
- [86] Jiang C W, Wu S T, Feng X S, Hu Q. A comparison study of a solar active-region eruptive filament and a neighboring non-eruptive filament. *Res. Astronomy Astrophys.*, 2016, 16(1): 18
- [87] Jiang C W, Feng X S. Testing a solar coronal magnetic field extrapolation code with the Titov-Démoulin magnetic flux rope model[J]. *Res. Astronomy Astrophys.*, 2016, 16(1): 15
- [88] Wu S T, Zhou Y F, Jiang C W, *et al.* A data-constrained three-dimensional magnetohydrodynamic simulation model for a coronal mass ejection initiation. *J. Geophys. Res. Space Physics*, 2016, 121, doi:10.1002/2015JA021615
- [89] Zhang M, Feng X S. A Comparative Study of Divergence Cleaning Methods of Magnetic Field in the Solar Coronal Numerical Simulation. *Front. Astron. Space Sci.*, 2016, 3:6, doi:10.3389/fspas.2016.00006
- [90] Zhao X H, Dryer M. Current status of CME/shock arrival time prediction. *Space Weather*, 2014, 12:448-469
- [91] Zhao X H, Feng X S. Influence of a CME's initial parameters on the arrival of the associated interplanetary shock at Earth and the shock propagational model version 3. *Astrophys. J.*, 2015, 809:44
- [92] Liu H L, Qin G. Improvements of the shock arrival times at the Earth model STOA [J]. *J. Geophys. Res. Space Physics*, 2015, 120:5290-5297, doi:10.1002/2015JA021072
- [93] Xu X J, Wang Y, *et al.* Direct evidence for kinetic effects associated with solar wind reconnection. *Scientific Reports*, 2015, 5: 8080
- [94] Zhao X H, Feng X S. Periodicities of solar activity and the surface temperature variation of the Earth and their correlations (in Chinese). *Chin Sci Bull (Chin Ver)*, 2014, 59: 1284-1292
- [95] Zhao X H, Feng X S. Correlation between solar activity and the local temperature of Antarctica during the past 11,000 years. *JASTP*, 2015, 122: 26-33

Magnetospheric Physics in China: 2014–2015

CAO Jinbin, YANG Junying

School of Space and Environment, Beihang University, Beijing 100191

* E-mail: jbcao@buaa.edu.cn

Key words

Geomagnetic storm
Substorm
Magnetic reconnection
Radiation belt
Magnetotail

Abstract

In the past two years, many progresses are made in magnetospheric physics by using the data of Double Star Program, Cluster, THEMIS, RBSP, Swarm missions etc., or by computer simulations. This paper briefly reviews these works based on papers selected from the 191 publications from January 2014 to December 2015. The subjects cover various sub-branches of magnetospheric physics, including geomagnetic storm, magnetospheric substorm, magnetic reconnection, solar wind-magnetosphere-ionosphere interaction, radiation belt, outer magnetosphere, magnetotail, plasmasphere, geomagnetic field, auroras and currents.

1 Geomagnetic Storms

Duan *et al.*^[1] presented measurements from Cluster spacecraft to investigate the energetic singly charged oxygen ions, O^+ , within the flux ropes in the nightside high-latitude magnetosheath during the initial phase of an intense storm on 24 October 2011. Three magnetic flux ropes were identified by Cluster 4 in the intervals from 20:10 UT to 20:20 UT. Unusually, large number density of energetic O^+ ions at energy of tens of keV was detected within these flux ropes. The number density of O^+ ions was above 0.1 cm^{-3} and the maximum value was about 0.25 cm^{-3} , 1 order of magnitude larger than the ambient value (0.01 cm^{-3}) in the magnetosheath. The O^+/H^+ ratio was as large as 0.08 within the flux ropes. Enhanced convection electric fields E_y ($10 \text{ mV}\cdot\text{m}^{-1}$) are associated with the flux rope and the high concentrations of energetic O^+ . The flux ropes, which are presumably produced by magnetic reconnection at the dayside magnetopause or cusp, are convected at a larger velocity than the tailward velocity of ambient flows in the magnetosheath. These observations together show that abundant energetic O^+ ions are carried by the flux ropes toward the tail in the nightside magnetosheath. Their observations present new evidence for

a chain linking the dayside to the nightside in the global O^+ transport process.

The impact of Geomagnetically Induced Currents (GICs) on the power networks at middle and low latitudes has attracted attention in recent years with the increase of large-scale power networks. Zhang *et al.*^[2] report the GIC monitored at two low-latitude 500 kV substations of China during the large storm of 17 March 2015. The GIC due to the Storm Sudden Commencement (SSC) was much higher than that during the storm main phase. This phenomenon is more likely to happen at low-latitude locations, highlighting the importance of SSC in inducing GIC in low-latitude power networks. Furthermore, they ran a global Magnetohydrodynamic (MHD) model to simulate the GIC during this SSC event by using the solar wind observation as input. The model results reproduced the main features of the GIC. The study also indicates that the eastward component of the geoelectric field is dominant for low-latitude locations during the SSC events. Further, topology and electrical parameters of the power grids make significant differences in the GIC levels.

The three-dimensional global Magnetohydrodynamic model (PPM-LR MHD) was employed by Han *et al.*^[3] to investigate the energy budget in the solar wind-mag-

netosphere system during the super magnetic storm on November 20, 2003, one of the biggest storms during the last decade with $Dst \sim -500$ nT. During this event, about 23% solar wind kinetic energy is transferred into the magnetosphere. The total energy input is estimated to be about 9.50×10^{17} J, about 14 times of a moderate storm. The energy dissipation *via* the inner magnetosphere is less than the energy input with the coupling efficiency of about 63.3%. The energy dissipated via ring current injection is less than that via high-latitude ionosphere at the initial stage of the super storm. Furthermore, both the simulation results and the empirical results indicate that the ratio of ring current injection to the total energy output increases with the enhancement of the magnetospheric activity level. These are consistent with the statistical results they have got before. The empirical equations underestimate the solar wind kinetic energy, the energy input, and the energy dissipation via high-latitude ionosphere compared with the simulation results; however, the coupling efficiency of the high-latitude ionosphere (23.4%) is close to the simulation result (23.1%) during the entire storm time period.

Poloidal ULF waves are capable of efficiently interacting with energetic particles in the ring current and the radiation belt. Using Van Allen Probes (Radiation Belt Storm Probes (RBSP)) data from October 2012 to July 2014, Dai *et al.*^[4] investigated the spatial distribution and storm time occurrence of Pc4 (7–25 mHz) poloidal waves in the inner magnetosphere. Pc4 poloidal waves are sorted into two categories: waves with and without significant magnetic compressional components. Two types of poloidal waves have comparable occurrence rates, both of which are much higher during geomagnetic storms. The noncompressional poloidal waves mostly occur in the late recovery phase associated with an increase of Dst toward 0, suggesting that the decay of the ring current provides their free energy source. The occurrence of dayside compressional Pc4 poloidal waves is found correlated with the variation of the solar wind dynamic pressure, indicating their origin in the solar wind. Both compressional and noncompressional waves preferentially occur on the dayside near noon at $L \sim 5$ –6. In addition, compressional poloidal waves are observed at magnetic local time 18–24 on the nightside. The location of the Pc4 poloidal waves relative to the plasmapause is investigated. The RBSP statistical results may shed light on the in-depth investigations of the generation and propagation of Pc4 poloidal waves.

A quantitative retrieval of 3D distribution of energetic ions as Energetic Neutral Atoms (ENA) sources is a challenging task. The voxel Computerized Tomography (CT) method was initially applied to reconstruct the 3D distribution of energetic ions in the magnetospheric Ring Current (RC) region from ENA emission images on board multiple spacecraft (Ma *et al.*^[5]). To weaken the influence of Low-Altitude Emission (LAE) on the reconstruction, the LAE-associated ENA intensities are corrected by invoking the thick-target approximation. To overcome the divergence in iteration due to discordant instrument biases, a differential ENA voxel CT method is developed. The method is proved reliable and advantageous by numerical simulation for the case of constant bias independent of viewing angle. Then this method is implemented with ENA data measured by the Two Wide-angle Imaging Neutral-atom Spectrometers mission which performs stereoscopic ENA imaging. The 3D spatial distributions and energy spectra of RC ion flux intensity are reconstructed for energies of 4–50 keV during the main phase of a major magnetic storm. The retrieved ion flux distributions seem to correspond to an asymmetric partial RC, located mainly around midnight favoring the post-midnight with $L = 3.5$ –7.0 in the equatorial plane. The RC ion distributions with magnetic local time depend on energy, with major equatorial flux peak for lower energy located east of that for higher energy. In comparison with the ion energy spectra measured by Time History of Events and Macroscale Interactions during Substorms-D satellite flying in the RC region, the retrieved spectrum from remotely sensed ENA images are well matched with the in situ measurements.

Yuan *et al.*^[6] presented the influence of precipitating energetic ions caused by Electromagnetic Ion Cyclotron (EMIC) waves on the subauroral ionospheric E region during a geomagnetic storm on 8 March 2008 with observations of the Meteorological Operational (METOP-02) of the Polar Orbiting Environmental Satellites (POES), a GPS receiver in Vaasa of Finland and Finnish network of search coil magnetometers. Conjugate observations of the POES METOP-02 satellite and Finnish network of search coil magnetometers have demonstrated that enhancements of the precipitating energetic ion flux within the proton anisotropic zone are attributed to the interaction between Ring Current (RC) ions and EMIC waves. With enhancements of the intensity of Pc1 waves observed by search coil magnetometers, the total

electron content observed by the GPS receiver accordingly increased, meaning that the enhancement of the ionospheric electron density is attributed to the precipitation of RC ions caused by EMIC waves. The electron density profiles derived by the International Reference Ionosphere (IRI-2007) model and with precipitating energetic protons observed by the POES METOP-02 satellite show that the energetic proton precipitation can cause the E layer peak electron density to increase from $1.62 \times 10^9 \text{ m}^{-3}$ to $5.05 \times 10^{11} \text{ m}^{-3}$ by 2.49 orders of magnitude. In comparison with the height-integrated conductivities derived by the IRI-2007 model, the height-integrated Pedersen and Hall conductivities derived with precipitating energetic protons increase by 2.4 and 2.34 orders of magnitude, respectively. Their result suggests that precipitating energetic ions caused by EMIC waves can lead to an obvious enhancement of the electron density and conductivities in the subauroral ionospheric E region during geomagnetic storms.

Coronal Mass Ejections (CMEs) and Corotating Interaction Regions (CIRs) are two significant contributors to interplanetary disturbances and geomagnetic disturbances, which also play as major drivers of geomagnetic storms to modulate the geo-space environment. In order to comprehensively investigate the characteristic temporal features of the solar wind activity and associated geomagnetic activity, a large amount of solar wind data and geomagnetic activity indices were analyzed in detail (Shen *et al.*^[7]). Firstly, using the public data of solar wind parameters and geomagnetic activity indices provided by the NASA OMNIWeb, the MATLAB codes are developed to deal with a number of key parameters including IMF B_z solar wind velocity, solar wind proton density, solar wind dynamic pressure, Dst , AE , and Kp for the entire Solar Cycle 23 from 1996 to 2008. The complete database with a full list of 269 CME events and 456 CIR events is identified. Case event studies and superposed epoch analyses are implemented to carefully investigate the statistical features of four important solar wind parameters (IMF B_z , solar wind speed, solar wind proton density, and solar wind dynamic pressure) and three major geomagnetic indices (Dst , AE , and Kp) associated with the two types of solar disturbances. Secondly, the minimum of Dst index is utilized to differentiate 355 isolated geomagnetic storms occurring during the Solar Cycle 23. These storms are further categorized according to the magnitude of Dst minimum into 145 weak storms, 123 moderate storms,

70 strong storms, 12 severe storms, and 5 extreme storms. Finally, superposed epoch analysis is applied to evaluate the statistics of solar wind parameters and geomagnetic indices corresponding to magnetic storms with different intensities. It is found that in general the linearly fitted slope of N_{sw} / P_{dyn} (where N_{sw} is the solar wind proton density and P_{dyn} the dynamic pressure) with respect to epoch time remains positive for CME events but negative for CIR events, which can act as a feasible means to distinguish CME and CIR events. On average, compared to CIR events, CME events have larger magnitudes of southward IMF B solar wind dynamic pressure, AE and Kp indices but smaller Dst (min). In principle, CMEs bear higher possibility to drive extremely intense (*i.e.*, super) geomagnetic storms. There are a large number of differences between CME and CIR events and their driven geomagnetic storms as well. Therefore, CME-driven storms and CIR-driven storms should be studied separately. The established database of CME and CIR events and geomagnetic storms and the quantitative statistical information in combination can provide a useful aid for better understanding the responses of Earth's plasma sheet, radiation belts, and ring current to various solar activities.

Using the data of Sun-synchronous satellite (Detection of Electro-Magnetic Waves Transmitted from Earthquake Regions) DEMETER, Zhima *et al.*^[8] investigated the storm time variations of ELF/VLF waves during the intense Coronal Mass Ejections (CME)-driven storms from 2005 to 2009. The results show that there is a good correlation between the enhancement of ELF/VLF waves and the CME events. Immediately following the enhanced wave activity driven by CMEs at the initial phase, the wave intensity decreases temporarily at the beginning of storm main phase. The strongest waves predominantly occur from the late main phase to early recovery phase. The ELF waves below 3 kHz are significantly intensified during the whole storm time, while the high-frequency waves above 3 kHz seem strengthened predominantly during the late main and early recovery phase. The ELF waves below 3 kHz can exist in a wide L shell range, with the intensity peaking at $L \sim 3$ and 4. High-frequency waves at $f > 9$ kHz exist mostly outside the plasmopause. The stronger ELF/VLF waves on the dayside can last longer time than those on the nightside.

Long-term variations of South Atlantic Anomaly (SAA) were generally derived by fitting a Gaussian-like

function to an averaged distribution of the proton flux at a certain altitude accumulated over time periods for a month or longer. These data do not show the short-term variation of SAA arising from geomagnetic storm effects whose time scale is less than a month. To investigate the short-term variations, the features of SAA for the high-energy protons detected by NOAA Polar Orbiting Environmental Satellites during 1998–2008 have been investigated with a 5 day running average method. Zou *et al.*^[9] found that the two SAA parameters for three proton channels reflect the maximal proton flux in SAA and the extension of SAA decreases several percent during geomagnetic storms. Possible reasons for the decreases of the two SAA parameters for high-energy protons are discussed. Proton losses at the outer boundary of the inner radiation belt can be explained by the field line curvature scattering mechanism, while the decrease of the proton flux near the center of SAA is probably caused by the enhanced neutral atmospheric density during geomagnetic storms. The study of the behavior of high-energy protons in SAA is useful for understanding of storm time and long-term variations of the radiation environment near Earth and for constructing dynamic radiation belt models.

2 Magnetospheric Substorms

An ion flux dropout near the Dipolarization Front (DF) at around $X_{\text{GSM}} = 11 R_E$ in the Earth's plasma sheet was observed by Time History of Events and Macroscale Interaction during Substorms (THEMIS) on March 31, 2009. The ion differential energy fluxes at energies from 450 eV to 150 keV measured by the ESA and SST instruments from THC began to decrease about 2 s before the detection of the DF and reached a local minimum 6 s later. Then, the ion fluxes gradually increased to form a dropout around the DF. The spatial extent of the dropout was about 4,000 km. For energies above 20 keV, the ion fluxes after the dropout are greater than those before it, contrary to the fluxes at energies below 20 keV. The associated ion density variation indicates that the ion flux dropout coincides with the ion density dropout. Taking advantage of multipoint observations, THD, THC, and THE detected the same DF consecutively. Only THC detected an obvious ion flux dropout; THD observed an indistinct one about 2 s before THC; no high-energy ($E > 30$ keV) ion flux dropout was observed by THE. Shi *et al.*^[10] suggests that the ion

flux dropout may evolve with the earthward-propagating DF, and its properties can depend on locations relative to the DF.

Substorms generally inject tens to hundreds of keV electrons, but intense substorm electric fields have been shown to inject MeV electrons as well. An intriguing question is whether such MeV electron injections can populate the outer radiation belt. Dai *et al.*^[11] presented observations of a substorm injection of MeV electrons into the inner magnetosphere. In the premidnight sector at $L \sim 5.5$, Van Allen Probes (Radiation Belt Storm Probes)-A observed a large dipolarization electric field ($50 \text{ mV} \cdot \text{m}^{-1}$) over ~ 40 s and a dispersionless injection of electrons up to ~ 3 MeV. Pitch angle observations indicated betatron acceleration of MeV electrons at the dipolarization front. Corresponding signals of MeV electron injection were observed at LANL-GEO, THEMIS-D, and GOES at geosynchronous altitude. Through a series of dipolarizations, the injections increased the MeV electron phase space density by 1 order of magnitude in less than 3 h in the outer radiation belt ($L > 4.8$). Observations of Dai *et al.*^[11] provide evidence that deep injections can supply significant MeV electrons.

Dipolarization Fronts (DFs) as earthward propagating Flux Ropes (FRs) in the Earth's magnetotail were presented and investigated with a three-dimensional (3D) global hybrid simulation for the first time (Lu *et al.*^[12]). In the simulation, several small-scale earthward propagating FRs were found to be formed by multiple X line reconnection in the near tail. During their earthward propagation, the magnetic field B_z of the FRs becomes highly asymmetric due to the imbalance of the reconnection rates between the multiple X lines. At the later stage, when the FRs approach the near-Earth dipole-like region, the anti-reconnection between the southward/negative B_z of the FRs and the northward geomagnetic field leads to the erosion of the southward magnetic flux of the FRs, which further aggravates the B_z asymmetry. Eventually, the FRs merge into the near-Earth region through the anti-reconnection. These earthward propagating FRs can fully reproduce the observational features of the DFs, *e.g.*, a sharp enhancement of B_z preceded by a smaller amplitude B_z dip, an earthward flow enhancement, the presence of the electric field components in the normal and dawn-dusk directions, and ion energization. Their results show that the earthward propagating FRs can be used to explain the DFs observed in the magnetotail. The thickness of the DFs is

on the order of several ion inertial lengths, and the electric field normal to the front is found to be dominated by the Hall physics. During the earthward propagation from the near-tail to the near-Earth region, the speed of the FR/DFs increases from about $150 \text{ km}\cdot\text{s}^{-1}$ to about $1000 \text{ km}\cdot\text{s}^{-1}$. The FR/DFs can be tilted in the GSM (x, y) plane with respect to the y (dawn-dusk) axis and only extend several Earth radii in this direction. Moreover, the structure and evolution of the FRs/DFs are non-uniform in the dawn-dusk direction, which indicates that the DFs are essentially 3D.

A large-scale two-dimensional (2D) particle-in-cell simulation was performed to investigate electron acceleration in the Dipolarization Front (DF) region during magnetic reconnection (Huang *et al.*^[13]). It is found that the DF is mainly driven by an ion outflow which also generates a positive potential region behind the DF. The DF propagates with an almost constant speed and gets growing, while the electrons in the DF region can be highly energized in the perpendicular direction due to betatron acceleration. For the first time, Huang *et al.*^[13] reveal that there exists a velocity threshold; only the electrons below the threshold can be trapped by the parallel electric potential in the DF region and then energized by betatron acceleration.

Ultralow Frequency (ULF) waves play an important role in transferring energy by buffeting the magnetosphere with solar wind pressure impulses. The amplitudes of magnetospheric ULF waves, which are induced by solar wind dynamic pressure enhancements or shocks, are thought to damp in one half a wave cycle or an entire wave cycle. Shen *et al.*^[14] report in situ observations of solar wind dynamic pressure impulse-induced magnetospheric ULF waves with increasing amplitudes. They found six ULF wave events induced by solar wind dynamic pressure enhancements with slow but clear wave amplitude increase. During three or four wave cycles, the amplitudes of ion velocities and electric field of these waves increased continuously by 1.3–4.4 times. Two significant events were selected to further study the characteristics of these ULF waves. They found that the wave amplitude growth is mainly contributed by the toroidal mode wave. Three possible mechanisms of causing the wave amplitude increase are discussed. First, solar wind dynamic pressure perturbations, which are observed in a duration of 20–30min, might transfer energy to the magnetospheric ULF waves continually. Second, the wave amplitude increase in the radial elec-

tric field may be caused by superposition of two wave modes, a standing wave excited by the solar wind dynamic impulse and a propagating compressional wave directly induced by solar wind oscillations. When superposed, the two wave modes fit observations as does a calculation that superposes electric fields from two wave sources. Third, the normal of the solar wind discontinuity is at an angle to the Sun-Earth line. Thus, the discontinuity will affect the dayside magnetopause continuously for a long time.

Simultaneous measurements from THEMIS spacecraft, GOES-11 and ground stations (Canadian Array for Realtime Investigations of Magnetic Activity or CARISMA, and 210 degrees Magnetic Meridian or MM) on March 18, 2009 allow the study of dynamic processes in the near-Earth magnetotail and corresponding Pi2 pulsations on the ground in great detail. Fast earthward flows along with traveling Alfvén waves and fast mode waves in the Pi2 band were observed by three Time History of Events and Macroscale Interactions during Substorms (THEMIS) probes (P3, P4 and P5) in the near-Earth plasma sheet. At the mid- to high-latitude nightside, the CARISMA stations located near the foot points of the three probes recorded Pi2s with two periods, about 80 s after the earthward fast flows observed by the P4 probe. The long- period Pi2 (140–150 s) belongs to the Transient Response Pi2 (TR Pi2), since the travel time of the Alfvén waves between the plasma sheet and CARISMA stations is very close to half the period of the long-period Pi2. The short-period Pi2 (60–80 s) has the same period band as the perpendicular velocity of the fast flows, which indicates that it may relate to the inertial current caused by periodic braking of the earthward fast flows. The 210 degrees MM stations located at the low-latitude duskside also observed Pi2s with the same start time, waveform and frequency, about about 120 s after the earthward fast flows. Strong poloidal oscillations are shown by GOES-11 (about 23 MLT) and the compressional component (B_b) is highly correlated with H components of the 210° MM stations, whereas the other two components (B_r and B_e) are not. These results of Luo *et al.*^[15] confirm that the low-latitude Pi2s are generated by cavity mode resonance, which is driven by an impulsive broadband source in the near-Earth magnetotail.

Diurnal variations of the SuperMAG auroral electrojet indices (SML and SMU) were examined for the pe-

riod of 1980–2010, and the differences between SML and SMU were especially analyzed (Wang *et al.*^[16]). The diurnal variation of SML with a maximum at around 11:00 UT has a prenoon-postnoon asymmetry. At solstices, the diurnal variation of SML is much stronger than that at equinoxes. For the SMU, two maxima are recorded in the diurnal variation with the bigger one at 17:00 UT and the smaller one at 04:00 UT. The seasonal variations are not obvious in the UT variation characteristics of SMU although the intensity of SMU is changed remarkably season by season. For both SML and SMU, the contributing stations are located at higher geomagnetic latitude around 16:00 UT and at lower geomagnetic latitude around 04:00 UT. These results indicate that: (i) the SML is mostly controlled by the convection electric field. Its diurnal variation is mainly correlated with the equinoctial and R-M hypothesis; (ii) the SMU is largely controlled by the ionospheric conductance. Its diurnal variation is tightly correlated with the solar radiation.

Pseudo-breakup events are thought to be generated by the same physical processes as substorms. Yao *et al.*^[17] reported the cross-tail current reduction in an isolated pseudo-breakup observed by three of the THEMIS probes (THEMIS A (THA), THEMIS D (THD), and THEMIS E (THE)) on 22 March 2010. During this pseudo-breakup, several localized auroral intensifications were seen by ground-based observatories. Using the unique spatial configuration of the three THEMIS probes, they have estimated the inertial and diamagnetic currents in the near-Earth plasma sheet associated with flow braking and diversion. They found the diamagnetic current to be the major contributor to the current reduction in this pseudo-breakup event. During flow braking, the plasma pressure was reinforced, and a weak electrojet and an auroral intensification appeared. After flow braking/diversion, the electrojet was enhanced, and a new auroral intensification was seen. The peak current intensity of the electrojet estimated from ground-based magnetometers, about 0.7×10^5 A, was about 1 order of magnitude lower than that in a typical substorm. They suggested that this pseudo-breakup event involved two dynamical processes: a current-reduction associated with plasma compression ahead of the earthward flow and a current-disruption related to the flow braking/diversion. Both processes are closely connected to the fundamental interaction between fast flows, the near-

Earth ambient plasma, and the magnetic field.

The nonadiabatic acceleration of plasma sheet ions is important to the understanding of substorm energetic injections and the formation of ring current. Previous studies show that nonadiabatic acceleration of protons by magnetic field dipolarization is hard to occur at $X > -10 R_E$ because the time-scale of dipolarization (several minutes) is much larger than the gyro period of protons there (several seconds). Wang *et al.*^[18] presented a case of nonadiabatic acceleration of plasma sheet ions observed by Cluster on October 30, 2006 at $(X_{GSM}, Y_{GSM}) = (-7.7, 4.7) R_E$. The non-adiabatic acceleration of ions is caused not by previously reported magnetospheric dipolarization but by the ultralow frequency (ULF) waves during magnetospheric dipolarization. The non-adiabatic acceleration of ions generates a new energy flux structure of ions, which is characterized by the usual energy flux increase of ions (28–80 keV) and a concurrent energy flux decrease of ions in a lower energy range (10 eV–20 keV). These new observations constitute a complete physical picture: The lower energy ions absorb the wave energy, and thus get accelerated to higher energy. They used a nonadiabatic model to interpret the ion energy flux variations. Both analytic and simulation results are in good agreement with the observations. This indicates that the nonadiabatic acceleration associated with ULF waves superposed on dipolarized magnetic field is an effective mechanism for ion energization in the near-Earth plasma sheet. The presented energy flux structures can be used as a proxy to identify the similar dynamic process.

Based on multi-satellite and ground observations, Nowada *et al.*^[19] investigated an influence of long-lasting and gradual enhancements of magnetic flux transport rate on the magnetotail fast flow duration. On March 10th, 2009, THEMIS-B, which was located in the central plasma sheet of middle distant magnetotail ($X_{GSM} \sim -25.8 R_E$), observed the fast flows with the velocity exceeding 300 km/s, lasting over 3 h for intense southward Interplanetary Magnetic Field (IMF) period. During long-lasting fast flows, *AL* index variations were very extensive and their recovery was much slow. Pi2 waves were observed at the ground observatories around the THEMIS's foot points and at low-/mid-latitudes. The aspect for these *AL* variations suggests Steady Magnetospheric Convection (SMC), but clear substorm signatures were also observed. Further magnetic dipolarization was detected by THEMIS-A at $X_{GSM} \sim$

$-8.2 R_E$ and its nearby THEMIS-E. Only THEMIS-A observed the associated energetic electron flux enhancements. Therefore, the fast flows occurred during substorm with energetic particle injections at “imitative” SMC, which would be driven by prolonged intense southward IMF. The cumulative transport rates of magnetic and Poynting fluxes consecutively and gradually enhanced. On the other hand, THEMIS-C detected much shorter fast flows with the duration of 37 min at $X_{GSM} \sim -18.1 R_E$ and weak/gradual substorm-associated dipolarization. However, the cumulative magnetic flux transport rate was enhanced only during the fast flow interval and was saturated after the fast flows. From different magnetic transport rate profiles at THEMIS-B and THEMIS-C, the realms of dipolar-configured field lines expanded to near THEMIS-C’s position responsible for long-lasting fast flow-associated consecutive and gradual magnetic flux pileup. Because the resultant “high-speed flow braking” region was retreated into a few R_E tailward direction, long-lasting fast flows were almost stemmed. These results suggest that the cumulative magnetic flux transport rate is one of the important factors to determine “fate” (duration) of the magnetotail fast flows.

During substorms energetic ions injected from the magnetotail plasma sheet can excite Electromagnetic Ion Cyclotron (EMIC) waves in the inner magnetosphere. As a signature of EMIC waves, the Interval of Pulsations of Diminishing Periods (IPDP) is observed by ground-based magnetometers (Zhou *et al.*^[20]). The generating mechanism of IPDP waves is closely associated with substorm injected energetic ions during substorms. In addition, the occurrence rate of IPDP waves in the inner magnetosphere is very important to study the dynamics of the magnetosphere. Firstly, with observations of magnetometers at MCMU and MSTK stations of CARISMA network in Canada and the GOES 11 satellite for the typical IPDP events, the relationship between IPDP and the energetic ions injected from the magnetotail plasma sheet during substorms was revealed. Then based on the observations of magnetometers at MCMU and MSTK stations of CARISMA network between April 2005 and May 2014, they statistically analyzed the occurrence rate distribution of IPDP events in seasons and Magnetic Local Time (MLT). The results for the typical case show that during substorms, energetic ions injected from the magnetotail plasma sheet can excite IPDP waves in the inner magnetosphere.

For the statistics, a total of 128 IPDP wave events have been simultaneously observed by both MCMU and MSTK stations. The maximum occurrence rate of the events is between 15 MLT and 18 MLT, corresponding to the region of plasmasphere plumes. The IPDP events have the least occurrence rate in winter (13.28%), the highest occurrence rate is in spring (32.81%). The least occurrence rate in winter should be related to the ionospheric conductivity while the highest in spring is associated with the spring-autumn asymmetry of substorm and geomagnetic activity. The case study and statistics show that IPDP events are mainly generated by energetic protons, which can be injected into the inner magnetosphere during substorms and drift westward and encounter the plasmaspheric plume. In addition, the occurrence rate of IPDP events is affected by the ionospheric conductivity and the occurrence rate of substorms.

The Van Allen probes, low-altitude NOAA satellite, MetOp satellite, and riometer are used to analyze variations of precipitating energetic electron fluxes and Cosmic radio Noise Absorption (CNA) driven by plasmaspheric hiss with respect to geomagnetic activities. The hiss-driven energetic electron precipitations (at $L \sim 4.7\text{--}5.3$, magnetic local time (MLT) $\sim 8\text{--}9$) are observed during geomagnetic quiet condition and substorms, respectively. Li *et al.*^[21] found that the CNA detected by riometers increased very little in the hiss-driven event during quiet condition on 6 September 2012. The hiss-driven enhancement of riometer was still little during the first substorm on 30 September 2012. However, the absorption detected by the riometer largely increased, while the energies of the injected electrons became higher during the second substorm on 30 September 2012. The enhancement of CNA observed by the riometer and calculated with precipitating energetic electrons is in agreement during the second substorm, implying that the precipitating energetic electrons increase CNA to an obviously detectable level of the riometer during the second substorm on 30 September 2012. The conclusion is consistent with Rodger *et al.* (2012), which suggest that the higher level of CNA prefers to occur in the substorms, because substorms may produce more intense energetic electron precipitation associated with electron injection. Furthermore, the combination of the observations and theory calculations also suggests that higher-energy electron (> 55 keV) precipitation contributes more to the CNA than the

lower energy electron precipitation. In this paper, the higher-energy electron precipitation is related to lower frequency hiss.

Dipolarization Fronts (DFs) are believed to play important roles in transferring plasmas, magnetic fluxes, and energies in the magnetotail. Using the Cluster observations in 2003, electromagnetic energy conversion at the DFs is investigated by case and statistical studies (Huang *et al.*^[22]). The case study indicates strongest energy conversion at the DF. The statistical study shows the similar features that the energy of the fields can be significantly transferred to the plasmas (load, $J \cdot E > 0$) at the DFs. These results are consistent with some recent simulations. Examining the electromagnetic fluctuations at the DFs, Huang *et al.* suggested that the wave activities around the lower hybrid frequency may play an important role in the energy dissipation.

Li *et al.*^[23] presented a statistical study of whistler waves behind Dipolarization Fronts (DFs) based on the Cluster satellites measurements during the years 2001–2007. They found 732 DFs during the 7 year tail periods ($X_{\text{GSM}} \leq -8 R_E$ and $|Y_{\text{GSM}}| \leq 10 R_E$) in the plasma sheet. By constraining the whistler waves in a 1 min interval behind the DFs (the maximum B_z), they found that 381 DFs (about 50%) are followed by whistler waves. They studied the occurrence rate of whistler waves, the wave characteristic parameters, and the corresponding electron distribution, not only in a global view but also in the local DF coordinate. In a global view, behind the DFs, the whistler waves mostly occur in the radial distance between 17 and 18 R_E . They have a higher occurrence rate on the dawnside than the duskside. On the other hand, in the local DF coordinate, whistler waves have a higher occurrence rate around the meridian of DF. In addition, the average wave amplitudes increase toward the dawnside of DF. Associated with the whistler waves, electron distributions have a dominant perpendicular anisotropy for electrons with energy higher than 5 keV. Lower energy electron distributions do not have such perpendicular anisotropy dominance. Moreover, the perpendicular anisotropy for electrons > 5 keV increases toward the dawnside of DF, which may be caused by the drift- betatron acceleration. They suggested that the free energy source for whistler waves behind the DFs is probably the perpendicular anisotropy of > 5 keV electrons caused by the betatron acceleration.

Fu *et al.*^[24] revealed where and how ions are acceler-

ated in the proximity of earthward propagating Dipolarization Fronts (DFs) in the magnetotail during a magnetospheric substorm on February 15, 2008. Two DFs were observed by multiple THEMIS spacecraft in the near- Earth magnetotail (about $-10 R_E$). They studied the ion dynamics associated with these DFs by comparing observed results with Large Scale Kinetic (LSK) simulation results. The LSK simulation reproduced the sudden ion energy flux enhancement concurrent with the arrival of the DF at the satellite locations. They found that ions can be accelerated to more than 100 keV of energy at the DF. These ions were initially non-adiabatically accelerated near magnetic reconnection site and then still non-adiabatically accelerated at the DF structure.

Broadband frequency waves around the Dipolarization Front (DF) are believed to play a crucial role in the particle dynamics. Using the Cluster observations, Huang *et al.*^[25] reported large-amplitude electromagnetic waves with frequencies just above the ion cyclotron frequency at the DF in the near-Earth magnetotail region. The waves have very large amplitudes of magnetic and electric field fluctuations, up to about 2 nT and about $10 \text{ mV} \cdot \text{m}^{-1}$, respectively. The magnetic fluctuations are predominately along the ambient magnetic field (B_0), while the electric fluctuations are primarily perpendicular to B_0 . The observed waves are highly oblique with a propagation angle of 100 with respect to the ambient magnetic field, and are also linearly polarized. These features are consistent with the properties of the ion Bernstein wave mode in the high plasma beta region, and also with the properties of current-driven ion cyclotron waves driven by the electromagnetic current-driven Alfvén instability. They also discussed the possibility of wave-particle interactions at the DF.

Huang *et al.*^[26] analyzed three Dipolarization Front (DF) events to investigate their dawn-dusk scales in the Earth's magnetotail using the Cluster measurements in year 2007, when the spacecraft separation is about 1.8 R_E (R_E is the Earth's radius) and is appropriate for investigating the DF scale. Based on the Minimum Variance Analysis (MVA) and the general shape of the DF, they found that Cluster detected the center and the flank (or just beyond the flank) of DF in the same event. This means that the scale of DF is about 3.6 R_E in the dawn-dusk direction, larger than that reported in previous studies. Using the semicircle function to fit the observations, they got the dawn-dusk scale of about

3.2–3.6 R_E , consistent with the rough estimation. Considering large separation among the spacecraft, the timing analysis cannot be used to obtain the normal of DF and the propagation velocity along the normal. One should be careful when performing timing analysis of DF using the Cluster data, and have to carry on MVA analysis to check the normal of DF before do timing analysis.

In order to investigate the suprathermal electron flux (> 30 keV) around Dipolarization Fronts (DFs), Wang *et al.*^[27] statistically studied the suprathermal electron flux variations and pitch angle distributions of hundreds of earthward propagating DFs observed by THEMIS spacecraft during its tail seasons in years 2008–2009. They focused on the electron flux variations across DFs and electron anisotropies behind DFs. They divided DF into three sectors in the equatorial plane: Dusk, central and dawn sectors. The sectors are defined according to the DF normals with respect to DF's meridian in the equatorial plane (the symmetric line of DF). They found that the events with electron flux increases and decreases behind the fronts had no particular dependence on the observation locations. In addition, there was no obvious dependence of electron anisotropy behind DF on the different sectors of DF.

Various plasma waves have been observed in the vicinity of Dipolarization Fronts (DFs) and the rarefaction regions behind them. It was suggested that these waves not only play crucial roles in regulating particle kinetics at the DFs but also may potentially affect the large-scale dynamics of the magnetotail. Zhou *et al.*^[28] presented the observations of large-amplitude electromagnetic waves at DFs that occurred during magnetospheric substorms. The DFs were embedded in either the tailward or earthward flows in the near-Earth magnetotail. The wave frequencies were near the local proton cyclotron frequency. The waves propagated at highly oblique angles with respect to the ambient magnetic field (about 80° – 100°). Their corresponding wavelengths were on the order of the local ion gyroradii. The major magnetic field fluctuations were along the background magnetic field, while the electric field fluctuations were predominantly perpendicular to the background magnetic field. The waves were compressional waves as there was an anti-correlation between the plasma density and the wave magnetic field strength. The electric potential associated with the waves reached to more than half of

the electron temperature, indicating the waves are nonlinear. They suggested that the waves were magnetosonic or ion Bernstein mode waves driven by the ion ring distribution. The waves were able to provide significant anomalous resistivity at the front, with major contributions from the electric field fluctuations. The effects of these waves on the electron pitch angle scattering and energy diffusion were also discussed.

Using test particle simulation, the acceleration of magnetotail protons is studied during substorm-associated dipolarization events. The effects of the ultra-low frequency waves on the proton acceleration process in the vicinity of equatorial plane are investigated. Meng *et al.*^[29] showed that particles are injected earthward during dipolarization. Protons with relatively low initial energies may not conserve their magnetic moment, and are non-adiabatically accelerated by the electromagnetic wave whose frequency is close to the proton gyro frequency. In addition, the final energies of the particles after the event are related to its initial energies at the dipolarization onset. For the protons whose initial energies are much lower than the cutoff energy, their energies are increased significantly after the event. The particles' energy increase have the same order of magnitude with the O^+ ions' in the dipolarization process, and it is related to the electromagnetic wave frequencies. However, for the protons whose initial energies are higher than the cutoff energy, their final energy level is not influenced by the wave and the energies are stable during the injection.

On 18 May 2011, the Time History of Events and Macroscale Interactions during Substorms satellite observed whistler mode waves associated with a magnetic dip behind a dipolarization front structure in the bursty bulk flow braking region. For the first time, Zhima *et al.*^[30] found that whistler mode waves are generated at the edges of magnetic dip rather than at the center (also known as “minimum-B-pocket”). Detailed wave analysis indicates that the waves are likely lower and upper band whistler mode chorus. They examined electron pitch angle distributions at the edges of dip and compare them with those at the center and far outside the magnetic dip. Results confirm that the positive temperature anisotropy and pancake distributions at the edges of magnetic dip provide free energy source for growth of the whistler mode waves. They also interpreted the whole physical process of how whistler mode waves generate in this event.

Lu *et al.*^[31] established a Hall-Finite Larmor Radius (FLR) MHD model by including Hall and finite Larmor radius (FLR) effects to study the Dipolarization Fronts (DFs) produced by the interchange instability in the magnetotail. The results indicate that the Hall effect on the scale of inertial length determines the distributions of electric field at DFs. The FLR effect can not only cause a dawn-dusk asymmetry of the DF structure but also can make the DF drift downward. The dawnward drifting of DF can be attributed to the ion diamagnetic velocity, which also causes alteration in the direction of the high-speed flow near the DF.

Electric fields associated with Dipolarization Fronts (DFs) have been investigated in the magnetotail plasma sheet using Cluster observations. Sun *et al.*^[32] studied each term in the generalized Ohm's law using data obtained from the multi spacecraft Cluster. Their results show that in the plasma flow frame, electric fields are directed normal to the DF in the magnetic dip region ahead of the DF as well as in the DF layer but in opposite directions. Case and statistical studies show that the Hall electric field is important while the electron pressure gradient term is much smaller. The ions decouple from the magnetic field in the DF layer and dip region ($E + V_i \times B \neq 0$), whereas electrons remain frozen-in ($E + V_e \times B = \nabla p_e / n_e$).

MERCURY Surface, Space ENVIRONMENT, GEOCHEMISTRY, and RANGING (MESSENGER) magnetic field measurements during the substorm expansion phase in Mercury's magnetotail have been examined for evidence of low-frequency plasma waves, *e.g.*, Pi2-like pulsations. It has been revealed that the B_y fluctuations accompanying substorm dipolarizations are consistent with pulses of field-aligned currents near the high-latitude edge of the plasma sheet. Detailed analysis of the B_y fluctuations reveals that they are near circularly polarized electromagnetic waves, most likely Alfvén waves. Soon afterward the plasma sheet thickened and MESSENGER detected a series of compressional waves. These Alfvénic and compressional waves have similar durations (10–20 s), suggesting that these waves may arise from the same source. Drawing on Pi2 pulsation models developed for Earth, they suggested that the Alfvénic and compressional waves reported at Mercury may be generated by the quasi-periodic sunward flow bursts in Mercury's plasma sheet. But because these waves are observed during the period with rapid mag-

netic field reconfiguration, Sun *et al.*^[33] could not fully exclude the possibility of standing Alfvén wave.

MERCURY Surface, Space ENVIRONMENT, GEOCHEMISTRY, and RANGING (MESSENGER) magnetic field and plasma measurements taken during crossings of Mercury's magnetotail from 2011 to 2014 have been examined for evidence of substorms. A total of 26 events were found during which an Earth-like growth phase was followed by clear near-tail expansion phase signatures (Sun and Slavin^[33]). During the growth phase, just as at Earth, the thinning of the plasma sheet and the increase of the magnetic field intensity in the lobe are observed, but the fractional increase in field intensity could be ~3 to 5 times that at Earth. The average timescale of the growth phase is ~1 min. The dipolarization that marks the initiation of the substorm expansion phase is only a few seconds in duration. During the expansion phase, lasting ~1 min, the plasma sheet is observed to thicken and engulf the spacecraft. The duration of the substorm observed in this paper is consistent with previous observations of Mercury's Dungey cycle. The reconfiguration of the magnetotail during Mercury's substorm is very similar to that at Earth despite its very compressed timescale.

Anti Dipolarization Fronts (ADFs), tailward moving structures in the Earth's magnetotail with sharp decreases in their magnetic B_z component, are thought to be mirror images of earthward propagating Dipolarization Fronts (DFs) generated on the opposite side of the reconnection site. Zhou *et al.*^[34] use ARTEMIS (Acceleration, Reconnection, Turbulence, and Electrodynamics of the Moon's Interaction with the Sun) observations and numerical simulations to study the role of ADFs in accelerating and reflecting ambient plasma sheet ions. In both case and statistical observations before ADF arrival, tailward streaming, energy-dispersed ions are seen first. After about 1 min, the ion fluxes are enhanced significantly with the peak shifted duskward, and then the peak gradually shifts back to the tailward direction until the ADF arrives. All these signatures are reproduced by their simulation model of ion acceleration and reflection on ADFs. They further examined typical ion trajectories before and after ADF reflection, to understand these seemingly complicated ion signatures as well as their similarities with and differences from the DF preceding signatures.

Dipolarizing flux bundles transport magnetic flux to

the inner and dayside magnetosphere, heat the plasma sheet, and provide a seed population to the radiation belt. The magnetic perturbation ahead of them, often referred to as a Dipolarization Front (DF), is asymmetric with a small B_z dip followed by a sharp B_z enhancement. The B_z dip is thought to be generated from dawnward currents carried by DF-reflected ions; after reflection, these earthward moving ions gyrate clockwise and contribute to dawnward diamagnetic currents ahead of the front. Using observations of hundreds of DFs, Pan *et al.*^[35] investigated this hypothesis. They found that the depth of the B_z dip as a function of the front azimuth depends on DF propagation speed and ambient plasma density. These statistical signatures support the hypothesis that the B_z dip is caused by ion reflection and suggest that secondary currents carried by these reflected ions can reshape the front significantly.

Dipolarization Fronts (DFs), earthward propagating structures in the Earth's magnetotail with sharp enhancements of the northward magnetic field, can reflect and accelerate ions in the ambient plasma sheet. The ion reflection and acceleration process, which generates earthward flows ahead of the DF, also imposes a dynamic pressure on the DF to decelerate its earthward motion. It has been shown that the ion reflection process is not symmetric, with stronger ion accelerations at the evening side of the DF than at its morning side, which implies dawn-dusk asymmetric reaction of the ambient plasma and consequently dawnward deflection of DFs. Zhou *et al.*^[36] examined this scenario in detail, by carrying out statistical studies based on Time History of Events and Macroscale Interactions during Substorms observations from 2008 to 2011. They demonstrated the important role of the ion reflection process in the long-standing problems regarding DF evolution and bursty flow braking in the near-Earth plasma sheet.

3 Magnetic Reconnection

Although Magnetic Reconnection (MR) on Earth's magnetopause has been extensively studied for many years, the details of the reconnected flux ropes on the dayside boundary has proven to be rather illusive in view of their geometry and magnetic topology. While theoretical models often assume open tube-like shapes, global simulations always show that flux ropes formed via reconnection at the magnetopause possess compli-

cated 3D structures. To reveal the natures/features of these flux ropes requires detailed multiple spacecraft measurements and may greatly improve their understanding of solar wind impact on the geospace environment. Pu *et al.*^[37] reported six case studies and a comprehensively statistical study based on ESA Cluster, CNSA TC-1 and NASA Themis measurements. They showed, for the first time, (i) the observed 3D large structure of the flux ropes across the dayside magnetospheric boundary; (ii) different field topologies seen, respectively, in the magnetospheric branch of the ropes, the ropes' azimuthally extended section, and the magnetosheath part of the ropes away from the magnetopause; and (iii) that magnetopause reconnection makes important contributions also to the formation of magnetospheric boundary layer of closed field lines. Evidence and process of multiple X-line reconnection that leads to appearance of magnetopause flux ropes are presented and discussed.

Fu *et al.*^[38] applied a new method, the First-Order Taylor Expansion (FOTE), to find magnetic nulls and reconstruct magnetic field topology, in order to use it with the data from the forthcoming MMS mission. They compared this method with the previously used Poincare Index (PI), and found that the two methods are generally consistent, except that the PI method can only find a null inside the Spacecraft (SC) tetrahedron, while the FOTE method can find a null both inside and outside the tetrahedron and also deduce its drift velocity. In addition, the FOTE method can (i) avoid limitations of the PI method such as data resolution, instrument uncertainty (B_z offset), and SC separation; (ii) identify 3D null types (A, B, As, and Bs) and determine whether these types can degenerate into 2D (X and O); (iii) reconstruct the magnetic field topology. They quantitatively tested the accuracy of FOTE in positioning magnetic nulls and reconstructing field topology by using the data from 3D kinetic simulations. The influences of SC separation ($0.05-1 d_i$) and null-SC distance ($0-1 d_i$) on the accuracy are both considered. They found that (i) for an isolated null, the method is accurate when the SC separation is smaller than $1 d_i$, and the null-SC distance is smaller than $0.25-0.5 d_i$; (ii) for a null pair, the accuracy is same as in the isolated-null situation, except at the separator line, where the field is nonlinear. They defined a parameter $\xi \equiv |(\lambda_1 + \lambda_2 + \lambda_3)| / |\lambda|_{\max}$ in terms of the eigenvalues (λ_i) of the null to quantify the quality

of their method, the smaller this parameter the better the results. Comparing to the previously used parameter ($\eta \equiv |\nabla \cdot B|/|\nabla \times B|$), ξ is more relevant for null identification. Using the new method, they reconstructed the magnetic field topology around a radial-type null and a spiral-type null, and find that the topologies are well consistent with those predicted in theory. They therefore suggested using this method to find magnetic nulls and reconstruct field topology with four-point measurements, particularly from Cluster and the forthcoming MMS mission. For the MMS mission, this null-finding algorithm can be used to trigger its burst-mode measurements.

Recent numerical simulations demonstrated that electron diffusion region develops into two-scale structure, *i.e.*, the inner electron diffusion region and the outer electron diffusion region. The outer diffusion region is manifested as super-Alfvénic electron jet embedded in central current sheet. However, the electron jets are deflected from neutral sheet with a weak guide field. Zhou *et al.*^[39] presented the in situ evidence of deflected super-Alfvénic electron jet in a reconnection region with a weak guide field in the Earth's magnetotail. The electron-scale jet was detected at about 37 ion inertial lengths from the X line. There was a strong electric field at the jet. The strong electric field at the jet was primarily balanced by Hall electric field, as the intense current was mainly carried by magnetized electrons. Another event in the magnetosheath also supports their conclusion that guide field deflects the electron jet away the neutral sheet.

Magnetic reconnection, as one important energy dissipation process in plasmas, has been extensively studied in the past several decades. Magnetic reconnection occurring in the downstream of a primary X line is referred to as secondary reconnection. Huang *et al.*^[40] used kinetic simulations to investigate the secondary reconnection in detail. They found that secondary reconnection is reversed by the compression caused by the outflowing jet originating from the primary reconnection site, which results in the erosion of the magnetic island between the two X lines. They showed the observational signatures expected in electromagnetic fields and plasma measurements in the Earth's magnetotail, associated with this mechanism. These simulation results could be applied to interpret the signatures associated with the evolution of earthward magnetic islands in the Earth's magnetotail.

Cluster spacecraft observed an earthward flowing plasmoid along with a Travelling Compression Region (TCR) structure in southern plasma sheet boundary layer (PSBL) at 21:09 UT of September 19, 2001. Lu *et al.*^[41] reconstructed the two-dimensional topology of the magnetic field structure observed by C1 using Grad-Shafranov reconstruction method. Results show that C1 passed through part of a plasmoid, which compressed the lobe magnetic field and formed a TCR. The size of the whole plasmoid structure in X direction is estimated to be about $3 R_E$. Furthermore, using multi-spacecraft observations, they found some detailed information about this structure. First, C1 observed bi-streaming electron components, which supports their suggestion that the spacecraft passed through closed field lines. Second, a small magnetic field perturbation within this plasmoid accompanied by slight decrease in electron flux suggests that a flux rope core might exist at the center of the plasmoid.

Magnetic islands are considered to play a crucial role in collisionless magnetic reconnection. Huang *et al.*^[42] use particle-in-cell simulations to investigate electric field E_z structure in the magnetic islands (including primary and secondary islands) with and without a guide field during magnetic reconnection. It is found that the electric field has multilayers in the primary island and a large bipolar structure in the secondary island in the absence of guide field. The electric field is provided by the Hall term $(J \times B)_z$ (mainly), the divergence of electron pressure tensor, and the convective term $(V_i \times B)_z$ in the outer and the inner region of primary island, while the electric field is much smaller (about 0) in the middle and the core region of primary island due to the cancelation of the three terms. The single bipolar electric field is primarily provided by the Hall term in the secondary island. In the presence of a guide field, the electric field has multiple layers in the primary island (about zero guide field case) and the secondary island. However, there still exists one single large sharp bipolar structure of electric field in the central region of the secondary island. The differences of electric field in the primary and secondary islands are essentially due to the variations of the current J_y . These features can be used as the observational criteria to identify different types of magnetic islands in the magnetosphere using the data of future mission, such as the Magnetospheric Multiscale mission.

Two consecutive magnetic flux ropes, separated by less than 30 s ($\Delta t < 30$ s), are observed within one magnetic reconnection diffusion region without strong guide field in the Earth's magnetotail by Cluster multi-spacecraft (Huang *et al.*^[43]). The flux ropes are characterized by bipolar signatures of the south-north magnetic field component B_z accompanied with strong core magnetic field B_y , intense current J and density depletions inside of them. In spite of the small but non-trivial global scale negative guide field ($-B_y$), there exists a directional change of the core fields of two flux ropes, *i.e.*, $-B_y$ for the first one, and $+B_y$ for the second one. The directions of the core fields are the same as the ambient cross-tail magnetic field component B_y just outside of flux ropes. Therefore, they suggested that the core field of flux ropes is formed by compression of the local preexisting B_y and that the directional change of core field is due to the change of local preexisting B_y . Such a change in ambient B_y might be caused by some microscale physics.

The precise mechanism for the formation of magnetic islands in the magnetotail and the subsequent evolution are still controversial. New investigations have provided the first observational evidence of secondary reconnection in the earthward outflow jet of primary reconnection in the magnetotail (Wang *et al.*^[44]). The secondary reconnection takes place $38 c \cdot \omega_{pi}^{-1}$ earthward from the primary reconnection site and results in the birth of a magnetic island observed. This generation mechanism is different from the widely used model of multiple reconnection X-lines. The duration of the secondary reconnection was approximate one ion gyration period (5s). The observations resemble recent numerical simulations where magnetic reconnection could spontaneously and transiently happen in the outflow jet, called secondary reconnection, which was used to explain the formation of the dipolarization fronts. Coincidentally, another magnetic island moving earthward passed through three satellites successively.

Wang *et al.*^[45] presented in situ observation of Double Layer (DL) and associated electron measurement in the sub-spin time resolution in the separatrix region during reconnection for the first time. The DL is inferred to propagate away from the X line at a velocity of about ion acoustic speed and the parallel electric field carried by the DL can reach $-20 \text{ mV} \cdot \text{m}^{-1}$. The electron displays a beam distribution inside the DL and streams

toward the X line with a local electron Alfvén velocity. A series of electron holes moving toward the X line are observed in the wake of the DL. The identification of multiple similar DLs indicates that the DLs are persistently produced and therefore might play an important role in energy conversion during reconnection. The observation suggests that energy dissipation during reconnection can occur in any region where the DL can reach.

Three earthward flowing magnetic flux ropes observed in the duskside plasma sheet at geocentric solar magnetospheric coordinate $X \sim -55 R_E$ by P1 and P2 of acceleration, reconnection, turbulence and electrodynamics of moon's interaction with the sun mission during 13:00 UT–15:00 UT on July 3, 2012, were studied by Tian *et al.*^[46]. The morphologies of the flux ropes were studied in detail based on Grad-Shfranov reconstruction method and electronic pitch angle distribution data. It is found that (i) the flux rope cross-sectional dimensions are $1.0 \times 0.78 R_E$, $1.3 \times 0.78 R_E$, and $2.5 \times 1.25 R_E$, respectively. The magnetic field lines were asymmetric about the center with field line compression on both sides of the current sheet at the leading region; (ii) the electron energy flux data presented asymmetry with larger electron flux and lower temperature in the precursor region. The flux ropes were blocked by the resistance of compressed particle density in the front central plasma sheet and the enhanced magnetic field on its sides; and (iii) it is found that the flux rope has a layered structure. From inside out, event 1 can be divided into three regions, namely electronic depletion core region, closed field line region, and the caudal area possible with fields connected with the ionosphere. It suggests that the flux ropes cannot merge with the tail magnetic field lines near the lunar orbit. Especially, the flux rope asymmetrical shape reflects the different reconnection processes that caused it on both sides of the magnetic structure. The events shown in this paper support the multiple X-line magnetic reconnection model for flux ropes with in situ observations.

With the upcoming Magnetospheric Multiscale mission by NASA to investigate Magnetic Reconnection (MR) in detail, it is imperative to identify more precisely the occurrence probabilities of observing MR signatures in different magnetospheric activity levels. An extensive investigation was conducted by Zhang *et al.*^[47] on the probabilities of observing MR feature at different magnetospheric activity levels with data from



Geotail satellite. A newly developed method is used to categorize the state of magnetosphere in five different activity levels. The result shows quantitatively the probabilities in encountering MR features for these five different activity levels, providing valuable guidance to satellite operations to enhance encounter of MR in the Earth's magnetotail.

Utilizing associated observations of Geotail and ACE satellites from the year of 1998 to 2005, Zhang *et al.*^[48] investigated the X lines in the near-Earth tail under different Interplanetary Magnetic Field (IMF) conditions. The X lines are recognized by the tailward fast flows with negative B_z . Statistically, the X lines in the tail can be observed for southward as well as northward IMF, but more frequently observed for southward IMF. A typical case on 26 April 2005 showed clear evidence that the X line can occur for northward IMF while the geomagnetic activity is particularly quiet. Further analysis showed that the X line-related solar wind has stronger E_y and B_z components for southward than northward IMF. In addition, the X line-related geomagnetic activities are stronger for southward than northward IMF.

For magnetic reconnection to proceed, the frozen-in condition for both ion fluid and electron fluid in a localized diffusion region must be violated by inertial effects, thermal pressure effects, or inter-species collisions. It has been unclear which underlying effects unfreeze ion fluid in the diffusion region. By analyzing in situ THEMIS (Time History of Events and Macroscale Interactions during Substorms) spacecraft measurements at the dayside magnetopause, Dai *et al.*^[49] presented clear evidence that the off-diagonal components of the ion pressure tensor is mainly responsible for breaking the ion frozen-in condition in reconnection. The off-diagonal pressure tensor, which corresponds to a non-gyrotropic pressure effect in this event, is a fluid manifestation of ion demagnetization in the diffusion region. From the perspective of the ion momentum equation, the reported non-gyrotropic ion pressure tensor is a fundamental aspect in specifying the reconnection electric field that controls how quickly reconnection proceeds.

Huang *et al.*^[50] carried out large-scale particle-in-cell kinetic simulations to demonstrate that a super-Alfvénic electron shear flow across the current layer can be spontaneously generated in the outflow region of magnetic reconnection, which is unstable to the electron Kelvin-Helmholtz (K-H) instability. The resulted K-H

vortex structures continuously drive the secondary magnetic reconnection and formation of secondary magnetic islands, which leads to strong electron energization in the outflow region.

With observations of magnetic reconnection and the related bursty bulk flow (BBF) in the magnetotail by Time History of Events and Macroscale Interactions during Substorms mission, Wu *et al.*^[51] investigated the process of the multistage acceleration of electrons in magnetotail reconnection events, which can be divided into three distinct stages: (i) First, electrons are accelerated in the vicinity of the X line where the electron temperature can be significantly raised while the energetic electron flux with the energy larger than tens of keV has no obvious enhancement. (ii) Second, electrons suffer the nonadiabatic acceleration in the pileup region of magnetic reconnection, which results in the obvious enhancement of the energetic electron flux and the small increase of the electron temperature in the earthward flow. (iii) At last, the energetic electron flux can be further raised in the BBFs due to adiabatic acceleration mechanisms. Their study indicated that low-energy electrons can be accelerated to a high energy with a multistage process in magnetic reconnection events, which ranges from the vicinity of the X line to the BBFs.

Two-dimensional particle-in-cell simulations were performed in Huang *et al.*^[52] to investigate the characteristics of these electron holes generated in the separatrix region of antiparallel magnetic reconnection. The electron holes with bipolar structures of the parallel electric field are formed in the border between the electron inflow channel (where electrons move toward the X line) and outflow channel (where electrons flow away from the X line), where the electrons satisfy the bump-on-tail distribution. Quasi-monochromatic electrostatic waves, which propagate with a speed near the bulk velocity of the fast electron beam, are first excited by the electron bump-on-tail instability. These waves then coalesce with each other, and at last electron holes are formed in the separatrix region, which then propagate away from the X line along the magnetic field lines.

A magnetic island plays an important role in magnetic reconnection. Using a series of two-dimensional particle-in-cell simulations, Huang *et al.*^[53] investigated the magnetic structures of a magnetic island formed during multiple X line magnetic reconnections, consid-

ering the effects of the guide field in symmetric and asymmetric current sheets. In a symmetric current sheet, the current in the x direction forms a tripolar structure inside a magnetic island during antiparallel reconnection, which results in a quadrupole structure of the out-of-plane magnetic field. With the increase of the guide field, the symmetry of both the current system and out-of-plane magnetic field inside the magnetic island is distorted. When the guide field is sufficiently strong, the current forms a ring along the magnetic field lines inside a magnetic island. At the same time, the current carried by the energetic electrons accelerated in the vicinity of the X lines forms another ring at the edge of the magnetic island. Such a dual-ring current system enhances the out-of-plane magnetic field inside the magnetic island with a dip in the center of the magnetic island. In an asymmetric current sheet, when there is no guide field, electrons flow toward the X lines along the separatrices from the side with a higher density and are then directed away from the X lines along the separatrices to the side with a lower density. The formed current results in the enhancement of the out-of-plane magnetic field at one end of the magnetic island and the attenuation at the other end. With the increase of the guide field, the structures of both the current system and the out-of-plane magnetic field are distorted.

Using the Cluster observation in the magnetotail, Wang *et al.*^[54] investigated the dynamic processes associated with a Bursty Bulk Flow (BBF) event. The BBF is inferred to be caused by magnetic reconnection proceeding to the lobe region in its tail, called "primary reconnection." On the BBF front, another reconnection was directly encountered by one of the four Cluster satellites, and no signatures of this reconnection were simultaneously measured by the satellite at the plasma sheet boundary. It indicates that this reconnection on the BBF front remained within the plasma sheet, called "secondary reconnection." The secondary reconnection moved earthward and was followed by a magnetic island. A few earthward moving pulses of B_z were detected between the island and the primary reconnection site. These B_z pulses, propagating faster than the island ahead of it, would lead to a more compressed B_z magnetic field in the wake of the island. The observational scenario is in accordance to the model proposed to explain the generation of dipolarization front in simulations. Furthermore, both electrons and ions were significantly accelerated in this process.

Plasma energy dispersion properties inside reconnection jet flows observed inside the low-latitude boundary layer are used to determine the distances of observing satellites to reconnection sites. The locations of the reconnection sites are then retrieved by tracing the modeled field lines by those distances. The controlling effects of the dipole tilt angle to the location of X lines or reconnection sites are investigated. Zhu *et al.*^[55] showed that the Earth's dipole tilt angles strongly modify the location of X lines predicted by Cooling *et al.*'s model, which is thought to be the result of magnetopause reshaping due to finite dipole tilt angles.

The dynamics of a secondary tearing instability is systematically investigated based on compressible Hall magnetohydrodynamic. It was found by Ma *et al.*^[56] that in the early nonlinear phase of magnetic reconnection before onset of the secondary tearing instability, the geometry of the magnetic field in the reconnection region tends to form a Y-type structure in a weak Hall regime, instead of an X-type structure in a strong Hall regime. A new scaling law is found that the maximum reconnection rate in the early nonlinear stage is proportional to the square of the ion inertial length ($\gamma \propto d_i^2$) in the weak Hall regime. In the late nonlinear phase, the thin elongated current sheet associated with the Y-type geometry of the magnetic field breaks up to form a magnetic island due to a secondary tearing instability. After the onset of the secondary tearing mode, the reconnection rate is substantially boosted by the formation of the X-type geometries of magnetic field in the reconnection regions. With a strong Hall effect, the maximum reconnection rate linearly increases with the increase of the ion inertial length ($\gamma \propto d_i^2$).

A new method for determination of the Alfvén wave energy generated during magnetic reconnection is introduced and used to analyze the results from two-dimensional MHD simulations. It was found by Wang *et al.*^[57] that the regions with strong Alfvén wave perturbations almost coincide with that where both magnetic-field lines and flow-stream lines are bent, suggesting that this method is reliable for identifying Alfvén waves. The magnetic energy during magnetic reconnection is mainly transformed into the thermal energy. The conversion rate to Alfvén wave energy from the magnetic energy is strongly correlated to the magnetic reconnection rate. The maximum conversion rate at the time with the peak reconnection rate is found

to be only about 4% for the cases with the plasma beta of 0.01, 0.1, and 1.0.

Nonlinear dynamics of magnetic reconnection with an external sub-Alfvénic parallel shear flow is investigated by using two-dimensional compressible Hall MHD simulation. Two pairs of slow shocks in the inflow region are generated by the sub-Alfvénic shear flow in the MHD simulation. With inclusion of Hall effects, it was found by Ma *et al.*^[58] that whistler waves are generated in the downstream region of slow shocks. The whistler waves propagating toward the reconnection region drive a large bursty enhancement in magnetic reconnection during its decaying phase.

Collisionless magnetic reconnection in a Harris current sheet with different initial thicknesses is investigated using a 2.5D Darwin particle-in-cell simulation with the magnetosonic open boundary condition. It was found by Sun *et al.*^[59] that the thicknesses of the ion dissipation region and the reconnection current sheet, when the reconnection rate E_r reaches its first peak, are independent of the initial thickness of the current sheet; while the peak reconnection rate depends on it.

Magnetic reconnection has long been believed to be an efficient engine for energetic electrons production. Four different structures have been proposed for electrons being energized: flux pileup region, density cavity located around the separatrix, magnetic island and thin current sheet. Zhou *et al.*^[60] compared the electron acceleration efficiency among these structures based on 12 magnetotail reconnection events observed by the Cluster spacecraft in 2001–2006. They used the flux ratio between the energetic electrons (> 50 keV) and lower energy electrons (< 26 keV) to quantify the electron acceleration efficiency. They did not find any specific sequence in which electrons are accelerated within these structures, though the flux pileup region, magnetic island and thin current sheet have higher probabilities to reach the maximum efficiency among the four structures than the density cavity. However, the most efficient electron energization usually occurs outside these structures. They suggested that other structures may also play important roles in energizing electrons. Their results could provide important constraints for the further modeling of electron acceleration during magnetic reconnection.

Recent studies show that the out-of-plane quadrupolar magnetic field in fast magnetic reconnection is dis-

torted in the presence of a guide field. It is asymmetric with respect to the current sheet. Lai *et al.*^[61] analyzed the spatial and amplitude asymmetries of the Hall magnetic field B_y and the Hall electric field E_z in reconnection with different guide fields by a series of 2.5D particle-in-cell simulations. They derived the relation between the asymmetry of B_y and E_z and the guide field strength. In addition, by analyzing the different terms in the generalized ohm's law, they found that the electric field E_z is mainly balanced by the Hall term, and the amplitude asymmetry is mainly caused by the Hall effect.

It has long been suggested that waves around the lower hybrid frequency play a significant role in magnetic reconnection. Zhou *et al.*^[62] statistically studied the distribution and possible roles of waves around lower hybrid frequency based on the wave data recorded by the Cluster spacecraft during 21 magnetotail reconnection events. They found that, as the plasma β increments, magnetic field fluctuations associated with waves increase while electric field fluctuations decrease. As β exceeds 10, both magnetic and electric field fluctuations decrease. Furthermore, a two-dimensional wave distribution is constructed based on the two-dimensional reconnection model. There are positive correlations between wave strength and energetic electron acceleration, as well as between wave strength and reconnection rate. Their results may be important for fully understanding the role of waves around lower hybrid frequency in the dissipation process of magnetic reconnection.

A large-scale two-dimensional electromagnetic particle-in-cell simulation was employed to study the magnetic island coalescence/merging process during magnetic reconnection with guide field. The merged island after coalescence is characterized by strong core field and plasma density dip at the island center. Zhou *et al.*^[63] found that the core field enhancement is caused by the out-of-plane magnetic field pileup, as well as the field line twisting due to Hall effect. There is an in-plane electric current loop, which is mainly carried by electrons, circumventing the enhanced core field region. Total force points away or tangentially to the surface of density dip within the merged island, which prevents electrons from higher-density region entering the lower density region between two merging islands. This is contrary to the force in the secondary island, inside which the total force points toward the island center and constrains plasma there. The coalescence process in-

volves a reconnection at the merging sheet between two islands. Electron frozen-in condition is violated locally along the merging sheet. It is contributed by both the divergence of electron pressure tensor and electron inertial. Energy dissipation is concentrated on the merging line during coalescence, while a train of dynamo ($\mathbf{j}' \cdot \mathbf{E}' < 0$) and dissipation ($\mathbf{j}' \cdot \mathbf{E}' > 0$) regions are distributed along the merging sheet after coalescence. Electrons and ions within the density dip at the island center are accelerated antiparallel to the ambient magnetic field, *i.e.*, along the out-of-plane direction. The resultant distribution can excite the Buneman instability and two-streaming instability, which probably account for the electrostatic solitary waves observed by satellite.

During reconnection, a Flux Pileup Region (FPR) is formed behind a dipolarization front in an outflow jet. Inside the FPR, the magnetic field magnitude and B_z component increase and the whistler-mode waves are observed frequently. As the FPR convects toward the Earth during substorms, it is obstructed by the dipolar geomagnetic field to form a near-Earth FPR. Unlike the structureless emissions inside the tail FPR, Fu *et al.*^[64] found that the whistler-mode waves inside the near-Earth FPR can exhibit a discrete structure similar to chorus. Both upper band and lower band chorus are observed, with the upper band having a larger propagation angle (and smaller wave amplitude) than the lower band. Most chorus elements they observed are rising-tone type, but some are falling-tone type. They noticed that the rising-tone chorus can evolve into falling-tone chorus within < 3 s. One of the factors that may explain why the waves are unstructured inside the tail FPR but become discrete inside the near-Earth FPR is the spatial inhomogeneity of magnetic field: they found that such inhomogeneity is small inside the near-Earth FPR but large inside the tail FPR.

4 Solar Wind-magnetosphere-ionosphere Interaction

Using the FAST/TEAMS observations on the declining phase of solar cycle 23 (SC23), Zhao *et al.*^[65] individually calculated the H^+ upflow rates during geomagnetic quiet times ($Kp \leq 2^+$) and disturbed times ($Kp \geq 3^+$) over the Southern (SH) and Northern (NH) high-latitude polar regions, respectively. They investigated into the long-term magnitude of upflow intensity and correlations between the hemispheres. It is found that the total

intensity is significantly enhanced during geomagnetic disturbed times by a factor of 1.04 and 1.45 for the northern and southern hemispheres, respectively. The enhancement in southern hemisphere is more dramatic than that in northern hemisphere, the hemispherically averaged intensities all arrive at about 22% during disturbed times while the quiet time upflow rate is about 15% and about 20%, respectively. The midnight and dawnside upflows are more sensitive to geomagnetic disturbance. The upflow rates increase remarkably at low boundary of aurora oval, and during disturbed times, the high occurrence upflow region spreads from the dayside cusp region towards the midnight auroral zone and towards lower invariant latitudes. In addition, the polar cusp region moves gradually to the dawnside during disturbed times.

Based on the Fast/TEAMS observations in southern hemisphere from 2000 to 2005 on the declining phase of the solar activity cycle 23, the following questions were comparatively discussed during magnetically quiet times ($Kp \leq 2^+$) and storms ($Kp \geq 3^+$). One was the hemispheric distribution characteristics of O^+ outflow rates and net outflow differential fluxes, and the other one was the characteristics of outflow ions, which were yielded in terms of correlations with the altitude, year and Magnetic Local Time (MLT). Results showed that the outflow events during storms were mainly scattered on magnetic invariant latitude (ILAT) from 50° to 70° which was lower than that from 60° to 70° ILAT during quiet times. The high occurrence areas turned up on the auroral oval area at 00:00–07:00 MLT before dawn and 16:00–24:00 MLT before midnight. There were remarkable low energy outflow O^+ (< 1 key) on the day-side polar cusp during quiet times, while the high energy outflow O^+ (1 key) rarely happened on the polar cusp. Specifically, Zhao *et al.*^[66] found that the outflow rates of high and low energy ions during storms exceeded those during quiet times by a factor of about 2.294 and about 1.572, respectively. As a result, the proportion of high and low energy outflow O^+ increased during magnetic storms. Their results also suggested that the O^+ outflow intensity increased from 2000 to 4200 km and had a positive correlation with the solar activities.

Electric field penetration is a consequence of solar wind interaction with planetary magnetosphere and/or ionosphere. For both Earth with intrinsic magnetosphere

and Mars/Venus without intrinsic magnetosphere, the penetration electric field causes various kinds of global and local electrodynamic response of the ionosphere to the solar wind electric field, especially the plasma motion in the ionosphere. Within the first 14 years of the twenty-first century, the cause and effect of the electric field penetration on Earth has been investigated extensively and understood more deeply. Wei *et al.*^[67] reviewed the progress acquired on the patterns and drivers of the penetration electric field, and its influences on the plasma distribution and the equatorial spread F in the mid- and low-latitude ionosphere. From the perspective of comparative study, they also shortly introduced the new results for Mars. What has become clear is that their understanding of electric field penetration has been significantly improved, but ultimately the crucial details of the global picture still remain unknown. Looking forward to the future research of the electric field penetration in Earth's ionosphere, the breakthrough relies on new instruments built up at different longitudes to improve the global coverage of the observation. An integrated network of instrument is necessary to reveal the longitude and local-time dependence of the electric field penetration and shed new light on the physical details of the global ionospheric processes driven by the electric field penetration.

Recently, Cluster observations have revealed the presence of new regions of solar wind plasma entry at the high-latitude magnetospheric lobes tailward of the cusp region, mostly during periods of northward interplanetary magnetic field. Observations from the Global Ultraviolet Imager (GUVI) experiment on board the TIMED spacecraft and Wideband Imaging Camera imager on board the IMAGE satellite are used to investigate a possible link between solar wind entry and the formation of transpolar arcs in the polar cap. Mailyan *et al.*^[68] focused on a case when transpolar arc formation was observed twice right after the two solar wind entry events were detected by the Cluster spacecraft. In addition, GUVI and IMAGE observations show a simultaneous occurrence of auroral activity at low and high latitudes after the second entry event, possibly indicating a two-part structure of the continuous band of the transpolar arc.

In He *et al.*^[69], a three-dimensional (3D) global hybrid simulation code and a 3D geocoronal hydrogen model are used to systematically study the Extreme Ul-

traviolet (EUV) emissions at 30.4 nm produced by Solar Wind Charge exchange (SWCX) in the Earth's magnetosheath, associated with different solar wind-interplanetary magnetic field (SW-IMF) conditions and different imaging perspectives. They found that the EUV emission intensities in the magnetosheath are highly variable from several mR to ~1200 mR and increase with the flow speed, the density, the temperature, and the $\text{He}^{2+}/\text{H}^+$ density ratio of the solar wind; the northward IMF leads to a minimum emission in the magnetosheath, whereas the southward IMF generates a maximum emission; with the increase of the magnitude of IMF, the emission pattern in the nightside splits from single field-aligned shape into a butterfly shape around the magnetic equator; and the EUV emissions vary with the imaging positions, reflecting different latitudinal and longitudinal information of the magnetosheath. It is noted that the SWCX EUV emissions in the magnetosheath for highly disturbed solar wind conditions should be considered in processing the Moon-based plasmaspheric EUV images. They suggested that EUV imaging of the global magnetosheath requires an EUV imager with large field-of-view, high-sensitivity, large dynamic range, and low intrinsic dark count rate. This investigation could provide us with an overall understanding on SWCX EUV emissions in the magnetosheath which can potentially be used to image the global magnetosheath to study the solar wind-magnetosphere coupling in the future.

Sun *et al.*^[70] simulated the Kelvin-Helmholtz wave (KHW)-induced X-ray emissions at the low-latitude magnetopause based on a global MHD code. A method was proposed to extract the KHW information from the X-ray intensity measured by a hypothetical X-ray telescope onboard a satellite assumed with a low Earth orbit. Specifically, the X-ray intensity at high latitude is subtracted from the intensity map as a background to highlight the role of KHW. Using this method, global features of KHW such as the vortex velocity, perturbation degree, spatial distribution, and temporal evolution could be evaluated from the X-ray intensity map. The validity of this method during intervals of solar wind disturbances is also verified. According to the simulation results, X-ray imaging of KHW is suggested as a promising observation technique to essentially see the large-scale configuration and evolution of KHW for the first time.

Using Cluster multi-spacecrafts observation data during January to April of each year from 2001 to 2006, Gou *et al.*^[71] studied the solar wind penetration events into the Earth's high-latitude magnetosphere. When the IMF is northward, although the formation of the entry layers depends on the direction of IMF, they pointed out that it mainly depends on the IMF B_x component and the influences of IMF B_y component could be weak.

In response to Interplanetary (IP) shocks, magnetic field may decrease/increase (negative/positive response) in nightside magnetosphere, while at high latitudes on the ground it has two-phase bipolar variations: preliminary impulse and Main Impulse (MI). Using global MHD simulations, Sun *et al.*^[72] investigated the linkage between the MI phase variation on the ground and the magnetospheric negative response to an IP shock. It is revealed that although the two phenomena occur at largely separated locations, the two phenomena are physically related and form a response chain. The velocity disturbances near the flanks of the magnetopause cause the magnetic field to decrease, resulting in a dynamo which thus powers the transient Field-Aligned Currents (FACs). These FACs further generate a pair of ionospheric current vortex, leading to MI variations on the ground. Therefore, they reported the intrinsic physically related chain response of the magnetospheric and ground magnetic field to IP shocks, and thus link the magnetospheric Sudden Impulse (SI) and ground SI together.

Prediction of the Shocks' Arrival Times (SATs) at the Earth is very important for space weather forecast. There is a well-known SAT model, Shock Time of Arrival (STOA), which is widely used in the space weather forecast. However, the shock transit time from STOA model usually has a relative large error compared to the real measurements. In addition, STOA tends to yield too much yes prediction, which causes a large number of false alarms. Therefore, Liu and Qin^[73] worked on the modification of STOA model. First, they gave a new method to calculate the shock transit time by modifying the way to use the solar wind speed in STOA model. Second, they developed new criteria for deciding whether the shock will arrive at the Earth with the help of the sunspot numbers and the angle distances of the flare events. It is shown that their work can improve the SATs prediction significantly, especially the prediction of flare events without shocks arriving at the Earth.

A fundamental statement in diffusion theory is provided by the so-called theorem on reduced dimensional-

ity. The latter theorem is saying that if the dimensionality of the turbulence is reduced, charged particles are tied to a single magnetic field line. If there is pitch-angle scattering and therewith parallel diffusion, this usually means that perpendicular transport is subdiffusive. Subdiffusive transport was found in numerous simulations for slab turbulence (Qin and Shalchi^[74]). However, it was unclear whether the theorem is valid for other models with reduced dimensionality such as the two-dimensional model. In the current paper, they simultaneously traced magnetic field lines and energetic particles and they computed the distance between the particle and the initial field line. They confirmed the aforementioned theorem for slab turbulence but they could not confirm it for two-dimensional turbulence. They also showed that particles are not tied to field lines for two-component turbulence.

Qin and Zhang^[75] modified the NonLinear Guiding Center theory for perpendicular diffusion by replacing the spectral amplitude of the two-component model of magnetic turbulence with that of the two-dimensional model (following Shalchi), and replacing the constant a^2 , which indicates the degree particles following the magnetic field line, with the variable a'^2 as a function of the magnetic turbulence. They combined the modified model with the NonLinear PARallel diffusion theory to solve perpendicular and parallel diffusion coefficients simultaneously. It is shown that the new model agrees better with simulations. Furthermore, they fitted the numerical results of the new model with polynomials, so that the parallel and perpendicular diffusion coefficients can be calculated directly without iteration of integrations, and many numerical calculations can be reduced.

Quantitatively estimating the energy input from the solar wind into the magnetosphere on a global scale is still an observational challenge. Wang *et al.*^[76] perform three-dimensional Magnetohydrodynamic (MHD) simulations to derive the energy coupling function. Based on 240 numerical test runs, they obtained an energy coupling function. They studied the correlations between the energy coupling function and a wide variety of magnetospheric activity, such as the indices of Dst , Kp , Ap , AE , AU , AL , the polar cap index, and the hemispheric auroral power. The results indicate that this energy coupling function gives better correlations than the epsilon function. This result is also applied to a storm event under northward interplanetary magnetic



field conditions. About 13% of the solar wind kinetic energy is transferred into the magnetosphere and about 35% of the input energy is dissipated in the ionosphere, consistent with previous studies.

Wang *et al.*^[77] investigates the conditions for producing rapid variations of Solar Energetic Particle (SEP) intensity commonly known as "dropouts." In particular, they used numerical model simulations based on solving the focused transport equation in the three-dimensional Parker interplanetary magnetic field to put constraints on the properties of particle transport coefficients in both directions perpendicular and parallel to the magnetic field. Their calculations of the temporal intensity profile of 0.5 and 5 MeV protons at the Earth show that the perpendicular diffusion must be small while the parallel mean free path is long in order to reproduce the phenomenon of SEP dropouts. When the observer is located at a larger solar radial distance, the perpendicular to parallel diffusion ratio for reproducing the dropouts should be even lower than that in the case of 1 AU distance. A shorter parallel mean free path or a larger radial distance from the source to observer will cause the particles to arrive later, making the effects of perpendicular diffusion more prominent and SEP dropouts disappear. All of these effects require the magnetic turbulence that resonates with the particles to be low everywhere in the inner heliosphere.

To develop an understanding of near-Earth space's response to solar activities and the coupling among different layers in geospace, China has initiated a ground based program to monitor China's geospace environment called the Meridian Space Weather Monitoring Project (Chinese Meridian Project). The effort consists of a chain of 15 ground-based observatories located roughly along 120°E longitude and 30°N latitude. Each observatory is equipped with multiple instruments to measure key parameters such as the baseline and time-varying geomagnetic field, as well as the middle and upper atmosphere and ionosphere from about 20 to 1000 kilometers. This project started collecting data in 2012. Wang^[78] gave a brief introduction to the Chinese Meridian Project, and presented recent scientific results mainly in ionospheric and atmospheric studies.

Shi *et al.*^[79] reported the in situ observation of a plasma vortex induced by a solar wind dynamic pressure enhancement in the nightside plasma sheet using multipoint measurements from Time History of Events

and Macroscale Interactions during Substorms (THEMIS) satellites. The vortex has a scale of 5–10 R_E and propagates several R_E downtail, expanding while propagating. The features of the vortex are consistent with the prediction of the Sibeck (1990) model, and the vortex can penetrate deep (about 8 R_E) in the dawn-dusk direction and couple to field line oscillations. Global magnetohydrodynamics simulations were carried out, and it was found that the simulation and observations are consistent with each other. Data from THEMIS ground magnetometer stations indicate a poleward propagating vortex in the ionosphere, with a rotational sense consistent with the existence of the vortex observed in the magnetotail.

Tracking the formation and full evolution of polar cap ionization patches in the polar ionosphere, Zhang *et al.*^[80] directly displayed the full Dungey convection cycle for southward Interplanetary Magnetic Field (IMF) conditions. This enables us to study how the Dungey cycle influences the patches' evolution. The patches were initially segmented from the dayside storm enhanced density plume at the equatorward edge of the cusp, by the expansion and contraction of the polar cap boundary due to pulsed dayside magnetopause reconnection, as indicated by in situ Time History of Events and Macroscale Interactions during Substorms (THEMIS) observations. Convection led to the patches entering the polar cap and being transported antisunward, while being continuously monitored by the globally distributed arrays of GPS receivers and Super Dual Auroral Radar Network radars. Changes in convection over time resulted in the patches following a range of trajectories, each of which differed somewhat from the classical twin-cell convection streamlines. Pulsed nightside reconnection, occurring as part of the magnetospheric substorm cycle, modulated the exit of the patches from the polar cap, as confirmed by coordinated observations of the ground magnetometers. After exiting the polar cap, the patches broke up into a number of plasma blobs and returned sunward in the auroral return flow of the dawn and/or dusk convection cell. The full circulation time was about 3h.

The evolution of life is affected by variations of atmospheric oxygen level and geomagnetic field intensity. Oxygen can escape into interplanetary space as ions after gaining momentum from solar wind, but Earth's strong dipole field reduces the momentum transfer effi-

ciency and the ion outflow rate, except for the time of geomagnetic polarity reversals when the field is significantly weakened in strength and becomes Mars-like in morphology. The newest databases available for the Phanerozoic era illustrate that the reversal rate increased and the atmospheric oxygen level decreased when the marine diversity showed a gradual pattern of mass extinctions lasting millions of years. Wei *et al.*^[81] proposed that accumulated oxygen escape during an interval of increased reversal rate could lead to the catastrophic drop of oxygen level, which is known to be a cause of mass extinction. They simulated the oxygen ion escape rate for the Triassic-Jurassic event, using a modified Martian ion escape model with an input of quiet solar wind inferred from Sun-like stars. The results show that geomagnetic reversal could enhance the oxygen escape rate by 3–4 orders only if the magnetic field was extremely weak, even without consideration of space weather effects. This suggests that their hypothesis could be a possible explanation of a correlation between geomagnetic reversals and mass extinction. Therefore, if this causal relation indeed exists, it should be a "many-to-one" scenario rather than the previously considered "one-to-one", and planetary magnetic field should be much more important than previously thought for planetary habitability.

Data from the two-spacecraft Acceleration, Reconnection, Turbulence and Electrodynamics of the Moon's Interaction with the Sun mission to the Moon have been exploited to characterize the lunar wake with unprecedented fidelity. The differences between measurements made by a spacecraft in the solar wind very near the Moon and concurrent measurements made by a second spacecraft in the near lunar wake are small but systematic. Zhang *et al.*^[82] established the perturbations of plasma density, temperature, thermal, magnetic and total pressure, field, and flow downstream of the Moon to distances of 12 lunar radii (R_M). The wake disturbances are initiated immediately behind the Moon by the diamagnetic currents at the lunar terminator. Rarefaction waves propagate outward at fast MHD wave velocities. Beyond about $6.5 R_M$, all plasma and field parameters are poorly structured which suggests the presence of instabilities excited by counter-streaming particles. Inward flowing plasma accelerated through pressure gradient force and ambipolar electric field compresses the magnetic field and leads to continuous increase in mag-

nitude of magnetic perturbations. Besides the downstream distance, the field perturbation magnitude is also a function of the solar wind ion beta and the angle between the solar wind and the Interplanetary Magnetic Field (IMF). Both ion and electron temperatures increase as a consequence of an energy dispersion effect, whose explanation requires fully kinetic models. Downstream of the Moon, the IMF field lines are observed to bulge toward the Moon, which is unexpected and may be caused by a plasma pressure gradient force or/and the pickup of heavy charged dust grains behind the Moon.

Previous studies have demonstrated that the Interplanetary Magnetic Field (IMF) can control the magnetospheric dynamics. Immediate magnetospheric responses to the external IMF have been assumed for a long time. The specific processes by which IMF penetrates into magnetosphere, however, are actually unclear. Solving this issue will help to accurately interpret the time sequence of magnetospheric activities (*e.g.*, substorm and tail plasmoids) exerted by IMF. With two carefully selected cases, Rong *et al.*^[83] found that the penetration of IMF into magnetotail is actually delayed by 1–1.5 h, which significantly lags behind the magnetotail response to the solar wind dynamic pressure. The delayed time appears to vary with different auroral convection intensity, which may suggest that IMF penetration in the magnetotail is controlled considerably by the dayside reconnection. Several unfavorable cases demonstrate that the penetration lag time is more clearly identified when storm/substorm activities are not involved.

On 24 August 2005, an impulse of solar wind dynamic pressure (P_{sw}) hit the magnetosphere. Using the high resolution geomagnetic field data from 15 ground stations and the data from Geotail and TC-1, Wang^[84] studied the geomagnetic pulsations at auroral latitudes driven by the sharp decrease of P_{sw} at the trailing edge of the impulse. The results show that the sharp decrease of P_{sw} can excite a global pulsation in the frequency range 4.3–11.6 mHz. The pulsation has a reversal of polarization between two auroral latitude stations, a larger Power Spectral Density (PSD) close to resonant latitude and increasing frequency with decreasing latitude. All these features indicate that the pulsations are associated with Field Line Resonance (FLR). The fundamental resonant frequency (the peak frequency of PSD between 4.3 and 5.8 mHz) is dependent on mag-

netic local time and is largest around magnetic local noon. This feature is due to the fact that the size of magnetospheric cavity is dependent on local time and smallest at noon. A second harmonic wave at about 10 mHz is also observed, which is strongest in the daytime sector, and becomes heavily attenuated in the night sector. The comparison of the PSDs of the pulsations driven by sharp increase and sharp decrease of P_{sw} shows that the frequency of pulsations is negatively proportional to the size of magnetopause. Since the FLR is excited by compressional cavity/waveguide waves, the above results indicate that the resonant frequency in the magnetospheric cavity/waveguide is controlled not only by solar wind parameters but also by magnetic local time of observation point.

Using the plasma data of Detection of Electro-Magnetic Emissions Transmitted from Earthquake Regions (DEMETER) satellite and the NRLMSISE-00 atmospheric model, Li *et al.*^[85] examined the semiannual and solar activity variations of the daytime plasma and neutral composition densities in the ionosphere-plasma-sphere transition region (about 670–710 km). The results demonstrate that the semiannually latitudinal variation of the daytime oxygen ions (O^+) is basically controlled by that of neutral atomic oxygen (O), whereas the latitude distributions of the helium and hydrogen ions (He^+ and H^+) do not fully depend on the neutral atomic helium (He) and hydrogen (H). The summer enhancement of the heavy oxygen ions is consistent with the neutral O enhancement in the summer hemisphere, and the oxygen ion density has significantly the summer-dense and winter-tenuous hemispheric asymmetry with respect to the dip equator. Although the winter enhancements of the lighter He^+ and H^+ ions are also associated with the neutral He and H enhancements in the winter hemisphere, the high-density light ions (He^+ and H^+) and electrons mainly appear at the low and middle magnetic latitudes ($|\lambda| < 50^\circ$). The equatorial accumulations of the light plasma species indicate that the light charged particles (He^+ , H^+ , and electron) are easily transported by some equatorward forces (*e.g.*, the magnetic mirror force and centrifugal force). The frequent Coulomb collisions between the charged particles probably lead to the particle trappings at different latitudes. Moreover, the neutral composition densities also influence their ion concentrations during different solar activities. From the low- $F_{10.7}$ year (2007–2008) to the high- $F_{10.7}$ year (2004–2005), the daytime

oxygen ions and electrons increase with the increasing neutral atomic oxygen, whereas the daytime hydrogen ions tend to decrease with the decreasing neutral atomic hydrogen. The helium ion density has no obvious solar activity variation, suggesting that the generation (via the neutral He photoionization) and loss (*via* the charge exchange with neutral nitrogen N_2 and/or the recombination with electrons) of the daytime He^+ ions are comparable during different solar activities.

Linear properties of Kinetic Alfvén Waves (KAWs) and Kinetic Slow Waves (KSWs) are studied in the framework of two-fluid magnetohydrodynamics. Zhao *et al.*^[86] obtained the wave dispersion relations that are valid in a wide range of the wave frequency ω and plasma-to-magnetic pressure ratio β . The KAW frequency can reach and exceed the ion-cyclotron frequency at ion kinetic scales, whereas the KSW frequency remains sub-cyclotron. At $\beta \sim 1$, the plasma and magnetic pressure perturbations of both modes are in anti-phase, so that there is nearly no total pressure perturbations. However, these modes also exhibit several opposite properties. At high β , the electric polarization ratios of KAWs and KSWs are opposite at the ion gyroradius scale, where KAWs are polarized in the sense of electron gyration (right-hand polarized) and KSWs are left-hand polarized. The magnetic helicity $\sigma \sim 1$ for KAWs and $\sigma \sim -1$ for KSWs, and the ion Alfvén ratio $R_{Ai} \ll 1$ for KAWs and $R_{Ai} \gg 1$ for KSWs. They also found transition wavenumbers where KAWs change their polarization from left-handed to right-handed. These new properties can be used to discriminate KAWs and KSWs when interpreting kinetic-scale electromagnetic fluctuations observed in various solar-terrestrial plasmas. This concerns, in particular, identification of modes responsible for kinetic-scale pressure-balanced fluctuations and turbulence in the solar wind.

The rapid change in the Earth's magnetosphere caused by solar wind disturbances has been an important part of the solar wind-magnetosphere interaction. However most of the previous studies focused on the perturbation of the Earth's magnetic field caused by solar wind dynamic pressure changes. Dong *et al.*^[87] studied the response of geosynchronous magnetic field and the magnetic field to the rapid southward turning of interplanetary magnetic field during the interval 13:50 UT–14:20 UT on 7 May 2007. During this event, B_z component of the interplanetary magnetic field decreased from 15 nT to –10 nT within 3 min (14:03 UT–

14:06 UT). The geosynchronous magnetic field measured by three geosynchronous satellites (GOES 10–12) first increased and then decreased. The variations of magnetic field strength in the morning sector (09:00 LT–10:00 LT) were much larger than those in the dawn sector (05:00 LT). Meanwhile, the H components of geomagnetic field on the ground have similar response features but exhibit latitude and LT dependent variations. Compared with H components, the D components do not have regular variations. Although the solar wind dynamical pressure encounters small variations, the magnetic field both in space and on the ground does not display similar variations. Therefore, the increase of geomagnetic field in the dawn sector is caused by the southward turning of IMF (interplanetary magnetic field) B_z . These results will help to better understand the coupling process of geomagnetic field and interplanetary magnetic field.

On 13 April 2002, four Cluster spacecraft with separations up to 127 km measured similar turbulence in the exterior cusp during northward Interplanetary Magnetic Field (IMF) B_z (Wang *et al.*^[88]). Both the power spectra of magnetic and electric field fluctuations resemble the classical Kolmogorov power law, with the scaling $f^{1.7}$ under the proton gyrofrequency f_{cp} (about 0.3 Hz), breaks near f_{cp} , and then steepens with the scalings $f^{2.8}$ and $f^{2.0}$ up to 10 Hz, respectively. The observed ratio of the electric to magnetic field is in agreement with the theoretical values, which reflects the features of Alfvén turbulence. The wave vector and dispersion relation of the turbulence are obtained using k-filtering technique. Wang *et al.*^[88] showed that the waves propagate quasi-perpendicularly to the background magnetic field. The similarity between the experimental and the theoretical dispersion relations indicates that the measured waves are kinetic Alfvén wave. The waves have right-handed elliptical polarization in the plane perpendicular to k . The main axis of polarization ellipse is perpendicular to the average magnetic field. These features furthermore indicate that the turbulence properties agree well with those of KAW mode. The observed KAW is much possibly produced through resonance mode conversion. They calculated the density gradient vector using multipoint density data and found that the waves propagate basically toward high-density region. The density gradient in the exterior cusp provides a favorable condition for the resonance converted KAW.

5 Radiation belt, Ring Current and Plasmasphere

Modulated High Frequency (HF) heating of the ionosphere provides a feasible means of artificially generating Extremely Low Frequency (ELF)/Very Low Frequency (VLF) whistler waves, which can leak into the inner magnetosphere and contribute to resonant interactions with high energy electrons. Combining the ray tracing method and test particle simulations, Chang *et al.*^[89] evaluated the effects of energetic electron resonant scattering driven by the discrete, multi-frequency artificially generated ELF/VLF waves. The simulation results indicate a stochastic behavior of electrons and a linear profile of pitch angle and kinetic energy variations averaged over all test electrons. These features are similar to those associated with single-frequency waves. The computed local diffusion coefficients show that, although the momentum diffusion of relativistic electrons due to artificial ELF/VLF whistlers with a nominal amplitude of about 1 pT is minor, the pitch angle scattering can be notably efficient at low pitch angles near the loss cone, which supports the feasibility of artificial triggering of multi-frequency ELF/VLF whistler waves for the removal of high energy electrons from the magnetosphere. They also investigated the dependences of diffusion coefficients on the frequency interval (Δf) of the discrete, multi-frequency waves. They found that there is a threshold value of Δf for which the net diffusion coefficient of multi-frequency whistlers is inversely proportional to Δf (proportional to the frequency components N_w) when Δf is below the threshold value but it remains unchanged with increasing Δf when Δf is larger than the threshold value. This is explained as being due to the fact that the resonant scattering effect of broadband waves is the sum of the effects of each frequency in the 'effective frequency band'. Their results suggest that the modulation frequency of HF heating of the ionosphere can be appropriately selected with reasonable frequency intervals so that better performance of controlled precipitation of high energy electrons in the plasmasphere by artificial ELF/VLF whistler waves can be achieved.

After lots of experiments by using 19–27 MeV differential energetic proton data based on the observation of SAMPEX from July of 1992 to June of 2004, it is found by Lu *et al.*^[90] that the change of $F_{10.7}$ and altitude

have a great influence on the distribution of differential energetic proton flux in South Atlantic Anomaly. During the geomagnetic quiet time at 540 ± 25 km altitude, the energetic proton flux in South Atlantic Anomaly decreased with the increasing of $F_{10.7}$, and the variation trend was flat when $F_{10.7} \geq 115$ sfu. It is found that there was obviously an anti-correlation between the absolute value of SYM- H and the differential energetic proton flux in South Atlantic Anomaly for storms with SYM- $H < -50$, and also there was a lasting effect on differential energetic proton flux in South Atlantic Anomaly. In addition, the proton flux could be significantly reduced in South Atlantic Anomaly during the main phase, while the proton flux showed a substantial resuming trend in the recovery phase of geomagnetic storms.

With consideration of magnetic Field Line Curvature (FLC) pitch angle scattering and charge exchange reactions, the O^+ (> 300 keV) in the inner magnetosphere loss rates are investigated by Ji and Shen^[91] using an eigenfunction analysis. The FLC scattering provides a mechanism for the ring current O^+ to enter the loss cone and influence the loss rates caused by charge exchange reactions. Assuming that the pitch angle change is small for each scattering event, the diffusion equation including a charge exchange term is constructed and solved; the eigenvalues of the equation are identified. The resultant loss rates of O^+ are approximately equal to the linear superposition of the loss rate without considering the charge exchange reactions and the loss rate associated with charge exchange reactions alone. The loss time is consistent with the observations from the early recovery phases of magnetic storms.

Qin and Shalchi^[92] revisited a well-known problem in diffusion theory, namely the 90° scattering problem. They used a test-particle code to compute the pitch-angle Fokker-Planck coefficient at 90° for different values of the turbulent magnetic field strength and the magnetic rigidity. They considered a slab model and compare their numerical findings with the analytical result provided by second-order quasilinear theory. They showed that the latter theory accurately describes 90° scattering. They also replaced the slab model by a more realistic two-component model to explore the influence of the turbulence model on 90° scattering.

Magnetic disturbances caused by the Earth's ring current, particularly during storm time activity, have a dominant effect on the geomagnetic field. Strong currents

and large kinetic and magnetic energies can change considerably local field geometry and depress the ground geomagnetic field. The multi-spacecraft magnetic measurements of Cluster allow extensive in situ coverage of the ring current. Shen *et al.*^[93] selected 48 storm time Cluster crossing events to investigate the variation of the local current density distribution and magnetic configuration of the ring current. They found direct evidence for the existence of an inner, eastward flowing current in addition to the dominant westward current, in the ring plane. The radius of curvature of the Magnetic Field Lines (MFLs) is found to be increasingly reduced at all local times during increasing storm activity, changing the resulting ring current magnetic geometry considerably, where the MFL configuration and the azimuthal current density distribution are asymmetric with the local time. During similar storm activity the radius of curvature of the local MFLs, R-c, is smallest on the nightside to duskside, medium on the dawnside, and largest on the dayside. This change in geometry may have significant influence on the spatial distribution of the particles with various energies in the plasmasphere, ring current, and radiation belts.

Theoretical bounce resonance diffusion coefficients from interactions between electrons and spatially confined waves are derived and validated. Roberts and Schulz bounce resonance diffusion coefficients assume waves to be present on the whole bounce trajectory of particles; therefore, those coefficients are not directly applicable to waves that have a finite spatial extent. Li *et al.*^[94] theoretically derived and numerically validated a new set of bounce resonance diffusion coefficients for spatially confined waves. They applied their analysis to magnetosonic waves, which are confined to equatorial regions, using a previously published magnetosonic wave model. They found that the bounce resonance diffusion coefficients are comparable to the gyroresonance diffusion coefficients. They concluded that bounce resonance diffusion with magnetosonic waves might play an important role in relativistic electron dynamics.

Superposed epoch analyses were performed on 193 significant relativistic electron flux dropout events, in order to study the roles of different solar wind parameters in driving the depletion of relativistic electrons, using about 16 years of data from the POES and GOES missions, and the OMNIWEB solar wind database. Gao *et al.*^[95] find that the solar wind dynamic pressure and interplanetary magnetic field (IMF) B_z play key roles in

causing the relativistic electron flux dropouts, but also that either large solar wind dynamic pressure or strong southward IMF B_z by itself is capable of producing the significant depletion of relativistic electrons. The relativistic electron flux dropouts occur not only when the magnetopause is compressed closer to the Earth but also when the magnetopause is located very far. Importantly, their results show that in addition to the large solar wind dynamic pressure, which pushes the magnetopause inward strongly and causes the electrons to escape from the magnetosphere, relativistic electrons can also be scattered into the loss cone and precipitate into the Earth's atmosphere during periods of strong southward IMF B_z , which preferentially provides a source of free energy for Electromagnetic Ion Cyclotron (EMIC) wave excitation. This is supported by the fact that the strongest electron precipitation into the atmosphere is found in the dusk sector, where EMIC waves are typically observed in the high-density plasmasphere or plume and cause efficient electron precipitation down to about 1 MeV.

The bandwidths and coherence coefficients of lower band whistler mode waves are analyzed using Time History of Events and Macroscale Interactions during Substorms (THEMIS) waveform data for rising tones, falling tones, and hiss-like emissions separately. Gao *et al.*^[96] also evaluate their dependences on the spatial location, electron density, the ratio of plasma frequency to local electron gyrofrequency (f_{pe}/f_{ce}), and the wave amplitude. Their results show that the bandwidth normalized by the local electron gyrofrequency (f_{ce}) of rising and falling tones is very narrow (about $0.01 f_{ce}$), smaller than that of the hiss-like emissions (about $0.025 f_{ce}$). Meanwhile, the normalized bandwidth of discrete emissions gradually decreases with increasing wave amplitude, whereas that of hiss-like emissions increases slowly. The coherence coefficient of rising and falling tones is extremely large (about 1), while the coherence coefficient of hiss-like emissions is smaller but is still larger than 0.5. For all categories of whistler mode waves, the normalized bandwidth increases at larger L shells. Furthermore, the normalized bandwidth is positively correlated with local f_{pe}/f_{ce} but is inversely correlated with the electron density. Interactions between radiation belt electrons and whistler mode waves have been widely described by quasi-linear diffusion theory. Their results suggest that although quasi-linear theory is not entirely applicable for modeling electron interactions with rising and falling tones due to their narrow bandwidth and

high coherence coefficient, it is suitable to treat wave-particle interactions between electrons and low-amplitude hiss-like emissions. Moreover, the correlations between the normalized bandwidth of chorus waves (especially the discrete emissions) and other parameters may provide insights for the generation mechanism of chorus waves.

Geomagnetic storms can either increase or decrease relativistic electron fluxes in the outer radiation belt. A statistical survey of 84 isolated storms demonstrates that geomagnetic storms preferentially decrease relativistic electron fluxes at higher energies, while flux enhancements are more common at lower energies. In about 87% of the storms, 0.3–2.5 MeV electron fluxes show an increase, whereas 2.5–14 MeV electron fluxes increase in only 35% of the storms. Superposed epoch analyses suggest that such "energy-dependent" responses of electrons preferably occur during conditions of high solar wind density which is favorable to generate magnetospheric Electromagnetic Ion Cyclotron (EMIC) waves, and these events are associated with relatively weaker chorus activities. Xiong *et al.*^[97] examined one of the cases where observed EMIC waves can resonate effectively with > 2.5 MeV electrons and scatter them into the atmosphere. The correlation study further illustrates that electron flux dropouts during storm main phases do not correlate well with the flux buildup during storm recovery phases. They suggested that a combination of efficient EMIC-induced scattering and weaker chorus-driven acceleration provides a viable candidate for the energy-dependent responses of outer radiation belt relativistic electrons to geomagnetic storms. These results are of great interest to both understanding of the radiation belt dynamics and applications in space weather.

Effects of magnetic field configuration on the day-night asymmetry of chorus occurrence rate are investigated using a recently developed hybrid code. Previous observational studies show that dayside chorus occurs in regions where the background magnetic field is nearly homogeneous; these observations suggest that the magnetic field configuration might play a significant role in the dayside chorus excitation. Tao *et al.*^[98] used a hybrid code to numerically study the threshold conditions of hot electron distributions required to excite chorus waves for different background magnetic field inhomogeneities. Their numerical experiments demonstrated



that in a magnetic field with smaller inhomogeneity, smaller temperature anisotropy and smaller number density of hot electrons are needed to excite chorus waves. This conclusion could help explain the higher occurrence rate of chorus waves on the dayside compared with that on the nightside especially in quiet times.

Trapped proton population in the inner radiation belt is highly dense, posing a potential danger to astronauts and man-made space assets traversing through this region. While being significantly stable within timescales up to hundreds of days, inner zone proton fluxes can exhibit considerable solar cycle variations, which have not been investigated comprehensively yet. To analyze the long-term variation of the South Atlantic Anomaly (SAA), Qin *et al.*^[99] adopted the proton flux data measured by NOAA 15 from 1999 through 2009 and perform statistical analyses on the basis of reasonable Gaussian fits. They reported that the variation of the peak proton flux in the SAA is anticorrelated with that of $F_{10.7}$ during a solar cycle. There also exists a phase lag of 685 days between the solar $F_{10.7}$ flux and the proton flux. Similar features are seen for changes of the SAA distribution area, which in addition shows a rapid decrease during the solar maximum and a slow increase during the solar minimum. They also found that the region where the proton flux peaks drifts westward year by year with larger drift rates during the solar minimum. The peak region shifts southward during the solar maximum but in the opposite direction during the solar minimum with higher shift speed. Enhancements in solar wind dynamic pressure can favor the north-south drift of the SAA.

Linear theory suggests that whistler mode wave growth rates are proportional to the ratio of hot electron (~1 to 30 keV) density to total electron density (N_h/N_t), whereas nonlinear wave theory suggests that an optimum linear growth rate is required to generate rising tone chorus from hiss-like emissions. Using the Time History of Events and Macroscale Interactions during Substorms waveform data collected by three probes over the past ~5 years, Gao *et al.*^[100] investigated the correlation between N_h/N_t and wave amplitude/wave occurrence rate for rising tone, falling tone, and hiss-like emissions separately. Statistical results show that the rising and falling tones preferentially occur in the region with a limited N_h/N_t range, whereas both the occurrence rate and wave amplitudes of hiss-like emissions become larger for higher values of N_h/N_t . Their statistical results

not only provide an important clue on the generation mechanism of hiss-like emissions, but also provide supporting experimental evidence for the nonlinear theory of generating rising tone chorus.

Chorus waves play an important role in energetic electron dynamics in the inner magnetosphere. Tao^[101] presented a new hybrid code, DAWN, to simulate the generation of chorus waves. The DAWN code is unique in that it models cold electrons using linearized fluid equations and hot electrons using particle-in-cell techniques. The simplified fluid equations can be solved with robust and simple algorithms. They demonstrated that discrete chorus elements can be generated using the code. Waveforms of the generated element show amplitude modulation or sub-packets, and the frequency sweep rate of the generated element is found to be consistent with that of observed chorus waves. Using the DAWN code, they then investigated the variation of wave intensity (B_w^2) with respect to linear growth rates on the equatorial plane. Their results demonstrate the importance of including nonlinear dynamics of chorus generation in understanding the whistler wave intensity modulation process in the inner magnetosphere.

Understanding how the relativistic electron fluxes drop out in the outer radiation belt under different conditions is of great importance. To investigate which mechanisms may affect the dropouts under different solar wind conditions, 1.5–6.0 MeV electron flux dropout events associated with 223 corotating interaction regions (CIRs) from 1994 to 2003 were studied by Yuan *et al.*^[102] using the observations of Solar, Anomalous, Magnetospheric Particle Explorer satellite. According to the superposed epoch analysis, it is found that high solar wind dynamic pressure with the peak median value of about 7nPa is corresponding to the dropout of the median of the radiation belt content (RBC) index to 20% of the level before stream interface arrival, whereas low dynamic pressure with the peak median value of about 3nPa is related to the dropout of the median of RBC index to 40% of the level before stream interface arrival. Furthermore, the influences of Russell-McPherron effect with respect to interplanetary magnetic field orientation on dropouts are considered. It is pointed out that under positive Russell-McPherron effect (+RM effect) condition, the median of RBC index can drop to 23% of the level before stream interface arrival, while for negative Russell-McPherron effect (-RM effect) events, the

median of RBC index only drops to 37% of the level before stream interface arrival. From the evolution of phase space density profiles, the effect of +RM on dropouts can be through nonadiabatic loss.

Through polarization and spectra analysis of the magnetic field observed by the Van Allen Probe A, Yu *et al.*^[103] presented two typical cases of O⁺ band Electromagnetic Ion Cyclotron (EMIC) waves in the outer plasmasphere or plasma trough. Although such O⁺ band EMIC waves are rarely observed, 18 different events of O⁺ band EMIC waves (16 events in the outer plasmasphere and two events in the plasma trough) are found from September 2012 to August 2014 with observations of the Van Allen Probe A. They found that the preferred region for the occurrence of O⁺ band EMIC waves is in $L=2-5$ and magnetic local time = 03:00–13:00, 19:00–20:00, which is in accordance with the occurrence region of O⁺ ion torus. Therefore, their result suggests that the O⁺ ion torus in the outer plasmasphere during geomagnetic activities should play an important role in the generation of EMIC waves in O⁺ band.

Utilizing the data from the magnetometer instrument which is a part of the Electric and Magnetic Field Instrument Suite and Integrated Science instrument suite on board the Van Allen Probe A from September 2012 to April 2014, when the apogee of the satellite has passed all the Magnetic Local Time (MLT) sectors, Wang *et al.*^[104] obtained the statistical distribution characteristics of Electromagnetic Ion Cyclotron (EMIC) waves in the inner magnetosphere over all magnetic local times from $L=3$ to $L=6$. Compared with the previous statistical results about EMIC waves, the occurrence rates of EMIC waves distribute relatively uniform in the MLT sectors in lower L shells. On the other hand, in higher L shells, there are indeed some peaks of the occurrence rate for the EMIC waves, especially in the noon, dusk, and night sectors. EMIC waves appear at lower L shells in the dawn sector than in other sectors. In the lower L shells ($L < 4$), the occurrence rates of EMIC waves are significant in the dawn sector. This phenomenon may result from the distribution characteristics of the plasmasphere. The location of the plasmapause is usually lower in the dawn sector than that in other sectors, and the plasmapause is considered to be the favored region for the generation of EMIC waves. In higher L shells ($L > 4$) the occurrence rates of EMIC waves are most significant in the dusk sector, implying

the important role of the plasmapause or plasmaspheric plume in generating EMIC waves. They have also investigated the distribution characteristics of the hydrogen band and the helium band EMIC waves. Surprisingly, in the inner magnetosphere, the hydrogen band EMIC waves occur more frequently than the helium band EMIC waves. Both of EMIC waves have peaks of occurrence rate in noon, dusk, and night sectors, and the hydrogen band EMIC waves have more obvious peaks than the helium band EMIC waves in the night sector, while the helium band EMIC waves are more concentrated than the hydrogen band EMIC waves in the dusk sector.

Electromagnetic Ion Cyclotron (EMIC) waves play an important role in the magnetospheric dynamics and can scatter relativistic electrons in the outer radiation belt into the loss cone leading to the rapid loss of relativistic electrons. Wang *et al.*^[105] presented characteristics of EMIC wave-driven Relativistic Electron Precipitation (REP) with observations of six Polar Orbiting Environmental Satellites (POES). They improved the algorithm and made it stricter. A total of 436,286 individual half orbits between 1998 and 2010 were inspected by this algorithm. The majority of selected events were observed at L values within the outer radiation belt ($3 < L < 7$) and more common in 18:00–22:00 magnetic local time. The distribution of normalized events follows the location of plasmapause contracting toward lower L value with the decrease of the Dst index, implying a strong link between detected events and the plasmapause. The cluster of normalized events moves to later afternoon sector where the peak occurrence of plasmaspheric plumes is located during geomagnetic storms. It is suggested that there is a connection between plasmaspheric plumes and detected events. Corresponding to the peak of event occurrence in 2003, solar wind dynamic pressure has a same peak. In addition, the minimum values of them are coincident. These results indicate that the increase of the solar wind dynamic pressure enhances the likelihood of EMIC wave-driven relativistic electron precipitation.

With coordinated observations of the NOAA 15 satellite and OUL magnetometer station in Finland, Wang *et al.*^[106] reported that the Electromagnetic Ion Cyclotron (EMIC) waves which were stimulated by the compression of the magnetosphere drive relativistic electron precipitation in geoquiescence on 1 Jan 2007. After an



enhancement of Solar Wind Dynamic Pressure (SWDP), a dayside Pc1 pulsation was observed by the OUL station. Such a Pc1 pulsation is caused by an EMIC wave which propagates from the generation source to lower altitudes. Simultaneously, the NOAA 15 satellite registered an enhancement of precipitating electron count rates with energies > 3 MeV within the anisotropic zone of protons. This phenomenon is coincident with the quasi-linear theoretical calculation presented in this paper. Their observations suggest that after a positive impulse of solar wind, the compression-related EMIC waves can drive relativistic electrons precipitation and play a pivotal role in the dynamic of radiation belts.

To improve their understanding of the role of Electromagnetic Ion Cyclotron (EMIC) waves in radiation belt electron dynamics, Ni *et al.*^[107] performed a comprehensive analysis of EMIC wave-induced resonant scattering of outer zone relativistic (>0.5 MeV) electrons and resultant electron loss time scales with respect to EMIC wave band, L shell, and wave normal angle model. The results demonstrate that while H^+ band EMIC waves dominate the scattering losses of about 1–4 MeV outer zone relativistic electrons, it is He^+ band and O^+ band waves that prevail over the pitch angle diffusion of ultra-relativistic electrons at higher energies. Given the wave amplitude, EMIC waves at higher L shells tend to resonantly interact with a larger population of outer zone relativistic electrons and drive their pitch angle scattering more efficiently. Obliquity of EMIC waves can reduce the efficiency of wave-induced relativistic electron pitch angle scattering. Compared to the frequently adopted parallel or quasi-parallel model, use of the latitudinally varying wave normal angle model produces the largest decrease in H^+ band EMIC wave scattering rates at pitch angles $< 40^\circ$ for electrons > 5 MeV. At a representative nominal amplitude of 1 nT, EMIC wave scattering produces the equilibrium state (*i.e.*, the lowest normal mode under which electrons at the same energy but different pitch angles decay exponentially on the same time scale) of outer belt relativistic electrons within several to tens of minutes and the following exponential decay extending to higher pitch angles on time scales from < 1 min to about 1 h. The electron loss cone can be either empty as a result of the weak diffusion or heavily/fully filled due to approaching the strong diffusion limit, while the trapped electron population at high pitch angles close to 90° remains in-

tact because of no resonant scattering. In this manner, EMIC wave scattering has the potential to deepen the anisotropic distribution of outer zone relativistic electrons by reshaping their pitch angle profiles to top-hat. Overall, H^+ -band and He^+ -band EMIC waves are most efficient in producing the pitch angle scattering loss of relativistic electrons at about 1–2 MeV. In contrast, the presence of O^+ -band EMIC waves, while at a smaller occurrence rate, can dominate the scattering loss of 5–10 MeV electrons in the entire region of the outer zone, which should be considered in future modeling of the outer zone relativistic electron dynamics.

Fifteen months of pitch angle resolved Van Allen Probes Relativistic Electron-Proton Telescope (REPT) measurements of differential electron flux were analyzed to investigate the characteristic variability of the pitch angle distribution of radiation belt ultra-relativistic (>2 MeV) electrons during storm conditions and during the long-term post storm decay. By modeling the ultra-relativistic electron pitch angle distribution as $\sin^n \alpha$, where α is the equatorial pitch angle, Ni *et al.*^[108] examined the spatio-temporal variations of the n value. The results show that, in general, n values increase with the level of geomagnetic activity. In principle, ultrarelativistic electrons respond to geomagnetic storms by becoming more peaked at 90° pitch angle with n values of 2–3 as a supportive signature of chorus acceleration outside the plasmasphere. High n values also exist inside the plasmasphere, being localized adjacent to the plasmopause and exhibiting energy dependence, which suggests a significant contribution from Electromagnetic Ion Cyclotron (EMIC) wave scattering. During quiet periods, n values generally evolve to become small, *i.e.*, 0–1. The slow and long-term decays of the ultra-relativistic electrons after geomagnetic storms, while prominent, produce energy and L -shell-dependent decay time scales in association with the solar and geomagnetic activity and wave-particle interaction processes. At lower L shells inside the plasmasphere, the decay time scales τ_d for electrons at REPT energies are generally larger, varying from tens of days to hundreds of days, which can be mainly attributed to the combined effect of hiss-induced pitch angle scattering and inward radial diffusion. As L shell increases to $L \approx 3.5$, a narrow region exists (with a width of about $0.5L$), where the observed ultra-relativistic electrons decay fastest, possibly resulting from efficient EMIC wave scattering.

As L shell continues to increase, τ_d generally becomes larger again, indicating an overall slower loss process by waves at high L shells. Their investigation based upon the $\sin^n \alpha$ function fitting and the estimate of decay time scale offers a convenient and useful means to evaluate the underlying physical processes that play a role in driving the acceleration and loss of ultra-relativistic electrons and to assess their relative contributions.

Although magnetospheric chorus plays a significant role in the acceleration and loss of radiation belt electrons, its global evolution during any specific time period cannot be directly obtained by spacecraft measurements. Using the low-altitude NOAA Polar-orbiting Operational Environmental Satellite (POES) electron data, Ni *et al.*^[109] developed a novel physics-based methodology to infer the chorus wave intensity and construct its global distribution with a time resolution of less than an hour. They described in detail how to apply the technique to satellite data by performing two representative analyses, *i.e.*, (i) for one specific time point to visualize the estimation procedure and (ii) for a particular time period to validate the method and construct an illustrative global chorus wave model. They demonstrated that the spatiotemporal evolution of chorus intensity in the equatorial magnetosphere can be reasonably estimated from electron flux measurements made by multiple low-altitude POES satellites with a broad coverage of L shell and magnetic local time. Such a data-based, dynamic model of chorus waves can provide near-real-time wave information on a global scale for any time period where POES electron data are available. A combination of the chorus wave spatiotemporal distribution acquired using this methodology and the direct space-borne wave measurements can be used to evaluate the quantitative scattering caused by resonant wave-particle interactions and thus model radiation belt electron variability.

Ionospheric modulation can artificially trigger ELF/VLF whistler waves, which can leak into the inner magnetosphere and contribute to resonant interactions with energetic electrons. Combining the ray tracing method and test particle simulations, Chang *et al.*^[110] investigated the propagation of these artificially generated ELF/VLF waves through the high ionosphere into the inner magnetosphere, and evaluate the subsequent effects of resonant scattering energetic electrons near the heart of the outer radiation belt. The results show

that the artificially triggered ELF/VLF waves become highly oblique in the magnetosphere and their spatial extent of L shell and magnetic latitude can be significantly controlled by the initial launch latitude. Corresponding to the principal first-order resonance, the energetic electrons from about 100 keV to 3 MeV can resonate with the artificial VLF waves with frequency above 10 kHz in the inner radiation belt, while in the outer radiation belt these hazardous electrons can resonate with ELF waves from about 100 Hz to 1 kHz. At $L = 4.5$ as the focus in this study, the artificial ELF waves can resonate with 1 MeV electron at the harmonics $N = -1, 1, 2$. In contrast, the Landau resonance rarely occurs for these energetic electrons. The results of test particle simulations indicate that while wave-induced changes in pitch angle and kinetic energy of a single electron are stochastic, the change averaged over all test electrons increases monotonically within the resonance timescale, which implies that resonant scattering is an overall characteristic of energetic electrons under the influence of the artificial whistler waves. Computed resonant scattering rates based on the test particle simulations indicate that artificial ELF/VLF waves with an observable in-situ wave amplitude of about 10 pT can drive efficient local pitch angle scattering of energetic electrons at the magnetic equator, thereby contributing considerably to their precipitation loss and magnetospheric electron dynamics. When the waves become highly oblique during the propagation, besides the fundamental first order resonance, higher order resonances can also drive efficient electron scattering. The results support the feasibility of generating artificially ELF/VLF whistler waves for controlled removal of energetic electrons in the Earth radiation belts.

Magnetosonic (MS) waves are linearly polarized emissions confined near the magnetic equator with wave normal angle near 90° and frequency below the lower hybrid frequency. Such waves, also termed equatorial noise, were traditionally known to be "temporally continuous" in their time-frequency spectrogram. Fu *et al.*^[111] showed for the first time that MS waves actually have discrete wave elements with rising-tone features in their spectrogram. The frequency sweep rate of MS waves, about $1 \text{ Hz}\cdot\text{s}^{-1}$, is between that of chorus and Electromagnetic Ion Cyclotron (EMIC) waves. For the two events they analyzed, MS waves occur outside the plasmapause and cannot penetrate into the plasmasphere; their power is smaller than that of chorus. They sug-



gested that the rising-tone feature of MS waves is a consequence of nonlinear wave-particle interaction, as is the case with chorus and EMIC waves.

By examining the compression-induced changes in the electron phase space density and pitch angle distribution observed by two satellites of Van Allen Probes (RBSP-A/B), Yu *et al.*^[112] found that the relativistic electrons (> 2 MeV) outside the heart of outer radiation belt ($L^* \geq 5$) undergo multiple losses during a storm sudden commencement. The relativistic electron loss mainly occurs in the field-aligned direction (pitch angle $\alpha < 30^\circ$ or $> 150^\circ$), and the flux decay of the field-aligned electrons is independent of the spatial location variations of the two satellites. However, the relativistic electrons in the pitch angle range of 30° – 150° increase (decrease) with the decreasing (increasing) geocentric distance ($|\Delta L| < 0.25$) of the RBSP-B (RBSP-A) location, and the electron fluxes in the quasi-perpendicular direction display energy-dispersive oscillations in the Pc5 period range (2–10 min). The relativistic electron loss is confirmed by the decrease of electron phase space density at high- L shell after the magnetospheric compressions, and their loss is associated with the intense plasmaspheric hiss, Electromagnetic Ion Cyclotron (EMIC) waves, relativistic electron precipitation (observed by POES/NOAA satellites at 850 km), and magnetic field fluctuations in the Pc5 band. The intense EMIC waves and whistler mode hiss jointly cause the rapidly pitch angle scattering loss of the relativistic electrons within 10 h. Moreover, the Pc5 ULF waves also lead to the slowly outward radial diffusion of the relativistic electrons in the high- L region with a negative electron phase space density gradient.

Fast mode magnetosonic waves are typically confined close to the magnetic equator and exhibit harmonic structures at multiples of the local, equatorial proton cyclotron frequency. Zhima *et al.*^[113] reported observations of magnetosonic waves well off the equator at geomagnetic latitudes from -16.5° to -17.9° and L shell of 2.7–4.6. The observed waves exhibit discrete spectral structures with multiple frequency spacings. The predominant frequency spacings are about 6 and 9 Hz, neither of which is equal to the local proton cyclotron frequency. Backward ray tracing simulations show that the feature of multiple frequency spacings is caused by propagation from two spatially narrow equatorial source regions located at L approximate to 4.2 and 3.7. The

equatorial proton cyclotron frequencies at those two locations match the two observed frequency spacings. Their analysis provides the first observations of the harmonic nature of magnetosonic waves well away from the equatorial region and suggests that the propagation from multiple equatorial sources contributes to these off-equatorial magnetosonic emissions with varying frequency spacings.

Quasi-Linear Theory (QLT) has been commonly used to study the Landau resonant interaction between radiation belt electrons and Magnetosonic (MS) waves. However, the long-parallel wavelengths of MS waves can exceed their narrow spatial confinement and cause a transit-time effect during interactions with electrons. Li *et al.*^[114] performed a careful investigation to validate the applicability of QLT to interactions between MS waves, which have a distribution in frequency and wave normal angle, and radiation belt electrons using test particle simulations. They showed agreement between these two methods for scattering rate of intense MS waves at $L = 4.5$ inside the plasmopause, but find a significant inconsistency for MS waves outside the plasmopause, due to the broad transit-time region. Consequently, they introduced a particle-independent criterion to justify the validity of QLT for MS waves: the wave spatial confinement should be longer than two parallel wavelengths.

Test particle simulation is a useful method for studying both linear and nonlinear wave-particle interactions in the magnetosphere. Recently Li *et al.*^[115] presented the detailed derivation process of the generalized resonance formulas, and suggests a check of the signs for self-consistency, which is independent of the choice of conventions, that is, the energy variation equation resulting from the momentum equations should not contain any wave magnetic components, simply because the magnetic field does not contribute to changes of particle energy. In addition, they showed that the wave centripetal force, which was considered small and was neglect in previous studies of nonlinear interactions, has a profound time derivative and can significantly enhance electron phase trapping especially in high frequency waves. This force can also bounce the low pitch angle particles out of the loss cone. They justified both the sign problem and the missing wave centripetal force by demonstrating wave-particle interaction examples, and comparing the gyro-averaged particle motion to the full particle motion under the Lorentz force.

The excitation of magnetospheric whistler-mode chorus in response to Interplanetary (IP) shocks is investigated using wave data from the Time History of Events and Macroscale Interactions during Substorms (THEMIS) spacecraft. As an example, Zhou *et al.*^[116] showed a typical chorus wave excitation following an IP shock event that was observed by THEMIS in the post-noon sector near the magnetopause on 3 August 2010. They then analyzed characteristic changes during this event and perform a survey of similar events during the period 2008–2014 using the THEMIS and OMNI data set. Their statistical analysis demonstrates that the chorus wave excitation/intensification in response to IP shocks occurs only at high L shells ($L > 8$) on the dayside. They analyzed the variations of magnetic curvature following the arrival of the IP shock and found that IP shocks lead to more homogeneous background magnetic field configurations in the near-equatorial dayside magnetosphere; and therefore, the threshold of nonlinear chorus wave growth is likely to be reduced, favoring chorus wave generation. Their results provide the observational evidence to support the concept that the geomagnetic field line configuration plays a key role in the excitation of dayside chorus.

Resonant pitch angle scattering by Electromagnetic Ion Cyclotron (EMIC) waves has been suggested to account for the rapid loss of ring current ions and radiation belt electrons. For the rising tone EMIC wave (classified as triggered EMIC emission), its frequency sweep rate strongly affects the efficiency of pitch-angle scattering. Based on the Cluster observations, He *et al.*^[117] analyzed three typical cases of rising tone EMIC waves. Two cases locate at the nightside (22.3 and 22.6 Magnetic Local Time (MLT)) equatorial region and one case locates at the duskside (18:00MLT) higher magnetic latitude ($\lambda = -9.3^\circ$) region. For the three cases, the time-dependent wave amplitude, cold electron density, and cold ion density ratio are derived from satellite data; while the ambient magnetic field, thermal proton perpendicular temperature, and the wave spectral can be directly provided by observation. These parameters are input into the nonlinear wave growth model to simulate the time-frequency evolutions of the rising tones. The simulated results show good agreements with the observations of the rising tones, providing further support for the previous finding that the rising tone EMIC wave is excited through the nonlinear wave growth process.

Ultralow frequency electromagnetic oscillations, in-

terpreted as standing hydromagnetic waves in the magnetosphere, are a major energy source that accelerates electrons to relativistic energies in the Van Allen radiation belt. Electrons can rapidly gain energy from the waves when they resonated via a process called drift resonance, which is observationally characterized by energy-dependent phase differences between electron flux and electromagnetic oscillations. Such dependence has been recently observed and interpreted as spacecraft identifications of drift resonance electron acceleration. Zhou *et al.*^[118] showed that in the initial wave cycles, the observed phase relationship differs from that characteristic of well-developed drift resonance. Their identification of such imprints provides a new understanding of how energy couples in the inner magnetosphere, and a new diagnostic for the generation and growth of magnetospheric hydromagnetic pulsations.

He *et al.*^[119] reported the multi-satellite (LANL, GOES-10 and Cluster) observation data of electron flux evolutions and chorus wave excitation in the radiation belt during the geomagnetic storm and substorm from 10 to 14 January, 2002. The seed (50–225 keV) electron flux increased 50 times in five hours during the storm main phase, and the relativistic (>0.6 MeV) electron flux increased about 60 times at night side during the recovery phase. In the meanwhile, the Cluster satellites detected intense chorus waves at MLT approximate to 3 when passing through the outer radiation belt. Using a Gaussian fit to the observed chorus spectra, they calculated the drift-averaged diffusion coefficients and then solve a 2D Fokker-Planck diffusion equation. They simulated the energetic electron flux evolutions driven by chorus waves in two cases: with and without seed electron injections. They showed that the energetic electron flux increases 79 times in three days with injection, comparable to the observation. However, the flux increases only 3 times in three days without injection, far below the observation. The current results suggest that the injected seed electrons and chorus waves play important roles in the buildup of the radiation belt electrons.

Interplanetary (IP) shocks have great impacts on Earth's magnetosphere, especially in causing global dynamic changes of energetic particles. In order to study the response of energetic electrons (50 keV–1.5MeV) at geosynchronous orbit to IP shocks, they systematically analyzed 215 IP shock events based on ACE, GOES, and LANL observations during 1998–2007. Liu and



Zong^[120] showed that after the shock arrival low-energy electron fluxes increase at geosynchronous orbit. However, in higher energy channels fluxes show smaller increases and eventually become unchanged or even decrease. The oscillations of electron fluxes following the shock arrival have also been studied in this paper. Statistical analysis revealed a frequency preference for 2.2 mHz and 3.3 mHz oscillations of energetic electron fluxes. The amplitude of these oscillations is larger under southward Interplanetary Magnetic Field (IMF) than under northward IMF. Furthermore, oscillations from high-energy and low-energy electron fluxes show different phase characteristics and power distributions. The wave power distribution of electron fluxes shows different dawn-dusk asymmetries for low-energy channels and high-energy channels. The results presented in this paper provide an energetic particle point of view of the magnetospheric response to the interplanetary shock impact.

During a substorm on 27 January 2004, energetic particle injections associated with ULF waves have been detected when Cluster fleet was traveling inbound in the Southern Hemisphere (Ren *et al.*^[121]). Substorm-injected energetic particles are strong and clearly modulated by these ULF waves. The ULF waves with the period of 1 min are probably the third harmonic mode. The periodic pitch angle dispersion signatures at 5.2–6.9 keV energy channel were detected by Cluster satellite. These thermal plasma have high coherence with the electric field of the third harmonic poloidal mode and satisfy the drift-bounce resonant condition of $N = 2$. In addition, ion outflows from the Earth's ionosphere (tens to hundreds of eV) are also observed to be modulated by these ULF waves. To the best of the authors' knowledge, Ren *et al.*^[121] is the first report to show that ULF waves can simultaneously interact with both substorm-injected “hot” particles from the magnetotail and cold outflow ions from the Earth's ionosphere.

Analysis of Cluster spacecraft data shows that intense Utralow Frequency (ULF) waves in the inner magnetosphere can be excited by the impact of interplanetary shocks and solar wind dynamic pressure variations. The observations reveal that such waves can be damped away rapidly in a few tens of minutes. Wang *et al.*^[122] examined mechanisms of ULF wave damping for two interplanetary shocks observed by Cluster on 7 November 2004 and 30 August 2001. The mechanisms considered are ionospheric joule heating, Landau damping,

and waveguide energy propagation. It is shown that Landau damping provides the dominant ULF wave damping for the shock events of interest. It is further demonstrated that damping is caused by drift-bounce resonance with ions in the energy range of a few keV. Landau damping is shown to be more effective in the plasmasphere boundary layer due to the higher proportion of Landau resonant ions that exist in that region.

6 Outer Magnetosphere

Hot flow anomalies (HFAs) frequently observed near Earth's bow shock are phenomena resulting from the interaction between interplanetary discontinuities and Earth's bow shock. Zhao *et al.*^[123] identified 199 HFA events using Cluster data from 2001 to 2010 and divide these events into four categories according to the dynamic pressure profile, namely, “- +,” “+ -,” “M,” and “W” types, where the symbols describe the profile of the dynamic pressure variations. They presented case studies to show the main characteristics of each type of HFAs. Normalized superposed epoch analyses show that variations of the magnetic field magnitude of - + and + - type HFAs are more dramatic than those of M and W types. The statistical study shows that the occurrence percentage of mature HFAs in W type HFAs is higher than that of - +, + -, and M types. Superposed epoch analysis result shows that variations of plasma parameters and magnetic field of mature HFAs are more dramatic than those of young HFAs, except for temperature. M and W type HFAs may be the later evolution stages of - + and + - type HFAs; on the other hand, four categories of HFAs may be due to the fact that the spacecraft crossed an HFA structure along different paths.

A three-dimensional adaptive Magnetohydrodynamic (MHD) model was used to investigate the energy flow from the solar wind to the magnetosphere in response to sudden turnings of the Interplanetary Magnetic Field (IMF) on 5 June 1998. During this dynamic period, the size of magnetospheric cavity and the energy input fluctuated enormously (Jing *et al.*^[124]). Due to the positive earth dipole tilt angle during the event, the distribution of energy transfer between northern and southern hemispheres of magnetopause is asymmetrical, with most energy transferred in the north hemisphere. The electromagnetic and mechanical energy inputs increase rapidly after the arrival of an interplanetary shock, while

the electromagnetic energy rises much more slowly after IMF turns from north to south. With a nearly invariable B_y component of IMF, under southward IMF the most electromagnetic energy is transferred near the plane anti-parallel to IMF clock angle, the most significant mechanical energy input occurs in the polar cusp of north hemisphere. In contrast, for northward IMF the electromagnetic energy is mostly transferred near the plane perpendicular to IMF clock angle, mechanical transferred energy occurs near equatorial plane of day-side magnetopause. Analyzing the distribution of the Poynting flux, they showed that the high-latitude reconnection causes different types of electromagnetic energy transfers into the magnetosphere during northward IMF especially with a large B_y component. It is also shown that the traditional energy transfer parameters from solar wind conditions do not include any of residual or hysteresis effects; therefore sometimes they do not reflected the right response to the solar wind variations.

The location and shape of the Earth's bow shock depend on the properties of the upstream solar wind, as well as the size and shape of the downstream magnetopause. The influence of the dipole tilt angle on the magnetopause is significant, especially at the high-latitude region, however, to date there is no bow shock model which depends on the dipole tilt angle. Using a physics-based global Magnetohydrodynamic (MHD) model, the Space Weather Modeling Framework (SWMF), Wang *et al.*^[125] investigated the effect of the dipole tilt angle on the location and shape of the bow shock, and their results show that (i) the subsolar standoff distance and the north-south asymmetry of bow shock increase with the increasing dipole tilt angle; (ii) with the dipole tilt angle positively increasing, the flaring angle of the bow shock increases in the northern hemisphere but keeps almost unchanged in the southern hemisphere, and the rotational asymmetry slightly decreases in the northern hemisphere and rapidly decreases in the southern hemisphere; and (iii) the influence of dipole tilt angle on the shape of the bow shock is north-south symmetric.

The equilibrium magnetopause location on the day-side is determined by the balance of pressure forces. Lu *et al.*^[126] used a physics-based global Magnetohydrodynamic (MHD) to examine contributions of different terms to this balance. They calculated the total pressure, as well as thermal and magnetic pressures just

inside and just outside the magnetopause. Their results show that (i) the total pressure just outside the magnetopause is enhanced with the increasing of B_z in both northward and southward Interplanetary Magnetic Field (IMF). For southward IMF the thermal pressure is dominant in the total pressure while the magnetic pressure is dominant for northward IMF when B_z is not small ($B_z > 5$ nT). For southward IMF larger solar wind dynamic pressure further enhances thermal pressure near the magnetopause while for northward IMF the dynamic pressure is more effectively converted to the magnetic pressure; (ii) the thermal pressure just outside the magnetopause is significantly enhanced with the increasing southward IMF as compared to the northward IMF case. However, this enhanced thermal pressure is not the only reason for the well-known earthward displacement of the magnetopause under southward IMF conditions. The dayside magnetic reconnection for southward IMF dramatically decreases magnetic pressure just inside the magnetopause. The combination of these two factors explains the earthward motion of the magnetopause for southward IMF.

Using the global Magnetohydrodynamic (MHD) simulation model, Wang *et al.*^[127] investigated the effects of the Interplanetary Magnetic Field (IMF) clock angle on the shape of bow shock, including its rotational asymmetry and subsolar point. For general northward IMF ($B_z > 0$), the rotational symmetry of the bow shock is broken by the effects of fast magnetosonic Mach number, and the cross-sectional line of the bow shock is an ellipse with the semi-major axis along the direction perpendicular to the IMF. The ratio or D -value between semi-major and semi-minor axis can be used to illustrate the extent of asymmetry of the bow shock. On the basis of the multiple parameters fitting, they obtained the changing relationship of both semi-axes with the clock angle and the distance away from the Earth. For general southward IMF ($B_z < 0$), the cross sectional line of the bow shock is highly asymmetrical under the multiple effects of magnetopause and fast magnetosonic Mach number. The effects of IMF clock angle on subsolar point depend mainly on the changing subsolar point of magnetopause as an obstacle. The distance of subsolar point of bow shock from the Earth increases with the increasing IMF clock angle for $B_z > 0$, and decreases with the increasing IMF clock angle for $B_z < 0$.

The numerical results from a physics-based global Magnetohydrodynamic (MHD) model were used to

examine the effect of the Interplanetary Magnetic Field (IMF), solar wind dynamic pressure, and dipole tilt angle on the size and shape of the magnetopause (Liu *et al.*^[128]). The subsolar magnetopause is identified using the plasma velocity and density, the cusps are identified using the thermal pressure, and the whole shape of the magnetopause is determined with the three-dimensional streamlines traced through the simulation domain. The magnetopause surface obtained from the simulations is fitted with a three-dimensional surface function controlled by ten configuration parameters, which provide a description of the subsolar magnetopause, the cusp geometry, the flaring angle, the azimuthal asymmetry, the north-south asymmetry, and the twisting angle of the magnetopause. Effects of the IMF, solar wind dynamic pressure, and dipole tilt angle on the configuration parameters are analyzed and fitted by relatively simple functions. It is found that the solar wind dynamic pressure mainly affects the magnetopause size; the IMF mainly controls the magnetopause flaring angle, azimuthal asymmetry, and twisting angle; and the dipole tilt angle mainly affects the magnetopause north-south asymmetry and the cusp geometry. The model is validated by comparing with available empirical models and observational results, and it is demonstrated that the new model can describe the magnetopause for typical solar wind conditions.

The Time History of Events and Macroscale Interactions during Substorms (THEMIS) observed several magnetopause crossings periodically at the duskside of magnetopause under southward Interplanetary Magnetic Field (IMF), with significant sunward returning flows inside the magnetopause (Yan *et al.*^[129]). The vortex features of the flows and the periodic enhancements in the calculated vorticity normal to the spacecraft plane could be found in the observation. The distortion of the magnetopause, the periodic features of vortex flows, the tailward propagation, and the evaluation of Kelvin-Helmholtz Instability (KHI) condition support the evidence of the Kelvin-Helmholtz vortices produced by the velocity shear at the duskside of magnetopause. Based on three-point simultaneous observations of the flow, the vorticity was calculated to be about 0.15 s^{-1} , similar to previous results. The tailward propagation of the vortices along the flank magnetopause was estimated to be about $292 \text{ km}\cdot\text{s}^{-1}$. The circular-induced electric field of several $\text{mV}\cdot\text{m}^{-1}$ was deduced perpendicular to the magnetic field when the magnetic field compression oc-

curred at the edges of the vortices.

Magnetic Decreases (MDs) are structures observed in interplanetary space with significant decreases in magnetic-field magnitude. Events with little or no change in the field direction are called Linear Magnetic Decreases (LMDs), the others are called nonlinear MDs (NMDs). Xiao *et al.*^[130] focused on LMD and NMD trains, where LMD trains are defined as at least three LMDs in a row and NMD trains as trains (\geq three MDs in a row) that are not all linear. A total of 16 273 MD trains (including 897 LMD trains and 15 376 NMD trains) were identified and studied. The details of the background magnetic-field and plasma (*e.g.* ion-density and velocity) features were examined and compared with the average solar-wind properties. LMD trains are found to occur in regions with relatively low magnetic-field strengths, high ion-number densities, and large plasma beta (β , ratio of the plasma thermal pressure to the magnetic pressure). In sharp contrast, NMD trains have plasma properties similar to the average solar wind. Forty-three LMD trains are related to Interplanetary Coronal Mass Ejections (ICMEs) (including 19 events that occurred in ICME sheaths and 24 in the ICME proper), while 222 LMD trains occurred in Corotating Interaction Regions (CIRs), and the remaining 632 events in the normal solar wind. The LMD trains that occurred in ICME sheaths are thought to be associated with the generation mechanism of the mirror-mode instability. Only 552 of the NMD trains are related to ICMEs (including 236 events in ICME sheaths and 316 in ICMEs proper), while 3889 (25%) NMD trains occurred in CIRs, and the remaining 71% occurred in the normal solar wind. Because the NMD trains have various plasma properties that differ from the LMD trains, they suggested that NMD trains may be generated by different mechanisms, for instance by a steepening of Alfvén waves.

Two-dimensional MHD simulations were performed to study the evolution of the Kelvin-Helmholtz (KH) instability at the Venusian ionopause in response to the strong flow shear in presence of the in-plane magnetic field parallel to the flow direction. The physical behavior of the KH instability as well as the triggering and occurrence conditions for highly rolled-up vortices are characterized through several physical parameters, including Alfvén Mach number on the upper side of the layer, the density ratio, and the ratio of parallel magnetic fields between two sides of the layer. Using these parameters, the simulations show that both the high

density ratio and the parallel magnetic field component across the boundary layer play a role of stabilizing the instability. In the high density ratio case, the amount of total magnetic energy in the final quasi-steady status is much more than that in the initial status, which is clearly different from the case with low density ratio. Lu *et al.*^[131] particularly investigated the nonlinear development of the case that has a high density ratio and uniform magnetic field. Before the instability saturation, a single magnetic island is formed and evolves into two quasi-steady islands in the non-linear phase. A quasi-steady pattern eventually forms and is embedded within a uniform magnetic field and a broadened boundary layer. The estimation of loss rates of ions from Venus indicates that the stabilizing effect of the parallel magnetic field component on the KH instability becomes strong in the case of high density ratio.

Based on Cluster observations, the propagation velocities and normal directions of Hot Flow Anomaly (HFA) boundaries upstream the Earth's bow shock are calculated. Twenty-one young HFAs, which have clear leading and trailing boundaries, were selected, and multi spacecraft timing method considering errors was employed for the investigation. According to the difference in the propagation velocity of the leading and trailing edges, Xiao *et al.*^[132] categorized these events into three groups, namely, contracting, expanding, and stable events. The contraction speed is a few tens of kilometers per second for the contracting HFAs, and the expansion speed is tens to more than hundred kilometers per second for expanding events. For the stable events, the leading and trailing edges propagate at almost the same speed within the error range. They further investigated what causes them to contract, expand, or stay stable by carefully calculating the thermal pressure of the young HFAs which have two distinct ion populations (solar wind beam and reflected flow). It is found that the extreme value of the sum of the magnetic and thermal pressure inside the HFAs compared with that of the nearest point outside of the leading edges is higher for expanding events and lower for contracting events, and there is no significant difference for the stable events, and the total pressure (sum of thermal, magnetic, and dynamic pressure) variation has a significant effect on the evolution for most (70%) of the HFAs, which implies that the pressure plays an important role in the evolution of young HFAs.

Using the solar wind data obtained from OMNI web,

Shen *et al.*^[133] find 1778 dynamic pressure enhancement events during Mar 2007 to Dec 2012. Then they checked the responses of Magnetospheric plasma flows to these events and find 64 responses show clear Sudden Impulse (SI) signatures from THEMIS observations. They superposed the initial responses of the flows in one plot to find two flow vortices exist at two sides of the near earth magnetotail respectively, which was not observed in-situ before. There are some ULF wave observations after initial responses.

The Interplanetary Magnetic Field (IMF) frozen in the solar wind, together with the solar EUV radiation, can significantly affect the location of Venusian bow shock. To recognize the IMF effect on the Venusian bow shock, Chai *et al.*^[134] investigated 1680 bow shock crossings recorded by Venus Express during the unusually long-lasting solar minimum (May 2006 to December 2010), of which the effect of solar EUV variation was significantly decreased. Their analysis shows that during the unusually long-lasting solar minimum, the effect of the solar EUV flux on the Venusian bow shock location is negligible. Neither solar wind dynamic pressure nor solar wind velocity has observable effect on the Venusian bow shock location. However, the IMF magnitude has a strong control of the Venusian bow shock location. They found that the size of Venusian bow shock linearly increases with the magnitude of the IMF component tangential to the bow shock surface, and this relationship can account for the perpendicular-parallel asymmetry and magnetic pole-equator asymmetry found in previous researches, as well as the magnetic dawn-dusk asymmetry discerned in this study.

It has been long known that the Venusian Bow Shock (BS) location is asymmetric from the observations of the long-lived Pioneer Venus Orbiter mission. The Venus Express (VEX) mission crossed BS near perpendicularly not only in the terminator region but also in the near-subsolar and tail regions. Taking the advantage of VEX orbit geometry, Chai *et al.*^[135] examined a large data set of BS crossings observed during the long-lasting solar minimum between solar cycles 23 and 24 and found that the Venusian BS asymmetries exhibit dependence of solar zenith angle. In the terminator and tail regions, both the magnetic pole-equator and north-south asymmetries are observed in Venusian BS location, which is similar to the Pioneer Venus Orbiter (PVO) observation near terminator. However, in the near-subsolar region, only the magnetic north-south is observed;



i.e., the BS shape is indented inward over magnetic south pole and bulged outward over magnetic north pole. The absence of the magnetic pole-equator asymmetry in the near-subsolar region suggests that the magnetic pole-equator asymmetry is mainly caused by the asymmetric wave propagation rather than the ion pickup process. The evident magnetic north-south asymmetry in solar minimum, which is not observed by PVO, suggests that even during the low long-lasting solar minimum, the ion pickup process is very important in Venusian space environment.

The Earth's dipole moment has been decaying over the past 1.5 centuries. The magnetosphere thus has been shrinking and the chance of geosynchronous magnetopause crossings has been increasing. Zhong *et al.*^[136] quantitatively evaluated the increasing exposure of geosynchronous orbit in the solar wind caused by the decay of dipole moment and the variation of solar wind condition and study the possible situation if such decay persists for several more centuries. The results show that the average subsolar magnetopause distance would move earthward by about $0.3 R_E$ per century, assuming the linear decreasing of the Earth's dipole moment at present rate. The minimum solar wind dynamic pressure required for geosynchronous magnetopause crossings will decrease by about 4 nPa (2 nPa) in the next 100 years under northward (southward) interplanetary magnetic field. Under normal solar wind conditions, the noon region of the geosynchronous orbit will be exposed to the solar wind in the next few centuries. These results suggest that the secular variations of geomagnetic field are of paramount importance for the understanding of space climate.

Mercury's magnetopause is unique in the solar system due to its relatively small size and its close proximity to the Sun. Based on 3 years of MErcury Surface, Space ENvironment, GEochemistry, and Ranging orbital Magnetometer and the Fast Imaging Plasma Spectrometer data, the mean magnetopause location was determined for a total of 5694 passes. Zhong *et al.*^[137] fitted these magnetopause locations to a three-dimensional nonaxially symmetric magnetopause which includes an indentation for the cusp region that has been successfully applied to the Earth. Their model predicts that Mercury's magnetopause is highly indented surrounding the cusp with central depth of $0.64 R_M$ and large dayside extension. The dayside polar magnetopause dimension is, thus, smaller than the equatorial magnetopause dimen-

sion. Cross sections of the dayside magnetopause in planes perpendicular to the Mercury-Sun line are prolate and elongated along the dawn-dusk direction. In contrast, the magnetopause downstream of the terminator plane is larger in the north-south than the east-west directions. Due to the northward offset of the internal dipole, the model predicts that solar wind has direct access to the surface of Mercury at middle magnetic latitudes in the southern hemisphere. During extremely high solar wind pressure conditions, the northern hemisphere middle magnetic latitudes may also be subject to direct solar wind impact.

The Mercury is experiencing significant variations of solar wind forcing along its large eccentric orbit. With 12 Mercury years of data from Mercury Surface, Space ENvironment, GEochemistry, and Ranging, Zhong *et al.*^[138] demonstrated that Mercury's distance from the Sun has a great effect on the size of the dayside magnetosphere that is much larger than the temporal variations. The mean solar wind standoff distance was found to be about 0.27 Mercury radii (R_M) closer to the Mercury at perihelion than at aphelion. At perihelion the subsolar magnetopause can be compressed below $1.2 R_M$ of about 2.5% of the time. The relationship between the average magnetopause standoff distance and heliocentric distance suggests that on average the effects of the erosion process appears to counter balance those of induction in Mercury's interior at perihelion. However, at aphelion, where solar wind pressure is lower and Alfvénic Mach number is higher, the effects of induction appear dominant.

The tearing instability with sub-Alfvénic streaming flow along the external magnetic field is investigated using resistive MHD simulation. It was found by Wu and Ma^[139] that the growth rate of the tearing mode instability is larger than that without the streaming flow. With the streaming flow, there exist two Alfvén resonance layers near the central current sheet. The larger perturbation of the magnetic field in two closer Alfvén resonance layers could lead to formation of the observed cone structure and can largely enhance the development of the tearing mode for a narrower streaming flow. For a broader streaming flow, a larger separation of Alfvén resonance layers reduces the magnetic reconnection. The linear growth rate decreases with increase of the streaming flow thickness. The growth rate of the tearing instability also depends on the plasma beta (β).

Huang *et al.*^[140] investigated the mid-latitudinal mag-

netopause locations under radial interplanetary field (RIMF) conditions. Among 262 (256) earthward (Sunward) RIMF events from years of 2001 to 2009, Cluster satellites have crossed the magnetopause 22(12) times, with 10 (7) events occurring at mid-latitudes. The observed midlatitudinal magnetopause positions are compared with two empirical magnetopause models (Shue98 model and the Boardsen00 model). The observation-model differences exhibit local time asymmetry. For earthward RIMF cases, the Shue98 model underestimates the magnetopause positions in the postnoon sector, while it overestimates the magnetopause positions in the dawn and dusk sectors. The Boardsen00 model generally underestimates the magnetopause after 06:00 MLT (Magnetic Local Time), with larger deviations in the postnoon sector as compared to those in the prenoon. For sunward RIMF cases, the selected events are mainly clustered around the dawn and dusk sectors. The comparison with the Shue98 model indicates contractions in the dawn and expansions in the dusk sector, while the comparison with Boardsen00 indicates general expansions, with larger expansions in the later local time sectors. The local time variations in the differences between observations and the Shue98 and the Boardsen00 models indicate that the real magnetopause could be asymmetrically shaped during radial IMF periods, which should be considered by magnetopause models.

Huang *et al.*^[141] presented a first statistical study of subproton- and electron-scale turbulence in the terrestrial magnetosheath using waveform data measured by the Cluster/STAFF search coil magnetometer in the frequency range [1, 180] Hz. It is found that clear spectral breaks exist near the electron scale, which separate two power-law-like frequency bands referred to as the dispersive and the electron dissipation ranges. The frequencies of the breaks f_b are shown to be well correlated with the electron gyroscale rather than with the electron inertial length. The distribution of the slopes below f_b is found to be narrow and peaks near -2.9 , while that of the slopes above f_b is found to be broader, peaking near -5.2 , with values as low as -7.5 . This is the first time that such steep power-law spectra are reported in space plasma turbulence. These observations provide new constraints on theoretical modeling of kinetic turbulence and dissipation in collisionless magnetized plasmas.

A three-dimensional adaptive Magnetohydrodynamic (MHD) model is used to study the dependences of the solar wind pressure coefficient on the upstream solar

wind parameters and the subsolar magnetopause flaring angle. The subsolar magnetopauses are determined under the different solar wind conditions, so that they could fit the flaring angles of the subsolar magnetopause. Wang *et al.*^[142] calculated the solar wind pressure coefficient by considering the thermal pressure and the magnetic pressure upstream the solar wind, as well as the dynamic pressure outside the magnetopause. By investigating the pressure conversion among the dynamic, thermal and magnetic pressure on the Sun-Earth line for the different orientations of the Interplanetary Magnetic Field (IMF), they studied the influence of the upstream solar wind parameters and the subsolar magnetopause flaring angle on the solar wind pressure coefficient, and the conclusions are as follows: (i) For the larger northward IMF ($B_z \geq 5$ nT), outside the magnetopause the magnetic pressure is dominant, while the thermal pressure is dominant for the southward IMF; (ii) The solar wind pressure coefficient is increased with the increasing IMF, and decreased with the IMF clock angle. Under the same other solar wind conditions, the solar wind pressure coefficient for the northward IMF is larger than that for the southward IMF. For the northward IMF the solar wind pressure coefficient decreases with the increasing solar wind dynamic pressure, while the solar wind pressure coefficient increases with the increasing dynamic pressure for southward IMF; the above results are the extensions of the observations; (iii) Moreover, for the first time, they found that the solar wind pressure coefficient is increased with the increasing subsolar magnetopause flaring angle.

Huiping *et al.*^[143] used a physics-based global Magnetohydrodynamic(MHD) model to investigate the location and shape of the Earth's bow shock. The bow shock locations in the simulations are identified by an automated search algorithm and are fitted by simple analytical functions. A global three dimensional bow shock model is constructed to include the effect of magnetopause and is parameterized by the fast magnetosonic Mach number, solar wind ram pressure, interplanetary magnetic field strength and magnetopause curvature radius. The model results are compared and agree well with the previous empirical and simulation models. They also found that both the shock standoff distance and the shock flaring angle decrease monotonically with increasing the fast magnetosonic Mach number. The size and location of bow shock on the equatorial plane and the meridian plane show obvious asymmetry.



A three-dimensional adaptive Magnetohydrodynamic (MHD) model was used to examine the electromagnetic energy flow from the solar wind to the magnetosphere. The magnetopause is determined by finding approximately the inner edge of the void encompassed by the solar wind stream lines, and the magnetopause is divided into nightside and dayside part by polar cusp region. Hao *et al.*^[144] found that the magnetopause energy transfer has close relations with solar wind conditions. The magnetopause area also effects energy transfer. For northward IMF, most of the electromagnetic energy flux inflow occurs near the polar cusps on magnetopause; for southward IMF the largest electromagnetic energy input into the magnetosphere occurs at the tail lobe behind the cusps. Under southward IMF conditions, more electromagnetic energy input can be identified as increasing solar wind density while it does not enhance as much for northward IMF. Their results suggest that the mechanisms proposed to electromagnetic energy transfer are mainly due to reconnection. If the electromagnetic energy coupling between the solar wind and the magnetosphere can be interpreted as a proxy for the reconnection efficiency, the efficiency during northward IMF is about 10%–30% of that for southward IMF under the solar wind conditions they considered.

7 Magnetotail

The penetration of Interplanetary Magnetic Field (IMF) B_y into the magnetosphere plays an important role in determining magnetospheric configuration and its dynamics. Using 9 years of Cluster data at the center of neutral sheet, Cao *et al.*^[145] statistically study the relations of the penetration of IMF B_y in the neutral sheet (NS) with IMF B_z and the Kp index. The correlation coefficient between NS B_y and IMF B_y is enhanced during the periods of southward IMF B_z and large Kp indexes. The penetration efficiency of IMF B_y , which is defined as the slope of the linear fit of the points in the B_y -IMF B_y space, is larger during southward IMF B_z than during northward IMF B_z . The penetration efficiency of IMF B_y also increases with increasing Kp index. Since the Kp index can be considered as an index of magnetospheric convection, this means that the penetration of IMF B_y into the magnetosphere is enhanced during the periods of strong magnetospheric convection. These results indicate that the IMF B_z and magnetospheric convection can influence the neutral sheet B_y and even magnetotail dynamics by changing the pene-

tration of IMF B_y .

On 3 August 2004, the enhancement of Ultra-Low-Frequency (ULF) waves with frequency less than the ion cyclotron frequency and the high-speed flows were observed by TC-1 at $X_{GSM} \sim -12R_E$ in the plasma sheet of the magnetotail. During the high-speed flows, the amplitude of the perpendicular component is roughly unchanged. For the parallel component, the amplitude accompanied with high peak flow is larger than that accompanied with low peak flow. After numerically analyzing the perturbed two-fluid model for drift-driven electromagnetic instability by the fully magnetized ions, Ma *et al.*^[146] found that: (i) For perpendicular propagation, the ratio of the cross-field drift to the Alfvén speed plays a role in the growth rate of the instability and the excited wave frequency. With the increase of the ratio, the growth rate increases and the excited wave frequency turns to positive from negative. (ii) For parallel propagation, the ratio of the ion thermal velocity to the Alfvén speed plays a role in the growth rate of the instability and the excited wave frequency, but the instability mode keeps unchanged. However, when the temperature is isotropic, the ratio of the cross-field ion drift to the Alfvén speed affects the growth rate and the excited wave frequency as well as the instability mode and the corresponding branches. When the plasma density, temperature, bulk velocity and magnetic field observed by TC-1 are input into the model equations, the numerical solutions show that the enhancements of the Power Spectrum Density (PSD) and the excited wave frequency are well consistent with what the theoretical model predicts for perpendicular propagation; while the enhancements of the power spectrum are consistent with what the theoretical model predicts with the former frequency less than the latter for parallel propagation. In addition to considering whether other factors such as the ion flow parallel to the magnetic field will affect the instability and the excited wave frequency, it is necessary to statistically further verify the correlation of ULF waves with the instabilities accompanied with high-speed flows.

In an attempt to study the flow bursts in the Earth's plasma sheet, Ma *et al.*^[147] selected an event that took place on August 7, 2004 in the expansion phase of a substorm, using data from the geomagnetic index, solar wind data, plasma and magnetic field observations from C1 Cluster satellite (the Cluster mission has 4 satellites) and from Double Star TC-1 satellite. In MHD approach,

TC-1 firstly observed the tailward flow, then the earthward, and finally the flow alternated in two directions. C1 firstly observed the earthward plasma flow, and then the tailward plasma flow. Before flow bursts are observed by TC-1 and C1, there are disturbances in local entropy with their tailward local entropy larger than those of the earthward. The kinetic features of the plasma flow observed by C1 are similar to those in MHD. However, kinetic characteristics of the plasma flow observed by TC-1 are far more than the description in MHD. The inadequacy mainly exists in two cases: (i) the firstly enhanced tailward flows given in MHD are found without significant increase of the energetic tailward flux; (ii) the almost stagnant flow in MHD is composed of the enhanced energetic ion flux in both earthward and tailward directions. The earthward flow burst observed by TC-1 might be multiple overshoots and rebounds. The earthward flow burst observed by C1 might be simply rebounded in the near-Earth. The pulsation observed by C1 is earlier than that observed by TC-1 with the former intensity less than that of the latter. After the energetic ion flux in the tailward direction is significantly enhanced, the power spectrum intensity of the ULF wave commences to increase obviously, which may suggest that the stream instability is closely correlated with ULF pulsations.

The motion and deceleration processes of plasma sheet high-speed flows have great significance to magnetospheric particle acceleration, magnetic field perturbation, magnetic flux transport, triggering of substorm, and the current system formation in the magnetotail. From February to April 2009, two satellites of the Time History of Events and Macroscale Interactions during Substorms mission, THA and THE, were often separated largely in Z direction, but had small X and Y separations. Such special configuration allows simultaneous observations of high-speed flows at the center and boundary of the plasma sheet (Shang *et al.*^[148]). With the hypothesis that parallel flow keeps the same speed during its earthward propagation while central plasma sheet stream uniformly or suddenly brakes on its way to the earth, they deduced the position where the deceleration begins to be between $13 R_E$ and $17 R_E$ downtail, where the near-earth reconnection is supposed to occur. In addition, their statistical results show that dipolarization fronts observed in the central plasma sheet are more prominent than those observed in the plasma sheet boundary layer ahead of the high-speed flow.

Utilizing multipoint observations by the Cluster satellites, Zhang *et al.*^[149] investigated the ion distributions of the Fast Bulk Flows (FBFs) in the plasma sheet. Simultaneous observation by C1 and C3 revealed that parallel-dominant and perpendicular-dominant components of the flows coexist and correspond to B_x dominant and B_z dominant magnetic field regions within the FBFs, respectively. In both cases, the ions distributions are characterized by a single-beam/crescent shape. In particular, no reflected ions are found within the FBFs. Statistical analysis showed that within the FBFs, the strength of the B_x component is typically less than 5 nT for B_z dominant regions and above 10 nT for B_x dominant regions. To distinguish between the parallel-dominant component of the FBFs and the field-aligned beams in the Plasma Sheet Boundary Layer (PSBL), they further statistically analyzed the tailward parallel flows (TPF) with positive B_z in the plasma sheet. The results indicated that the FBFs tend to have higher velocity, weaker B , and higher magnetic tilt angle (θ_{MTA}) than the TPFs/PSBL beams.

Utilizing C3/Cluster satellite observations from the year of 2001 to 2006, Zhang *et al.*^[150] investigated the Earthward Flow (EF) and Tailward Flow (TF) at $B_z > 0$ in the plasma sheet. They found that the EF and the TF have similar spatial distributions. Both characteristics are independent of the distance beyond $14 R_E$. Both flows are deflected while closer to the Earth. Statistical results further showed that the EF/TF occur in the central plasma sheet as well as the plasma sheet boundary layer and can be observed during quiet times and periods of geomagnetic activity. A typical event reveals that the EF and the TF have different plasma population. A Transition Region (TR) can be formed at the interface between the EF and TF. Very significant duskward components appeared in bulk velocities for both populations. It appears that the vortical-like structure can be formed near the TR. The magnetic field within the TR is twisted and strongly fluctuates. No clear magnetic flux pileups are observed inside the TR.

Zhang *et al.*^[151] statistically analyzed and compared the Earthward Flow (EF) and the Tailward Flow (TF) in the plasma sheet. It is found that the properties of the EF/TF in the Central Plasma Sheet (CPS) and the Outer Plasma Sheet (OPS) are distinctly different. The main conclusions include that (i) the EFs occur in both the CPS and the OPS while the TFs mainly occur in the OPS, (ii) both flows are dominantly convective in the



CPS and parallel in the OPS, (iii) in the CPS, the EF and the TF have similar characteristics, including their bulk velocities and ion densities and E_y components. Both flows tend to have isotropic temperatures; (iv) in the OPS, the EFs tend to have higher ion velocity, density, and E_y than the TF. The EFs tend to have anisotropic temperatures, while the TFs tend to have more isotropic temperatures. As a whole, combined characteristics of the EF and the TF are consistent with (i) reflection at the magnetic mirror point near the Earth for parallel flows in the OPS and (ii) bouncing off/back from the dipolar field closer to the Earth for convective flows in the CPS.

Pang *et al.*^[152] used the data of Cluster from 2001 to 2009 to study the polytropic processes of Central Plasma Sheet (CPS) ions. They first adopted the approach of MHD Bernoulli Integral (MBI) to identify homogeneous streamflow tubes (quasi-invariant MBI regions) and then calculate the polytropic index of ions for those streamflow tubes whose outward electromagnetic energy ratios < 0.05 . The central plasma sheet is actually a complicated system, which comprises many streamflow tubes with different polytropic relations and the transition layers in between. The polytropic indexes of the CPS ions range from 0.1 to 1.8 and have a quasi-Gaussian distribution. The median polytropic index is 0.93 for $AE < 200$ nT and 0.91 for $AE \geq 200$ nT. Thus, there is no obvious difference between the polytropic indexes of the quiet time and the substorm time CPS ions, which suggests that the thinning and thickening processes of plasma sheet during substorm times do not change obviously the polytropic relation of the CPS ions. The statistical analysis using different (< 0.05 , 0.025, and 0.01) shows that the outward emission of electromagnetic energy is an effective cooling mechanism and can make the polytropic index to decrease and shift toward isobaric. It is inferred that the CPS ions as a whole much likely behave in a way between isobaric and isothermal.

Pang *et al.*^[153] studies the effective polytropic index in the Central Plasma Sheet (CPS) by using the method of Kartalev *et al.* (2006), which adopts the denoising technique of Haar wavelet to identify the homogeneous MHD Bernoulli Integral (MBI) and has been frequently used to study the polytropic relation in the solar wind. They chose the quiet CPS crossing by Cluster C1 during the interval of 08:51:00 UT–09:19:00 UT on 03

August 2001. In the central plasma sheet, thermal pressure energy per unit mass is the most important part in MBI, and kinetic energy of fluid motion and electromagnetic energy per unit mass are less important. In the MBI, there are many peaks, which correspond to isothermal or near isothermal processes. Their result indicates that the CPS is not uniform even during quiet time and the blanket applications of polytropic law to plasma sheet may return misleading value of polytropic index. The polytropic indexes in homogeneous regions with a high correlation coefficient basically have good regression significance and are thus credible. These results are very important to understand the energy transport in magnetotail in the MHD frame.

Wang *et al.*^[154] used the global Magnetohydrodynamic (MHD) simulation to investigate effects of the Interplanetary Magnetic Field (IMF) on the twisting of the magnetotail. It is shown that the cross section of the magnetotail is elongated along a certain direction close to the IMF orientation. The elongated direction twists with the IMF orientation, magnitude, and the distance away from Earth, and the quantitative relationship has been given. In addition, the current sheet has a similar twisting behavior as the magnetotail magnetopause, with a smaller twisting angle. Their simulated results fall within the range that people have deduced from observations.

A statistical survey of 560 fast flows in midnight central plasma sheet is performed by Li *et al.*^[155] based on Time History of Events and Macroscale Interactions during Substorms (THEMIS) observations during its first two tail phases. From superposed epoch analysis, no significant substorm activities are found to be associated with the occurrence of fast flows beyond $X = -15 R_E$. Considering the associations with substorm activities, the fast flows inside of $X = -15 R_E$ can be classified into two obvious classes: short duration (< 2.0 min) and long duration (> 4.0 min). Substorm breakups are shown to be more closely correlated to short-duration fast flows. Furthermore, the onset of short-duration fast flows in the dipolarization region ($X = -9$ to $-11 R_E$) is almost simultaneous with the onset of substorm breakups and dipolarizations. On the other hand, time delays of 2–4 min are both found in the near-Earth region ($X = -7$ to $-9 R_E$) and in the near-tail region ($X = -11$ to $-15 R_E$). Assuming that short-duration fast flows are generated by the force imbalance caused by cross-tail current

disruption, these features are consistent with the predictions made by the cowlings electrojet current loop and the cross-tail current disruption substorm models. In comparison, although more magnetic flux is transported toward Earth for long-duration fast flows, no clear substorm breakup is closely associated with them. The analysis of 2D ion velocity distribution further shows some differences. For short-duration fast flows, multiple crescent-shaped ion populations are found. However, for long-duration fast flows, there exists only a single crescent-shaped ion population. The difference may be an important signature for distinguishing these two classes of fast flows.

Unambiguous knowledge of magnetic field structure and the electric current distribution is critical for understanding the origin, evolution, and related dynamic properties of Magnetic Flux Ropes (MFRs). A survey of 13 MFRs in the Earth's magnetotail was conducted by Yang *et al.*^[156] by means of Cluster multipoint analysis. It is shown that the selected flux ropes with the bipolar signature of the south-north magnetic field component generally lie near the equatorial plane, as expected, and that the magnetic field gradient is rather weak near the axis center, where the curvature radius is large. It is found that the stronger the current density, the smaller the angles between the magnetic field and current in MFRs. The direct observations show that only quasi force-free structure is observed, and it tends to appear in the low plasma beta regime (in agreement with the theoretic results). The quasi force-free region is generally found to be embedded in the central portion of the MFRs, where the current is approximately field aligned and proportional to the strength of core field. It is shown that about 60% of surveyed MFRs can be globally approximated as force free. The force-free factor is found to be non-constantly varied through the quasi force-free MFR, suggesting that the force-free structure is nonlinear.

Observations by the Cluster spacecraft on 3 August 2004 are presented as an example of flapping motions of the magnetotail current sheet excited by nonadiabatic ions. It is found that the current sheet up-down motions are exactly corresponding to alternating hemispherical asymmetries of the bouncing ion population. Wei *et al.*^[157] showed that those hemisphere-asymmetric non-adiabatic ion populations are present in the magnetic field configuration with an effective finite guiding component due to the local current sheet inclination. These results demonstrate that the current sheet flapping mo-

tion is a self-organized circulation process between the alternating hemispherical asymmetries of the nonadiabatic ion population inside the plasma sheet and the current sheet equilibrium itself.

The magnetotail current sheet frequently moves in the north-south direction, which named current sheet flapping. A statistical survey of Geotail data showed that the flapping motions of the current sheet might be related to the plasma bursty bulk flows BBFs. Current sheet flapping association with fast plasma flows in the plasma sheet and Pi2 pulsation was also observed by THEMIS observations. These observations also pointed out the close relationship between current sheet flapping and the Z component of the ion flow velocity. During the repeated crossings of the current sheet by the spacecraft, the ion velocity V_z showed obviously periodic oscillations. A single observation case is discussed by Wei and Cai^[158] to reveal that the associated observation BBFs may be the local ions flow. The Cluster FGM, CIS, PEACE and RAPID data will be used to analyze the current sheet flapping case. The CL soft will be used to calculate the current. In the magnetotail, on Oct 26, 2002 the Cluster crosses southward the central current sheet in a distance of $19 R_E$ to Earth. The current sheet flapping case associated by high speed ions flow was observed by Cluster on Oct 26, 2002. This flapping case periodic is very good. The FFT analyses show the period of the current sheet flapping is about 2 min, the amplitude is about 20 nT. The velocity values changed periodically. The x component of ions velocity reaches $400 \text{ km}\cdot\text{s}^{-1}$. The z component of ion velocity is up to $600 \text{ km}\cdot\text{s}^{-1}$. The energy range from 50–100 keV electrons and 10 keV ions flux is enhanced during the spacecrafts across current sheet center. When the spacecrafts move to the current sheet boundary, the energy of ions and electrons flux is decreasing. The current density is also flapping periodically. The velocity vector distribution show the particles motion is not a single direction. Base on the velocity and current vector analyses, the local particles motion is vortex motion. This current sheet flapping is highly cyclical event and lasts for about 10 minutes. This result show the current sheet flapping may be induced by a self-circulation process not the BBF compressed the magnetosphere.

Flux ropes in the Earth's magnetotail are widely believed to play a crucial role in energy transport during substorms and the generation of energetic particles. Previous kinetic simulations are limited to the lo-

cal-scale regime, and thus cannot be used to study the structure associated with the geomagnetic field and the global-scale evolution of the flux ropes. The evolution of flux ropes in the magnetotail under a steady southward interplanetary magnetic field were studied with a newly developed three-dimensional global hybrid simulation model for dynamics ranging from the ion Larmor radius to the global convection time scales by Lu *et al.*^[159]. Magnetic reconnection with multiple X-lines is found to take place in the near-tail current sheet at geocentric solar magnetospheric distances from $x = -30R_E$ to $-15 R_E$ around the equatorial plane ($z = 0$). The magnetotail reconnection layer is turbulent, with a nonuniform structure and unsteady evolution, and exhibits properties of typical collisionless fast reconnection with the Hall effect. A number of small-scale flux ropes are generated through the multiple X-line reconnection. The diameter of the flux ropes is several R_E , and the spatial scale of the flux ropes in the dawn-dusk direction is on the order of several R_E and does not extend across the entire section of the magnetotail, contrary to previous models and MHD simulation results and showing the importance of the three-dimensional effects. The non-uniform and unsteady multiple X-line reconnection with particle kinetic effects leads to various kinds of flux rope evolution.

Hao *et al.*^[160] presented in situ observations of a shock-induced substorm-like event on 13 April 2013 observed by the newly launched Van Allen twin probes. Substorm-like electron injections with energy of 30–500 keV were observed in the region from $L \sim 5.2$ to 5.5 immediately after the shock arrival (followed by energetic electron drift echoes). Meanwhile, the electron flux was clearly and strongly varying on the ULF wave time scale. It is found that both toroidal and poloidal mode ULF waves with a period of 150 s emerged following the magnetotail magnetic field reconfiguration after the Interplanetary (IP) shock passage. The poloidal mode is more intense than the toroidal mode. The 90° phase shift between the poloidal mode B_r and E_a suggests the standing poloidal waves in the Northern Hemisphere. Furthermore, the energetic electron flux modulations indicate that the azimuthal wave number is ~ 14 . Direct evidence of drift resonance between the injected electrons and the excited poloidal ULF wave has been obtained. The resonant energy is estimated to be between 150 keV and 230 keV. Two possible scenarios on ULF wave triggering are discussed: vortex-like flow structure-

driven field line resonance and ULF wave growth through drift resonance. It is found that the IP shock may trigger intense ULF wave and energetic electron behavior at $L \sim 3$ to 6 on the nightside, while the time profile of the wave is different from dayside cases.

In space plasmas, charged particles are frequently observed to possess a high-energy tail, which is often modeled by a kappa-type distribution function. The formation of the electron kappa distribution in generation of parallel propagating whistler waves is investigated by Tao and Lu^[161] using fully nonlinear Particle-In-Cell (PIC) simulations. They demonstrated that for interactions between electrons and parallel propagating whistler waves, a non-Maxwellian high-energy tail can be formed, and a kappa distribution can be used to fit the electron distribution in time-asymptotic limit. The κ -parameter is found to decrease with increasing initial temperature anisotropy or decreasing ratio of electron plasma frequency to cyclotron frequency. The results might be helpful to understanding the origin of electron kappa distributions observed in space plasmas.

Until now it is still questionable whether ions are accelerated to energies above 100 keV in the near-Earth Current Sheet (CS), in the vicinity of a possible near-Earth neutral line. By using 11 years of 3D energetic ion flux data for protons, helium, and oxygen (~ 150 keV–1 MeV) from the RAPID instrument on board Cluster 4, Luo *et al.*^[162] statistically studied the energetic ion acceleration by investigating ion anisotropies in the near-Earth magnetotail ($-20 R_E < X < -16 R_E$). It is found that the earthward (tailward) anisotropy of the energetic (>150 keV) ions (protons, He^+ , and O^+) tend to become higher as the earthward (tailward) plasma bulk flows (measured by Cluster Ion Spectrometry experiment) become stronger. During such periods the presence of a strong acceleration source tailward (earthward) of Cluster spacecraft (S/C) is confirmed by the hardening energy spectra of the earthward (tailward) energetic ion flows. A good statistical correlation between tailward bulk flow, negative B_z , and the tailward anisotropy of energetic ions indicates that the strong ion acceleration might be related to a near-Earth reconnection, which occurred earthward of the Cluster S/C. The energetic ion anisotropies do not show a clear dependence on the AE index, which may indicate that the acceleration source (s) for the energetic ions could be spatially localized.

The penetration of the plasma sheet into the inner magnetosphere is important to both ring current forma-

tion and spacecraft charging at geosynchronous orbit. Using hot ion data recorded by HIA of TC-1/DSP, establishes an empirical model of the Inner Boundary of Ion Plasma Sheet (IBIPS) on the near equatorial plane. All IBIPS are located inside geocentric radial distance of $9 R_E$. Cao *et al.*^[163] divided Local Times (LT) into eight local time bins and found that during quiet times ($Kp \leq 2$), the IBIPS is closest to the Earth on the pre-midnight side (LT = 19:30–21:30) and farthest on the dawn side (LT = 04:30–07:30), which differs from previous spiral models. The geocentric radius of IBIPS in each local time bin can be described by a linear fitting function: $R_{ps} = A + B \cdot Kp$. The changing rates of the radius of IBIPS relative to Kp index on the midnight side (LT = 22:30–01:30) and post-night side (LT = 01:30–04:30) are the two largest (0.66 and 0.67), indicating that the IBIPS on the night side (LT = 22:30–04:30) moves fastest when Kp changes. Since the IBIPSs in different local times bins have different changing rates, both the size and shape of IBIPS change when Kp varies. The correlation coefficients between the radius of IBIPS and the instantaneous Kp increase with the increase of ΔT (the time difference between IBIPS crossing time and preceding Kp interval), which suggests that with the increase of ΔT , the radius of IBIPS is more and more controlled by instantaneous Kp , and the influence of preceding Kp becomes weaker. The response time of IBIPS to Kp is between 80 and 95 min. When $\Delta T > 95$ min, the correlation coefficient basically keeps unchanged and only has a weak increase, suggesting that the IBIPS is mainly determined by the convection electric field represented by instantaneous Kp .

Duan *et al.*^[164] studied Energetic Electron Bursts (EEBs) (40–250 keV) in the Plasma Sheet (PS) and their relation to Bursty Bulk Flows (BBFs) using the data recorded by Cluster from 2001 to 2009. The EEBs in the PS can be classified into four types. Three types of EEBs are dispersionless, including EEBs accompanied with BBFs ($V > 250 \text{ km} \cdot \text{s}^{-1}$) but without Dipolarization Front (DF); EEBs accompanied with both Dipolarization Front (DF) and BBF; and EEBs accompanied with DF and fast flow with $V < 250 \text{ km} \cdot \text{s}^{-1}$. One type of EEB, *i.e.*, EEBs not accompanied with BBFs and DFs, is dispersed. The energetic electrons (40–130 keV) can be easily transported earthward by BBFs due to the strong dawn-dusk electric field embedded in BBFs. The DFs in BBFs can produce energetic electrons (40 to

250 keV). For the EEBs with DF and BBFs, the superposed epoch analyses show that the increase of energetic electron flux has two phases: gradual increase phase before DF and rapid increase phase concurrent with DF. In the PS around $x = -18 R_E$, 60%–70% of EEBs are accompanied with BBFs, indicating that although hitherto there have been various acceleration mechanisms of energetic electrons, most of the energetic electrons in the PS are related with magnetic reconnection. The corresponding ratio between EEBs and BBFs shows a dawn-dusk asymmetry.

Using in situ observations from THEMIS A, D and E during the 2008–2011 tail season, Yao *et al.*^[165] presented a statistical study of the evolution of pressure gradients in the near-Earth tail during Bursty Bulk Flow (BBF) convection. They identified 138 substorm BBFs and 2197 non-substorm BBFs for this study. They found that both the pressure and the B_z component of the magnetic field were enhanced at the arrival of BBFs at the spacecraft locations. They suggested that the increase of B_z during non-substorm BBFs is associated with flux pile-up. However, the much stronger enhancement of B_z during substorm BBFs implies the occurrence of magnetic field dipolarization which is caused by both the flux pile-up process and near-Earth current disruption. Furthermore, a bow-wave-like high pressure appears to be formed at the arrival of substorm BBFs, which is responsible for the formation of region-1-sense FACs. The azimuthal pressure gradient associated with the arrival of substorm BBFs lasts for about 5 min. The enhanced pressure gradient associated with the bow wave is caused by the braking and diversion of the Earthward flow in the inner plasma sheet. The results from this statistical study suggest that the braking and azimuthal diversion of BBFs may commonly create azimuthal pressure gradients, which are related to the formation of the FAC of the substorm current wedge.

Effects of a fast flow in the tail plasma sheet on the generation of Kinetic Alfvén Waves (KAWs) in the high-latitude of the near-Earth magnetotail were investigated by Guo *et al.*^[166]. Firstly, the plasma sheet becomes thinned and the dipolarization of magnetic field appears around $(x, z) = (-10.5R_E, 0.3R_E)$, where R_E is the radius of the Earth. Then, shear Alfvén waves are excited in the plasma sheet, and the strong earthward flow is braked by the dipole-like magnetic field. These

waves propagate along the magnetic field lines toward the polar regions later. Subsequently, KAWs with $k_{\perp} \gg k_{\parallel}$ are generated in the high-latitude magnetotail due to the existence of the non-uniformity of the magnetic field and density in the polar regions. Their simulation provides a mechanism for the generation of the observed low-frequency shear Alfvén waves in the plasma sheet and kinetic Alfvén waves in the high-latitude near-Earth magnetotail, whose source is suggested to be the flow braking in the low-latitude plasma sheet.

Li *et al.*^[167] reported the observation of mirror mode structures by Cluster spacecraft at around $X \sim -16 R_E$ in the Earth's magnetotail. The wavelength of the mirror structure is larger than 7000 km, corresponding to tens of ion gyroradii. Features of the mirror structures are similar to those detected in the magnetosheath: the anti-correlation between the magnetic field strength and plasma density, zero phase velocity in the plasma rest frame and linear polarization. The structures were observed in a region bounded by two dipolarizations during a substorm intensification. Thus, the dipolarization process may provide a plasma condition facilitating the growth of the mirror mode structures. Another interesting feature is the electron dynamics within the mirror structures. Thermal electron energy flux has an enhancement at 0° and 180° pitch angles inside the magnetic dips of the first three mirror structures and an enhancement at 90° pitch angle inside the magnetic dip of the last structure. The different electron distribution inside the mirror structures might be a result of different evolution stages of the mirror wave. The last structure may be in the nonlinear stage of the mirror instability, whereas the three others with quasi-sinusoidal waveforms may be in the linear stage. In addition, they found that intense whistler waves were confined within the magnetic dips. They conjectured that whistler waves observed in the first three dips were generated in a remote region, then trapped in the mirror mode troughs and transported toward the spacecraft; while the whistler wave detected in the last dip was excited locally by the electron anisotropy instability.

The current system associated with the boundary of plasma bubbles in the Earth's magnetotail has been studied by employing Cluster multipoint observations. Sun *et al.*^[168] investigated the currents in both the Dipolarization Front (DF, leading edge of the plasma bubble) and the trailing edge of the plasma bubble. The distribution of currents at the edge indicates that there is a cur-

rent circuit in the boundary of a plasma bubble. The field-aligned currents in the trailing edge of the plasma bubble are flowing toward the ionosphere (downward) on the dawnside and away from the ionosphere (upward) on the duskside, in the same sense as region-1 current. Together with previous studies of the current distributions in the DF and magnetic dip region, they obtained a more complete picture of the current system surrounding the boundary of plasma bubble. This current system is very similar to the substorm current wedge predicted by MHD simulation models but with much smaller scale.

A flapping wave was observed by THEMIS-B (P1) and THEMIS-C (P2) probes on the dawn side of the magnetotail, while the solar wind was generally stable. The magnetic activity was quite weak, suggesting that this flapping wave was generated by an internal instability, which normally occurs during magnetic quiet times. Sun *et al.*^[169] showed that the flapping wave was propagating downward with a tail-aligned scale of at least $3.7 R_E$ and did not show much change in shape during its propagation from P1 to P2. Correlation analysis employed to estimate the time lag between the corresponding half waveforms of P1 and P2 shows that the propagating velocities along the current sheet normal directions were close to each other in the beginning, but increased linearly later on. The average wavelength of the flapping wave is approximately $4 R_E$. Theoretical analysis suggests that the ballooning type wave model may not be the mechanism for the observed flapping wave, but that the magnetic double-gradient instability model is a more plausible candidate.

A new approach of Electron Magnetohydrodynamics (EMHD) was developed by including the anisotropy of the electron pressure tensor to take Biermann battery effect into account. Based on the model, the dispersion relation of slow and fast electron magnetosonic modes were derived (Ji *et al.*^[170]). A Korteweg-de Vries equation was then obtained from the wave equation to get a solution of one-dimensional slow-mode soliton. Furthermore, according to measurements of Cluster and Time History of Events and Macroscale Interactions during Substorms, they found a good agreement between the theory and observations of magnetic field depression and perpendicular pressure increase.

8 Plasmasphere

The Moon-based Extreme Ultraviolet Camera (EUVC)

aboard China's Chang'E-3 (CE-3) mission has successfully imaged the entire Earth's plasmasphere for the first time from the side views on lunar surface (He *et al.*^[171]). An EUVC image on 21 April 2014 is used in this study to demonstrate the characteristics and configurations of the Moon-based EUV imaging and to illustrate the determination algorithm of the plasmopause locations on the magnetic equator. The plasmopause locations determined from all the available EUVC images with the Minimum L Algorithm are quantitatively compared with those extracted from in situ observations (Defense Meteorological Satellite Program, Time History of Events and Macroscale Interactions during Substorms, and Radiation Belt Storm Probes). Excellent agreement between the determined plasmapauses seen by EUVC and the extracted ones from other satellites indicates the reliability of the Moon-based EUVC images as well as the determination algorithm. This preliminary study provides an important basis for future investigation of the dynamics of the plasmasphere with the Moon-based EUVC imaging.

Liu *et al.*^[172] presented a dynamic plasmopause location model established based on 5 years of Time History of Events and Macroscale Interactions during Substorms (THEMIS) measurements from 2009 to 2013. In total, 5878 plasmopause crossing events are identified, sufficiently covering all 24 Magnetic Local Time (MLT) sectors. Based on this plasmopause crossing database, they investigated the correlations between plasmopause locations with solar wind parameters and geomagnetic indices. Input parameters for the best fits are obtained for different MLT sectors, and finally, they chose five input parameters to build a plasmopause location model, including 5 min-averaged SYM- H , AL , and AU indices as well as hourly-averaged AE and Kp indices. Two out-of-sample comparisons on the evolution of the plasmopause is shown during two magnetic storms, demonstrating good agreement between model results and observations. Two major advantages are achieved by this model. First, this model provides plasmopause locations at 24:00 MLT sectors, still providing good consistency with observations. Second, this model is able to reproduce dynamic variations of the plasmopause on time-scales as short as 5 min.

Lin *et al.*^[173] searched the plasma and magnetic field data of the Time History of Events and Macroscale Interactions during Substorms (THEMIS) probes B and C during 2008 and 2009 for observation evidences of the

Kelvin-Helmholtz Instability (KHI). Fourteen KHI events with rolled-up vortices are identified under the northward Interplanetary Magnetic Field (IMF) at the Low-Latitude Boundary Layer (LLBL). They collected another 42 events reported from the observations of the Geotail, Double Star TC-1, and Cluster for a statistical study of the KH wave properties. All the 56 rolled-up KH wave events are quantitatively characterized by the dominant period, phase velocity, and the wavelength. They further explored the relationship between the KH wave period and the solar wind velocity (V_{SW}) and the IMF clock angle. It is found that the KH period tends to be shorter under a higher V_{SW} , and longer with a larger IMF clock angle. The spatial distribution of the KH wavelength shows a longitudinal growth with increasing distance from the subsolar point along the flank magnetopause. The statistical results provide new insights for the development of KH waves and their connection with the interplanetary conditions and deepen our understanding of the KHI at the magnetopause.

The magnetospheric particle drift theory in (U, B) coordinates provides a convenient tool for analyzing particle drift trajectories from plasma sheet to the inner magnetosphere. However, in this drift theory, the Alfvén layer for a realistic asymmetric magnetic field model cannot be obtained due to numerical difficulty. Zhang *et al.*^[174] developed a new technique to calculate electron Alfvén layer for Volland-Stern electrical potential model and dipole+T89 geomagnetic field model. The results show that for realistic asymmetric field models, the dawn and dusk separators are not in the dawn-dusk meridian but asymmetric and tilt toward the dayside. The stagnant point of the electron Alfvén layer is always located in the duskside separator. Compared with the electron Alfvén layers calculated from Volland-Stern electric field model and dipole magnetic field model, the new electron Alfvén layer becomes closer to the Earth and meanwhile rotates clockwise. This rotation makes the point closest to the Earth in the Alfvén layer shift from dawnside to nightside. The newly calculated geosynchronous Alfvén layer crossings cannot only explain the observed geosynchronous access of plasma sheet thermal (0.913 and 2.783 keV) electrons as previous studies did but also the geosynchronous access of plasma sheet energetic (10.472 and 31.039 keV) electrons. This new technique can be used to calculate Alfvén layer for any asymmetric field models and may become an important compliment to the classical mag-



netospheric particle drift theory in the (U, B) coordinates.

A new empirical model of plasmopause location as functions of magnetic local time and geomagnetic indices has been developed based on the observations from THEMIS mission. Liu and Liu^[175] used the two-year data of electron density inferred from spacecraft potential to identify the plasmopause crossings and create a database of plasmopause locations. The database is further used to build up an empirical model of plasmopause related to magnetic local time based on the equation from O'Brien and Moldwin (2003). The new model is compared with previous plasmopause location models. It is found that their newly developed model is the best in predicting plasmopause locations among the existing models. The models based on Kp and Dst indices are better than the model based on AE index, suggesting that the plasmopause location is controlled by large scale convection of the magnetosphere.

Yuan *et al.*^[176] reported in situ observations by the Cluster spacecraft of plasmaspheric electron heating in the plasmaspheric plume. Electron heating events were accompanied by enhancements of Electromagnetic Ion Cyclotron (EMIC) waves in the increased density ducts on the negative density gradient side for two substructures of the plasmaspheric plume. Electron heating is much stronger for the pitch angle of 0° and 180° than for the pitch angle of 90° . Theoretical calculations of the Landau resonant interaction between electrons and observed EMIC waves demonstrate that Landau damping of oblique EMIC waves is a reasonable candidate to heat cold electrons in the presence of O^+ ions in the outer boundary of the plasmaspheric plume. Therefore, this observation is considered in situ evidence of plasmaspheric electron heating through Landau damping of EMIC waves in plasmaspheric plumes.

Modulated High-Frequency (HF) heating of the ionosphere provides a feasible means of artificially generating Extremely Low-Frequency (ELF)/Very Low-Frequency (VLF) whistler waves, which can leak into the inner magnetosphere and contribute to resonant interactions with high energy electrons in the plasmasphere. By ray tracing the magnetospheric propagation of ELF/ VLF emissions artificially generated at low-invariant latitudes, Chang *et al.*^[177] evaluated the relativistic electron resonant energies along the ray paths and show that propagating artificial ELF/VLF waves can resonate with electrons from about 100 keV to

about 10 MeV. They further implemented test particle simulations to investigate the effects of resonant scattering of energetic electrons due to triggered monotonic/single-frequency ELF/ VLF waves. The results indicate that within the period of a resonance timescale, changes in electron pitch angle and kinetic energy are stochastic, and the overall effect is cumulative, that is, the changes averaged over all test electrons increase monotonically with time. The localized rates of wave-induced pitch-angle scattering and momentum diffusion in the plasmasphere are analyzed in detail for artificially generated ELF/VLF whistlers with an observable in-situ amplitude of about 10 pT. Their investigation further supports the feasibility of artificial triggering of ELF/ VLF whistler waves for removal of high-energy electrons at lower L shells within the plasmasphere. Moreover, their test particle simulation results show quantitatively good agreement with quasi-linear diffusion coefficients, confirming the applicability of both methods to evaluate the resonant diffusion effect of artificial generated ELF/VLF whistlers.

9 Geomagnetic Field, Auroras and Currents

Dunlop *et al.*^[178] showed for the first time, with direct, multi-spacecraft calculations of electric current density, and other methods, matched signatures of Field-Aligned Currents (FACs) sampled simultaneously near the ionosphere at low (about 500 km altitude) orbit and in the magnetosphere at medium (about $2.5 R_E$ altitude) orbits using a particular Swarm and Cluster conjunction. The Cluster signatures are interpreted and ordered through joint mapping of the ground/magnetospheric footprints and estimation of the auroral zone boundaries (taken as indication of the boundaries of Region 1 and Region 2 currents). They found clear evidence of both small-scale and large-scale FACs and clear matching of the behavior and structure of the large-scale currents at both Cluster and Swarm. The methodology is made possible through the joint operations of Cluster and Swarm, which contain, in the first several months of Swarm operations, a number of close three-spacecraft configurations.

Based on the auroral electron/ion precipitation boundary database observed by the DMSP satellites during 1984–2009, Niu *et al.*^[179] statistically investigated the characteristics of the nightside equatorial

boundaries of the electron precipitation (B1E) and the ion precipitation (B1I) in the Northern/Southern Hemispheres (NH/SH). Most of the boundaries are located between magnetic latitude (MLAT) of 60° – 70° with the mean MLAT for B1E/B1I to be 64.30° N/ 63.22° N and 64.48° S/ 63.26° S in the NH and SH, respectively, indicating that B1E and B1I in both hemispheres are located in conjugated magnetic field lines with B1E $\sim 1.2^{\circ}$ poleward of B1I; that the MLAT of B1E and B1I in both hemispheres shift to lower MLAT (from $\sim 70^{\circ}$ to $\sim 55^{\circ}$) as geomagnetic activity increases; that MLAT of both B1E and B1I and their differences slowly decrease from dusk to midnight with some difference in both hemispheres during different levels of geomagnetic activities; that B1E and B1I in both hemisphere decrease linearly with Kp and exponentially with Dst , AE , and $SYM-H$, respectively, demonstrating that auroral particle precipitation is closely related with geomagnetic activity; that in different Magnetic Local Time (MLT) sectors, the changing rates of the boundaries with Kp are different, and the rates of B1E are generally larger than that of B1I, implying that the difference between B1E and B1I reduce with increasing geomagnetic activity. Compared with previous studies, the statistical results based on the long-term large database in this paper can well reflect the properties of the equatorial boundaries of auroral precipitation and may be used for physical modeling or space weather forecasting in future.

A large database of more than 18000 subauroral ion drift (SAID) events from DMSP observations from 1987 to 2012 was used by Zhang *et al.*^[180] to systematically investigate the features of SAID. SAID occurs mostly at $\sim 62^{\circ}$ – 60° magnetic latitude (MLAT) and $\sim 22:15/22:45$ magnetic local time (MLT) for geomagnetically quiet conditions and at $\sim 58^{\circ}$ – 56° MLAT and $\sim 22:15/22:45$ MLT for geomagnetically disturbed conditions in the North Hemisphere (NH)/South Hemisphere (SH), respectively. Significant north-south asymmetries in SAID occurrence, shape, and geomagnetic activity variations are found in this statistical study. The latitudinal width of a SAID is larger in the NH than in the SH. An interesting finding of this work is that the SAID occurrence probability peaks have an $\sim 180^{\circ}$ difference in longitude between the two hemispheres in the geographic coordinates for both geomagnetically quiet and disturbed conditions. The SAID width peaks in almost the same geomagnetic meridian zone with a geomagnetic longitude of $\sim 80^{\circ}$ – 120° in both hemispheres.

Significant hemispheric asymmetries and spike signatures with sharp dips are found in all the latitudinal profiles of the horizontal velocities of SAIDs. The SAID is highly correlated to geomagnetic activity, indicating that the location and evolution of the SAID might be influenced by global geomagnetic activity, auroral dynamics, and the dynamics of ring currents.

The solar cycle, seasonal, and diurnal variations of the subauroral ion drifts (SAIDs) were investigated for the first time to use such a large database of 18226 SAID events observed by the DMSP satellites during 1987–2012 (He *et al.*^[181]). Statistical results show that SAIDs occur mostly at 60.1° invariant latitude and 2230 magnetic local time with a typical half width of 0.57° , move equatorward during high solar activities with large widths, and have two occurrence peaks in spring and fall equinoxes and two valleys in summer and winter solstices. The seasonal variation of SAID latitude has two valleys in spring and fall, and SAID width has a valley distribution with a minimum in summer. SAIDs exhibit a clear day-to-night difference in latitude. The diurnal variation of SAID width has a morning valley and an afternoon peak. The generation mechanism of SAID associated with the electron precipitation and the downward field-aligned current is also supported in this study.

To test the current-generation model of subauroral polarization stream (SAPS), Wang *et al.*^[182] investigated the relative positions of Field-Aligned Currents (FACs) with respect to SAPS in a statistical way by using CHAMP (CHALLENGING Minisatellite Payload) and DMSP (Defense Meteorological Satellite Program) satellite observations as well as model simulations. Comparative studies have been performed for consecutive CHAMP observations in different Magnetic Local Time (MLT) sectors with respect to SAPS. The latitude of the peak westward zonal wind deduced from CHAMP measurements has been used to represent the location of the SAPS peak. Both the density and the sheet current strength of R2 (region 2) FACs are enhanced when SAPS occur. Subsequently R2 FACs decay in intensity and correspondingly the centers retreat poleward. The latitudes of the center of the R2 FAC, small-and medium-scale FACs, and SAPS shift equatorward with increasing MLT. The SAPS peaks are located between R2 and R1 (region 1) FAC peaks in all MLT bins under study. The SAPS peaks are closer to R2 centers in the later MLT sectors. The peaks of small-and medium-

scale FACs are located poleward of SAPS, mainly in the upward R1 FACs region. The upward R1 FACs are partly closed by the downward R1 FACs in the dawn-morning sector. Based on model simulation, when R2 shifts equatorward to the subauroral region, the plasma flow also shifts equatorward with its peak located poleward of that of R2 FACs. Both the model and observations provide evidence that SAPS behave as caused by a magnetospheric current source.

Wang *et al.*^[183] has investigated the configuration of Field-Aligned Currents (FACs) during a long period of radial Interplanetary Magnetic Field (IMF) on 19 May 2002 by using high-resolution and precise vector magnetic field measurements of CHAMP satellite. During the interest period IMF B_y and B_z are weakly positive and B_x keeps pointing to the Earth for almost 10 h. The geomagnetic indices Dst is about -40 nT and AE about 100 nT on average. The cross polar cap potential calculated from Assimilative Mapping of Ionospheric Electrodynamics and derived from DMSP observations have average values of 10–20 kV. Obvious hemispheric differences are shown in the configurations of FACs on the dayside and nightside. At the south pole FACs diminish in intensity to magnitudes of about $0.1 \text{ A}\cdot\text{m}^{-2}$, the plasma convection maintains two-cell flow pattern, and the thermospheric density is quite low. However, there are obvious activities in the northern cusp region. One pair of FACs with a downward leg toward the pole and upward leg on the equatorward side emerge in the northern cusp region, exhibiting opposite polarity to FACs typical for duskward IMF orientation. An obvious sunward plasma flow channel persists during the whole period. These ionospheric features might be manifestations of an efficient magnetic reconnection process occurring in the northern magnetospheric flanks at high latitude. The enhanced ionospheric current systems might deposit large amount of Joule heating into the thermosphere. The air densities in the cusp region get enhanced and subsequently propagate equatorward on the dayside. Although geomagnetic indices during the radial IMF indicate low-level activity, the present study demonstrates that there are prevailing energy inputs from the magnetosphere to both the ionosphere and thermosphere in the northern polar cusp region.

Based on the data of French DEMETER satellite, Yan *et al.*^[184] attempted to make a statistical analysis of variations of electron density before $37 M_w \geq 7.0$ earthquakes in the world during January 2005 to December

2009. The orbits, recorded in local nighttime by the satellite, were chosen by a range of longitude 20° and latitude 15° during the 9 days around these earthquakes, with 7 days before and 1 day after. Among the 37 earthquakes, electron density perturbations were detected before 19 events, accounting for nearly 51% of the total. The anomalies represent positive before 18 events and occurred mostly within 1–6 days before the shocks, part of which appeared more than one time. It is more easily to observe the electron density disturbance around the equatorial and low-latitude regions than high latitudes. The disturbance amplitude presents a positive correlation with the magnitude of earthquakes basically, while the depth of earthquakes does not show significant relationship with the perturbation. It is noted that before several events, the anomalies were likely associated with the combined effect of earthquakes and geomagnetic activity and revealed a higher disturbance level. As the seismoionospheric coupling process is complex, it is necessary to conduct more observations of multi-parameters on the ground, in the atmosphere and ionosphere synchronously.

Based on the seventh generation of International Geomagnetic Reference Field, the non-dipole magnetic fields for 1900–2000 (interval is 5 years) were calculated by Zeng *et al.*^[185]. The distribution ranges are very large, and the intensities are very strong for the following five magnetic anomalies: Eastern Asian positive anomaly, Oceanian negative anomaly, Southern Atlantic positive anomaly, African negative anomaly and Northern American positive anomaly. The intensity of Southern Atlantic positive anomaly is the biggest. The intensity of Eastern Asian positive anomaly is the second before 1990. The intensity of African negative anomaly exceeds the Eastern Asian anomaly and becomes the second since 1990. The increasing rate of magnetic anomaly intensity (absolute value) of African negative anomaly is the largest (average annual variation rate is $67.1 \text{ nT}\cdot\text{a}^{-1}$), that of Southern Atlantic positive anomaly is the second (that is $64.8 \text{ nT}\cdot\text{a}^{-1}$), that of Oceania negative anomaly is the third (that is $49.6 \text{ nT}\cdot\text{a}^{-1}$). The location changes of magnetic anomaly center of African and Southern Atlantic anomaly are the fastest in the all of the magnetic anomalies.

During the first several months of the three-spacecraft Swarm mission all three spacecraft came repeatedly into close alignment, providing an ideal opportunity for validating the proposed dual-spacecraft method

for estimating current density from the Swarm magnetic field data^[186]. Two of the Swarm spacecraft regularly fly side-by-side in closely similar orbits, while the third at times approaches the other two. This provides a data set which under certain assumptions of stationarity of the magnetic field can produce 2, 3, 4, 5 (or more) point measurements, which can be cross compared. Dunlop *et al.*^[186] found that at low Earth orbit the use of time-shifted positions allow stable estimates of current density to be made and can verify temporal effects as well as validating the interpretation of the current components as arising predominantly from field-aligned currents. The four- spacecraft configurations can resolve the full vector current and therefore can check the perpendicular as well as parallel current density components directly, together with the quality factor for the estimates directly (for the first time in situ at low Earth orbit).

Compared to the recently improved understanding of the nightside diffuse aurora, the mechanism(s) responsible for the dayside diffuse auroral precipitation remains limitedly understood. Shi *et al.*^[187] investigated the dayside diffuse aurora observed by the all-sky imagers of Chinese Arctic Yellow River Station in the time interval of 02:00 UT–10:00 UT (05:00–13:00 magnetic local time) on 2 January 2006. In this interval, the intensity of dayside diffuse aurora is highly correlated with the solar wind dynamic pressure with a maximum coefficient of 0.89. Moreover, there are similar spectra characteristics in the Pc5 range between the intensity of dayside diffuse aurora and solar wind dynamic pressure (proton density) during a portion of the time interval, in which the interplanetary magnetic field B_z is northward. The observation indicates that changes in solar wind dynamic pressure can efficiently modulate the magnitude of the dayside diffuse aurora, except when the interplanetary magnetic field is southward. The enhancement of the solar wind dynamic pressure can provide favorable circumstances for dayside chorus wave generation, so they considered that the dayside chorus could be a candidate for the production of the dayside diffuse aurora. Furthermore, since the compressional Pc4–Pc5 pulsations can also modulate the intensity of whistler mode chorus waves, the solar wind dynamic pressure modulates the dayside diffuse aurora through affecting dayside chorus wave activity and the associated scattering process.

A comprehensive analysis of long-term and multispectral auroral observations made in the Arctic and Antarctica demonstrates that the dayside auroral ovals

in two hemispheres are both presented in a two-peak structure, namely, the prenoon 09:00 Magnetic Local Time (MLT) and postnoon 15:00 MLT peaks^[188]. The two-peak structures of dayside ovals, however, are asymmetric in the two hemispheres; *i.e.*, the postnoon average auroral intensity is more than the prenoon one in the Northern Hemisphere but less in the Southern Hemisphere. The hemispheric asymmetry cannot be accounted for by the effect of the interplanetary magnetic field B_y component and the seasonal difference of ionospheric conductivities in the two hemispheres, which were used to interpret satellite-observed real-time auroral intensity asymmetries in the two hemispheres in previous studies. Hu *et al.*^[188] suggested that the hemispheric asymmetry is the combined effect of the prenoon-postnoon variations of the magnetosheath density and local ionospheric conductivity.

Derivation of Equivalent Current Systems (ECS) from a global magnetospheric Magnetohydrodynamics (MHD) model is very useful in studying magnetosphere-ionosphere coupling, ground induction effects, and space weather forecast. Zhang *et al.*^[189] introduced an improved method to derive the ECS from a global MHD model, which takes account of the obliqueness of the magnetic field lines. By comparing the ECS derived from this improved method and the previous method, they found that the main characteristics of the ECS derived from the two methods are generally consistent with each other, but the eastward-westward component of the geomagnetic perturbation calculated from the ECS derived from the improved method is much stronger than that from the previous method. They then compared the geomagnetic perturbation as a function of the Interplanetary Magnetic Field (IMF) clock angle calculated from the ECS derived from both methods with the observations. The comparison indicates that the improved method can improve the performance of the simulation. Furthermore, it was found that the incomplete counterbalance of the geomagnetic effect produced by the ionospheric poloidal current and Field-Aligned Current (FAC) contributes to most of the eastward-westward component of geomagnetic perturbation.

Although it has been a long time since the beginning of research on the auroral Hemispheric Power (HP), less has been done on the differences of HP among storms driven by different interplanetary disturbances. According to different drivers, all the storm events during 2001–2008 are divided into three categories, namely

helmet streamer Corotating Interaction Regions (CIRs), pseudo-streamer CIRs and Interplanetary Coronal Mass Ejection (ICMEs) driven events. A superposed epoch analysis is performed to investigate the relative differences of HP during geomagnetic storms driven by different disturbances^[190]. The background solar wind parameters, geomagnetic activity and the effectiveness of coupling function have been studied. In addition, Chen *et al.*^[190] investigated the hemispheric asymmetry of HP in the three types of storms. The statistic results show that HP favors storms driven by pseudo-streamer CIRs and ICMEs than storms driven by helmet streamer CIRs before the storm onset. It is inferred that the occurring of the so-called "calm before the storm" effect is less correlated with the Russell-McPherron effect, but might be a result of the Newell coupling function. The maximum of HP during helmet streamer CIR storms is greater than that during pseudo-streamer CIR and ICME storms. The possible reason is larger interplanetary magnetic field component $|B_z|$ and higher solar wind number density related to helmet streamer CIRs. The difference value of HP between two hemisphere (winter minus summer) increases with Kp when Kp is less than or equal to 4, which is consistent with the prediction of the ionospheric conductivity feedback model. For $Kp > 4$, HP favors winter hemisphere during storms driven by helmet streamer CIRs and ICMEs, but summer HP is larger or close to winter HP during storms driven by pseudo-streamer CIRs.

Earth's proton aurora occurs over a broad MLT region and is produced by the precipitation of low-energy (2–10 keV) plasmashet protons. Proton precipitation can alter chemical compositions of the atmosphere, linking solar activity with global climate variability. Previous studies proposed that electromagnetic ion cyclotron waves can resonate with protons, producing proton scattering precipitation. A long-outstanding question still remains whether there is another mechanism responsible for the proton aurora. By performing satellite data analysis and diffusion equation calculations, Xiao *et al.*^[191] showed that fast magnetosonic waves can produce trapped proton scattering that yields proton aurora. This provides a new insight into the mechanism of proton aurora. Furthermore, a ray-tracing study demonstrates that magnetosonic wave propagates over a broad MLT region, consistent with the global distribution of proton aurora.

References

- [1] Duan S P, Dai L, Wang C, Lui A T Y, Liu Z X, He Z H, Zhang Y C, Dandouras I, Reme H. Cluster observations of unusually high concentration of energetic O⁺ carried by flux ropes in the night-side high-latitude magnetosheath during a storm initial phase. *Journal of Geophysical Research-Space Physics*, 2015, 120(10): 8317-8326
- [2] Zhang J J, Wang C, Sun T R, Liu C M, Wang K R. GIC due to storm sudden commencement in low-latitude high-voltage power network in China: Observation and simulation. *Space Weather-the International Journal of Research and Applications*, 2015, 13(10): 643-655
- [3] Han J P, Wang C, Li H. Energetics characteristics of the super magnetic storm on November 20, 2003 based on 3D global MHD simulation. *Science China-Earth Sciences*, 2014, 57(12): 3035-3046
- [4] Dai L, Takahashi K, Lysak R, Wang C, Wygant J R, Kletzing C, Bonnell J, Cattell C A, Smith C W, MacDowall R J, *et al.* Storm time occurrence and spatial distribution of Pc4 poloidal ULF waves in the inner magnetosphere: A Van Allen Probes statistical study. *Journal of Geophysical Research-Space Physics*, 2015, 120(6): 4748-4762
- [5] Ma S Y, Yan W N, Xu L. Tomographic reconstruction of storm time RC ion distribution from ENA images on board multiple spacecraft. *Journal of Geophysical Research-Space Physics*, 2015, 120(11): 9334-9354
- [6] Yuan Z G, Xiong Y, Li H M, Huang S Y, Qiao Z, Wang Z Z, Zhou M, Wang D D, Deng X H, Raita T, *et al.* Influence of precipitating energetic ions caused by EMIC waves on the subauroral ionospheric E region during a geomagnetic storm. *Journal of Geophysical Research-Space Physics*, 2014, 119(10): 8462-8471
- [7] Shen X F, Ni B B, Gu X D, Zhou C, Liu Y, Xiang Z, Zhao Z Y. A statistical analysis of solar wind parameters and geomagnetic indices for the Solar Cycle 23. *Chinese Journal of Geophysics-Chinese Edition*, 2015, 58(2): 362-370
- [8] Zhima Z R, Cao J B, Liu W L, Fu H S, Wang T Y, Zhang X M, Shen X H. Storm time evolution of ELF/VLF waves observed by DEMETER satellite. *Journal of Geophysical Research-Space Physics*, 2014, 119(4): 2612-2622
- [9] Zou H, Li C F, Zong Q G, Parks G K, Pu Z Y, Chen H F, Xie L, Zhang X G. Short-term variations of the inner radiation belt in the South Atlantic anomaly. *Journal of Geophysical Research-Space Physics*, 2015, 120(6): 4475-4486
- [10] Shi X, Chen T, Zhang L, Duan S, Liu J, He Z. Ion flux dropout observed near dipolarization front. *Chinese Science Bulletin*, 2014, 59(34): 4790-4796
- [11] Dai L, Wang C, Duan S P, He Z H, Wygant J R, Cattell C A, Tao X, Su Z P, Kletzing C, Baker D N, *et al.* Near-Earth injection of MeV electrons associated with intense dipolarization electric fields: Van Allen Probes observations. *Geophysical Research Letters*, 2015, 42(15): 6170-6179
- [12] Lu S, Lu Q M, Lin Y, Wang X Y, Ge Y S, Wang R S, Zhou M, Fu H S, Huang C, Wu M Y, *et al.* Dipolarization fronts as earthward propagating flux ropes: A three-dimensional global hybrid simulation. *Journal of Geophysical Research-Space Physics*, 2015, 120(8): 6286-6300
- [13] Huang C, Wu M Y, Lu Q M, Wang R S, Wang S. Electron acceleration in the dipolarization front driven by magnetic reconnection.

- Journal of Geophysical Research-Space Physics, 2015, 120(3): 1759-1765
- [14] Shen X C, Zong Q G, Shi Q Q, Tian A M, Sun W J, Wang Y F, Zhou X Z, Fu S Y, Hartinger M D, Angelopoulos V. Magnetospheric ULF waves with increasing amplitude related to solar wind dynamic pressure changes: The Time History of Events and Macroscale Interactions during Substorms (THEMIS) observations. *Journal of Geophysical Research-Space Physics*, 2015, 120(9): 7179-7190
- [15] Luo H, Chen G X, Du A M. Multipoint observations of Pi2 pulsations and correlation with dynamic processes in the near-Earth magnetotail on March 18, 2009. *Science China-Earth Sciences*, 2014, 57(2): 359-371
- [16] Wang Y, Du A M, Chen G X, Cao X, Zhang Y, Li M, Liu X C, Guo J P. Comparing the diurnal variations in the SuperMAG auroral electrojet indices SML and SMU. *Chinese Science Bulletin*, 2014, 59(29-30): 3877-3883
- [17] Yao Z H, Pu Z Y, Owen C J, Fu S Y, Chu X N, Liu J, Angelopoulos V, Rae I J, Yue C, Zhou X Z, et al. Current reduction in a pseudo-breakup event: THEMIS observations. *Journal of Geophysical Research-Space Physics*, 2014, 119(10): 8178-8187
- [18] Wang Z Q, Cao J B, Reme H, Dandouras I, Ma Y D. Nonadiabatic acceleration of plasma sheet ions related to ion cyclotron waves. *Science China-Technological Sciences*, 2014, 57(12): 2434-2440
- [19] Nowada M, Fu S Y, Parks G K, Pulkkinen T I, Pu Z Y. An influence of long-lasting and gradual magnetic flux transport on fate of magnetotail fast plasma flows: An energetic particle injection substorm event study. *Planetary and Space Science*, 2014, 101: 135-148
- [20] Zhou M X, Yuan Z G, Li H M, Wang D D, Yu X D, Wang Z Z, Qiao Z. Statistical study of IPDP events observed by the CARISMA network of magnetometers. *Chinese Journal of Geophysics-Chinese Edition*, 2015, 58(7): 2235-2241
- [21] Li H M, Yuan Z G, Yu X D, Huang S Y, Wang D D, Wang Z Z, Qiao Z, Wygant J R. The enhancement of cosmic radio noise absorption due to hiss-driven energetic electron precipitation during substorms. *Journal of Geophysical Research-Space Physics*, 2015, 120(7): 5393-5407
- [22] Huang S Y, Fu H S, Yuan Z G, Zhou M, Fu S, Deng X H, Sun W J, Pang Y, Wang D D, Li H M, et al. Electromagnetic energy conversion at dipolarization fronts: Multispacecraft results. *Journal of Geophysical Research-Space Physics*, 2015, 120(6): 4496-4502
- [23] Li H M, Zhou M, Deng X H, Yuan Z G, Guo L X, Yu X D, Pang Y, Huang S Y. A statistical study on the whistler waves behind dipolarization fronts. *Journal of Geophysical Research-Space Physics*, 2015, 120(2): 1086-1095
- [24] Fu S, Ashour-Abdalla M, Deng X H, El-Alaoui M, Zhou M, Richard R L, Walker R J, Yuan Z G. Ion dynamics associated with substorm dipolarization fronts. *Science China-Earth Sciences*, 2014, 57(10): 2543-2551
- [25] Huang S Y, Yuan Z G, Ni B, Zhou M, Fu H S, Fu S, Deng X H, Pang Y, Li H M, Wang D D, et al. Observations of large-amplitude electromagnetic waves and associated wave-particle interactions at the dipolarization front in the Earth's magnetotail: A case study. *Journal of Atmospheric and Solar-Terrestrial Physics*, 2015, 129: 119-127
- [26] Huang S Y, Fu H S, Vaivads A, Yuan Z G, Pang Y, Zhou M, Khotyaintsev Y V, Deng X H, Andre M, Zhang L, et al. Dawn-dusk scale of dipolarization front in the Earth's magnetotail: multi-cases study. *Astrophysics and Space Science*, 2015, 357(1): 961-966
- [27] Wang Y, Zhou M, Deng X H. Statistical study on the suprathermal electrons properties around dipolarization fronts in Earth's magnetotail. *Science China-Technological Sciences*, 2015, 58(6): 961-966
- [28] Zhou M, Ni B B, Huang S Y, Deng X H, Ashour-Abdalla M, Nishimura Y, Yuan Z G, Pang Y, Li H M. Observation of large-amplitude magnetosonic waves at dipolarization fronts. *Journal of Geophysical Research-Space Physics*, 2014, 119(6): 4335-4347
- [29] Meng X, Cao J, Wang T, Ma Y. Nonadiabatic acceleration of protons in the near-earth magnetotail during substorm dipolarization. *Chinese Journal of Space Science*, 2014, 34(6): 794-801
- [30] Zhima Z R, Cao J B, Fu H S, Liu W L, Chen L J, Dunlop M, Zhang X M, Shen X H. Whistler mode wave generation at the edges of a magnetic dip. *Journal of Geophysical Research-Space Physics*, 2015, 120(4): 2469-2476
- [31] Lu H Y, Cao J B, Ge Y S, Zhang T L, Nakamura R, Dunlop M W. Hall and finite Larmor radius effects on the dipolarization fronts associated with interchange instability. *Geophysical Research Letters*, 2015, 42(23): 2469-2476
- [32] Sun W J, Fu S Y, Parks G K, Pu Z Y, Zong Q G, Liu J, Yao Z H, Fu H S, Shi Q Q. Electric fields associated with dipolarization fronts. *Journal of Geophysical Research-Space Physics*, 2014, 119(7): 5272-5278
- [33] Sun W J, Slavin J A, Fu S Y, Raines J M, Sundberg T, Zong Q G, Jia X Z, Shi Q Q, Shen X C, Poh G K, et al. MESSENGER observations of Alfvénic and compressional waves during Mercury's substorms. *Geophysical Research Letters*, 2015, 42(15): 6189-6198
- [34] Zhou X Z, Pan D X, Angelopoulos V, Liu J, Runov A, Li S S, Li J Z, Zong Q G, Fu S Y. Ion acceleration and reflection on magnetotail antidipolarization fronts. *Geophysical Research Letters*, 2015, 42(21): 9166-9175
- [35] Pan D X, Zhou X Z, Shi Q Q, Liu J, Angelopoulos V, Runov A, Zong Q G, Fu S Y. On the generation of magnetic dips ahead of advancing dipolarization fronts. *Geophysical Research Letters*, 2015, 42(11): 4256-4262
- [36] Zhou X Z, Angelopoulos V, Liu J, Runov A, Pan D X. Asymmetric braking and downward deflection of dipolarization fronts: Effects of ion reflection. *Geophysical Research Letters*, 2014, 41(20): 6994-7001
- [37] Pu Z Y, Zhong J, Lv L Q. 3d Structure of Reconnected Flux Ropes at Earth's Magnetopause: Results from Multiple Spacecraft Observations. 2014 Xxxith Ursi General Assembly and Scientific Symposium (Ursi Gass), 2014
- [38] Fu H S, Vaivads A, Khotyaintsev Y V, Olshevsky V, Andre M, Cao J B, Huang S Y, Retino A, Lapenta G. How to find magnetic nulls and reconstruct field topology with MMS data?. *Journal of Geophysical Research-Space Physics*, 2015, 120(5): 3758-3782
- [39] Zhou M, Deng X H, Tang R X, Pang Y, Xu X J, Yuan Z G, Huang S Y. Evidence of deflected super-Alfvénic electron jet in a reconnection region with weak guide field. *Journal of Geophysical Research-Space Physics*, 2014, 119(3): 1541-1548
- [40] Huang S Y, Zhou M, Yuan Z G, Fu H S, He J S, Sahraoui F, Aunai N, Deng X H, Fu S, Pang Y, et al. Kinetic simulations of secondary reconnection in the reconnection jet. *Journal of Geophysical Research-Space Physics*, 2015, 120(8): 6188-6198
- [41] Lu S W, Zong Q G, Vogiatzis I, Wang Y F, Tian A M. Recon-



- struction of plasmoid and traveling compression region in the near-Earth magnetotail. *Science China-Technological Sciences*, 2015, 58(2): 330-337
- [42] Huang S Y, Zhou M, Yuan Z G, Deng X H, Sahraoui F, Pang Y, Fu S. Kinetic simulations of electric field structure within magnetic island during magnetic reconnection and their applications to the satellite observations. *Journal of Geophysical Research-Space Physics*, 2014, 119(9)
- [43] Huang S Y, Pang Y, Yuan Z G, Deng X H, He J S, Zhou M, Fu H S, Fu S, Li H M, Wang D D, *et al.* Observation of directional change of core field inside flux ropes within one reconnection diffusion region in the Earth's magnetotail. *Chinese Science Bulletin*, 2014, 59(34): 4797-4803
- [44] Wang R, Nakamura R, Zhang T, Du A, Baumjohann W, Lu Q, Fazakerley A N. Evidence of transient reconnection in the outflow jet of primary reconnection site. *Annales Geophysicae*, 2014, 32(3): 239-248
- [45] Wang R S, Lu Q M, Khotyaintsev Y V, Volwerk M, Du A M, Nakamura R, Gonzalez W D, Sun X, Baumjohann W G, Li X, *et al.* Observation of double layer in the separatrix region during magnetic reconnection. *Geophysical Research Letters*, 2014, 41(14): 4851-4858
- [46] Tian A M, Shi Q Q, Zong Q G, Du J, Fu S Y, Dai Y N. Analysis of magnetotail flux rope events by ARTEMIS observations. *Science China-Technological Sciences*, 2014, 57(5): 1010-1019
- [47] Zhang L Q, Lui A T Y, Baumjohann W, Wang J Y. Probabilities of magnetic reconnection encounter at different activity levels in the Earth's magnetotail. *Advances in Space Research*, 2015, 56(4): 736-741
- [48] Zhang L Q, Wang J Y, Baumjohann W, Reme H, Dai L, Dunlop M W, Chen T, Huang Y. X lines in the magnetotail for southward and northward IMF conditions. *Journal of Geophysical Research-Space Physics*, 2015, 120(9): 7764-7773
- [49] Dai L, Wang C, Angelopoulos V, Glassmeier K H. In situ evidence of breaking the ion frozen-in condition via the non-gyro-tropic pressure effect in magnetic reconnection. *Annales Geophysicae*, 2015, 33(9): 1147-1153
- [50] Huang C, Lu Q M, Guo F, Wu M Y, Du A M, Wang S. Magnetic islands formed due to the Kelvin-Helmholtz instability in the outflow region of collisionless magnetic reconnection. *Geophysical Research Letters*, 2015, 42(18): 7282-7286
- [51] Wu M Y, Huang C, Lu Q M, Volwerk M, Nakamura R, Voros Z, Zhang T L, Wang S. In situ observations of multistage electron acceleration driven by magnetic reconnection. *Journal of Geophysical Research-Space Physics*, 2015, 120(8): 6320-6331
- [52] Huang C, Lu Q M, Wang P R, Wu M Y, Wang S. Characteristics of electron holes generated in the separatrix region during antiparallel magnetic reconnection. *Journal of Geophysical Research-Space Physics*, 2014, 119(8)
- [53] Huang C, Lu Q M, Lu S, Wang P R, Wang S. The effect of a guide field on the structures of magnetic islands formed during multiple X line reconnections: Two-dimensional particle-in-cell simulations. *Journal of Geophysical Research-Space Physics*, 2014, 119(2): 798-807
- [54] Wang R S, Lu Q M, Du A M, Nakamura R, Lu S, Huang C, Liu C X, Wu M Y. In situ observation of magnetic reconnection in the front of bursty bulk flow. *Journal of Geophysical Research-Space Physics*, 2014, 119(12)
- [55] Zhu C B, Zhang H, Ge Y S, Pu Z Y, Liu W L, Wan W X, Liu L B, Chen Y D, Le H J, Wang Y F. Dipole tilt angle effect on magnetic reconnection locations on the magnetopause. *Journal of Geophysical Research-Space Physics*, 2015, 120(7): 5344-5354
- [56] Ma Z W, Wang L C, Li L J. Reconnection dynamics with secondary tearing instability in compressible Hall plasmas. *Physics of Plasmas*, 2015, 22(6)
- [57] Wang L C, Li L J, Ma Z W, Zhang X, Lee L C. Energy of Alfvén waves generated during magnetic reconnection. *Physics Letters A*, 2015, 379(36): 2068-2072
- [58] Ma Z W, Wu L N, Li L J, Wang L C. Bursty magnetic reconnection under slow shock-generated whistler waves. *Journal of Geophysical Research-Space Physics*, 2014, 119(9)
- [59] Sun H E, Ma Z W, Huang J. Reconnection properties in collisionless plasma with open boundary conditions. *Physics of Plasmas*, 2014, 21(7)
- [60] Zhou M, Li T, Deng X, Huang S, Li H. Comparisons of electron acceleration efficiency among different structures during magnetic reconnection: a Cluster multicasestudy. *Annales Geophysicae*, 2015, 33(12): 1469-1478
- [61] Lai X S, Zhou M, Deng X H, Li T M, Huang S Y. How Does the Guide Field Affect the Asymmetry of Hall Magnetic and Electric Fields in Fast Magnetic Reconnection?. *Chinese Physics Letters*, 2015, 32(9)
- [62] Zhou M, Li H M, Deng X H, Huang S Y, Pang Y, Yuan Z G, Xu X J, Tang R X. Characteristic distribution and possible roles of waves around the lower hybrid frequency in the magnetotail reconnection region. *Journal of Geophysical Research-Space Physics*, 2014, 119(10): 8228-8242
- [63] Zhou M, Pang Y, Deng X H, Huang S Y, Lai X S. Plasma physics of magnetic island coalescence during magnetic reconnection. *Journal of Geophysical Research-Space Physics*, 2014, 119(8)
- [64] Fu H S, Cao J B, Cully C M, Khotyaintsev Y V, Vaivads A, Angelopoulos V, Zong Q G, Santolik O, Macusova E, Andre M, *et al.* Whistler-mode waves inside flux pileup region: Structured or unstructured?. *Journal of Geophysical Research-Space Physics*, 2014, 119(11): 9089-9100
- [65] Zhao K, Jiang Y, Men K P, Huang L F, Fu S. Interhemispheric comparisons of ionospheric upflow H⁺ at various geomagnetic activity levels using FAST observations. *Chinese Journal of Geophysics-Chinese Edition*, 2014, 57(11): 3715-3728
- [66] Zhao K, Jiang Y, Ding L G, Huang L F. Statistical analysis of outflow ionospheric O⁺ on the declining phase of solar cycle 23 using Fast observations. *Planetary and Space Science*, 2014, 101: 170-180
- [67] Wei Y, Zhao B Q, Li G Z, Wan W X. Electric field penetration into Earth's ionosphere: a brief review for 2000-2013. *Science Bulletin*, 2015, 60(8): 748-761
- [68] Mailyan B, Shi Q Q, Kullen A, Maggiolo R, Zhang Y, Fear R C, Zong Q G, Fu S Y, Gou X C, Cao X, *et al.* Transpolar arc observation after solar wind entry into the high-latitude magnetosphere. *Journal of Geophysical Research-Space Physics*, 2015, 120(5): 3525-3534
- [69] He F, Zhang X-X, Wang X-Y, Chen B. EUV emissions from solar wind charge exchange in the Earth's magnetosheath Three-dimensional global hybrid simulation, *Journal of Geophysical Research: Space Physics*, 2015. 120(1), 138-156
- [70] Sun T R, Wang C, Wei F, Sembay S. X-ray imaging of Kelvin-Helmholtz waves at the magnetopause. *Journal of Geophysical Research-Space Physics*, 2015, 120(1): 266-275

- [71] Gou X C, Shi Q Q, Tian A M, Fu S Y, Zong Q G, Dunlop M W, Pu Z Y. Solar Wind Penetration into the High-latitude Magnetosphere: Cluster Observations. 2014 Xxxith Ursi General Assembly and Scientific Symposium (Ursi Gass), 2014
- [72] Sun T R, Wang C, Zhang J J, Pilipenko V A, Wang Y, Wang J Y. The chain response of the magnetospheric and ground magnetic field to interplanetary shocks. *Journal of Geophysical Research-Space Physics*, 2015, 120(1): 157-165
- [73] Liu H L, Qin G. Improvements of the shock arrival times at the Earth model STOA. *Journal of Geophysical Research-Space Physics*, 2015, 120(7): 5290-5297
- [74] Qin G, Shalchi A. Perpendicular diffusion of energetic particles: Numerical test of the theorem on reduced dimensionality. *Physics of Plasmas*, 2015, 22(1)
- [75] Qin G, Zhang L H. The Modification of the Nonlinear Guiding Center Theory. *Astrophysical Journal*, 2014, 787(1)
- [76] Wang C, Han J P, Li H, Peng Z, Richardson J D. Solar wind-magnetosphere energy coupling function fitting: Results from a global MHD simulation. *Journal of Geophysical Research-Space Physics*, 2014, 119(8)
- [77] Wang Y, Qin G, Zhang M, Dalla S. A Numerical Simulation of Solar Energetic Particle Dropouts during Impulsive Events. *Astrophysical Journal*, 2014, 789(2)
- [78] Wang Chi. Recent Advances in Chinese Meridian Project. *Chin. J. Space Sci.*, 2014, 34(5): 535-543
- [79] Shi Q Q, Hartinger M D, Angelopoulos V, Tian A M, Fu S Y, Zong Q G, Weygand J M, Raeder J, Pu Z Y, Zhou X Z, et al. Solar wind pressure pulse-driven magnetospheric vortices and their global consequences. *Journal of Geophysical Research-Space Physics*, 2014, 119(6): 4274-4280
- [80] Zhang Q H, Lockwood M, Foster J C, Zhang S R, Zhang B C, McCrea I W, Moen J, Lester M, Ruohoniemi J M. Direct observations of the full Dungey convection cycle in the polar ionosphere for southward interplanetary magnetic field conditions. *Journal of Geophysical Research-Space Physics*, 2015, 120(6): 4519-4530
- [81] Wei Y, Pu Z Y, Zong Q G, Wan W X, Ren Z P, Fraenz M, Dubinin E, Tian F, Shi Q Q, Fu S Y, et al. Oxygen escape from the Earth during geomagnetic reversals: Implications to mass extinction. *Earth and Planetary Science Letters*, 2014, 394: 94-98
- [82] Zhang H, Khurana K K, Kivelson M G, Angelopoulos V, Wan W X, Liu L B, Zong Q G, Pu Z Y, Shi Q Q, Liu W L. Three-dimensional lunar wake reconstructed from ARTEMIS data. *Journal of Geophysical Research-Space Physics*, 2014, 119(7): 5220-5243
- [83] Rong Z J, Lui A T Y, Wan W X, Yang Y Y, Shen C, Petrukovich A A, Zhang Y C, Zhang T L, Wei Y. Time delay of interplanetary magnetic field penetration into Earth's magnetotail. *Journal of Geophysical Research-Space Physics*, 2015, 120(5): 3406-3414
- [84] Wang Z Q. Global frequency distributions of pulsations driven by sharp decrease of solar wind dynamic pressure. *Science China-Earth Sciences*, 2015, 58(12): 2211-2219
- [85] Li L Y, Cao J B, Yang J Y, Berthelier J J, and Lebreton J P. Semiannual and solar activity variations of daytime plasma observed by DEMETER in the ionosphere-plasmasphere transition region. *Journal of Geophysical Research-Space Physics*, 2015, 120(12): 10640- 10653
- [86] Zhao J S, Voitenko Y, Yu M Y, Lu J Y, Wu D J. Properties of Short-Wavelength Oblique Alfvén and Slow Waves. *Astrophysical Journal*, 2014, 793(2)
- [87] Dong Y X, Cao J B, Liu W L, Zhang L, Li L Y. Response of magnetic fields at geosynchronous orbit and on the ground to the sudden changes of IMF B-Z. *Science China-Technological Sciences*, 2014, 57(2): 360-367
- [88] Wang T Y, Cao J B, Fu H S, Liu W L, Dunlop M. Turbulence in the Earth's cusp region: The k-filtering analysis. *Journal of Geophysical Research-Space Physics*, 2014, 119(12)
- [89] Chang S S, Ni B B, Zhao Z Y, Gu X D, Zhou C. Test particle simulations of resonant interactions between energetic electrons and discrete, multi-frequency artificial whistler waves in the plasmasphere. *Chinese Physics B*, 2014, 23(8)
- [90] Lu J, Zhang X, Lin R, Fei H E, Jiang Y. Dynamic distribution features of energetic proton in south atlantic anomaly based on the observation of SAMPEX. *Chinese Journal of Space Science*, 2015, 35 (2): 192-202
- [91] Ji Y, Shen C. The loss rates of O⁺ in the inner magnetosphere caused by both magnetic field line curvature scattering and charge exchange reactions. *Physics of Plasmas*, 2014, 21(3)
- [92] Qin G, Shalchi A. Detailed numerical investigation of 90 degrees scattering of energetic particles interacting with magnetic turbulence. *Physics of Plasmas*, 2014, 21(4)
- [93] Shen C, Yang Y Y, Rong Z J, Li X, Dunlop M, Carr C M, Liu Z X, Baker D N, Chen Z Q, Ji Y, et al. Direct calculation of the ring current distribution and magnetic structure seen by Cluster during geomagnetic storms. *Journal of Geophysical Research-Space Physics*, 2014, 119(4): 2458-2465
- [94] Li X X, Tao X, Lu Q M, Dai L. Bounce resonance diffusion coefficients for spatially confined waves [J]. *Geophysical Research Letters*, 2015, 42(22): 9591-9599
- [95] Gao X L, Li W, Bortnik J, Thorne R M, Lu Q M, Ma Q L, Tao X, Wang S. The effect of different solar wind parameters upon significant relativistic electron flux dropouts in the magnetosphere. *Journal of Geophysical Research-Space Physics*, 2015, 120(6): 4324-4337
- [96] Gao X, Li W, Thorne R M, Bortnik J, Angelopoulos V, Lu Q, Tao X, Wang S. Statistical results describing the bandwidth and coherence coefficient of whistler mode waves using THEMIS waveform data. *Journal of Geophysical Research-Space Physics*, 2014, 119(11): 8992-9003
- [97] Xiong Y, Xie L, Pu Z Y, Fu S Y, Chen L J, Ni B B, Li W, Li J X, Guo R L, Parks G K. Responses of relativistic electron fluxes in the outer radiation belt to geomagnetic storms. *Journal of Geophysical Research-Space Physics*, 2015, 120(11): 9513-9523
- [98] Tao X, Lu Q, Wang S, Dai L. Effects of magnetic field configuration on the day-night asymmetry of chorus occurrence rate: A numerical study. *Geophysical Research Letters*, 2014, 41(19): 6577- 6582
- [99] Qin M R, Zhang X G, Ni B B, Song H Q, Zou H, Sun Y Q. Solar cycle variations of trapped proton flux in the inner radiation belt. *Journal of Geophysical Research-Space Physics*, 2014, 119(12)
- [100] Gao X, Li W, Thorne R M, Bortnik J, Angelopoulos V, Lu Q, Tao X, Wang S. New evidence for generation mechanisms of discrete and hiss-like whistler mode waves. *Geophysical Research Letters*, 2014, 41(14): 4805-4811
- [101] Tao X. A numerical study of chorus generation and the related variation of wave intensity using the DAWN code. *Journal of Geophysical Research-Space Physics*, 2014, 119(5): 3362-3372
- [102] Yuan C J, Zong Q G, Wan W X, Zhang H, Du A M. Relativistic electron flux dropouts in the outer radiation belt associated with



- corotating interaction regions. *Journal of Geophysical Research-Space Physics*, 2015, 120(9): 7404-7415
- [103] Yu X D, Yuan Z G, Wang D D, Li H M, Huang S Y, Wang Z Z, Zheng Q, Zhou M X, Kletzing C A, Wygant J R. In situ observations of EMIC waves in O⁺ band by the Van Allen Probe A. *Geophysical Research Letters*, 2015, 42(5): 1312-1317
- [104] Wang D D, Yuan Z G, Yu X D, Deng X H, Zhou M, Huang S Y, Li H M, Wang Z Z, Qiao Z, Kletzing C A, et al. Statistical characteristics of EMIC waves: Van Allen Probe observations. *Journal of Geophysical Research-Space Physics*, 2015, 120(6): 4400-4408
- [105] Wang Z Z, Yuan Z G, Li M, Li H M, Wang D D, Li H M, Huang S Y, Qiao Z. Statistical characteristics of EMIC wave-driven relativistic electron precipitation with observations of POES satellites: Revisit. *Journal of Geophysical Research-Space Physics*, 2014, 119(7): 5509-5519
- [106] Wang D D, Yuan Z G, Deng X H, Zhou M, Huang S Y, Li M, Li H M, Li H M, Raita T, Pang Y. Compression-related EMIC waves drive relativistic electron precipitation. *Science China-Technological Sciences*, 2014, 57(12): 2418-2425
- [107] Ni B B, Cao X, Zou Z Y, Zhou C, Gu X D, Bortnik J, Zhang J C, Fu S, Zhao Z Y, Shi R, et al. Resonant scattering of outer zone relativistic electrons by multiband EMIC waves and resultant electron loss time scales. *Journal of Geophysical Research-Space Physics*, 2015, 120(9): 7357-7373
- [108] Ni B B, Zou Z Y, Gu X D, Zhou C, Thorne R M, Bortnik J, Shi R, Zhao Z Y, Baker D N, Kanekal S G, et al. Variability of the pitch angle distribution of radiation belt ultrarelativistic electrons during and following intense geomagnetic storms: Van Allen Probes observations. *Journal of Geophysical Research-Space Physics*, 2015, 120(6): 4863-4876
- [109] Ni B B, Li W, Thorne R M, Bortnik J, Green J C, Kletzing C A, Kurth W S, Hospodarsky G B, Pich M D S. A novel technique to construct the global distribution of whistler mode chorus wave intensity using low-altitude POES electron data. *Journal of Geophysical Research-Space Physics*, 2014, 119(7): 5685-5699
- [110] Chang S S, Ni B B, Zhao Z Y, Wang F, Li J X, Zhao J J, Gu X D, Zhou C. Test particle simulation of resonant interaction between energetic electrons in the magnetosphere and ELF/VLF waves generated by ionospheric modification. *Acta Physica Sinica*, 2014, 63(6)
- [111] Fu H S, Cao J B, Zhima Z, Khotyaintsev Y V, Angelopoulos V, Santolik O, Omura Y, Taubenschuss U, Chen L, Huang S Y. First observation of rising-tone magnetosonic waves. *Geophysical Research Letters*, 2014, 41(21): 7419-7426
- [112] Yu J, Li L Y, Cao J B, Yuan Z G, Reeves G D, Baker D N, Blake J B, Spence H. Multiple loss processes of relativistic electrons outside the heart of outer radiation belt during a storm sudden commencement. *Journal of Geophysical Research-Space Physics*, 2015, 120(12): 10275-10288
- [113] Zhima Z, Chen L J, Fu H S, Cao J B, Horne R B, Reeves G. Observations of discrete magnetosonic waves off the magnetic equator. *Geophysical Research Letters*, 2015, 42(22): 9694-9701
- [114] Li J X, Ni B B, Xie L, Pu Z Y, Bortnik J, Thorne R M, Chen L J, Ma Q L, Fu S Y, Zong Q G, et al. Interactions between magnetosonic waves and radiation belt electrons: Comparisons of quasi-linear calculations with test particle simulations. *Geophysical Research Letters*, 2014, 41(14): 4828-4834
- [115] Li J X, Bortnik J, Xie L, Pu Z Y, Chen L J, Ni B B, Tao X, Thorne R M, Fu S Y, Yao Z H, et al. Comparison of formulas for resonant interactions between energetic electrons and oblique whistler-mode waves. *Physics of Plasmas*, 2015, 22(5)
- [116] Zhou C, Li W, Thorne R M, Bortnik J, Ma Q L, An X, Zhang X J, Angelopoulos V, Ni B B, Gu X D, et al. Excitation of dayside chorus waves due to magnetic field line compression in response to interplanetary shocks. *Journal of Geophysical Research-Space Physics*, 2015, 120(10): 8327-8338
- [117] He Z G, Zong Q G, Liu S Q, Wang Y F, Lin R L, Shi L Q. Frequency sweep rates of rising tone electromagnetic ion cyclotron waves: Comparison between nonlinear theory and Cluster observation. *Physics of Plasmas*, 2014, 21(12)
- [118] Zhou X Z, Wang Z H, Zong Q G, Claudepierre S G, Mann I R, Kivelson M G, Angelopoulos V, Hao Y X, Wang Y F, Pu Z Y. Imprints of impulse-excited hydromagnetic waves on electrons in the Van Allen radiation belts. *Geophysical Research Letters*, 2015, 42(15): 6199-6204
- [119] He Z G, Zhu H, Liu S Q, Zong Q G, Wang Y F, Lin R L, Shi L Q, Gong J C. Correlated observations and simulations on the buildup of radiation belt electron fluxes driven by substorm injections and chorus waves. *Astrophysics and Space Science*, 2015, 355(2): 245-251
- [120] Liu Y, Zong Q G. Energetic electron response to interplanetary shocks at geosynchronous orbit. *Journal of Geophysical Research-Space Physics*, 2015, 120(6): 4669-4683
- [121] Ren J, Zong Q G, Wang Y F, Zhou X Z. The interaction between ULF waves and thermal plasma ions at the plasmaspheric boundary layer during substorm activity. *Journal of Geophysical Research-Space Physics*, 2015, 120(2): 1133-1143
- [122] Wang C R, Rankin R, Zong Q G. Fast damping of ultralow frequency waves excited by interplanetary shocks in the magnetosphere. *Journal of Geophysical Research-Space Physics*, 2015, 120(4): 2438-2451
- [123] Zhao L L, Zong Q G, Zhang H, Wang S. Case and statistical studies on the evolution of hot flow anomalies. *Journal of Geophysical Research-Space Physics*, 2015, 120(8): 6332-6346
- [124] Jing H, Lu J Y, Kabin K, Zhao J S, Liu Z Q, Yang Y F, Zhao M X, Wang M. MHD simulation of energy transfer across magnetopause during sudden changes of the IMF orientation. *Planetary and Space Science*, 2014, 97: 50-59
- [125] Wang M, Lu J Y, Yuan H Z, Kabin K, Liu Z Q, Zhao M X, Li G. The dipole tilt angle dependence of the bow shock for southward IMF: MHD results. *Planetary and Space Science*, 2015, 106: 99-107
- [126] Lu J Y, Wang M, Kabin K, Zhao J S, Liu Z Q, Zhao M X, Li G. Pressure balance across the magnetopause: Global MHD results. *Planetary and Space Science*, 2015, 106: 108-115
- [127] Wang J Y, Huang Z H, Wang C, Liu Z Q. Effects of the interplanetary magnetic field clock angle on the shape of bow shock. *Science China-Earth Sciences*, 2015, 58(7): 1228-1234
- [128] Liu Z Q, Lu J Y, Wang C, Kabin K, Zhao J S, Wang M, Han J P, Wang J Y, Zhao M X. A three-dimensional high Mach number asymmetric magnetopause model from global MHD simulation. *Journal of Geophysical Research-Space Physics*, 2015, 120(7): 5645-5666
- [129] Yan G Q, Mozer F S, Shen C, Chen T, Parks G K, Cai C L, McFadden J P. Kelvin-Helmholtz vortices observed by THEMIS at the duskside of the magnetopause under southward interplanetary magnetic field. *Geophysical Research Letters*, 2014, 41(13): 4427-4434

- [130] Xiao T, Shi Q Q, Tian A M, Sun W J, Zhang H, Shen X C, Shang W S, Du A M. Plasma and Magnetic-field characteristics of magnetic decreases in the solar wind at 1 AU: Cluster-C1 observations. *Solar Physics*, 2014, 289(8): 3175-3195
- [131] Lu H Y, Cao J B, Zhang T L, Fu H S, Ge Y S. Evolution of Kelvin-Helmholtz instability at Venus in the presence of the parallel magnetic field. *Physics of Plasmas*, 2015, 22(6)
- [132] Xiao T, Zhang H, Shi Q Q, Zong Q G, Fu S Y, Tian A M, Sun W J, Wang S, Parks G K, Yao S T, *et al.* Propagation characteristics of young hot flow anomalies near the bow shock Cluster observations. *Journal of Geophysical Research: Space Physics*, 2015, 120(6): 4142-4154
- [133] Shen X C, Shi Q Q, Tian A M, Fu S Y, Zong Q G, Pu Z Y. Initial Responses of Magnetospheric Plasma Flows to the Dynamic Pressure Enhancements. 2014 Xxxith Ursi General Assembly and Scientific Symposium (Ursi Gass), 2014
- [134] Chai L, Fraenz M, Wan W, Rong Z, Zhang T, Wei Y, Dubinin E, Zhong J, Han X, Barabash S. IMF control of the location of Venusian bow shock The effect of the magnitude of IMF component tangential to the bow shock surface. *Journal of Geophysical Research: Space Physics*, 2014, 119(12): 9464-9475.
- [135] Chai L, Wan W, Fraenz M, Zhang T, Dubinin E, Wei Y, Li Y, Rong Z, Zhong J, Han X, *et al.* Solar zenith angle-dependent asymmetries in Venusian bow shock location revealed by Venus. *Express Journal of Geophysical Research: Space Physics*, 2015, 120(6): 4446-4451
- [136] Zhong J, Wan W X, Wei Y, Fu S Y, Jiao W X, Rong Z J, Chai L H, Han X H. Increasing exposure of geosynchronous orbit in solar wind due to decay of Earth's dipole field. *Journal of Geophysical Research-Space Physics*, 2014, 119(12)
- [137] Zhong J, Wan W X, Slavin J A, Wei Y, Lin R L, Chai L H, Raines J M, Rong Z J, Han X H. Mercury's three-dimensional asymmetric magnetopause. *Journal of Geophysical Research-Space Physics*, 2015, 120(9): 7658-7671
- [138] Zhong J, Wan W X, Wei Y, Slavin J A, Raines J M, Rong Z J, Chai L H, Han X H. Compressibility of Mercury's dayside magnetosphere. *Geophysical Research Letters*, 2015, 42(23)
- [139] Wu L N, Ma Z W. Linear growth rates of resistive tearing modes with sub-Alfvénic streaming flow. *Physics of Plasmas*, 2014, 21(7)
- [140] Huang T, Wang H, Shue J H, Cai L, Pi G. The dayside magnetopause location during radial interplanetary magnetic field periods: Cluster observation and model comparison. *Annales Geophysicae*, 2015, 33(4): 437-448
- [141] Huang S Y, Sahraoui F, Deng X H, He J S, Yuan Z G, Zhou M, Pang Y, Fu H S. Kinetic Turbulence in the Terrestrial Magnetosheath: Cluster Observations. *Astrophysical Journal Letters*, 2014, 789(2)
- [142] Wang M, Lu J Y, Li G. The study of the solar wind pressure coefficient. *Chinese Journal of Geophysics-Chinese Edition*, 2014, 57(11): 3804-3811
- [143] Huiping H, Jianyong L, Zhou Q, Wang M, Yang Y, Liu Z, Pei S. Simulation of Three-dimensional Earth's Bow Shock. *Chinese Journal of Space Science*, 2015, 35(1): 1-8
- [144] Hao J, Lu J, Jiang Y, Wang M, Hu H, Liu Z. Electromagnetic energy transfer across the magnetopause. *Chinese Journal of Space Science*, 2015, 34(3): 269-277
- [145] Cao J, Duan A, Dunlop M, Wei X, Cai C. Dependence of IMF By penetration into the neutral sheet on IMF B_z and geomagnetic activity. *Journal of Geophysical Research: Space Physics*, 2014, 119(7): 5279-5285
- [146] Ma Y D, Cao J B, Fu H S, Yang J Y, Lu H Y, Yang J, Wang Z Q. ULF wave accompanied with high-speed flows observed by TC-1 in the near magnetotail and the instability analysis. *Chinese Journal of Geophysics-Chinese Edition*, 2014, 57(11): 3754-3765
- [147] Ma Y D, Cao J B, Fu H S, Reme H, Dandouras I, Yang J Y, Wang Z Q, Tao D, Yang J. MHD and kinetic analysis of flow bursts in the Earth's plasma sheet. *Science China-Technological Sciences*, 2014, 57(1): 55-66
- [148] Shang W S, Yao Z H, Shi Q Q, Sun W J, Fu S Y, Liu J, Tian A M, Zong Q G, Pu Z Y, Xiao T, *et al.* Braking of high-speed flows in the magnetotail: THEMIS joint observations. *Chinese Science Bulletin*, 2014, 59(3): 326-334
- [149] Zhang L Q, Dai L, Baumjohann W, Reme H, Dunlop M W, Wei X H. Parallel-dominant and perpendicular-dominant components of the fast bulk flow: Comparing with the PSBL beams. *Journal of Geophysical Research-Space Physics*, 2015, 120(11): 9500-9512
- [150] Zhang L Q, Wang J Y, Baumjohann W, Reme H, Dunlop M W. Earthward and tailward flows in the plasma sheet. *Journal of Geophysical Research-Space Physics*, 2015, 120(6): 4487-4495
- [151] Zhang L Q, Baumjohann W, Wang J Y, Reme H, Dunlop M W, Chen T. Statistical characteristics of slow earthward and tailward flows in the plasma sheet. *Journal of Geophysical Research-Space Physics*, 2015, 120(8): 6199-6206
- [152] Pang X X, Cao J B, Liu W L, Ma Y D, Lu H Y, Yang J Y, Li L Y, Liu X, Wang J, Wang T Y, *et al.* Polytropic index of central plasma sheet ions based on MHD Bernoulli integral. *Journal of Geophysical Research-Space Physics*, 2015, 120(6): 4736-4747
- [153] Pang X X, Cao J B, Liu W L, Ma Y D, Lu H Y, Yang J Y, Li L Y, Liu X, Wang J, Wang T Y, *et al.* Case study of small scale polytropic index in the central plasma sheet. *Science China-Earth Sciences*, 2015, 58(11): 1993-2001
- [154] Wang J Y, Wang C, Huang Z H, and Sun T R. Effects of the interplanetary magnetic field on the twisting of the magnetotail: Global MHD results [J]. *Journal of Geophysical Research-Space Physics*, 2014, 119(3): 1887-1897.
- [155] Li H, Wang C, Fu S Y. Classification of fast flows in central plasma sheet: Superposed epoch analysis based on THEMIS observations. *Journal of Geophysical Research-Space Physics*, 2014, 119(9)
- [156] Yang Y Y, Shen C, Zhang Y C, Rong Z J, Li X, Dunlop M, Ma Y H, Liu Z X, Carr C M, Reme H. The force-free configuration of flux ropes in geomagnetotail: Cluster observations. *Journal of Geophysical Research-Space Physics*, 2014, 119(8)
- [157] Wei X H, Cai C L, Cao J B, Reme H, Dandouras I, Parks G K. Flapping motions of the magnetotail current sheet excited by nonadiabatic ions. *Geophysical Research Letters*, 2015, 42(12): 4731-4735
- [158] Wei X H, Cai C L. Observations of current sheet flapping associated with high speed flow in the magnetotail. *Chinese Journal of Geophysics-Chinese Edition*, 2015, 58(10): 3449-3456
- [159] Lu S, Lin Y, Lu Q M, Wang X Y, Wang R S, Huang C, Wu M Y, Wang S. Evolution of flux ropes in the magnetotail: A three-dimensional global hybrid simulation. *Physics of Plasmas*, 2015, 22(5)
- [160] Hao Y X, Zong Q G, Wang Y F, Zhou X Z, Zhang H, Fu S Y, Pu Z Y, Spence H E, Blake J B, Bonnell J, *et al.* Interactions of energetic electrons with ULF waves triggered by interplanetary shock: Van Allen Probes observations in the magnetotail. *Journal of*



- Geophysical Research-Space Physics, 2014, 119(10): 8262-8273
- [161] Tao X, Lu Q. Formation of electron kappa distributions due to interactions with parallel propagating whistler waves. *Physics of Plasmas*, 2014, 21(2)
- [162] Luo H, Kronberg E A, Grigorenko E E, Franz M, Daly P W, Chen G X, Du A M, Kistler L M, Wei Y. Evidence of strong energetic ion acceleration in the near-Earth magnetotail. *Geophysical Research Letters*, 2014, 41(11): 3724-3730
- [163] Cao J B, Zhang D, Reme H, Dandouras I, Sauvaud J A, Fu H S, Wei X H. Preliminary empirical model of inner boundary of ion plasma sheet. *Advances in Space Research*, 2015, 56(6): 1194-1199
- [164] Duan A Y, Cao J B, Dunlop M, Wang Z Q. Energetic electron bursts in the plasma sheet and their relation with BBFs. *Journal of Geophysical Research-Space Physics*, 2014, 119(11): 8902-8915
- [165] Yao Z H, Pu Z Y, Du A M, Angelopoulos V, Owen C J, Liu J, Chu X N, Cao X, Fu S Y, Zong Q G, et al. Pressure gradient evolution in the near-Earth magnetotail at the arrival of BBFs. *Chinese Science Bulletin*, 2014, 59(34): 4804-4808
- [166] Guo Z F, Hong M H, Lin Y, Du A M, Wang X Y, Wu M Y, Lu Q M. Generation of kinetic Alfvén waves in the high-latitude near-Earth magnetotail: A global hybrid simulation. *Physics of Plasmas*, 2015, 22(2)
- [167] Li H M, Zhou M, Deng X H, Yuan Z G, Huang S Y. Electron dynamics and wave activities associated with mirror mode structures in the near-Earth magnetotail. *Science China-Technological Sciences*, 2014, 57(8): 1541-1551
- [168] Sun W J, Fu S Y, Pu Z Y, Parks G K, Slavin J A, Yao Z H, Zong Q G, Shi Q Q, Zhao D, Cui Y B. The current system associated with the boundary of plasma bubbles. *Geophysical Research Letters*, 2014, 41(23): 8169-8175
- [169] Sun W J, Fu S Y, Shi Q Q, Zong Q G, Yao Z H, Xiao T, Parks G. THEMIS observation of a magnetotail current sheet flapping wave. *Chinese Science Bulletin*, 2014, 59(2): 154-161
- [170] Ji X F, Wang X G, Sun W J, Xiao C J, Shi Q Q, Liu J, Pu Z Y. EMHD theory and observations of electron solitary waves in magnetotail plasmas. *Journal of Geophysical Research-Space Physics*, 2014, 119(6): 4281-4289
- [171] He F, Zhang X-X, Chen B, Fok M-C, Nakano S. Determination of the Earth's plasmopause location from the CE-3 EUVC images. *Journal of Geophysical Research: Space Physics*, 2016, 121(1), 296-304
- [172] Liu X, Liu W, Cao J B, Fu H S, Yu J, Li X. Dynamic plasmopause model based on THEMIS measurements. *Journal of Geophysical Research-Space Physics*, 2015, 120(12): 10543-10556
- [173] Lin D, Wang C, Li W Y, Tang B B, Guo X C, Peng Z. Properties of Kelvin-Helmholtz waves at the magnetopause under northward interplanetary magnetic field: Statistical study. *Journal of Geophysical Research-Space Physics*, 2014, 119(9)
- [174] Zhang D, Cao J B, Wei X H, Li L Y. New technique to calculate electron Alfvén layer and its application in interpreting geosynchronous access of PS energetic electrons. *Journal of Geophysical Research-Space Physics*, 2015, 120(3): 1675-1683
- [175] Liu X, Liu W L. A new plasmopause location model based on THEMIS observations. *Science China Earth Science*, 2014, 57(10): 2552-2557
- [176] Yuan Z G, Xiong Y, Huang S Y, Deng X H, Pang Y, Zhou M, Dandouras I, Trotignon J G, Fazakerley A N, Lucek E. Cold electron heating by EMIC waves in the plasmaspheric plume with observations of the Cluster satellite. *Geophysical Research Letters*, 2014, 41(6): 1830-1837
- [177] Chang S S, Ni B B, Bortnik J, Zhou C, Zhao Z Y, Li J X, Gu X D. Resonant scattering of energetic electrons in the plasmasphere by monotonic whistler-mode waves artificially generated by ionospheric modification. *Annales Geophysicae*, 2014, 32(5): 507-518
- [178] Dunlop M W, Yang J Y, Yang Y Y, Xiong C, Luhr H, Bogdanova Y V, Shen C, Olsen N, Zhang Q H, Cao J B, et al. Simultaneous field-aligned currents at Swarm and Cluster satellites. *Geophysical Research Letters*, 2015, 42(10): 3683-3691
- [179] Niu Y Y, Zhang X X, He F, Jiang Y. Statistical characteristics of the equatorial boundary of the nightside auroral particle precipitation. *Science China-Earth Sciences*, 2015, 58(9): 1602-1608
- [180] Zhang X-X, He F, Wang W, Chen B. Hemispheric asymmetry of subauroral ion drifts: Statistical results. *Journal of Geophysical Research: Space Physics*, 2015, 120(6), 4544-4554
- [181] He F, Zhang X X, Chen B. Solar cycle, seasonal, and diurnal variations of subauroral ion drifts: Statistical results. *Journal of Geophysical Research: Space Physics*, 2014, 119(6): 5076-5086
- [182] Wang H, Luhr H, Ridley A, Huang T. The spatial distribution of region 2 field-aligned currents relative to subauroral polarization stream. *Annales Geophysicae*, 2014, 32(5): 533-542
- [183] Wang H, Luhr H, Shue J H, Frey H U, Kervalishvili G, Huang T, Cao X, Pi G, Ridley A J. Strong ionospheric field-aligned currents for radial interplanetary magnetic fields. *Journal of Geophysical Research-Space Physics*, 2014, 119(5): 3979-3995
- [184] Yan X X, Shan X J, Cao J B, Tang J. Statistical analysis of electron density anomalies before global $M_w \geq 7.0$ earthquakes (2005-2009) using data of DEMETER satellite. *Chinese Journal of Geophysics-Chinese Edition*, 2014, 57(2): 364-376
- [185] Zeng L, Cao J, Wei X. Global changes of the geomagnetic field during 1980-2010. *Progress in Geophysics*, 2014, 29(1): 116-121
- [186] Dunlop M W, Yang Y Y, Yang J Y, Luhr H, Shen C, Olsen N, Ritter P, Zhang Q H, Cao J B, Fu H S, et al. Multispacecraft current estimates at swarm. *Journal of Geophysical Research-Space Physics*, 2015, 120(10): 8307-8316
- [187] Shi R, Hu Z J, Ni B B, Han D S, Chen X C, Zhou C, Gu X D. Modulation of the dayside diffuse auroral intensity by the solar wind dynamic pressure. *Journal of Geophysical Research-Space Physics*, 2014, 119(12)
- [188] Hu Z J, Ebihara Y, Yang H G, Hu H Q, Zhang B C, Ni B B, Shi R, Trondsen T S. Hemispheric asymmetry of the structure of dayside auroral oval. *Geophysical Research Letters*, 2014, 41(24): 8696-8703
- [189] Zhang J J, Wang C, Tang B B. Improved method to derive equivalent current systems from global MHD simulations. *Science China-Earth Sciences*, 2014, 57(1): 167-173
- [190] Chen X, Fu S Y, Zheng L, Yang L P, Cui Y B. Auroral hemispheric power during geomagnetic storms driven by different interplanetary disturbances. *Chinese Journal of Geophysics-Chinese Edition*, 2014, 57(11): 3766-3776
- [191] Xiao F L, Zong Q G, Wang Y F, He Z G, Su Z P, Yang C, Zhou Q H. Generation of proton aurora by magnetosonic waves. *Scientific Reports*, 2014, 4

New Understanding Achieved from 2 Years of Chinese Ionospheric Investigations

LIU Libo^{1,2,3}, WAN Weixing^{1,2,3}

1. Key Laboratory of Earth and Planetary Physics, Institute of Geology and Geophysics, Chinese Academy of Sciences, Beijing 100029

2. Beijing National Observatory of Space Environment, Institute of Geology and Geophysics, Chinese Academy of Sciences, Beijing 100029

3. Geoscience School, University of the Chinese Academy of Sciences, Beijing 100049

* E-mail: liul@mail.iggcas.ac.cn

Key words

Ionosphere
Ionospheric climatology
Ionospheric dynamics
Ionospheric coupling
Planetary ionospheres
Ionospheric disturbance

Abstract

In the mainland of China, the number of ionospheric research groups is more than 10. Around 110 articles related to ionospheric physics have been published during 2014–2015. In this annual national report of the Committee on Space Research (COSPAR), we will outline some recent progress in ionospheric studies conducted by the Chinese mainland scientists in the past two years. These investigations cover the ionosphere responses to geomagnetic activities; ionospheric climatology and structures; couplings between the ionosphere, plasmasphere and lower atmosphere, and possible seismic signatures in the ionosphere; ionospheric irregularities and scintillation; ionospheric models, data assimilation and simulations; ionospheric dynamics and electrodynamics; progresses in the observation methodology and technique; and planetary ionospheres. Such investigations will strengthen our ability to monitor the ionosphere, provide a better understanding of the ionospheric states and the underlying fundamental processes, and improve the ionospheric modeling, forecasting, and related applications.

1 Ionosphere Responses to Geomagnetic Activities

The most fascinating issue encountered in ionospheric studies is the ionosphere's response to geomagnetic activities; especially what drives the ionosphere away from its normal states and how to more precisely forecast such changes in the ionosphere.

A poorly understood question is the Long-duration Positive Storms (LPSs) in the equatorial ionosphere. Here, the LPSs are identified as the relative deviation of the F₂ layer peak density (N_mF_2) exceeds 25% for more than 6 hours. Kuai *et al.*^[1] conducted a statistical analysis of the equatorial ionospheric LPS effects that occurred in

1998–2010. During the decade, 250 geomagnetic storms (minimum $Dst < -50$ nT) occurred, and only 204 storms were available for ionosonde observations at Jicamarca (12.0°S, 283.2°E), Peru. The occurrence of the 46 identified LPSs tends to decay approximately exponentially on the days after the main phase of geomagnetic storms. The disturbed electric fields are found to be essential in forming the equatorial LPSs. During the daytime LPSs, the disturbed zonal electric fields are mostly westward; for the nighttime LPSs, the significant uplifting of the F₂ layer is mostly caused by an eastward electric field.

There are a few reports on the occurrences of a Tongue of Ionization (TOI) in the ionosphere under weak to moderately disturbed geomagnetic conditions.

Utilizing the Global Positioning System (GPS) Total Electron Content (TEC), the Defense Meteorological Satellite Program (DMSP) measured the in situ total ion concentration and ion drift velocity, the Super Dual Auroral Radar Network (SuperDARN) measured the polar ion convection patterns, and the electron density profiles were obtained from the Poker Flat Incoherent Scatter Radar (PFISR). Liu *et al.*^[2] investigated the source and development of TOI during a moderate geomagnetic storm on October 14, 2012, as shown in Figure 1. Their results demonstrated that the TEC enhancements mainly come from the topside ionosphere, obvious changes are absent in the bottomside ionosphere and vertical plasma drifts. Additionally, there were no signatures of penetration of electric fields in the equatorial electrojet data and upward ion drifts at high latitudes.

The ionospheric responses to the geomagnetic activities driven by the co-rotating interaction region (CIR) events have become a hot topic in recent ionospheric studies. Chen *et al.*^[3] analyzed the effect of the weaker geomagnetic activities on the ionospheric variability during the 2007–2009 deep solar minimum. The effect of weaker geomagnetic activities on the Global Electron Content (GEC) shorter-term variation was significant during 2007–2009, when it was under relatively quiet

geomagnetic activity. The values of GEC were positively correlated with A_p . In contrast, the GEC variation was poorly correlated with A_p at shorter-term scales during 2003–2005, except under strong geomagnetic disturbance. Statistically, the contributions to the GEC shorter-term variations were comparable with the solar irradiance, geomagnetic activity, and meteorological sources during 2007–2009.

Chen *et al.*^[4] conducted an epoch analysis of global ionospheric responses to the recurrent geomagnetic activities. They analyzed 79 CIR events from 2004 to 2009. At high and middle latitudes, the TEC showed significant positive responses on the first day of the epoch. At all latitudes, most of the positive TEC effects always occurred 2–6 h after the CIR started at the local daytime and 10–18 h later at local nighttime. Case studies indicate that the positive response had a strong dependence on the southward component of the interplanetary magnetic field (IMF B_z) and solar wind speed. Negative responses following at the high latitudes of the American continent were related to the storm-time thermospheric composition (O/N_2) changes. During the recovery phase, the TEC positive disturbance at low latitudes sometimes could last 2–4 days, whereas at the middle to high latitudes the disturbance lasted only for 1 day in most cases. Moreover, the ionospheric response in North America was stronger than in Europe and Asia.

Liu *et al.*^[5] used the three-year observations of the Fabry Perot Interferometers (FPI) at Xinglong (40.2°N, 117.4°E) and Millstone Hill (42.6°N, 71.5°W) to study the Planetary Wave-Type oscillations (PWTOs) in thermospheric winds at a height of 250 km. The oscillations with periods of 4–19 days exhibit annual and semiannual variations. As an extension, Liu *et al.*^[6] included the 11-year (1989–1995 and 2010–2013) FPI data to investigate the 6–30 day oscillations of the thermospheric winds. There are prominent quasi-27-day oscillations in the zonal winds, highly correlated to the same periodic oscillations in Kp and SW during the solar maximum. The high correlation of the PWTOs to the solar wind speed and Kp indicates that the oscillations in the thermospheric neutral winds may possibly be influenced by the CIRs, the related high-speed solar wind, and the recurrent geomagnetic activity.

Liu *et al.*^[7] used observations by multiple instruments including GPS TEC, the critical frequency of F_2 -layer (f_0F_2) and peak height (h_mF_2) from ionosondes, vertical ion drift measurements from C/NOFS, and far ultraviolet

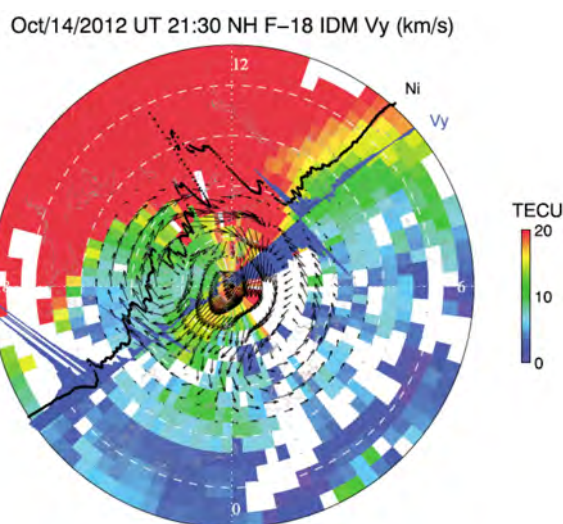


Fig. 1 Polar view of absolute TEC, cross-track velocity (V_y , blue line), and total plasma density (N_i , dark dotted line) in the magnetic latitude (40° – 90°) and the magnetic local time coordinate. The y -axes for V_y and N_i are perpendicular to the orbit. The plasma convection pattern observed by SuperDARN is also superimposed. The DMSP progressed from the nighttime sector to the morning sector. After Liu *et al.*^[2]

airglow measured by the Thermosphere-Ionosphere-Mesosphere Energetics and Dynamics (TIMED)/Global Ultraviolet Imager (GUVI) to investigate the profound negative ionospheric disturbances at the middle and low latitudes during the July 14–17, 2012, geomagnetic storm. They ascribed a strong inhibition of the Equatorial Ionization Anomaly (EIA) over East Asia in the recovery phase on July 16 to the combined effects of the intrusion of neutral composition disturbance zone and the long-lasting daytime westward Disturbance Dynamo Electric Field (DDEF). The daytime periodical intrusion of the negative phases appeared in the American longitudes for three consecutive days in the recovery phase of the storm.

The altitudinal dependence of the ionospheric responses to geomagnetic storms is yet to be resolved. Lei *et al.*^[8] combined the TEC data measured by the Jason, CHAMP, GRACE, and SAC-C satellites, the in situ electron densities from CHAMP and GRACE, and the vertical $E \times B$ drifts from the ROCSAT-1 to examine the ionospheric responses to the October 2003 superstorms. Strong positive storm effects were observed in the daytime TEC when IMF B_z was southward during the two main phases of the October 2003 storms. The TEC enhancement events occurred at the times with enhancements in the upward vertical drift, indicating a critical role of the electric fields in the electron density enhancements during these superstorms.

Chen *et al.*^[9] studied the response of topside ionospheric diffusive fluxes to the October 2002 geomagnetic storms. The daytime upward diffusive flux decreased and nighttime downward diffusive flux increased during the two geomagnetic storms. The variations in the diffusive velocity and flux during the main and recovery phases of storms were caused by changes in the ionospheric scale height.

Lei *et al.*^[10] used observations from the ground-based GPS receiver network, CHAMP and GRACE satellites, and ionosondes to examine the ionospheric variations over the Pacific Ocean and the American continent during the October 2003 superstorms. The topside TEC at low and middle latitudes showed significant increases during storms, while the bottomside TEC did not show considerable changes, indicating that the lower ionosphere made a minor contribution to the positive phase of the ionosphere. Their results suggested that the TEC increases at low and middle latitudes were also associated with the storm variations in the effective plasma

scale height.

Mao *et al.*^[11] investigated the ionospheric response of the October 2, 2013, storm in China. A wave structure was detected with periods of about 1–2 h and a horizontal speed about $680 \text{ m} \cdot \text{s}^{-1}$, propagating equatorward in the 200 to 400 km height range. In the low latitudes, compared with those in a quiet day, the storm day $h_m F_2$ increased considerably, accompanied by a notable decrease in TEC and $N_m F_2$, which might be a result of the eastward Prompt Penetration Electric Field (PPEF) and the subsequent westward DDEF. The storm-time TEC enhancement mainly occurred in the topside ionosphere, as revealed from the relative contributions of the topside and bottomside TEC.

Ding *et al.*^[12] conducted a comparative study of the Large-Scale Traveling Ionospheric Disturbances (LSTIDs). They identified a sum of 390 LSTIDs in China and 363 events in North America from the 2011–2012 observations. These LSTIDs propagated dominantly in south-, north-, and westward directions. The southward-moving LSTIDs over North America follow the similar diurnal and seasonal variations in geomagnetic disturbances, but they do not show such close relationships over China. The northward LSTIDs are mainly observed in China, mostly during geomagnetic active periods. Westward-traveling LSTIDs may be excited by the moving solar terminator, which is seen during local sunrise over both the regions.

Effectively and accurately extracting the ionospheric disturbance is important to study an ionospheric storm. Wang *et al.*^[13] introduced a new method, Spectral Whitening Method (SWM), to identify the aperiodic disturbances in the ionosphere. Although it is similar to the commonly used MMM (monthly median method), the SWM yields a better background than the MMM. The disturbances identified by the SWM have a Gaussian-type distribution, which simplifies further statistical analysis by virtue of the well-known characteristics of the Gaussian-type distributions, and also simplifies the comparisons of the disturbances at different times. Chen *et al.*^[14] introduced the single-station index J_s and the planetary index J_p to measure the ionospheric state. The J_s index describes the local ionospheric variations well, while the J_p index captures the overall features of the ionospheric variations. The J_p index is closely correlated with the *Dst* index, but is not affected by solar activity.

Yuan *et al.*^[15] presented the influence of precipitating energetic ions caused by the Electromagnetic Ion Cy-

clotron (EMIC) waves in the sub-auroral ionospheric E region during the March 8, 2008 geomagnetic storm with observations being made by the Meteorological Operational (METOP-02) of the Polar Orbiting Environmental Satellites (POES), a GPS receiver in Vaasa of Finland, and the Finnish network of search coil magnetometers. The enhancements of the precipitating energetic ion flux within the proton anisotropic zone are found to be attributed to the interaction between the ring current ions and EMIC waves. With enhancements of the intensity of Pc1 waves, TEC increased accordingly. The result suggests that the precipitating energetic ions caused by the EMIC waves can lead to an obvious enhancement of the electron density and conductivities in the sub-auroral ionospheric E region during geomagnetic storms.

With observations of the Van Allen probes, low-altitude NOAA satellite, MetOp satellite, and a riometer, Li *et al.*^[16] analyzed the variations in precipitating energetic electron fluxes and cosmic radio noise absorption driven by the plasmaspheric hiss with respect to geomagnetic activities.

2 Ionospheric Climatology and Structures

The mid-latitude trough is a salient structure in the mid-latitude ionosphere. Yang *et al.*^[17] used the TEC data from 2000 to 2014 to statistically investigate its seasonal and magnetic local time variations. The trough depth increases with the solar flux index ($F_{10.7}$) and decreases with the solar zenith angle. The trough equatorward half-width decreases as the geomagnetic activity increases.

F-lacuna manifests itself as a partial or total disappearance of normal ionogram traces. F-lacuna is frequently observed at Zhongshan Station, Antarctica, during geomagnetic disturbances. Yang *et al.*^[18] presented the temporal characteristics of the F-lacuna and its correlation with geomagnetic activity, interplanetary magnetic field, and collocated TEC. Magnetic local time distribution of the F-lacuna occurrence exhibits a dawn–dusk asymmetry. The magnetic activity is found to have a strong positive correlation with the F_2 and total lacuna. It is worth mentioning that the F-lacuna is associated with the simultaneous TEC condition, which has a positive correlation with the F_1 -lacuna occurrence and a strong negative correlation with the F_2 and total lacuna. Yang *et al.*^[19] simulated the combined effect of

soft precipitation and electric field on the polar ionosphere near the cusp region. Results showed that the F region electron density decreases effectively, when the local electric field exceeds $80 \text{ mV}\cdot\text{m}^{-1}$.

The nighttime enhancement in electron density is a unique ionospheric phenomenon. Zhang *et al.*^[20] collected the f_0F_2 data recorded from 4 Japanese ionosonde stations from 1948 to 2011 to investigate the variations of nighttime enhancements. Their results show seasonal solar activity variations in the nighttime electron density enhancements. The pre-midnight enhancements have a higher occurrence probability in the summer months than in the winter months and an opposite one for the post-midnight enhancements. The nighttime enhancement occurrence clearly shows a negative solar activity dependence.

Chen *et al.*^[21] investigated the global features of the nighttime enhancement of N_mF_2 based on the ionospheric electron density profiles measured by the Constellation Observing System for Meteorology, Ionosphere, and Climate (COSMIC) during the 2007–2009 solar minimum. The results indicated that the nighttime enhancement of N_mF_2 with duration longer than 2 hours mainly appears in the winter hemisphere with dips larger than 45° . The magnitude of N_mF_2 enhancement reaches maxima (minima) at the geomagnetic latitude of about 40° – 50° (60° – 70°), with larger magnitude in the northern winter hemisphere than in the southern winter hemisphere (Figure 2). The longitudinal variation of the nighttime enhancements is also evident, especially in the southern winter hemisphere.

The dusk-to-night enhancement in N_mF_2 is a popular mid-latitude phenomenon in the summer hemisphere. Chen *et al.*^[22] collected the ionosonde observations in East Asia–Australia to investigate the dusk-to-night enhancement in mid-latitude summer N_mF_2 . The results indicated that the dusk-to-night enhancement is remarkably dependent on the latitudinal location and is asymmetrical between the southern and northern ionosonde stations more evidently in the northern hemisphere. The dusk-to-night enhancement shows opposite trends with solar activity, which is somewhat different from previous conclusions.

Le *et al.*^[23] carried out case-control simulations on the mechanisms of the nighttime enhancements in the low-latitude ionosphere, which was reported in Liu *et al.*^[24] Figure 3 illustrates the modeling results and observations over Sanya (109.6°E , 18.3°N ; dip lat. 12.8°N ,

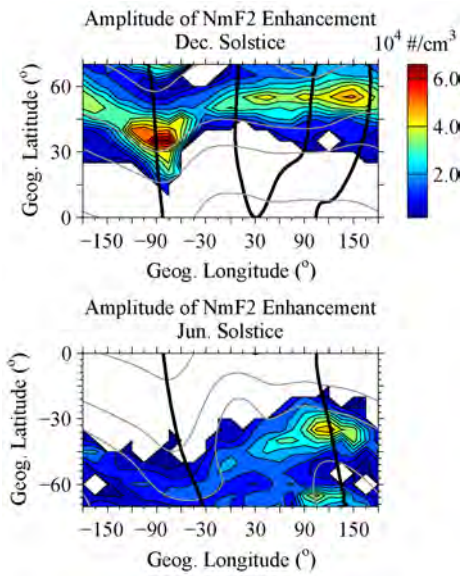


Fig. 2 Magnitude of N_mF_2 nighttime enhancement (top) in the northern winter hemisphere and (bottom) in the southern winter hemisphere. The black thick lines denote the zero geomagnetic declination; the grey lines are dip isolines (from top to bottom: dip=80°, 60°, 45°, and 0° for the northern winter hemisphere and dip=0°, -45°, -60°, and -80° for the southern winter hemisphere). After Chen *et al.*^[21]

geomagnetic latitude 8.2°N). Their results confirm the earlier conclusion that the westward electric field is the main driving force for the nighttime enhancement. The

phase of the electric field is important in forming the enhancement. Delayed westward electric field can produce significant post-midnight enhancement as observed at Sanya. The equatorward neutral wind is found to modulate the formation of the nighttime enhancement at geomagnetic latitudes below 15°N. The combined effects of the two drivers cause significant equatorward/downward plasma flux, which results in the enhancement of the electron density and drop in the ionospheric peak height.

The EIA is the most significant structure in the low latitudinal and equatorial ionosphere. The TEC over the equatorial ionization anomaly region do not always have two crests; sometimes there is only an obvious single crest. Huang *et al.*^[25] analyzed the morphological features of the single crest phenomenon in the TEC around the 120°E longitude during the geomagnetic quiet periods compared with the International Reference Ionosphere extended to Plasmasphere (IRI-Plas) model. Their results show that the single crest phenomena mainly occurred during the extremely low solar activity days, the corresponding f_oF_2 showed an obvious asymmetry or even only a single peak.

Using the COSMIC radio occultation measurements, Luan *et al.*^[26] investigated the hemispheric asymmetry (or summer–winter difference) of the EIA crests. The

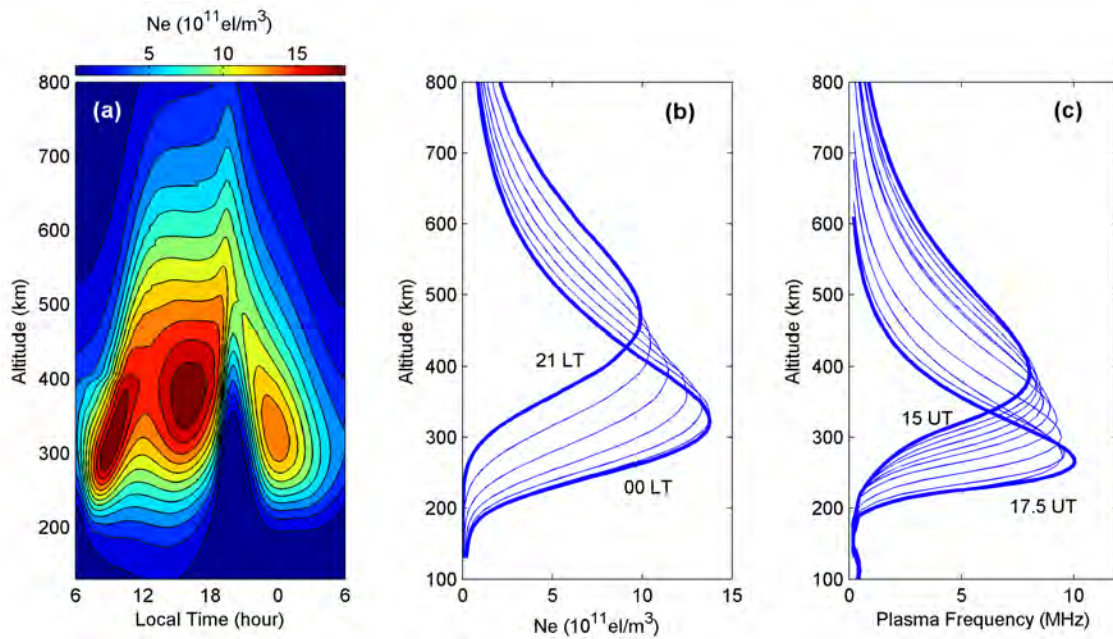


Fig. 3 (a) Temporal variation of the simulated electron density on DOY=82 at Sanya. (b) Height profiles of the simulated electron density from 21:00 LT to 00:00 LT at an interval of 0.5 h. (c) Height profiles of the ionogram-derived electron density measured from 15:00 UT to 17:30 UT at an interval of 15 min over Sanya on May 28, 2012. After Le *et al.*^[23]

results indicated that the inflection point of the EIA hemispheric asymmetry index occurs in the morning. The EIA asymmetry in the afternoon depends on the solar flux, and there is no dependency in the morning. Luan *et al.*^[27] first reported the daytime double crests of $h_m F_2$. Evident double crests of $h_m F_2$ occurred at around $\pm 10^\circ$ geomagnetic latitude with a trough over the magnetic equator during low solar activity and at March equinox. They named this phenomenon as Equatorial Height Anomaly (EHA) of the ionospheric F_2 layer. The double crests become less obvious during the September equinox and disappear at solstices.

It is an interesting to note how the ionosphere varies when solar Extreme Ultraviolet (EUV) irradiance decreases far below the normal levels. Taking the constraint of zero TEC under the case when the solar EUV disappears, Chen *et al.*^[28] extrapolated the ionospheric variations under extremely low solar EUV conditions based on JPL TEC maps and the EUV flux measured by the solar EUV Monitor onboard the Solar Heliospheric Observatory satellite (SOHO/SEM). The results indicated that there are four types of nonlinear variation trends of TEC versus EUV over the whole EUV range from zero to the solar maximum level. The climatological features of nighttime TEC under extremely low solar EUV conditions may differ from those during normal solar cycles. With a continuous decrease in solar EUV, GEC should vary largely in accordance with the GEC-EUV trend during the normal solar cycles and the seasonal fluctuation of the GEC declines.

As for the ionospheric response to the solar EUV variations, Chen *et al.*^[29] further presented the different responses of the global ionosphere to the solar cycle and solar rotation variations in EUV based on the daily mean GEC and SOHO/SEM EUV flux. There is a significant time lag effect for the solar rotation variations of the GEC and EUV; it generally shows a decreasing trend with decreasing solar activity, and a 1-day lag dominates. In contrast, there is no evident time lag effect for the solar cycle variations of GEC and EUV. The GEC versus EUV slopes are different for the solar cycle and for three solar rotation variations; the slope of the solar cycle is significantly higher than that of solar rotation by about 40%. Their results indicate the possible difference between the ionospheric climatology and weather.

Following the prolonged and extremely quiet solar activity from 2008 to 2009^[30], the 24th solar cycle started

slowly. The observations of sunspots, $F_{10.7}$, and EUV irradiance all indicate that the Sun is very inactive in the first half of the solar cycle 24, which makes the current solar cycle the weakest since solar cycle 14. Similarly, $f_0 F_2$ and GEC are both significantly lower than the previous solar cycles. The current weak solar cycle is challenging our knowledge of the thermosphere-ionosphere system^[31-32].

Based on the DEMETER satellite observations, Zhang *et al.*^[33-34] studied the solar cycle variations in the electron density in the topside ionosphere (660–710 km) during low solar activity years in 2005–2010, in which the electron density N_e reduced by more than 50% in three years, from 2006 to 2008, at the equatorial and middle latitudes. Zhang^[35] revealed the overestimation of N_e by the IRI model. There is only an equatorial peak structure in N_e at 660 km during solar minimum, not the double-crest structure predicted in the IRI model. Zhang *et al.*^[36] found an abnormal enhancement in the solstitial asymmetry between both the hemispheres during 2008–2009.

By using the observations of the IAP (Instrument d'Analyse du Plasma) onboard the DEMETER satellite, Zhang *et al.*^[38] analyzed the solar cycle variations in ion density (N_i), composition (O^+ , H^+ , and He^+), and temperature (T_i) at local time 10:30 and 22:30 during 2005–2010. N_i and daytime T_i shows positive correlation with solar flux, while $[H^+]$, $[He^+]$, and nighttime T_i varies negatively with solar flux.

The Chapman scale height (H_m) measures the electron density profile of the F_2 layer. H_m is an important parameter in extrapolating the topside electron density profile from the bottom side. Using the Beijing digisonde observations from 2010 to 2014, Xie *et al.*^[39] analyzed the diurnal and seasonal solar activity variations of H_m . They also explored the correlations between H_m and $f_0 F_2$, $h_m F_2$ and the IRI lower thickness parameter B_0 . Based on the EISCAT Svalbard Radar (ESR) observations, Qiao *et al.*^[40] statistically studied the H_m at high latitudes. With observations of the ESR between 1997 and 2008, they analyzed the statistical characteristics of the polar H_m with local time, season, and solar activity under quiet geomagnetic conditions. It shows a diurnal trend, reaching a maximum in the morning, a minimum in the afternoon, the highest amplitude in summer.

Luan *et al.*^[41] investigated the longitudinal variations of the nighttime auroral E-layer electron density. With

the data of COSMIC and TIMED/GUVI, they found that, in winter, a relatively larger electron density was located in 120° – 310° magnetic longitude in the northern hemisphere and in 170° – 360° magnetic longitude in the southern hemisphere. The greater maximum density occurred in the northern hemisphere than in the southern one, which was generally associated with the more intense auroral precipitation intensity during the local winter. In the local summer and equinox, the longitudinal variations of the electron density were the combined results of the auroral precipitation and solar radiation.

Climatological features of N_mF_2 in the Arctic and Antarctic stations are investigated and compared using long-term observations from the dynasonde measurements at Tromso station, the ESR measurements at Longyearbyen station, and the DPS-4 digisonde measurements at Zhongshan station, Antarctica^[42]. Xu *et al.*^[43] found that N_mF_2 increases linearly with solar activity indices most of the time at all three stations, illustrating that the solar radiation is the primary factor in the formation of the ionosphere. There exists an apparent “saturation effect” at Zhongshan in the southern summer and an “amplification effect” at Tromso and Longyearbyen in the northern winter. For the diurnal variations, N_mF_2 is highly sensitive to solar activity variations at around noon in Tromso, around magnetic noon in Longyearbyen, and between the two in Zhongshan. Zhang *et al.*^[44] simulated in further detail the winter N_mF_2 in both hemispheres for the solar minimum. The N_mF_2 peak at Zhongshan station is due to the transportation of the photoionization, while the auroral precipitation is the main cause for the major features of N_mF_2 at Svalbard.

The additional stratification of the F_2 layer, the so-called F_3 layer, is a phenomenon in the equatorial and low-latitude ionosphere. Zhao *et al.*^[45] collected electron density profiles data for about 8 years using the COSMIC radio occultation technique to study the F_3 layer. They identified the F_3 layer through the altitude differential profile featuring two maxima existing in the selected electron density profiles (see Figure 4). There were ~37000 (bottomside) and 25000 (topside) cases of F_3 layer out of ~1.27 million occultations from April 2006 to August 2014. The latitude distribution shows a tendency to form a single crest at a high altitude. They further built an empirical model of the F_3 layer occurrence.

Various dynamic processes in the solar wind-magnetosphere-ionosphere coupling can directly be in-

involved in the polar ionosphere along the magnetic field lines and can generate various irregularities in the polar ionosphere. The most common irregularity is the polar cap patch, in which the motion and associated density gradients give variable disturbances to the high-frequency radio communications, over-the-horizon radar location errors, and disruption and errors to satellite navigation and communication. Therefore, it is very helpful to study the formation mechanism and evolution feature of the polar cap patches for understanding the solar wind-magnetosphere-ionosphere coupling process, and can provide further physical basis for modeling the polar ionosphere. Zhang *et al.*^[46] reviewed the recent progresses by the Chinese community regarding the formation mechanism and evolution feature of the polar cap patches.

Further, by tracking the formation and full evolution of the polar cap patches in the polar ionosphere, Zhang *et al.*^[47] directly observed the full Dungey convection cycle for southward IMF conditions. The patches were initially segmented from the dayside storm enhanced density plume at the equatorward edge of the cusp, by the expansion and contraction of the polar cap boundary due to pulsed dayside magnetopause reconnection. Convection led to the anti-sunward patches entering the polar cap. Changes in convection over time resulted in the patches following a range of trajectories, each of which differed somewhat from the classical twin-cell convection streamlines. Pulsed nightside reconnection, occurring as a part of the magnetospheric substorm cycle, modulated the exit of the patches from the polar cap. After being ejected from the polar cap, the patches broke up into a number of plasma blobs and returned sunward in the auroral return flow of the dawn and/or dusk convection cell. The full circulation lasts for about 3 hours.

3 Ionosphere, Plasmasphere, and Lower Atmosphere Couplings, and Their Possible Seismic Signatures in the Ionosphere

The atmospheric tides are an important agent in the coupling between ionosphere and lower atmosphere. Wan and Xu^[48] reviewed the progress in this field made by Chinese scholars. Ren *et al.*^[49] simulated the influence of the Diurnal Eastward-3 non-migrating (DE3) tide mode on the equinoctial asymmetry of the zonal mean ionospheric electron density by separately including the September and March DE3 tide at the lower boundary of the GCITEM-IGGCAS model. Compared

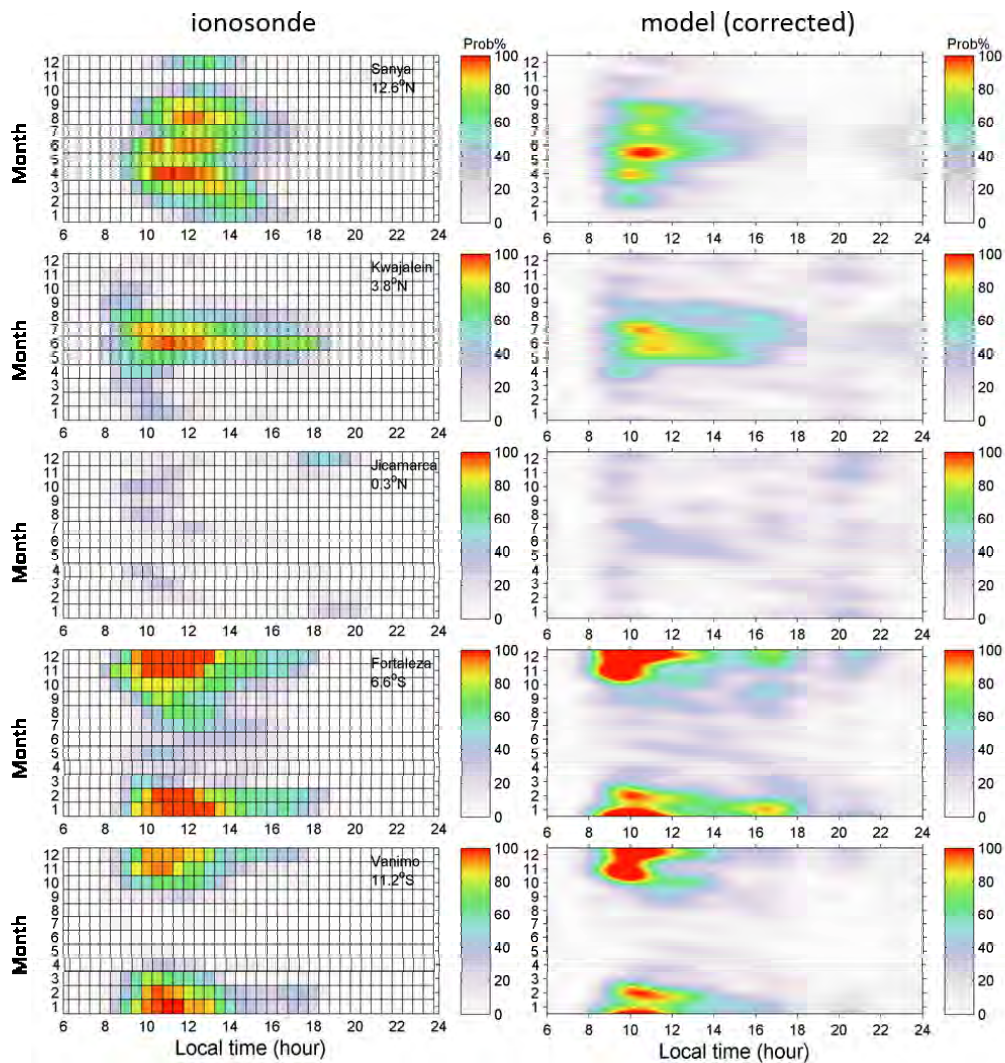


Fig. 4 Left panels represent the occurrence probabilities calculated from five ground ionosonde observations, while the right panels show the corrected reconstructed occurrence of F_3 at corresponding sites based on the COSMIC data. After *Zhao et al.*^[45]

with the September case, the March DE3 tide mainly decreases the lower ionospheric zonal mean electron density and increases the electron density at higher altitudes. In the low-latitude ionosphere, the DE3 tide drives an EIA structure, which suggests that the DE3 tide affects the longitudinal mean equatorial vertical $E \times B$ plasma drifts. The EIA equinoctial asymmetry decreases with solar activity. The non-migrating tides from the lower atmosphere may significantly modulate the structure of the ionosphere and the thermosphere. Lei *et al.*^[50] investigated the modulation of the non-migrating tides on both the EIA and the Equatorial Thermosphere Anomaly (ETA) on the basis of the Thermosphere-Ionosphere Electrodynamics General Circulation Model (TIE-GCM) simulations. Both the EIA and the ETA display an obvious zonal wave-4

structure. The simulations reveal that the zonal wave-4 structure of the ETA is mainly caused by the direct response of the upper thermosphere to the diurnal eastward wave number 3 and semidiurnal eastward wave number 2 non-migrating tides from the lower atmosphere. The ion-neutral coupling is only a minor contributor.

Wang *et al.*^[51] used the JPL global ionospheric maps from 1999 to 2013 to analyze the tidal patterns in the ionospheric TEC. The space-time spectral analysis results showed significant seasonal variations in the amplitudes of DE2, DE3, SPW3, and SPW4. The tidal components have a prominent latitudinal asymmetry and a saturation effect on the solar activity.

The ion-neutral collision frequency is a critical parameter in the ionosphere-thermosphere coupling. In previous studies, the effect of neutral winds was ne-

glected in the derivation of the ion-neutral collision frequency at high latitudes. Based on the TIE-GCM simulations, Dang *et al.*^[52] evaluated the effect of the neutral wind on the estimation of the ion-neutral frequency from the ion momentum equation. Their results illustrated that, even at high latitudes, the effects of the neutral wind should always be considered in deriving the ion-neutral collision frequency, especially at night.

An earthquake initiates varying degrees of the movement of the earth–atmosphere boundary. The excited atmospheric waves at the air–ground interface will propagate up to the upper atmosphere and affect the distribution of neutral and charged particles. Song *et al.*^[53] studied the coseismic ionospheric disturbances during the May 12, 2008, Wenchuan Earthquake. The acoustic gravity waves were excited by the partial transformation of the acoustic waves that originated from the energy release of the earthquake near the epicenter. The directional preferences of the coseismic ionospheric disturbances may be associated with the oblique geomagnetic field lines and the background wind filtering effect.

Coseismic Ionospheric Disturbances (CIDs) after the tsunamigenic 2011 Tohoku Earthquake (Tohoku EQ, M_w 9.1) were observed thousands of kilometers away from the epicenter. Zhao and Hao^[54] conducted a retrospective investigation of the CIDs and geomagnetic responses to the 2008 Wenchuan Earthquake (M_w 7.9) using multiple observations of TEC, HF Doppler, and ground magnetometer. This is the very first report to present the CIDs recorded by different techniques at co-located sites simultaneously. Their results indicated that compared to the Tohoku case, the main directional lobe of the Wenchuan event is more distinct; it is perpendicular to the direction of the fault rupture. They further suggested that the different fault slips (inland or submarine) may affect the couplings of the lithosphere with the atmosphere.

It is helpful to identify the differences between seismo-ionospheric anomalies and quiet geomagnetic disturbances events. Xu *et al.*^[55] investigated the local time variation of Q-disturbances using the f_0F_2 data spanning ~ 3 solar cycles. A remarkable difference is presented in the local time variation of f_0F_2 between the earthquake-triggered and Q-disturbance events. Their results showed a well-pronounced nighttime peak for positive disturbances induced by the Q-disturbance events, and the positive disturbances related to earthquakes mainly in daytime, especially during local afternoon.

In the ionosphere, there is an electromagnetic field abnormality before large earthquakes. Zhao *et al.*^[56] took the full-wave method to simulate the electromagnetic field abnormality at ULF in the ionosphere before two large earthquakes at different latitudes. The results show that the variations in the electric field before earthquakes seem to be related to the background ionospheric electron density and ion densities. The effect of the background plasma density on the electric field is larger at lower latitudes. The ion density hardly affects the field intensity. At the ULF band, the wave attenuation in the ionosphere is larger for higher frequency.

Zhang *et al.*^[57] studied the local nighttime perturbations in the ULF electric field (DC–15 Hz) observed by the DEMETER satellite (at 660–710 km) around strong earthquakes, especially over the two seismic regions of Indonesia and Chile located at equatorial and mid-latitude areas. Their results showed that the amplitude of the quasi-static electric field perturbations varies from 1.5 to 16 $\text{mV}\cdot\text{m}^{-1}$ over the epicentral area, mostly occurring in the upper ionosphere 1 day before the earthquakes. Shen *et al.*^[58] found that the N_e – T_e correlation median values at different seismic levels showed a clear decrease with earthquakes $>M7$. The close relationship among different parameters shows a clue to the coupling mechanism between the earthquake preparation processes and ionospheric disturbances.

Anomalous radon emanation around the epicenter is proposed to be a process to change the atmospheric electrical conditions. The modified electric fields probably cause ionospheric anomalies before earthquakes. Xu *et al.*^[59] numerically solved the electric potential equation in the presence of a vertical electric field of $1 \text{ kV}\cdot\text{m}^{-1}$ on the ground and considering the effect of radon emanation on atmospheric conductivity. Their results show that radon emanation can strengthen the atmospheric conductivity and increase the daytime ionospheric electric field by about 60%.

The study of the anomalous ionospheric variations before earthquakes has attracted the attention of geophysicists for many years, which has also been considered to be a possible method to identify the ionospheric earthquake precursors. Le *et al.*^[60] gave a brief summary of the recent progresses in this field. It is not confirmed whether these anomalies are really related to incoming earthquakes; there are many debates or doubts regarding this in the community. There are still no exact, direct, and integrated observations from the lithosphere to the

atmosphere and ionosphere, while the ionosphere has high day-to-day variations. To further investigate the pre-earthquake ionospheric anomalies, more rigorous work involving the observations of ground-based satellites at various heights and locations over the earthquake preparatory zone will be important. If various possible anomalies can be simultaneously measured at various heights, which self-consistently crosscheck each other, it will further help us to identify the pre-seismic anomaly and understand the possible mechanism for the pre-earthquake anomalies.

4 Ionospheric Irregularities and Scintillations

The ionospheric E- and F-region electron density irregularities may induce the GPS L-band ionospheric scintillation. Liu *et al.*^[61] investigated the statistical behavior of GPS ionospheric scintillation over Sanya. They found that the amplitude scintillation has an equinoctial maximum occurrence. Two GPS receivers are installed over Sanya with a short distance to estimate the zonal drifts of irregularities. The estimated drifts show a similar behavior during the two equinoxes, slowly decreasing from $150 \text{ m}\cdot\text{s}^{-1}$ at post-sunset to $50 \text{ m}\cdot\text{s}^{-1}$ near midnight. The initiation of scintillation is about 25 min earlier during September–October than that during March–April.

Ionograms recorded at Sanya during 2012–2013 were analyzed by Zhu *et al.*^[62] to investigate the occurrence characteristics of the spread-F and Satellite Traces (STs). The diurnal spread-F peaks post-sunset in equinox and post-midnight in the summer months. The spread-F during equinox mostly consists of spread-F (RSF) associated with the equatorial F-region irregularities. Not all RSF events were preceded by STs. The monthly mean $h_m F_2$ around sunset is apparently higher on RSF days than on non-RSF days, indicating both the sunset rapid rising of the F-layer and the presence of the lower F-region density perturbations are important factors for the equinoctial RSF onset and development. The summer midnight frequency spread-F over Sanya might be the local generation of F-region irregularities, not resulting from the decaying post-sunset equatorial RSF.

A vertical shear in the evening zonal plasma drifts is often measured by incoherent scatter radars near the magnetic equator with westward drifts below the F region peak and eastward drifts above. Li *et al.*^[63] re-

ported observations of a clear shear structure in the zonal drifts of 3 m irregularities inside spread-F backscatter plumes measured with a 47.5 MHz coherent scatter radar operated at Sanya. The spread-F 3 m irregularities are found to move westward at the lowest altitudes, while at higher altitudes the 3 m irregularities drift eastward. The vertical shear of zonal drifts was centered at an altitude of $\sim 300 \text{ km}$ altitude over Sanya, which maps an apex altitude of $\sim 650 \text{ km}$ at the magnetic equator, apparently higher than the usually observed apex altitudes of 250–450 km of the zonal velocity shear.

The generation of post-midnight F region irregularities at lower latitudes has been studied in recent years. Zhang *et al.*^[64] carried out a comparative study of ionospheric scintillations and spread F by analyzing the December 2011–November 2012 data recorded by a digital ionosonde, a GPS scintillation, and a TEC receiver collocated at Sanya. A good consistency exists between the temporal variations of GPS scintillation (represented by the S_4 index) and of ionogram spread F (represented by the QF index) in the pre-midnight period during equinox. However, in the post-midnight period during equinox and in the period from post-sunset to pre-sunrise during June solstice, moderate spread F is seen without concurrent GPS scintillations.

Huang *et al.*^[65] studied the ionospheric scintillation variations over the anomaly region using GPS measurements at the Shenzhen (22.59°N , 113.97°E) station of the Chinese Meridian Project. The L-band scintillation data extend from December 2010 to April 2014. Their results show that the scintillation events mainly occurred at the inner edge of the northern EIA crest in China. A total of 512 TEC depletions and 460 events of loss of lock are observed. Both kinds of events are likely to increase during high solar activity, especially the strong scintillations are often simultaneously accompanied by the TEC depletions and the loss of lock of the GPS receiver.

Using the data from an all-sky imager, a GPS monitor, and a digisonde around Xinglong, Sun *et al.*^[66] reported the generation, amplification, and dissipation of mesoscale Field-aligned Irregularity Structures (FAIs) at about 150 km, associated with a Medium-scale Traveling Ionospheric Disturbance (MSTID) event. Their detailed analysis illustrated that the mesoscale FAIs grew rapidly when they experienced southeast winds with a speed of about $100 \text{ m}\cdot\text{s}^{-1}$ measured by a FPI. A northeast polarization electric field within a depleted

airglow front can play a controlling role in the development of the mesoscale FAIs.

The daytime mid-latitude E region FAI is a rare phenomenon, especially in a solar eclipse. Only four cases of the E region FAIs were observed during the solar eclipse of 2009. The daytime FAIs observed by Chen *et al.*^[67] suggest that the eclipse-induced gravity waves and the weak ambient conductivity in the lunar shadow were likely responsible for the E region FAIs. Their observations address the outstanding question of the source of the mid-latitude E region FAIs.

Chen *et al.*^[68] discovered a surprising consistency between the striation tilt of the QP echoes and the drift direction of the plasma blobs. There are continuous echo traces, whereas the QP striation changed from negative to positive, and vice versa (Figure 5). A negative echo striation of the QP FAIs was recorded during the measured southward drift of the plasma blobs, and a positive one during the northward drift. Thus, the northward/southward-drifting striated FAIs in the view field of a coherent scatter radar might result in the positive/negative QP echo striation in the range-time-intensity plots.

Yang *et al.*^[69] investigated the equatorial ionospheric scintillations during the November 20, 2003, magnetic storm. The storm triggered GPS scintillations at Vanimo, an equatorial station. Severe depletions of the electron density are observed over Vanimo, and simultaneously

the enhancements present in its adjacent northern and southern regions are also seen. It is suggested that the prompt penetration of the eastward electric field associated with the southward turning of the IMF B_z elevates the ionospheric plasma to certain heights by the $E \times B$ mechanism, then the plasma drifts along magnetic lines to lower latitudes, thus forming the great north-south gradient of electron density and scintillations at the Vanimo station.

Meng *et al.*^[70] simulated the effects of ionospheric electron temperature and density by high-power radio waves. The model includes equations of energy conservation and continuity equation for electrons. The background information comes from the IRI-2007 and the neutral atmospheric model (NRLMSISE-00). The results show that the powerful high-frequency radio waves heat the ionospheric electrons, more efficiently for the X mode waves. The heating results in the rise in the collision frequency and the decrease in the loss rate of electrons. As a consequence, the electron density is modified. The perturbations of electron temperature and density gradually become saturated.

5 Ionospheric Models, Data Assimilation, and Simulations

Based on a two-layer Empirical Orthogonal Function (EOF) technique, Zhang *et al.*^[71] built an updated

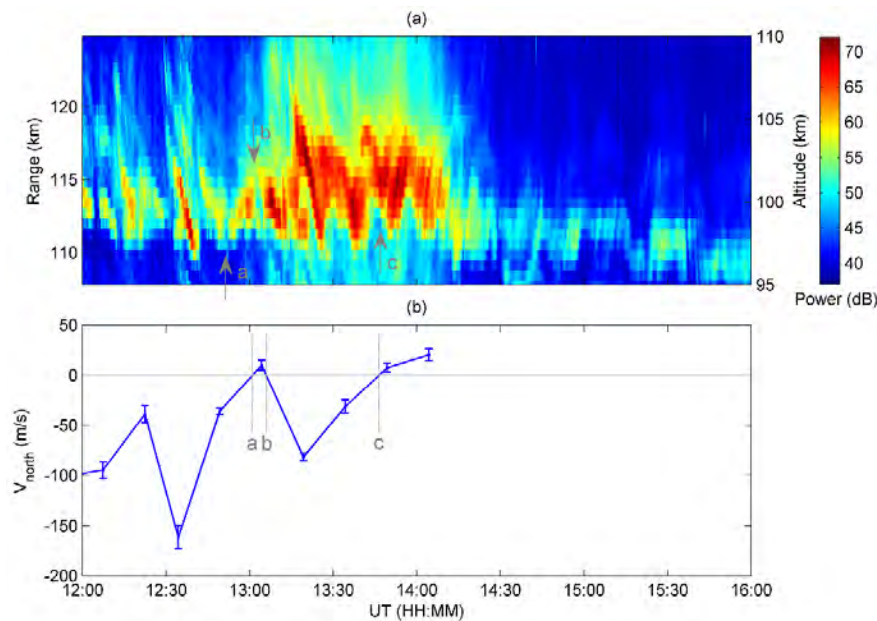


Fig. 5 (a) Range-Time-Intensity (RTI) plot showing the variable QP echoes on August 7, 2013. The left and right vertical axes show the radar range and altitude of the irregularities, respectively. (b) Mean velocities of the E-region plasma in the magnetic north direction. The sampling rate of the velocity was 15 min. After Chen *et al.*^[68]

global model of $h_m F_2$ by combining the data from COSMIC/FORMOSAT-3 RO measurements and from global ionosonde stations (including 10 Chinese stations). Their model reproduces the observational measurements of COSMIC RO and digisondes reasonably well, and it also has a better performance than the well-known IRI model.

The Chapman scale measures the shape of the profile of plasma density in the F_2 layer of the ionosphere. Liu *et al.*^[72] collected the in situ observations of plasma density at an altitude of 600 km from the ROCSAT-1 satellite and of simultaneous F peak parameters from an ionosonde operated at Wuhan (30.6°N, 114.4°E) in China to estimate the topside plasma density profiles by using the Chapman- α function and further retrieve the Chapman-scale height. They presented the climatology of the Chapman-scale height, which is significantly different from those at the ground-based ionograms, indicating that further improvements are required in the present extrapolation of the topside electron density profiles from the ground-based ionosonde observations.

The Vary-Chap profile can well represent the topside ionospheric electron density profiles. Wang *et al.*^[73] used the electron density profiles retrieved from the COSMIC ionospheric radio occultation observations to estimate the Vary-Chap scale heights. Their results showed that the Vary-Chap scale height was measured to be 400–550 km in 2007 at the mid-latitudes, with a prominent altitudinal dependence as well as diurnal and seasonal variations. The Vary-Chap scale heights are not closely correlated with the neutral or plasma-scale heights. Wang *et al.*^[74] used the maximum entropy method to model the features of the derived Vary-Chap scale heights.

Huang *et al.*^[75] developed a new empirical model of the topside plasma density around 600 km under relatively quiet geomagnetic conditions in terms of more than 5 years of ROCSAT-1 observations. The model results are in good agreement with observations from Hinotori, C/NOFS satellites, and the Incoherent Scatter Radar (ISR) at Arecibo. Their model highlights the importance of the effect of orbit altitude in improving the accuracy of plasma density variations in the topside ionosphere.

Ercha *et al.*^[76–77] developed a regional TEC mapping technique over China and its adjacent areas (70–140°E, 15–55°N). They adopted a Kalman filter data assimilation scheme to assimilate the Global Navigation Satellite Systems (GNSS) data from the Crustal Movement

Observation Network of China and International GNSS Service (IGS) networks. The background model they used is the IRI model. The regional TEC maps are generated at a spatial and temporal resolution of $1^\circ \times 1^\circ$ and 5 min, respectively.

Zhao *et al.*^[78] constructed a model 1 hour ahead of the prediction of $f_0 F_2$ with the AdaBoost-BP algorithm. Compared with other prediction methods, the effectiveness of the prediction model was verified by the data from nine ionosonde stations in the East-Asian region. Their model achieves a better performance as compared to BP neural network, support vector regression, and the IRI model.

Based on the Alouette/ISIS topside sounding observations, Zhu *et al.*^[79] developed a new topside profiler, which describes the topside ionosphere as a composite of two separate layers, the O^+ layer and the light-ions (H^+ and He^+) layer. The light-ions layer is characterized by an alpha-Chapman function with a scale height as a linear function of altitude. This new profiler performs the best among six topside profilers in the representing data from ISIS-1&2 and Alouette-1&2 observations. Meanwhile, the light ions contribute dominantly to the topside-ionospheric total electron content, especially in the night magnetic low and mid-latitudes.

Yu *et al.*^[80] developed an Ionosphere Data Assimilation Analysis System (IDAAS) to reconstruct a three-dimensional ionosphere with the GPS slant TEC and ionosonde data in China by using the IRI model as a background ionosphere and applying the Kalman filter to update the state with observations. Their results show that inversed slant TEC, $N_m F_2$, and vertical TEC all demonstrate great improvement of agreement with those observed from the ionosondes and TOPEX satellite independently. Based on the IDAAS system, Yu *et al.*^[81] investigated the deviation relative to the slant-to-vertical conversion (STV). The results indicate that the relative deviation induced by the slant-to-vertical conversion may be significant in certain instances; generally, the IDAAS TEC map is much closer to the “true TEC” than the STV TEC map.

Yu *et al.*^[82] constructed the maps of the ionospheric layer parameters ($f_0 F_2$, $h_m F_2$, $M(3000)F_2$, and $f_0 E$) over China based on an EOF analysis using the 20th solar cycle observations from 24-ionosonde in Asia. They decomposed the EOF modes from the IRI-07, assimilated the EOF patterns to get information on the amplitudes from ionosonde observations, which is further used

to construct the Chinese Ionospheric Maps (CIMs) of the layer parameters.

6 Ionospheric Dynamics and Electrodynamic

It is well known that the equatorial ionospheric vertical plasma drift does not represent a dawn enhancement in the statistical scenario, while the recent case measurements pointed out its existence. Zhang *et al.*^[83] for the first time investigated the occurrence of the dawn enhancement in the equatorial ionospheric vertical plasma drift from ROCSAT-1 observations. They found that, during geomagnetic quiet times, the dawn enhancements occur most frequently in June solstice and least frequently in December solstice. Their statistical survey shows that the occurrence depends on the magnetic declination, with peaks in regions near 320° longitude and during June solstice. The dawn enhancement occurs easily in regions with a large sunrise time lag in the conjugated E regions.

The altitude-varying structure of the plasma vertical drift has become an interesting research topic in recent years. Qian *et al.*^[84] carried out a simulation study on the impact of the altitude-dependent plasma drift on the equatorial ionosphere in the evening, under geomagnetically quiet conditions. F₃ layers in electron densities in the equatorial F region and “arch” latitudinal structures extending to lower middle latitudes were seen in the simulations driven by the observed altitude-dependent drift, indicating the importance of the altitudinal gradients in the vertical plasma drift velocity. The neutral winds do not have a significant effect on the simulated F₃ layers.

Based on the coordinated observations by the ISR, ionosonde, magnetometers, and GPS receivers, Xiong *et al.*^[85] investigated the electrodynamic effects on the equatorial and low-latitude ionosphere during the intense solar flare (X1.5/2B) on September 13, 2005. At the initial stage of the flare, the ISR and ionosonde measurements at Jicamarca show decreases of 10.14 m/s and 20 km in the upward vertical $E \times B$ drift velocity and the F₂-region peak height, respectively, while the Equatorial Electrojet (EEJ) strength over America indicates a sudden increase of 53.7 nT. The decrease in the upward vertical $E \times B$ drift velocity reveals the weakening of the eastward electric field during the flare. It suggests that the flare-induced increase in the Cowling conductivity

changes the ionospheric dynamo electric field and further results in the weakening of the eastward electric field and the decrease in the upward vertical $E \times B$ drift velocity.

As a consequence of the interactions of solar wind with the planetary magnetosphere and/or ionosphere, the penetration electric field induces strong electrodynamic processes in the ionospheres. Wei *et al.*^[86] discussed the recent understanding of the electric field penetration, especially the role of the magnetosphere during the electric field penetration, the patterns and drivers of the penetration electric field, and its influences on the equatorial spread F and the plasma distribution in the mid- and low-latitude ionosphere.

Chen *et al.*^[87] studied the latitude dependence of the lag in ionospheric response to solar eclipses. The rapid temperature drop in the lunar shadow during an eclipse will induce plasma flux from the protonosphere, which possibly makes up for the ionization loss. A greater downward plasma flux was generated at higher latitudes with a larger dip angle, and the ionosphere responses later.

7 Observation Methodology and Technique Progresses

The meridian project promoted the development of ground-based observation techniques and methodology, especially the ionospheric and upper atmospheric monitoring instruments. Chinese Journal of Geophysics published a Topic Issue with an aim to highlight the findings in the field of space physics and space weather^[88]. There are 38 articles published after peer-review. The issue mainly refers to some reports presented at a workshop on data processing and scientific analysis based on the meridian project. The subject of these investigations includes ionosphere, middle and upper atmosphere, geomagnetism and magnetosphere, solar activity and solar wind. In particular, there are two articles reporting the findings in planetary space environment.

With the development of BeiDou Navigation Satellite System (BDS), the signals from more than 30 GNSS satellites can be received, which will greatly strengthen the observation of ionosphere in China (see Figure 6). Xiong *et al.*^[89] utilized the TEC observations from BDS, GLONASS, and GPS to construct the ionospheric map, and investigate the travelling ionospheric disturbances, ionospheric irregularities, and ionospheric responses to solar flares. The results show that three systems of BDS, GLONASS, and GPS are obviously superior to any single

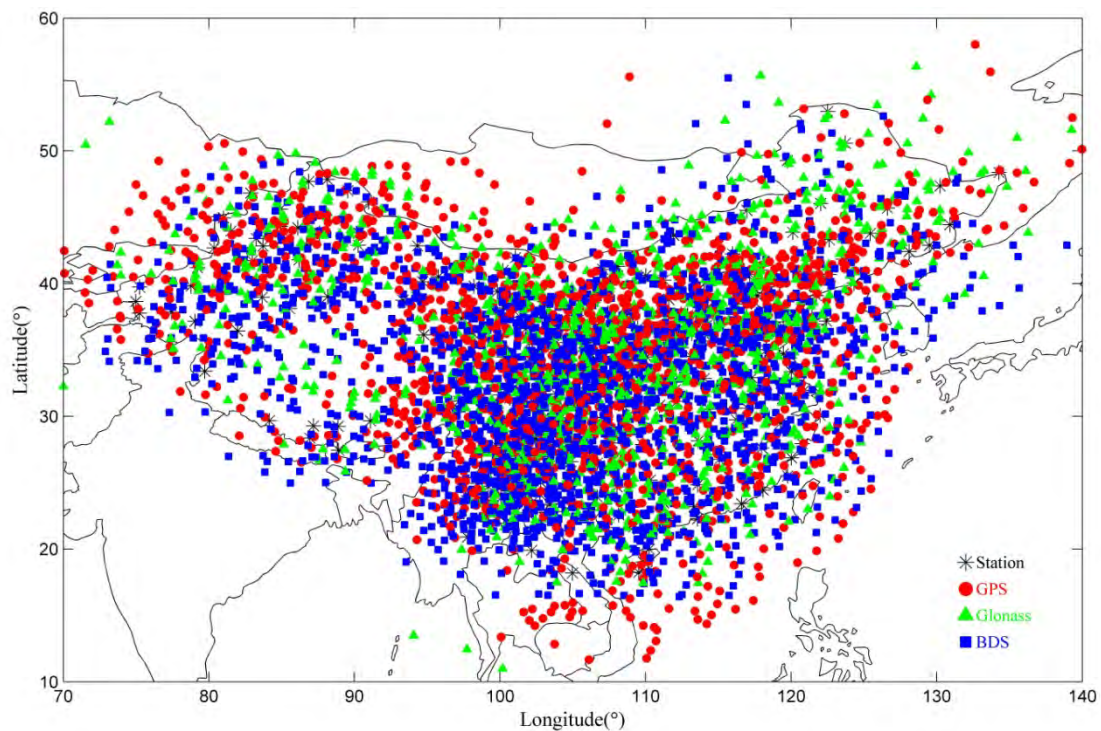


Fig. 6 Distribution of the intersection points between the ionospheric shell and the line from the satellite to the receiver over China at 12:00 LT on December 10, 2013. After Xiong *et al.*^[89]

GNSS system. With the wide setup of the multisystem GNSS receivers, it can serve as a solid base for monitoring and forecasting space weather and for the study of the ionosphere climatology and satellite navigation.

Global ionospheric TEC map (GIM) is one of the most important IGS products. Function-based and grid-based modeling methods are adopted by the IGS Ionospheric Associate Analysis Center (IAAC) individually to release the daily GIMs. The function-based modeling method takes a predefined function to estimate the GIM, so it cannot reflect the subtle variation in the ionospheric TEC due to the smoothed distribution of TEC on a large scale. In contrast, the grid-based modeling captures the detailed pictures of the ionospheric TEC around the stations; however, it becomes poor over the ocean. Li *et al.*^[90] proposed a Spherical Harmonic function Plus generalized Trigonometric Series function (SHPTS) to improve the accuracy of the GIM computation. Compared with the existing approaches, the SHPTS could improve the ionospheric TEC estimates over the area significantly.

The Crustal Movement Observation Network of China (CMONOC), which includes the GNSS stations across mainland China, provides the continuous monitoring of the ionosphere over China. A series of approaches for the GNSS-based ionospheric remote sens-

ing and software have been proposed and developed by the Institute of Geodesy and Geophysics (IGG) in Wuhan^[91]. The retrieval of the ionospheric observables based on the Precise Point-Positioning (PPP) technique significantly improves the accuracy of the GNSS-based TEC, the IGGDCB approach for Differential Code Biases (DCB) estimation abandons the dependence on a large amount of global distributed stations, the proposed Generalized Triangular Series Function (GTSF) algorithm can capture the subtle variations in local ionospheric TEC.

The ionospheric tomography inverse algorithms are usually an ill-conditioned problem. The main methods to resolve the ill-posed problem are the constraint algorithms in the process of the ionospheric electron density inversion. Wen *et al.*^[92] proposed a Fitting Method by Selection of the Parameter Weights (FMSPW) to resolve the ill-posed problem. The correlation of the neighboring electron density is analyzed to devise a new scheme for constructing the parameter weights matrix, which efficiently resolved the ill-posed problem of the ionospheric tomography system.

Interferometry is useful in revealing fine-scale structures of ionospheric irregularity. Li *et al.*^[93] installed another receiving array of four 5-element Yagi antennas

in the north of the main East-West array of the Sanya VHF radar to implement the multiple interferometry baselines with components parallel and perpendicular to the magnetic meridian. These baselines provide an interferometer capability to detect the three-dimensional picture of low-latitude ionospheric Field-Aligned Irregularity (FAI) over Sanya. Using multiple non-colinear receiving baselines, an experiment for which the Sanya VHF radar operated as an interferometer was performed on July 10, 2013. The interferometry results show fine-scale structures of E-region FAI with a zonal scale size of 15 km or less. The periodic variations of the echo intensity shown in radar Range-Time-Intensity (RTI) maps were produced by spatially separated E-region irregularity patches. The patches drifted westward with a velocity of about $40\text{--}60\text{ m}\cdot\text{s}^{-1}$ and could be associated with propagating gravity waves.

Li *et al.*^[94] conducted an experiment on the spatial domain interferometry observations of meteor trail irregularities in August 2013 using the Sanya VHF coherent radar. They have observed more than 3000 Range-Spread meteor trail echoes (RSTEs). Among the trail echoes, the spatial structure of the meteor trail irregularities responsible for a single long-duration RSTE event persisting for ~ 4 min was reconstructed. This RSTE was found to be initially generated at altitudes of 90–115 km and aligned along the radar-beam boresight.

After about the first minute of the trail lifetime, the trail echo appeared only in a narrow altitude range of 94–98 km. The trail irregularities at lower range gates moved perpendicular to the geomagnetic field. The eastward drifts of the RSTE irregularities were found to decrease with altitude, *e.g.*, from $80\text{ m}\cdot\text{s}^{-1}$ at ~ 94 km to $20\text{ m}\cdot\text{s}^{-1}$ at ~ 100 km.

Regarding the radar meteor trail echoes, a long-standing question is how high the meteor echo can be detected in the Earth's atmosphere. Using the Sanya VHF coherent radar, Li *et al.*^[95] made interferometer measurements (Figure 7) from July 11 to August 10, 2013. They have found a new class of range-spread high-altitude meteor trail echoes, some of which appeared at ~ 170 km altitude lasting for more than 10 s. A statistical analysis on the local time dependence of the identified high-altitude meteor trail echoes events shows a maximum around 00:00LT–04:00LT. At altitudes above 130 km, the classical ablation-ionization process responsible for the formation of normal meteor trails in the 70–110 km region cannot be responsible for the formation of the high-altitude meteor trails. The results imply that there could be much more meteor mass input due to meteoroid sputtering at high altitudes in the Earth's atmosphere than was previously thought.

A Fabry-Perot Interferometer (FPI) system was deployed in Kelan (38.7°N , 111.6°E), central China, in

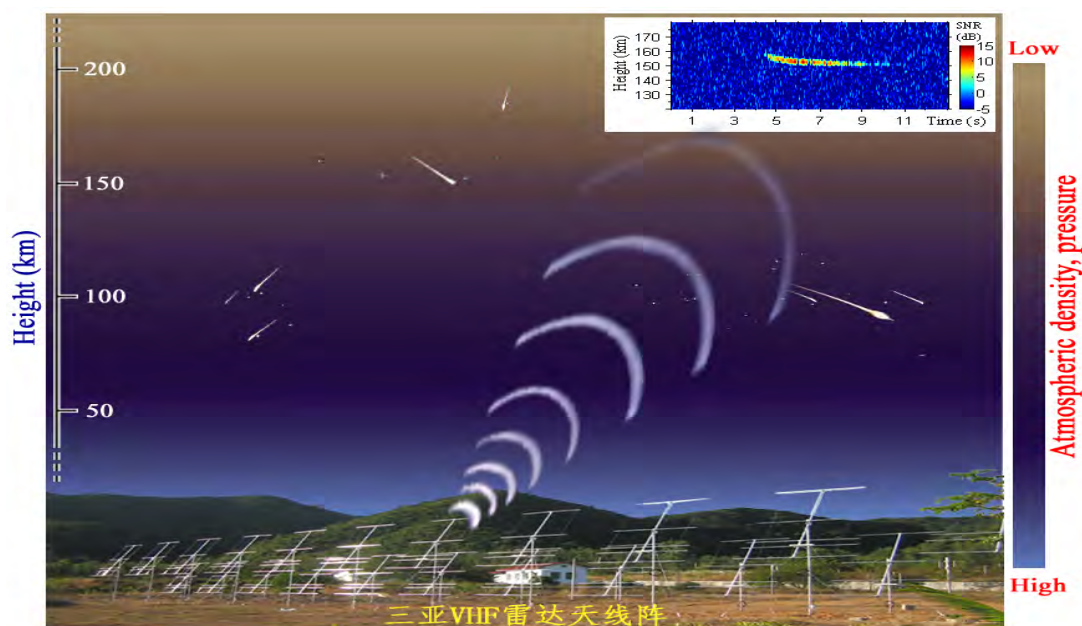


Fig. 7 Observations of a new class of range-spread High Altitude Meteor trail Echoes (HAMES) appeared above an altitude of 130 km, lasting more than 5 s by using the Sanya VHF radar interferometer. The right top inset shows a high-altitude meteor trail echo detected by the Sanya radar. After Li *et al.*^[95]



November 2011, which observes the airglows at wavelengths of 892.0 nm, 557.7 nm, and 630.0 nm emissions in the upper atmosphere, to derive the wind and temperature at heights of around 87 km, 97 km, and 250 km, respectively. Yu *et al.*^[96] validated the measurements from late 2011 through 2013 and investigated the morphology of wind in the mesosphere and thermosphere. Wang and Wang^[97] proposed an improved method for wind retrieval for ground-based Fabry-Perot Interferometer (FPI). The method can reduce the disturbance of bad fringes and advance the retrieval precision. The error calculation has considered the influence of the airglow intensity, CCD dark noise, and background emissions.

Wang and Wang^[98] improved the Atmospheric Ultraviolet Radiance Integrated Code (AURIC v1.2) to AURIC-2012. It can be used for the batch simulation of airglow globally, and also for batch retrieval along with satellite observations, such as O/N₂, electron density etc. The model supplies possibilities for further substitution of other modules. The limb column emission intensity (L-CEI) and Volume Emission Rate (VER) were calculated using the AURIC-2012 and were compared with the measurements of the TIMED/GUVI and Doppler Interferometer (TIDI), respectively.

Ding *et al.*^[99] presented the preliminary measurements of the Qujing incoherent scatter radar mainly including the variation of the ionospheric power profile and electron density. Combining the collocated ionosonde, they investigated some typical space weather characteristics including the wave-like disturbance, the location of the northern crest of the equatorial ionospheric abnormality, the enhancement of electron density after sunset, the ionospheric disturbance during a geomagnetic storm, and the day-to-day variations. These measurements show that the Qujing incoherent scatter radar may act as a good tool for ionospheric studies over southwestern China.

Hu *et al.*^[100–101] and Sun *et al.*^[102] validated the ionospheric peak parameters (N_mF_2 and h_mF_2) retrieved from COSMIC measurements by using the ground-based ionosonde measurements. Their results indicate that the ionospheric peak parameters from both measurements are generally in good agreement. However, the discrepancies between the COSMIC N_mF_2 and ionosonde N_mF_2 vary with longitude. The correlations coefficients between COSMIC N_mF_2 and ionosonde N_mF_2 at Sanya are inversely correlated with solar activities.

Fu *et al.*^[103] newly designed an instrument called Far Ultraviolet Nighttime Ionospheric Photometer (FNIP) for Low Earth Orbit (LEO) missions to observe the night airglow nadir at OI 135.6 nm emission. The OI 135.6 nm emission is produced by ionospheric O⁺ + e recombination. The horizontal information on the nighttime ionosphere will be obtained with a spatial resolution of about 1.6°×3.8°. This simple, highly robust instrument achieves a sensitivity of about 400 counts/s/ Rayleigh at 135.6 nm with stray light less than 2%, excluding the OI 130.4 nm emission and Herzberg oxygen bands.

Mapping function is important in converting the slant TEC to vertical TEC. Zhong *et al.*^[104] utilized the GNSS observations from LEO satellites to study the LEO-based mapping function. They compared the vertical TEC converted by these mapping functions and the vertical TEC directly calculated by the model to discuss different mapping functions. For the LEO-based TEC conversion, their results show that the ionospheric effective height increases linearly with the orbit altitudes, and the F&K mapping function along with the ionospheric effective height from the centroid method is more suitable.

Zhong *et al.*^[105] examined whether the long-term variation of the GPS differential code biases (DCBs) is associated with the ionospheric variability. The GPS DCBs released by IGS is compared with the estimated DCBs from LEO satellites. The results showed that, though the GPS DCBs show solar-cycle-like variations, their long-term variation is not contributed to the ionospheric variation. Instead, it is attributed to the GPS satellite replacement with different satellite types and the zero-mean condition imposed on all the satellite DCBs.

8 Planetary Ionospheres

Unlike Earth, Venus and Mars have no global intrinsic dipolar field, thus their ionospheres directly interact with solar wind rather than the indirect interaction via coupling, with the magnetosphere in between. Such a direct interaction produces some plasma regimes and/or structures that are different from the observations in the Earth's magnetosphere. The Martian ionosphere has a definite upper boundary, which is called ionopause, separating the solar wind and ionospheric plasma. The ionopause is usually identified from as a significant density gradient from an ionospheric electron density profile. An alternative indicator of ionopause is the

Photoelectron Boundary (PEB) determined from the electron energy spectrum at some specific energy range. To investigate the difference of them, Han *et al.*^[106] have examined the Mars Express data during 2005–2013, taking the electron density profile from Mars Advanced Radar for Subsurface and Ionospheric Sounding (MARSIS) and PEB from Analyzer of Space Plasmas and Energetic Atoms (ASPERA-3). They found that the average position of the PEB is ~ 200 km higher than that of the ionopause, which corresponds to 10^3 cm^{-3} in the electron density profile. The discrepancy can be explained by the cross-field transport of photoelectrons.

The Venusian ionosphere interaction with solar wind produces an induced magnetosphere, and also affects the bow shock. Such an interaction is strongly controlled by IMF and produces asymmetries relative to the IMF direction in the Venusian space environment. By examining a large dataset of bow shock crossings observed by Venus Express (VEX) during its long-lasting solar minimum between solar cycles 23 and 24, Chai *et al.*^[107] have investigated the control factors of the Venusian bow shock location and found that both the IMF magnitude and direction have the most important effect on the bow shock location. Chai *et al.*^[108] also found a significant hemispheric asymmetry in the Venusian bow shock location along the solar wind convection electric field, which proves that the ion pickup process by IMF is very important in the Venusian space environment.

Knowledge of the magnetic field morphology of the magnetotail in the near-Venus wake is essential, but it has rarely been surveyed. Rong *et al.*^[109] used the VEX magnetic field measurements to draw the global magnetic field morphology in the near-Venus magnetotail. They found that the draped magnetic field lines are directed equatorward in the region $0\text{--}1.5 R_V$ (R_V , Venus radius, 6052 km) downtail as it looks like “sinking” into the Venus umbra. They estimated the thickness of the magnetotail current sheet and the current density at the sheet center, and found that the tailward $\mathbf{j} \times \mathbf{B}$ force is stronger near the $+E$ -hemispheric flank. In contrast, the average magnetic field structure near the $-E$ -hemispheric flank is irregular, which suggests that dynamic activities preferentially appear there.

Venusian magnetotail exhibits evident flapping motion, but it is still unknown whether the induced current sheet exhibits a similar flapping motion in the Earth’s magnetotail. The major challenge in studying the Venusian magnetotail’s flapping motion is how to use the

single-point measurement to resolve the flapping properties. Recently, Rong *et al.*^[110] developed a new single-point technique, which is capable of qualitatively distinguishing the different flapping types, as well as the propagation direction. Rong *et al.*^[111] subsequently applied this technique to study the Venusian magnetotail flapping. The flapping comprises non-propagating steady flapping and the propagating kink-like flapping (Figure 8). The sources triggering the kink-like waves are located near the magnetotail flanks, not in the central region of the current sheet.

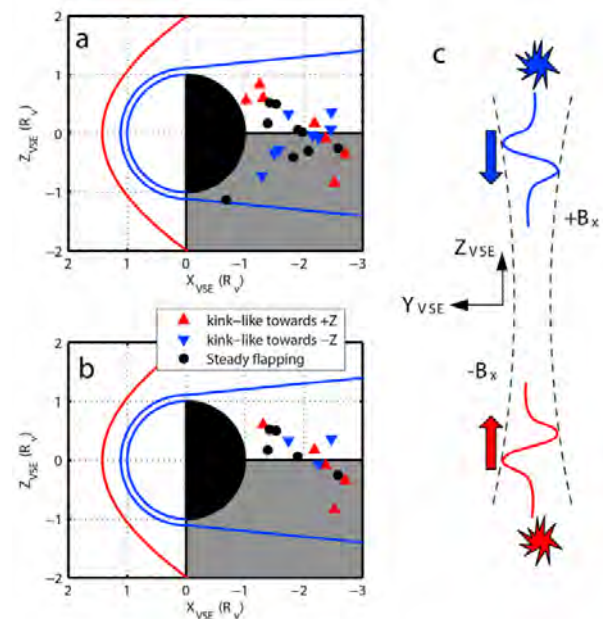


Fig. 8 Locations of the investigated flapping events of the Venusian magnetotail. (a) All events regardless of the plasma characteristics and (b) only the events associated with energetic plasma flux are shown. (c) An illustration of the propagation of “kink-like” flapping in the YZ plane is also presented. After Rong *et al.*^[111]

With the knowledge of planetary ionospheres, it is possible to understand the Earth’s paleoionosphere. Wei *et al.*^[112] built a theoretical model to describe the solar wind interaction with the paleoionosphere during a geomagnetic reversal, based on a similar model on Mars. They found that the oxygen ion escape driven by the solar wind can explain the drops in atmospheric oxygen level during the Phanerozoic era, which is thought to be related to biological mass extinctions.

Competing Interests

The authors declare that they have no competing interests.



Acknowledgements

Libo Liu greatly gratifies many colleagues for kindly providing their articles and pictures for the preparation of this national report. They are Yiding Chen, Huijun Le, Jing Liu, Manlian Zhang, Xiukuan Zhao, Ying Zhang, Jie Zhu, Linfeng Huang, Tao Yu, Bo Xiong, Qian Song, Haiyong Xie, Lianhuan Hu, Feng Ding, Zhipeng Ren, Tian Mao, Guozhu Li, Zonghua Ding, Gang Chen, Yongqiang Hao, Yong Wei, Tong Xu, Xuemin Zhang, Shufan Zhang, Houmao Wang, Zhigang Yuan, Jiuhou Lei, Xiaoli Luan, Beichen Zhang, Zhengping Zhu, Yanhong Chen, Qinghe Zhang, Xinliang Huo, Hanxian Fang, Shenggao Yang, and Biqiang Zhao. This research was supported by National Natural Science Foundation of China (41231065, 41321003), National Key Basic Research Program of China (2012CB825604), and the projects of Chinese Academy of Sciences (KZZD-EW- 01-3).

References

- [1] Kuai J, Liu L, Liu J, Zhao B, Chen Y, Le H, Wan W. The long-duration positive storm effects in the equatorial ionosphere over Jicamarca. *J. Geophys. Res. Space Phys.*, 2015, 120:1311- 1324
- [2] Liu J, Nakamura T, Liu L, Wang W, Balan N, Nishiyama T, Hairston M R, Thomas E G. Formation of polar ionospheric tongue of ionization during minor geomagnetic disturbed conditions. *J. Geophys. Res. Space Phys.*, 2015, 120: 6860-6873
- [3] Chen Y, Liu L, Le H, Wan W. Geomagnetic activity effect on the global ionosphere during 2007–2009 deep solar minimum. *J. Geophys. Res. Space Phys.*, 2014, 119:3747-3754
- [4] Chen Y, Wang W, Burns A G, Liu S, Gong J, Yue X, Jiang G, Coster A. Ionospheric response to CIR-induced recurrent geomagnetic activity during the declining phase of solar cycle 23. *J. Geophys. Res. Space Phys.*, 2015, 120:1394-1418
- [5] Liu X, Xu J, Zhang S, Jiang G, Zhou Q, Yuan W, Noto J, Kerr R. Thermospheric planetary wave-type oscillations observed by FPIs over Xinglong and Millstone Hill. *J. Geophys. Res. Space Phys.*, 2014, 119: 6891-6901
- [6] Liu X, Xu J, Zhang S-R, Zhou Q, Yuan W. Solar activity dependency of multiday oscillations in the nighttime thermospheric winds observed by Fabry-Perot interferometer. *J. Geophys. Res. Space Phys.*, 2015, 120:5871-5881
- [7] Liu J, Liu L, Nakamura T, Zhao B, Ning B, Yoshikawa A. A case study of ionospheric storm effects during long-lasting southward IMF B_z -driven geomagnetic storm. *J. Geophys. Res. Space Phys.*, 2014, 119:7716-7731
- [8] Lei J, Wang W, Burns A G, Yue X, Dou X, Luan X, Solomon S C, Liu YC-M. New aspects of the ionospheric response to the October 2003 superstorms from multiple-satellite observations. *J. Geophys Res Space Phys.*, 2014, 119:2298-2317
- [9] Chen G M, Xu J, Wang W, Lei J, Zhang S R. The responses of ionospheric topside diffusive fluxes to two geomagnetic storms in October 2002. *J. Geophys. Res. Space Phys.*, 2014, 119: 6806-6820
- [10] Lei J, Zhu Q, Wang W, Burns A G, Zhao B, Luan X, Zhong J, Dou X. Response of the topside and bottomside ionosphere at low and middle latitudes to the October 2003 superstorms. *J. Geophys. Res. Space Phys.*, 2015, 120:6974-6986
- [11] Mao T, Sun L, Hu L, Wang Y, Wang Z. A case study of ionospheric storm effects in the Chinese sector during the October 2013 geomagnetic storm. *Adv. Space Res.*, 2015, 56:2030-2039
- [12] Ding F, Wan W, Li Q, Zhang R, Song Q, Ning B, Liu L, Zhao B, Xiong B. Comparative climatological study of large-scale traveling ionospheric disturbances over North America and China in 2011–2012. *J. Geophys. Res. Space Phys.*, 2014, 119:519-529
- [13] Wang J S, Chen Z, Huang C M. A method to identify aperiodic disturbances in the ionosphere. *Ann. Geophys.*, 2014, 32:563-569
- [14] Chen Z, Wang J S, Huang C M, Huang L F. A new pair of indices to describe the relationship between ionospheric disturbances and geomagnetic activity. *J. Geophys. Res. Space Phys.*, 2014, 119. doi:10.1002/2014JA020438
- [15] Yuan Z, Xiong Y, Li H, Huang S, Qiao Z, Wang Z, Zhou M, Wang D, Deng X, Raita T, Wang J. Influence of precipitating energetic ions caused by EMIC waves on the subauroral ionospheric E region during a geomagnetic storm. *J. Geophys Res Space Phys.*, 2014, 119:8462-8471
- [16] Li H, Yuan Z, Yu X, Huang S, Wang D, Wang Z, Qiao Z, Wygant JR (2015) The enhancement of cosmic radio noise absorption due to hiss-driven energetic electron precipitation during substorms. *J. Geophys Res Space Physics* 120: 5393–5407. doi:10.1002/2015JA021113
- [17] Yang N, Le H, Liu L (2015) Statistical analysis of ionospheric mid-latitude trough over the Northern Hemisphere derived from GPS total electron content data. *Earth Planets Space* 67:196. doi:10.1186/s40623-015-0365-1
- [18] Yang S, Zhang B, Fang H, Liu J, Zhang Q, Hu H, Liu R, Li C (2014) F-lacuna at cusp latitude and its associated TEC variation. *J. Geophys Res Space Physics* 119. doi: 10.1002/2014JA020607
- [19] Yang S, Zhang B, Zhang Q, Fang H, Liu J, Zhou X, Zhang J (2014) Numerical simulation of the role of dayside magnetic reconnection in polar cap patch formation. *Chinese J Geophys. (in Chinese)* 57:3551-3557
- [20] Zhang Y, Liu L, Chen Y, Liu J, Yu Y, Li M (2015) Nighttime electron density enhancements at middle and low latitudes in East Asia. *SCIENCE CHINA Earth Sciences* 58:551-561. doi:10.1007/s11430-014-4953-x
- [21] Chen Y, Liu L, Le H, Wan W, Zhang H. N_mF_2 enhancement during ionospheric F_2 region nighttime: A statistical analysis based on COSMIC observations during the 2007–2009 solar minimum. *J. Geophys. Res. Space Phys.*, 2015, 120:10083–10095
- [22] Chen Y, Liu L, Le H, Wan W, Zhang H. Dusk-to-nighttime enhancement of mid-latitude N_mF_2 in local summer: Inter-hemispheric asymmetry and solar activity dependence. *Ann. Geophys.*, 2015, 33:711-718
- [23] Le H, Liu L, Chen Y, Zhang H, Wan W. Modeling study of nighttime enhancements in F region electron. *J. Geophys. Res Space Phys.*, 2014, 119: 6648-6656
- [24] Liu L, Chen Y, Le H, Ning B, Wan W, Liu J, Hu L. A case study of postmidnight enhancement in F-layer electron density over Sanya of China. *J. Geophys. Res. Space Phys.*, 2013, 118:4640-4648
- [25] Huang L, Wang J, Jiang Y, Huang J, Chen Z, Zhao K. A preliminary

- nary study of the single crest phenomenon in Total Electron Content (TEC) in the equatorial anomaly region around 120°E longitude between 1999 and 2012. *Adv. Space Res.*, 2014, 54:2200-2207
- [26] Luan X, Wang P, Dou X, Liu Y C M. Interhemispheric asymmetry of the equatorial ionization anomaly in solstices observed by COSMIC during 2007–2012. *J. Geophys. Res. Space Phys.*, 2015, 120:3059-3073
- [27] Luan X, Lei J, Dou X, Dang T. (2015) Double crests of peak height in the equatorial ionospheric F₂ layer observed by COSMIC. *J. Geophys. Res. Space Phys.*, 121. doi:10.1002/2015JA021611
- [28] Chen Y, Liu L, Le H, Wan W. How does ionospheric TEC vary if solar EUV irradiance continuously decreases. *Earth, Planets Space*, 2014, 66:52
- [29] Chen Y, Liu L, Le H, Wan W, Zhang H. Discrepant responses of the global electron content to the solar cycle and solar rotation variations of EUV irradiance. *Earth Planets Space*, 2015, 67:80. doi:10.1186/s40623-015-0251-x
- [30] Liu L, Chen Y, Le H, Kurkin V I, Polekh N M, Lee C C. The ionosphere under extremely prolonged low solar activity. *J. Geophys. Res. Space Phys.*, 2011, 116: A04320. doi:10.1029/2010JA016296
- [31] Hao Y, Shi H, Xiao Z, Zhang D. Weak ionization of the global ionosphere in solar cycle 24. *Ann. Geophys.*, 2014, 32:809-816
- [32] Yu S, Hao Y, Zhang D, Xiao Z. Low ionization level of northern midlatitude ionosphere in solar cycle 24. *Chin. J. Geophys.*, 57:3512-3522
- [33] Zhang X, Qian J, Shen X. Solar cycle variation of the electron density in the topside ionosphere at local nighttime observed by DEMETER during 2006–2008. *J. Geophys. Res. Space Phys.*, 2014, 119:3803-3814
- [34] Zhang X, Shen X, Liu J, Zeren Z, Yao L, Ouyang X, Zhao S, Yuan G, Qian J. The solar cycle variation of plasma parameters in equatorial and mid latitudinal areas during 2005–2010. *Adv. Space Res.*, 2014, 54:306-319
- [35] Zhang X. Electron density comparison between IRI 2007 and DEMETER satellite data in solar minimum year. *Terr. Atmos. Ocean Sci.*, 2014, 25:559-571
- [36] Zhang X, Shen X, Liu J, Yao L, Yuan G, Huang J. The asymmetrical features in electron density during extreme solar minimum. *Adv. Space Res.*, 2014, 54: 2236-2248
- [37] Zhang X, Shen X, Yuan G. The solar cycle variations of plasma parameters and their correlations at topside ionosphere from DEMETER during 2005–2010. *Adv. Space Res.*, 2015, 56:1374-1388
- [38] Zhang X, Shen X, Yuan G. The solar cycle variations of plasma parameters and their correlations at topside ionosphere from DEMETER during 2005–2010. *Adv. Space Res.*, 2015, 56:1374-1388
- [39] Xie H, Ning BQ, Liu LB, *et al.* Statistical analysis of the ionospheric Chapman scale height at Beijing. *Chin. J. Geophys.*, 2014, 57:3523-3531
- [40] Qiao Z, Yuan ZG, Qi F, *et al.* Statistical characteristics of the polar ionospheric scale height around the peak height of F2 layer with observations of the ESR radar: Quiet days. *Sci. China Tech. Sci.*, 2015, 58:687-694
- [41] Luan X, Wang W, Dou X, Burns A, Yue X. Longitudinal variations of the nighttime E layer electron density in the auroral zone. *J. Geophys. Res. Space Phys.*, 2015, 120:825-833
- [42] Xu S, Zhang B, Liu R, Guo L, Wu Y. Comparative studies on ionospheric climatological features of N_mF₂ among the Arctic and Antarctic stations. *J Atmos Solar-Terr Phys.*, 2014, 119:63-70
- [43] Xu S, Zhang B, Liu R, Guo L, Wu Y. Comparative studies on solar activity variations of N mF₂ at the Arctic and Antarctic Stations. *Chin. J. Geophys.*, 2014, 57:3502-3511
- [44] Zhang B, Yang S, Xu S, Liu R, Häggström I, Zhang Q, Hu Z, Huang D, Hu H. Diurnal variation of winter F region ionosphere for solar minimum at both Zhongshan Station, Antarctica, and Svalbard Station, Arctic. *J. Geophys. Res. Space Phys.*, 2015, 120:9929-9942
- [45] Zhao B, Zhu J, Xiong B, Yue X, Zhang M, Wang M, Wan W. An empirical model of the occurrence of an additional layer in the ionosphere from the occultation technique: Preliminary results. *J. Geophys. Res. Space Phys.*, 2014, 119:10204-10218
- [46] Zhang Q H, Zhang B C, Yang S G, Wang Y. Research progress of the plasma patches in the polar ionosphere. In Shi J K, Ye Y H, Liu Z X ed. *Adv Space Res*, 5, Science Press, 2015:352-378
- [47] Zhang Q H, Lockwood M, Foster J, Zhang S R, Zhang B C, McCrea I, Moen J, Lester M, Ruohoniemi J M. Direct observations of the full Dungey convection cycle in the polar ionosphere for southward interplanetary magnetic field conditions. *J. Geophys. Res. Space Phys.*, 2015, 120:4519-4530
- [48] Wan W, Xu J. Recent investigation on the coupling between the ionosphere and upper atmosphere. *Sci. China Earth Sci.*, 2014, 57:1995-2012
- [49] Ren Z, Wan W, Xiong J, Liu L. Influence of DE3 tide on the equinoctial asymmetry of the zonal mean ionospheric electron density. *Earth Planets Space*, 2014, 66:117. doi:10.1186/1880-5981-66-117
- [50] Lei J, Thayer JP, Wang W, Yue J, Dou X. Nonmigrating tidal modulation of the equatorial thermosphere and ionosphere anomaly. *J. Geophys. Res. Space Phys.* 2014, 119:3036-3043
- [51] Wang S, Huang S, Fang H. Wave-3 and wave-4 patterns in the low- and mid-latitude ionospheric TEC. *J. Atmos. Solar-Terr. Phys.*, 2015, 132:82-91
- [52] Dang T, Lei J, Dou X, Wan W. Feasibility study on the derivation of the O⁺-O collision frequency from ionospheric field-aligned observations. *J. Geophys. Res. Space Phys.*, 2015, 120:6029-6035
- [53] Song Q, Ding F, Yu T, Wan W, Ning B, Liu L, Zhao B. GPS detection of the coseismic ionospheric disturbances following the 12 May 2008 M7.9 Wenchuan earthquake in China. *Sci. China: Earth Sci.*, 2015, 58:151-158
- [54] Zhao B, Hao Y. Ionospheric and geomagnetic disturbances caused by the 2008 Wenchuan earthquake: A revisit. *J. Geophys. Res. Space Phys.*, 2015, 120: 5758-5777
- [55] Xu T, Hu YL, Wang FF, Chen Z, Wu J. Is there any difference in local time variation in ionospheric F₂-layer disturbances between earthquake-induced and Q-disturbance events. *Ann Geophys.*, 2015, 33:687-695
- [56] Zhao S, Zhang X, Zhao Z, Shen X. The numerical simulation of electric field perturbation before large earthquakes. *Ann. Geophys.*, 2014, 32:1487-1493
- [57] Zhang X, Shen X, Zhao S, Yao L, Ouyang X, Qian J. The charac-



- teristics of quasistatic electric field perturbations observed by DEMETER satellite before large earthquakes. *J. Asian Earth Sci.*, 2014, 79:42-52
- [58] Shen X H, Zhang X, Liu J, Zhao S F, Yuan G P. Analysis of the enhanced negative correlation between electron density and electron temperature related to earthquakes. *Ann. Geophys.*, 2015, 33:471- 479
- [59] Xu T, Zhang H, Hu Y, Wu J. Electric field penetration into the ionosphere in the presence of anomalous radon emanation. *Adv. Space Res.*, 2015, 55:2883-2888
- [60] Le H, Liu J, Zhao B, Liu L. Recent progress in ionospheric earthquake precursor study in China: A brief review. *J. Asian Earth Sci.*, 2015, 114:420-430
- [61] Liu K, Li G, Ning B, Hu L, Li H. Statistical characteristics of low-latitude ionospheric scintillation over China. *Adv. Space Res.*, 2015, 55:1356-1365
- [62] Zhu Z, Lan J, Luo W, Sun F, Chen K, Chang S. Statistical characteristics of ionogram spread-F and satellite traces over a Chinese low-latitude station Sanya. *Adv. Space Res.*, 2015, 56:1911-1921
- [63] Li G, Ning B, Liu L, Abdu MA, Wan W, Hu L. Shear in the zonal drifts of 3-m irregularities inside spread-F plumes observed over Sanya. *J. Geophys. Res. Space Phys.*, 2015, 120:8146-8154
- [64] Zhang Y, Wan W, Li G, Liu L, Hu L, Ning B. A comparative study of GPS ionospheric scintillations and ionogram spread F over Sanya. *Ann. Geophys.*, 2015, 33:1421-1430
- [65] Huang L, Wang J, Jiang Y, Chen Z, Zhao K. A study of GPS ionospheric scintillations observed at Shenzhen. *Adv. Space Res.*, 2014, 54:2208-2217
- [66] Sun L, Xu J, Wang W, Yue X, Yuan W, Ning B, Zhang D, de Meneses F C. Mesoscale field-aligned irregularity structures (FAIs) of airglow associated with medium-scale traveling ionospheric disturbances (MSTIDs). *J. Geophys. Res. Space Phys.*, 2015, 120:9839- 9858
- [67] Chen G, Wu C, Zhao Z, Zhong D, Qi H, Jin H. Daytime E region field-aligned irregularities observed during a solar eclipse. *J. Geophys. Res. Space Phys.*, 2014, 119, doi:10.1002/2014JA020666
- [68] Chen G, Jin H, Huang X, Zhong D, Yan C, Yang G. Strong correlation between quasiperiodic echoes and plasma drift in the E region. *J. Geophys. Res. Space Phys.*, 2015, 120. doi:10.1002/2015JA021566
- [69] Yang S G, Fang H X, Niu J. A case study on effect of the magnetic storm of 20 November 2003 on GPS ionospheric scintillation at Vanimo station. *Adv. Space Res.*, 2015, 56:1992-2000
- [70] Meng X, Fang H X. Preliminary simulation of heating effects of the lower ionosphere in Nanjing District. *Chin. J. Geophys.*, 2014, 57:3642-3649
- [71] Zhang M, Liu L, Wan W, Ning B. An update global model of hmF2 from values estimated from ionosonde and COSMIC/FORMOSAT- 3 radio occultation. *Adv. Space Res.*, 2014, 53:395-402
- [72] Liu L, Huang H, Chen Y, Le H, Ning B, Wan W, Zhang H. Deriving the effective scale height in the topside ionosphere based on ionosonde and satellite in-situ observations. *J. Geophys. Res. Space Phys.*, 2014, 119:8472-8482
- [73] Wang S, Huang S, Fang H. Topside ionospheric Vary-Chap scale height retrieved from the COSMIC/FORMOSAT-3 data at mid-latitudes. *Adv. Space Res.*, 2015, 56:893-899
- [74] Wang S, Huang S, Fang H. New method for deriving the topside ionospheric Vary-Chap scale height. *Radio Sci.*, 2015, 50:866-875
- [75] Huang H, Chen Y, Liu L, Le H, Wan W. An empirical model of the topside plasma density around 600 km based on ROCSAT-1 and Hinotori observations. *J. Geophys. Res. Space Phys.*, 2015, 120:4052- 4063
- [76] A E, Huang W, Yu S, Liu S, Shi L, Gong J, Chen Y, Shen H. A regional ionospheric TEC mapping technique over China and adjacent areas on the basis of data assimilation. *J. Geophys. Res. Space Phys.*, 2015, 120:5049-5061
- [77] A Ercha, Huang W G, Liu S Q, *et al.* A regional ionospheric TEC mapping technique over China and adjacent areas: GNSS data processing and DINEOF analysis. *Sci. China Inf. Sci.*, 2015, 58:107201(11). doi: 10.1007/s11432-015-5399-2
- [78] Zhao X, Ning B, Liu L, Song G. A prediction model of short-term ionospheric foF2 based on AdaBoost. *Adv. Space Res.*, 2014, 53:387-394
- [79] Zhu J, Zhao B, Wan W, Ning B, Zhang S. A new topside profiler based on Alouette/ISIS topside sounding. *Adv. Space Res.*, 2015, 56:2080-2090
- [80] Yu T, Tian M, Wang Y, Zeng Z, Xia C, Wu F, Le W. Simulation study of slant-to-vertical deviation in two dimensional TEC mapping over ionosphere equatorial anomaly. *Adv. Space Res.*, 2014, 54:595-603
- [81] Yu T, Mao T, Wang Y, Zeng Z, Wang J, Fang H. Using the GPS observations to reconstruction the ionosphere in three-dimensional by an Ionospheric Data Assimilation and Analysis System (IDAAS). *Science China: G*, 2014, 57:2210-2219
- [82] Yu Y, Wan W, Xiong B, Ren Z, Zhao B, Zhang Y, Ning B, Liu L. Modeling Chinese ionospheric layer parameters based on EOF analysis. *Space Weather* 2015, 13:339-355
- [83] Zhang R, Liu L, Chen Y, Le H. The dawn enhancement of the equatorial ionospheric vertical plasma drift. *J. Geophys. Res. Space Phys.*, 2015, 120. doi: 10.1002/2015JA021972
- [84] Qian C, Lei J, Wang W. A simulation study on the impact of altitudinal dependent vertical plasma drift on the equatorial ionosphere in the evening. *J. Geophys. Res. Space Phys.*, 2015, 120:2918-2925
- [85] Xiong B, Wan W, Zhao B, Yu Y, Wei Y, Ren Z, Liu J. Response of the American equatorial and low-latitude ionosphere to the X1.5 solar flare on 13 September 2005. *J. Geophys. Res. Space Phys.*, 2014, 119:10336-10347
- [86] Wei Y, Zhao B, Li G, Wan W. Electric field penetration into Earth's ionosphere: a brief review for 2000–2013. *Sci. Bull.*, 2015, 60:748-761
- [87] Chen G, Wu C, Huang X, Zhao Z, Zhong D, Qi H, Huang L, Qiao L, Wang J. Plasma flux and gravity waves in the midlatitude ionosphere during the solar eclipse of 20 May 2012. *J. Geophys. Res. Space Phys.*, 2015, 120: doi:10.1002/2014JA020849
- [88] Liu L, Wan W. A brief overview on the issue on space physics and space weather. *Chin. J. Geophys.*, 2014, 57:3493-3501
- [89] Xiong B, Wan W, Ning B, Hu L, Ding F, Zhao B, Li J. Investigation of mid- and low-latitude ionosphere based on BDS, GLONASS and GPS observations. *Chin. J. Geophys.*, 2014, 57:3586- 3599
- [90] Li Z, Yuan Y, Wang N, Hernandez-Pajares M, Huo X. SHPTS: towards a new method for generating precise global ionospheric

- TEC map based on spherical harmonic and generalized trigonometric series functions. *J. Geodesy*, 2015, 89: 331-345
- [91] Yuan Y, Li Z, Wang N, Zhang B, Li H, Li M, Huo X, Ou J. Monitoring the ionosphere based on the Crustal Movement Observation Network of China. *Geodesy Geodyn.*, 2015, 6:73-80
- [92] Wen D, Zhang X, Zhang G, Ou J, Yuan Y. Tomographic reconstruction of ionospheric electron density based on the fitting method by selection of the parameter weights. *Chin. J. Geophys.*, 2014, 57:2395-2403
- [93] Li G Z, Ning B Q, Hu L H. Interferometry observations of low-latitude E-region irregularity patches using the Sanya VHF radar. *Sci. China Tech. Sci.*, 2014 57:1552-1561
- [94] Li G, Ning B, Chu Y H, Reid I M, Hu L, Dolman B K, Xiong J, Jiang G, Yang G, Yan C. Structural evolution of long-duration meteor trail irregularities driven by neutral wind. *J. Geophys. Res. Space Phys.*, 2014, 119:10348-10357
- [95] Li G, Ning B, Wan W, Reid IM, Hu L, Yue X, Younger J P, Dolman B K. Observational evidence of high-altitude meteor trail from radar interferometer. *Geophys. Res. Lett.*, 2014, 41:6583-6589
- [96] Yu T, Huang C, Zhao G, Mao T, Wang Y, Zeng Z, Wang J, Xia C. A preliminary study of thermosphere and mesosphere wind observed by Fabry-Perot over Kelan. *China. J. Geophys. Res. Space Phys.*, 2014, 119:4981-4997
- [97] Wang H, Wang Y. Error calculation and analysis for an improved wind retrieval method based on the ground-based Fabry-Perot interferometer measurements. *Adv. Space Res.*, 2015, 56:1815-1821
- [98] Wang H M, Wang Y M. Airglow simulation based on the atmospheric ultraviolet radiance integrated code of 2012. *Sci. China: Earth Sci.*, 2015, 58:1-11
- [99] Ding Z, Yu L, Dai L, Xu Z, Wu J. The preliminary measurement and analysis of the power profiles by the Qujing incoherent scatter radar. *Chin. J. Geophys.* 2014, 57:3564-3569
- [100] Hu L, Ning B, Liu L, Zhao B, Chen Y, Li G. Comparison between ionospheric peak parameters retrieved from COSMIC measurement and ionosonde observation over Sanya. *Adv. Space Res.*, 2014, 54:929-938
- [101] Hu L, Ning B, Liu L, Zhao B, Li G, Wu B, Huang Z, Hao X, Chang S, Wu Z. Validation of COSMIC ionospheric peak parameters by the measurements of an ionosonde chain in China. *Ann. Geophys.*, 2014, 32:1311-1319
- [102] Sun L, Zhao B, Yue X, Mao T. Comparison between ionospheric character parameters retrieved from FORMOSAT3 measurement and ionosonde observation over China. *Chinese J. Geophys.*, 2014, 57:3625-3632
- [103] Fu L, Peng R, Shi E, Peng J, Wang T, Jiang F, Jia N, Li X, Wang Y. Far ultraviolet nighttime ionospheric photometer. *Astrophys. Space Sci.*, 2015, 355:1-7
- [104] Zhong J, Lei J, Dou X, Yue X. Assessment of vertical TEC mapping functions for space-based GNSS observations. *GPS Solut*, 2015 doi:10.1007/S10291-015-0444-6
- [105] Zhong J, Lei J, Dou X, Yue X. Is the long-term variation of the estimated GPS differential code biases associated with ionospheric variability. *GPS Solut*, 2015. doi:10.1007/S10291-015-0437-5
- [106] Han X, Fraenz M, Dubinin E, Wei Y, Andrews DJ, Wan W, He M, Rong Z, Chai L, Zhong J, Li K, Barabash S. Discrepancy between ionopause and photoelectron boundary determined from Mars Express measurements. *Geophys. Res. Lett.*, 2014, 41:8221-8227
- [107] Chai L, Fraenz M, Wan W, Rong Z, Zhang T, Wei Y, Dubinin E, Zhong J, Han X, Barabash S. IMF control of the location of Venusian bow shock: The effect of the magnitude of IMF component tangential to the bow shock surface. *J. Geophys. Res. Space Phys.*, 2015, 119:9464-9475
- [108] Chai L, Wan W, Fraenz M, Zhang T, Dubinin E, Wei Y, Li Y, Rong Z, Zhong J, Han X, Futaana Y. Solar zenith angle-dependent asymmetries in Venusian bow shock location revealed by Venus Express. *J. Geophys. Res. Space Phys.*, 2015, 120:4446- 4451
- [109] Rong Z J, Barabash S, Futaana Y, Stenberg G, Zhang T L, Wan W X, Wei Y, Wang X D, Chai L H, Zhong J. Morphology of magnetic field in near-Venus magnetotail: Venus express observations. *J. Geophys. Res. Space Phys.*, 2014, 119:8838-8847
- [110] Rong Z J, Barabash S, Stenberg G, Futaana Y, Zhang T L, Wan W X, Wei Y, Wang X D. Technique for diagnosing the flapping motion of magnetotail current sheets based on single-point magnetic field analysis. *J Geophys Res Space Phys.*, 2015, 120:3462-3474
- [111] Rong Z J, Barabash S, Stenberg G, Futaana Y, Zhang T L, Wan W X, Wei Y, Wang X D, Chai L H, Zhong J. The flapping motion of the Venusian magnetotail: Venus Express observations. *J. Geophys. Res. Space Phys.*, 2015, 120:5593-5602
- [112] Wei Y, Pu Z, Zong Q, Wan W, Ren Z, Fraenz M, Dubinin E, Tian F, Shi Q, Fu S, Hong M. Oxygen escape from the Earth during geomagnetic reversals: implications to mass extinction. *Earth Planet Sci. Lett.*, 2014, 394:94-98

Advances in the Researches of the Middle and Upper Atmosphere in China in 2014–2016

CHEN Zeyu¹, XU Jiyao², HU Xiong², CHEN Hongbin³, CHEN Wen³, WEI Ke³, BIAN Jianchun³, TIAN Wenshou⁴, ZHANG Shaodong⁵, REN Rongcai⁶, DOU Xiankang⁷

1. LAGEO, Institute of atmospheric physics, Chinese Academy of Sciences, Beijing 100029
2. National Space Science Center, Chinese Academy of Sciences, Beijing 100190
3. Institute of atmospheric physics, Chinese Academy of Sciences, Beijing 100029
4. School of Atmospheric Sciences, Lanzhou University, Lanzhou 730000
5. School of Electronic Information, Wuhan University, Wuhan 430072
6. LASG, Institute of atmospheric physics, Chinese Academy of Sciences, Beijing, 100029
7. School of Earth and Space Sciences, University of Science and Technology of China, Hefei 230026

* E-mail: chb@mail.iap.ac.cn

Key words

Middle and upper atmosphere
Dynamical and chemical process
Observation infrastructure

Abstract

In this report we summarize the research results by Chinese scientists in 2014–2016. The focuses are placed on the researches of the middle and upper atmosphere, specifically the researches associated with ground-based observation capability development, dynamical processes, and properties of circulation and chemistry-climate coupling of the middle atmospheric layers.

1 Studies on Airglow Radiation

Gao *et al.*^[1] analyzed the vertical structure of OH day-glow using the data from observations by the Sounding of the Atmosphere using Broadband Emission Radiometry (SABER) instrument on the Thermosphere-Ionosphere-Mesosphere Energetics and Dynamics (TIMED) satellite from January 2002 to June 2014. They found that there is a double-layer structure in the distributions of 12-year averaged OH airglow emission, [O₃], and [H] during the daytime. The upper layer of OH day-glow is located in the mesopause region (~88 km) at a similar altitude to that of the OH nightglow. The lower layer is situated in the range of 70–85 km. The double-layer structure of OH day-glow emission is a long-term stable structure and is mainly caused by photochemical processes involving [O₃]. It is also modulated by back-

ground atmospheric temperature and [H]. Liu *et al.*^[2] studied the rotation temperature derived from OH airglow emission spectra at OH (8–3) band, which were observed by the ground-based spectrometer from December 2011 to December 2013. The comparison between OH rotation temperature and SABER temperature showed that the mean rotation temperature of OH (8–3) band is 203.0±11.2 K with 5.5 K warmer than SABER's. Both have obviously seasonal variations, *e.g.*, the annual amplitude of 10.8 K, the semiannual amplitude of 2.7 K. Liu *et al.*^[3] used the OH (9–4, 8–3, 6–2, 5–1, and 3–0) band airglows to evaluate Einstein coefficient by comparing the ground-based temperature derived from five sets of Einstein coefficients and SABER/TIMED temperature. They showed that of the five sets of coefficients, the rotational temperature derived with Langhoff *et al.*'s (1986) set is most consistent with SABER. Based

on these comparisons, they get a set of optimal Einstein coefficients for rotational temperature derivation. The use of a standard set of Einstein coefficients will be beneficial for comparing rotational temperatures observed at different sites.

2 Studies on Thermosphere

Geomagnetic storm can be clarified to two classes: Coronal Mass Ejections (CMEs) driven storms and the Co-rotating Interaction Regions (CIRs) driven storms. Chen *et al.*^[4] carried out a statistical study to assess the relative importance of each kind of storm to satellite orbital decay. They showed that CIR storms have a slightly larger effect on total orbital decay than CME storms do in a statistical sense. During the declining phase and the minimum years of a solar cycle, CIR storms occur frequently and quasi-periodically. These storms have a large effect on thermospheric densities and satellite orbits because of their relatively long duration. Xu *et al.*^[5] studied the latitudinal, longitudinal, and height dependences of the multi-day oscillations of thermospheric densities observed by CHAMP and GRACE satellites during 2002–2010 and the globally averaged thermospheric densities from 1967 to 2007. They find that the main multi-day oscillations in thermospheric densities are 27-, 13.5-, 9-, and 7-day oscillations. The high correlation coefficients between the density oscillations and the $F_{10.7}$ or A_p index indicate that these oscillations are externally driven. The multi-day, periodic oscillations of thermospheric density exhibit strong latitudinal and longitudinal variations in the geomagnetic coordinate and oscillate synchronously at different heights. Jiang *et al.*^[6] investigated the responses of the lower thermospheric temperature to the 9-day and 13.5-day oscillations of recurrent geomagnetic activity and solar radiation. They found that the zonal mean temperature in the lower thermosphere oscillated with periods of near 9 and 13.5 days in the height range of 100–120 km. These oscillations were more strongly correlated with the recurrent geomagnetic activity than with the solar EUV. The amplitudes of 9-day and 13.5-day oscillations increase with latitudes and altitudes. Simulation results from NCAR-TIME-GCM reproduced these oscillations and indicated that recurrent geomagnetic activity is the main cause of the 9-day and 13.5-day variations in the lower thermosphere temperature, and the contribution from solar EUV

variations is minor. Liu *et al.*^[7] investigated the climatology of multiday oscillations with periods of 4–19 days using three-year (2010–2013) observations of thermospheric winds (at ~ 250 km) during declining solar phase by Fabry-Perot interferometers (FPIs) at Xinglong (XL, 40.2°N, 117.4°E) and Millstone Hill (MH, 42.6°N, 71.5°W). They found that these oscillations occur more frequently in the months from May to October and coincide with the summertime preference of middle-latitude ionospheric electron density oscillations. Oscillations with periods of 4–19 days exhibit annual and semiannual variations and are correlated to both the Solar Wind speed (SW) and K_p . These studies indicate that the oscillations in the thermospheric neutral winds may possibly be influenced by CIRs, the related high-speed solar wind, and the recurrent geomagnetic activity. Liu *et al.*^[8] analyzed an 11-year (1989–1995 and 2010–2013) nighttime thermospheric wind (at ~ 250 km) data set from FPI at MH to investigate multiday oscillations (6–30 days) in the thermospheric nighttime winds. They found that there exist prominent quasi 27-day oscillations in the thermospheric zonal wind during solar maximum and quasi 13.5 day oscillations in the zonal wind occur during the solar maximum and increasing phases. The multiday oscillations in the thermospheric winds are more correlated with K_p and SW than $F_{10.7}$. Further analyses illustrated that the zonal wind is more sensitive to SW than the meridional wind. Sun *et al.*^[9] analyzed the simultaneous observations from an all-sky imager, a GPS monitor, a digisonde and a Fabry-Perot Interferometer (FPI) Xinglong (40.4°N, 30.5°N magnetic latitude), China, on 17/18 February 2012. They find the evolution (generation, amplification, and dissipation) of mesoscale field-aligned irregularity structures (FAIs) (~ 150 km) associated with a Medium-Scale Traveling Ionospheric Disturbance (MSTID) event. The mesoscale FAIs had an obvious northwestward relative velocity to main-body MSTIDs. The direction of this relative velocity was roughly parallel to the depleted fronts and was mostly controlled by the intensity of the depleted fronts. A northeastward polarization electric field within a depleted airglow front can play a controlling role in the development of the mesoscale FAIs. Chen *et al.*^[10] studied the O^+ field-aligned ambipolar diffusive velocities V_d and fluxes Φ_d in the topside ionosphere using the observed profiles observed by incoherent scatter radar experiment conducted at Millstone Hill (288.5°E, 42.6°N) from 4 October to 4 No-

vember 2002. Two geomagnetic storms took place during this period. By comparing V_d and Φ_d during different phases of the two storms and quiet times, they proposed that storm time variations in diffusive velocity were more likely the results of storm time changes in the plasma vertical profile, rather than the cause of these plasma density changes. Yao *et al.*^[11] compared the meridional and zonal winds derived from the Kelan FPI wind model with those based on Meteor Radar wind observations at Beijing (39.92°N, 116.39°E), and those calculated from horizontal wind models, *i.e.*, HWM93 and HWM07, at Kelan. They found that the Kelan FPI wind patterns agreed well with the Meteor Radar winds and the HWM07 model results, but less well with the HWM93 model in the mesopause region. The comparison indicates that there were large discrepancies between the Kelan FPI winds and the HWM07 model results, which were mainly due to differences in the annual variation in the nighttime meridional wind.

3 Solar Effect on the East-Asian Monsoon System

Solar radiation is the primary energy source for the motion of the atmosphere, and the most important interdecadal timescale is the 11-year solar cycle. During winters with high solar activity (HS), robust warming appeared in northern Asia in response to a positive AO phase (Tan and Chen^[12]). However, during winters with Low Solar activity (LS), the surface warming was much less in the presence of a positive AO phase. Possible mechanism for this 11-year solar cycle modulation is suggested to be the indirect influence of solar activity on the AO structure. On the other hand, the relationship between the EAWM and the following summer monsoon (EASM) is also modulated by the 11-year solar cycle (Zhou and Chen^[13]). The EAWM-ENSO relationship depends on the solar cycle with more robust relationship in the LS categories. There tends to be a much stronger EASM after a weak EAWM associated with ENSO during the LS phases than during the HS phases. Different evolution of SST anomalies in the HS and LS years are further demonstrated, and thus explain why a closer EAWM-EASM relationship is established during LS years than HS years. These findings extend earlier ones by emphasizing the modulation effect of solar cycle on the AO&ENSO and the East Asian climate relationship, which has practical use for climate prediction.

4 Dynamical Processes in the Middle Atmosphere

4.1 Tides

Xu *et al.*^[14] studied the nonlinear interaction between Stationary Planetary Waves (SPWs) and tides in the stratosphere and mesosphere using the global temperature data from 11 years (2002–2012) SABER/TIMED observations. The holistic behavior of the nonlinear interactions between all SPWs and tides is analyzed from the point of view of energetics. The results indicate that the intensities of nonmigrating diurnal, semidiurnal, terdiurnal, and 6 h tides are strongest during winter and almost vanish during summer, synchronous with SPW activity. Thus nonlinear interactions between SPWs and tides in the stratosphere and the lower mesosphere may be an important source of the nonmigrating tides that then propagate into the upper mesosphere and lower thermosphere. Liu *et al.*^[15] studied the global structure and seasonal variations of the migrating 6-h tide from the stratosphere to the lower thermosphere using 10 years of SABER/TIMED temperature data. The amplitudes of the migrating 6-h tide increase with altitudes. In the stratosphere, the migrating 6-h tide peaks around 35°N/S. The migrating 6-h tide is stronger in the southern hemisphere. Annual, semiannual, 4- and 3-month oscillations are the four dominant seasonal variations of the tidal amplitude. Both ozone heating in the stratosphere and the background atmosphere probably affect the generation and the seasonal variations of the migrating 6-h tide. In addition, the non-linear interaction between different tidal harmonics is another possible mechanism. Liu *et al.*^[16] examined modulations of the temperature migrating diurnal tide (DW1) by latitudinal gradients of zonal mean zonal wind using the temperature data from SABER/TIMED and Empirical Orthogonal Function (EOF) analysis. The result shows that latitudinal gradient of zonal mean zonal wind increases with altitudes and displays clearly seasonal and interannual variability. These variations are in a similar manner as the DW1. The resembling spatial-temporal features suggest that in the upper tropic MLT probably plays an important role in modulating semiannual, annual, and quasi-biennial oscillations in DW1 at the same latitude and altitude. Yu *et al.*^[17] studied seasonal variations of MLT tides using meteor radar chain. The seasonal variations of different tides in the mesosphere and lower thermosphere are investigated from wind obser-

vations of a meteor radar chain on the basis of Hough mode decomposition. Pronounced semiannual oscillation (SAO) is presented in the diurnal component, while latitude-dependent seasonal variation is found in the semidiurnal and terdiurnal components. At the low/mid-latitude stations, the semiannual/annual oscillation is relatively stronger. Hough mode decomposition is utilized to extract the dominant tidal modes of each decomposed component. It is found the (1, 1) mode dominates the diurnal component with apparent SAO, (2, 4) mode of the semidiurnal component is strong in the autumn and winter months (after the September equinox). Ren *et al.*^[18] studied the influence of DE3 tide on the equinoctial asymmetry of the zonal mean ionospheric electron density. Through respectively adding September DE3 tide and March DE3 tide at the low boundary of GCITEM-IGGCAS model, we simulate the influence of DE3 tide on the equinoctial asymmetry of the zonal mean ionospheric electron density. The influence of DE3 tide on the equinoctial asymmetry of the zonal mean electron density varies with latitude, altitude and solar activity level. Compared with the density driven by September DE3 tide, the March DE3 tide mainly decreases the lower ionospheric zonal mean electron density, and mainly increases the electron density at higher ionosphere. In the low-latitude ionosphere, DE3 tide drives an Equatorial Ionization Anomaly structure (EIA) at higher ionosphere in the relative difference of zonal mean electron density, which suggests that DE3 tide affect the longitudinal mean equatorial vertical $E \times B$ plasma drifts. Although the lower ionospheric equinoctial asymmetry driven by DE3 tide mainly decreases with the increase of solar activity, the asymmetry at higher ionosphere mainly increases with solar activity. However, EIA in equinoctial asymmetry mainly decreases with the increase of solar activity. Li *et al.*^[19] studied yearly variations of the stratospheric tides. The three main tidal components, *i.e.*, the migrating components DW1, SW2 and the non-migrating component DE3, at the two stratospheric altitudes (20 and 43 km) and in the latitude range between $\pm 60^\circ$, are obtained from the temperature data of National Centers for Environmental Prediction (NCEP) Climate Forecast System Reanalysis (CFSR) during the interval from 1979 to 2010. The yearly variations of the main tidal components may demonstrate that the CFSR reanalysis data can be used as a supplementary observation in the investigation of the stratospheric tidal components. Li *et*

al.^[20] studied the variability of nonmigrating tides. This paper deals with the variability of the nonmigrating tides detected from the observation of the SABER instrument on board the TIMED satellite during the 11-year solar period from 2002 to 2012. We found that the properties of the spatial distribution and large time scale variation of the DE3 component are similar to those of the previous works, which used the interpolated data with 2-month resolution. Practically, the higher-resolution data were used to reveal the day-to-day variability of the DE3 component. The day-to-day variability of the DE3 component may be explained by the variance of the absolute amplitudes and the contribution of the wave phases, and the later seems to play more important role.

4.2 GWs

Chen *et al.*^[21] simulated generation of stratospheric gravity waves in upper-tropospheric jet stream accompanied with a cold vortex over Northeast China in June 2010, using WRF ARW. The results reveal that pronounced stratospheric GWs are generated by the jet stream as they emerge from the exit region of jet stream.

To identify oceanic regions for which convection is a major source of Gravity Waves (GWs), Jia *et al.*^[22] analyzed the correlation between sea surface temperature and absolute values of Gravity Wave Momentum Flux (GWMF) deduced from satellite data. Convective GWs are identified at the Eastern coasts of the continents and over the warm water regions formed by the warm ocean currents, in particular the Gulf Stream and the Kuroshio. Potential contributions of tropical cyclones to the excitation of the GWs are discussed. Convective excitation can be identified well into the mid-mesosphere. In propagating upward, the centers of GWMF formed by convection shift poleward. Some indications of the main forcing regions are even shown for the upper Mesosphere/Lower Thermosphere (MLT).

Jia *et al.*^[23] investigated the Gravity Wave (GW) variability during the Sudden Stratosphere Warming (SSW) in 2008 and 2009 using the COSMIC temperature profiles together with zonal wind and geopotential height data from NCEP/NCAR reanalysis. GWs were enhanced at the edge of the polar vortex where the background wind was strong, whereas the areas with the largest GW amplitudes did not always correspond with those with the strongest background wind. In 2008, the magnitudes of the zonal mean GW enhancements dur-



ing the downward progression were relatively stable, whereas a clear reduction was detected as the GW enhancement was progressing downward in 2009.

Xu *et al.*^[24] developed a no-gap OH airglow all-sky imager network for the first time in northern China since February 2012. The network is composed of 26 all-sky airglow imagers that make observations of OH airglow gravity waves and cover an area of about 2000 km east and west and about 1400 km south and north. In the study, the authors reported a series of Concentric Gravity Wave (CGW) events nearly every night during the first half of August 2013. Further analysis on two representative CGW events illustrated that on CGW was likely launched by a single thunderstorm. The temporal and spatial analyses indicate that the CGW horizontal wavelength agrees with the GW dispersion relation within 300 km from the storm center. Another CGW event was launched by two very strong thunderstorms on 09 August 2013. These CGWs have multi-scales with horizontal wavelength ranging from less than 10 km to 200 km.

Liu *et al.*^[25] studied the diurnal variations of turbulence parameters (turbulence kinetic energy and turbulence diffusivity) in the tropical oceanic upper troposphere. This study used the four times per day radio sounding data on the Kexue#1 scientific observation ship of South China Sea Monsoon Experiment (SCSMEX) in 1998 and the concurrent mesoscale convective systems derived from TRMM (tropical rain-fall measuring mission)satellite. They found that the diurnal variations of turbulence parameters averaged over May and June are strongly correlated with the diurnal variations of MCSs with correlation factors of 0.79 and 0.94, respectively. This indicates that the turbulence and its diurnal variations over the tropic oceanic upper stratosphere region are highly related to the MCSs. Liu *et al.*^[26] simulated gravity waves (GWs) breaking and their contributions to the formation of large winds ($\geq 100 \text{ m}\cdot\text{s}^{-1}$) and wind shears ($\geq 40 \text{ m}\cdot\text{s}^{-1}\cdot\text{km}^{-1}$) in the Mesosphere and Lower Thermosphere(MLT). They showed that the momentum deposited by breaking GWs accelerates the mean wind. The resultant large background wind increases the GW's apparent horizontal phase velocity and decreases the GW's intrinsic frequency and vertical wavelength. Both the accelerated mean wind and the decreased GW vertical wavelength contribute to the enhancement of wind shears. This, in turn, creates a favorable condition for the occurrence of GW instability, breaking, and momentum deposition, as well as mean

wind acceleration, which further enhances the wind shears. Liu *et al.*^[27] performed 64 numerical experiments to simulate GWs with different wavelengths propagating in the migrating diurnal and semidiurnal tidal background. They found that both migrating diurnal and semidiurnal tides strongly modulate the occurrence of GW breaking, and the resulted large winds and wind shears. The simulated large winds and wind shears are in good agreement with those from the rocket-sounding chemical release measurements. Moreover, the occurrence of large wind shears highly depends on the phases of migrating tides in local time, which is in agreement with the reported lidar observations. This study revealed that the nonlinear interactions between GWs breaking and the migrating diurnal and semidiurnal tides may play an important role in driving the large winds and wind shears in the MLT region and their local time dependence. Liu *et al.*^[28] used a 6-year (2007–2013) temperature data set from SOFIE/AIM to extract Gravity Waves (GWs) in the polar stratosphere and mesosphere of both hemispheres. They showed that GWs are stronger in the winter than in the summer and exhibit strong annual variation. GWs are stronger in the Southern Polar Region (SPR) than in the Northern Polar Region (NPR) except in the summer months. This is likely because there are stronger and longer-lasting zonal wind jets in the SPR stratosphere. The longitudinal variations of PE in the winter polar stratosphere are consistent with the elevated regions. The correlations between GW potential energy and the column Ice Water Content (IWC, an indicator of the polar mesosphere cloud) exhibit longitudinal and annual variations.

Wei *et al.*^[29] found that orographic wave excited by the TP propagate upward into the stratosphere and breaks near 150 hPa, leading to a strong attenuation of momentum flux and the release of energy into basic flows. Meanwhile, vertical turbulent mixing is extremely increased and turbulent exchange coefficient enhances by more than eight times during a short period (within 1 hour). Large turbulent mixing process causes air transports from the troposphere to the stratosphere.

4.3 Planetary Waves

Liu *et al.*^[30] studied 5 day Planetary Waves (PWs) in the polar stratosphere and mesosphere using the temperature and column Ice Water Content (IWC) of Polar Mesospheric Clouds (PMCs) measured simultaneously by the Solar Occultation for Ice Experiment (SOFIE) on

board NASA's Aeronomy of Ice in the Mesosphere satellite from 2007 to 2014. They found that the 5-day PWs in temperature are stronger in the polar winter stratosphere and mesosphere and exhibit substantial inter-hemispheric asymmetry. The strength of 5 day waves coincide with those of the eastward jet in each hemisphere. This indicates that the 5-day PWs might be generated from barotropic/baroclinic instability in the polar stratosphere. In the same study, the authors also showed that the phase shifts of W1 5-day PW in temperature relative to that in IWC have a mean of -2.0 h (0.3 h) with a standard deviation of 3.8 h (4.2 h) in the northern (southern) polar region. This indicates that the formation of the W1 5-day PW in PMCs is controlled mainly by the W1 5-day PW in temperature and influenced by other factors. Extending the broad spectral method proposed by Zhang *et al.* (2013) and applying 11 years (1998–2008) of radiosonde data from 92 stations in the Northern Hemisphere, Zhang *et al.*^[31] investigated latitudinal, continuous vertical and seasonal variability of Medium- and High-frequency Gravity Waves (MHGWs) parameters in the lower atmosphere (2–25 km). The latitudinal and vertical distributions of the wave energy density and horizontal momentum fluxes as well as their seasonal variations exhibit considerable consistency with those of inertial gravity waves. Despite the consistency, the MHGWs have much larger energy density, horizontal momentum fluxes and wave force. The derived intrinsic frequencies are more sensitive to the spatiotemporal variation of the buoyancy frequency, and at all latitudinal regions they are higher in summer.

Gan *et al.*^[32] reported the seasonal variations of the westward propagating 6.5-day planetary wave in the Mesosphere and Lower Thermosphere (MLT). A case study (around day 130 in year 2003) revealed an extraordinarily strong 6.5-day wave event. They found that intensive dissipation of 6.5-day wave in the mesopause region induced an extra meridional circulation, which could result in a net upward and downward transportation of atomic oxygen and molecular nitrogen, thus, the depletion of thermospheric O/N₂ ratio. Using meteor radar, radiosonde and satellite observations over 20°N and NCEP/NCAR reanalysis data during 81 days from 22 December 2004 to 12 March 2005, Huang *et al.*^[33] observed a quasi-27-day oscillation propagating from the troposphere to the mesosphere. The oscillation attains a large amplitude of about $12\text{m}\cdot\text{s}^{-1}$ in the eastward wind shear region of the troposphere. When the wind

shear reverses, its amplitude rapidly decays, and the background wind gradually evolves to be westward. They further suggested that the quasi-27-day oscillation may be an atmospheric response to forcing due to the convective activity with a period of about 27 days in the tropical region.

Using Extended Canadian Middle Atmosphere Model (eCMAM), Gan *et al.*^[34] validated the migrating and non-migrating diurnal tidal modes with SABER temperature observation. It is found that the major tidal modes in temperature were well simulated by eCMAM with realistic lower atmosphere physics, parameterizations of gravity wave in the middle atmosphere and ion drag in the ionosphere. The simulated diurnal tides exhibited consistent spatial structure and seasonal and inter-annual characteristics compared with 11-year observations, indicative of further utilization of tidal-related research. Using observation data from the Wuhan University (WHU) VHF radar in 2012, Huang *et al.*^[35] studied the primary features of the DT and its variability in the lower atmosphere over Chongyang (114.14°E , 29.53°N). They found that dominant diurnal oscillations exist in the lower atmosphere at middle latitudes, and the diurnal tide shows remarkable height, season, and short-term variability. The background wind could be responsible for diurnal tide height and season variability. The short-term variation in the tidal source and the coupling with planetary waves could be responsible for short-term variability of diurnal tide.

5 Stratospheric Processes

5.1 Sudden Stratospheric Warming

Shuai *et al.*^[36] reported a study on the Elevated Stratosphere (ES) events in the winter of 2006, 2009 and 2010 at 70° N. The studies are based on the SABER/TIMED temperature measurements in the period from 2003 to 2011. Their results indicated that the ES events occur only after the major Sudden Stratospheric Warming (SSW) accompanying with the polar vortex splitting. They suggested that in the ES events, enhancement of gravity wave activity could be observed at ~ 80 km between late January and early February, corresponding to the ES occurrence height and time.

Hu *et al.*^[37] investigated the boreal spring Stratospheric Final Warming (SFW) and its interannual and interdecadal variability. They found that the earliest SFW occurs in mid-March whereas the latest SFW

happens in late May. The early/late SFW events in boreal spring correspond to a quicker/slower transition of the stratospheric circulation. The earlier breakdown of the Stratospheric Polar Vortex (SPV), as for the winter Stratospheric Sudden Warming (SSW) events is driven mainly by wave forcing; and in contrast, the later breakdown of the SPV exhibits more characteristics of its seasonal evolution. In addition, the SFW onset time before the mid-1990s is 11 days earlier than that afterwards. Hu *et al.*^[38–39] then demonstrates relationship between intensity and occurrence of major stratospheric Sudden Warming Events (SSWs) in midwinter and the seasonal timing of Stratospheric Final Warming events (SFWs) in spring. Specifically, early spring SFWs that on average occur in early March tend to be preceded by non-SSW winters, while late spring SFWs that on average take place up until early May are mostly preceded by SSW events in midwinter. Planetary wave activity and western Eurasian high may play a role.

Pogoreltsev *et al.*^[40] suggested that nonlinear interaction between planetary waves and mean flow could provide a favorable condition for the Sudden Stratospheric Warming (SSW) initiation. Their results demonstrated that the nonlinear wave-wave and wave-mean flow interactions could play an important role before and during SSW.

Xue *et al.*^[41] investigated the modulation effect of QBO on the connection between ENSO and the summer South Asian High (SAH). Their results suggested that the boreal summer SAH was more significantly influenced by preceding ENSO events in the easterly phase of the QBO than in the westerly phase. This change in the ENSO-SAH relationship in the different QBO phases was attributable to the change in the ENSO-induced sea surface temperature anomalies over the tropical Indian Ocean. This result highlights the modulation effect of the QBO on the impacts of ENSO events, and the QBO should be taken into consideration when ENSO is used to predict the Asian monsoon variations.

Guo *et al.*^[42] found double-core structure of ozone valley over the Tibetan Plateau and presumed its possible mechanisms. From Microwave Limb Sounder (MLS) ozone (O_3) data, a double core structure of the ozone valley over the TP is found with one depletion center in upper stratosphere named the upper core, and another depletion center, named the lower core, is observed in the upper troposphere/lower stratosphere. The analysis indicates that the zonal deviation of ozone at the upper

core is nearly -1 DU while its counterpart's deviation at the lower core is nearly -15 DU. Large scale atmospheric circulation and terrain effects play an important role in the ozone valley at the lower core. In contrast, photochemistry reactions of odd chlorine including chlorine atoms (Cl) and chlorine monoxide (ClO) dominate the ozone valley at the upper core.

Zhang *et al.*^[43] reported that the Total column Ozone Low (TOL) over the TP during winter and spring is deepening over the recent decade. Based on the analysis of multiple regression model, the thermal dynamical processes associated with the TP warming accounts for more than 50% of TCO decline during winter for the period 1979–2009. According to the Chemistry-Climate Model (CCM) simulations, the increases in NO_x emissions in East Asia and global tropospheric N_2O mixing ratio for the period 1979–2009 contribute to no more than 20% reductions in TCO during this period.

Xie *et al.*^[44] found that El Niño Modoki has had a significant effect on tropical ozone since the 1980s, alongside that of the QBO, and canonical El Niño. Based on EOF analysis, it was found that the leading mode of TCO variability, accounting for $\sim 28\%$ of the variance, is associated with El Niño Modoki events, and the other modes are related to the QBO and canonical El Niño. Since El Niño Modoki activity leads tropical ozone changes by 3–4 months, it could serve as a predictor for tropical ozone variations. Xie *et al.*^[45] revealed that the continuous expansion of the area of the Indo-Pacific Warm Pool (IPWP) since the 1980s represents an increase in the total heat energy of the IPWP available to heat the tropospheric air. This process lifts the tropical cold-point tropopause height and leads to the observed long-term cooling trend of the tropical Cold-Point Tropopause Temperature (CPTT). In addition, Modoki activity is an important factor in modulating the interannual variations of the tropical CPTT through significant effects on overshooting convection.

Wang *et al.*^[46] revealed that the Carbon Oxide (CO) surface emissions explain most of the semi-annual oscillation signals in the tropical upper troposphere, with the remainder being attributed to dynamical and chemical processes. The CO Annual Oscillation (AO) in the lower stratosphere primarily results from combined effects of dynamical and chemical processes while the dynamical and chemical processes make opposite contributions to the CO AO signals. CO surface emissions tend to weaken the amplitude of the CO annual cycle in

the tropical lower stratosphere, while the annual variations in the meridional component of the BD circulation can amplify the annual variations of CO above 30 hPa.

5.2 Stratosphere Climate Change Simulation

Hu *et al.*^[47] used a state-of-the-art general circulation model and found that, in the Southern Hemisphere, the stratospheric ozone depletion leads to a cooler and stronger Antarctic stratosphere, while the stratospheric ozone recovery has the opposite effects. In the Northern Hemisphere (NH), the impacts of the stratospheric ozone depletion on polar stratospheric temperature are not opposite to that of the stratospheric ozone recovery; *i.e.*, the stratospheric ozone depletion causes a weak cooling and the stratospheric ozone recovery causes a statistically significant cooling. Particularly interesting is that stratospheric ozone changes have opposite effects on the stationary and transient wave fluxes in the NH stratosphere.

Wang *et al.*^[48] investigated the impact of the assumed N₂O increases on stratospheric chemistry and dynamics using a series of idealized simulations with a CCM. In a future cooler stratosphere the net yield of NO_y from N₂O is shown to decrease in a reference run following the IPCC A1B scenario, but NO_y can still be significantly increased by extra increases of N₂O over 2001–2050. Meanwhile, the ozone depleting potential of N₂O varies with the time period and is influenced by the environmental conditions.

Shang *et al.*^[49] showed that CH₄ emission increases will accelerate the BD circulation. However, the BD circulation in the tropics at 100 hPa weakens as CH₄ emissions increase in East Asia and strengthens when CH₄ emissions increase in North America. A 50% increase of CH₄ emissions in North America has a greater influence on the stratospheric ozone increases than the same CH₄ emissions increase in East Asia. CH₄ emission increases in East Asia and North America reduce the concentration of tropospheric hydroxyl radicals and increase the concentration of mid-tropospheric ozone in the Northern Hemisphere midlatitudes.

Zhang *et al.*^[50] revealed that the longitudinal dependence of mid-latitude ozone anomalies associated with ENSO events during the period January–February–March is found to be related to planetary waves. The wave trains affect ozone in the Upper Troposphere and Lower Stratosphere (UTLS) by modulating the mid-latitude tropopause height and cause Total Ozone Column

(TOC) anomalies by changing the vertical distributions of ozone. In addition, changes in synoptic-scale Rossby wave breaking can also influence ozone through modulating eddy-driven meridional circulation in the UTLS. Based on the above mechanisms, Zhang *et al.*^[51] further found that the maximum response of the TOC to ENSO shifts northward from southern China in winter to northern China in summer. The seasonal shift of the centre of TOC anomalies is related to the seasonal shift of the location of East Asia westerly jet, accompanied by tropopause height changes and anomalous circulation induced by Rossby wave trains along the jet. The differences in the TOC between El Niño and La Niña events can cause up to 6%–10% clear-sky erythema UV changes over the middle and lower reaches of the Yangtze River in winter and the northwestern Tibetan Plateau (TP) during spring.

Hu *et al.*^[52] showed that increases in SST and the SST meridional gradient could intensify the subtropical westerly jets and significantly weaken the northern polar vortex. Global uniform SST increases produced a more significant impact on the southern stratosphere than the northern stratosphere, while SST gradient increases produced a more significant impact on the northern stratosphere. The asymmetric responses of the northern and southern polar stratosphere to SST meridional gradient changes were found to be mainly due to different wave properties and transmissions in the northern and southern atmosphere.

Using E-P flux in quasi-geostrophic spherical coordinates and its transformation form weighted by zonal annular total mass (Shi *et al.*^[53]). Subsequently, Shi *et al.*^[54] reported recent latitudinal-structure changes in the boreal Brewer-Dobson circulation. The global ozone chemistry and related trace gas data records for the stratosphere data (GOZCARDS) show that the tropical lowermost stratospheric WV increased by 18% per decade during 2001–2011 and the boreal mid-latitude lower stratospheric HCl rose 25% per decade after 2006. This may result from a slowdown of the tropical upwelling and a speedup of the mid-latitude downwelling, which is also supported by composite analysis of Eliassen-Palm Flux (EPF), zonal wind and regression of temperature on the EPF from the ERA-Interim data.

5.3 STE Processes

Using reanalysis datasets, Wei *et al.*^[55] indicated that the relationship between the second mode of East Asian

Winter Monsoon (EAWM) and the Stratospheric Polar Vortex (SPV) increased suddenly since the late 1980s. The SPV-related circulation and planetary wave activities are intensified in the latter period. The global warming and ozone depletion are further suggested to cause this change.

Reflection of stratospheric planetary waves and its impact on tropospheric cold weather over Asia during January 2008 was investigated by Nath *et al.*^[56]. They found that a wave packet emanating from Baffin Island/coast of Labrador propagated eastward, equatorward and was reflected over Central Eurasia and parts of China, which in turn triggered the advection of cold wind from the northern part of the boreal forest regions and Siberia to the subtropics. Extreme cold weather occurred in the wide region of Central Eurasia and China during the second ten days of January 2008. Nath *et al.*^[57] further studied the impact of planetary wave reflection on tropospheric blocking over the Urals-Siberia region in this event by employing time-lagged singular value decomposition analysis on the geopotential height field. The results clearly showed that around mid-January the upward component of the high-latitude wave guide was very weak, it was only the downward component that could have contributed to the development of the blocking high over the Urals-Siberia region.

Shi *et al.*^[58] studied stratosphere-troposphere exchange caused by a deep convection in warm sector and abnormal subtropical front of a cutoff low over East Asia in June 2009, using cloud profile radar data from Cloudsat, temperature of black body from FY-2C, atmospheric compositions from Aura/MLS, meteorological data from the ECMWF and HYSPLIT4 trajectory model. The analysis shows that intense stratosphere-troposphere exchange occurs in the abnormal subtropical front zone due to the convective injection into stratospheric intrusions. On the scatter plot of ozone and water vapor these are two special gathering areas with both high (low) concentrations of the two species. Chen *et al.*^[59] simulated a typical cold vortex over northeast China during June 19–23 2010 using WRF model and investigated the stratosphere-troposphere exchange process through Wei formula. Results showed that the Cross-Tropopause mass Flux (CTF) induced by the cold vortex was controlled by Stratosphere-to-Troposphere Transport (STT). The time evolution of the CTF exhibited three characteristics: (1) the predominance of the STT during the pre-formation stage; (2) the formation

and development of the cold vortex, in which the CTF varied in a fluctuating pattern from Troposphere-to-Stratosphere Transport (TST) to STT to TST; and (3) the prevalence of the STT during the decay stage.

Xu *et al.*^[60] found that the higher orography has a significant influence on the STE processes with its effect having an evident diurnal variation. In the morning and evening time, the upward motions due to forcing lift of the high orography are strong and inhibit the STE. In the afternoon, the thermal effects of the high orography enhance and the turbulent mixing above the height of the orography of 2.5 km is critical, with an increase of 1% when the average orographic height rises 100 m.

Yang *et al.*^[61] found, using WRF model, that deep convection over the TP can inject dust aerosols into the stratosphere. When there is no overshooting convection, vertical motions cannot transport aerosols directly into the lower stratosphere. However, small scale diffusion and mixing processes can slowly transport aerosols in the upper troposphere into the lower stratosphere using a few hours of time. Zhang *et al.*^[62] reported that vertical transport of dust aerosols is closely related to background horizontal winds. In the absence of the cloud microphysical processes, when a deep convergence zone of northerly and southerly winds forms over the TP, the vertical motions resulted from the convergence could transport dust aerosols, originated from the Taklimakan desert, to the lower stratosphere with an evident inclined transport pathway. Tian *et al.*^[63] showed that the distributions of water vapor over the TP from 2005 to 2008 are characterized by a minimum over the southern TP from March to April, and a maximum over the southern TP from July to October near tropopause region at 100 hPa. The low water vapor at 215 hPa over the center of the TP is related to the sinking of dry air from the UTLS region.

5.4 Studies on the Troposphere

Liu *et al.*^[64] found that the effects of the QBO on tropical tropopause and OLR are most significant in winter and autumn while relatively insignificant in spring and summer. The tropical tropopause height and temperature anomalies associated with the QBO exhibit a belted distribution in the tropics while the OLR anomalies have both positive and negative anomalies along the equator. The buoyancy frequency anomalies and Convective Potential Energy (CAPE) anomalies associated

with the QBO are spatially in accordance with the QBO-induced OLR anomalies, suggesting that the QBO can affect tropical convective activities through modulating the static stability and the CAPE in the tropical troposphere.

Based on the satellite observations and reanalysis data, Shi *et al.*^[65] showed the distribution of Cloud Top Above the Tropopause (CTAT) events and its effect on water vapor and temperature structures in the Upper Troposphere and Lower Stratosphere (UTLS) over East China. The maximum frequency of CTAT in boreal summer is located in Asian monsoon region. Meanwhile, the maximum frequency of CTAT in mid-latitudes is located in Northeast Asia. Composite analysis suggested that “dry above-moist below” and “cold above-warm below” structure in the UTLS along 15°–35°N over East Asia-West Pacific region may be associated with tropical cyclones, the opposite structure in the UTLS along 35°–50°N may be related to extratropical cyclones.

Zheng *et al.*^[66] analyzed the variation of tropical tropopause height 1919–2011. The results indicate an increase linear trend of tropopause height which contributed by tropical convection, total ozone and tropospheric air temperature. With the linear trend removed, tropical tropopause varies significantly at periods of 18.2, 28.6 and 40 months. 18.2-month variation may be related to ozone and tropospheric temperature induced by monsoon. 28.6-month variation may be attributed to the quasi-biennial variation of ozone induced by the lower stratospheric zonal wind. 40-month period is mainly responsible for ENSO.

Zhang *et al.*^[67] presented the intense interaction between the Tropopause Inversion Layer (TIL) and the Inertial Gravity Wave (IGW) activities by using a high vertical resolution radiosonde data set at a midlatitude station for the period 1998–2008. It is found that the TIL not only could inhibit the upward propagation of IGWs from below but also imply the possible excitation links between the TIL and IGW. The results also indicate that the enhanced wind shear layer just 1 km above the tropopause may result in the IGW breaking and intensive turbulence. The effect of the IGW-induced intensive turbulence could significantly cool the tropopause, which makes the tropopause colder and sharper and finally forms the TIL.

Zhang *et al.*^[68] studied the diurnal variation of the Planetary Boundary Layer Height (PBLH) by using the eight-times-daily sampling data from an intensive ra-

diosonde observation campaign at Yichang (111°E, 30°N), China in August 2006 and January 2007. It was found that the PBLH in both summer and winter months showed diurnal changes and the daily cycle was deeper in summer; the morning rise began at 07:00 LT/10:00 LT in summer/winter and the evening transition occurred at 1900 LT in both seasons; the maximum height occurred in the afternoon for most cases, except some peaks found in the winter night.

6 Development of Infrastructure

Based on the 1 min backscatter ratio R profiles from the all-day lidar measurements in Wuhan, China (30.5°N, 114.4°E), Kong and Yi^[69] calculated the hourly Convective Boundary Layer (CBL) height with the variance method. The computed CBL height sequence displays the regular diurnal cycle of the CBL top. The diurnal variation of the CBL height shows an obvious seasonal dependence which coincides with the annual variation of the local surface temperature. The surface fine particle concentration generally has a more complex diurnal cycle than that expected from the CBL-dilution/CBL-accumulation effect. They suggested that the seasonal behavior of the surface fine particle concentration mainly depends on the seasonal variation in available volume (determined by the CBL height) for aerosol dispersion.

A spectrally resolved Raman lidar has been built by Liu and Yi^[70] to measure atmospheric N₂ Stokes vibrational-rotational Raman spectra. The lidar applies a double-grating polychromator with a reciprocal linear dispersion of $\sim 0.12 \text{ nm}\cdot\text{mm}^{-1}$ for the wavelength separation and a 32-channel linear-array photomultiplier tube for sampling the spectral signals. A comparison shows an excellent agreement between the lidar-measured and theoretically-calculated spectra. A new temperature retrieval approach without needing a calibration from reference temperature data has been developed. The temperature derived from the new lidar and method is comparable to that from local radiosonde.

Acknowledgement Thank to Dr. Ling Chao from the CAS/IAP for his effort on text compilation.

References

- [1] Gao H, J Xu, W Ward, A K Smith, G M Chen. Double-layer structure of OH dayglow in the mesosphere, *J. Geophys. Res. Space*



- Physics, 2015, 120, 5778-5787
- [2] Liu W, Xu J, and Yuan W. Seasonal variation of OH rotational temperature measured over Beijing, China. *Chinese J. Geophys.*, 2015, 58(5): 1467-1474
 - [3] Liu W, Xu J, Smith A K, Yuan W. Comparison of rotational temperature derived from ground-based OH airglow observations with TIMED/SABER to evaluate the Einstein coefficients. *J. Geophys. Res. Space Physics*, 2015, 120, doi:10.1002/2015JA021886
 - [4] Chen G M, J Xu, Wang W, Burns A G. A comparison of the effects of CIR- and CME-induced geomagnetic activity on thermospheric densities and spacecraft orbits: Statistical studies. *J. Geophys. Res. Space Physics*, 2014, 119, doi:10.1002/2014JA019831
 - [5] Xu J, Wang W, Zhang S, Liu X, Yuan W. Multiday thermospheric density oscillations associated with variations in solar radiation and geomagnetic activity. *J. Geophys. Res. Space Physics*, 2015, 120, doi:10.1002/2014JA020830
 - [6] Jiang G, Wang W, Xu J, Yue J, Burns A G, Lei J, Mlynczak M G, Rusell J M. Responses of the lower thermospheric temperature to the 9 day and 13.5 day oscillations of recurrent geomagnetic activity. *J. Geophys. Res. Space Physics*, 2014, 119, doi:10.1002/2013JA019406
 - [7] Liu X, Xu J, Zhang S R, Jiang G, Zhou Q, Yuan W, Noto J, Kerr R. Thermospheric planetary wave-type oscillations observed by FPIs over Xinglong and Millstone Hill. *J. Geophys. Res. Space Physics*, 2014, 119: 6891–6901
 - [8] Liu X, Xu J, Zhang S R, Zhou Q, Yuan W. Solar activity dependency of multiday oscillations in the night time thermospheric winds observed by Fabry-Perot interferometer. *J. Geophys. Res. Space Physics*, 2015, 120: 5871–5881
 - [9] Sun L, Xu J, Wang W, Yue X, Yuan W, Ning B, Zhang D, Menees F C de. Mesoscale field-aligned irregularity structures (FAIs) of airglow associated with medium-scale traveling ionospheric disturbances (MSTIDs). *J. Geophys. Res. Space Physics*, 2015, 120, doi:10.1002/2014JA020944
 - [10] Chen G M, Xu J, Wang W, Lei J, Zhang S R. The responses of ionospheric topside diffusive fluxes to two geomagnetic storms in October 2002. *J. Geophys. Res. Space Physics*, 2014, 119: 6806–6820
 - [11] Yao X, Yu T, Zhao B, Yu Y, Liu L, Ning B, Wan W. Climatological modeling of horizontal winds in the mesosphere and lower thermosphere over a mid-latitude station in China. *Adv. Space Res.* 2015, 56: 1354-1365
 - [12] Tan Benkui, Chen Wen. Progress in the study of the dynamics of extratropical atmospheric teleconnection patterns and their impacts on East Asian climate. *J. Meteor. Res.*, 2014, 28(5): 780-802
 - [13] Zhou Qun, Chen Wen. Impact of the 11-year solar cycle on the relationship between the East Asian winter monsoon and the following summer monsoon and the related processes. *Climatic and Environmental Research (in Chinese)*, 2014, 19(4): 486-496
 - [14] Xu J, Smith A K, Liu M, Liu X, Gao H, Jiang G, Yuan W. Evidence for non-migrating tides produced by the interaction between tides and stationary planetary waves in the stratosphere and lower mesosphere. *J. Geophys. Res.*, 2014, 119, doi: 10.1002/2013JD020150
 - [15] Liu M, Xu J, Yue J, Jiang G. Global structure and seasonal variations of the migrating 6-h tide observed by SABER/TIMED. *Science China: Earth Sciences*, 2015, 58: 1216–1227
 - [16] Liu M, Xu J, Liu H, Liu X. Possible modulation of migrating diurnal tide by latitudinal gradient of zonal wind observed by SABER/TIMED. *Science China: Earth Sciences*, 2015, doi: 10.1007/s11430-015-5185-4
 - [17] Yu Y, Wan W, Ren Z, Xiong B, Zhang Y, Hu L, Ning B, Liu L. Seasonal variations of MLT tides revealed by a meteor radar chain based on Hough mode decomposition. *J. Geophys. Res. Space Physics*, 2015, 120: 7030–7048
 - [18] Ren Z, Wan W, Xiong J, Liu L. Influence of DE3 tide on the equinoctial asymmetry of the zonal mean ionospheric electron density. *Earth Planets Space*, 2014, 66(117), doi:10.1186/1880-5981-66-117
 - [19] Li X, Wan W, Yu Y, Ren Z. Yearly variations of the stratospheric tides seen in the CFSR reanalysis data. *Adv. Space Res.*, 2015, 56(9): 1822-1832
 - [20] Li X, Wan W, Ren Z, Liu L, Ning B. The variability of nonmigrating tides detected from TIMED/SABER observations. *J. Geophys. Res. Space Physics*, 2015b, 120, doi:10.1002/2015JA021577
 - [21] Chen D, Chen Z Y, Lü D R. Simulation of the generation of stratospheric gravity waves in upper-tropospheric jet stream accompanied with a cold vortex over Northeast China. *Chinese J. Geophys.*, 2014, 57(1): 10-20
 - [22] Jia J Y, Preusse P, Ern M, *et al.* Sea surface temperature as a proxy for convective gravity wave excitation: a study based on global gravity wave observations in the middle atmosphere. *Ann. Geophys.*, 2014, 32: 1373-1394
 - [23] Jia Y, Zhang S D, Yi F, Huang C M, Huang K M, Gan Q, Gong Y. Observations of gravity wave activity during stratospheric sudden warmings in the Northern Hemisphere. *Sci. China Tech. Sci.*, 2015, doi: 10.1007/s11431-015-5806-3
 - [24] Xu J, Li Q, Yue J, Hoffmann L, Straka W C, Wang C, Liu M, Yuan W, Han S, Miller S D, *et al.* Concentric gravity waves over northern China observed by an airglow imager network and satellites. *J. Geophys. Res. Atmos.*, 2015, 120: 11058–11078
 - [25] Liu X, Xu J, Yuan W. Diurnal variations of turbulence parameters over the tropical oceanic upper troposphere during SCSMEX. *Sci. China Tech. Sci.*, 2014, doi: 10.1007/s11431-013-5445-5
 - [26] Liu X, Xu J, Liu H L, Yue J, Yuan W. Simulations of large winds and wind shears induced by gravity wave breaking in the mesosphere and lower thermosphere (MLT) region. *Ann. Geophys.*, 2014, 32, 543–552
 - [27] Liu X, Xu J, Yue J, Liu H L, Yuan W. Large winds and wind shears caused by the nonlinear interactions between gravity waves and tidal backgrounds in the mesosphere and lower thermosphere. *J. Geophys. Res. Space Physics*, 2014, doi: 10.1002/2014JA020221
 - [28] Liu X, Yue J, Xu J, Wang L, Yuan W, Russell J M, Hervig M E. Gravity wave variations in the polar stratosphere and mesosphere from SOFIE/AIM temperature observations. *J. Geophys. Res. Atmos.*, 2014, 119: 7368–7381
 - [29] Wei D, Tian W, Chen Z Y, *et al.* Upward transport of air masses during an occurrence of orographic wave in the UTLS over the Tibetan Plateau. *Chinese J. Geophys.*, (in Chinese, in press).
 - [30] Liu X, J. Yue J, Xu J, Yuan W, Russell J M, Hervig M E. Five-day wave in polar stratosphere and mesosphere temperature and mesospheric ice water measured by SOFIE/AIM. *J. Geophys. Res. Atmos.*, 2015, 120: 3872–3887
 - [31] Zhang S D, Yi F, Huang C M, Huang K M, Zhang Y H, Gong Y, Gan Q. Spatial and seasonal variability of high frequency gravity waves in lower atmosphere revealed by U.S. radiosonde data. *Ann. Geophys.*, 2014, 32: 1129-1143
 - [32] Gan Q, Yue J, Chang L C, Wang W B, Zhang S D, Du J. Observations of thermosphere and ionosphere changes due to the dissipative 6.5-day wave in the lower thermosphere. *Ann. Geophys.*, 2015, 33, 913-922
 - [33] Huang K M, Zhang S D, Yi F, Huang C M, Gan Q, Gong Y, Zhang Y H. Nonlinear interaction of gravity waves in a nonisothermal and dissipative atmosphere. *Ann. Geophys.*, 2014, 32, 263-275
 - [34] Gan Q, Du J, Ward W E, Beagley S R, Fomichev V I, Zhang S D. Climatology of the diurnal tides from eCMAM30 (1979 to 2010)

- and its comparison with SABER. *Earth Planets Space*, 2014, 66, doi:10.1186/1880-5981-66-103
- [35] Huang C M, Zhang S D, Zhou Q, Yi F, Huang K M, Gong Y, Zhang Y H, Gan Q. WHU VHF radar observations of the diurnal tide and its variability in the lower atmosphere over Chongyang (114.14° E, 29.53° N), China. *Ann. Geophys.*, 2015, 33: 865-874
- [36] Shuai J, Huang C M, Zhang S D, Yi F, Huang K M, Gan Q, Gong Y. Elevated stratopause events during 2003 – 2011 revealed by SABER/TIMED temperature observations. *Chinese J. Geophys.*, 2014, 57(8): 2465-2472
- [37] Hu J G, Ren R C, Xu H M. The boreal spring stratospheric final warming and its interannual and interdecadal variability. *Sci. China Earth Sci.*, 2014, 57(4): 710-718
- [38] Hu J G, Ren R C, Xu H M. Occurrence of winter stratospheric sudden warming events and the seasonal timing of spring stratospheric final warming. *J. Atmos. Sci.*, 2014, 71: 2319-2334
- [39] Hu J G, Ren R C, Xu H M, *et al.* Seasonal timing of stratospheric final warming associated with the intensity of stratospheric sudden warming in preceding winter. *Sci. China Earth Sci.*, 2015, 58(4): 615–627
- [40] Pogoreltsev A I, Savenkova E N, Aniskina O G, Ermakova T S, Chen W, Wei K. Interannual and intraseasonal variability of stratospheric dynamics and stratosphere-troposphere coupling during northern winter. *Journal of Atmospheric and Solar-Terrestrial Physics*, 2015, 136, 187-200
- [41] Xue X, Chen W, Chen S, Zhou D. Modulation of the connection between boreal winter ENSO and the South Asian High in the following summer by the stratospheric Quasi-biennial Oscillation. *J. Geophys. Res. Atmos.*, 2015, 120, 7393-7411
- [42] Guo D, Su Y C, Shi C H, *et al.* Double core of ozone valley over the Tibetan Plateau and its possible mechanisms. *J. Atmos. Sol.-Terr. Phys.*, 2015, 127-131
- [43] Zhang J, Tian W, Xie F, *et al.* Climate warming and decreasing total column ozone over the Tibetan Plateau during winter and spring. *Tellus B*, 2014, 66
- [44] Xie F, Li J, Tian W, *et al.* The relative impacts of El Nino Modoki, canonical El Nino, and QBO on tropical ozone changes since the 1980s. *Environmental Research Letters*, 2014, 9(6): 064020
- [45] Xie F, Li J, Tian W, *et al.* Indo-Pacific warm pool area expansion, Modoki activity, and tropical cold-point tropopause temperature variations. *Scientific reports*, 2014, 4
- [46] Wang C, Tian W, Zhang J, *et al.* Model study of the impacts of emissions, chemical and dynamical processes on the CO variability in the tropical upper troposphere and lower stratosphere. *Tellus B*, 2015, 67
- [47] Hu D, Tian W, Xie F, *et al.* Impacts of stratospheric ozone depletion and recovery on wave propagation in the boreal winter stratosphere. *Journal of Geophysical Research: Atmospheres*, 2015, 120: 8299-8317
- [48] Wang W, Tian W, Dhomse S, *et al.* Stratospheric ozone depletion from future nitrous oxide increases. *Atmospheric Chemistry and Physics*, 2014, 14: 12967-12982
- [49] Shang L, Liu Y, Tian W, *et al.* Effect of methane emission increases in East Asia on atmospheric circulation and ozone. *Advances in Atmospheric Sciences*, 2015, 32(12): 1617-1627
- [50] Zhang J, Tian W, Wang Z, *et al.* The Influence of ENSO on Northern Midlatitude Ozone during the Winter to Spring Transition. *Journal of Climate*, 2015, 28: 4774-4793
- [51] Zhang J, Tian W, Xie F, *et al.* Influence of the El Niño southern oscillation on the total ozone column and clear-sky ultraviolet radiation over China. *Atmospheric Environment*, 2015, 120: 205-216
- [52] Hu D, Tian W, Xie F, *et al.* Effects of meridional sea surface temperature changes on stratospheric temperature and circulation. *Advances in Atmospheric Sciences*, 2014, 31(4): 888-900
- [53] Shi C H, Xu T, Cai J, *et al.* The E-P flux calculation in spherical coordinates and its application. *Trans. Atmos. Sci.*, 2015, 38(2): 267-272
- [54] Shi C H, Guo D, Xu J J, *et al.* The latitudinal structure of recent changes in the boreal Brewer-Dobson circulation. *Atmos. Chem. Phys. Discuss.*, 2015, 15(17): 24403-24417
- [55] Wei K, M Takahashi, Chen W. Long-term changes in the relationship between stratospheric circulation and East Asian winter monsoon. *Atmospheric Science Letters*, 2015, 16: 359-365
- [56] Nath D, Chen W, Wang L, Ma Y. Planetary wave reflection and its impact on tropospheric cold weather over Asia during January 2008. *Adv. Atmos. Sci.*, 2014, 31(4), 851-862
- [57] Nath D, Chen W. Impact of planetary wave reflection on tropospheric blocking over the Urals-Siberia region in January 2008. *Adv. Atmos. Sci.*, 2016, 33(3), 309-318
- [58] Shi C H, Li H, Zheng B, *et al.* Stratosphere-troposphere exchange corresponding to a deep convection in warm sector and abnormal subtropical front induced by a cutoff low over East Asia. *Chinese J. Geophys.*, 2014, 57(1): 21-30
- [59] Chen D, Lü D R, Chen Z Y. Simulation of the stratosphere–troposphere exchange process in a typical cold vortex over northeast China. *Sci. China Earth Sci.*, 2014, 57(7): 1452-1463
- [60] Xu P, Tian W, Zhang J, *et al.* A simulation study of the transport of the stratospheric ozone to the troposphere over the northwest side of the Tibetan Plateau in spring. *Acta Meteorologica Sinica*, 2015, 73(3): 529-545
- [61] Yang Q, Tian W, Long X, *et al.* Transport of Dust Aerosols from Troposphere to Stratosphere over Qinghai-Xizang Plateau. *Plateau Meteorology*, 2014, 33(4): 887-899
- [62] Zhang J, Tian W, Long X, *et al.* Fact and Simulation of Dust Aerosol Transported to Stratosphere during a Strong Dust Storm in South Xinjiang. *Plateau Meteorology*, 2015, 34: 991-1004
- [63] Tian H, Tian W, Luo J, *et al.* Characteristics of Water Vapor Distribution and Variation in Upper Troposphere and Lower Stratosphere over Qinghai-Xizang Plateau. *Plateau Meteorology*, 2014, 33(1): 1-13
- [64] Liu W, Tian W, Shu J, *et al.* Effects of Quasi-biennial Oscillation on Tropical Tropopause and Deep Convective Activities. *Advances in Earth Science*, 2015, 30(6): 724-736
- [65] Shi C H, Chang S J, Sheng X Y, *et al.* The effects of cloud top above tropopause events on the structures of the upper troposphere and lower stratosphere in summer over East Asia. *Trans. Atmos. Sci.*, 2015, 38(6): 804-810
- [66] Zheng B, Shi C H. Factors contributing to linear trends of the tropical tropopause height and causes of their interannual variability from 1979 to 2011. *J. Trop. Meteorol.*, 2015, 31(3): 300-309
- [67] Zhang Y, Zhang S, Huang C, Huang K, Gong Y, Gan Q. The interaction between the tropopause inversion layer and the inertial gravity wave activities revealed by radiosonde observations at a mid-latitude station. *J. Geophys. Res. Atmos.*, 2015, 120, 8099–8111
- [68] Zhang Y H, Zhang S D, Huang C M, Huang K M, Gong Y, Gan Q. Diurnal variations of the planetary boundary layer height estimated from intensive radiosonde observations over Yichang, China. *Sci China Tech Sci*, 2014, 57: 2172–2176
- [69] Kong W, Yi F. Convective boundary layer evolution from lidar backscatter and its relationship with surface aerosol concentration at a location of a central China megacity. *J. Geophys. Res. Atmos.*, 2015, 120, 7928–7940
- [70] Liu F C, Yi F. Lidar-measured atmospheric N₂ vibrational-rotational Raman spectra and consequent temperature retrieval. *Optics Express*, 2014, 22 (23): 27833-27844

Development of Operational Space Environment Technology System

GONG Jiancun^{1,2}, CAI Yanxia^{1,2}, LIU Siqing¹, SHI Liqin¹, LU Guorui¹, CHEN Zhaofeng¹, BAO Lili¹

1. Center for Space Science and Applied Research, Chinese Academy of Sciences, Beijing 100190

2. University of Chinese Academy of Sciences, Beijing 100049

Key words

Space environment
technology system
multi-client web framework
e SpaceWx
SWASAP
PPSWAP

Abstract

With the increasing of users and the demands which are transforming from the monotonous traditional service to network service, we have developed multiple space environment web applications including browse-client, rich-client and mobile-client applications during the past few years. The architecture of operational space environment technology system (OSETS) that these applications rely on is described and the description of structural optimization of the architecture is provided. To demonstrate the evolution of the OSETS, three web application examples for e SpaceWx, Space Weather Situation Awareness Picture (SWASAP), Plug-and-Play SWx Analysis and Plotting Program (PPSWAP) are presented.

1 Introduction

Adverse conditions in the space environment can influence the performance and reliability of space-based and ground-based technological system that we rely on and can endanger human life or health. Increased reliance on technology, especially space-based technology, has resulted in significant growth in interest and need for space environment products.

Space environment technology system, which provides timely, accurate and reliable products to the end user with technology of computer and network, is an important aspect of research on space environment. With the support of china manned space engineering and the national 863 program, the OSETS in Space Environment Prediction Center (SEPC), NSSC, CAS) has been developed for more than 20 years from some original single independent software to now highly integrated operational system. OSETS works on integration of real-time monitor data, mature prediction

models, effects analysis and services 24/7.

With the increase in the number of users and the demands which are transforming from the monotonous traditional service to network service, OSETS is performing great changes and reforms. The network version software becomes one kind of software developing trend. Using the web technology removes geographical barriers to getting the space environment data and products, reduces the costs of information dissemination, and enables collaboration among people in different geographic locations.

In this paper, we discuss the innovation achievements in the transformation of OSETS over the past few years in SEPC. In the next Section we briefly present the architecture of multi-client web framework. In Section 3 we provide examples of application software we have built based on the concept of the web architecture. Finally in the conclusion, and from SEPC experience in the making of web-based applications, we expose the next challenges for the development of the OSETS.

2 Multi-client Web Framework Architecture

2.1 Architecture Concept

The multi-client web framework concept described here is based on the experience of SEPC in developing a broad variety of space environment web applications over the past years. The server cluster, web service and Apache HTTP Server are key technologies of the framework, which is scalable for the integration of distributed applications. In Section 2.1, we introduce the overall architecture concept. In Section 2.2 and 2.3, we describe the performance optimization in the multi-client web framework. In Section 2.4, we provide an example of how the multi-client web framework is used for PPSWAP.

The multi-client web framework meeting our integration needs is deployed within SEPC as the common web platform for the development and operation of web applications. As shown in the Fig.1, the framework uses the hierarchical structure, which is divided into four layers: client layer, business layer, data access layer and storage layer.

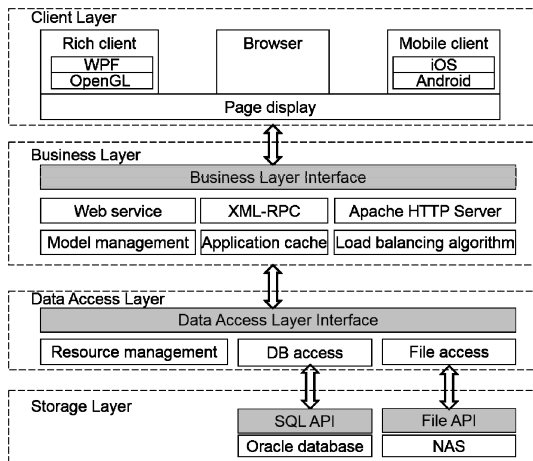


Fig. 1 Multi-client web framework architecture Client layer

(1) Client Layer

The client layer, which can be classified into 3 categories: browsers (IE, Chrome, Firefox ...), rich clients (applications written for the desktop), mobile clients (phone, pad ...), provides UI design. The browser-based web applications utilize a traditional B/S structure, the primary benefit of which is the client only needs to install a browser to have easy access to web pages of space environment applications. Rich-clients-based and

mobile-clients-based applications have more diversified display technologies and more flexible data request methods, which are implemented by web service. As a result, customized solutions are allowed by the above two type clients when displaying text, tables, images and other information.

(2) Business Layer

Business layer provides three functions: responding to requests from clients, executing space environment models on servers and dealing with problems caused by high concurrency.

Web service and XML-RPC are used to provide a range of interfaces to the client layer. For browser-based web applications, the Apache HTTP Server is used to deploy the web site. Based on the above three methods, requests from clients can be responded.

Space environment model management module manages inputs, outputs and restricted condition of space environment models, based on which space environment models can be executed on servers methodically.

Server cluster is a key technology to deal with problems caused by high concurrency. Business layer manages the load information of each server cluster and designs different algorithms to achieve cluster load balancing. Additionally, catching strategy is very important to optimize business processing.

(3) Data Access Layer

Data access layer manages the remote access to databases, file storage servers and other resources. In the multi-client web framework, in order to improve the scalability of the integration of different space environment applications, uniform database and file interface specifications are utilized by each space environment application, which facilitates the upgrade of the software and hardware in the future.

(4) Storage Layer

Storage layer persistently stores various data, including the historical and real-time space environment monitoring data, the product data calculated by forecasters and space environment models, and the management data for servers and space environment models. Oracle Database and Network-Attached Storage (NAS) are the key components of storage layer, on the basis of which the multi-client web framework can provide 24/7 operational services.

In the multi-client web framework, clients can reuse formerly stored display solutions, and servers release

"plug and play" services, then a new space environment application is developed and added to the framework, which is scalable.

2.2 Dispatcher-based Web Server Cluster System in the Multi-client Web Framework

As the amount of applications grows ever larger, the multi-client web framework is found to be unstable when dealing with large number of concurrent users. The single-server mode cannot meet the demand of high concurrency, consequently, a dispatcher-based web server cluster technology is applied, which improves the performance, scalability and reliability.

As shown in Fig.2, performance optimization of the multi-client web framework is mainly reflected in the design of the dispatcher and three server clusters: Web Server Cluster, File Server Cluster and Model Calculation Server Cluster (Section 1.3 discusses this further).

Dispatcher-based web server cluster system consists of a dispatcher and multiple web servers distributed in the LAN. The dispatcher is responsible for receiving requests from clients, and assigning requests to the cluster server nodes, based on load balancing algorithm. The entire cluster system has a virtual IP address, which makes the system look like a single machine on the outside. Dispatcher-based web server cluster can handle requests concurrently, achieve fine-grained load balancing, speed up the process and shorten the time delay.

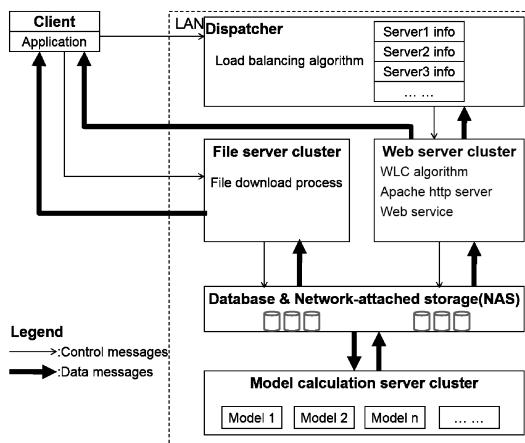


Fig. 2 Performance optimization of the multi-client web framework

2.3 Three Clusters in the Multi-client Web Framework

In the multi-client web framework, there are file type

data and numerical type data. File type data is generally bigger, taking up more network resources, which leads to the slower response of the numerical type data request, or even leads to response failed, degrading the user experience. To solve this problem, we divide the traditional cluster into two parts: Web Server Cluster and File Server Cluster. Accordingly, we adopt different response methods to implement diversion with respect to numerical and file type requests. Meanwhile, with an increasing number of the space environment models, the calculation burden is heavy, so the space environment model calculation adopts the cluster technology as well. In summary, based on the characteristics of space environment web applications, the multi-client web framework includes three server clusters (1) Web Server Cluster (2) File Server Cluster (3) Model Calculation Server Cluster. To achieve load balancing, the multi-client web framework designs and implements different load balancing algorithms for three server clusters respectively.

Web Server Cluster responds to client requests. When a numerical type request happens, the node of Web Server Cluster queries the Oracle Database and the NAS, and replies information directly. When a file type request happens, according to Weighted Least-Connection (WLC) algorithm, the node selects the target file downloading server, and then replies queried file index and the target server information to client applications.

File Server Cluster provides downloading services of image and text files. Based on a file index, the client initiates file downloading requests to the target server of File Server Cluster.

Model Calculation Server Cluster executes space environment models to get the space environment forecasts, alerts, and other products. Model Calculation Server Cluster has a task scheduling server, which selects suitable cluster nodes to execute new tasks.

2.4 Example

As a detailed example of how the multi-client web framework is used for the PPSWAP based on rich client, we describe the progress of downloading Huairou Solar Observing Station $H\alpha$ image observed on February 1, 2016. In Fig.3, we illustrate this progress by following the control flow and data flow through these numbered steps.

- (1) Client initiates a request to the dispatcher. The key parameters of the request are:

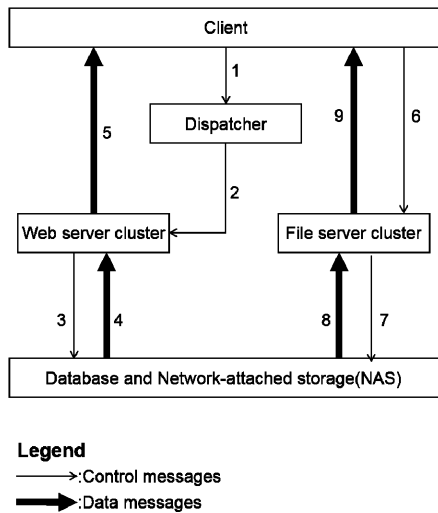


Fig. 3 Control and data flow of Huairou Solar Observing Station $H\alpha$ image downloading progress

- Request type: “file type”
- Start date: “2016-02-01”
- End date: “2016-02-01”
- Content name:
“CAS_SUNCHROMO_HA_FD_IMAGE”

- (2) Dispatcher forwards the request to the web server. According to the load balancing algorithm, the dispatcher chooses a target server from the Web Server Cluster, and forwards the request to the chosen web server through the MAC address modification method.
- (3) The chosen web server reads and analyzes the content of request, then accesses to the Oracle Database through standard SQL API.
- (4) The Oracle Database generates the storage index of Huairou Solar Observing Station $H\alpha$ image observed on February 1, 2016, and returns the index to the chosen web server.
- (5) The chosen web server replies to the client. Depending on the returned index of the Oracle Database, the chosen web server generates the file of the storage index. Meanwhile, based on the WLC (Weighted Least-Connection) algorithm it selects the target file downloading server from the File Server Cluster. The chosen web server replies to the client with the index file and the IP of the chosen file server. This technology effectively reduces the network pressure.
- (6) In accordance with the storage index of Huairou Solar Observing Station $H\alpha$ image, the client initiates the file downloading request to the chosen

sen file server.

- (7) The chosen file server reads and analyzes request content, then accesses the Network Attached Storage (NAS) through standard file API.
- (8) The NAS server replies with image files.
- (9) The chosen file server forwards image files to the client.

Only successful progresses are described in the above nine steps. In our actual work, many failures and exceptions are addressed.

3 Examples of Distributed Network Applications

Based on the multi-client web framework architecture, SEPC has developed multiple space environment web applications, which belong to the client layer of the architecture. The functions and features of three web application examples for e SpaceWx, SWSAP and PPS-WAP are presented in the following section.

3.1 e SpaceWx app for Smartphone

The e SpaceWx app, China’s first professional mobile application in space environment forecast domain, was released in Nov. 2014, providing space environment services at all time and places. The app is designed to meet the requirements of space environment monitor, forecast and alert service, characteristic of accuracy, timeliness, and comprehensiveness, furthermore, strengthen the ability of space environment service. The accomplishment was on the basis of technical and scientific achievements during the past decade including a series of prior-warning and safeguarding technologies in space environment research such as data characteristic extracting and analyzing technology, model forecasting technology, safeguarding and serving technology, products distributing by mobile web technology. e SpaceWx is an example of mobile client.

There are four primary function-modules of e SpaceWx.

- Up-to-the-minute forecast products, which can be obtained through the forecast function-module, consist of daily report and forecast on solar-geophysical activity and products by different kinds of models, for instance, solar and geomagnetic indices forecast models of $F_{10.7}$, Ap , Kp , AE and Dst , coronal hole index model, GEO relativistic electron flux model, magnetopause & bow-shock model, and sudden ionosphere disturbance model, and all the models are developed by SEPC.



Fig. 4 The e Space Wx app is aimed at providing space environment services through Smartphone.

- The alert function-module automatically pushes space weather alerts to the users when environmental disturbances occurred, sorted into four event-types of solar X-ray flare alert, solar proton event alert, geomagnetic storm alert and GEO relativistic electron enhancement alert, which are labeled as yellow, orange and red color-scales depending on the effect on people and systems analogous to hurricanes, tornadoes, and earthquakes that convey severity. Moreover, when the environmental disturbances exceed the orange-level, forecasters will issue particular bulletins so that users can understand the event cause, evolution, and possible effects in detail through the news function.
- The monitor function-module supplies abundant real-time observing data including solar, interplanetary, geomagnetic field, energetic particles, and ionosphere domains of space environment. Besides the internet-shared data such as SDO, SOHO solar images, ACE solar wind parameters (distributed by SWPC), and Dst index (distributed by WDC), the geomagnetic field, cosmic ray, ionospheric scintillation and TEC disturbing data observed by SEPC are also supplied.
- The user-favorite function-module stores the in-

terested products list, user can choose and change the list to define his own interface to directly access interested forecast, alert and monitor products efficiently and rapidly.

The iPhone and Android version of e SpaceWx are both accessible to download from app stores or from the official website of SEPC www.sepc.ac.cn. Hundreds of users have downloaded up to now, and the UI and function design are appreciated. China Science Daily made a special report on this by the headline titled “Space Environment Forecast in the Pocket”.

3.2 SWSAP (Space Weather Situation Awareness Picture)

SWSAP is implemented to enable SEPC to assess and predict the risk of space environment to satellites in orbit regarding the radiation, atmosphere, geomagnetic environment effects, and the fragmentation debris orbiting Earth. The source code of SWSAP is written in C++ and runs on Microsoft Windows operating system. SWSAP is an example of rich-client application.

SWSAP is composed of five major software function modules.

- Radiation Environment Module. This module is developed to calculate the spatial flux distribution

of energetic particles in the terrestrial space, especially of the radiation belt, utilizing the models of AP8, AE8 and Geomagnetic Transmission. The radiation environment along the orbit is calculated when the orbit elements are acquired, from which the effects and risk to satellites are assessed and predicted with respect to single event effect, radiation injury effect and surface charging effect, visualized as labels with different colors corresponding to the risk levels. The time periods when the satellite starts crossing radiation belt are also calculated.

- Atmosphere Environment Module. The global spatial distribution of the atmosphere density in the upper atmosphere is calculated utilizing the MSISE-2000 model, from which the orbital decay risk is assessed for each LEO satellite.
- Magnetopause Environment Module. The Earth's dynamic magnetopause and bow shock shapes driven by real-time solar wind parameters are empirically modeled, and results are displayed with the geomagnetic field in the background. The sub-solar distance of the magnetopause is modeled to determine whether a Geosynchronous Magneto-

pause Crossing (GMC) occurs, and if so, the dawn-side and dusk-side longitudes of the crossing points are then calculated which is referred to determine a GEO satellite whether crosses magnetopause or not.

- Debris Environment Module. This module evaluates the possibility of collision risk of debris to satellites and judging whether a possible collision has occurred between the satellite and debris.
- Fault Diagnosis Module. This module guides users to determine whether a fault of the satellite is caused by space environment factors based on expert system.

In the process of developing SWSAP, the issues of visual effects and the accelerated rendering of big volume data are hard to cope with. We adopted the improved Ray-casting algorithm to render high-quality 3D space environment scenes in real time. In order to accelerate rendering speed, the graphics workstation that adopts parallel algorithms based on GPU is used to replace the ordinary PC.

SWSAP has been installed at some departments in China, such as satellite operation management department and satellite navigation department.

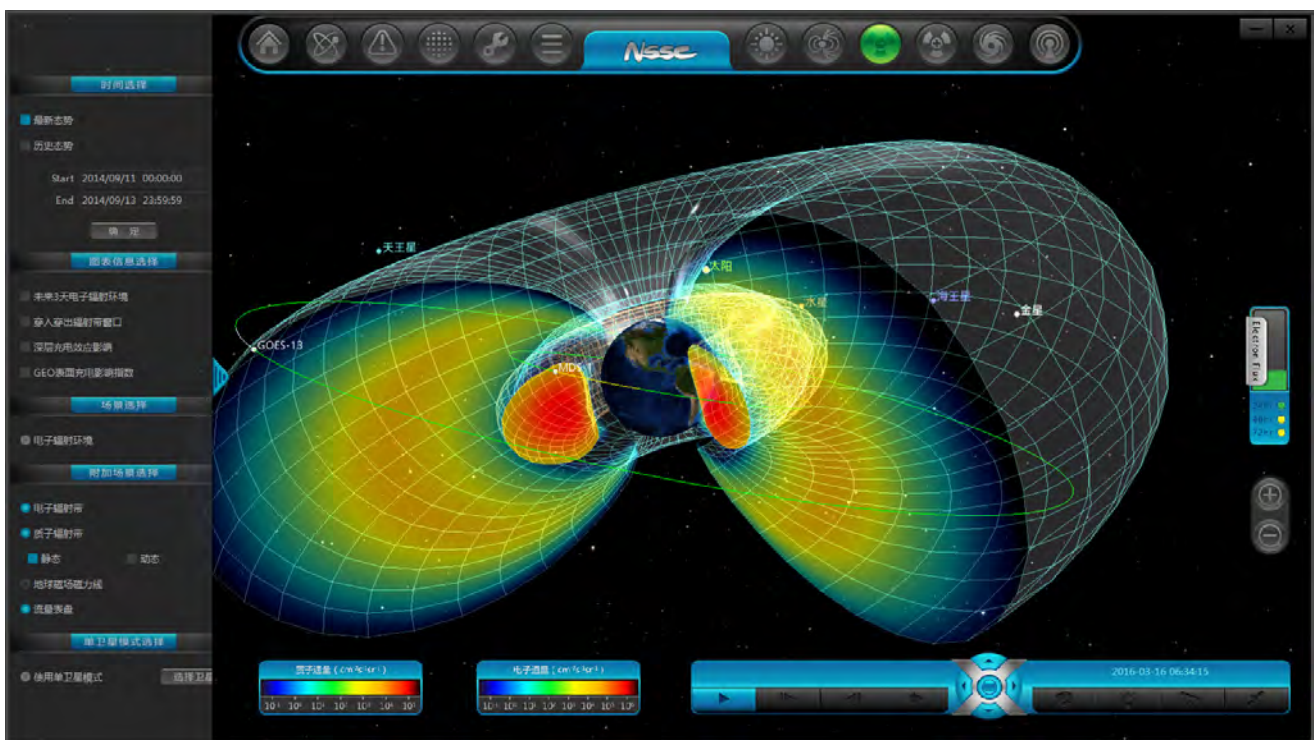


Fig. 5 Screen shot of the SWSAP showing radiation environment .Colors of each orbit indicate the radiation risk levels. Green, yellow and red means the satellite is in a safe, dangerous and very dangerous radiation environment, respectively.

in the form of charts, movies, and statistical tables, which will be displayed on the right area of the interface by clicking the left data list menu of the interface. Forecasters can optionally assemble all kinds of space environment information and define personal interfaces with requested data for space environment analysis through utilizing the function of historical data inquiry and space environment events statistical results inquiry.

The message board as well as the instant messenger is also integrated as the chat room service to strengthen the communication and information sharing between forecasters.

Considering that this software provides convenient interaction between user and application, we aim to make it possible for both domestic and international space environment forecasters and researchers to have open access to this software in the web-based form, which is downloaded at <http://eng.sepc.ac.cn/sfdownload.php>.

4 Conclusion

OSETS is the key of transition from achievement in space environment research into operational products. OSERS based on multi-client web framework architecture is proposed as an innovative system for users demand for network service including operational space environment data, products, effect analysis etc. Like other web-based system, OSETS has four main attributes: wide accessibility, flexibility, reusability and user-friendliness, which is realized by the optimization in the multi-client web framework.

The e SpaceWx, SWSAP and PPSWAP are the typical web applications based on OSETS. These applications allow anywhere on the network to access a rich supply of space environment data and product conveniently. Meanwhile, SWSAP and PPSWAP, which are rich-client applications, are often characterized by the ability to perform many functions such as calculation and plotting without net connection.

In the future, with the development of space environment and information technology, OSERS will be developed towards digital and intelligent towards.

References

- [1] Tobiska W K, Bouwer S D. Distributed networks enable advances in US space weather operations. *Advances in Space Research*, 2011, **47**(12): 2223-2234
- [2] Nicula B, Marqué C, Berghmans D. Visualization of Distributed Solar Data and Metadata with the Solar Weather Browser. *Solar Physics*, 2008, **248**(2): 225-232
- [3] Crowley G, Guhathakurta M, Oh S J, et al. Space Weather Gets Real—on Smartphones. *Space Weather-the International Journal of Research & Applications*, 2010, **8**(10): 898-907
- [4] Génot V, Jacquy C, Bouchemit M, et al. Space Weather applications with CDDP/AMDA. *Advances in Space Research*, 2010, **45**(9): 1145-1155
- [5] Sanz A L, García M N M, Batista V F L. XML Based Integration of Web, Mobile and Desktop Components in a Service Oriented Architecture[C]// *International Symposium on Distributed Computing and Artificial Intelligence, DCAI 2008*. Spain: University of Salamanca, 2008: 565-573
- [6] Ghemawat S, Gobioff H, Leung S T. The Google file system[C]// *Acm Sigops Operating Systems Review*. ACM, 2003: 29-43.

Observations from FENGYUN Satellites

Tang Yunqiu¹, Li Yingying¹, Zhang Jiashen¹, Wang Jingsong²

1. National Satellite Meteorological Center/National Center for Space Weather, China Meteorological Administration, Beijing 100081

2. Department of Integrated Observations, China Meteorological Administration, Beijing 100081

* E-mail: tangyq@cma.gov.cn

Key words

FY satellites
Polar-orbiting satellite
Geostationary Satellite

Abstract

Fengyun (FY) Satellite has a polar-orbiting series and a geostationary series. Up to now, 7 polar-orbiting (FY-1A/B/C/D and FY-3A/B/C) and 7 geostationary (FY-2A/B/C/D/E/F/G) satellites were launched. FY data has been being intensively applied not only to meteorological monitoring and prediction but also to many other fields regarding ecology, environment, disaster and so on.

1 Development of FENGYUN Satellites

Since initiation of FENGYUN (FY) meteorological satellite program in 1970, China has developed and successfully launched 7 polar-orbiting satellites and 7 geostationary satellites. The FY polar-orbiting system has been upgraded to the new generation or FY-3 series with satellite payload instruments increased from 1 to 10, extending the observation spectrum from visible and infrared to ultraviolet and microwave, and realizing three dimensional measurements of the atmosphere. The geostationary system, operating in dual satellite constellation and with an orbital storage as back-up, has become more stable and reliable for the service^[1].

1.1 FENGYUN Polar-orbiting Meteorological Satellites

1.1.1 FY-1 Program

FY-1 is the first generation of FENGYUN polar-orbiting meteorological satellites. The FY-1 polar-orbiting, sun-synchronous meteorological satellite program started in 1980's. Four satellites, namely the FY-1A/B/C/D were launched to provide visible and infrared radiometry measurement for weather and Earth environment

monitoring. Derived products include the Vegetation Index (NDVI), Sea Surface Temperature (SST), water vapor content, atmospheric aerosol optical thickness and so on. FY-1D is the last model of the FY-1 series and is operationally.

1.1.2 FY-3 Program

FY-3 is the second generation of FENGYUN polar orbiting meteorological satellites^[2-3]. The FY-3 is a new polar-orbiting, sun-synchronous meteorological satellite series planned to cover the duration of 2008–2021. The first three models FY-3A, B and C were launched in May 2008, November 2010 and September 2013, respectively. And FY-3D will be launched at the end of 2016. FY-3E is an early morning orbit satellite, which is scheduled to be launched in 2018. China is planning to launch a FengYun-3 Precipitation Radar (FY-3R) satellite at 2020 in order to monitor the strong precipitation accompanying disastrous weather events like typhoon mainly. The FY-3R will operate in a non- sun-synchronous circular orbit with an inclination of 50°C, and the flight altitude is about 407 km. The primary payloads on the FY-3R are the precipitation measurement radar (PMR), the microwave radiation imager (MWRI), the Medium Resolution Spectral Imager (MERSI) and the

**Tab. 1** Chronology of FENGYUN polar-orbiting meteorological satellites

Satellite	launch date	instrument	nature	design life
FY-1A	7 Sept. 1988	MVISR(Multichannel Visible Infrared Scanning Radiometer)	experimental	2 years
FY-1B	3 Sept. 1990	MVISR	experimental	2 years
FY-1C	10 May 1999	MVISR	operational	2 years
FY-1D	15 May 2002	MVISR	operational	2 years
FY-3A	27 May 2008	VIRR (Visible and Infra-Red Radiometer), MERSI (Medium Resolution Spectral Imager), IRAS (Infrared Atmospheric Sounder), MWTS (Micro-Wave Temperature Sounder), MWHS (Micro-Wave Humidity Sounder), MWRI (Micro-Wave Radiation Imager), SBUS (Solar Backscatter Ultraviolet Sounder), TOU (Total Ozone Unit),SIM(Solar Irritation Monitor), ERM (Earth Radiation Monitor), SEM (Space Environment Monitor)	experimental	3 years
FY-3B	Nov. 5 2010	VIRR, MERSI, IRAS, MWTS, MWHS, MWRI, SBUS, TOU, SIM, ERM, SEM	experimental	3 years
FY-1A	7 Sept. 1988	VIRR, MERSI, IRAS, MWTS, MWHS, MWRI, GNOS (GNSS Occultation Sounder), SBUS, TOU, SIM, ERM, SEM	experimental	5 years

global navigation satellites system (GNSS) occultation sounder (GNOS).

Compared with FY-1 satellite, the FY-3 satellite is more capable in terms of vertical temperature and humidity sounding, ozone detection, and microwave, visible, infrared imaging. Future FY-3 models will carry the atmospheric composition detection payload to support the greenhouse gas monitoring for climate change study.

1.2 FENGYUN Geostationary Meteorological Satellites

1.2.1 FY-2 Program

FY-2 is the first generation of FENGYUN geostationary meteorological satellites. The FY-2 geostationary satellite program has produced 6 spacecraft models (FY-2A/B/C/D/E/F) since 1997 and will continue with FY-2G/H in the future. Two FY-2 satellites at 86.5°E and at 105°E constitute a dual satellite constellation for operational observation. FY-2 satellites carry the Visible and

Infrared Spin Scan Radiometer (VISSR) capable of cloud imagery of 5 spectral channels. Derived products include the Atmospheric Motion Vector (AMV), Sea Surface Temperature (SST), Outgoing Long wavelength Radiation (OLR) and so on^[4].

1.2.2 FY-4 Program

FY-4 is a new geostationary meteorological satellite series planned to cover the duration of 2016–2020. Compared with FY-2 satellites, the main objective of FY-4 series is to monitor rapid changing weather systems and improve warning and forecasting capability. This will be accomplished by providing.

- (1) High temporal and spatial resolution imaging in over 14 spectral bands in Visible (VIS), Near Infrared (NIR) and Infrared (IR) spectral regions.
- (2) Lightning imaging.
- (3) High spectral resolution IR sounding observations over China and adjacent regions.
- (4) Space weather monitoring and warning.

Development of FY-4 series is in parallel with other new generation meteorological satellites in the world. It is intended to make better contribution to the World Meteorological Organization (WMO) global observing system.

2 Data Sharing and Service

FENGYUN satellite data is provided to both domestic and international users via the following ways^[5]:

- (1) Direct Broadcast Service: Users with appropriate

Tab. 2 Chronology of FENGYUN geostationary meteorological satellites

Satellite	Launch	Instrument	Nature	Design Life
FY-2A	10 June 1997	VISSR(Visible and Infra-red Spin Scan Radiometer)	experimental	3 years
FY-2B	25 June 2000	VISSR	experimental	3 years
FY-2C	19 Oct. 2004	VISSR	operational	3 years
FY-2D	8 Dec. 2006	VISSR	operational	3 years
FY-2E	23 Dec. 2008	VISSR	operational	3 years
FY-2F	13 Jan. 2012	VISSR	operational	4 years
FY-2G	31 Dec. 2014	VISSR	operational	4 years

receiving equipment can directly receive data transmission of each operational FENGYUN satellite.

(2) DVB-S Dissemination System: The CMACast system uses the DVB technology to disseminate real-time products to subscribers.

(3) Internet: The FENGYUN Satellite Data Service Network* is one of the way to download real-time or historical products.

(4) FTP Service: For users demanding for large bulk data in real-time or near-real-time, the system initiatively pushes the data to user-specified FTP servers.

(5) Manual service: If large volume data is requested and has been approved by China Meteorological Administration, manual service is also available.

The website has become one of the main accesses to FENGYUN satellite data for global users. Users can easily obtain data, use the Web GIS platform to browse the satellite imagery, customize the content and format of the required data after a quick registration.

3 Weather, Natural Disaster and Environmental Monitoring

In 2014–2015, FENGYUN satellites were operationally used to monitor weather, large-scale meteorological disasters, weather-induced secondary natural hazards and environment changes, and provide geophysical parameters for scientific research in climate change and its variability, climate diagnosis, and predictions. FENGYUN satellites render global and regional meteorological information for aviation, ocean navigation, agriculture, forestry, marine activities, hydrology, and many other economic sectors^[6-8]. All monitoring results and analysis were promptly provided by CMA to the public and government for decision making. Some typical examples are shown as follows.

3.1 Monitoring of Strong Convection Weather

Strong convection weather monitoring is one of the main applications of meteorological satellite service. In 2014–2015, FENGYUN satellites played an effective and timely role in monitoring heavy rainfalls and strong convection weathers over China, the products such as rainfall estimation, strong convection animation were generated by CMA for the public and government's information which proved very important for disasters prevention and reduction. Figure 1, 2 and 3 are the pro-

ducts of FY-2G to monitor heavy downpour over Northeastern part of Southwest China and Jiangnan region in August, 2015.

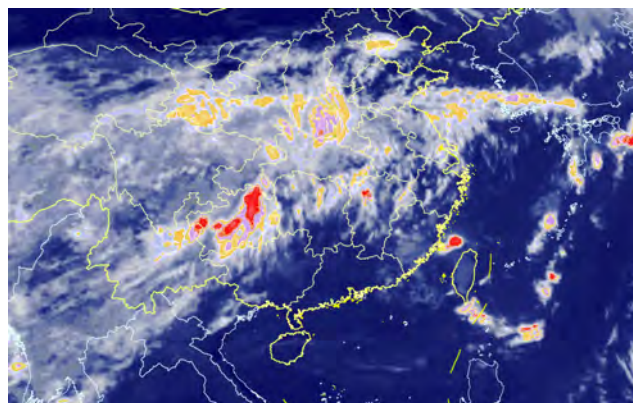


Fig. 1 Infrared image by FY-2G at 10:00 (Beijing Time) of 18 August 2015

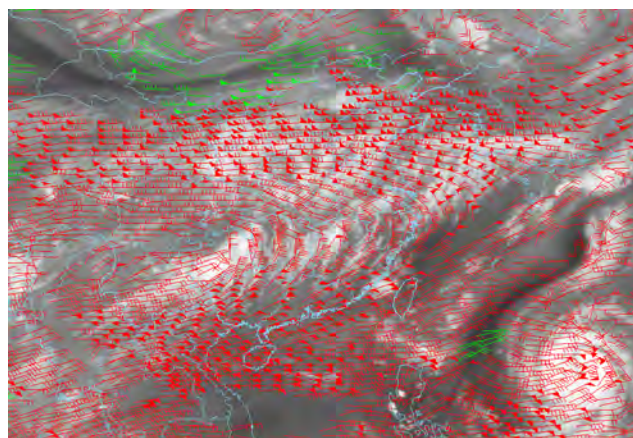


Fig. 2 Cloud wind and Steam images by FY-2G at 13:30 (Beijing Time) of 18 August 2015

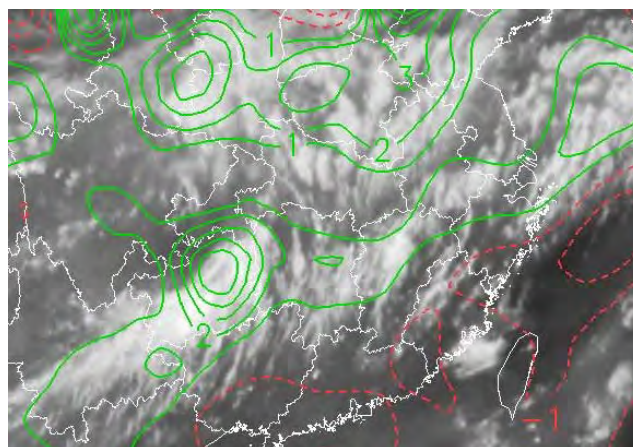


Fig. 3 Cloud wind upper level divergence images by FY-2G at 13:30 (Beijing Time) of 18 August 2015

*Website: <http://satellite.cma.gov.cn>

3.2 Monitoring of Tropical Cyclone

In July 2015, Typhoons CHAN-HOM, LINFA and NANNGKA made their debut on the Northwest Pacific waters one after another. NSMC tracked down their path and monitored their possible development, landfall and strength using the satellite remote sensing products stemmed from multiple sources (Figure 4), demonstrating the typhoon monitoring capabilities enabled by the multi-sourced satellite data. The observation provided important support to typhoon positioning and forecast operations at the National Meteorological Center.

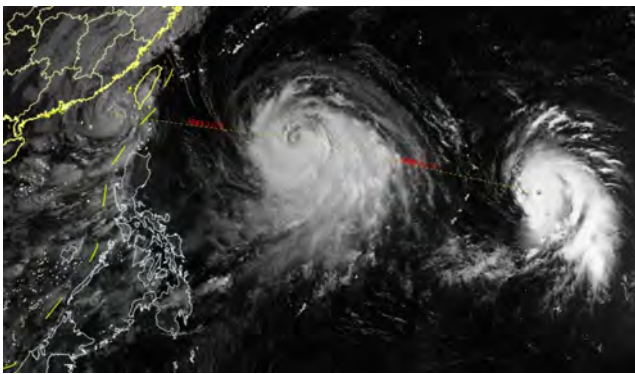


Fig. 4 Visible images generated by FY-2 at 07:32 (Beijing Time) of 8 July 2015

3.3 Monitoring of Sand and Dust

The FENGYUN satellites data were effective in imaging the sand and dust storms and estimating the strength, to provide useful information for the forecasters at the national weather consultation meeting.

Affected by cold weather in March, 2014, the north-western part of China and the Inner Mongolia area reported dust weathers. The following are the monitoring results stemmed from FENGYUN satellites.

The image derived from FY-3B satellite on 17 March depicts the extensive dust weather in the western part of Inner Mongolia, Ningxia, and the northern part of Shanxi. Figure 5 which collected by FY-3B satellite in the morning of March 19 shows the dust weather in the eastern part of Xinjiang, the western part of Gansu, and the northwestern part of Qinghai, covering an area of 67000 square kilometers. In the afternoon of 19 March the sphere of dust weather moved eastwards with more areas affected (Figure 6).

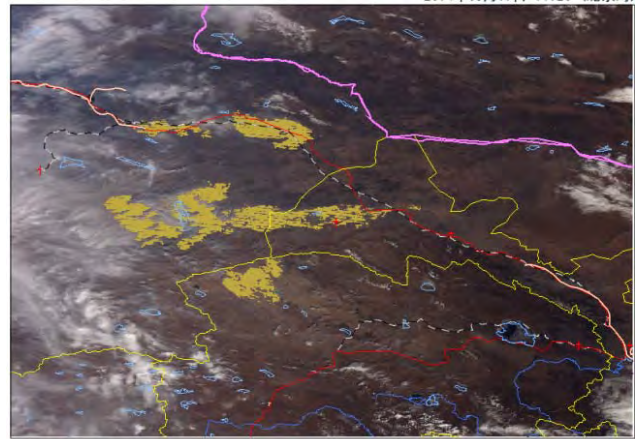


Fig. 5 Dust weather image generated by FY-3B at 11:20 (Beijing Time) of 19 March 2014



Fig. 6 Dust weather image derived from FY-3B at 14:50 (Beijing Time) of 19 March 2014

3.4 Monitoring of Droughts

Sustained abnormally dry weather brought droughts to Liaoning and Jilin in July-August, 2014. The drought maps built on FY-3C/MERSI data from August 1 to August 12 show that the central, western and southern parts of Liaoning (Figure 7) and the western and eastern parts of Jilin (Figure 8) suffered mild or moderate droughts.

3.5 Monitoring of Heavy Fog

The images collected by FY-2E meteorological satellite at 08:00 (Beijing Time) of March 30, 2015 show that heavy fog prevailed over the Bohai Sea, the Yellow Sea, eastern Shandong, southern Liaoning, eastern Sichuan, western Hubei and southern Henan, with an affected area up to 570 000 km² (Figures 9 and 10).

3.6 Monitoring of Volcano Eruption

Calbuco volcano, sitting in the southern part of Chile

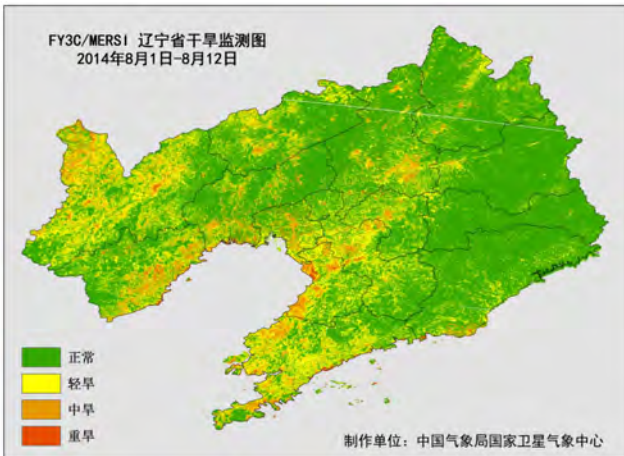


Fig. 7 A drought map for Liaoning derived from FY-3C/ MERSI data from 1 August to 12 August

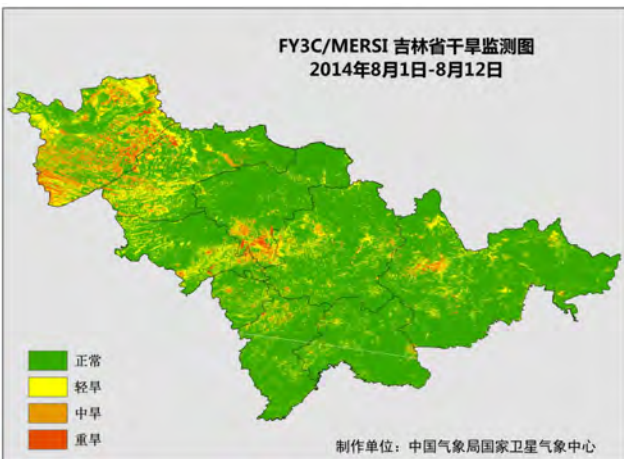


Fig. 8 A drought map for Jilin derived from FY-3C/ MERSI data from 1 August to 12 August

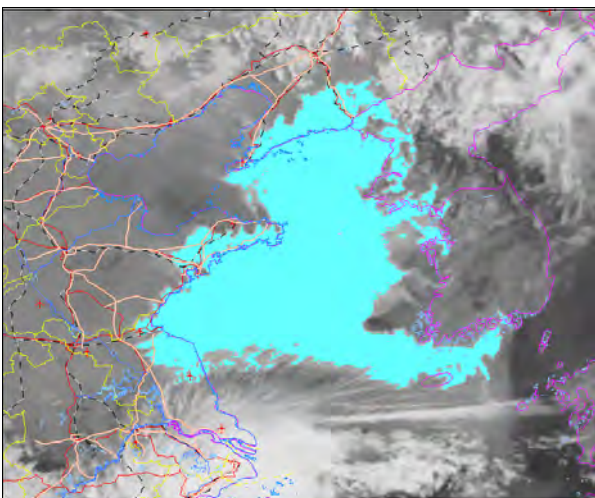


Fig. 9 A fog map generated by FY-2E at 08:00(Beijing Time) of 30 March 2015, showing the heavy fog over the Yellow Sea and the Bohai Sea

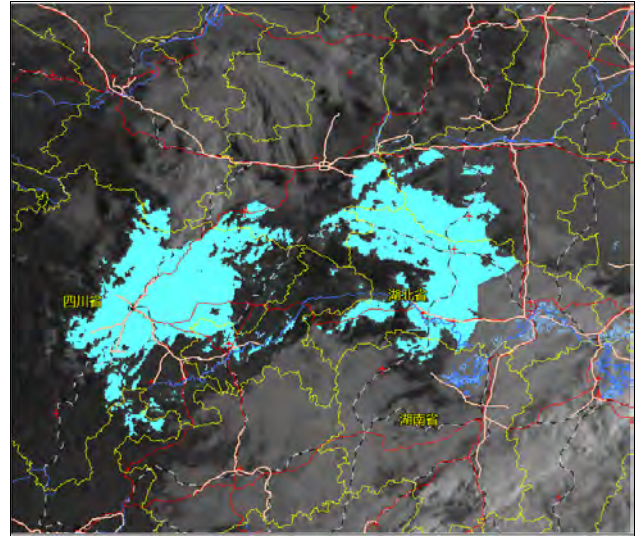


Fig. 10 A fog map generated by FY-2E at 08:00(Beijing Time) of 30 March 2015 showing the heavy fog over Sichuan, Hubei and other areas

(72.6°W/41.33°S) made an eruption at 18:00UTC of 22 April 2015. In the early morning of 23 April Calbuco volcano erupted again. It was remaining in eruption on 24 April.

The volcano eruption was monitored by the VIRR data derived from FY-3C. It can be seen in Figure11 that the volcanic ash was steadily heading for the northeast due to the prevailing southwesterly winds in the locality, affecting its neighbor Argentina. The monitoring results collected at 13:50UTC of April 23 showed that San Martin de los Andes in the southwestern part of Argentina has been covered by thick volcanic ash clouds, with a height up to 15 km.

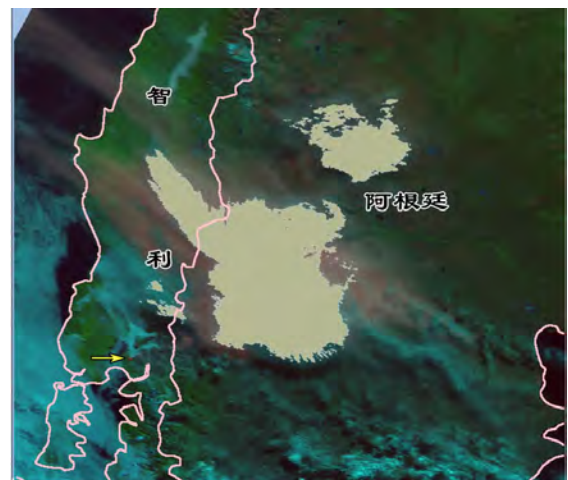


Fig. 11 A Calbuco volcanic eruption map derived from FY-3C data

3.7 Monitoring the Change of a Lake Body

In mid and late May 2015 many areas in southern China reported heavy rainfalls. On 14 May, some parts of southern Dongting Lake registered a rainfall up to 50mm. A rainfall map based on FENGYUN satellite data collected on 21 May and 12 May. One can see a noticeably enlarged lake body on May 21. It was estimated that the lake body reached some 1130 square kilometers on May 21, or 420 square kilometers up compared with the one on 12 May with an area increase by 60% (Figure 12).

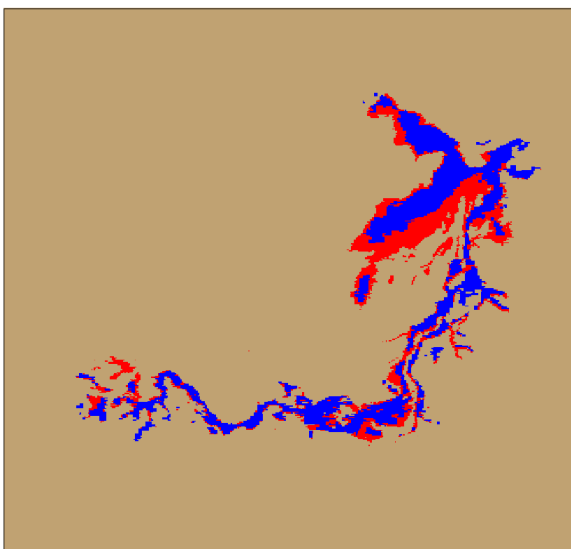


Fig. 12 The changed water body of Dongting Lake between 21 May and 12 May 2015

Compared with the size of lake body recorded on 12 May 2014, the water body of Dongting Lake on 21 May 2015 was enlarged by some 24%.

3.8 Monitoring of Monthly Earth Surface Temperature

A monthly maximum surface temperature monitoring result for August 2015 shows that a wide range of Chinese territories, including the southwestern part of Northeast China, most part of Inner Mongolia, most part of North China, the eastern part of the Huanghuai Valley, Northwest China, the northeastern and central part of the Southern Yangtze River Delta region, and the eastern and central part of South China, had a monthly maximum surface temperature exceeding 40°C, while the central and western part of Northwest China and the western part of Inner Mongolia having a monthly max-

imum surface temperature exceeding 60°C.

3.9 Monitoring of Haze

In fourth quarter of 2015, the combined effects encouraged the repeated incidences of hazy weather in northern China. FENGYUN satellites spotted 17 incidences of hazy weather in October, 11 in November and 7 in December. Hazy weather mainly prevailed over the northern and northeastern part of China, affecting the Huanghuai Basin as well. Some severe hazy weather processes were reported, including the one that occurred in early November across the northeastern and northern part of China. Beijing reported two red labeled heavy pollution processes during 8–10 December and 19–22 December.

An image stemmed from FY-3B at 14:00(Beijing Time) of 20 December showed that in the cloudless areas or the areas with few clouds, an array of areas have witnessed moderate or severe haze, including Beijing, the central and southern part of Hebei, most part of Henan, western Shandong, most part of Hubei, Shanxi and Shaanxi. In the above-mentioned areas, the AAI collected by FY-3B/TOU sat between 3.5 and 4.5 (Figure 13), suggesting an obvious aerosol impact on the areas.

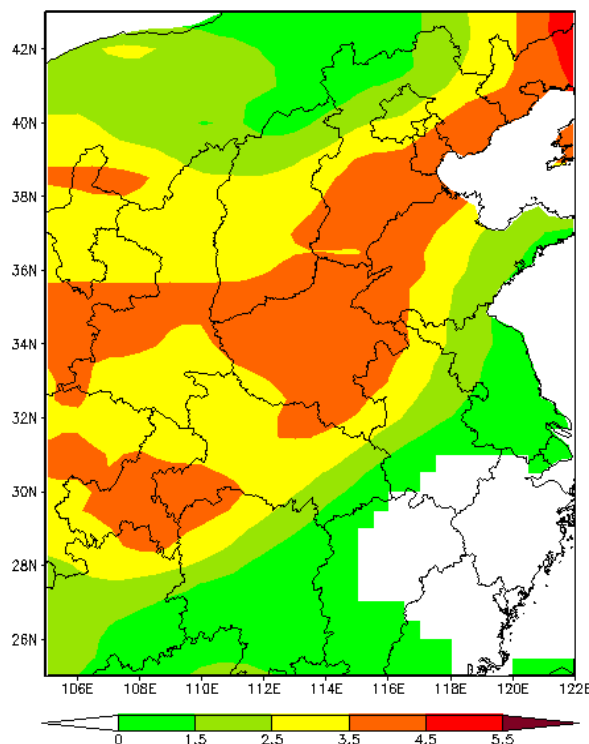


Fig. 13 Absorbing Aerosol Index (AAI) collected by FY-3B/TOU in the afternoon of 20 December 2015

3 Future Plan

With growing demands for weather and climate information for disaster prevention and reduction, climate change response, and for the development of science and society, it is important for further development of FENGYUN satellites and raise of applications to the higher level^[9-10].

The FENGYUN program will continue to support major development projects such as the subsequent FY-2 satellite, FY-3 satellite, FY-4 satellite and ground application system, in order to comprehensively raise the satellite observational capacity with high temporal and special resolution and in all-weather conditions; to develop the three-dimensional sounding of the atmosphere for the support of weather forecast; to improve the quality of satellite data and products and promote the satellite applications in the fields such as weather, climate, disaster prevention and reduction, ecotype, agriculture and forestry.

References

[1] Wang Jingsong, Zhang Jiashen, Tang Yunqiu. Fengyun satellites:

achievements and future [J]. *Chin. J. Space Sci.*, 2010, **30**(5): 468-473

- [2] Yang Jun, Dong Chaohua, Lu Naimeng, et al. The New generation Fengyun Polar-orbiting Meteorological Satellite of China: Operational Products and Applications [M]. Beijing: Science Press, 2011
- [3] Tang Yunqiu, Zhang Jiashen, Wang Jingsong. FY-3 meteorological satellites and the applications[J]. *Chin. J. Space Sci.*, 2014, **34**(5): 703-709
- [4] LYU Qingqing, Sun Anlai, Zhang Jiashen. FY-2F meteorological satellite and its applications [J]. *Aeros. China*, 2012, **21**(3): 10-13
- [5] Qian Jianmei, Sun Anlai, Xu Zhe, et al. Fengyun series meteorological satellite data archiving and service system [J]. *J. Appl. Meteor. Sci.*, 2012, 23(3): 369-376
- [6] Fang Zongyi. The evolution of meteorological satellites and the insight from it[J]. *Adv. Meteor. Sci. Technol.*, 2014, **4**(6): 27-34
- [7] Zhang Peng, Yang Lei, Gu Songyan, et al. Meteorological requirements for the early-morning-orbit satellite [J]. *Adv. Meteor. Sci. Technol.*, 2015, 5(2): 6-12
- [8] Xu Wanzhi, Zhu Chuntao, Chen Zhongyu, et al. The comprehensive analysis of a heavy air pollution episode in North China region in February, 2014 [J]. *Environ. Monit. China*, 2015, 31(6): 34-40
- [9] China Meteorological Administration. Long-Term Plan for Fengyun Meteorological Satellites[R]. Beijing: China Meteorological Administration, 2010
- [10] China Meteorological Administration. China's Meteorological Satellites and Associated Application Development Planning (2011-2015)[R]. Beijing: China Meteorological Administration, 2012

Progress of 2014–2016 China’s Earth Observation and Earth Science

GUO Huadong, XIAO Han, MA Jianwen

Institute of Remote Sensing and Digital Earth, Chinese Academy of Sciences, Beijing 100094

Key words

Earth observation
Earth science
Climate change
Sustainable development

Abstract

Earth observation technology in China has entered a period of rapid development. Earth observation data and Earth system science are moving from a theoretical and experimental stage toward an application stage. The support given by Earth observation data and Earth system science play an increasingly important role in global change, regional sustainable development, extreme events, and the development of social and economic needs. This field is also moving towards systematization, platforms, and standardized development. In December 2015, nearly 200 parties of the United Nations Framework Convention on Climate Change agreed in Paris to make arrangements for global action in response to climate change by 2020. The national Development and Reform Commission and the Ministry of Housing and Urban-Rural Development of China jointly issued a climate change adaptation strategy for cities in 2016 and then elevated national action to respond to climate change. China’s Earth Observation and Earth Science development is facing new challenges as it supports the national civil space infrastructure and high-resolution Earth observation system.

China's economy is shifting from natural resource-oriented growth to human resource-and science-oriented growth. The national governance system has achieved significant progress in its modernization^[1]. At the same time, Earth observation technology in China has entered a period of rapid development^[2–3]. The new Earth observation technologies are used to build the national economy^[4–5]. They are playing an important role in the fields of global change, “The Belt and Road Initiative”, new-pattern urbanization, food security, and ecological security.

1 Development of Earth Observation

A historic agreement was made at the 2015 United Nations Climate Change Conference in Paris. A large amount of scientific research and discoveries from Earth observation were presented to respond to climate change. For example, carbon scientists readjusted nearly a century of temperature change in China and made a homogeniza-

tion temperature sequence set at one hundred years for the first time. They found that over the past one hundred years the temperature increased by 1.2°C to 1.5°C in China while the previous national assessment result was 0.5°C to 0.8°C^[6]. Afterwards, a quantitative evaluation of the status quo of China's terrestrial carbon sink and potential was implemented. Enhanced measurements of terrestrial carbon sink will continue to play an important role in carbon sequestration in China^[7]. Series results show that the impact of climate change in China has been underestimated, meaning that the impact of climate change on extreme weather events in our country is greater than previously thought.

1.1 “Earth Observation Big Data for Climate Change Research” Selected for UN “Projects to Watch”

The Big Data Climate Challenge is a global competition

hosted by the United Nations Global Pulse, an initiative of the UN Secretary-General on big data. The Challenge was launched in May 2014 to unearth fresh evidence of the economic dimensions of climate change around the world using data and analytics. “Earth Observation Big Data for Climate Change Research” by the Institute of Remote Sensing and Digital Earth (RADI), Chinese Academy of Sciences, was selected for “Projects to Watch”. Among the seven “Projects to Watch” in this competition, the RADI project was the only one from China^[8].

“Earth Observation Big Data for Climate Change Research” originated from a National Basic Research Program of China (973 Program) project titled “Earth Observation for Sensitive Factors of Global Change”. Based on huge, abundant datasets obtained from four synchronous satellite-aerial-ground observation experiments on the Tibetan Plateau and the Bohai Rim of China, the project aims to explore new theories, technologies and methods for climate change studies through Earth observation; develop an assimilation model using multi-source heterogeneous spatial data; acquire characteristics of the sensitive factors of climate change; develop a simulation platform for regional climate change studies; and conduct conceptual research on global change scientific satellites. The experiment has reaped fruitful results. The datasets obtained from the experiments contribute to national policy-making in climate change and sustainable development. Six articles were especially cited by the 5th IPCC Assessment Report and made academic contributions to climate change research.

1.2 Glacial Melt Research

The South Pole, the North Pole and the Tibetan Plateau are called the “three poles” of the Earth. Not only are they the world's largest cold storage and important carbon sinks, but also the least area affected by human activities and environmental pollution globally. The environments of the “three poles” are undergoing dramatic changes and becoming sensitive areas, and are research hotspots for global change science. The Global Climate Observing System (GCOS) proposed 50 key climate variables, or ECVs, 28 of which depend on satellite observations^[9]. Earth observation may be the most economical, quantitative, objective, reliable and convenient manner to get to know those special areas^[10–12].

1.2.1 Trends in Glacial Mass Change in High Asia from Satellite Gravity Observations^[13]

The change in equivalent water quality of glaciers in High Asia and its adjacent regions were separated and extracted using 32 Mascon results based on the GRACE RL05 Level-2 products for time-varying gravity field models in frequency domain. The spatial characteristics of glacier mass change in High Asia indicate that glacier mass loss is dominated by positive growth in the inland areas of the Tibetan Plateau, while the edge region is dominated by negative growth, with the most serious loss in southeastern Tibet. The average quality changes in glacier mass were $-2.8 + 0.9$ Gt/a, $-3.3 + 1.5$ Gt/a, $-9.9 + 2.1$ Gt/a and $5 + 0.8$ Gt/a in the Pamirs and Tianshan Mountains, Kunlun Mountains, Himalayas, and Karakoram Mountains. The average overall quality change of glacier mass was $-11.0 + 2.9$ Gt/a in High Asia.

1.2.2 Significant Scientific Discoveries by Remote Sensing in Antarctica^[14]

Due to the geographical remoteness, the icy areas of East Antarctica are among the least understood places on Earth by far. Through analysis of satellite remote sensing and other means, scientists speculate that below the ice sheet of the Princess Elizabeth area in East Antarctica lies the largest canyon and subglacial lakes in the world. China's 32nd Antarctic expedition team used “Snow Eagle 601”, the first polar fixed-wing aircraft in China to study the region with scientific instruments such as ice radar, a gravimeter, magnetometer, laser altimeter and high precision differential GPS. They conducted a large-scale, systematic scientific investigation of Princess Elizabeth. The detection area so far has covered 866,000 square kilometers. Using observation data, Chinese scientists took the lead in making three important scientific discoveries.

1.3 Frontiers of Earth Observation Research

In an analysis of the literature in recent years, research frontiers were ranked by total citations and the top publications in the field of Earth science were extracted. Some research frontiers such as surface temperature and precipitation, satellite inversion of surface emissivity research, the relationship between sea level and global temperature, and the role of atmospheric black carbon in the climate system, showed the most activity or were de-

veloping the most rapidly^[15].

1.3.1 Research on Land Emissivity Calculated by Satellite Retrieval

Surface temperature is an important physical parameter for basic research and applications. It can provide spatial and temporal variation information about surface energy balance, and can be used as input for surface process modeling and to verify the output of models. Therefore, it was listed as one of the priority parameters of measurement by the International Geosphere-Biosphere Program (IGBP).

Measuring surface emissivity can help gain information such as soil moisture, surface evaporation, soil heat flux, and soil thermal inertia. The importance of land surface emissivity is increasing and strong interest has been shown in developing space-based measurements for land surface emissivity. Using satellite remote sensing data to invert land surface emissivity has brought more attention to remote sensing science and applications. It may push the development of quantitative thermal infrared remote sensing and promote new developments in passive microwave remote sensing in the future. A variety of algorithms have been developed for land surface emissivity based on space-based thermal infrared data and passive microwave remote sensing data, expanding the applications of polar orbit satellite observation data. At the same time, studies on satellite inversion of surface emissivity also face many challenges, such as establishing a theoretical basis, methods, validation of test methods, and level of precision.

1.3.2 Research on the Relation between Sea Level and Global Temperature

Sea level rise is a global phenomenon caused by global warming, rapidly melting ice caps and glaciers, and the upper thermal expansion of the oceans. According to the UN IPCC “Climate Change 2014 Synthesis Report”, global sea level rose by 0.19 m on average between 1901 and 2010. The IPCC predicts that by the end of the 21st century, global sea level will rise 0.26 to 0.55 m on average. In a scenario of high concentrations of greenhouse gas emissions, sea level could even reach 0.45 to 0.82 m. Sea level rise in the future may lead to proportioned typhoon and storm surge disasters, flooding, severe erosion of the coastline, and saltwater intrusion, and important resources such as beaches and fisheries may be threat-

ened. More than 70% of the world’s population lives in coastal plains. Sea level rise will have significant negative impacts on many aspects of human and natural environments. As a result, global sea level change and regional interaction have not only received great attention from governments, but from scientists who see it as a core research question in Earth science.

1.3.3 Role of Atmospheric Black Carbon in the Climate System

Black carbon in soot is the main absorbent of visible radiation from the Sun in the atmosphere. Artificially produced around the world, it plays a unique and important role in Earth's climate system. It can be mixed with other aerosols to form widely distributed atmospheric brown clouds during transmission, and, in turn, affect the hydrologic cycle. Black carbon settled on the surface of snow and ice can also increase the absorption of heat, accelerating snow and glacial melt. A large number of scientific studies have shown that black carbon emissions have become the second largest factor of the current global warming after carbon dioxide emissions. On the whole, so far, black carbon emissions have not yet been given as great importance at the political level as carbon dioxide emissions have, but its scientific significance has been fully proved and widely recognized. Academia believes that the reduction of black carbon emissions can play an immediate role in mitigating climate change, and also help open a new chapter for future climate change policy.

1.3.4 Moon-based Earth Observation for Large Scale Geoscience Phenomenon

Moon-based Earth observation is a new initiative for the study of Earth science. Installing sensors on the Moon to carry out Earth observation has distinct advantages that will enhance Earth observation capabilities and vigorously promote the in-depth study of Earth science issues. Specifically, Moon-based Earth observation is able to: (1) deepen our understanding of the dynamics of the solid Earth; (2) improve our understanding of the global energy balance; (3) simultaneously observe Earth's magnetosphere, ionosphere, atmosphere, biosphere, hydrosphere, and lithosphere to study the interaction between various layers; and (4) study celestial gravitational influence on the Earth system. The macroscopic Earth observation



potential of a Moon-based, multi-sensor platform will unprecedentedly guarantee a global-scale integration of multiple layers. Consequently, it is possible to give new answers to a series of key scientific questions about coupling multiple global layers.

2 Progress of Earth Observation Applications and Basic Research

2.1 Earth Observation for the Belt and Road Initiative and New-pattern Urbanization Strategies

2.1.1 EO Applications in the Development of the Silk Road Economic Belt and the 21st-century Maritime Silk Road^[16]

Chinese President Xi Jinping created an initiative jointly building a “Silk Road Economic Belt” and a “21st-century Maritime Silk Road” (hereinafter referred to as the Belt

and Road), which have attracted close attention from around the world^[17]. The Belt and Road initiative, an international vision, involves a wide geographic range, and a variety of fields.

Space technologies can help develop modern agriculture and modern tourism along the Belt and Road. For example, to better develop modern agriculture we can analyze the distribution of water resources, the spatial structure of agriculture and agricultural development opportunities, and the dominant central cities and urbanization patterns. It can promote the development of a tourism economy, thus developing digital tourism, virtual tourism, science and technology tourism, and so on.

Space technologies can help construct “the Silk Road Space Information Network” to form a large-scale view of Asia, Africa and Europe covering all regions along the Silk Road. At present, the Arctic remote sensing satellite ground station, the fourth in China but the first built abroad, has begun construction in Sweden. The capacity



Fig. 1 Remote Sensing Satellite Receiving Stations along the Silk Road in Asia, Africa and Europe.

Note: In the upper left is a diagram of the Silk Road Economic Belt and 21st Century Maritime Silk Road (the Belt and Road). On the right is a coverage map of the satellite remote sensing ground station network (light blue line), which is being built, and the new Silk Road spatial information network. The bottom picture is a coverage relationship diagram of the Belt and Road (red dashed line) and the “six stations network”.

to receive the satellite data will cover the Arctic and Europe. With the aid of this platform, China may have an advantage in outputting virtual ground stations, data processing technology, and spatial information applications to the countries and regions along the Belt and Road. The construction of the Belt and Road space-based big data sharing system, data interoperability services, Internet services and international business communication areas are also more likely.

The Belt and Road's construction is characterized by openness, cooperation, and win-win relationships. The Belt and Road is not only a road for economies and trade, but also a road for science, education, and cultural exchange. Science and technology can fully embody its international strategic significance and support economic and social development.

2.1.2 Understanding the Hu-Huanyong Line with Earth observation^[18]

In 1935, Chinese geographer Hu Huanyong drew out a line, the population density contrast line, connecting Aihui in Heilongjiang Province to Tengchong in Yunnan Province. This line is called the Hu-Huanyong Line (Hu Line). Using population distribution and density diagrams in 1933, he found that there was a geographical population boundary from Aihui to Tengchong. The line extends 45° northeast from Tengchong. At that time, 36% of the land fed 96% of the population in the southeast and nearly 64% of the country held 4% of the population in the northwest. Still today, the proportion of the population is

tion is still unbalanced. Prime Minister Li Keqiang put forward the question more than once: should the Hu Line be broken? Can it be broken? And how?

The Hu Line is a scientific phenomenon formed by complicated natural conditions and human activities over thousands of years and spanning thousands of kilometers. Researching the line has been a long-term, systematic process. Using the advantages of space technology with the concept of big data and technical support, research can consider nature, economics, and society as a base for studying the effect. The basic database for research includes: the Landsat data series since 1978, data from the United States Defense Meteorological Satellite Program showing global light at night from 1992–2010, China Resources Satellite remote sensing data, 1-km Chinese urban density grid datasets at the end of the 1980s, 2000s, and 2010, seven statistical population datasets since 1935, the 30-m and 90-m DEM data of China, 753 national meteorological datasets, and statistical socioeconomic data for China including six western provinces (autonomous regions). Scientists have analyzed the data and come to some conclusions.

The Hu Line could be broken. The population density boundary is dynamic and changing. The Hu Line as the modern population density boundary, does not have a reason why it could never be broken. While the proportion of population and GDP accounted for in the territory northwest of the Hu Line is slowly rising, the prosperity of all of China needs to spread into the western region, across the Hu Line. The East and West of China need to



Fig. 2 Relationship between the Belt and Road and the Hu Line

be planned as a whole, with coordinated and balanced development.

2.2 Application of Earth observation in the Field of Disaster Reduction

Disaster management involves many aspects of natural and social sciences. It fully reflects the multi-disciplinary, multi-field cooperation in the process of academic research. Earth observation technology could play a greater role in responding to natural disasters and emergencies with data standards and sharing mechanisms for disaster risk management.

2.2.1 Application of a Gas Remote Sensing Technique to Earthquake Monitoring ^[19]

Different materials have different characteristics of absorption, reflection and radiation at different wavelengths of electromagnetic waves. Because the spectral characteristics of trace gases mainly appear in the infrared band (especially thermal infrared band), we mainly use thermal infrared high spectral resolution data to recognize and invert atmospheric trace gas groups. With the development of satellite remote sensing technology, seismic observation uses many techniques such as infrared remote sensing, InSAR, and gas inversion. Because these techniques have many advantages, such as strong macroscopic characteristics, high precision, repeated short observation cycle, and indifference to ground conditions, they have become an important means of observation for researching fault activity and finding anomalies before and after earthquakes, and they improve earthquake monitoring to a certain extent.

Of course, the abnormal geochemical gases monitored by remote sensing satellites are the result both of the interaction of the lithosphere and atmosphere. So, the abnormality moves not only because of the abnormal geological background of the lithosphere, influence of surface topography and human activities, but also by the atmospheric effects of climate, weather and other factors. Because of this, some abnormal gas has nothing to do with the earthquake, and earthquake abnormality does not yet have evaluation criteria. But the use of satellite hyperspectral technology can give full play to the advantage that remote sensing is not limited by ground conditions in monitoring geochemical gas from an earthquake anomaly. It can provide a new technical means for earthquake monitoring, and provide new indexes for earthquake

monitoring and prediction. It is conducive to promoting the development of earthquake monitoring and prediction and improving the reliability of earthquake prediction.

2.2.2 Application of UAV in Disaster Reduction

High-precision Unmanned Aerial Vehicle (UAV) remote sensing is an advanced surveying and investigation technology that has developed rapidly in recent years. As an important means of obtaining spatial data, UAV has the advantage of being real-time, flexible, high-resolution, and cost-effective, and it can gather information in dangerous environments without other risk.

At least 123 people were killed in a massive explosion that ripped through a chemical storage facility in the port of Tianjin in August 2015. The blast brought serious destruction followed by the danger of chemical spills and fire hazards. At this point, UAV played a key role. Equipped with an infrared camera and GPS navigation, a UAV flew into the core area of the explosion and took a 360° panorama. In recent years, UAV have been widely used in various fields, such as land supervision, flood disasters, meteorology disasters, geological disasters, and forest fire disasters, as well as in express delivery and investigations of drug smuggling.

2.2.3 Geological Hazard Investigation and Monitoring System Based on Domestic Satellites

The national geological disaster information system integrates investigation and monitoring data of 2,020 counties (cities). It set up a multi-source, multi-scale database of geological disasters in the country, built a unified information platform, realized the construction of national geological disaster database standardization, and provided effective support for government management, scientific research and public disaster prevention. It was also a breakthrough in some core technology for domestic remote sensing surveying and identification of geological disasters, and for the Beidou-2 satellite's high-precision deformation monitoring. The monitoring accuracy reached 3 mm (horizontal) and 6 mm (vertical direction), and can replace the existing GPS system. With the results in the application, the national geological disaster information system can carry out technology training for domestic satellite surveying of geological disasters to 31 nationwide geological environment monitoring stations and relevant business units. It was successfully applied in

a 1:5,000,000-scale geological disaster surveying project in the provinces of Gansu and Sichuan. It greatly promoted the industrialization of the application.

3 Progress of Earth Observation Infrastructure

3.1 High-resolution Earth Observation System^[20]

The implementation of a major national project titled, "High Resolution Earth Observation System," will establish a space-based, near-space and air-based Earth observation system with quasi real-time, all-weather ability to obtain all kinds of spatial data at high spatial, spectral, and temporal resolutions, with wide coverage in one of the Earth observing systems. In August 2014, the Gaofen-II satellite was successfully launched, earning achievements that brought China's remote sensing satellites into the sub-meter era.

The major users of the satellite are the Ministry of Land and Resources, Ministry of Environmental Protection, Ministry of Agriculture, the Ministry of Housing and Urban Construction, the Ministry of Transport, and the State Forestry Bureau. The data of Gaofen-II was used in the investigation and monitoring of mineral resources, land utilization, forest resource monitoring and so on.

Specifically, during the orbit test of Gaofen-II, earthquakes struck Ludian in Yunnan Province, Kangding in Sichuan Province, and Chile; there was a debris flow disaster in India; an APEC meeting in Beijing; and other major events that were provided effective support and services by Gaofen-II.

Gaofen-IV, capable of minutes of continuous observation, was successfully launched on December 10, 2015. It is China's first geostationary-orbit, high-resolution optical imaging satellite. The first run and data transfer was on January 3, 2016.

According to the plan, China will continue to develop a Gaofen-III radar satellite and a Gaofen-V nanoscale spectral resolution hyperspectral satellite, and accelerate the Gaofen-VI and VII satellite projects. By 2020, China's Earth observation system should provide space-time coordinated, all-weather, global-range observation at high resolutions.

3.2 National Civil Space Infrastructure and Long-term Development Plan^[21]

The National Development and Reform Commission,

Ministry of Finance, and State Administration of Science, Technology and Industry for National Defense jointly formed the "National Civil Space Infrastructure and Long-term Development Plan (2015–2025)" with other departments in order to comprehensively promote the healthy and rapid development of the national civilian space infrastructure and to increase the scale and industrialization of spatial resource applications. It was approved by the State Council in October 2015. In order to explore the civil infrastructure market and new mechanisms of commercial development, the plan supports and guides social capital participation in the construction and application of national civil space infrastructure, and actively carries out application demonstrations of multilevel remote sensing, communication, integrated navigation in regional industrialization, internationalization and the development of science and technology. The plan reinforces cross-domain resource sharing and comprehensive information services, and accelerates integration with the Internet of Things, cloud computing, big data and other new concepts and applications. The plan promotes the sustainable development of the satellite industry, and improves support for and abilities in China's space infrastructure that benefit economic and social development. According to the plan, China will gradually build up a national civil space infrastructure composed of a satellite remote sensing system, satellite communications and broadcasting system, and satellite navigation and positioning system. It will use advanced technology that is independently controllable with a rational layout, global coverage and capability to meet the demands of industry, regional development, modernization, and national security, improving people's livelihood.

3.3 National Key Research and Development Plans Begin

The national key research and development plan is very important in the reform of national science and technology management. The national key research and development plan focuses more on major social welfare research related to the national economy—areas that need long-term evolution such as agriculture, energy resources, environment, ecological balance, and health. It also focuses on important scientific problems, common key technologies and products, and major international scientific and technological cooperation concerning the core competitiveness of the industry, overall capability of in-



dependent innovation and forward-looking strategies for national security.

3.3.1 Earth Observation and Navigation^[22]

In February 2016, the Ministry of Science and Technology issued a notice in the national key research and development plan about important guidelines for specific projects in Earth observation and navigation. In the future, special "Earth observation and navigation" projects will focus on nine directions: new mechanisms and systems for advanced remote sensing technology, baseline and transmission calibration technology for measuring space radiation, an integrated high-performance air and space monitoring network, applications of Earth system science and regional monitoring with remote sensing, new mechanisms and methods of navigation and positioning, core technology of navigation and location-based services, global framework for location services, spatial information services for urban agglomeration of regional economies and urbanization, and spatial information services for emergency response. The study will be initiated with 45 key tasks.

3.3.2 Global Change and Response^[23]

In March 2016, the Ministry of Science and Technology issued another notice, now on guidelines for projects specific to global change and response. These projects focus on four directions and deploy five types of research tasks relevant to these key questions. These directions include: characterization and simulation of key processes, mechanisms, and tendencies of global change; technological research and development of big data products and their integration regarding global change influences, risk, mitigation and adaptation; an Earth system model developed with independent intellectual property rights; and sustainable responses to global change. The following research tasks help support the projects: data assimilation and a big data platform; research on the verification of global change, key processes and dynamic mechanisms; research and development of Earth system modeling, prediction, and forecasting; global change impact and risk assessment; and mitigation and adaptation of global change research and sustainable transitions.

4 Perspective of Trends in the Industrialization of Earth Observation

Earth observation systems are not only a critical infra-

structure related to economic construction and social development, but also a transformation of China's economic development with great market value. After 20 years of development, China's Earth observation industry value chain has taken a basic form. The upstream is aerospace, aviation and other data acquisition platforms; the downstream is the Digital Earth platform, geographic information and location service platforms. The product is information and database systems and the terminal services are customers such as government, enterprises, scientific research, education, the public and international cooperators. The annual growth rate of the data and information industry is 20%, the number employed is more than 40 million, the output value is totaled at more than 300 billion Yuan and is expected to reach 800 billion Yuan in 2020^[24]. The data and information industry has become a key contributor to China's innovation-driven growth.

China published and implemented guidelines on certain policies and measures for promoting entrepreneurship and innovation. Aiming to integrate the Internet with traditional industries, the Internet Plus action plan was launched. With the guidance of the state, the establishment of a network integrating airborne and spaceborne data involved in Earth observation will make full use of comprehensive, multi-source information, and Digital Earth platform technology, which will help build an "Internet+ space-based information service system" based on population, resource, and environmental data. Promoting the application of satellite remote sensing data in development and prosperity relies on accelerating a data commonwealth and commercial products. This conforms with a country oriented toward public entrepreneurship and innovation and will also demonstrate the benefits of remote sensing data for value-added products that guide the various types of market players actively involved in applying the data.

References

- [1] The central committee of the communist party of China to develop thirteenth five-year plan for national economic and social development (approved by the 18th session of the central committee of the fifth plenary session of the communist party of China, October 29, 2015. <http://politics.people.com.cn/n/2015/1103/c1001-27772701-2.html>(in Chinese)
- [2] Major National Science and Technology Infrastructure Mid-Long Term Plan (2012-2030). Earth System and Environmental Science Field, 2012 (in Chinese)
- [3] Vision 2020: The Emerging Trends in Science & Technology and Strategic Option of China. Chinese Academy of Sciences. Science



- Press, 2014(in Chinese)
- [4] Guo Huadong, Ma Jianwen, Xiao Han, et al. 2012-2014 China's earth observation and earth science development. *Chin. J. Space Sci.*, 2014, 34(5): 721-732
- [5] Guo Huadong, Ma Jianwen, Lu Feng, Wen Lichun. 2001-2011 China's earth observation and earth science development. *Space Science Activities in China, National Report 2010-2012. CNCOSPAR*, 2012: 126-138
- [6] China's third national assessment report on climate change. Ministry of Science and Technology and China meteorological administration. Paris 2015 UN climate change conference.
- [7] Liu Zhu, Guan Dabo, Wei Wei, et al. Reduced carbon emission estimates from fossil fuel combustion and cement production in China. *Nature*, 2015, 524(7565): 335-338
- [8] Big Data Climate Challenge winners show how big data can drive climate action. United Nations Climate Summit 2014. <http://www.un.org/climatechange/summit/2014/09>
- [9] Global Observing Systems Information Center. 2013. GCOS Essential Climate Variables (ECV) Data Access Matrix. <http://gosic.org/ios/MATRICES/ECV/ECV-matrix.htm>. 2016-2-10
- [10] Tomasi C, Kokhanovsky A A, Lupi A, et al. Aerosol remote sensing in polar regions. *Earth-Science Reviews*. 2015, 140: 108-157
- [11] Young D A, Schroeder D M, Blankenship D D, et al. The distribution of basal water between Antarctic subglacial lakes from radar sounding. *Philosophical Transactions of the Royal Society A: Mathematical, Physical & Engineering Sciences*. 2016, 374 (2059). doi: 10.1098/rsta.2014.0297
- [12] Bolch T, Yao T, Kang S, et al. A glacier inventory for the western Nyainqentanglha range and the Nam Co Basin, Tibet, and glacier changes 1976-2009. *Annals of Glaciology*. 2010, 4(3): 419-433
- [13] Zhu C D, Lu Y, Shi H L, et al. Trends of glacial mass changes in high Asia from satellite gravity observations. *Chinese journal of geophysics-Chinese edition*. 2015, 58(3): 793-801
- [14] Three significant scientific discoveries were discovered by remote sensing in the Antarctica. 2016. <http://news.china.com/domestic/945/20160119/21207396.html> (in Chinese)
- [15] Research Fronts 2015. Thomson Reuters & National Science Library Chinese academy of sciences. http://ip-science.thomsonreuters.com.cn/press/research_fronts_2015.pdf
- [16] Research Reports: progress of earth observation technology industrialization in China, China to 2050 Space Science and Technology Development Roadmap Continue Research Projects. Group on Space Applications, May 2015 (in Chinese)
- [17] Vision and Actions on Jointly Building Silk Road Economic Belt and 21st-Century Maritime Silk Road. Issued by the National Development and Reform Commission, Ministry of Foreign Affairs, and Ministry of Commerce of the People's Republic of China, with State Council authorization. 2015, <http://finance.people.com.cn/n/2015/0328/c1004-26764666.html> (in Chinese)
- [18] Research Reports: Spatial-temporal cognition the three questions asked by the prime minister, Chinese Academy of Sciences Supported Consulting and Appraising, December 2015(in Chinese)
- [19] Cui Y, LI J, WANG Y, et al. Application of gas remote sensing technique to earthquake monitoring. *Advances in earth science*, 2015, 30(2): 284-294
- [20] High-resolution Earth Observation System Major Projects. Major Projects Engineering Center, State Administration of Science, Technology and Industry for National Defence, PRC, April 2014. <http://www.sastind.gov.cn/n25770/index.html> (in Chinese)
- [21] National Civil Space Infrastructure and Long-term Development Plan (2015-2025). National Development and Reform Commission, Ministry of finance, State Administration of Science, Technology and Industry for Nation Defence, 2015. <http://www.ndrc.gov.cn/>
- [22] Notice of the national key research and development plan about the important specific project guide in earth observation and navigation. Ministry of Science and Technology (MOST). 2016. http://www.most.gov.cn/mostinfo/2016/201602/t20160218_124155.htm(in Chinese)
- [23] Notice of the national key research and development plan about the important specific project guide in global change and response. Ministry of Science and Technology (MOST). http://www.most.gov.cn/mostinfo/2016/201603/t20160308_124540.htm (in Chinese)
- [24] The National Development and Reform Commission, jointly with the National Administration of Surveying, Mapping and Geoinformation. The National Geographic Information Industry Development Plan (2014–2020), 2014 (in Chinese). http://www.mlr.gov.cn/zwgk/ghjh/201408/t20140814_1326957.htm

National Report on Space Medicine Progress in 2014–2016

LI Yinghui, ZHANG Xiaoyou, WAN Yumin, DING Bai, LIU Zhaoxia, LING Shukuan, BAI Yanqiang, CHEN Shanguang

State Key Lab of Space Medicine Fundamentals and Application, China Astronaut Research and Training Center, Beijing 100094

* E-mail: yinghuidd@vip.sina.com

Key words

Spaceflight
Space medicine
Progress

Abstract

The progress of China Spaceflight makes a great impetus for the development of space medicine. With the developing of China Space Station, our national space medicine has attained great achievements. In this paper, the basic research of Space Medicine and its application in China during 2014–2016 are briefly reviewed.

1 Introduction

After the rendezvous and docking mission, space medicine has great development: (i) found the technology of astronauts' selection and training; (ii) achieved the technology of astronauts' health guarantee and life supporting in short-term flight; (iii) developed the technology of medicine experiments on-orbit. Now, researches are focused on the key questions during long-term space flight. With the developing of Space Station mission, we systematically plan to carry out spaceflight experiments in China Space Station, which will be an important supporting to build Chinese Space Station.

In this paper, the Space medicine Progress in China during 2014–2016 is briefly introduced.

2 Medical Monitoring and Treatment

After the rendezvous and docking mission, China's astronauts health care system was found successfully, including crew medical selection and training, traditional Chinese medicine and western medicine prevention, on-orbit countermeasure and protection of physiological effects of weightlessness, medical treatment, *etc.* It provides support for astronauts' life and work on-orbit.

(1) The protection effects of Electroacupubcture (EA) stimulating Neiguan caves on maladjustment of cardiovascular function under short-term simulated weightlessness were investigated. Compared with pre-HDBR, orthostatic tolerance and cardiac systolic function in control group decreased significantly after HDBR ($P < 0.05$), while these variables remained unchanged due to daily 30 min EA ($P > 0.05$). In addition, heart rate variability analysis revealed that EA at PC 6 made high-frequency ranges of R-R interval decreased while increasing low-frequency ranges of R-R interval, which indicated an elevated heart sympathetic tone. So, HDBR for 4 days can lead cardiac systolic function and orthostatic tolerance to a significant decrease. EA treatment at Neiguan caves was highly effective in activating peripheral sympathetic nervous system and activating Renin-Angiotensin-Aldosterone System (RAAS), which might be responsible for improved orthostatic tolerance (Sun Jing, 2014).

(2) Wang Desheng researched the effects of neiguan acupoint stimulation on the cardiac functional changes in simulated weightlessness rats and explored the new countermeasure against cardiac functional changes in weightlessness environment. Simulated weightlessness mainly results in decrease of the left ventricular function,

cardiac structural and cardiovascular regulatory changes, and neiguan acupoint stimulation may alleviate these disadvantageous influences and may have a good foreground in countermining the cardiac functional changes in weightlessness environment.

(3) Li Dijie reported the effects of traditional Chinese compound prescription-Qiang Gu Kang Wei Prescription (QGKWP) on bone metabolism of tail suspended rats. Compared with TS, QGKWP significantly increased the BMD of femur, tibia and lumbar vertebrae. QGKWP also promoted serum ALP and BGLAP level. Quantitative IHC analysis showed that QGKWP increased the expression of collagen I and osteopontin in femur of TS rats. So QGKWP partially reverses the effects induced by TS and may be a potential countermeasure for bone loss.

3 Microgravity Physiological Effects and Countermeasures

Based on a series of Earth experiments and spaceflight missions, lots of astronauts' data in microgravity and simulated weightlessness environment were acquired, and astronauts databases in short-term spaceflight was founded, including physiologic function, endocrine function, biochemistry indexes. Therefore, the protection of physiological effects of weightlessness in long-term spaceflight was explored. And many space medicine research techniques were tested and verified.

(1) Using system biology method and technology, mechanism of physiological effects induced by weightlessness are researched, including cardiovascular deconditioning, vestibular dysfunction, bone loss, muscle atrophy, immunology dysfunction and so on. Through these studies, physiology adaption and readaption theory in different gravity level was built and provides foundation for development of the countermeasure against physiological deconditioning.

(2) Aiming at extended duration involved in the long-term spaceflight mission, several experiments were carried out including 15–60-day HDBR. In these experiments, the effects of an integrated counter measures were validated containing thigh cuff, penguin suit, lower body negative pressure device (LBNP), bicycle ergometer and expander. The integrated countermeasure systems provided supports for the spaceflight.

(3) By combining with cardiopulmonary function test, isokenic strength test, foot force test and bio mechanism

test, an advanced zero-gravity locomotion stimulated system was established. The subject force loading system can provide loading similar to one gravity force. With this system, the leg motion compensation apparatus counterbalance to the running leg's gravity. The system is very important for designing and evaluating the Space Station treadmill.

(4) Liu Gang reported the effects of simulated weightlessness on human brain cognition and influences of some Chinese traditional medicines on them. Results showed that: after HDBR, in control group, the size of activation area and the signal intensity in bilateral frontal lobe and anterior cingulate gyrus decreased significantly compared to those before HDBR; in taking traditional Chinese medicine group, the brain activation map was similar to those before HDBR. So the brain activation map corresponding to the executed function changes significantly. It is suggested that weightlessness has significant reverse impact on brain cognitive function. Taking traditional Chinese medicine can improve the regulatory cognition function of related brain area.

(5) Li Jinglong reported the effects of hindlimb unloading with different duration on exercise endurance of mice and the possible mechanism. Results showed that hindlimb unloading for 7, 14 and 28 d induced decreases of exercise endurance compared with control group respectively ($P < 0.001$). The decreases of exercise endurance were concomitant with loss of soleus muscle mass respectively. The expression of Troponin I-SS decreased and expression of Troponin I-FS increased during unloading-induced muscle atrophy. The contents of MHC-I fibers lost after 7, 14 and 28 d of hindlimb unloading respectively. Therefore, exercise endurance capacity decreased continuously with the hindlimb unloading, which was accompanied by slow-twitch muscle atrophy and the loss of slow fibers. So the decreased exercise endurance induced by hindlimb unloading may be contributed by the slow-twitch muscle atrophy and the selective loss of slow fibers.

(6) Liu Junli studied inhibitory effect of oral administration of Strontium Ranelate (SR) and bovine Collagen Peptide (CP) on bone loss in tail suspended rats. Results showed that TS rats supplemented with SR&CP showed osteoprotective effects: significant inhibition in reductions of their serum ALP and OC levels and femoral BMD, as well as improvement the microarchitecture of their femurs. So oral administration SRCP

can significantly inhibit bone loss of TS rats and provide theoretical basis for the prevention and treatment of osteoporosis under microgravity.

(7) Li Xiaotao investigated the effects of 4 d HDBR as simulated microgravity on aerobic power and anaerobic power, and the protective effects of artificial gravity combined with moderate exercise. Results showed cumulative exercise stress index, maximal oxygen consumption, anaerobic threshold, and minimum anaerobic power decreased while percent of anaerobic power drop increased significantly ($P < 0.05$) in the control group after HDBR. However, no significant change was detected in peak anaerobic power, average anaerobic power. No significance was detected in all the above parameters in the countermeasure group. It is suggested that exercise capacity reduced after 4 d HDBR. The aerobic power was affected seriously, while the anaerobic power was affected a little. Moderate exercise based on artificial gravity preserved both aerobic power and anaerobic endurance during 4 d HDBR.

(8) Zhong Guohui studied the physiological adaptations to microgravity involving alterations in cardiovascular systems. Compared with the control, the Hindlimb Unloading (HU) group of mice showed reduced LV-EF (Ejection Fraction) and LV-FS (Fractional Shortening). However, mice that were allowed to recover for 7 days after HU (HR-7d) showed increased LVIDs (systolic LV Internal Diameter) and LV Vols (systolic LV Volume). Mice that recovered for 14 days (HR-14d) returned to the normal state. In comparison, RV-EF and RV-FS didn't recover to the normal conditions till being reloaded for 14 days. Compared with the control, RVIDd (diastolic RV Internal Diameter) and RV Vols (diastolic RV Volume) were reduced in HU group and recovered to the normal conditions in HR-7d and HR-14d groups, in which groups RVIDs (systolic RV internal diameter) and RV Vols (systolic RV Volume) were increased. Histological analysis and cardiac remodeling gene expression results indicated that HU induces left and right ventricular remodeling. Western blot demonstrated that the phosphorylation of HDAC4 and ERK1/2 and the ratio of LC3-II / LC3-I, were increased following HU and recovered following HR in both LV and RV, and the phosphorylation of AMPK was inhibited in both LV and RV following HU, but only restored in LV following HR for 14 days. These results indicate that simulated microgravity leads to car-

diac remodeling, and the remodeling changes can be reversed. Furthermore, in the early stages of recovery, cardiac remodeling may be intensified. Finally, compared with the LV, the RV is not as easily reversed. Cardiac remodeling pathways, such as, HDAC4, ERK1/2, LC3-II and AMPK were involved in the process.

(9) Proteomic analysis was performed on mouse soleus subjected to Hindlimb Unloading (HU) and Hindlimb Reloading (HR) to identify new dysregulated proteins. Following HU, the mass and cross-sectional area of muscle fibers decreased, but they recovered after HR. Proteomic analyses revealed 9 down-regulated and 7 up-regulated proteins in HU, and 2 down-regulated and 5 up-regulated proteins in HR. The dysregulated proteins were mainly involved in energy metabolism, protein degradation, and cytoskeleton stability. Among the dysregulated proteins, were fatty acid binding protein 3, α -B crystalline, and transthyretin. These results indicate that muscle atrophy induced by unloading is related to activation of proteolysis, metabolic alterations toward glycolysis, destruction of myofibrillar integrity, and dysregulation of Heat Shock Proteins (HSPs). The dysregulated proteins may play a role in muscle atrophy and the recovery process (Wang Fei, 2015).

(10) Su Longxiang reported the effects of space on *Klebsiella pneumoniae* after spaceflights. A strain of *Klebsiella pneumoniae* was sent to space for 398 hours by ShenZhou VIII. After the space mission, the flight strains LCT-KP289 exhibited a much higher cotrimoxazole resistance level, and changes in metabolism relative to the ground control strain LCT-KP214.73 SNPs and the copy number variation of the plasmid are identified in the flight strain. There are 232 up-regulated genes and 1,879 down-regulated expression genes respectively, which almost belong to metabolism. According to proteomics, there are 57 up-regulated proteins and 125 down-regulated expression proteins. In summary, the mutation of *ytfG* gene may influence the fructose and mannose metabolic process of *Klebsiella pneumoniae* during space flight, which may be beneficial to the field of space microbiology and make potential therapeutic strategies to combat or prevent infection of astronauts.

(11) Mental Workload(MW)-based adaptive system has been found to be an effective approach to enhance the performance of human-machine interaction and to avoid human error caused by overload. The results show that the performance of regression model trained on

working memory task and tested on multi-attribute task with the feature subset picked-out were significantly improved when compared to the performance in the same condition with all features. It can be inferred that there do exist some MW-related EEG features that can be picked out and there are something in common between MW of a relatively simple task and a complex task. This study provides a promising approach to measure MW across tasks (Ke Yufeng, 2014).

(12) Xiao Y examined how error related negativity (ERN) of a four-choice reaction time task was reduced in the mental fatigue condition and investigated the role of sustained attention in error processing. Forty-one recruited participants were divided into two groups. In the fatigue experiment group, 20 subjects performed a fatigue experiment and an additional continuous Psychomotor Vigilance Test (PVT) for 1 h. In the normal experiment group, 21 subjects only performed the normal experimental procedures without the PVT test. Fatigue and sustained attention states were assessed with a questionnaire. Event-related potential results showed that ERN ($p < 0.005$) and peak ($p < 0.05$) mean amplitudes decreased in the fatigue experiment. ERN amplitudes were significantly associated with the attention and fatigue states in electrodes Fz, FC1, Cz, and FC2. These findings indicated that sustained attention was related to error processing and that

4 Cellular and Molecular Research

The scientific issues for the long term space-flight medicine were preliminarily explored. A large amount of cellular and molecular studies have been performed including onboard and ground experiments to disclose intracellular changes under space environment.

(1) Liang Meng reported the effects of simulated microgravity on the activity of Wnt/ β -catenin signaling pathway in osteocytes for clarifying the occurrence mechanism of bone loss induced by microgravity. The results of simulated microgravity group to be compared with control group are: the mRNA's expression of Cyclin D1 and Lef-1 was significantly decreased ($P < 0.05$), but of CX43 and SOST was significantly increased ($P < 0.05$), while the expression of Wnt3a, Lrp5 and β -catenin had no significant difference; Moreover, the protein's expression of β -catenin, Cyclin D1 and CX43 was significantly decreased ($P < 0.05$), but of Lef-1 and Sclerostin was significantly increased ($P < 0.05$), while

the expression of Wnt3a, Lrp5/6 and CX43 had no significant difference. So, the activity of Wnt/ β -catenin signaling pathway declines in osteocytes under simulated microgravity.

(2) Sun Weijia reported that osteoclasts secrete microRNA-enriched exosomes, by which miR-214 is transferred into osteoblasts to inhibit their function. In a coculture system, inhibition of exosome formation and secretion prevented miR-214 transportation. Exosomes specifically recognized osteoblasts through the interaction between ephrinA2 and EphA2. In osteoclast-specific miR-214 transgenic mice, exosomes were secreted into the serum, and miR-214 and ephrinA2 levels were elevated. Therefore, these exosomes have an inhibitory role in osteoblast activity. miR-214 and ephrinA2 levels in serum exosomes from osteoporotic patients and mice were up-regulated substantially. These exosomes may significantly inhibit osteoblast activity. Inhibition of exosome secretion *via* Rab27a small interfering RNA prevented ovariectomized-induced osteoblast dysfunction in vivo. Taken together, these findings suggest that exosomemediated transfer of microRNA plays an important role in the regulation of osteoblast activity. Circulating miR-214 in exosomes not only represents a biomarker for bone loss but could selectively regulate osteoblast function.

(3) Ling Shukuan researched whether CKIP-1 was also involved in the regulation of physiological cardiac hypertrophy. The results of Q-PCR and western blotting revealed the higher levels of CKIP-1 in the heart from swimming mice. The results of echocardiography and histology demonstrated that CKIP-1-deficient mice after swimming exhibited pathological cardiac hypertrophy. The phosphorylation of HDAC4 in the heart of CKIP-1 deficient mice, a key molecule in the signaling cascade of pathological hypertrophy, increased more than that in wild type controls. Transgenic mice with cardiac-specific overexpression of CKIP-1 showed a similar physiological cardiac hypertrophy in response to swimming compared to wild-type controls. And the phosphorylation of HDAC4 in heart of CKIP-1 TG mice didn't change after swimming, but still decreased compared to the wild-type controls. These results indicate that CKIP-1 can regulate physiological cardiac hypertrophy by up-regulating the dephosphorylation of HDAC4. Swimming which is mechanical stress for physiological hypertrophy can lead to pathological cardiac hypertrophy in CKIP-1-deficient mice.

(4) Researches showed that miR-214 is up-regulated during osteoclastogenesis from bone marrow monocytes (BMMs) with Macrophage Colony Stimulating Factor (M-CSF) and Receptor Activator of Nuclear Factor- κ B Ligand (RANKL) induction, which indicates that miR-214 plays a critical role in osteoclast differentiation. Overexpression of miR-214 in BMMs promotes osteoclastogenesis, whereas inhibition of miR-214 attenuates it. We further find that miR-214 functions through PI3K/Akt pathway by targeting phosphatase and tensin homolog (Pten). In vivo, osteoclast specific miR-214 transgenic mice (OC-TG214) exhibit down-regulated Pten levels, increased osteoclast activity, and reduced bone mineral density. These results reveal a crucial role of miR-214 in the differentiation of osteoclasts, which will provide a potential therapeutic target for osteoporosis (Zhao Chenyang, 2015).

5 Environmental Medicine Research

Further understandings were acquired for the impact of space environments on human's physiological status. It provides powerful support and important basis to the measurements research for space medicine and the subsequent space station mission engineering design.

(1) Ran Yuanyuan reported the radio protective effects of Dragon's Blood (a Chinese traditional herb, DBE). Results showed that DBE significantly promoted the recovery of peripheral blood cells and the morphology of bone marrow histopathology in irradiated mice. Histology bone marrow confirmed the protective effect of DBE, as shown by an increased number of hematopoietic cells and a reduction of apoptosis. In a megakaryocytic apoptotic model, DBE ($50 \mu\text{g}\cdot\text{mL}^{-1}$) markedly alleviated GM-CSF withdrawal-induced apoptosis and cell-cycle arrest of Mo7e cells. DBE ($50 \mu\text{g}\cdot\text{mL}^{-1}$) also significantly decreased the ratio of Bax expression to Bcl-2 expression, inhibited the active caspase-3 expression, and increased the activation of ERK1/2 protein level. These findings suggest that DBE effectively promotes hematopoiesis in irradiated mice, attenuates cell apoptosis and cell cycle arrest through the decrease of Bax/Bcl-2 ratio and the reduction of active caspase-3 expression, and increases cell proliferation in factor-depleted Mo7e cells, which is likely associated with the activation of ERK1/2 pathway, not AKT pathway.

(2) Researches showed that the morphology and proliferation of osteoblastic MC3T3-E1 cells was influ-

enced by Static Magnetic Fields (SMFs) with different responses. The cell proliferation was increased after treated by HiMF (16T). HiMF promoted the differentiation of MC3T3-E1 cells at both early and mineralization stages. As for osteoclast, under HyMF ($<5 \mu\text{T}$), the survival of preosteoclasts Raw264.7 was decreased and differentiated into more matured osteoclasts with reduced formation of podosomes. Besides, Raw264.7 cell showed elevated osteoclastogenesis in HpMF and MMF, but reduced in HiMF. HyMF and MMF (0.2–0.4 T) disrupted the balance of bone remodeling with decreased bone formation and increased bone resorption. Therefore, exposure to the environments with magnetic intensity far away the geomagnetic field was harmful to bone metabolism. On the contrary, HiMF had positive effects on bone remodeling. It indicates that HiMF may be a potential physical therapy for both maintenance and treatment of bone health. Above all, these results will contribute to our better understanding of the geomagnetic field's function on the health of human beings, prediction of the potential effects of the hypomagnetic fields of deep space on the health of astronaut, and understanding of the mechanism of SMF as physical therapy on bone disorders (Zhang Jian, 2014).

6 Considerations for Future

With the basic research of space medicine and the verification by space flight, breakthroughs will be made in a number of key technologies in space medical and biological research. Consequently, series of innovative scientific outcomes of basic research in space medicine will be achieved.

In Chinese Space Station mission, the systematically developed space medicine experiments cover: (i) long-term on-orbit health risk management, (ii) advanced medical monitoring and treatment technology, (iii) mental health and performance management, (iv) long-term on-orbit environment biological safety management, and (v) development of a series of technique platform to carry out prospective and groundbreaking space medicine experiments on-orbit.

It will provide important basis and make a great impetus for the development of space medicine.

Reference

- [1] Liang X, Zhang L, Shen H, *et al.* Effects of a 45-day head-down bed



- rest on the diurnal rhythms of activity, sleep and heart rate. *Biological Rhythm Research*, 2014, 45(4): 596-601
- [2] Liu Z, Wan Y, Zhang L, *et al.* Alterations in heart rate and activity rhythms of three orbital astronauts on a space mission. *Life Sciences in Space Research*, 2015, 4: 62-66
- [3] Chen S. Advances in human space research - lessons learned and future directions//*Human Performance in Space- Advancing Astronautics Research in China*. Washington DC: AAAS Press, 2014: 2
- [4] Guo J, Qu W, Chen S, Chen X, Lv K, Huang Z, Wu Y. Keeping the right time in space: importance of circadian clock and sleep for physiology and performance of astronauts. *Military Medical Research*, 2014, 1: 23
- [5] Wang D, Zhang L, Liang X, Shen H, *et al.* Space meets time: impact of gravity on circadian/diurnal rhythms//*Human performance in space - advancing astronautics research in China*, 2014: 15-17
- [6] Guo Shuangsheng, Dong Wenping, Ai Weidang, *et al.* Research on regulating technique of material flow for 2-person and 30-day integrated CELSS test. *Acta Astronautica*, 2014(100): 140-146
- [7] Liu Hong, Fu Yuming, Xie Beizhen, *et al.* Bioregenerative life support experiment for 90 days in a closed integrative experimental facility LUNAR PALACE 1//40th COSPAR Scientific Assembly. Russia Moscow: COSPAR, 2014: 270
- [8] Guo Shuangsheng, Ai Weidang, Fei Jinxue, *et al.* Kinetics characteristics of trace gases for a 2-person 30-day integrated CELSS test. *Environmental Science and Pollution Research*, 2015, 22(9): 7020-7024
- [9] Liu Gang, Zeng Yawei, Li Ke, *et al.* Effects of simulated weightlessness on human brain cognition and interferences of traditional Chinese medicines. *Space Medicine & Medical Engineering*, 2014, 27(2): 89-93
- [10] Li Jinglong, Zhang Peng, He Jian, *et al.* Effects of hindlimb unloading on exercise endurance of mice and its mechanism. *Space Medicine & Medical Engineering*, 2015, 28(2): 85-88
- [11] Liu Junli, Song Shujun, Si Shaoyan, Guo Yanchuan. Inhibitory effect of oral administration of strontium ranelate and bovine collagen peptide on bone loss in tail suspended rats. *Space Medicine & Medical Engineering*, 2015, 28(6): 432-436
- [12] Li Xiaotao, Gao Yuan, Zhao Jiangdong, *et al.* Effects of Artificial Gravity Combined with Moderate Exercise on Aerobic and Anaerobic Powers after 4 d Head-down Bed Rest. *Space Medicine & Medical Engineering*, 2016, 29(2): 95-100
- [13] Li Dijie, Chen Zhihao, Liu Zonglin, *et al.* Qiang Gu Kang Wei Prescription increases bone mineral density of load-bearing bone in tail suspended rats. *Space Medicine & Medical Engineering*, 2016, 29(1): 1-8
- [14] Sun Jing, Li Xiaotao, Yang Changbing, *et al.* Effects of electroacupuncture on cardiovascular regulatory function under 4-day head-down bed rest. *Space Medicine & Medical Engineering*, 2014, 27(2): 146-148
- [15] Wang Desheng, Zhang He, Du Fang, *et al.* Research on Neiguan Acupoint stimulation against cardiac functional changes in simulated weightlessness rats. *Space Medicine & Medical Engineering*, 2014, 27(6): 403-407
- [16] Liang Meng, Yang Xiao, Fan Yubo, Sun Lianwen. Effects of simulated microgravity on wnt/ β -catenin pathway in osteocytes. *Space Medicine & Medical Engineering*, 2014, 27(3): 164-167
- [17] Sun Weijia, Zhao Chenyang, Li Yuheng. Osteoclast-derived microRNA-containing exosomes selectively inhibit osteoblast activity. *Cell Discovery*, 2016, 2, 16015. DOI:10.1038/celldisc.2016.15
- [18] Zhao Chenyang, Sun Weijia, Zhang Pengfei. MiR-214 promotes osteoclastogenesis by targeting Pten/PI3k/Akt pathway. *RNA Biology*, 2015, 12(3): 343-353
- [19] Wang Fei, Zhang P, Liu H, Fan M, Chen X. Proteomic analysis of mouse soleus muscles affected by hindlimb unloading and reloading. *Muscle & Nerve*, 2015, 52(5): 803-811

Space Life Science of China in 2015

MA Hong¹, LÜ Xuefei¹, DAI Rongji¹, LI Yujuan¹, ZHANG Yongqian¹,
LI Xiaoqiong¹, WANG Rui¹, QING Hong¹, LI Qiang², SUI Li³,
ZHUANG Fengyuan¹, DENG Yulin^{1*}

1. School of Life Science, Beijing Institute of Technology, Beijing 100081

2. Department of Space Radiobiology, Key Laboratory of Heavy Ion Radiation Biology and Medicine, Institute of Modern Physics, Chinese Academy of Sciences, Lanzhou 730000

3. Beijing Tandem Accelerator Nuclear Physical National Laboratory (BTANL), Nuclear Physics Department, China Institute of Atomic Energy, Beijing 102413

* E-mail: deng@bit.edu.cn

Key words

Space life sciences
Space payload
Simulated microgravity
Ionizing radiation

Abstract

With the human space exploration activities, space life science is an emerging interdisciplinary and it covers a wide range of research. Based on our country's manned space station and recoverable satellite science experimental platform, the development of space life science research is very important to acquire new knowledge or new innovation in technology, to give further services to the human space exploration activities, to improve the national economic and social development. Based on present situation, both theoretical and applied researches were continuously performed in the 2015. Here, we review and summarize the researches on space life sciences which were contributed by Chinese scientists.

1 Payload in Space Life Science

1.1 Payload for Cell Culture

The research of space cell culture and online observation module is supported by the National Key Scientific Instrument and Equipment Development Project. The research intends to develop a general space cell culture module and a special space cell culture module. The general one has the functions of cell culture and growth condition monitoring, cell Immobilization, cell automatic transfer and subculture function, and data processing. The special module is used for connecting the material and information interfaces of existing space cell reactor units, to meet the needs of the special requirements for scalable cell culture conditions.

In the later part of the study, scientists in Beijing Institute of Technology have developed a spacecraft payload with automated and integrated cell perfusion culture and real-time optical microscopic imaging function,

to study the biological effects of nerve cells and immune cells and their interactions under space microgravity and radiation environment. The payload has a power supply interface, a 1553B telemetry bus interface and an Ethernet data interface, which are all connected with the spacecraft. The payload size is 300 mm×250 mm×250 mm, weights about 15 kg. The device is equipped with circuit boards, microfluidic cell culture and detection units and a few cell samples. In 2017, the payload will carry out scientific experiments on a certain type of aircraft of the China Academy of Space Technology.

1.2 Biological Sample Processing Equipment

With the progress of space technology, biological Sample Processing has become an important field of space life science research. Cell is the basic unit of organism structure and function. Some intracellular important compounds including proteins and nucleic acids are vital

to space life science research. Under the special space environment, some common processing in ground environment is very difficult to apply in microgravity condition. Based on the manned space flight project and major national instruments development, and the relevant technology principles, an automatic and integrated device is developed for biological samples processing and separation on the premise of considering the space environment.

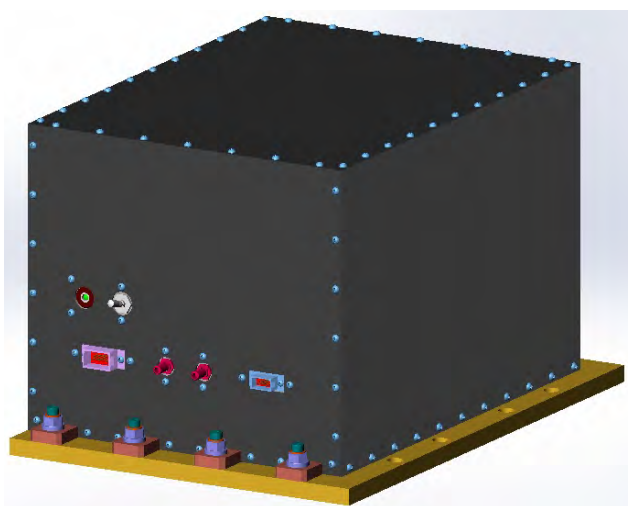


Fig. 1 Payload design

The space biological sample processing device (Fig.2) is composed of five principal modules, such as cell pre-treatment unit, ultrafiltration membrane unit, free flow electrophoresis chip unit, boric chromatography column unit and the communication unit. In order to provide the theoretical basis and technical support for development of space biological sample processing device, the research was focused on the related key technologies for biological sample processing using Jurkat and SH-SY5Y cells as samples. The conditions of cell washing and cell lysis were investigated. The effective lysis buffer for simultaneously extraction of intracellular proteins and nucleic acids was obtained by optimizing the chemical composition of the lysis buffer. The study proposed a

chemical and mechanical lysis method using mechanical vibration imposed on the membrane. The result indicated that this lysis approach enhanced the concentration of the intracellular nucleic acids. The optimum separation conditions for extraction of intracellular biological macromolecules were determined by exploring the effects of ultrafiltration membrane on the biological macromolecules content (Table 1). Subsequently, the off-line methods for separation and determination of free flow electrophoresis chip and boric acid temperature-sensitive affinity chromatography column. The results showed that the intracellular proteins and nucleic acids (Table 2) as well as DNA and RNA (Table 3) were effectively separated on their principles by optimizing the separation performance.

1.3 Gene Amplification on Microfluidic Chip

Microfluidic chip was a field of multidisciplinary intersection including physics, chemistry, biochemistry,

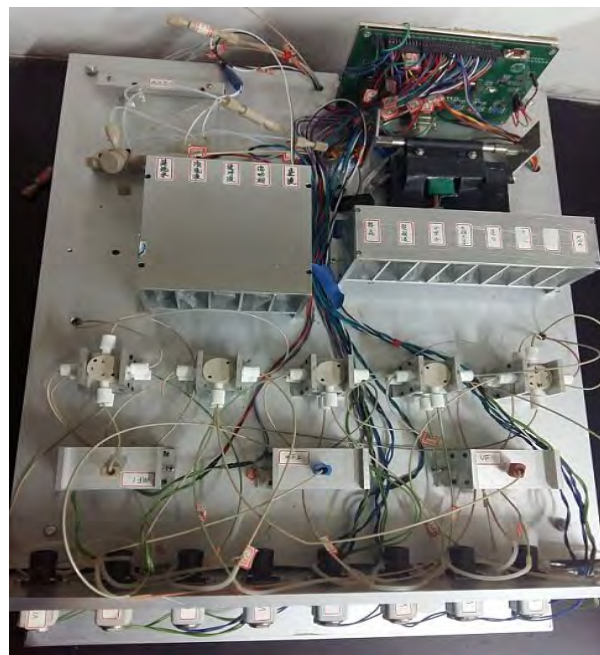


Fig. 2 Photograph of inner structure in the integrated space biological sample processing device

Table 1 Extraction of biological macromolecules using ultrafiltration in different membrane molecular weight cut-off

MWCO	Jurkat				SH-SY5Y			
	DNA (ng·μl ⁻¹)	loss rate (%)	RNA (ng·μl ⁻¹)	loss rate (%)	DNA (ng·μl ⁻¹)	Loss rate (%)	RNA (ng·μl ⁻¹)	loss rate (%)
Before	247.7	0	973.7	0	217.7	0	1013	0
5 K	245.3	0.97	961.7	1.23	215.3	1.10	987.7	2.50
10 K	240.3	2.99	891.3	8.46	208.3	7.53	898.7	11.28
30 K	232.7	6.06	794.7	18.38	199.3	8.45	812	19.84

Table 2 Effects of buffer pH and voltage on the DNA purity at the flow rate of $0.048 \text{ ml}\cdot\text{min}^{-1}$

Buffer pH	Voltage (V)				
	100	150	200	250	300
4.0	1.62	1.68	1.54	1.46	1.37
4.5	1.67	1.69	1.59	1.42	1.31
5.0	1.59	1.52	1.44	1.38	1.28
5.5	1.57	1.49	1.38	1.44	1.30
6.0	1.42	1.45	1.33	1.24	1.19
6.5	1.38	1.32	1.20	1.01	0.95

Tab. 3 Nuclear acid contents of different distillates at 10°C and 50°C in off-line mode (Concentration units $\mu\text{g}\cdot\text{mL}^{-1}$)

T	Substance	Time (T)				
		0–2min	2–4min	4–6min	6–10min	10–20min
10°C	DNA	0	18	2	0	0
	RNA	0	3	11	7	0
50°C	RNA	0	14	30	5	0

nanotechnology, biotechnology, electronics, medical science and mechnology, *etc.* Microfluidic chip with the advantages of small size, low sample consumption, rapid detection rate, high detection sensitivity and easy realization of high flux and automation was more and more widely used in the area of gene amplification. To date, various kinds of quantitative PCR technique, such as real-time PCR, digital PCR, and droplet PCR have been realized on the microfluidic chip over the years. In addition, other gene amplification techniques such as Short Tandem Repeats (STRs) PCR and Loop-mediated isothermal amplification (LAMP) was also applied more and more widely in microfluidic chip.

A new material named Norland Optical Adhesive 81 (NOA81) was fabricated for microfluidic chip with the advantages of greater solvent and pressure resistance, low auto-fluorescence, impermeability to air and water vapor, especially fast and easy fabrication and good biocompatibility. Our work related to gene amplification was carried out on this kind of NOA81 microfluidic chip.

1.3.1 PCR on the Coppered NOA81 Chip

In this study, the Copper Target Ion Beam Sputtering Deposition (CTIBSD) method was used for improving the thermal performance of commercial ceramic Peltier and several PCR chips were made of NOA81 in a few minutes by UV soft lithography technology. The thermal uniformity and heat transfer rate of coppering Peltiers were simulated by Comsol to investigate the

improved effect of coppering Peltier. Besides the simulation, the thermal distribution on the Peltiers with different thickness copper film was measured through the line average temperature measuring method. The cooling rate of the PCR chip with coppering Peltier also was tested according to the PCR program. The results of the simulation and measurement showed that the CTIBSD method could greatly improve the thermal performance of Peltier and the PCR time of the PCR chip could be reduced by the increasing of the heat transfer rate. A practical application in gene amplification was realized successfully on the PCR chip which the heat resource supplied by the coppering Peltier. With the excellent thermal performance of coppering Peltier, the novel NOA81 chip could apply in the field of Point Of Care Testing (POCT) and forensic analysis in the future.

1.3.2 PCR on BSA Coated NOA81 Chip

Norland Optical Adhesive 81 (NOA81) is an excellent material of microfluidic chip, but this chip has been rarely used in the field of gene amplification due to the existence of inhibition on the Polymerase Chain Reaction (PCR). In this study, a NOA81 PCR chip (NP-chip) was developed with a simple, fast fabrication method. To overcome the inhibition effect, a simple Bovine Serum Albumin (BSA) coated method was introduced and the BSA coated pH and concentration was optimized for a better gene amplification effect. The PCR results of HLA-DRB1 indicated that the BSA coated method

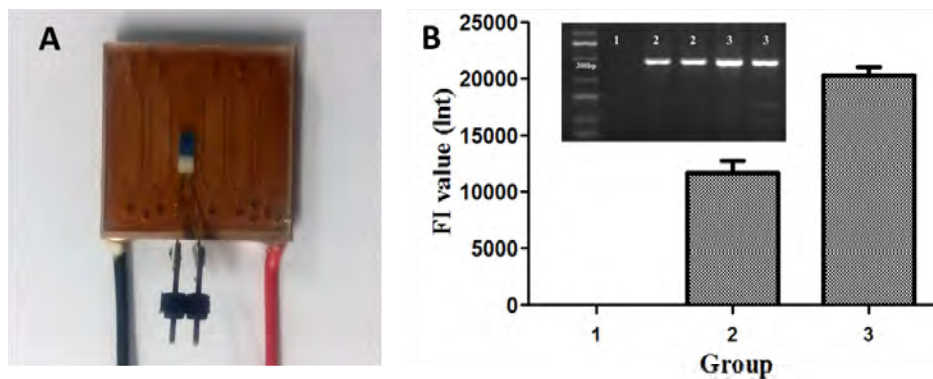


Fig. 3 The coppered NOA81 chip and PCR results on the coppered NOA81 chip. A was the picture of the coppered NOA81 chip. B was the PCR results on the coppered NOA81 chip, (i) Group 1, 2, 3 was the negative control group, experiment group and the positive group respectively. (ii) The picture in the figure was the agarose gel electrophoresis result of three groups. (iii) The histogram was the gray value corresponding to the agarose gel electrophoresis of HLA-DRB1 gene

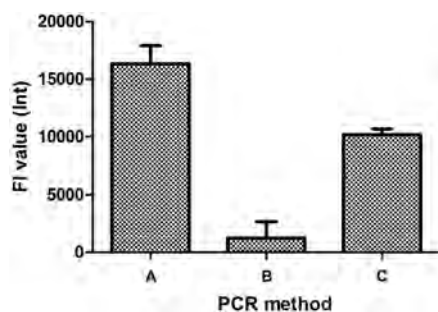


Fig. 4 The FI value of HLA-DRB1 PCR products with different BSA coated methods (A) in-tube PCR method (B) on-chip PCR method without BSA coating (C) on-chip PCR method with pH4, 5 mg/ml BSA coating

could greatly improve the PCR efficiency on the NP-chip.

Moreover, two kinds of PCR were successful performed on the NP-chip to validate the effectiveness of the BSA coated method. (i) gene mutation of anti EBV variable region gene (AEB-HC6-6) was observed under the condition of cobalt radiation. (ii) Short Tandem Repeats (STRs) PCR was performed on the NP-chip as the multiple-primers PCR. The results showed that the NP-chip with BSA coated was able to successfully realize single and multiple primers gene amplification. With further improvement of the precise temperature controlling, this kind of NP-chip would be widely applied in gene amplification and promote the development of the miniature gene amplification device in the fields of care testing (PCOT) and forensic detection, etc.

1.3.3 LAMP on the NOA81 Chip and Device

Against the food safety issues caused by pathogenic microorganism pollution, we introduced a microfluidic

chip based on the loop-mediated isothermal amplification which was applied successfully to detect the pathogenic microorganism rapidly. We chose the NOA81 as the material of the microfluidic chip and developed a simple and fast fabrication method by the technology of soft lithography. With the BSA treatment, the rapid detection of Salmonella was successfully realized on the NOA81 LAMP Microfluidic chip (NLM-chip) and NLM-chip device. This NLM-chip device has the advantages of small size, low sample consumption, mild reaction conditions, rapid detection, high detection sensitivity, visual detection and so on. If the temperature control of the NLM-chip is further optimized and the miniature peripheral control system is developed, the NLM-chip device will be widely used in the rapid detection of food pathogenic microorganism in real time and on site.

1.4 Protein Analysis on Microfluidic Chip

Protein chip analysis module is mainly used to study the changes in a variety of proteins of the body in cases of space microgravity environment and high radiation. Space biotechnology, space life science, space medicine research and the biology research are of great significance. This module is used to carry out the biology experiments under the conditions of space environment, and provide a platform for the space life science research.

Protein chip analysis module is based on microfluidic chip technology. According to the antigen antibody specificity reactions in protein chip analytical instruments designed by ourselves, we implemented particular qualitative and semi-quantitative real-time fluorescence protein detection. Figure 6 shows the principle diagram of the prototype.

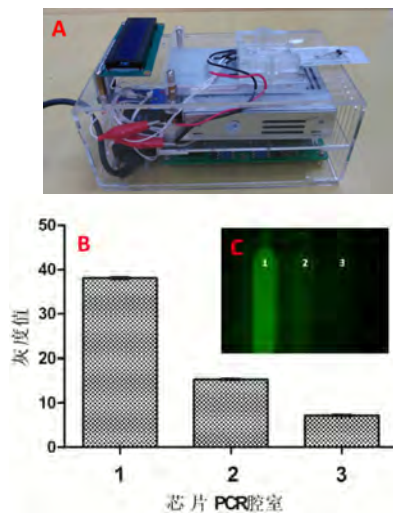


Fig. 5 The NLM-chip device and LAMP result on the NLM-chip device. A was the picture of NLM-chip and NLM-chip device. B was the gray intensity analysis results of Salmonella LAMP result on the NLM-chip. C was the NLM-chip LAMP results of Salmonella with the fluorescence visual method (1:the positive sample of Salmonella with prepared concentration; 2: the negative sample of Salmonella; 3: the negative control)

This machine is composed of three parts: liquid road system, testing system and control system. The liquid road system is composed of four liquid storage containers, two pumps, one valve and a microfluidic chip. And the chip is the core of the liquid road system. Figure 7 shows the design sketch and the real figure of the chip. Protein chip is mainly used for probe hybridization of

target protein, the cover layer is produced by PDMS materials, while the substrate by glass. Some kinds of antibody are fixed on the substrate of the chip, which will catch the corresponding antigens that are dyed in the previous operations. According to the strength of the fluorescence intensity to determine the concentration of the samples.

The light source of the detector is a LED. Through a series of optical components, the light focuses on the microfluidic chip channel to realize the chip antigen antibody markers of fluorescence excitation. Figure 8 shows the working principle of the testing system.

In Fig.9, (a) shows the software control interface. (b) shows the detection interface. The FITC dye is excited by 495 nm light, and the emission wavelength is 525 nm. We collected the following waveform signals, in which each peak is corresponding to a fluorescent point. (c) shows the temperature control interface.

1.5 Capillary Electrophoresis Equipment for Space Bio-separation and -analysis

Space exploration can't be carried out without analytical instruments. Since its introduction into analytical practice, capillary electrophoresis has become a frequently used separation method for determining substances in various matrices. To adapt to the reality in space bio-separation and -analysis including limited space load, heavy research work for astronauts and valuable sample, a smart capillary electrophoresis equipment with high

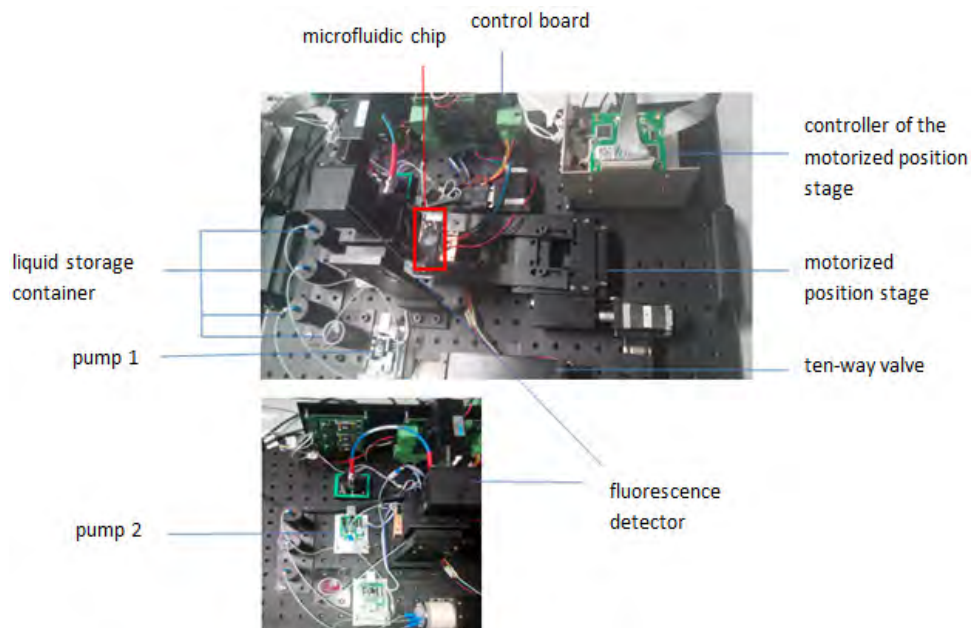


Fig. 6 The principle diagram of the prototype

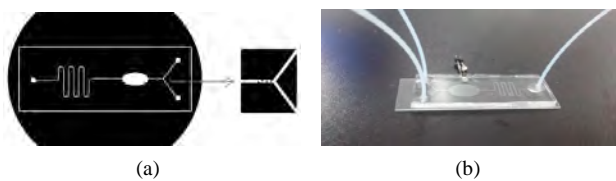


Fig. 7 Chip design. (a) design sketch, (b) real figure of the chip

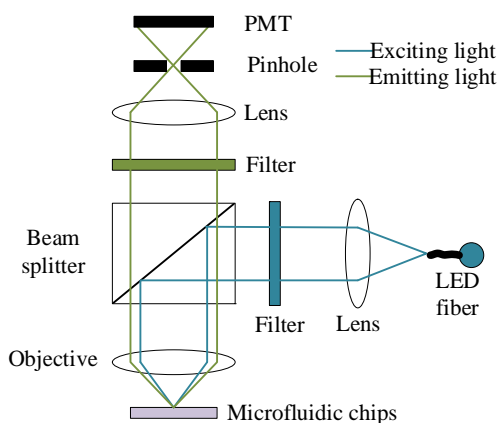


Fig. 8 Working principle of the testing system

performance has been designed and built, which is featured with impact structure, light, low power consumption, automation, less sample and reagent consumption. The instrument comprises eight units: injection and washing, high-voltage power, temperature control, detection, signal processing, power supply and main control board. A peristaltic pump was adopted, which can support high pressure and bidirectional output. Together

with electric selector valve, electric displacement modules and responsive corrosion solenoid valve, an automatic injector was built, characterized with cleaning the loading channel and the separation channel orderly without dead volume. The use of the novel injector can decrease sample consumption, shorten analysis time, and improve reproducibility of the separation results greatly. Modular detector and quickly replaced joints simplifies the installation of the entire system. The thermostat unit using semiconductor coolers controls capillary temperature, which has lots of advantages, compared with traditional air cooling or liquid cooling, including small size, light weight, low power consumption, and little noise. In addition, in the aspect of the hardware control, a high-performance power supply control circuit board was used to convert the power supplied by the space cabin into the stable voltage and current the components require for work, and FPGA, as the core control unit, combined with digital phase-sensitive technology to achieve high sensitivity fluorescence signal detection in non darkroom environment. The system is highly automatic and integrated, easy to assemble and maintain, with stable performance, which can achieve good separation and analysis of biological samples in the space environment.

1.6 Miniature Bio-chemistry Mass Spectrometer

With the increasing amount of space missions, there are pressing demands for bio-chemical analyses in outer

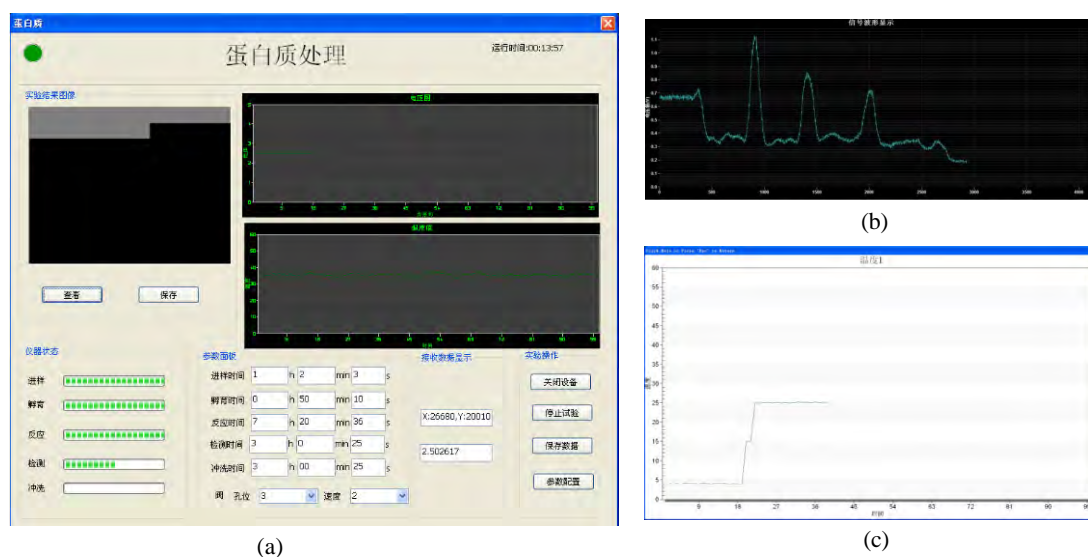


Fig. 9 The software control interface

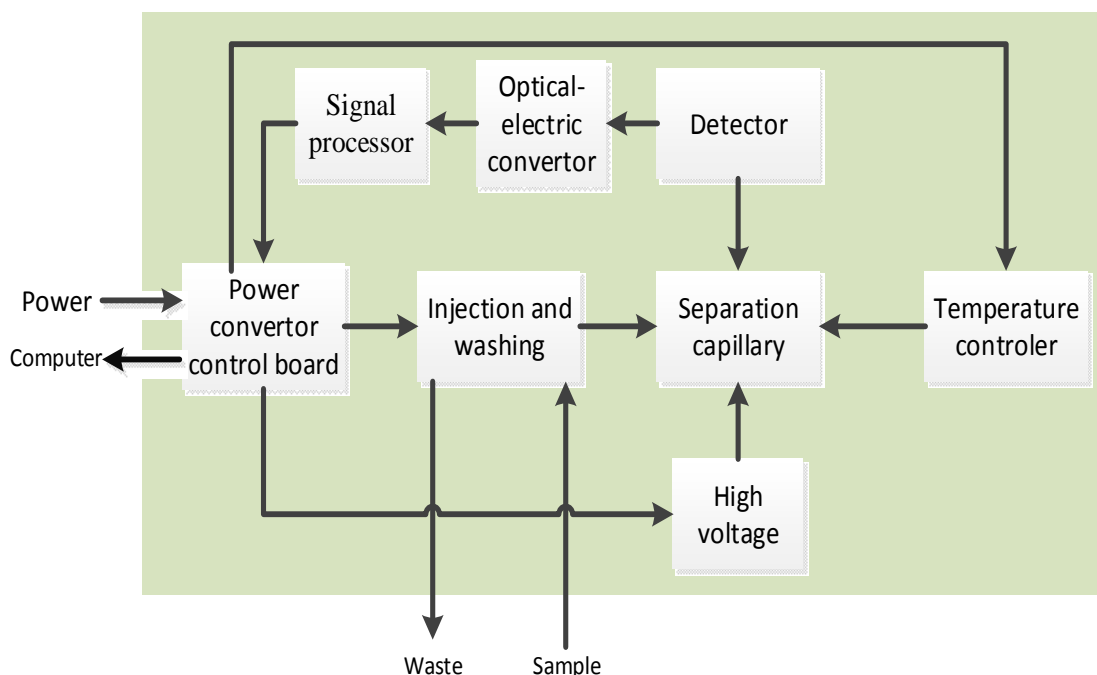


Fig. 10 The diagram of the functional block of self-built capillary electrophoresis apparatus

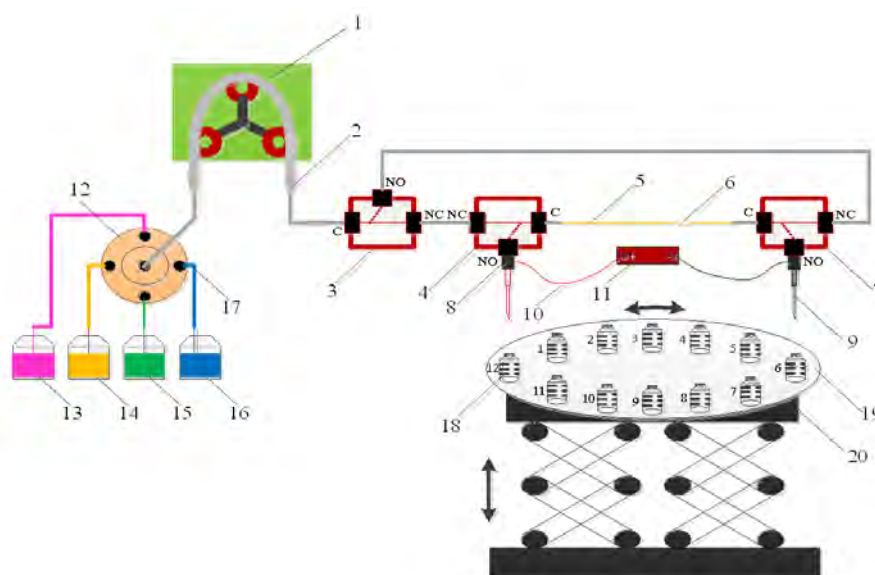


Fig. 11 Schematic of cleaning and injecting unit of capillary electrophoresis equipment. 1 peristaltic pump, 2 silicone hoses, 3, 4 three-way solenoid valve, 5 capillary, 6 detection window, 7 three-way solenoid valve, 8 adapter, 9 stainless steel threaded needles, 10 high voltage wire, 11 high voltage power supply module, 12 electric selector valve, 13 water reservoir, 14 cleaning fluid reservoir, 15 buffer fluid reservoir, 16 waste reservoir, 17 hard tube, 18 liquid reagent bottle, 19 rotational displacement unit, 20 lifter displacement unit.

space environments, for example, the detection of organic compounds to explore the signature of life on other planets; performing biology experiments in outer space to study the bio-effects of zero gravity. Mass spectrometry technique is a powerful bio-chemistry analysis method, which could detect trace amount of chemi-

cals in complex matrices. For space explorations, we need to develop miniaturized mass spectrometers, so that we could perform bio-chemical analyses on the spot for space missions. Within the past 4 years, scientists in BIT have developed several miniature mass spectrometer prototypes, specially designed for bio-chemical

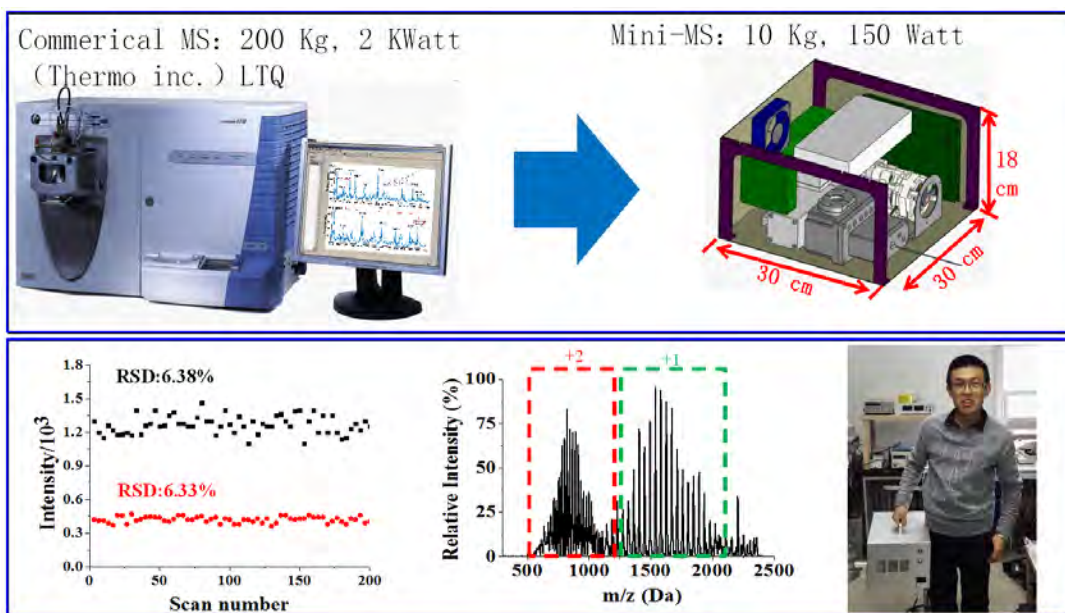


Fig. 12 The miniaturized mass spectrometers

analyses. As shown in the following Figure, the mini-MS developed in BIT could achieve a mass range of 100–2000 Th, and could couple with different ionization techniques for the direct analyses of analytes within different matrices, such as organic compounds, peptides within water and soil.

2 Biological Study in the Ground-based Simulated Microgravity

Research in microgravity is indispensable to disclose the impact of gravity on biological processes and organisms. Ground-based simulators of microgravity are valuable tools for preparing spaceflight experiments. The various microgravity simulators that are frequently used by gravitational biologists are based on different physical principles. The effects of ground-based microgravity on biological specimens were investigated by using simulators^[1]. In this section, current heterogeneous researches are discussed critically, and a summary is given for comprehensive understanding of the influence.

2.1 Microbe Research in Simulated Microgravity Conditions

The research group from Beijing Institute of Technology found increased transgene expression mediated by recombinant adeno-associated virus in human neuroglia cells under the microgravity circumstance. The space environment has the special characteristic of radiation,

noise particularity, weightlessness, which has an adverse effect on astronauts’ muscles, bones, neuron, and immunity system. Some reports prove that chemotherapy and radiotherapy can increase the activity of this recombinant Adeno-Associated Virus (AAV) which is widely used in gene therapy. In their study, recombinant AAV2 (rAAV2) was packaged firstly with gene of enhanced Green Fluorescence Protein (eGFP), which was used to infect neuroglia cells, like U87 and U251 cell line under the microgravity circumstance and detected by fluorescence microscopy and flow cytometry, the results show that microgravity affects adhesion ability of cells, promotes the transgene expression induced by rAAV2 in cells and causes different changes of virus infection receptors at different time point. These findings may broaden current understanding of microgravity effect on rAAV with significant implications in gene therapy and mechanism of increased virus pathogenicity in space microgravity.

To investigate the effect of simulated microgravity on growth, morphology, protein expression and virulence gene expression of *Klebsiella Pneumoniae* (KPN), Group in Anhui medical university, 306 hospital of the people’s liberation army studied of effect of simulated microgravity on biological characteristics of *Klebsiella pneumoniae*. In their study, KPN was divided into simulated microgravity group and control group in the experiment. The former group was in the ambient of

simulated microgravity in a clinostat. The bacterial growth curves, morphological changes in electron microscopy, and protein expression were detected by SELDI-TOF-MS, and the expression of 4 virulence genes (*ureA*, *wabG*, *uge* and *fimH*) by Real-Time fluorescence quantitative PCR (RT-PCR) in both groups. Results compared with the control group, the growth of KPN under simulated microgravity was accelerated, and the total bacterial count increased in microgravity group. The bacterial morphology in microgravity group was changed under Scanning Electron Microscopy (SEM), and thinner and longer bacteria were increased. The Transmission Electron Microscopy (TEM) analysis revealed increase in cytoplasmic granular substance in microgravity group. Proteome analysis showed that the expression of 18 proteins was changed, half of which up-regulated and the rest were down-regulated. Those 18 proteins were searched in the protein library. And 21 proteins of a similar molecular mass were retrieved, 13 of which, proteins with known functions, were closely related to bacterial life activities. RT-PCR results showed that four virulence genes of KPN were down-regulated. Conclusion Upon exposure to simulated microgravity, the growth and reproduction of KPN are accelerated and enhanced. The bacterial morphology is changed. The strain's protein expression and four virulence genes expression are also changed. Therefore, microgravity can change the characteristics of KPN.

Under microgravity environment, virulence and pathogenicity of conditions pathogen can be increased or reduced. Caries disease is prior to oral bacteria under the multiple factors, including *s. mutans*, which is widely regarded as one of the main cause of caries bacteria. Researchers of Anhui medical university want to observe the effects of simulated microgravity environment on the growth of *s. mutans*, morphology and ability to produce acid, synthesis of extracellular polysaccharide and GTFs mRNA expression. Their study showed that simulated microgravity for 2–12 h can accelerate *s. mutans* growth. *S. mutans* under simulated microgravity environment has the obvious morphological changes. And then the pH value of *s. mutans* bacteria liquid has no obvious change after 24 h under simulated microgravity environment, but the activity of synthetic water soluble and water insoluble extracellular polysaccharides significantly inhibit and mRNA expression of *gtfB*, *gtfC* or *GTF D* has obvious inhibitory effect.

2.2 Human Biological Effects in Simulated Microgravity Conditions

With the development of manned space technology and space biotechnology, the biological behaviors of cells and the involved molecular mechanisms in space have gradually become a hot topic and frontier of the space biology. Mechanical stimulation plays key roles in regulating the development and function of cells. Studies have demonstrated that mechanical stimulation participated in the proliferation, differentiation, migration and apoptosis of chondrocytes. In recent years, researchers have made significant achievements in biological behaviors of cells responding to microgravity environment by means of space simulation technology.

Researchers from Military academy of medical sciences and Affiliated hospital of Armed police logistics college focused on the effect of microgravity on bone mesenchymal stem cells differentiation to osteogenesis. BMSCs were harvested from femur of mouse and then subcultured in vitro to the 4th generation. The numbers of BMSCs in microgravity condition were more than that in normal gravity condition after 4 days' culture ($P < 0.05$). Alizarin red staining results showed that after 10 days' induction, lots of calcium nodules were found in normal group, while barely nodules could be found in microgravity group at the same time. The qPCR demonstrated that microgravity condition inhibits the expression of osteogenic gene. The Western Blot results were nearly consistency with qPCR, and the osteogenesis-related protein was inhibited in microgravity condition. We can see that microgravity can promote the proliferation of BMSCs and inhibit the differentiation to osteogenesis.

Another group from Beijing Institute of Technology focused on the effects of short-term simulated microgravity on neuron cells. They investigated effects of 1-day simulated microgravity on apoptosis and activity of NOS of primary cells from cortex and cerebellum of SD neonatal rats. In their study, primary cells were obtained from cortex and cerebellum of SD neonatal rats. After cultured for 7 days, primary cells of the two brain areas were randomly divided into control group and simulated microgravity group. The microgravity group was treated with clinostat for 1 day and control group was cultured in the same incubator. After that, flow cytometry was carried out to investigate apoptosis and activity of NOS of the two kinds of primary cells. The results show apoptosis and activity of NOS of primary

cells from the two brain areas showed no difference between simulated microgravity group and control group. But there were fine differences in apoptosis between the changes of cortex and cerebellum. Their data indicated that apoptosis and activity of NOS of primary cells from cortex and cerebellum seemed not to be affected by 1-day simulated microgravity, but the responses of cortex and cerebellum to simulated microgravity had a little difference from each other.

2.3 Pharmacodynamic Study

Researchers from Beijing Institute of Technology carried out some pharmacodynamic study of candidate drug against space microgravity or radiation biological effects.

2.3.1 Protective Effects of Dragon's Blood on Nervous Tissue

Dragon's Blood could mitigate against the injury in rats' brain induced by tail-suspension. Dragon's Blood could significantly reduce the level of oxidative stress and TNF- α , IFN- γ , IL-6 caused by tail-suspension. It could play protective role by decreasing the apoptosis and the expression of Caspase-3 in rat brain. It down-regulated the expression of c-jun, which possibly decreases the secretion of inflammatory cytokines. The study also found that Dragon's Blood could enhance the expression of neurotrophic factor BDNF in brain, which plays an important role on nutrition protection.

2.3.2 Protective Effects of Dragon's Blood on Cardiovascular Tissue

Dragon's Blood could significantly avoid the change in hemorheology induced by tail-suspension, such as the increase of hematocrit and blood viscosity, and the decrease of erythrocyte deformation. Dragon's Blood could significantly reduce the level of oxidative stress and NO/iNOS/SSAO in heart and blood. Dragon's Blood also played an important role in decreasing the expression of iNOS/SSAO. All the results showed that Dragon's Blood could improve cardiovascular function in simulated weightlessness condition.

2.3.3 Pharmacokinetic Study of Loureirin A and Loureirin B in Dragon's Blood under Simulated Weightlessness Condition

An HPLC-MS/MS method for the quantification of

loureirin A and B in rat plasma, urine, feces, and bile was developed for the first time. The pharmacokinetic parameters between normal and simulated weightless group showed that AUC(0–T) was similar. Compared with the normal group, there are two peaks in simulated weightless group and the eliminated time is extended. The apparent volume of distribution V_c was about one third of normal group. It showed that the absorption rate and disposition of Dragon's Blood were changed in simulated microgravity.

After oral administration of Dragon's Blood, cumulative excretion amount of loureirin A and loureirin B in rat urine were 2.94 ± 0.81 and 0.36 ± 0.16 μg at 72 h, respectively. The cumulative excretion of loureirin A was much higher than loureirin B in urine. Of the total dose, 5.35% of loureirin A and 5.46% of loureirin B were excreted from feces at 60 h. The cumulative amounts of loureirin A and loureirin B in rat bile reached 4.49 ± 0.98 and 5.11 ± 0.83 μg , respectively, at 36 h after dosing, accounting for $(0.54 \pm 0.04)\%$ and $(0.56 \pm 0.1)\%$ of the total dose. The cumulative excretion of loureirin A was similar with loureirin B in feces and urine.

2.3.4 Pharmacokinetic Study of Loureirin B Monomer under Simulated Weightlessness Condition

Pharmacokinetic study showed that the AUC_{0–t} of both oral and intravenous administration decreased, which meant the absorption of loureirin B significantly decreased after tail-suspension. Compared with the normal group, there were two peaks in the concentration-time curve in simulated weightlessness group after OA. The apparent volume of distribution V_d both increased in two simulated weightlessness group. And the eliminated rate of oral administration significantly fell down. The bioavailability is $(26.5 \pm 7.5)\%$ in normal group and $(47.2 \pm 7.0)\%$ in simulated weightlessness group, respectively, and the simulated weightlessness group showed a significant increase. All the results showed that the adoption, distribution, metabolism and the bioavailability of loureirin B changed notably in simulated weightlessness condition.

2.3.5 Pharmacokinetic Study of Multiple Components in Dragon's Blood under Simulated Weightlessness Condition

An HPLC-MS/MS method for the quantification of LA,

LB, LC, PTS and DHF in rat plasma, urine, feces, and bile was developed for the first time. The pharmacokinetic parameters of normal and simulated weightless group showed that they are influenced by the chemical structure. Compared with the normal group, AUC(0-T) of flavonoids is lower in simulated weightless group. AUC(0-T) of LA is $30.5 \pm 2.4 \mu\text{g} \cdot \text{L}^{-1} \cdot \text{h}^{-1}$ in normal but $18.1 \pm 5.4 \mu\text{g} \cdot \text{L}^{-1} \cdot \text{h}^{-1}$ in simulated weightless group. AUC (0-T) of diphenylethene in simulated weightless group is higher than that in normal. AUC(0-T) of PTS is $447 \pm 78.6 \mu\text{g} \cdot \text{L}^{-1} \cdot \text{h}^{-1}$ in normal but $548 \pm 92.4 \mu\text{g} \cdot \text{L}^{-1} \cdot \text{h}^{-1}$ in simulated weightless group. Tmax in simulated weightless group is later than that in normal. Compared with the normal group, there are two peaks in simulated weightless group for dihydrochalcones. It showed that the absorption rate and disposition of Dragon's Blood were changed in simulated microgravity.

Compared with the normal group, cumulative excretion amount of compound in rat urine in simulated weightless group is higher, after oral administration of Dragon's Blood. The cumulative excretion amount of LA in simulated weightless group is 5 times of that in normal. The cumulative excretion of compounds in simulated weightless group was much higher than that in normal in bile. The cumulative excretion amount of diphenylethenes in rat feces in simulated weightless group is much higher than that in normal. But the cumulative excretion amount of flavone in rat feces is opposite.

2.3.6 Pharmacokinetic Study of Promethazine and Its Combination with Ephedrine under Simulated Weightlessness Condition

A LC-MS/MS method for the quantification of promethazine and ephedrine simultaneously in rat plasma was established, which was used to determine the content of target drugs in the plasma and calculate pharmacokinetic parameters. The results had shown that it had a significant effect of the pharmacokinetics studies in different tail-suspended cycles.

In different dosing groups, the change trends of Ke and T1/2 are consistent of promethazine and ephedrine between normal and simulated weightless groups. Compared with the normal group, there are two or three peaks in simulated weightless groups. The parameters showed that Ke was lower in each stimulated microgravity group than normal group, while T1/2 extended over the normal group, indicating that the elimination of

the drug in rats slows down in simulated weightlessness conditions.

After injecting promethazine, it showed that AUC0-t and Cmax of 3 days and 7 days tail-suspended groups were significantly decreased compared with those of normal group, whose parameters were AUC0-t $662.9 \pm 8.3 \mu\text{g} \cdot \text{L}^{-1} \cdot \text{h}^{-1}$ and Cmax $486.9 \pm 8.5 \mu\text{g} \cdot \text{L}^{-1}$. It presents a significant reduction of absorption in short-term simulated weightlessness rats by intramuscular injection of promethazine. The V_d elevated 12.95 times and 3.97 times to the ground group, whose apparent volume of distribution was $28.0 \pm 0.04 \text{L} \cdot \text{kg}^{-1}$, and the Cl were extended 8.57-fold and 3.36-fold to the ground group, whose clearance rate was $3.6 \pm 0.3 \text{L} \cdot \text{h}^{-1} \cdot \text{kg}^{-1}$. It indicated that slowing down of the clearance rate was after short-term simulated weightlessness intramuscular injection of promethazine.

After administration of the combination of promethazine and ephedrine, compared with the ground group, the AUC0-t and Cmax of promethazine increased significantly in the tail-suspended group, indicating that it significantly raised the absorption of PH after i.m. the PH-EH mixture under the conditions of simulated weightlessness. Unlike administered promethazine alone, the V_d reduced 67.28% and 13.56% to the ground group, whose apparent plasma volume of distribution was $317.7 \pm 0.7 \text{L} \cdot \text{kg}^{-1}$. The Cl was shortened 12.39% and 5.38% to the ground group, whose clearance rate was $93.2 \pm 0.1 \text{L} \cdot \text{h}^{-1} \cdot \text{kg}^{-1}$.

Compared with the ground group, ephedrine in 7 days and 21 days tail-suspended groups, the AUC0-t and Cmax increased significantly, indicating that in the medium-term simulated weightlessness cycles, the absorption of ephedrine increased significantly in rats plasma after intramuscular the mixture of PH-EH.

3 Basic Research for Underlying Mechanisms of Radiation Injury

3.1 Radiobiological Effect of Ground-based Simulated at BTANAL

Beijing Tandem Accelerator Nuclear Physical National Laboratory (BTANL) is an important base for low energy nuclear physics research in China. The Laboratory is attached to the Nuclear Physics Department of China Institute of Atomic Energy (CIAE). The application of nuclear technique and research related to radiobiology is

one of the important fields of the Laboratory. The main experimental facility is HI-13 Tandem Accelerator, which can produce several kinds of ions from p to 235U, and the corresponding linear energy transfer (LET, from several to ten thousands) and Range (from dozens to thousands) in water of these ions is very suitable to research on the mechanism of radiobiological effects. The features of experimental terminal for radiobiology is very good, beam uniformity is better than 95% at 5 cm×5 cm area, dose measurement accuracy is better than 90%, dose rate is adjustable in several μGy to dozens of Gy. Based on this platform, the research on interaction of high LET radiation with biological matters related to radioprotection and estimation of risk to crews in case of exposure to high LET radiation, such as space or nuclear radiation environment, as well as the application of heavier ions and protons therapy were carried out.

3.1.1 Clustered DNA Damage Induced by Protons or Heavy Ions Radiation.

Clustered DNA damage is considered as a critical type of lesions induced by ionizing radiation, which can be converted into the fatal or strong mutagenic complex double strand breaks (DSBs) during the damage process in the cells. The results obtained by irradiation of plasmid DNA showed that the protons with the LET of ~ 3.6 keV·μm⁻¹ produced more potentially lethal DSBs than low LET γ-rays radiation (0.2keV·μm⁻¹), induced about 1.6 fold more non-DSB clustered DNA damages than the prompt DSB, and the DNA damage yields by protons were greater than that by γ-rays, specifically by 6 fold for the isolated type of DNA damage and 14 fold for the clustered damage. Furthermore, the spectrum of damages was also demonstrated to be depended on the radiation quality, with protons producing more DSBs relative to clusters than do γ-rays.

Clustered DNA damage assessed by γ-H2AX foci induced in normal (MEF) cells irradiated with γ-rays (0.2 keV·μm⁻¹), 7Li (70.2 keV·μm⁻¹) or 12C (12.6 keV·μm⁻¹) ions indicated that the average number of γ-H2AX foci per cell was a function of time post-irradiation for all the radiations, and the peak of γ-H2AX formation was at 2h after ionizing radiation. The persistence of high number of foci depended on the radiation. The frequency of production was by the order: 7Li >12C > γ-rays. An increase in the size of γ-H2AX foci with the times post-irradiation induced by high LET ion beams was

found, as compared with γ-rays irradiation. Moreover, the foci size increased with increasing LET, which suggested the size of γ-H2AX foci is an accurate parameter to correlate the radiation quality and DSBs repair, which can reflect complexity and severity of clustered DNA damage.

3.1.2 mRNA Expression of Genes PIG3 and Cell Cycle Changes of AHH-1 Cells Induced by Protons and Thermal Neutrons Radiation

p53 is a well-known tumor suppressor gene. PIG3 is downstream gene of p53 induced by DNA damage and play important role in many physiological and pathological responses, such as cell cycle arrest, apoptosis, aging and so on. The results obtained by proton and thermal neutrons irradiation of AHH-1 showed that the mRNA expression of genes PIG3 increased in linear-quadratic correlation with dose increased, and the quantity or time of appearance for proton was much more and earlier than that of thermal neutrons. Both of them also induced G2/M arrest in similar time-response with each of PIG3 expression. Moreover, G1 arrest was also detected in protons irradiated AHH-1 and followed by G2/M arrest. In conclusion, the effect on AHH-1 from protons was more significant than that of thermal neutrons. The mRNA expression of g PIG3 may be provided a valuable candidate for developing a novel radiation molecular biological dosimeter.

3.2 Carbon Ion Radiation-induced Long-term Brain Injury

Hippocampus is a major component involved in particle radiation-induced long-term brain injury and behavioral changes. A number of accelerator-based studies have shown that particle exposure leads to various hippocampus-related changes of the behavior for rodents, such as impaired spatial memory and cognitive performance and even Alzheimer's disease-like changes. The research group from the Division of Medical Physics, Institute of Modern Physics, Chinese Academy of Sciences found that exposure of immature mouse hippocampus to carbon ions caused an LET-dependent behavior pattern change after maturation and an LET-dependent differential molecular response. Carbon ions with higher LET values (70–100 keV·μm⁻¹) more readily elicited a reduced cognitive performance of the mice, as evidenced by their declining performance in spatial

learning and memory, cognitive ability, and depression-related behavioral tasks. In the same experiment, as a vulnerable neurodegeneration-related signaling pathway, autophagic flux was intact in the hippocampal cells of the mature mice after irradiation. However, persistently high content of nuclear Nrf2 in the hippocampal cells were observed in the mice exposed to relatively low-LET ($10\text{--}20\text{ keV}\cdot\mu\text{m}^{-1}$) carbon ions, and might account for the unchanged behavioral patterns as well as the subsequent increased radioresistance of the hippocampal cells in these mice.

Another group in BIT established a brain localized heavy ion irradiated rat model. Wistar rats, with the body weight of $180\text{ g} \pm 10\text{ g}$ were exposed at Heavy Ion Research Facility in Lanzhou (HIRFL). Rats in the experimental group were irradiated with single high dose of 15 Gy vertically on the back of the head with a $^{12}\text{C}^{6+}$ ion beam ($165\text{ MeV}\cdot\mu\text{m}^{-1}$ primary energy; LET, $30\text{ KeV}\cdot\mu\text{m}^{-1}$; intensity, $0.3\text{--}0.5\text{ Gy}\cdot\text{min}^{-1}$). The long-term biological effects on the central nervous system, including neuronal atrophy, cell apoptosis were examined. The data showed that atrophy in the parietal cortex and occipital cortex was induced. Widely scattered TUNEL-positive cells were found from one month to three months after irradiation, which indicated that, rat brain suffered extensive injury after direct irradiation.

3.3 By-stand Effect of Carbon Ion Radiation-induced Neural Injury

Previous reports indicated bystander effects of ironing radiation can be induced in non-targeted organs. However, in the present studies related to biological effects of space heavy ion radiation mainly focus on the relative low dose ($< 4\text{ Gy}$), whole body irradiation, short term ($< 7\text{ days}$) and superimposed effects, leading to the big question to explain the cascade reactions and regulatory sequences after irradiation. Therefore, investigation about the direct and indirect effects after localized irradiation, especially the brain localized heavy ion irradiation would greatly benefit to understanding the mechanism of damage after whole body space heavy ion irradiation and the development of astronaut health care technology.

Researchers established a rat model with brain localized heavy ion irradiation and profound study about the bystander effects in thymus, peripheral blood and spleen; evaluation of the bystander effects in peripheral

organs, such as cardiac muscle, lung, liver, trachea, kidney, stomach and aorta; finding of conditioned medium mediated effects from neuron and glia cells to immune cells. Firstly, local brain irradiation derived damages in the peripheral immune organs (thymus and spleen) and blood were evaluated. In the thymus, atrophy process was accelerated after brain-localized heavy ion radiation. The cortex thinning and increased number of apoptosis cells was found, which shown time-dependent features. Compared with the thymus in control group, oxidative stress and T-cell development were disturbed. Genes related to the T-cell development, such as c-kit, Rag1 and Sca1 were down-regulated in transcriptional level. However, the proportion of CD8+ T-cells increased significantly. Thymic microenvironment was also affected. GC and GR related apoptotic pathway was triggered and inflammatory factors secretion was disordered. Whereas, CD3+ T-cells were not apparently decreased. Transcriptome sequencing found that, multiple pathways associated with cell adhesion are changed, which led to the decrease of the thymus pathogen clearance ability. For the spleen, stromal cells decreased significantly while the number of hemosiderin-positive macrophages, extracellular matrix, and TUNEL-positive cells increased when the time was prolonged compared with that in control group. T cells subtypes distribution was also disturbed. The proportion of CD3+CD4-CD8+ and CD3+CD4+CD8-T-cells elevated in chronological order. What's more, secretion, inflammation and immunosuppression, including TNF- α , IFN- γ , IL-6, SSAO and IL-10 were triggered. In the peripheral blood, the number of total lymphocyte and leukocyte decreased notably. Red blood cells and platelet were also affected. However, the total number of T lymphocyte did not altered.

Secondly, brain-localized heavy ion radiation induced injury in peripheral organs. Increased myocardial hypotrophy, focal fibrosis and inflammation factors (SSAO, PEG2, iNOS, IL-6, TNF- α and CCL20) were found. In lungs, edema surrounding blood vessels and apoptosis cells were observed. Epithelial cells in the trachea one month after irradiation presented increased apoptosis while mucosa and submucosa presented apoptosis three months after irradiation. Increased apoptosis was found only at three months after irradiation in the kidney. Gastric muosa epithelial cells showed great TUNEL-positive signal and atrophy after irradiation.

SSAO, TNF- α , CCL20, iNOS, IL-6 and PGE2 increased significantly three months after irradiation. Hence, evident bystander effects in fundamental peripheral organs were caused after brain localized heavy ion irradiation. Parenchymatous organs showed great injury than that in non-parenchymatous organs.

Thirdly, cytokines in conditioned medium could mediate bystander effect on immune cells. Based on a neuro-immune interaction cell model, researchers found that, U87 conditioned medium can strongly enhance its viability and the SH or U87 and SH co-culture conditioned medium made limited effect compared to the U87 conditioned medium. But for U937 cells, the viability was significantly enhanced after U87 and SH conditioned medium treatment, which was even higher than the U87 conditioned medium. U87 conditioned medium can evidently enhance the cell viability of THP-1, U937 and Jurkat cells. Presumably, synergistic effect of the cytokines may be involved in the activations. Then, cytokines and chemokines involved in the interaction and their effects were studied. Certainly, different combination of glioblastoma cell and neuroblastoma cell resulted in different secretions, which lead to different effect on different immune cells. This observation implicated that direct communication would be progressed in the co-culture condition. Information exchange progresses via liposome, exosome, as well as other mediators which contain various molecular constituents of their cell of origin, including proteins and RNA. Membrane vesicle trafficking was found in SH or U87 and SH co-culture conditions. Effects of the neural cells damage after irradiation on peripheral immune cells were evaluated. Medium conditioned by neural cells receiving 5 Gy of radiation increased the viability of both THP-1 and Jurkat cells compared with medium conditioned by mock-irradiated neural cells. Significantly less THP-1 cells migrated when exposed to the conditioned medium of irradiated compared with mock-irradiated cells. These data indicate that neural cell injury caused by carbon ion radiation may enhance the proliferation of peripheral immune T-cells and decrease the migration and invasion of monocytes. In conclusion, developing research about the injury in central nervous system and its bystander effects under simulated space heavy ion radiation condition in the manned space flight is conducive to deeply know the space radiation injury and to effectively evaluate and prevent, as well as fur-

ther clarification of whole-body irradiation induced overlapping effect.

3.4 DNA Mismatching during PCR Reaction Exposed to Space Environment

Astronauts will face serious health threaten during space flights. The two major factors that may lead to astronauts' physiological dysfunction are space radiation and microgravity. The heavy ion radiation, which is one of the important components of charged particles in orbit, can cause all kinds of DNA damages and gene mutation. The microgravity also can affect a series of cell physiology functions, including cytoskeleton remodeling, DNA modification, interactions between molecules, etc.

Antibodies are the most important molecules in adaptive humoral immunity. They can bind antigens with high affinity and specificity. The iconic antibody molecule consists of four polypeptide chains, two identical heavy (H) chains and two identical light (L) chains. Both the H and L chains consist of a variable (V) domain and a constant (C) region. The C region is encoded by a C gene and the V region is encoded by V genes which including three kinds of genes (the V, D, J genes). The V genes encode the antigen-binding regions of antibodies. Despite a clear sequence homology among V sequences from different species, there is a marked plasticity in the organization of the region and in the mechanism for the generation of antibody diversity. The C region's sequence is constant relatively compares with V region, and is a key structure for binding Fc receptors and complements.

Besides the immune functions, antibody is also a kind of biology element which is conserved between human and other vertebrates including sharks the evolutionary oldest living organisms. And the constant (C) regions are conserved domains between mammalian animals. Do the space radiation and microgravity cause gene mutation in the encoding genes of antibody? How does it happen? Are there different between the constant (C) region and variable (V) region genes when the gene mutation happens caused by space radiation and microgravity? Will the C region encoding genes be more constant than V region? The relationship between the sequence and stability of genes is one of the still unsolved issues in biological evolution. Does the mechanism of C region's radiation resistant similar with the principle of biological evolution? In this project of basic biological

research for ISS international space flight, they will detect the rules of gene mutation in antibody encoding genes under space environment. This project will be helpful to answer those questions. In this project, the mutagenic efficiency of space radiation will be studied by detecting the gene mutation rules on the on-orbit antibody DNA fragments amplification products in a mini-sized microfluidic chip PCR device after space flight.

References

- [1] Zhang Yushi. Protective effect of Drageny I on nervous system and pharmacokinetic study in rats under the simulated microgravity condition. Beijing: Master thesis of Beijing Institute of Technology, 2011
- [2] Chen Bo. Protective effect of Drageny I on cardiovascular system and pharmacokinetic study in rats under the simulated weightlessness condition. Beijing: Master thesis of Beijing Institute of Technology, 2012
- [3] Chen Bo, Deng Li, Ou Wanlu, Zheng Zhifeng, Deng Yulin, LI yujuan. Protective Effects of Dragon's Blood on Blood Coagulation and NO/iNOS Level in Myocardium and Serum of Rats in Simulated Microgravity. *J. B. Inst. Technol.*, 2016 25: 152-8(in Chinese)
- [4] Li Yujuan, Zhang Yushi, Chen Bo, Gan Lin, Deng Li, DenYulin. Pharmacokinetics of Loureirin B in the Plasma of Rats under Simulated Weightlessness. *Space Med. Med. Eng.*, 2014 27: 79-83
- [5] Yujuan Li, George Q Li, Yongzhi Li, Yulin Deng, Li Deng. Development and application of an UHPLC-MS method for comparative pharmacokinetic study of phenolic components from dragon's blood in rats under simulated microgravity environment. *J. Pharm. Biomed. Anal.*, 2016 121: 91-8
- [6] Deng Li. Pharmacokinetic study of Dragon's blood in rats under the simulated weightlessness condition. Beijing: Master thesis of Beijing Institute of Technology, 2014
- [7] Deng Li, Zheng Zhifen, Ou Wanlu, Chen Bo, Deng Yulin, Li Yujuan. Excretion Study of Pterostilbene in the Urine and Feces of Normal and Simulated Weightless Rats. *Space Med. Med. Eng.*, 2015, 28(2): 89-93
- [8] Gan Lin. Pharmacokinetic study of Promethazine and Ephedrine combination in rats under the simulated microgravity condition. Beijing: Master thesis of Beijing Institute of Technology, 2013
- [9] DeCarolis N A, P D Rivera, F Ahn, et al. Fe Particle Exposure Results in a Long-Lasting Increase in a Cellular Index of Genomic Instability and Transiently Suppresses Adult Hippocampal Neurogenesis. *Life Sci. Space Res. (Amst)*, 2014, 2: 70-79
- [10] Rivera P D, Shih H Y, LeBlanc J A, et al. Acute and Fractionated Exposure to High-LET (56) Fe HZE-Particle Radiation Both Result in Similar Long-Term Deficits in Adult Hippocampal Neurogenesis. *Radiat. Res.*, 2013, 180: 658-667
- [11] Shukitt-Hale B, Casadesus G, McEwen J J, et al. Spatial learning and memory deficits induced by exposure to iron-56-particle radiation. *Radiat. Res.*, 2000, 154: 28-33
- [12] Joseph J A, Hunt W A, Rabin B M, et al. Possible "accelerated striatal aging" induced by 56Fe heavy-particle irradiation: implications for manned space flights. *Radiat. Res.*, 1992, 130: 88-93
- [13] Joseph J A, Hunt W A, Rabin B M, et al. Deficits in the sensitivity of striatal muscarinic receptors induced by 56Fe heavy-particle irradiation: further "age-radiation" parallels. *Radiat. Res.*, 1993, 135: 257-261
- [14] Manda K, Ueno M, Anzai K. Memory impairment, oxidative damage and apoptosis induced by space radiation: ameliorative potential of alpha-lipoic acid. *Behav. Brain Res*, 2008, 187: 387-395
- [15] Denisova N A, Shukitt-Hale B, Rabin B M, et al. Brain signaling and behavioral responses induced by exposure to (56) Fe-particle radiation. *Radiat. Res*, 2002, 158: 725-734
- [16] Cherry J D, Liu B, Frost J L, et al. Galactic cosmic radiation leads to cognitive impairment and increased abeta plaque accumulation in a mouse model of Alzheimer's disease. *PLoS One*, 2012, 7: e53275
- [17] Ye F, Zhao T, Liu X, et al. Long-term Autophagy and Nrf2 Signaling in the Hippocampi of Developing Mice after Carbon Ion Exposure. *Sci. Rep.*, 2015, 5: 18636
- [18] Lei R, Zhao T, Li Q, Wang X, Ma H, Deng Y. Carbon Ion Irradiated Neural Injury Induced the Peripheral Immune Effects in vitro or in vivo. *Int. J. Mol. Sci.*, 2015, 12: 28334-46
- [19] Sui L, Zhang X L, Kong F Q, et al. Diagnostics and Measurements of 7Li Ion Beam on the New Terminal at HI-13 Tandem Accelerator for Biological Samples Irradiation. *Nucl. Phys. Rev.*, 2015, 32: 259-264
- [20] Sui L, Wang Y, Wang X, et al. Clustered DNA damage induced by protons radiation in plasmid DNA. *Chinese Sci. Bull.*, 2013, 58: 3217-3223
- [21] Sui L, Zhang X L, Kong F Q, et al. Clustered DNA damage induced by high LET radiation in normal cells, PTCOG'53, 2014
- [22] Kong F Q, Ma N R, Sui L et al. mRNA expression of Genes PIG3 and cell cycle changes of AHH-1 cells induced by protons. *Atomic Energy Science and Technology*, 2015, 49: 955-960 (in Chinese)

Microgravity Material Research in China: 2016

XIE Wenjun¹, LUO Xinghong², ZHANG Xingwang³, YU Yude³

1. North Western Polytechnical University, Xi'an 710072

2. Institute of Metal Research, Chinese Academy of Sciences, Shenyang 110016

3. Institute of Semiconductors, Chinese Academy of Sciences, Beijing 100083

* E-mail: yudeyu@semi.ac.cn

Key words

Undercooling
Simulation
Crystallization
Microgravity
Superalloys solidification

Abstract

We firstly review recent research works of high undercooling and rapid solidification of metallic alloys under ground simulation conditions in Northwestern Polytechnical University and secondly under normal gravity and microgravity of binary to quinary Nickel-base single crystal alloys with different contents of W, Ta, Al and Ti elements were comparatively investigated by Institute of Metal Research using drop tube, thirdly solidification and crystal growth of SJ10-Recoverable Scientific Experiment Satellite by institute of semiconductors.

A High Undercooling and Rapid Solidification of Metallic Alloys under Ground Simulation Conditions

1 Space Environment Simulation by Electrostatic and Acoustic Levitation

Electrostatic levitation is an efficient method for the study of undercooling and solidification of high temperature melts under containerless condition. Wei and his coworkers developed an electrostatic levitator based on a systematic optimization of the electric field, position detecting, sample charging and voltage feedback control^[1]. Various types of materials such as metals, inorganic materials and polymers were stably levitated^[2]. This apparatus can also levitate various kinds of plant seeds and flower buds such as coral berry, peppers, soybeans, wheat grains and mushroom^[3]. Using this levitator, the density and ratio of specific heat to emissivity of Ni₇Zr₂ intermetallic alloy^[4] and Zr_{91.2}Si_{8.8} eutectic alloy^[5] have been measured, which is found to vary linearly with temperature at solid and liquid states.

The obtained maximum undercooling of Ni₇Zr₂ and Zr_{91.2}Si_{8.8} alloy melts reaches 317 K and 371 K, respectively. The eutectic growth velocity of Zr_{91.2}Si_{8.8} alloy was measured to be 1 mm·s⁻¹ for lamellar eutectic and 90 mm/s for anomalous eutectic.

Acoustic levitation is another practical technique for containerless processing of materials, especially for those with poor conductivity and low melting temperature. In order to improve the stability of single-axis acoustic levitator, Wei and his group carried out a series of optimum design of the reflector^[6]. Two kinds of flexible reflectors were proposed. One kind is those with a deformable reflecting surface, and the other kind is those with an elastic support, both of which are self-adaptive to the change of acoustic radiation pressure^[6].

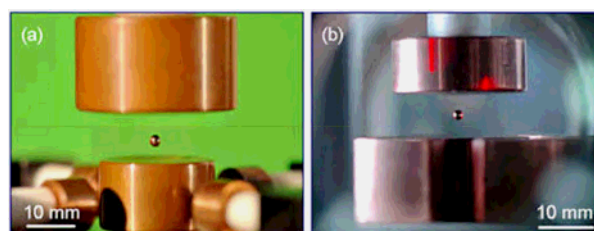


Fig. 1 Electrostatic levitation of metallic materials:

(a) Ti-6Al-4V alloy in air, (b) Ir in vacuum^[2].

With the elastic reflector, the levitation stability can be remarkably enhanced by reducing the decay time and amplitude of the sample vibration^[7]. The containerless melting and solidification of several alloys have been successfully achieved by applying the elastically supported reflector and with the assistance of a YAG laser beam. An interesting phenomenon is the appearance of surface wave patterns on the acoustically levitated and solidified eutectic alloy samples^[8]. To understand the solidification mechanism under acoustic levitation condition, the fluid dynamics of levitated drops was also extensively studied. In addition to the general vertical vibration and axisymmetric shape oscillation^[9], a special kind of non-axisymmetric mode, i.e. sectorial oscillation was observed^[10]. The sectorial oscillation was excited by parametric resonance and the eigenfrequency can be well described by a modified Rayleigh equation. The internal fluid always flows between the extended sections and the compressed sections^[11]. They also discovered a kind of vortex flow rotating in the meridional plane of the steadily levitated drop^[12].

2 Thermophysical Properties of Undercooled Liquid Multicomponent Alloys

The thermophysical properties of undercooled metallic melts are difficult to measure because of the severe requirements for experimental conditions. Applying the electromagnetic levitation techniques and incorporating the oscillating drop method and drop calorimetry method, Wei and his coworkers have measured the surface tension and specific heat of a series of undercooled liquid alloys in Ti-Al binary system^{[13],[14]}, Ti-Al-Nb ternary system^{[15][16]} and Ni-based multicomponent systems^{[17][18]}. For Ti-Al system, the maximum undercoolings of Ti₈₀Al₂₀, Ti₅₅Al₄₅, Ti₄₉Al₅₁ alloys are obtained to be 257 K (0.13T_L), 259 K (0.143T_L), 324 K (0.19T_L), respectively. Their surface tension varies linearly with temperature in the experimental range. The specific heat of liquid Ti₈₀Al₂₀ and Ti₄₉Al₅₁ alloys are determined to be 33.01 and 31.27 J·mol⁻¹·K⁻¹ in the superheated and undercooled states. For Ti-Al-Nb system, the maximum undercoolings of Ti₅₀Al₄₅Nb₅ and Ti₄₅Al₄₅Nb₁₀ alloys are 268 K (0.146T_L) and 287 K (0.15T_L), respectively. The specific heat of liquid Ti₄₅Al₄₅Nb₁₀ alloy is determined to be 32.72 J·mol⁻¹·K⁻¹ over a broad temperature range of 1578–2010K. The surface tension of Ti-Al-Ni

alloys decreases linearly with the increase of temperature. For Ni-based multicomponent alloys, the maximum undercoolings of Ni₉₀Cu₅Fe₅, Ni₈₀Cu₁₀Fe₁₀, Ni₈₅Cu₅Fe₅Sn₅, Ni₈₀Cu₅Fe₅Sn₅Ge₅, and Ni₇₅Cu₅Fe₅Co₅Sn₅Ge₅ alloys are 272 K (0.15T_L), 252 K (0.15T_L), 349 K (0.21T_L), 363 K (0.22T_L), and 363 K (0.22T_L), respectively. The specific heats of Ni₈₀Cu₁₀Fe₁₀ and Ni₇₅Cu₅Fe₅Co₅Sn₅Ge₅ alloys are measured to be 41.67 and 41.49 J·mol⁻¹·K⁻¹, respectively. The surface tension of Ni₉₀Cu₅Fe₅, Ni₈₅Cu₅Fe₅Sn₅, and Ni₈₀Cu₅Fe₅Sn₅Ge₅ alloys are determined as 1.799, 1.546 and 1.357 N/m at their liquidus temperatures, and with their temperature coefficients to be -4.972×10^{-4} , -5.057×10^{-4} , and -5.385×10^{-4} N·m⁻¹·K⁻¹, respectively. Based on these directly measured values, other thermophysical parameters such as viscosity and diffusion coefficient can also be derived.

Computer simulation is an efficient way to investigate the structure and thermodynamical properties of undercooled liquid metals and alloys at atomic scale. Wei and coworkers carried out an extensive Molecular Dynamics (MD) simulation on the structures and thermophysical properties of undercooled liquid Ni, Fe, Cu, Co, Ti, Pd, Pt, Ag, Au and Rh pure metals^[19], and Fe-Cu binary^[20] and Ni-Cu-Fe ternary^[21] systems. The densities, specific heats, and atomic order parameters were obtained and analyzed for these metals and alloys by MD simulation, and some results were compared with the measured data or existing theories, which shows reasonable consistency. As a complementary study, the structure, elastic and thermodynamic properties of crystalline alloys and compounds were conducted by a First-principle calculation^[22]. Differential Scanning Calorimetry (DSC) and laser flash method were also employed to determine the enthalpy of fusion, undercoolibility and thermal diffusivity of the multicomponent alloys^[23].

3 Rapid Solidification Kinetics and New Materials Development

Dendrites and eutectics are the two elementary growth patterns in solidification. Rapid dendritic growth kinetics of undercooled liquid alloys was quantitatively studied by Wei and coworkers with the help of electromagnetic levitation and glass fluxing methods. The dendrite growth velocities of γ -Fe, α -Ni, and Ni₃Sn phases were measured in undercooled Fe-based and Ni-based alloys. Generally, the growth velocity varies with the increase of undercooling according to a power or exponential

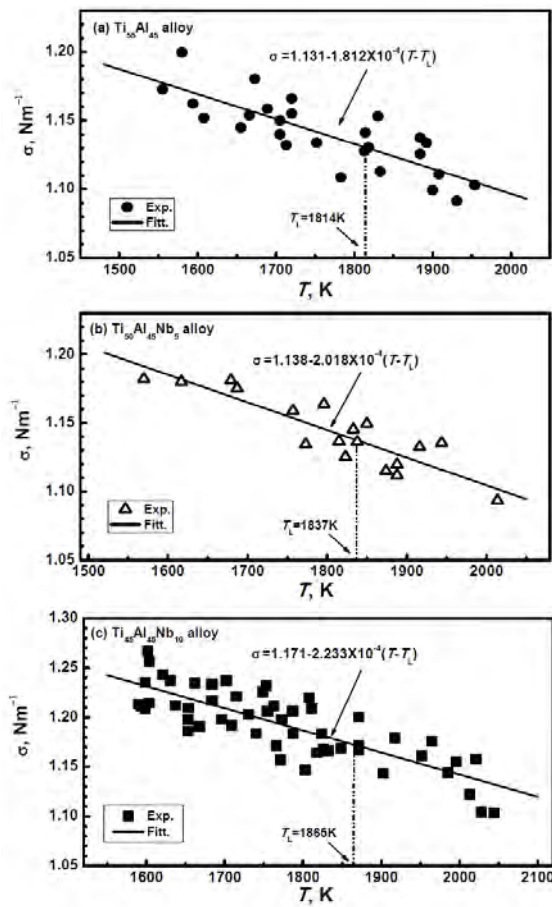


Fig. 2 Surface tension of liquid Ti-Al and Ti-Al-Nb alloys versus temperature:

(a) $\text{Ti}_{55}\text{Al}_{45}$ alloy, (b) $\text{Ti}_{50}\text{Al}_{45}\text{Nb}_5$ alloy, and (c) $\text{Ti}_{45}\text{Al}_{45}\text{Nb}_{10}$ alloy^[16].

law. The measured maximum velocities of γ -Fe dendrite attains 15 and 30.4 m/s in $\text{Fe}_{50}\text{Cu}_{50}$ ^[24] and $\text{Fe}_{62.5}\text{Cu}_{27.5}\text{Sn}_{10}$ ^[25] alloys, respectively. The dendritic growth velocity of undercooled pure Fe was also determined as a reference, which reaches 69 $\text{m}\cdot\text{s}^{-1}$ ^[24]. The growth velocity of α -Ni phase in undercooled liquid $\text{Ni}_{90}\text{Cu}_5\text{Mo}_5$ ^[26] and $\text{Ni}_{85}\text{Cu}_5\text{Mo}_5\text{Ge}_5$ ^[27] alloys approached 32 and 28 m/s, respectively. The Ni_3Sn compound grows dendritically like a solid solution phase with a nonfaceted manner in $\text{Ni}_{66}\text{Sn}_{31.7}\text{Ge}_{2.5}$ alloy^[28] and the maximum velocity was measured to be only 0.38 m/s. At high undercoolings, a morphological transition usually takes place from well-developed dendrites to equiaxed grains, and the rapid growth velocity leads to a significant solute trapping. Rapid eutectic growth in Ni-Sn^[29], Al-Ge^[30], and Al-Cu-Si^[31] systems was investigated under acoustic levitation and free fall conditions. It was found that a lamellar eutectic to anomalous eutectic transition usually takes place if the undercooling is large enough.

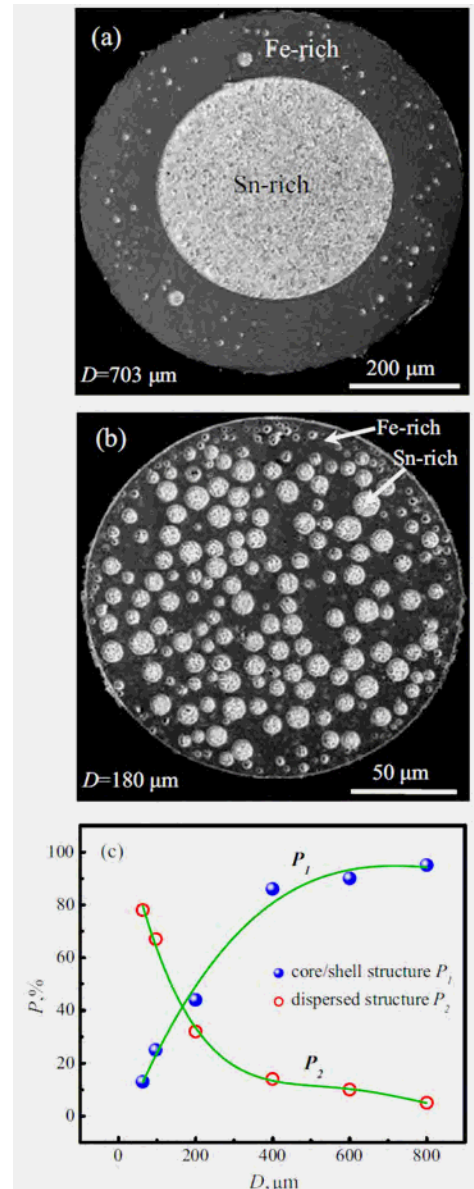


Fig. 3 Two typical microstructures of ternary $\text{Fe}_{62}\text{Sn}_{34}\text{Ge}_4$ immiscible alloy droplets solidified inside drop tube: (a) two-layer core/shell microstructure at $D=703\ \mu\text{m}$, (b) dispersed microstructure at $D=180\ \mu\text{m}$, and (c) the formation probabilities of core/shell and dispersed microstructures versus alloy droplet diameter^[36].

Peritectic and monotectic solidification processes are sensitive to undercooling and often exhibits immiscibility, which is a great challenge for the fabrication of homogeneously dispersed materials. Wei and his group performed extensive exploration on the undercooling, phase separation and microstructural characterization of these two kinds of solidification by means of drop tube, glass fluxing, and acoustic levitation. Peritectic phase forms via peritectic transformations in most cases. Once

the undercooling exceeds a critical value, the peritectic phase grows directly from the undercooled liquid by suppressing the primary phase nucleation and peritectic transformation. This has been demonstrated experimentally in Cu-Sn system^[32]. The ternary Fe-Cu-Sn^[25], Fe-Cu-Si^[33], and Co-Cu-Ni^[34] alloys possess a metastable immiscibility gap. If the alloy melts were undercooled into this gap, liquid phase separation is possible to become the dominant solidification mechanism, and a morphological transition from dendrites to macrosegregation was observed in the solidified microstructures. During the free fall of Fe-Sn-Si^[35], Fe-Sn-Ge^[36] and Co-Cu-Pb^[37] ternary alloy droplets, core-shell structures of two or three layers were frequently formed after solidification owing to the liquid phase separation and the reduced gravity. But for sufficiently small droplets, the macrosegregation can be suppressed so as to form a homogeneously dispersed microstructure. The phase separation of Al-Cu-Sn alloy^[38] under acoustic levitation condition shows a laterally-layered macro-segregation which is much special as compared to the vertically-layered pattern under normal condition.

In addition, the dynamic solidification of binary and ternary alloys was also carried out with the introduction of ultrasonic vibration. The published experimental results of Wei's group include the eutectic growth of Sn-Pb^[39] and Ag-Cu-Ge alloys^[40], peritectic solidification of Sb-Sn^[41] and Cu-Sn alloys^[42], and monotectic solidification of Al-Cu-Sn alloy^[43]. Generally, the ultrasound stimulates nucleation and hinders the bulk undercooling. For most of the tested alloys, the primary phases were remarkably refined by the ultrasound, and the faceted phases have a tendency to grow in a non-faceted manner at high ultrasonic energy. Spherical eutectic cells of (Sn) + (Pb) and spherical monotectic cells of (Al) + (Sn) + θ (Al₂Cu) formed in ultrasonic field and the volume fraction increases with the ultrasound power. Strong ultrasound facilitates or even completes the peritectic transformation ($L + \varepsilon \rightarrow \eta$) in Cu₃₀Sn₇₀ alloy which occurs only to a very limited extent under static condition.

References

- [1] L. Hu, H.P. Wang, W.J. Xie, B. Wei. Electrostatic levitation under the single-axis feedback control condition. *Science China-Physics Mechanics & Astronomy*, 2010, 53: 1438-1444
- [2] L. Hu, H.P. Wang, L.H. Li, B. Wei. Geometric optimization of electrostatic fields for stable levitation of metallic materials. *Science China-Technological Sciences*, 2013, 56: 53-59
- [3] L. Hu, H.P. Wang, L.H. Li, B. Wei. Electrostatic Levitation of Plant Seeds and Flower Buds. *Chinese Physics Letters*, 2012, 29: 064101
- [4] L.H. Li, L. Hu, S.J. Yang, W.L. Wang, B. Wei. Thermodynamic properties and solidification kinetics of intermetallic Ni₇Zr₂ alloy investigated by electrostatic levitation technique and theoretical calculations. *Journal of Applied Physics*, 2016, 119:035902
- [5] L. Hu, L.H. Li, S.J. Yang, B. Wei. Thermophysical properties and eutectic growth of electrostatically levitated and substantially undercooled liquid Zr_{91.2}Si_{8.8} alloy. *Chemical Physics Letters*, 2015, 621: 91-95
- [6] Z.Y. Hong, W.J. Xie, B. Wei. Acoustic levitation with self-adaptive flexible reflectors. *Review of Scientific Instruments*, 2011, 82: 074904
- [7] Z.Y. Hong, W.J. Xie, B. Wei. Vibration Characteristics of Acoustically Levitated Object with Rigid and Elastic Reflectors. *Chinese Physics Letters*, 2010, 27: 014301
- [8] D.L. Geng, W.J. Xie, N. Yan, B. Wei. Surface waves on floating liquids induced by ultrasound field. *Applied Physics Letters*, 2013, 102: 041604
- [9] D.L. Geng, W.J. Xie, N. Yan, B. Wei. Vertical vibration and shape oscillation of acoustically levitated water drops. *Applied Physics Letters*, 2014, 105: 104101
- [10] C.L. Shen, W.J. Xie, B. Wei. Parametrically excited sectorial oscillation of liquid drops floating in ultrasound. *Physical Review*, 2010, E 81: 046305
- [11] C.L. Shen, W.J. Xie, Z.L. Yan, B. Wei. Internal flow of acoustically levitated drops undergoing sectorial oscillations. *Physics Letters A*, 2010, 374: 4045-4048
- [12] Z.L. Yan, W.J. Xie, B. Wei. Vortex flow in acoustically levitated drops. *Physics Letters A*, 2011, 375: 3306-3309
- [13] K. Zhou, H.P. Wang, B. Wei. Determining thermophysical properties of undercooled liquid Ti-Al alloy by electromagnetic levitation. *Chemical Physics Letters*, 2012, 521: 52-54
- [14] K. Zhou, H.P. Wang, J. Chang, B. Wei. Specific heat measurement of stable and metastable liquid Ti-Al alloys. *Applied Physics A-Materials Science & Processing*, 2011, 103: 135-137
- [15] K. Zhou, H.P. Wang, B. Wei. Thermophysical properties of substantially undercooled liquid Ti-Al-Nb ternary alloy measured by electromagnetic levitation. *Philosophical Magazine Letters*, 2013, 93: 138-141
- [16] K. Zhou, H.P. Wang, J. Chang, B. Wei. Surface tension measurement of metastable liquid Ti-Al-Nb alloys. *Applied Physics A-Materials Science & Processing*, 2011, 105: 211-214
- [17] J. Chang, H.P. Wang, K. Zhou, B. Wei. Surface tension measurement of undercooled liquid Ni-based multicomponent alloys. *Philosophical Magazine Letters*, 2012, 92: 428-435
- [18] J. Chang, H.P. Wang, K. Zhou, B. Wei. Thermophysical properties and rapid solidification of an undercooled liquid hexabasic Ni-based alloy. *Philosophical Magazine Letters*, 2013, 93:254-263
- [19] H.P. Wang, S.J. Yang, B. Wei. Molecular dynamics prediction of density for metastable liquid noble metals. *Chemical Physics Letters*, 2012, 539: 30-34
- [20] H.P. Wang, B. Wei. Positive excess volume of liquid Fe-Cu alloys resulting from liquid structure change. *Physics Letters A*, 2010, 374: 4787-4792
- [21] H.P. Wang, J. Chang, B. Wei. Density and related thermophysical

- properties of metastable liquid Ni-Cu-Fe ternary alloys. *Physics Letters A*, 2010, 374: 2489-2493
- [22] L.H. Li, W.L. Wang, L. Hu, B. Wei. First-principle calculations of structural, elastic and thermodynamic properties of Fe-B compounds. *Intermetallics*, 2014, 46: 211-221
- [23] W. Zhai, K. Zhou, L. Hu, B. Wei. Determination of the enthalpy of fusion and thermal diffusivity for ternary $\text{Cu}_{60-x}\text{Sn}_x\text{Sb}_{40}$ alloys. *Journal of Chemical Thermodynamics*, 2016, 95: 159-163
- [24] S.B. Luo, W.L. Wang, J. Chang, Z.C. Xia, B. Wei. A comparative study of dendritic growth within undercooled liquid pure Fe and $\text{Fe}_{50}\text{Cu}_{50}$ alloy. *Acta Materialia*, 2014, 69: 355-364
- [25] Z.C. Xia, W.L. Wang, S.B. Luo, B. Wei. Liquid phase separation and rapid dendritic growth of highly undercooled ternary $\text{Fe}_{62.5}\text{Cu}_{27.5}\text{Sn}_{10}$ alloy. *Journal of Applied Physics*, 2015, 117: 054901
- [26] J. Chang, H.P. Wang, K. Zhou, B. Wei. Rapid dendritic growth and solute trapping within undercooled ternary Ni-5%Cu-5%Mo alloy. *Applied Physics A-Materials Science & Processing*, 2012, 109: 139-143
- [27] J. Chang, H.P. Wang, B. Wei. Rapid Solidification Characteristics of Highly Undercooled Liquid Ni-Cu-Mo-Ge Quaternary Alloy under Electromagnetic Levitation Condition. in: Wu Y, Deng W, (Eds.). *Proceedings of the AASRI International Conference on Industrial Electronics and Applications*, 2015, 2: 22-25
- [28] W.L. Wang, H.Y. Qin, Z.C. Xia, B. Wei. Primary dendrite growth of Ni₃Sn intermetallic compound during rapid solidification of undercooled Ni-Sn-Ge alloy. *Chinese Science Bulletin*, 2012, 57: 1073-1077
- [29] D.L. Geng, W.J. Xie, B. Wei. Containerless solidification of acoustically levitated Ni-Sn eutectic alloy. *Applied Physics A-Materials Science & Processing*, 2012, 109: 239-244
- [30] N. Yan, D.L. Geng, Z.Y. Hong, B. Wei. Ultrasonic levitation processing and rapid eutectic solidification of liquid Al-Ge alloys. *Journal of Alloys and Compounds*, 2014, 607: 258-263
- [31] N. Yan, D.L. Geng, Z.Y. Hong, B. Wei. Rapid solidification of acoustically levitated Al-Cu-Si eutectic alloy under laser irradiation. *Chinese Science Bulletin*, 2011, 56: 912-918
- [32] W. Zhai, B.B. Wei. Direct nucleation and growth of peritectic phase induced by substantial undercooling condition. *Materials Letters*, 2013, 108: 145-148
- [33] S.B. Luo, W.L. Wang, Z.C. Xia, Y.H. Wu, B. Wei. Solute redistribution during phase separation of ternary Fe-Cu-Si alloy. *Applied Physics A-Materials Science & Processing*, 2015, 119: 1003-1011
- [34] D.Y. Zang, H.P. Wang, F.P. Dai, D. Langevin, B. Wei. Solidification mechanism transition of liquid Co-Cu-Ni ternary alloy. *Applied Physics A-Materials Science & Processing*, 2011, 102: 141-145
- [35] W.L. Wang, Z.Q. Li, B. Wei. Macrosegregation pattern and microstructure feature of ternary Fe-Sn-Si immiscible alloy solidified under free fall condition. *Acta Materialia*, 2011, 59: 5482-5493
- [36] Y.H. Wu, W.L. Wang, Z.C. Xia, B. Wei. Phase separation and microstructure evolution of ternary Fe-Sn-Ge immiscible alloy under microgravity condition. *Computational Materials Science*, 2015, 103: 179-188
- [37] N. Yan, W.L. Wang, S.B. Luo, L. Hu, B. Wei. Correlated process of phase separation and microstructure evolution of ternary Co-Cu-Pb alloy. *Applied Physics A-Materials Science & Processing*, 2013, 113: 763-770
- [38] N. Yan, Z.Y. Hong, D.L. Geng, W.L. Wang, B. Wei. Phase separation and structure evolution of ternary Al-Cu-Sn immiscible alloy under ultrasonic levitation condition. *Journal of Alloys and Compounds*, 2012, 544: 6-12
- [39] W. Zhai, Z.Y. Hong, W.J. Xie, B. Wei. Dynamic solidification of Sn-38.1% Pb eutectic alloy within ultrasonic field. *Chinese Science Bulletin*, 2011, 56: 89-95
- [40] W. Zhai, X.Y. Lu, B. Wei. Microstructural evolution of ternary $\text{Ag}_{33}\text{Cu}_{42}\text{Ge}_{25}$ eutectic alloy inside ultrasonic field. *Progress in Natural Science-Materials International*, 2014, 24: 642-648
- [41] W. Zhai, B.B. Wei. Peritectic solidification characteristics of Sb-Sn alloy under ultrasonic vibration. *Materials Letters*, 2015, 138: 1-4
- [42] W. Zhai, Z.Y. Hong, X.L. Wen, D.L. Geng, B. Wei. Microstructural characteristics and mechanical properties of peritectic Cu-Sn alloy solidified within ultrasonic field. *Materials & Design*, 2015, 72: 43-50
- [43] W. Zhai, H.M. Liu, B. Wei. Liquid phase separation and monotectic structure evolution of ternary $\text{Al}_{62.6}\text{Sn}_{28.5}\text{Cu}_{8.9}$ immiscible alloy within ultrasonic field. *Materials Letters*, 2015, 141: 221-224

B Microgravity Material Research Activities in IMR in the Past Two Years

Nickel-base single crystal superalloys are susceptible to various solidification defects in preparation, which are detrimental to properties. Investigations show that gravity plays an important role in alloy solidification process and defect formation. However, it is difficult to reveal the gravity effects and study the mechanisms through traditional ground-based solidification experiments. Under microgravity conditions, the effects of gravity on solidification process can be neglected. Therefore, under the financial support of the National Natural Science Foundation of China (No. 51171196), using the microgravity environment produced by a 50m long drop tube, the dendritic morphologies, characteristics sizes and solute distribution formed under normal gravity and microgravity of binary to quinary Nickel-base single crystal alloys with different contents of W, Ta, Al and Ti elements were comparatively investigated. Besides, Al-Cu alloys and DZ483 nickel-base superalloys were also investigated to explore the effect of microgravity on equiaxial dendrites and the influence of solidification segregation on liquid densities in mushy zone.

The results indicate that:

Under microgravity condition, the primary dendrite arm spacing of Ni-4.9%Al, Ni-9.6%W and Ni-5.9%Ta binary alloys were all increased, and the macrosegregation of the three alloys were more significant. Under normal gravity condition, apparent macrosegregation of solute elements were observed in the three alloys, while,

no such tendency could be found under microgravity condition.

Under microgravity condition, the dendrites of Ni-5%Al-8%W, Ni-5%Al-6%Ta, Ni-5%Al-8%W-4%Ti and Ni-5%Al-8%W-4%Ti-3%Ta alloys are more developed, the primary dendrite arm spacing were increased, the secondary arms were longer, and developed tertiary dendrites appeared.

Under microgravity condition, the secondary dendrite arm spacing of Ni-5%Al-8%W and Ni-5%Al-8%Ta were decreased, while those of Ni-5%Al-8%W-4%Ti and Ni-5%Al-8%W-4%Ti-3%Ta were increased.

Under normal gravity condition, along upward growth direction in ternary to quinary alloys, Al contents in primary dendrite arm had tendency to increase, W and Ti contents had tendency to decrease; while under microgravity condition, the change tendency of the three elements were not apparent. No obvious influence of gravity level on Ta content in dendrite arms could be found.

The addition of Ta or Ti into alloys significantly accelerated their solidification processes under normal gravity condition, and increased the difference between the primary dendrite arm spacing formed under the two gravity conditions.

Compared with under normal gravity condition, except the microsegregation of Al was always weaker, those of the other elements could be either stronger or weaker in ternary to quinary alloys under microgravity condition. The addition of Ti into alloys was beneficial to weaken the microsegregation of Al and W, and the addition of Ta into alloys was beneficial to weaken the microsegregation of W, while the segregation of Ti and Ta themselves did not appear to be much different between the two gravity levels.

Research on Al-Cu alloys indicates that the primary and secondary dendrite arm spacing became smaller, and microsegregation became weaker under microgravity condition. Due to smaller density of primary equiaxed dendrites, they floated above the top of epitaxially growing columnar dendrites under the effect of gravity. Under microgravity however, because there was no buoyancy convection, some of the equiaxed dendrites were engulfed by epitaxially growing columnar dendrites. Besides, gravity environment was evidently more conducive to the growth of equiaxed dendrites, and promoted coarsening of equiaxed dendrites and interdendritic eutectic.

Research on mushy zone density of DZ483 alloy indicates that due to different segregation behavior of various alloy elements and precipitation of MC carbides, especially the strong segregation of Ta and Ti in-between dendrites and W in dendrites, the density of liquid in mushy zone inverted. This will arouse thermosolutal convection under the effect of gravity, and make freckles easier to form. MC carbides precipitate at temperature slightly below the liquidus can retard the quick reduce of liquid density to a certain extent, this supplies an idea to control the precipitation of MC carbides by adjusting C content in alloy so that to avoid the occurrence of freckles.

To summarize the above results, the conclusions can be drawn as follows:

1. Microgravity environment can enlarge or shrink dendrite arm spacing, and can weaken or enhance microsegregation, depending on the density, content, redistribution behavior of solute elements. Various elements work together, change the density of melt in front of liquid/solid interface, and therefore, change local concentration distribution, which alter the growth speed, solute transportation and supercooling degree there, resulting in the change of dendrite structure, interdendritic structure, precipitate morphology and amount.

2. Buoyancy convection does not always increase effective diffusion coefficient, it may also decrease effective diffusion coefficient, especially in area among dendrites, which is related with local solute concentration and probably radial temperature gradient.

3. Due to lighter or heavier respectively, Al and W initiate buoyancy convection and result in macrosegregation. However, no such tendency are observed aroused by Ti and Ta. This may be because they speed up solidification process under normal gravity. Therefore, Al and W are apt to produce channel effect, but Ti and Ta can decrease their segregation.

4. Under normal gravity, once equiaxed dendrites formed, they will rise above and are repelled by upward growing columnar dendrites if they are lighter; While, they will be engulfed by upward growing columnar dendrites and form stray grains if they are heavier.

5. Density inversion occurs in mushy zone because of solute segregation, which may produce thermo-solutal convection under gravity, and therefore make freckles easier to form. Precipitation of carbides at the temperature slightly below liquidus may suppress the rapid de-

crease of melt density, which could be applied to avoid the occurrence of freckle.

Besides the above works, under the support of the manned space flight project (No. TGJZ80701-2-RW018), by using the microgravity environment in space, and combining with ground-based comparison experiments, the dendritic morphologies, characteristics sizes as well as solute segregation and defect formation under normal gravity and microgravity of an AlCuMgZn single crystal alloy are planning to comparatively investigated during Tiangong II mission. The aim of this work is also to explore the role of gravity in dendrite growth process and solute segregation as well as solidification defect formation. At the present, almost all the ground-based preparation tests and examinations, such as sample and ampoule design, process experiment and optimization, matching experiment together with the multifunctional space material experiment device and mechanical environmental test, etc., have been finished. It is planned that Tiangong II space laboratory will be launched later in 2016. During its flight, an AlCuMgZn single crystal sample encapsulated in quartz ampoule will conduct directional solidification in the multifunctional space material experiment device boarded on it, meanwhile, same experiment under equivalent conditions on the ground will be performed as well to supply a reference object. After the space experiment is finished and the sample is recovered, the samples experimented both in space and on the ground will be comparatively analyzed to get the results.

C Solidification and Crystal Growth in Space: Materials Science Program in the SJ10-Recoverable Scientific Experiment Satellite

The virtual absence of gravity-dependent phenomena in microgravity allows an in-depth understanding of fundamental events that are normally obscured and therefore are difficult to study quantitatively on earth^[1-2]. Particular interest is that the low-gravity environment aboard spacecraft provides a unique platform to synthesize alloys of semiconductors and metals with homogeneous composition distributions, on both the macroscopic and microscopic scales, due to the much reduced buoyancy-driven convection^[1]. Moreover, the easy realization of detached solidification in microgravity suppresses the formation of defects such as dislocations and twins, and thereby the crystallographic perfection is

greatly increased^[3-4].

Motivated by these facts, the materials science program in the SJ-10 recoverable scientific experiment satellite mainly focuses on the following issues: i) the growth of large-size semiconductor crystals with uniform composition and low defect density, and high quality metal alloys or composites that cannot be obtained from ground; (ii) understanding how the gravity-driven phenomena affect the crystal growth, and elucidating the site occupation of doping atoms, revealing the liquid/solid interfacial structures, as well as clarifying the microstructure evolution of the metal alloys (or composites) during the solidification process. We hope our program not only provides new sights into the crystal growth mechanism, but also guides the terrestrial crystal preparations.

The materials science program in the SJ-10 recoverable satellite, which is led by Prof. X. W. Zhang from the Institute of Semiconductors, Chinese Academy of Sciences, includes 8 experimental tasks: 1) space growth of GaMnSb diluted magnetic semiconductors, 2) space synthesis and characterization of high-performance thermoelectric semiconductors, 3) new generation of infrared semiconductors grown in space, 4) space growth, numerical simulation and characterization of InGaSb ternary photoelectric crystals, 5) space solidification and defect control of the super alloy single crystals, 6) interfacial phenomena during the melting of the tin-based alloys, 7) synthesis of metal matrix composites by self-propagating reaction under microgravity environment, and 8) the wettability of molten metal and preparation of metal matrix composites in space^[5]. The series of scientific experiments will be carried out successively in the same multiple materials processing furnace with precise controls on the ampoule moving speed and the temperature gradient, and as a result the total load mass can be considerably reduced.

The scientific ampoules have been designed and fabricated under strict quality control procedures. In order to verify their high-safeties, multiple rounds of mechanical tests have been performed under the simulated conditions. Moreover, a large number of terrestrial crystal growth experiments have been carried out using the multiple materials processing furnace to achieve the optimal growth parameters (see, for instance, Fig. 4). Now the materials science program in the SJ-10 recoverable satellite enters the critical stage and the final preparations are under way to ensure the success of our experiments.

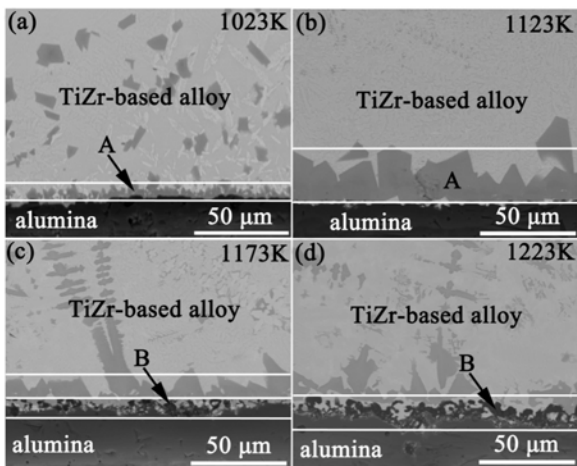


Fig. 4 SEM images at the interfaces of the $\text{Ti}_{32.8}\text{Zr}_{30.2}\text{Ni}_{5.3}\text{Cu}_9\text{Be}_{22.7}/\text{Al}_2\text{O}_3$ system synthesized at 1023 K (a), 1123 K (b), 1173K (c) and 1223 K (d) with saturation time of 60 minutes.

Reference

- [1] V. I. Strelov, I. P. Kuranova, B. G. Zakharov, A. E. Voloshin. Crystallization in Space: Results and Prospects. *Crystallogr.* 2014, 59:781
- [2] N. F. Chen, X. R. Zhong, L. Y. Lin, M. Zhang, Y. S. Wang, X. W. Bai, J. Zhao. Comparison of field effect transistor characteristics between space-grown and earth-grown gallium arsenide single crystal substrates. *Appl. Phys. Lett.* 2001, 78: 478
- [3] T. Duffar, P. Dusserre, F. Picca, S. Lacroix, N. Giacometti. Bridgman growth without crucible contact using the dewetting Phenomenon. *J. Cryst. Growth*, 2000, 211: 434
- [4] D. M. Herlach, R. F. Cochrane, I. Egry, H. J. Fecht, A. L. Greer. Containerless processing in the study of metallic melts and their solidification, *Int. Mater. Rev.*, 1993, 38:273
- [5] W. R. Hu, J. F. Zhao, M. Long, X. W. Zhang, Q. S. Liu, M. Y. Hou, Q. Kang, Y. R. Wang, S. H. Xu, W. J. Kong, H. Zhang, S. F. Wang, Y. Q. Sun, H. Y. Hang, Y. P. Huang, W. M. Cai, Y. Zhao, J. W. Dai, H. Q. Zheng, E. K. Duan, J. F. Wang. Space program SJ-10 of microgravity research. *Microgravity Sci. Tec.*, 2014, 26, 159

The background of the entire page is a stylized illustration of three satellites in orbit around the Earth. The Earth is shown as a glowing blue and green sphere. The satellites are depicted with solar panels and various instruments, orbiting in elliptical paths. The overall color scheme is dark blue and green, with white text on semi-transparent grey boxes.

Chief Editor XIANGLI Bin

Deputy Chief Editor WU Ji

Responsible Editor LI Lei

Editorial Staffs SONG Yana
SUN weiyong
LI Li

Secretariat Contact

LI Xiaoyu, XU Yongjian

CNCOSPAR Secretariat

Tel: 86 10 6258 6404

Fax: 86 10 6263 2257

E-mail: xuyongjian@nssc.ac.cn